Modelling the Anaestheto-Dynamic Phase Transition of the Cerebral Cortex

A thesis submitted
for the degree of
Doctor of Philosophy
in Physics
by

David Alistair Steyn-Ross

The
University
of Waikato
*Te Whare Wānanga
o Waikato*

January 2002
The University of Waikato

Abstract

This thesis examines a stochastic model for the electrical behaviour of the cerebral cortex under the influence of a general anaesthetic agent. The modelling element is the macrocolumn, an organized assembly of $\sim 10^5$ cooperating neurons (85% excitatory, 15% inhibitory) within a small cylindrical volume (~ 1 mm^3) of the cortex. The state variables are h_e and h_i, the mean-field average soma voltages for the populations of excitatory (e) and inhibitory (i) neurons comprising the macrocolumn. The random fluctuations of h_e about its steady-state value are taken as the source of the scalp-measured EEG signal. The randomness enters by way of four independent white-noise inputs representing fluctuations in the four types (e-e, i-e, e-i, i-i) of subcortical activity.

Our model is a spatial and temporal simplification of the original set of eight coupled partial differential equations (PDEs) due to Liley *et al.* [Neurocomputing **26-27**, 795 (1999)] describing the electrical rhythms of the cortex. We assume (i) spatial homogeneity (i.e., the entire cortex can be represented by a single macrocolumn), and (ii) a separation of temporal scales in which all inputs to the soma "capacitor" are treated as fast variables that settle to steady state very much more rapidly than do the soma voltages themselves: this is the "adiabatic approximation." These simplifications permit the eight-equation Liley set to be collapsed to a single pair of first-order PDEs in h_e and h_i. We incorporate the effect of general anaesthetic as a *lengthening* of the duration of the *inhibitory* post-synaptic potential (PSP) (i.e., we are modelling the GABAergic class of anaesthetics), thus the effectiveness of the inhibitory firings increases monotonically with anaesthetic concentration.

These simplified equations of motion for $h_{e,i}$ are transformed into Langevin (stochastic) equations by adding small white-noise fluctuations to each of the four subcortical spike-rate averages. In order to anchor the analysis, I first identify the $t \to \infty$ steady-state values for the soma voltages. This is done by turning off all noise sources and setting the dh_e/dt and dh_i/dt time derivatives to zero, then numerically locating the steady-state coordinates as a function of anaesthetic effect λ, the scale-factor for the lengthening of the inhibitory PSP. We find that, when plotted as a function of λ, the steady-state soma voltages map out a reverse-S trajectory consisting of a pair of stable branches—the upper (active, high-firing) branch, and the lower (quiescent, low-firing) branch—joined by an unstable mid-branch. Because the two stable phases are not contiguous, the model predicts that a transit from one phase to the other must be first-order discontinuous in soma voltage, and that the downward (induction) jump from active-awareness to unconscious-quiescence will be hysteretically separated from (i.e., will occur at a larger concentration of anaesthetic than) the upward (emergence) jump for the return of consciousness.

By reenabling the noise terms, then linearizing the Langevin equations about one of the stable steady states, we obtain a two-dimensional Ornstein–Uhlenbeck (Brownian motion) system which can be analyzed using standard results from stochastic calculus. Accordingly, we calculate the covariance, time-correlation, and spectral matrices, and find the interesting predictions of vastly increased EEG fluctuation power, attended by simultaneous redistribution of spectral energy towards low frequencies with divergent increases in fluctuation correlation times (i.e., critical slowing down), as the macrocolumn transition points are approached. These predictions are qualitatively confirmed by clinical measurements reported by Kuizenga *et al.* [British Journal of Anaesthesia **80**, 725 (1998)] of the so-called EEG biphasic effect. He used a slew-rate technique known as aperiodic analysis, and I demonstrate that this is approximately equivalent to a frequency-scaling of the power spectral density.

Changes in the frequency distribution of spectral energy can be quantified using the notion of spectral entropy, a modern measure of spectral "whiteness." We compare the spectral entropy predicted by the model against the clinical values reported recently by Viertiö-Oja *et al.* [Journal of Clinical Monitoring **16**, 60 (2000)], and find excellent qualitative agreement for the induction of anaesthesia.

To the best of my knowledge, the link between spectral entropy and correlation time has not previously been reported. For the special case of Lorentzian spectrum (arising from a 1-D OU process), I prove that spectral entropy is proportional to the negative logarithm of the correlation time, and uncover the formula which relates the discrete H_1 Shannon information to the continuous H_2 "histogram entropy," giving an unbiased estimate of the underlying continuous spectral entropy H_ω. The inverse entropy–correlation relationship suggests that, to the extent that anaesthetic induction can be modelled as a 1-D OU process, cortical state can be assessed either in the time domain via correlation time or, equivalently, in the frequency domain via spectral entropy.

In order to investigate a thermodynamic analogy for the anaesthetic-driven ("anaesthetodynamic") phase transition of the cortex, we use the steady-state trajectories as an effective equation of state to uncouple the macrocolumn into a pair of (apparently) independent "pseudocolumns." The stable steady states may now be pictured as local minima in a landscape of potential hills and valleys. After identifying a plausible temperature analogy, we compute the analogous entropy and predict discontinous entropy change—with attendant "heat capacity" anomalies—at transition. The Stullken dog experiments [Stullken *et al.*, Anesthesiology **46**, 28 (1977)], measuring cerebral metabolic rate changes, seem to confirm these model predictions.

The penultimate chapter examines the impact of incorporating NMDA, an important *excitatory* neurotransmitter, in the adiabatic model. This work predicts the existence of a new stable state for the cortex, midway between normal activity and quiescence. An induction attempt using a pure anti-NMDA anaesthetic agent (e.g., xenon or nitrous oxide) will take the patient to this mid-state, but no further. I find that for an NMDA-enabled macrocolumn, a GABA induction can produce a *second* biphasic power event, depending on the brain state at commencement. The latest clinical report from Kuizenga *et al.* [British Journal of Anaesthesia **86**, 354 (2001)] provides apparent confirmation.

Preface

A Brief History

In December 1997, Dr Jamie Sleigh, a senior anaesthetist at Waikato Hospital (who had been putting people to sleep for years), presented Waikato University theoretical physicist Dr Moira Steyn-Ross with an interesting challenge. It had become increasingly apparent to Dr Sleigh that conscious-awareness and anaesthetic-induced unconsciousness are completely disjoint mental states which do not grade smoothly from one to the other as anaesthetic concentration is increased. Rather, it is as if, at a critical level of anaesthetic concentration, a switch is flipped and the patient's brain makes a sudden, dramatic (and fortunately reversible!) change of phase to its unaware state. Hence Dr Sleigh's formidable challenge: Could Dr M. Steyn-Ross please craft a set of equations which would model the patient response to anaesthetic as if it were a thermodynamic phase change?

Serendipitously, Dr Steyn-Ross and I learned that Dr David Liley, a biophysicist from Swinburne University of Technology, Melbourne, Australia, would be visiting his parents in Hamilton the following month. So I arranged that the four of us (J. Sleigh, M. Steyn-Ross, D. Liley, A. Steyn-Ross) should meet, and that January gathering marked the start of a vigorous and productive collaboration. We soon learned that Dr Liley had strong views about which cortical model should be used—namely: his one! Having promptly settled that matter, discussion then turned to how the Liley model could be modified to incorporate the effect of a GABAergic induction agent such as the anaesthetic propofol which was known to lengthen the opening times of the chloride ion channel controlled by the GABA_A receptor. It was decided that we could model this drug-induced change as a *lengthening* of the inhibitory neuron's postsynaptic impulse response, with the degree of prolongation to be proportional to drug concentration.

While the Liley cortical mean-field equations for the average neuron voltage have been carefully constructed to be neurophysiologically plausible, they are mathematically daunting: eight first- and second-order, nonlinear partial differential equations. Moira realized that the Liley equations could be "solved" if one were to make two bold and drastic simplifying assumptions. First, the averaged soma voltages are to evolve on time scales much *slower* than those of the invading inhibitory and excitatory impulses. Second: the cortex might be imagined as being spatially homogeneous. Then the eight equations become two—a pair of first-order ordinary differential equations in h_e and h_i, the population-average excitatory and inhibitory neuron voltages. These simplified cortical equations define what we call the "adiabatic model."

Moira's plan of attack was to determine the awake and anaesthetized steady states for the homogeneous "adiabatic" brain, and then, by incorporating subcortical white-noise perturbations to generate a pseudo EEG signal, calculate the theoretical spectrum for small fluctuations about those steady states using the tools of stochastic calculus. Her preliminary calculations had shown that there could be *three* stationary points for a given value of anaesthetic concentration, so, on the basis of her earlier work on optical bistability, she predicted that a detailed map of the cortical steady states would reveal the "cubic" S-bend signature of a classic first-order phase transition.

My contributions to the research began at this point. My first task was to locate numerically the accurate locus of steady states as a function of anaesthetic concentration, and to establish their stability with respect to small disturbances. The anticipated S-bend with *unstable mid-branch* emerged, and now the cortex could reside either on the top ("conscious") branch or the bottom ("unconscious") branch, and, at critical values of anaesthetic, would be forced to switch states. So far so good.

The next step was to calculate the pseudo-EEG fluctuation spectrum for the white-noise-forced adiabatic equations. Using the stochastic analysis techniques detailed in C. W. Gardiner's *Handbook of Stochastic Methods*, Moira derived equations for the EEG spectral variation with anaesthetic. I coded these, and plotted the predicted variation in fluctuation power. But we were both rather dismayed by my initial results—the model seemed to be telling us that the total fluctuation power *increases* as the point of induction is approached, completely contradicting our naive expectation that fluctuations would diminish as the inhibitory effects of anaesthetic started to "bite." However, when Jamie saw the results, he was delighted! He told us that it is well-known within the community of anaesthesiologists that EEG power shows a "biphasic" response to anaesthetic: low doses of general anaesthetic tend to produce an excited brain response; larger doses produce the expected suppressed response. The biphasic effect had been nicely demonstrated in a 1998 paper by Karel Kuizenga, an anaesthestist working in The Netherlands, so we contacted him, requesting access to some of his published results.

Our biphasic "discovery" was in October 1998. By December of the following year we had published our findings in *Physical Review E* in what we now refer to as "Paper 0" (Steyn-Ross *et al.*, 1999).[1] This was accompanied by an APS-sponsored *Focus* article "Freezing into Unconsciousness" published at the Americal Physical Society web site.[2] Shortly afterwards, we were contacted by Dr Hanna Viertiö–Oja from the Finland medical instrumentation company, Datex-Ohmeda. Hanna is part of a design team for a novel depth-of-anaesthesia monitor that utilizes EEG spectral entropy as an index for patient awareness. She felt that a phase-transition model might provide the essential theoretical foundation for the Datex-Ohmeda instrument. An invitation followed from Datex-Ohmeda for Moira to speak at the World Congress of Anaesthesiologists in Montreal, Canada in June 2000.

Moira wanted to develop a statistical mechanics formalism that would permit extraction of a cortical entropy and a cortical "heat capacity" from the model, but first we needed a

---

[1] "Theoretical EEG stationary spectrum for a white-noise-driven cortex: Evidence for a general anesthetic-induced phase transition," M. L. Steyn-Ross, D. A. Steyn-Ross, J. W. Sleigh, D. T. J. Liley, *Phys. Rev. E*, **60**, 7299–7311, 1999.

[2] The Americal Physical Society *Focus* story can be viewed at `http://focus.aps.org/v4/st30.html`

(non-thermal!) cortical "temperature." I investigated a range of inverse mappings between anaesthetic concentration and an analogous temperature that I called cortical *excitability*, Θ. Moira suggested using the locus of steady states as an effective equation of state, thereby decoupling the excitatory and inhibitory neural populations within the macrocolumn into a pair of "independent" *pseudocolumns*. That decoupling was crucial. It permitted the construction of free-energy hills and valleys (potential functions), thence the calculation of entropy and "heat" capacity changes with anaesthetic, and the prediction of a "heat" capacity anomaly (release of latent "heat") at the point of phase change. Jamie uncovered a significant paper published in 1977 by Stullken and colleagues that seems to confirm the notion that as the brain is "cooled" with anaesthetic, there exists a region intermediate between consciousness and unconsciousness in which cortical metabolic requirements decline precipitously. We can interpret this anomalous *non*-consumption of energy as signalling the *release* of latent energy as the brain transits from its disordered conscious state to its well-ordered unconscious state. Our thermodynamics analogy was written up in Paper 1 (Steyn-Ross *et al.*, 2001a)[3] which appeared in July 2001.

Meanwhile, our research group had been enlivened by the arrival of MSc student Ms Lara Wilcocks. Her research task was to run stochastic simulations of both the full Liley equations and the adiabatically simplified set. Her simulations confirmed the number and nature of the steady states I had calculated numerically from the adiabatic theory, and her simulation spectra were able to be brought into exact agreement with theory once I'd established the precise scale factors that need to be applied to the discrete Fourier tranform process. (It seems that these scale factors are normally ignored, since I found no mention of them in the standard signal processing texts.) For me, the most satisfying aspect of Lara's simulations was the confirmation of a pronounced growth of fluctuation power as the point of induction is approached—this is the "cornucopia" graph of Fig. 7.8 on p. 141. We investigated the theoretical and simulation behaviour of spectral entropy, and found excellent qualitative agreement with Hanna Viertiö–Oja's clinical measurements of spectral entropy of patient EEG records. Intrigued by the apparent inverse relationship between the correlation time T of the cortical fluctuations and their spectral entropy H_ω, I discovered that for a particular spectral distribution (Lorentzian or Cauchy), there exists a simple closed relationship: $H_\omega = -\log_e T$. This simulation and spectral entropy work was written up as Paper 2 (Steyn-Ross *et al.*, 2001b),[4] and published simultaneously with Paper 1.

Contents Overview

This thesis is a comprehensive report of the work I have done helping to develop and test a physics-based theory of anaesthesia. I have included here all the work I did for Papers 0, 1, and 2. Also reported is some recently completed research, outlined below but not yet published: entropy estimation for continuous frequency spectra, and the modelling of anaesthetic effects for an NMDA-enabled macrocolumn.

---

[3] "Toward a theory of the general-anesthetic-induced phase transition of the cerebral cortex: I. A thermodynamics analogy," M. L. Steyn-Ross, D. A. Steyn-Ross, J. W. Sleigh, L. C. Wilcocks, **64**, 011917, (2001).

[4] "Toward a theory of the general-anesthetic-induced phase transition of the cerebral cortex: II. Numerical simulations, spectral entropy, and correlation times," D. A. Steyn-Ross, M. L. Steyn-Ross, L. C. Wilcocks, J. W. Sleigh, **64**, 011918, (2001).

The reader will find that I have attempted throughout to give full acknowledgement of the contributions by the various members of the cortical research team. In general terms, Moira provided the theoretical backbone for the stochastic and thermodynamic approach, David was ever the staunch advocate for and defender of the Liley neuron, Jamie ensured that the physics and mathematics stayed true to the biology, and Lara stress-tested my assumptions and calculations with her careful simulations and independent insights.

The thesis proceeds as follows.

Chapter 1 lays the foundations for an electrical model of anaesthesia. I outline the three modern theories of anaesthetic action, and explain how our electrical model, based on the Liley equations, aims to incorporate the main ideas from the prevailing ion-channel theory. I give a rapid tutorial of some essential concepts of neurophysiology (e.g., resting, reversal, and action potentials of a nerve cell), then explain how these ideas were built into the Hodgkin–Huxley electrical model of the nerve cell. This classic model is held in high regard because it successfully predicts the formation and propagation of nerve action potentials. I discuss the Tuckwell subthreshold (non-firing) model neuron, then demonstrate that the Liley model for a macrocolumn (an assembly of cooperating neurons) can be regarded as a mean-field generalization of the Tuckwell neuron.

In **Chapter 2** I present a brief survey of continuous and discrete Fourier transform theory germane to the analysis of EEG and other random time-series.

The main business of the thesis gets under way in **Chapter 3** where I locate the macrocolumn steady states for both the standard Liley equations and for a restricted case which ignores cell reversal potentials. In **Chapter 4** I examine the stability of these steady states.

Chapter 5 introduces white-noise driving terms into the macrocolumn equations, thereby transforming them into stochastic differential (Langevin) equations. Linearizing these about steady state gives a two-dimensional Ornstein–Uhlenbeck (Brownian motion) system that can be analyzed using well-established methods from stochastic calculus. Of paramount interest to EEG studies are the small *voltage fluctuations* about macrocolumn steady state and in particular, the *statistics* of these fluctuations: the variance, spectral distribution, and correlation time. For the first time, one can now make predictions about how the statistical character of the EEG fluctuations is expected to change with anaesthetic. The model makes three significant predictions:

- there will be a *surge in fluctuation power* at the point of anaesthetic induction, and again at the point of emergence into wakefulness;
- there will be a pronounced *redistribution of spectral power towards low frequencies* as the point of induction is approached;
- a *return journey* into anaesthetic-unconsciousness and back will exhibit *hysteresis behaviour* (i.e., the emergence point will occur at a weaker level of anaesthetic than that required at induction).

The aperiodic EEG analysis by Kuizenga of patients undergoing propofol induction seems to confirm the first and third of these predictions.

Chapter 6 describes a thermodynamics analogy for the conscious-to-unconscious phase transition. By utilizing the trajectory of steady states as an "equation of state," the excitatory and inhibitory neural populations become effectively uncoupled, allowing the computation of hills-and-valleys potential functions for the cortical free energy. I test several arbitrary but plausible inverse mappings between anaesthetic concentration and cortical "temperature," and from a subset of these compute the analogous thermodynamic entropy and heat capacity. A discontinuity in heat capacity is predicted—a "latent heat" effect—arising, presumably, from changes in macrocolumn "bonding." I give an interpretation of a 1977 experiment by Stullken that supports the notion of a biological "heat capacity" for the cerebral cortex.

As a prelude to the stochastic macrocolumn simulations described in **Chapter 7**, I run a simple one-dimensional Ornstein–Uhlenbeck simulation as a validation test case to provide guidance on the choice of quadrature time-step, Fourier transform scale factors and window functions. I report L. Wilcock's simulation results for the full and adiabatic macrocolumn equations, and demonstrate good agreement between simulation and theory for changes in spectral distribution and power level as a function of anaesthetic effect.

In **Chapter 8** I discuss the several different kinds of entropy that might be used to quantify the state of order in the cortex. I show that the form of *spectral* entropy used in the EEG literature is fundamentally flawed—it assumes (falsely) that one can use the (discrete) information entropy H_1 to estimate the spectral entropy H_ω of the underlying (continuous) spectrum. This flaw becomes obvious in the limit $\Delta\omega \to 0$: H_1 fails to converge; in fact, it grows without limit. I show that the correct estimator is obtained by applying a "histogrammed" entropy measure H_2. I compute the theoretical spectral entropy for an ideal Lorentzian spectrum, and show that there is a direct logarithmic proportionality with correlation time. For the adiabatic macrocolumn spectrum, I calculate the predicted changes in spectral entropy, and find excellent qualitative agreement when compared with patient EEG records furnished by H. Viertiö-Oja.

Chapter 9 is an attempt to generalize the adiabatic model for the case of dissociative (anti-NMDA) anaesthetics. The published Liley model is designed for synaptic receptors which have "fast" kinetics (i.e., they decay on a timescale of a few milliseconds). This is a good fit for the (excitatory) AMPA and kainate receptors, and also for the (inhibitory) GABA receptors. Our adiabatic simplification then assumes that these synaptic timescales are very much shorter than the membrane timeconstant of the macrocolumn, and, by a *moderate* lengthening of the IPSP, we achieve a plausible model for the GABAergic class of anaesthetics. However, the *dissociative* class of general anaesthetics (e.g., nitrous oxide and xenon) work by shutting down or *antagonizing* the excitatory NMDA receptor, and this receptor has "slow" kinetics: its EPSP that can extend out to ~100 ms or longer. In this chapter I investigate the implications of enabling slow NMDA receptor action, then antagonizing this action with progressive increases in dissociative anaesthetic concentration. The model predicts the existence of a new state of unconsciousness hovering between normal conscious-awareness and fully-induced anaesthetic unresponsiveness.

Chapter 10 is a brief summary of work accomplished and an outline of future research directions. There are two appendices. The first provides details for simulating the non-adiabatic, spatially-homogeneous Liley equations (the so-called "full" equations); the second is a MATLAB algorithm I developed for numerically integrating the thermodynamic potential functions of Chapter 6.

Original Contributions

I consider myself lucky to have been part of a such refulgent research team! But, because this document is a thesis, I need to state which components of the research originated with me. In general, unless otherwise stated, all numerical calculations and all graphic presentations are my own work. Here is a list of my main contributions:

- treatment of the Liley neuron as a generalization of the Tuckwell neuron; design of equivalent circuits for Liley neuron and macrocolumn (Chap. 1);
- derivation of $\Delta t/N$ forms for discrete Fourier transform normalizations (Chap. 2);
- development of algorithms to locate steady states of the GABAergic (Chap. 3) and NMDA-enabled (Chap. 9) macrocolumns, and to establish their stability with respect to small perturbations (Chaps 4 & 9);
- coding of equations derived by M. Steyn-Ross for the fluctuation spectrum of the adiabatic macrocolumn (Chap. 5);
- justification of equilibrium treatment for non-equilibrium steady states; investigation of inverse mappings between anaesthetic concentration and cortical "temperature" for thermodynamic analogy; interpretation of the Stullken dog results (Chap. 6);
- comparison of L. Wilcocks' numerical simulation results against adiabatic-theory predictions for fluctuation intensity, spectral distribution and spectral entropy change with anaesthetic (Chap. 7);
- discovery of direct logarithmic relationship between spectral entropy and correlation time for a Lorentzian spectrum; establishing the histogram "correction" to enable unbiased estimation of the entropy of a continuous spectrum from a discrete spectral sample (Chap. 8);
- modifications to Liley equations to permit modelling of NMDA-antagonist anaesthetic agents; discovery of a "dissociated" state lying between normal consciousness and anaesthetic unconsciousness; prediction of "peak-splitting" during normal GABAergic induction (Chap. 9).

Acknowledgements

I wish to acknowledge with considerable gratitude the contributions and help received from a host of colleagues:

Dr Moira Steyn-Ross, Dr Jamie Sleigh, Dr David Liley, Ms Lara Wilcocks: I have relished being able to argue, disagree, and be corrected by each of you in turn; working with you individually and as a team has been an honour and a privilege;

Dr Howell Round and Assoc. Prof. Ian Craig for a friendly, relaxed, light-handed supervision, and for their implicit confidence that I would simply get the job done;

Dr Michael Cree for guru assistance with some of the intricate arcaneries of LaTeX formatting;

Dr Hanna Viertiö-Oja of Datex-Ohmeda, Finland for supplying her patient-75 spectral entropy records, and for several thoughtful and detailed communications on aspects of the model;

Dr Karel Kuizenga for his courteous and prompt responses to our requests to access his propofol induction records.

Dedication

I dedicate this thesis—

To my wife Moira
To my sons Jason and Joshua
To my mother Ms Ruth Gatfield
And to the memory of my father, William David Ross.

You have all been most patient.

Contents

List of Figures

List of Tables

Acronyms and Abbreviations

1D, 2D	one-dimensional, two-dimensional
AMPA	α-amino-3-hydroxy-5-methyl-4 isoxazole propionic acid (a neurotransmitter associated with the fast-decaying "early" current in the excitatory postsynapse; cf. NMDA)
AP5, APV	2-amino-5-phosphonovalerate (an NMDA-blocking agent)
CMR	cerebral metabolic rate
DE	differential equation
ECoG	electrocorticogram (brain activity recorded via electrodes attached directly to the cerebral cortex; cf. EEG)
EEG	electroencephalogram (brain activity recorded via scalp electrodes; cf. ECoG)
EPSC	excitatory postsynaptic current
EPSP	excitatory postsynaptic potential
DFT	discrete Fourier transform
GABA	γ-aminobutyric acid (an inhibitory neurotransmitter)
GHK	Goldman–Hodgkin–Katz formula for membrane voltage
IPSC	inhibitory postsynaptic current
IPSP	inhibitory postsynaptic potential
LOC	loss of consciousness
MAC	minimum anaesthetic concentration (a standard measure of anaesthetic potency)
MEG	magnetoencephalogram (brain activity recorded via magnetic-field probes)
NOS	nitric oxide synthase (an enzyme that catalyzes production of NO, nitric oxide)
NMDA	N-methyl-D-aspartate (a neurotransmitter associated with the slowly-decaying "late" current in the excitatory postsynapse; cf. AMPA)
OAAS	observer assessment of alertness and sedation (a measure of patient awareness)
ODE	ordinary differential equation
OU	Ornstein–Uhlenbeck (random process describing the velocity of a Brownian particle)
PDE	partial differential equation
PDF	probability density function
PSP	postsynaptic potential
SDE	stochastic differential equation (Langevin equation)
rms	root-mean square

Chapter 1

Foundations for an Electrical Model of Anaesthesia

1.1 The Anaesthesia State

The ability to safely and reversibly render a patient unconscious is an essential element of modern surgical medicine. Most surgical procedures would be completely impossible were it not for a series of discoveries, dating from the 1840s, that certain gaseous and volatile agents can induce a state of *general anaesthesia*, defined as follows—

> —a state of controlled and reversible unconsciousness characterized by lack of pain sensation (analgesia), lack of memory (amnesia), muscle relaxation, and relatively depressed reflex responses.[1]

It is the task of the clinical anaesthetist to administer anaesthetic drugs in doses that will not only guarantee adequate anaesthesia with minimal side-effects for the duration of the surgical intervention, but also enable fast emergence from anaesthesia at the end of the intervention.

1.1.1 Stages of Anaesthesia

Guedel (1937) identified four distinct stages in the induction of general anaesthesia:

1. **Analgesia and Amnesia:** Patient experiences pain relief and dreamy disorientation, but remains conscious.
2. **Delirium:** Patient has lost consciousness, blood pressure rises, breathing can become irregular, pupils dilate. Sometimes there is breath-holding, swallowing, uncontrolled violent movement, vomiting, and uninhibited response to stimuli.
3. **Surgical anaesthesia:** Return of regular breathing, relaxation of skeletal muscles, eye movements slow, then stop. This is the level at which surgery is safe.
4. **Respiratory paralysis:** Anaesthetic crisis—respiratory and other vital control centres cease to function, death from circulatory collapse will follow without assisted ventilation and circulatory support.

Some of the patient responses during stage-2 can be medically worrisome. Because of this, most anaesthetic protocols seek to minimise stage-2 duration, or, with appropriate premedication, to bypass this stage altogether. The "ideal" anaesthetic protocol yields a quick and smooth induction to stage-3, and allows a rapid recovery.

---

[1] Source: `www.cvm.msu.edu/courses/VM303` (course notes for Veterinary Technology students)

1.1.2 Motivation for EEG Monitoring

As a matter of standard practice, an anaesthetist will "titrate to effect," i.e., will adjust the drug administration amount and rate according to the clinical response of the patient. For example, if the patient moves or vocalizes in response to surgical incision, opens her eyes, or suddenly changes her pattern of breathing, then the level of anaesthesia is inadequate and the drug level must be increased. However, these important clinical indicators of inadequate anaesthesia will be unavailable if muscle-relaxant drugs have been applied, in which case the anaesthetist has to rely on autonomic responses such as increases in heart rate and blood pressure, transpiration (sweating) and lacrimation (tear formation). But these indirect measures of anaesthetic depth can themselves be diminished by disease and by some co-medications, thus increasing the risk of either under- or overdosing the anaesthetic drug (Kuizenga, 2001).

It is prudent to reduce this risk by using an alternative measure of the patient's level of anaesthesia: the electrical activity of the brain itself. Scalp-mounted electrodes monitoring the activity of the cerebral cortex give voltage-vs-time traces referred to as the EEG (electroencephalogram). Alterations in anaesthetic–blood concentrations produce significant changes in the spectral character (amplitude and frequency distribution) of the EEG fluctuations. The relationship between anaesthetic concentration and its effect on the EEG will be investigated in detail later in this thesis.

Although it is of primary concern to the anaesthetist to ensure the patient is safely and comfortably transported from an initial state of conscious awareness to a sufficiently deep plane within stage-3 anaesthesia, the safety and comfort aspects of the transition are *not* the focus of this thesis. Instead, we will be examining the changes in the state of consciousness from a physics perspective, attempting to identify transition behaviours that are shared with other changes of state that occur in the physical world.

1.1.3 The Anaestheto-Dynamic Phase Transition

As naive (i.e., non-medically trained) observers seeking simple explanations for anaesthetic-induced loss of consciousness, it seems not unreasonable for us to assume that there exists a roughly linear rule-of-thumb for the dose–response relationship, such as: "increases in drug concentration leads to proportionate reductions in brain response." Unfortunately this intuition is immediately contradicted by the anomalous patient responses exhibited at the stage-2 (delirium) depth of anaesthesia. A general anaesthetic is administered with the aim of quieting or *inhibiting* brain response to noxious stimuli, and yet, on route to the stage-3 fully-inhibited state, the patient transits through a "wild" uncontrolled state of delirium and *uninhibited* response to stimuli. This is a most interesting paradox: the end-state of inhibition is preceded by an intermediate stage of excitation. As we shall see later, this observation supports the idea that the conscious → unconscious transition is analogous to a classical first-order thermodynamic phase transition in physics. For this reason, I have coined the phrase "anaestheto-dynamic phase transition" to describe the abrupt change in the state of consciousness induced by a general anaesthetic agent.

1.2 Effect of Anaesthetics on Bioluminescence

Researchers have reported that the volatile anaesthetics ether ($CH_3{\cdot}CH_2{\cdot}O{\cdot}CH_2{\cdot}\ CH_3$), halothane ($CF_3{\cdot}CHClBr$), chloroform ($CHCl_3$), and cyclopropane ($C_3H_6$) reversibly reduce the intensity of light emissions from luminescent bacteria (White and Dundas, 1970; Halsey and Smith, 1970). This followed earlier work by Ueda (1965) showing that the light emission from the firefly lantern extract luciferase was reversibly suppressed by both ether and halothane. (In all cases the *wavelength* of the emitted light was unaffected.)

The anaesthetic concentration required to depress bioluminescent intensity by 50% was found to be very simililar to the concentrations required for clinical induction in humans. Because of this remarkable scale invariance (i.e., the light-emitting complex in photo-bacteria and fireflies, and the central nervous system in humans, all seem to respond in similar ways to similar concentrations of a given anaesthetic), and because light intensity can be be easily and accurately measured, bioluminescence provided a very useful means for quantifying and comparing anaesthetic potency.

Figure 1.1 shows the bioluminescence dose–response curve for ether reported by Halsey and Smith (1970). At an ether partial pressure of 0.026 atm, the luminous intensity has reduced to to 50% of its original (zero ether) value. This partial pressure is similar to the 0.032 atm value they quote for the abolition of the righting instinct in 50% of mice exposed to ether (prior to the bioluminescence work, small mammals had been used to calibrate anaesthetic potency).

Of particular interest to us is the observation that luminescence is *stimulated* by low doses of ether ($P \sim 0.009$ atm). Halsey and Smith reported that stimulation also occurred at low levels

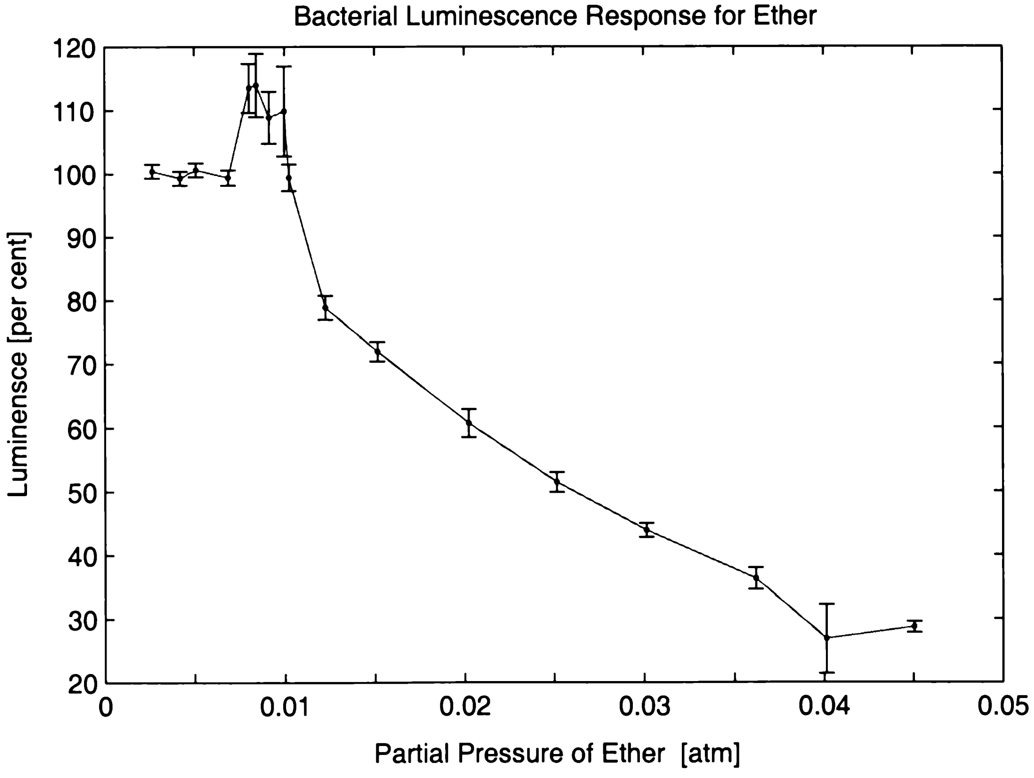

Figure 1.1: Dose–response curve showing the effect of the volatile anaesthetic ether on the luminous intensity of the bacteria *Photobacterium phosphoreum*. [Source: Halsey and Smith (1970)]

of chloroform, halothane, and nitrous oxide (though for the latter two agents they described the increase as "not statistically significant," presumably because the error bars became very large during this transition phase). Apart from noting the low-dose stimulation effect, neither Halsey and Smith nor White and Dundas proffered any explanation of this paradoxical excitation by an inhibitory agent. The anomalous boost in light output seems to have been viewed as a curiosity rather than an indicator of a deeper phenomenon.

Thus it is apparent that two quite dissimilar organisms exhibit similar but paradoxical, dis-inhibitory responses to low-concentration anaesthetic: the human patient enters a delirium phase of unsteady, feverish activity (stage-2 of general anaesthesia), and the photobacterium enters an overactive phase of strongly fluctuating light intensity. In both cases, at higher concentrations the anomalous excitation dies away, and the organism response becomes quieter in a monotonically dose-dependent manner.

If we picture deep-anaesthesia and conscious-awareness as being two opposite states that bracket stage-2 delirium, then the dramatic fluctuations of stage-2 indicate that a change of phase is imminent. It will become evident as this thesis proceeds that this picture is consistent with clinical recordings of brain activity during induction of general anaesthesia, and is also consistent with model predictions for changes in EEG activity during induction of an inhibited, low-firing cortical state.

1.3 Theories of Anaesthetic Action

1.3.1 Ion-Channel Theory

Although general anaesthetics have been in use for over 150 years, the way in which they work has remained a puzzle and a source of some controversy. The prevailing view is as summed up in the title of a recent paper by Franks and Lieb (1997): "Anaesthetics set their sites on ion channels." These authors argue that inhibition occurs when the anaesthetic molecule binds to a specific site on the $\mathrm{GABA_A}$ (γ-aminobutyric acid) receptor of the postsynaptic neuron, causing its chloride-ion channels to remain open longer, so more $\mathrm{Cl^-}$ ions enter the postsynaptic neuron, and it becomes hyperpolarized (i.e., more negative), and therefore less likely to fire.

Figure 1.2(a) shows the arrival of an action potential at the terminal of the presynaptic neuron and the subsequent release of messenger chemicals (neurotransmitters) which diffuse across the gap (synapse) separating the pre- and postsynaptic neurons. The incoming GABA neurotransmitter momentarily opens the $\mathrm{Cl^-}$ channels, allowing a brief inward flux of $\mathrm{Cl^-}$ ions and consequent negative-going "impulse response" in the postsynaptic neuron (Fig. 1.2(b)). The duration of the inhibitory impulse response is *increased* in the presence of anaesthetic. In our modelling work, we will assume that the characteristic decay time of this inhibitory postsynaptic potential (IPSP) scales proportionately with anaesthetic concentration.

Figure 1.3 presents a simple block-diagram representation of the $\mathrm{GABA_A}$ receptor. The GABA molecule provides the "key" which unlocks the $\mathrm{Cl^-}$ channel via an unspecified catalytic reaction represented by the triangle.

This enhancement of inhibitory effect is thought to be the basis of the so-called *GABAergic* anaesthetics, such as the intravenous agent propofol (2:6 di-isopropylphenol), which are capable

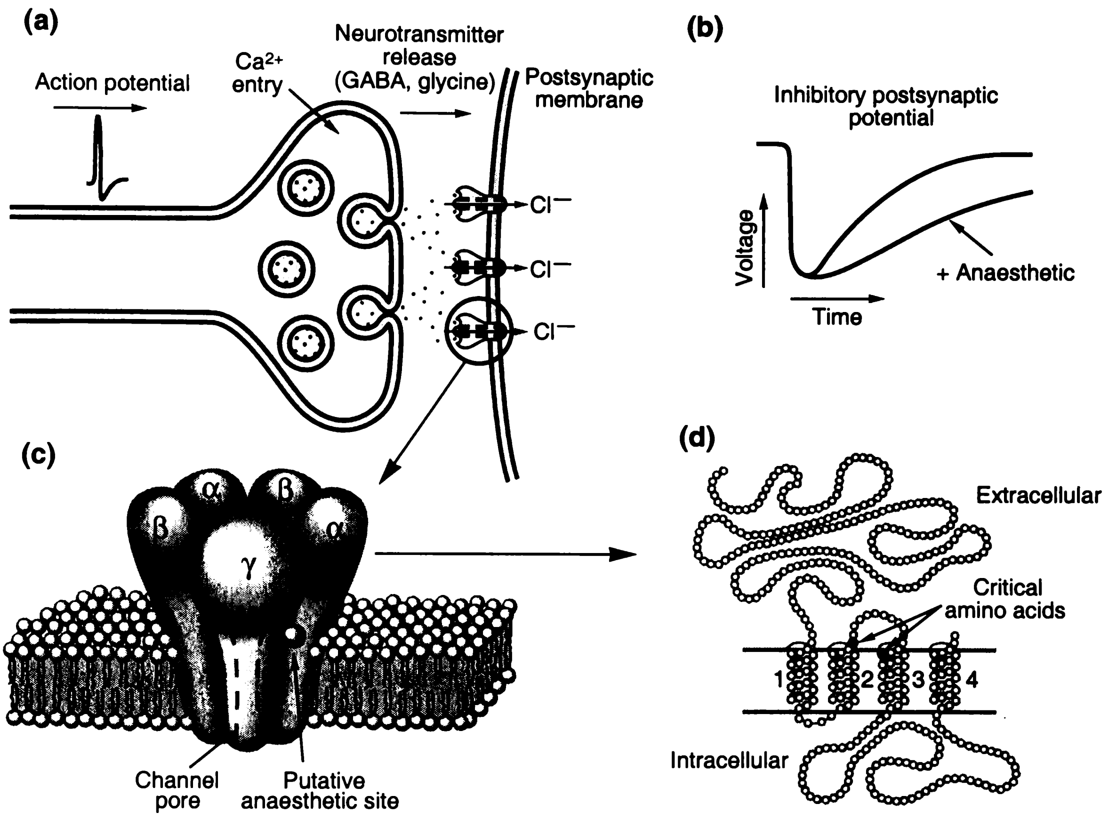

Figure 1.2: GABAergic model for anaesthetic action. (a) An action potential arriving at the terminal of an inhibitory neuron results in the release of GABA neurotransmitter which diffuses across the synaptic junction to the membrane of the postsynaptic neuron, opening chloride-permeable GABA$_A$ receptor channels, causing the postsynaptic neuron to become hyperpolarized as Cl$^-$ ions enter. (b) The main effect of GABAergic anaesthetics (such as propofol) is to prolong channel opening, and hence to increase postsynaptic inhibition. (c) Each channel consists of five protein subunits; the structure of a single subunit is shown in (d). [Source: Fig. 1 of Franks and Lieb (1997)]

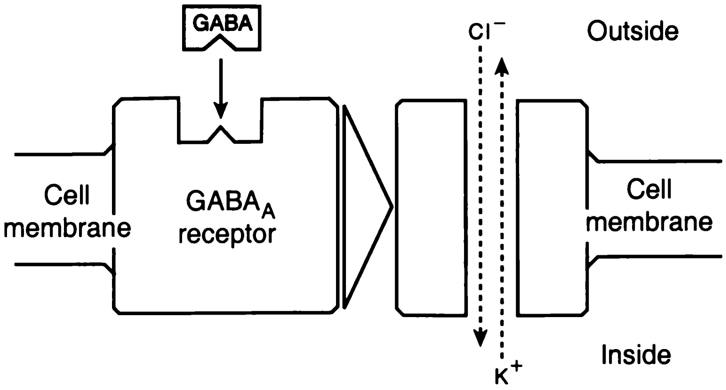

Figure 1.3: Simplified view of the GABA-controlled chloride channel illustrated in Fig. 1.2(c). Activation occurs when the GABA neurotransmitter binds to the GABA$_A$ receptor molecule. The chloride channel opens, and Cl$^-$ ions diffuse down the concentration gradient into the postsynaptic neuron, causing it to become hyperpolarized (more negative) and less likely to fire.

of inducing a fully-unconscious state. The bulk of this thesis (Chapters 3–8) will be concerned with modelling GABAergic action.

There is a second class of agents referred to as *dissociative anaesthetics*, such as nitrous oxide (N_2O) and xenon (Xe), which do not ordinarily induce full anaesthesia. The dissociatives are thought to act by suppressing the excitatory effectiveness of the NMDA (*N*-methyl-D-aspartate) receptor complex on the postsynaptic neuron (Franks *et al.*, 1998; Jevtovic-Todorovic *et al.*, 1998), so are referred to *NMDA-antagonists.* Figure 1.4 shows a simplified block-diagram of the NMDA receptor. Modelling the action of this receptor is complicated by the fact that the duration of the excitatory postsynaptic response to a presynaptic action potential depends not only on anaesthetic concentration (greater concentrations lead to EPSPs of *shorter* duration), but also on the voltage state of the receiving neuron (the Mg^{2+} block in the ion channel is only removed when the neuron is depolarized). Chapter 9 develops a model for NMDA-antagonist effect based on laboratory measurements reported by Hestrin *et al.* (1990).

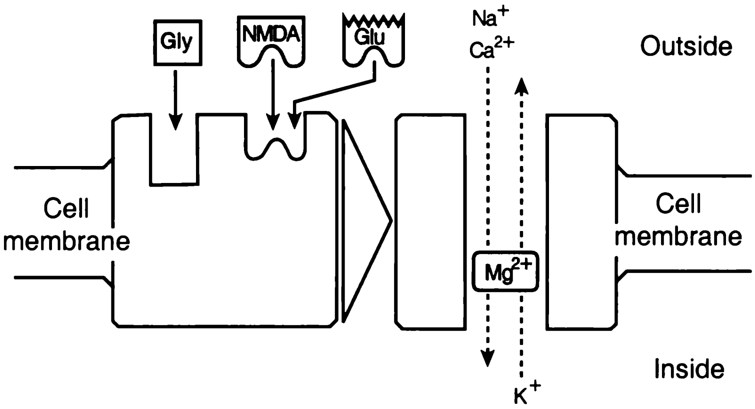

Figure 1.4: The NMDA receptor complex. Activation (i.e., excitation) occurs when glycine (Gly) and one of either of glutamate (Glu) or NMDA bind to the receptor molecule. In its unactivated configuration, a magnesium ion blocks the channel within the receptor. On activation, the Mg^{2+} ion is removed, and other ions are then free to diffuse down their concentration gradients: Na^+ and Ca^{2+} ions enter the cell, causing the cell to become depolarized (less negative). Dissociative anaesthetics such as nitrous oxide and xenon are NMDA-antagonists (i.e., they reduce activation of the NMDA receptor). [Based on Fig. 1 of Thomas and Riley (1998)]

1.3.2 Volume-Change Theory and Pressure Reversal

The ion-channels theory of Franks and Lieb (described above) asserts that anaesthetics act on specific sites on receptor proteins to alter the ionic conductance through membrane pores.

Ueda (2001) maintains a vigorous counterview—he argues that the action of anaesthetics is both *nonspecific* and *physical.* A bewildering array of chemical agents can induce anaesthesia;[2] such chemical diversity militates against the idea of a common, specific receptor. For Ueda, the key observation that anaesthetic action is physical is the fact that anaesthesia can be *reversed* by application of pressure. Johnson and Flagler (1951) reported that the spontaneous swimming motion of tadpoles disappeared when they were anaesthetized with various liquid anaesthetics,

---

[2] e.g., alcohols, alkanes, ketones, ethers, barbiturates, isoflurane, nitrogen (at ~150 atm pressure), xenon, ...

or when unanaesthetized tadpoles were exposed to hydrostatic pressures of 200–350 atmospheres. However, when anaesthetized tadpoles were exposed to hydrostatic pressures of 150–350 atm, spontaneous swimming motions reappeared! Johnson and Miller (1970) studied the ability of a newt to right itself under the influence of anaesthetics and pressure. Butanol, ether, or nitrogen anaesthetic was administered in sufficient dose to abolish the righting reflex. Application of pressure, either hydrostatically or with the non-anaesthetic helium, restored the righting reflex at about 150 atm. Application of pressure alone led to progressive loss of righting reflex above 150 atm.

From the observation that pressure reverses anaesthesia, Ueda concludes that "the volume of the anaesthetized state is *larger* than the awake state [...]; an *increase* in the partial molar volume of the system is the crucial condition for anaesthesia" [my italics] but unfortunately he never defines what he means by "system." Also not addressed is the idea that since application of pressure *alone* can induce an anaesthetic state, then apparently the anaesthetized state can be either *larger or smaller* than the awake state, depending on whether the state was induced by chemical agent (anaesthetic) or by physical agent (pressure).

It seems plausible that pressurizing an organism will cause non-specific bulk changes in its neural membrane conformation which *could* disrupt ionic conduction, thereby altering the electrical state of the neural network and leading to loss of consciousness. But it seems much less plausible that bulk pressurization should be able to reverse an anaesthesia induced by a chemical agent acting at specific site. Therefore pressure reversal seems inexplicable in the Franks and Lieb ion-channel theory.

The Ueda volume-change theory says that all anaesthetics act nonspecifically at the bilipid membrane, yet this claim is contradicted by the growing body of experimental evidence demonstrating site specificity for anaesthetic agents.

At this stage of knowledge, neither theory is complete. Worse, the theories seem to be mutually exclusive and irreconcilable. Nevertheless, because in our modelling work we want to assume a direct relationship between the electrical state of the cerebral cortex and the state of patient awareness, we will take the ion-channel theory as our starting point and reluctantly leave the pressure-reversal paradox as an unresolved puzzle.

1.3.3 NMDA-Disruption Hypothesis

Recently Flohr, Glade, and Motzko (2000) have put up a theory of general anaesthesia which asserts that anaesthetic loss of consciousness *always* involves disruption of one or more NMDA-dependent processes. Flohr states that *all* agents that directly inactivate the NMDA synapse or its subsequent plastic processes (some of which are shown in Flohr's NMDA diagram reproduced below as Fig. 1.5) possess dissociative anaesthetic properties. He argues that the anaesthetic action of agents that primarily act upon other targets, such as the GABAergic anaesthetics, can be explained as an *indirect* effect on the NMDA receptor.

Referring to Fig. 1.5, it is plausible that the working conditions of the NMDA receptor could be modified by inhibitory ($GABA_A$) and excitatory (AMPA) synapses located in the vicinity of the receptor. Flohr presents experimental evidence which demonstrates that propofol, generally classified as a GABAergic agent, partially blocks the uptake of radio-labelled MK-801, an NMDA

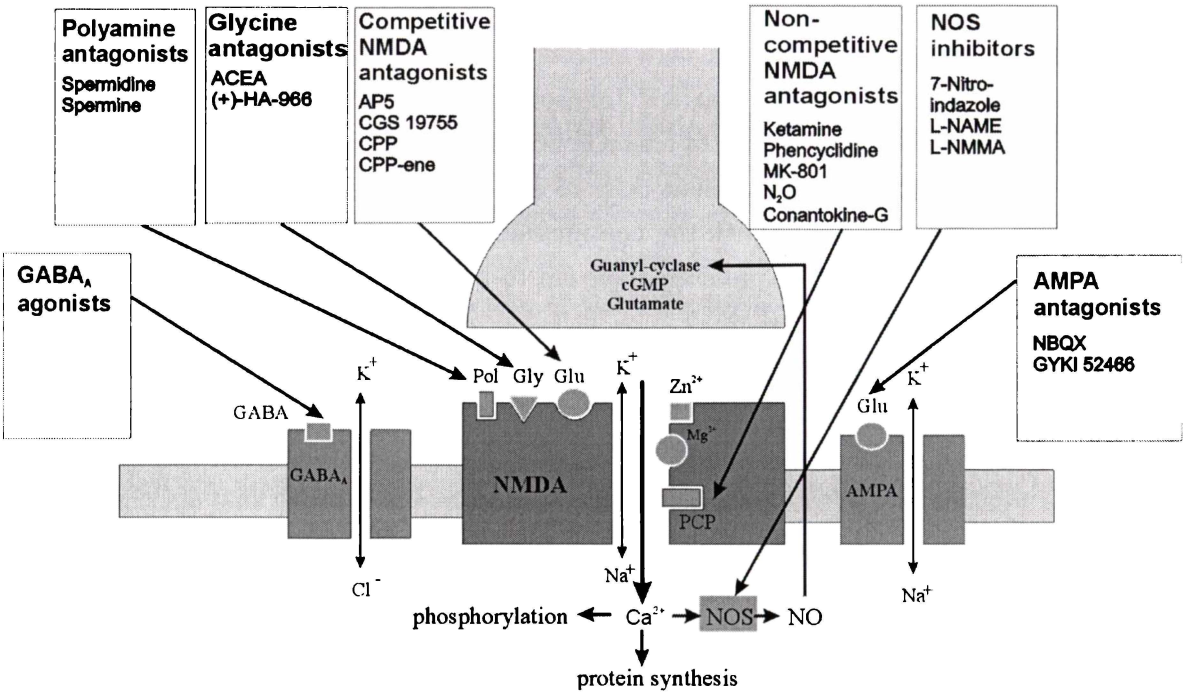

Figure 1.5: The Flohr model of the NMDA synapse as a target of anaesthetics. Schematic representation of the NMDA receptor channel complex with its regulatory sites and its neighbouring GABA_A and AMPA receptors which can influence the working conditions of the NMDA receptor. All listed agents have anaesthetic properties; arrows indicate possible interaction sites. [Source: Fig. 2 of Flohr *et al.* (2000)]

antagonist that binds to the PCP site within the NMDA channel. Thus propofol is found to be both GABAergic and (weakly) NMDA-antagonistic.

It will become apparent in Chap. 9 that our ion-channel model for the NMDA-enabled macrocolumn (local assembly of cooperating neurons) makes predictions that are nicely consistent with the Flohr hypothesis. For induction via a GABAergic agent, our theory predicts *two* cortical activity peaks: the first of these peaks marks the transition to what I call the "dissociated" state, and the second peak is the transition to the deeper state of unresponsiveness required for surgery. Our "dissociated state" is an intermediate region of equilibrium states which only comes into existence when slow NMDA-mediated currents are incorporated into the model.

There is fresh clinical support also: Part of Chap. 9 is an analysis of clinical data (kindly furnished by our colleague K. Kuizenga), measuring changes in EEG activity during slow (20-min) propofol infusions, and this also shows two surges in cerebral cortex activity (Fig. 9.16). Loss of responsiveness to verbal command generally occurs prior to the first peak, and, according to the model, the first peak is an NMDA feature. Thus, just as the Flohr hypothesis would predict,[3] the GABAergic anaesthetic propofol appears to display an NMDA-antagonisic behaviour during the preliminary phase of the induction.

---

[3] Though it is worth pointing out that I only became aware of the Flohr NMDA-disruption hypthesis several months *after* the NMDA-modelling work of Chap. 9 had been completed.

1.4 Elements of Neurophysiology

Before we examine the Liley "average neuron" which forms the basis of our anaesthetic model, we need to introduce some basic concepts of nerve cell biology, and also make more concrete some of the neurophysiological terms we have already used in the foregoing discussion.

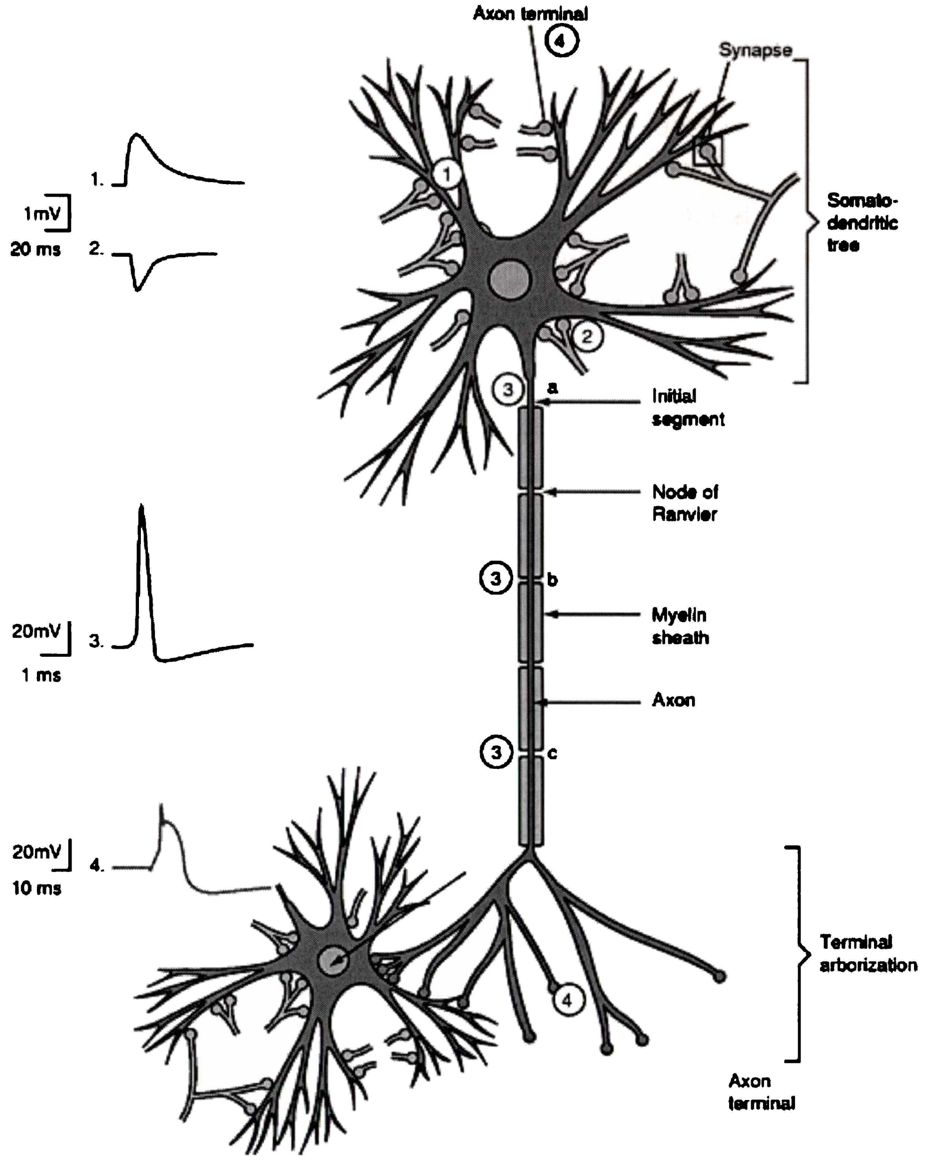

Figure 1.6: Schematic view of a prototypical neuron. Neurotransmitters released at the axon terminal (4) (at top of figure) of a presynaptic neuron (not shown) induce small excitatory (1) or inhibitory (2) voltage pulses in the dendritic branches of the receiving neuron. These incoming voltage events propagate to the soma where they are summed. If a threshold voltage is exceeded, a large voltage spike (action potential) is generated (3a) and propagated down the axon (3b, 3c) towards the terminal arborization (telodendria), where neurotransmitters are released to stimulate the next neuron. (The diagram represents a "white-matter" neuron, since its axon is sheathed with myelin, a white fatty insulator, whose effect is to increase transmission velocity. For "grey-matter" neurons such as the those of the cerebral cortex, the myelin coating is absent.) [From Hammond (2001, Fig. 1.5)]

1.4.1 The Cortical Nerve Cell

Our brains and spinal cords contain specialized cells called *nerve cells* or *neurons*[4] which collectively form the central nervous system. The stereotypical neuron (see Fig. 1.6) consists of a *cell body* or *soma*, *dendrites*, *axon*, and *telodendria*. The *dendrites* form a dense root-like structure which converge at the *soma*. The dendrites sample electrical stimulus currents from the local neural environment, and feed these currents forward to the soma where they are integrated to produce a change in the internal voltage of the cell.

If the voltage change is small (i.e., *subthreshold*), then the voltage change propagates slowly and passively only a short distance along the axon, decaying exponentially as it travels. This decaying voltage transient is referred to as a *local potential*.

If the voltage change is sufficient to raise the soma voltage V_m above a threshold level (i.e., $V_m \gtrsim -60$ mV), then an *action potential* is triggered and *actively* propagated along the axon, away from the cell body towards the *telodendria* or *terminal branches* of the neuron. The arrival of an action potential at a terminal branch causes *neurotransmitters* (messenger chemicals) to be released from the terminal, and these convey a chemical impulse to the next neuron by diffusing across the extracellular junction or *synapse* that separates the sending (*presynaptic*) and receiving (*postsynaptic*) neurons. The impinging neurotransmitters generate currents in the postsynaptic cell by altering the ion permeability of the postsynaptic membrane, thereby allowing ions to diffuse across it.

1.4.2 The Resting Neuron

In any measurement of the cellular transmembrane potential difference, it is standard practice to take the extracellular ionic "sea" in which the neuron is bathed as defining the zero potential level. Relative to this external reference, the potential of the ionic fluid inside most nerve cells is found to be approximately -70 mV when the cell is "at rest," i.e., when the cell is not receiving stimuli from its dendritic tree. This steady transmembrane electrical tension provides the source of potential energy required for the propagation of electrical action signals. The cell resting voltage (usually referred to as the *resting membrane potential*) arises from an imbalance in ion concentrations either side of the membrane. The ionic imbalance is actively maintained by a metabolic process called the *sodium-potassium pump* that moves three Na^+ ions out of the cell for every two K^+ ions that enter.

1.4.3 Nernst Potential

Table 1.1 shows the intracellular and extracellular concentrations of the four most important ionic species which can cross the nerve membrane through ion-specific *pores* or *channels*. The *Nernst potential* listed in the final column is an ideal equilibrium voltage calculated from classical membrane theory (see, for example, Sect. 2.6 of Tuckwell (1988a)) for the diffusion of a single ion across a membrane permeable only to that ion. The Nernst potential V_X for a single ionic species X, whose respective concentrations outside and inside the cell are $[\mathrm{X}]_o$ and $[\mathrm{X}]_i$, is given by:

---

[4] Some authors spell neuron as *neurone*.

Table 1.1: Typical ion concentrations (in mmol/L) and Nernst potentials (mV) for a resting neuron. The Nernst potentials were calculated using Eq. (1.1) for a neuron at body temperature (37°C) giving $RT/F = 26.7$ mV. [From Silbernagl and Despopoulos (1996)]

	Concentration		
Ion	Inside	Outside	Nernst Potential
Na^+	10	140	+70
K^+	140	4	−95
Cl^-	4	103	−87
Ca^{2+}	$<10^5$	5	>350

$$V_X = V_i - V_o = \frac{RT}{zF} \log_e \frac{[X]_o}{[X]_i} \qquad \text{(Nernst potential)} \tag{1.1}$$

or sometimes stated as a Boltzmann factor for the concentration ratio,

$$\frac{[X]_i}{[X]_o} = \exp\left[-zFV_X/RT\right] = \exp\left[-ze(V_i - V_o)/kT\right] \tag{1.2}$$

where T is the absolute temperature, $R = 8.314\ \mathrm{J\,K^{-1}\,mol^{-1}}$ is the ideal gas constant, z is the signed valence of the ion (e.g., $z = -1$ for Cl^-), $F = 9.648 \times 10^4\ \mathrm{C\,mol^{-1}}$ is the Faraday constant, $k = 1.381 \times 10^{-23}\ \mathrm{J\,K^{-1}}$ is the Boltzmann constant, $e = 1.602 \times 10^{-19}$ C is the elementary charge, and $R/F = k/e$.

1.4.4 Reversal Potential

Suppose the transmembrane voltage is initially zero, while the concentration of, say, potassium (K^+) is initially higher inside than outside. Potassium will tend to diffuse down its concentration gradient to the outside, but every K^+ ion that leaves will add to a growing charge imbalance across the membrane, with the inside becoming progressively more negative. Eventually the inwards electric force on the K^+ ions will exactly balance the outwards diffusive force, and the transmembrane K^+ ion flux stops. For typical nerve cells, the Nernst potential for K^+ is approximately −90 mV (cf Table 1.1), i.e., when the inside of the cell membrane is 90 mV negative with respect to the outside of the cell membrane, the K^+ ion flux is zero.

If the membrane voltage is made more negative, then K^+ ions will be dragged back into the cell against the concentration gradient, and the direction of the ion flux will be reversed. For this reason, the Nernst potential for a given ion is also referred to as the *reversal potential* since it is the point of equilibrium about which the ion current changes sign.

1.4.5 Resting Membrane Potential

When the only permeant ions are potassium, sodium, and chloride, the membrane potential can be predicted using the *Goldman-Hodgkin-Katz* (GHK) formula,

$$V = \frac{RT}{F} \log_e \left[\frac{P_K[K]_o + P_{Na}[Na]_o + P_{Cl}[Cl]_i}{P_K[K]_i + P_{Na}[Na]_i + P_{Cl}[Cl]_o} \right] \tag{1.3}$$

or

$$V = \frac{RT}{F} \log_e \left[\frac{[\mathrm{K}]_o + P'_{\mathrm{Na}}[\mathrm{Na}]_o + P'_{\mathrm{Cl}}[\mathrm{Cl}]_i}{[\mathrm{K}]_i + P'_{\mathrm{Na}}[\mathrm{Na}]_i + P'_{\mathrm{Cl}}[\mathrm{Cl}]_o} \right] . \tag{1.4}$$

In the limiting case where the permeability of a single ion domininates, the GHK equation reduces the Nernst equation (1.1) for that ion. Here, P_{X} is the permeability for ion X (with units the same as speed), and P'_{X} is the (dimensionless) relative permeability of X with respect to potassium,

$$P'_{\mathrm{Na}} = P_{\mathrm{Na}}/P_{\mathrm{K}} \tag{1.5a}$$

$$P'_{\mathrm{Cl}} = P_{\mathrm{Cl}}/P_{\mathrm{K}} . \tag{1.5b}$$

In the resting state the ratios for the values $\mathrm{P_K} : \mathrm{P_{Na}} : \mathrm{P_{Cl}}$ are approximately 1 : 0.05 : 0.25 (i.e., the resting cell is 20 times more permeable to potassium than to sodium). Substituting these relative permeabilities, together with the ionic concentrations from Table 1.1, into Eq. (1.4) gives a resting membrane voltage of

$$V_{\mathrm{rest}} = -70.2 \text{ mV},$$

about 20 mV higher than the reversal potentials for potassium or chloride ions. In contrast, at the peak of the action potential, the potassium permeability is not substantially changed, but the sodium permeability increases by a factor of about 500 because of the opening of voltage-gated sodium channels. Equation (1.4) predicts that the membrane voltage will reach a maximum value of

$$V_{\mathrm{peak}} = +56.9 \text{ mV},$$

about 13 mV below the reversal potential for sodium.

1.5 Hodgkin–Huxley Model Neuron

1.5.1 Neuron Equivalent Circuit

Table 1.1 shows that potassium is in excess inside the nerve cell, while sodium and chloride are in deficit. The tendency of each ion to diffuse down its concentration gradient can be represented as an electric battery whose voltage, calculated from the Nernst formula of Eq. (1.1), conveys the magnitude and direction of the concentration gradient. (For chloride, a negative ion, conventional current will be an apparent diffusion *against* the concentration gradient, so the battery direction is reversed.) The fact that the sodium and potassium batteries point in opposite directions turns out to be critical for electrical signalling.

The pioneering work by Hodgkin and Huxley (1952) modelled the membrane of the squid giant axon as a capacitor in parallel with distinct conduction paths for each of the major ionic species ($\mathrm{Na^+}$, $\mathrm{K^+}$, $\mathrm{Cl^-}$); see Fig. 1.7. They posited that the driving force for a given ion is proportional to the difference between the membrane potential V and the Nernst potential for that ion. Defining the *outwards* current direction as *positive*, then the $\mathrm{Na^+}$ current in Fig. 1.7 can be written:

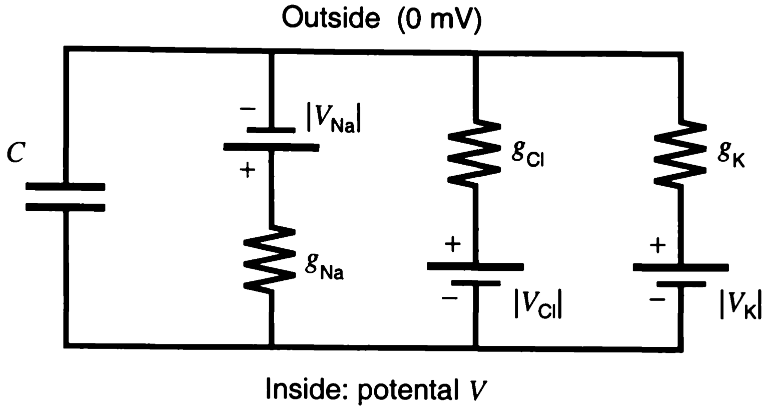

Figure 1.7: Electrical circuit used by Hodgkin and Huxley to represent a patch of nerve membrane at rest. Each ion channel is modelled as a conductance (inverse resistance) driven by battery whose magnitude and direction is given by the Nernst potential of the ion.

$$I_{\mathrm{Na}} = (V - V_{\mathrm{Na}})\, g_{\mathrm{Na}} \tag{1.6a}$$

where the coefficient g_{Na} is the *sodium conductance* [units: Ω^{-1}]. We can write parallel expressions for the potassium and chloride currents

$$I_{\mathrm{K}} = (V - V_{\mathrm{K}})\, g_{\mathrm{K}} \tag{1.6b}$$

$$I_{\mathrm{Cl}} = (V - V_{\mathrm{Cl}})\, g_{\mathrm{Cl}}\,. \tag{1.6c}$$

Thus for the resting nerve cell, the conventional current for Na^+ ions will be in the negative direction (i.e., directed inwards), while for K^+ and Cl^- ions the conventional current will be positive (outwards).

In general, the conductance is *not* constant: it depends on both the membrane voltage V and its history. However, defining conductance in this way (with the $V - V_{\mathrm{X}}$ term factored out; X is one of Na^+, K^+, or Cl^-) simplifies the functional form of g_{X} since it does not have to change sign as V crosses the Nernst potential V_{X} and the current reverses direction.

For their Fig. 1.7 circuit, Hodgkin and Huxley wrote the total membrane current as the sum of capacitive and ionic currents,

$$I = C\frac{dV}{dt} + I_{\mathrm{ion}} \tag{1.7}$$

where the ionic current is the sum of the individual channel contributions

$$I_{\mathrm{ion}} = I_{\mathrm{Na}} + I_{\mathrm{K}} + I_{\mathrm{Cl}} \tag{1.8}$$

giving the total current as

$$I = C\frac{dV}{dt} + (V - V_{\mathrm{Na}})\, g_{\mathrm{Na}} + (V - V_{\mathrm{K}})\, g_{\mathrm{K}} + (V - V_{\mathrm{Cl}})\, g_{\mathrm{Cl}}\,. \tag{1.9}$$

At rest, $I = 0$ and $C\,dV/dt = 0$, and Eq. (1.9) predicts a resting voltage that is the weighted sum of Nernst potentials,

$$V_{\text{rest}} = \frac{g_{\text{Na}}V_{\text{Na}} + g_{\text{K}}V_{\text{K}} + g_{\text{Cl}}V_{\text{Cl}}}{g_{\text{Na}} + g_{\text{K}} + g_{\text{Cl}}} . \qquad (1.10)$$

Tuckwell (1988b, pp. 5–6) points out that Eq. (1.10) is linear in the Nernst potentials for the various ions, while the GHK prediction of Eq. (1.3) is *not* linear in the individual Nernst potentials, except when only one kind of ion is involved. This inconsistency arises from the fact that *conductance* and *permeability* are not interchangeable concepts (Koester, 1991, p.90). Permeability depends on the state of the membrane, while conductance also depends on the concentration of surrounding ions.[5]

For the present work we will assume a nominal resting voltage of −70 mV, as calculated using the GHK formula on p. 12.

1.5.2 Modelling the Action Potential

When a synaptic or other injected current drives the membrane voltage from its −70-mV resting level to a threshold of approximately −60 mV, a population of voltage-dependent Na^+ channels, normally closed at rest, opens abruptly, thereby increasing the sodium conductance g_{Na} and leading to a rapid influx of Na^+ ions, driving the membrane voltage towards the sodium reversal potential V_{Na}. Within a fraction of a millisecond, the Na^+ channels begin to close or "inactivate." At the same time, voltage-dependent K^+ channels sense the voltage upswing on the leading edge of the action potential, and open to produce a large outward current. The combined effect of Na^+ channel inactivation and K^+ channel activation result in an abrupt downswing to terminate the action potential.

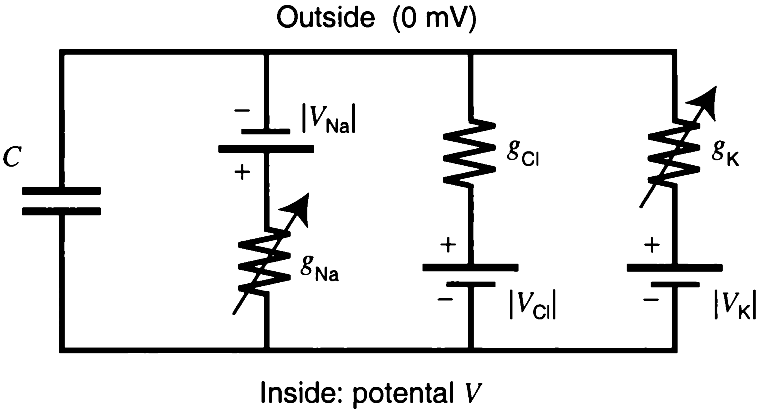

Figure 1.8: Hodgkin and Huxley equivalent circuit used to model the formation of an action potential. The g_{Na} and g_{K} rest conductances of Fig. 1.7 are replaced by voltage- and time-dependent functions. Once the membrane voltage crosses a trigger threshold (about 10 mV above V_{rest}), voltage-gated sodium channels turn on, increasing sodium conductance and inward sodium current, further depolarizing the membrane, leading to regenerative increases in sodium conductance and membrane voltage. After a delay, the voltage-gated potassium channels turn on, eventually restoring the membrane to its resting voltage. See Fig. 1.9.

Tuckwell (1988b, pp. 44–57) gives a good account of the classic Hodgkin–Huxley model for the formation of the action potential in a nerve membrane. What follows is a brief summary.

---

[5] For example, the membrane could be highly permeable to K^+, but if the surrounding K^+ concentrations are low, the conductance (ionic current per unit voltage difference) will be low.

In order to describe their experimental measurements of the action potential in the squid giant axon, Hodgkin and Huxley found it necessary to replace the constant Na^+ and K^+ conductances of Fig. 1.7 with variable conductances as indicated in Fig. 1.8. These variable conductances were expressed in terms of a *sodium activation* variable m, a sodium *inactivation* variable h, and a *potassium activation* variable n:

$$g_{\mathrm{Na}} = \bar{g}_{\mathrm{Na}} m^3 h \tag{1.11a}$$

$$g_{\mathrm{K}} = \bar{g}_{\mathrm{K}} n^4 \tag{1.11b}$$

where $\bar{g}_{\mathrm{Na}}$ and $\bar{g}_{\mathrm{K}}$ are the measured maximum conductance values for Na^+ and K^+ ions. Each of the m, h, and n activation or inactivation variables is dimensionless, takes values in the range [0,1], and obeys an ordinary differential equation of the form

$$\frac{dm}{dt} = \alpha_m(1-m) - \beta_m m \tag{1.12a}$$

$$\frac{dh}{dt} = \alpha_h(1-h) - \beta_h h \tag{1.12b}$$

$$\frac{dn}{dt} = \alpha_n(1-n) - \beta_n n \tag{1.12c}$$

The three α_j and β_j ($j \in \{m, h, n\}$) are voltage-dependent coefficients whose voltage dependence was established by curve fitting to conductance data obtained in a detailed series of voltage-clamp experiments. Setting total current I in Eq. (1.9) to zero, we can write the Hodgkin–Huxley equation for the action potential as,

$$C\frac{dV}{dt} = (V_{\mathrm{Na}} - V)\,\bar{g}_{\mathrm{Na}} m^3 h + (V_{\mathrm{K}} - V)\,\bar{g}_{\mathrm{K}} n^4 + (V_{\mathrm{Cl}} - V)\,g_{\mathrm{Cl}}\,. \tag{1.13}$$

Figure 1.9 shows the numerically evaluated solution of Eqs(1.12–1.13). We observe that the dynamic range of the action potential (upper graph of Fig. 1.9) is constrained to lie entirely within the bounds defined by the reversal potentials for Na^+ (upper bound) and K^+ (lower bound). Although the Liley model neuron makes no attempt to follow the dynamics of the action potential (its focus instead is on the accurate following of synaptic *inputs* rather than the axon action "output"), the notion that a pair of reversal potentials place upper and lower bounds on membrane voltage excursions will be preserved.

1.6 The Tuckwell Neuron

The Hodgkin–Huxley neuron provides a faithful mathematical model of the action potential. However, action potentials are never seen in scalp EEG records. This is because *action* potentials have very fast rise and fall times which are strongly low-pass filtered by the cerebrospinal fluid, skull, and scalp tissue that intervene between the brain surface and scalp electrode. In fact, what is seen at the scalp are the much more slowly varying fluctuations in the spatially- and temporally-averaged *local* potentials of the excitatory neurons.

In order to model the EEG signal, we need to be able to calculate the soma voltage which results from a membrane integration of all the incoming presynaptic activity: the inflowing

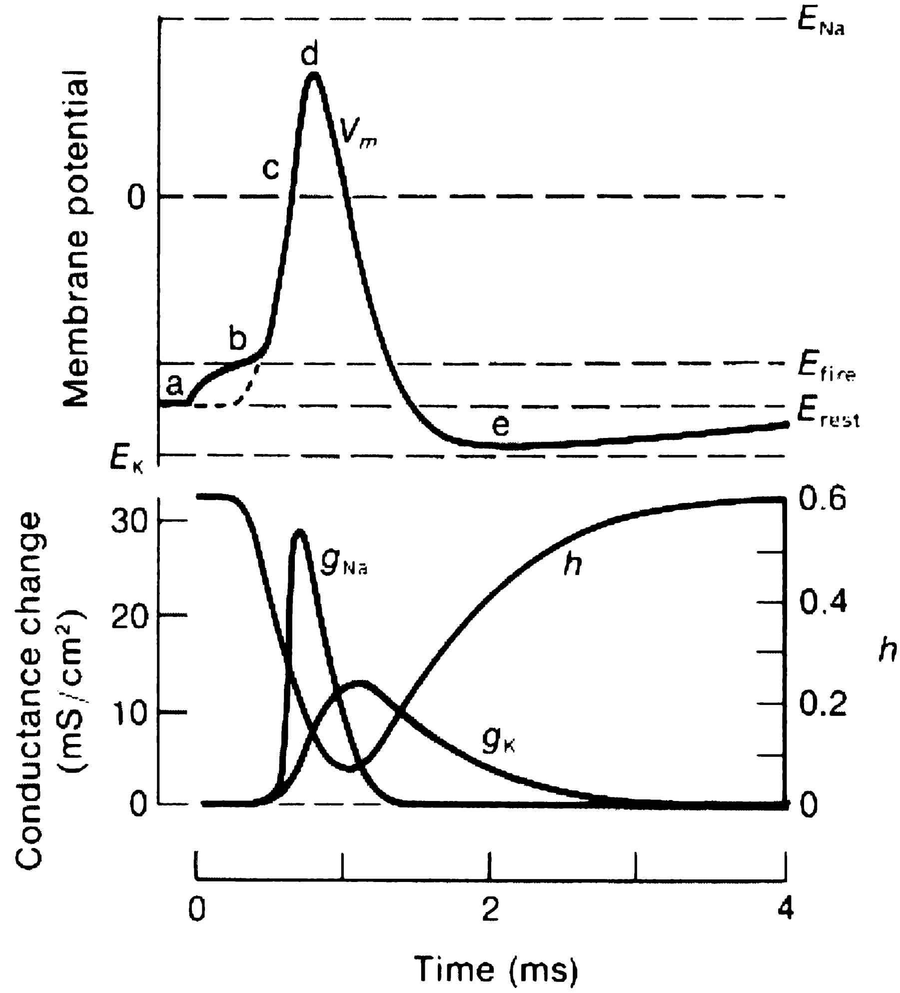

Figure 1.9: Predictions from the Hodgkin–Huxley model for the formation of an action potential (top figure) via differentially-timed changes in sodium and potassium conductances (bottom figure). Here, V_m is the membrane voltage, E_{fire} is the firing threshold, E_{Na} and E_{K} are the sodium and potassium Nernst potentials. Also plotted in the lower figure is the sodium inactivation parameter h. [From Halsey and Smith (1970), after Hodgkin and Huxley (1952)]

EPSCs (excitatory postsynaptic currents) minus the outflowing IPSCs (inhibitory postsynaptic currents). But no matter how high the integrated soma voltage gets, the neuron is *not* permitted to fire off action potentials!—otherwise the soma voltage time-series will contain spikes. Instead, the averaged *effect* of a train of action potentials on the neural population can be preserved via a sigmoid (i.e., S-shaped; see Fig. 3.2 on p. 42) mapping from average soma voltage to average spike-rate, and it is this output spike-*rate* (not the spikes themselves) which will determine the presynaptic activity and hence the average postsynaptic voltage.

The Liley neuron (to be described shortly) models the formation of (spike-free) EEG by interacting excitatory and inhibitory populations of neurons. Because the Liley neuron never "fires," it is intuitively helpful to approach it as a generalization of the *Tuckwell subthreshold neuron* described in Tuckwell (1988b, p. 9).

The first step is to replace the Fig. 1.7 sodium, chloride, and potassium batteries, and their associated conductances, with a single battery V_{rest} in series with resting conductance g_{rest}. The resulting circuit is shown in Fig. 1.10. The neuron is maintained in this −70 mV resting state by various ion pumps working in the background to keep the ion concentration gradients, and therefore the ion batteries, fully "charged."

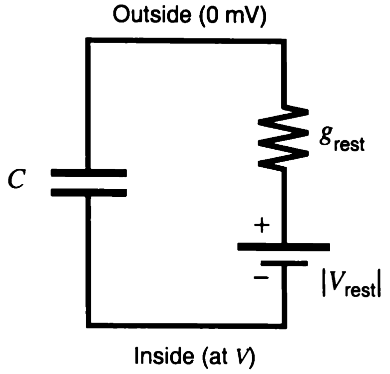

Figure 1.10: Equivalent circuit of the resting neuron. The combined effects of the Na$^+$, Cl$^-$, and K$^+$ non-gated ion channels of Fig. 1.7 are represented here by a single channel of constant conductance g_{rest} driven by an eternal battery of voltage $V_{\text{rest}} = -70$ mV.

Next, we couple in the synaptic inputs. For simplicity, we will follow Tuckwell in assuming that there is only one ion species involved in excitation and only one involved in inhibition. Then their Nernst potentials will be the synaptic reversal potentials, denoted V_E and V_I. The circuit for the Tuckwell neuron appears in Fig. 1.11.

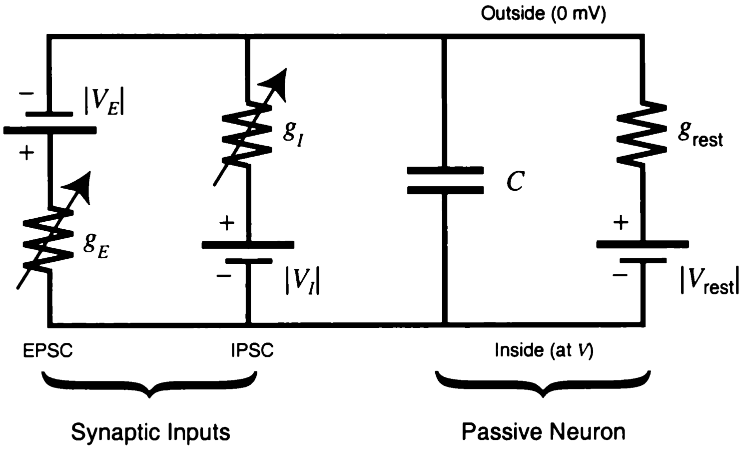

Figure 1.11: The Tuckwell subthreshold neuron. The membrane capacitor integrates synaptic input currents to give a graded local potential V; the *population-average* local potential is assumed to be proportional to scalp-measured EEG. This neuron never fires off an action potential.

Total currents sum to zero, giving

$$C\frac{dV}{dt} = (V_{\text{rest}} - V)\,g_{\text{rest}} + (V_E - V)\,g_E + (V_I - V)\,g_I\,. \tag{1.14}$$

Looking ahead a little (see Table 3.1[6] on p. 40), Liley chooses reversal potentials which roughly correspond to those of sodium for an excitatory neurotransmitter release, and to potassium for an inhibitory neurotransmitter release:

$$\begin{aligned} V_E &= +45\text{ mV} \approx V_{\text{Na}}, \\ V_I &= -90\text{ mV} \approx V_{\text{K}}\,. \end{aligned}$$

---

[6] But note the change in nomenclature: $V_E \to h_e^{\text{rev}}$; $V_I \to h_i^{\text{rev}}$

However, as already pointed out in Sect. 1.3.1, it is the increase in *chloride* permeability which is the source of GABAergic anaesthetic action, suggesting that the appropriate IPSP reversal potential would be V_{Cl} rather than V_{K}. Examining the reversal potentials listed in Table 1.1 (p. 11) we see that $V_{\mathrm{Cl}} \approx -90$ mV, so it seems reasonable to assume that for the purposes of modelling anaesthetic action, an ingress of Cl^- is equivalent to an egress of K^+—either of these ion fluxes will tend to hyperpolarize the nerve cell.

1.7 The Liley Neuron

Although there are some common elements between the Liley neuron and the Tuckwell subthreshold neuron, the Liley model (Liley, 1997; Liley *et al.*, 1999, 2002) is much more ambitious. The Liley model is an attempt to reproduce the scalp-measured EEG signal generated by a cortical *macrocolumn*: an organized assembly of excitatory and inhibitory neurons acting cooperatively within a small volume of the cerebral cortex. Figure 1.12 is a schematic representation

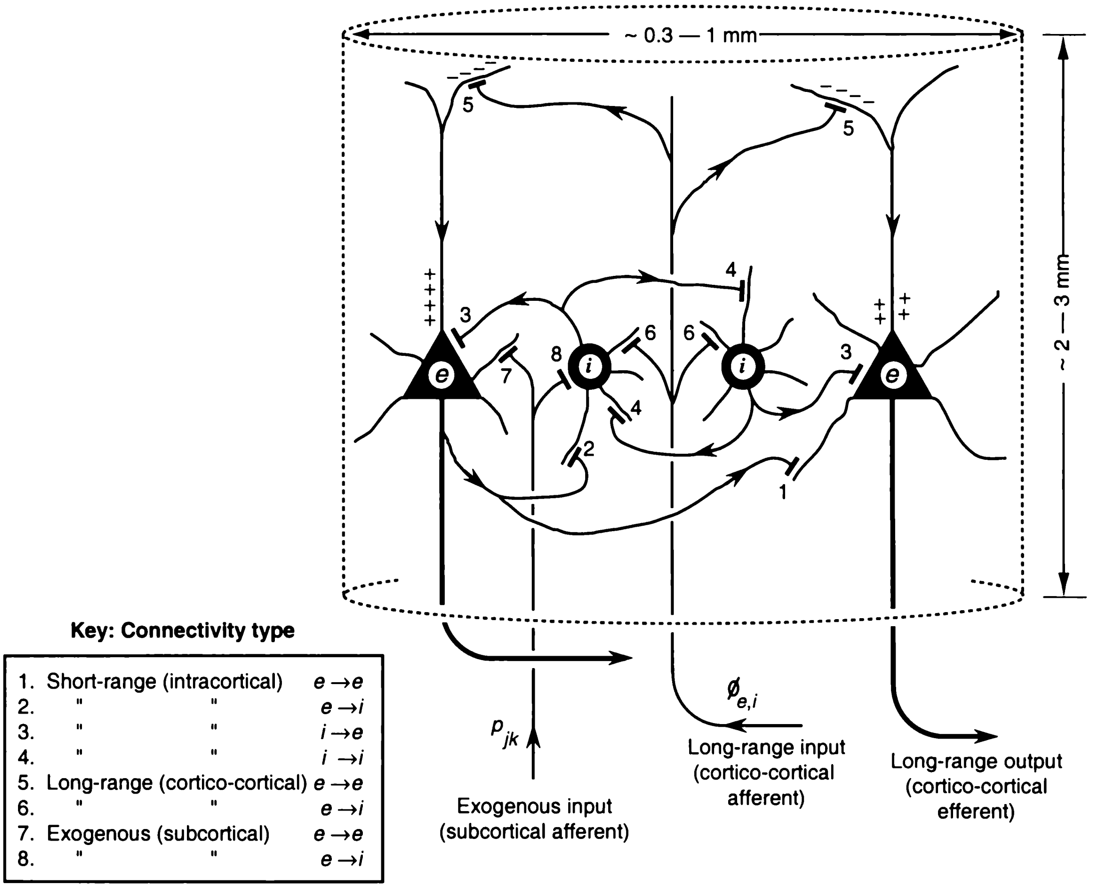

Figure 1.12: Schematic representation of the connective topology within a cortical macrocolumn. Only four of the ~100,000 neurons are shown. Triangles are excitatory (pyramidal) cells which receive excitatory input via apical dendrites (e.g., connection type 5) and basal dendrites (1, 7); and inhibitory input directly at the cell body (3). Circles are inhibitory (stellate or basket) cells receiving input from dendritic connections (2, 4, 6) and at the cell body (8). Excitatory output from the macrocolumn is via trunk-lines (axons) shown bold. The symbol $\phi_{e,i}$ represents long-range input to the excitatory and inhibitory populations from distant macrocolumns, and p_{jk} represents input from the subcortex (e.g., thalamus and brainstem). (For clarity, I have omitted p_{ie} and p_{ii} exogenous inputs corresponding to connection types 9 and 10 respectively.) [Drawn from sketches supplied by J. Sleigh and D. Liley (personal communication)]

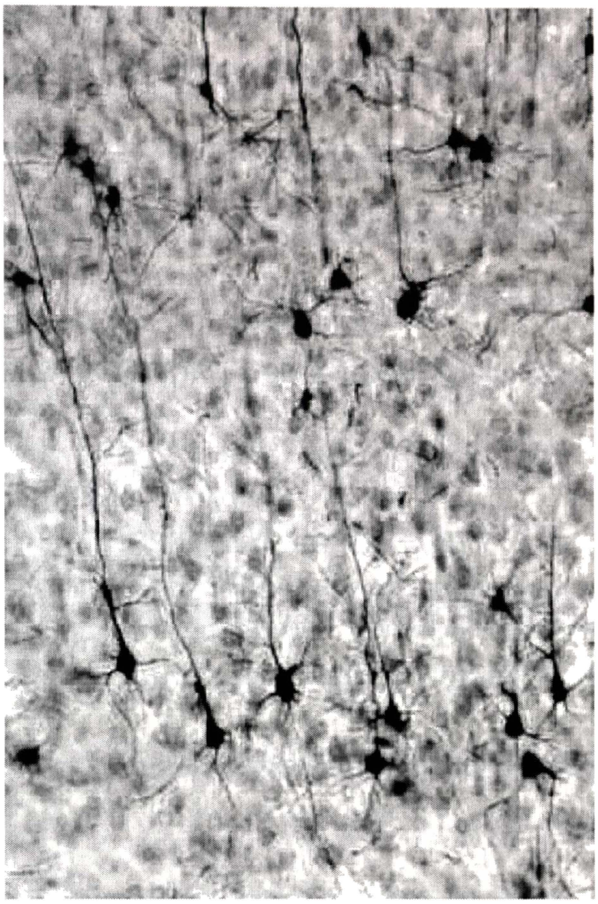

Figure 1.13: Photomicrograph of Golgi-stained pyramidal cells in a neural preparation. The Golgi method, based on silver reagents used in photography, randomly stains about 1–2% of exposed nerve cells. The long parallel traces are the dendritic spines which descend to apex of the pyramidal-shaped cell body. The axon exits from the base of the cell. These are excitatory nerve cells; the parallel alignment of their dendritic trees provides an efficient dipole radiation pattern when the cells act cooperatively. [Source of graphic: M. Nelson lecture notes at `http://soma.npa.uiuc.edu/courses/bio303`]

Figure 1.14: Higher magnification view of pyramidal nerve cells and their parallel dendritic structure. [Source of graphic: C. L. Williams lecture notes at `http://www.duke.edu/web/psy91/williams`]

of such an assembly which can be thought of as occupying a cylindrical volume of diameter ~0.3–1 mm, and containing 40 000–100 000 neurons. The excitatory (pyramidal) cells make up ~85% of the total number of neurons, and the inhibitory (stellate and basket) cells comprise the balancing 15% (Braitenberg and Schüz, 1991).

There are actually *two* Liley "neurons" per macrocolumn. The first "neuron" is a spatial average representing the *population of excitatory neurons*, and the second represents the *population of inhibitory neurons* within the macrocolumn. The average membrane voltage of the excitatory population is given the symbol h_e, and is assumed to be proportional to the scalp EEG, while the average voltage of the inhibitory population is written h_i, and is assumed to have negligible *direct* effect on the EEG. Nevertheless, the inhibitory population plays a crucial moderating role on the behaviour of the excitatory population, so exerts a powerful *indirect* effect on the EEG.

There are two reasons why (direct) h_i contributions to EEG are thought to be negligible. First, excitatory neurons outnumber inhibitory neurons by about 6:1. Second, microscopic examinations of stained cortical preparations reveal that the dendrites and axons of the excitatory neurons tend to line up perpendicular to the cortical surface and parallel to each other (see Figures 1.13 and 1.14), thus their dendritic currents act as a palisade of small, aligned *current dipoles*[7] whose electric fields sum with increasing area. In contrast, the inhibitory neurons are smaller and have their dendrites oriented at random with nearly spherical symmetry, so their electric field is mainly limited to the region of dendritic arborization with negligible influence at the scalp.

1.7.1 Mapping from Tuckwell → Liley

In Fig. 1.15 I have drawn up two Tuckwell-like subthreshold "average neurons." One "neuron" represents the *population* of excitatory neurons in the macrocolumn, and the other represents the population of inhibitory neurons. The following list gives the symbol remappings I have

---

[7] A current dipole is an abstraction that has the dimensions of current times length; the length is usually taken as infinitesimal. [Source: Wellcome Trust Laboratory for MEG Studies, `www.aston.ac.uk/psychology/meg`]

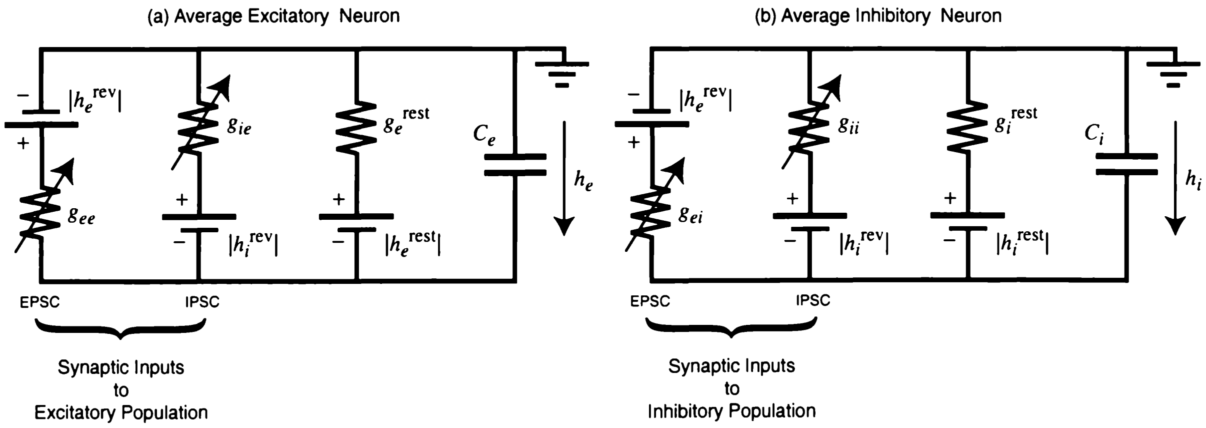
(a) Average Excitatory Neuron

(b) Average Inhibitory Neuron

Figure 1.15: Equivalent circuit for the (a) excitatory and (b) inhibitory neural populations comprising the macrocolumn of Fig. 1.12. This is the Liley generalization of the Tuckwell subthreshold neuron of Fig. 1.11.

used to transform from the single Tuckwell neuron of Fig. 1.11 to the Liley population neurons of Fig. 1.15:

Tuckwell neuron	$\longrightarrow$	**Liley "neurons"**	
V	$\longrightarrow$	h_e, h_i	membrane voltage
V_E	$\longrightarrow$	h_e^{rev}	excitatory reversal potential = +45 mV
V_I	$\longrightarrow$	h_i^{rev}	inhibitory reversal potential = −90 mV
V_{rest}	$\longrightarrow$	$h_e^{\text{rest}}, h_i^{\text{rest}}$	resting potential = −70 mV
C	$\longrightarrow$	C_e, C_i	membrane capacitance
g_E	$\longrightarrow$	g_{ee}, g_{ie}	conductance for excitatory-reversal battery
g_I	$\longrightarrow$	g_{ei}, g_{ii}	conductance for inhibitory-reversal battery
g_{rest}	$\longrightarrow$	$g_e^{\text{rest}}, g_i^{\text{rest}}$	conductance for resting-potential battery

The $h_{e,i}$ equations of motion for the Fig. 1.15 circuit are,

$$C_e \frac{dh_e}{dt} = \left(h_e^{\text{rev}} - h_e\right) g_{ee} + \left(h_i^{\text{rev}} - h_e\right) g_{ie} + \left(h_e^{\text{rest}} - h_e\right) g_e^{\text{rest}} \tag{1.15a}$$

$$C_i \frac{dh_i}{dt} = \left(h_e^{\text{rev}} - h_i\right) g_{ei} + \left(h_i^{\text{rev}} - h_i\right) g_{ii} + \left(h_i^{\text{rest}} - h_i\right) g_i^{\text{rest}} . \tag{1.15b}$$

In the *absence* of synaptic inputs, we can define a pair of membrane time-constants,

$$\tau_e = C_e / g_e^{\text{rest}} \equiv C_e R_e \tag{1.16a}$$

$$\tau_i = C_i / g_i^{\text{rest}} \equiv C_i R_i \tag{1.16b}$$

where R_e, R_i are the excitatory and inhibitory membrane resistances. Provided the time-averaged synaptic conductances are small (i.e., the synaptic PSPs are brief and infrequent), then the $\tau_{e,i}$ time-"constants" give us the decay time for the cell to relax back to its resting voltage. If synaptic activity is high, the time-averaged synaptic conductances g_{jk} will be no longer negligible, so the total membrane resistance will be lowered, and the response times will be *faster* than the nominal relaxation times defined in Eq. (1.16) (Tuckwell, 1988b, p. 7). In other words, the *effective* membrane time-"constant" is actually membrane-voltage dependent. For the present modelling work, we will follow Liley in taking the membrane time-constant as a fixed number.

Dividing Eq. (1.15) by g_e^{rest}, g_i^{rest} and rearranging gives,

$$\tau_e \frac{dh_e}{dt} = \left(h_e^{\text{rest}} - h_e\right) + \left(h_e^{\text{rev}} - h_e\right) \frac{g_{ee}}{g_e^{\text{rest}}} + \left(h_i^{\text{rev}} - h_e\right) \frac{g_{ie}}{g_e^{\text{rest}}} \tag{1.17a}$$

$$\tau_i \frac{dh_i}{dt} = \left(h_i^{\text{rest}} - h_i\right) + \left(h_e^{\text{rev}} - h_i\right) \frac{g_{ei}}{g_i^{\text{rest}}} + \left(h_i^{\text{rev}} - h_i\right) \frac{g_{ii}}{g_i^{\text{rest}}} . \tag{1.17b}$$

These equations of motion are directly comparable with the standard Liley formulation given below as Eq. (1.20). We see that the conductance ratios of Eq. (1.17) become voltage ratios in Eq. (1.20):

$$\frac{g_{jk}}{g_k^{\text{rest}}} = \frac{V_{jk}}{\left|h_j^{\text{rev}} - h_k^{\text{rest}}\right|}, \quad \text{where} \quad j,k \in \{e,i\}. \tag{1.18}$$

The denominators of both sides are constants, so there is a direct proportionality between synaptic conductance g_{jk} and voltage increment V_{jk} at the C_k capacitor,

$$V_{jk} \propto g_{jk}. \tag{1.19}$$

Note that V_{jk} is *not* the voltage across the g_{jk} conductance; V_{jk} is the *incremental change* in the h_k soma voltage resulting from an incremental change in the g_{jk} input conductance.

1.7.2 Local Feedback within the Macrocolumn

Not immediately apparent from Fig. 1.15 is the fact that the two circuits are very strongly coupled; this fact is hinted at by the double-subscripting on the four synaptic conductances in Fig. 1.15. For example, g_{ei} implies an $e \rightarrow i$ effect, and is read, "the average conductance determined at the inhibitory neuron because of synaptic spike-rate input from an excitatory source." This excitatory source could be spike-output from the *local* macrocolumn, or from a *distant* macrocolumn somewhere else in the cortex via cortico-cortical connection, or *exogenous* input coming up from the subcortex (e.g., thalamus or brainstem). These various connection types appear in the macrocolumn schematic of Fig. 1.12 (p. 18).

By definition, a subthreshold neuron never fires off an action potential. To avoid having to incorporate the detailed and complicated Hodgkin–Huxley action-potential dynamics, yet still

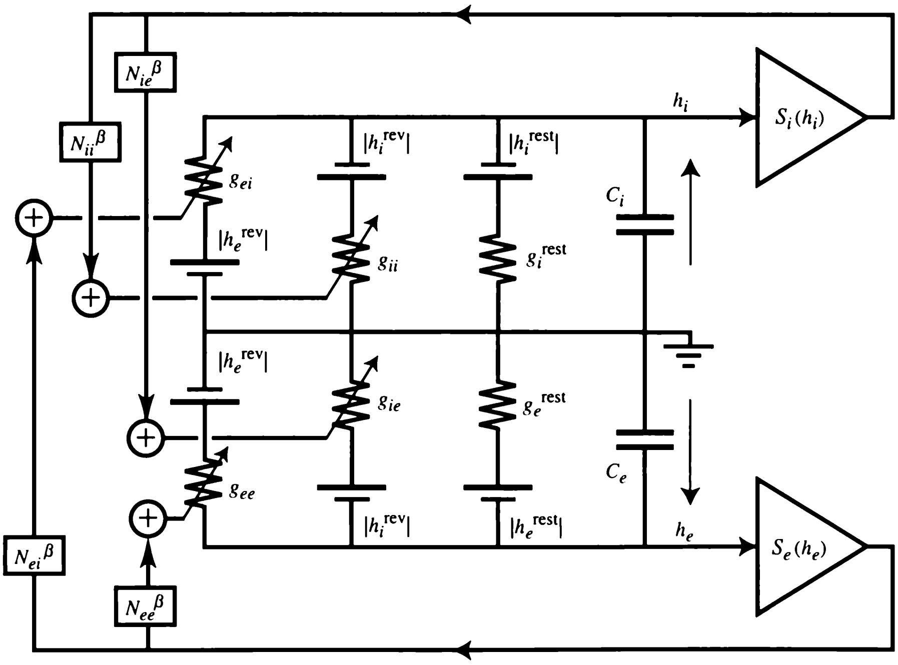

Figure 1.16: Equivalent circuit for the Liley macrocolumn with local feedbacks explicitly shown. The excitatory and inhibitory output voltages $h_{e,i}$ are coupled back to the four g_{jk} synaptic input conductances via a pair of nonlinear (sigmoidal) voltage-to-spike-rate converters represented by the $\mathcal{S}_e(h_e)$ (lower) and $\mathcal{S}_i(h_i)$ (upper) triangles. The four N_{jk}^{β} boxes are constant multiplicative scale-factors that represent the degree of *local* inter-connectedness between the excitatory and inhibitory populations within the macrocolumn. All possible local feedbacks are allowed: $e \rightarrow e$, $e \rightarrow i$, $i \rightarrow e$, $i \rightarrow i$.

retain the spatially-averaged *effect* of neural activity arriving at the synaptic input receptors, the Liley model adopts an early idea from Wilson and Cowan (1972): that there exists a nonlinear sigmoidal mapping from soma voltage (input) to average firing rate (output). This spike-rate output then feeds back to the synaptic inputs to alter the population average soma voltage.

The $\mathcal{S}_e(h_e)$ and $\mathcal{S}_i(h_i)$ sigmoids used here (listed in Eq. (3.6) and plotted in Fig. 3.2) are S-shaped functions defined in terms of a preset maximum firing rate ($\mathcal{S}_{e,i}^{\max} = 1000\ \mathrm{s}^{-1}$), a threshold voltage ($\theta_{e,i} = -60$ mV), and a threshold "gain"[8] (g_e, $g_i = 0.28, 0.14\ (\mathrm{mV})^{-1}$).

Figure 1.16 shows how the excitatory and inhibitory soma voltages are coupled back into the four g_{jk} conductances via the pair of voltage-to-pulse-rate sigmoid functions; all possible local feedback types ($e \rightarrow e$, $e \rightarrow i$, $i \rightarrow e$, $i \rightarrow i$) are explicitly included. Equations (1.22, 1.23) below show how the sigmoid functions enter the Liley model.

1.7.3 The Liley Equations

I will now present the Liley macrocolumn equations, and then address the simplifications we will be applying in order to "solve" the Liley equations in the present context of modelling anaesthesia.

In their 1999 *Neurocomputing* paper, Liley, Cadusch, and Wright listed eight PDEs as defining their one-dimensional mean-field equations for population-average soma voltages. The first equation pair gives the equation of motion for the excitatory soma voltage h_e and the inhibitory soma voltage h_i:

$$\tau_e \frac{dh_e}{dt} = \left(h_e^{\mathrm{rest}} - h_e\right) + \left(h_e^{\mathrm{rev}} - h_e\right)\frac{V_{ee}(h_e)}{\left|h_e^{\mathrm{rev}} - h_e^{\mathrm{rest}}\right|} + \left(h_i^{\mathrm{rev}} - h_e\right)\frac{V_{ie}(h_i)}{\left|h_i^{\mathrm{rev}} - h_e^{\mathrm{rest}}\right|} \tag{1.20a}$$

$$\tau_i \frac{dh_i}{dt} = \left(h_i^{\mathrm{rest}} - h_i\right) + \left(h_e^{\mathrm{rev}} - h_i\right)\frac{V_{ei}(h_e)}{\left|h_e^{\mathrm{rev}} - h_i^{\mathrm{rest}}\right|} + \left(h_i^{\mathrm{rev}} - h_i\right)\frac{V_{ii}(h_i)}{\left|h_i^{\mathrm{rev}} - h_i^{\mathrm{rest}}\right|}\,. \tag{1.20b}$$

The τ_e, τ_i are the excitatory and inhibitory *RC* (resistance–capacitance) membrane time-constants. The four V_{jk} appearing on the right are the postsynaptic potential (PSP) changes in soma voltage arising from presynaptic inputs. For example, V_{ie} is inhibitory presynaptic input invading the excitatory membrane, and V_{ei} is excitatory presynaptic input invading the inhibitory membrane. The correspondence between Eq. (1.20) and the previously discussed conductance form of Eq. (1.17) has already been noted.

Tuckwell (1988a, p. 93) observes that experimental measurements of the PSPs shows a rapid-rise, slow-decay curve which is well approximated by the so-called *alpha-function*:

$$V_{\mathrm{PSP}} = \gamma t \exp(1 - \gamma t) \tag{1.21}$$

where the time-to-peak is given by $t = 1/\gamma$. The peak height is unity, and the total area under the curve is $1/\gamma$. Sample alpha-function plots are shown in Fig. 1.17. Because the alpha-function is a good representation of the PSP, Liley selects a particular form of second-order differential equation for the V_{jk} such that the alpha-function serves as the Green's function (impulse response) for the DE.

---

[8] The two sigmoid gain constants g_e, g_i are *not* to be confused with the four g_{jk} conductances; despite unfortunately similar nomenclature, the concepts are distinct.

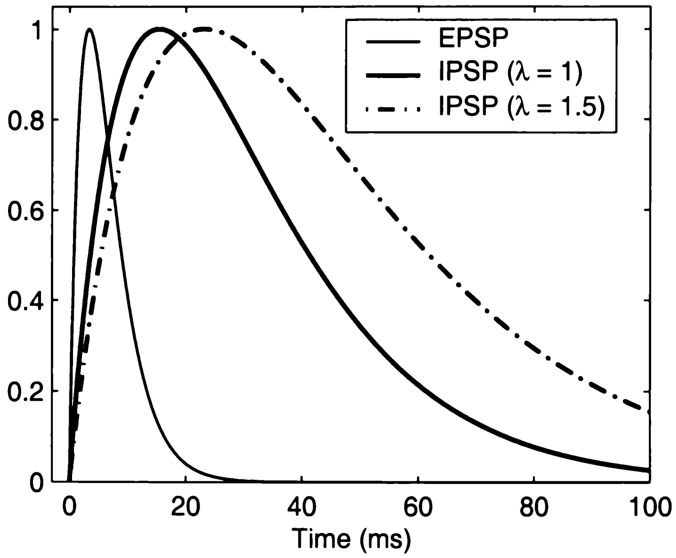

Figure 1.17: Impulse response for excitatory (light curve), inhibitory (bold), and anesthetic-modified inhibitory (bold-dashed) postsynaptic membranes. These curves are plots of the alpha function $V_{\text{PSP}} = \gamma t \exp(1 - \gamma t)$ of Eq. (1.21). For application to the Liley model, the heights are scaled by the respective EPSP and IPSP amplitudes, $G_{e,i} = 0.18, 0.37$ mV. The rate constants, in $(\text{ms})^{-1}$, for the three curves are $\gamma_e = 0.30$, $\gamma_i = 0.065$, $\overline{\gamma_i} = 0.043$. The symbol λ is our dimensionless anaesthetic-effect scale factor giving the lengthening of the IPSP duration: $(\overline{\gamma_i})^{-1} = \lambda/\gamma_i$.

The equations for the four V_{jk} PSPs are:

$$\left(\frac{d}{dt} + \gamma_e\right)^2 V_{ee}(h_e) = \left[N_{ee}^{\beta}\, S_e(h_e) + \phi_e(h_e) + p_{ee}\right] G_e \gamma_e e \tag{1.22a}$$

$$\left(\frac{d}{dt} + \gamma_e\right)^2 V_{ei}(h_e) = \left[N_{ei}^{\beta}\, S_e(h_e) + \phi_i(h_e) + p_{ei}\right] G_e \gamma_e e \tag{1.22b}$$

$$\left(\frac{d}{dt} + \gamma_i\right)^2 V_{ie}(h_i) = \left[N_{ie}^{\beta}\, S_i(h_i) + p_{ie}\right] G_i \gamma_i e \tag{1.23a}$$

$$\left(\frac{d}{dt} + \gamma_i\right)^2 V_{ii}(h_i) = \left[N_{ii}^{\beta}\, S_i(h_i) + p_{ii}\right] G_i \gamma_i e \tag{1.23b}$$

The first pair of equations give the time-evolution of an EPSP: the voltage response to an excitatory neurotransmitter impulse[9] arriving at the synapse of an excitatory (Eq. (1.22a)) or inhibitory (Eq. (1.22b)) nerve cell. The time-course of the response is set by the excitatory rate-constant γ_e (see Table 3.1 on p. 40 for values), and the amplitude by G_e, the EPSP peak. The second equation pair describes the time-course of IPSP: the voltage response to an inhibitory impulse[10] arriving at the synapse of an excitatory (Eq. (1.23a)) or inhibitory (Eq. (1.23b)) nerve cell. The IPSP amplitude G_i and duration γ_i^{-1} are respectively larger and longer than the corresponding EPSP values—see Fig. 1.17 and Table3.1.

Note that the general characterizations—

---

[9] A δ-function-shaped flux of *excitatory* chemical flooding the AMPA or kainate receptor causing momentary ingress of Na^+ ions and consequent *depolarizing* (positive-going) voltage increment.

[10] A δ-function-shaped flux of *inhibitory* chemical flooding the GABA$_\text{A}$ receptor causing momentary egress of K^+ or ingress of Cl^- ions and consequent *hyperpolarizing* (negative-going) voltage increment; the presence of GABAergic anaesthetic prolongs the duration of the IPSP.

$$\text{EPSP} \equiv \text{“excitatory event”}$$
$$\text{IPSP} \equiv \text{“inhibitory event”}$$

are *not* always true. For example, if the soma voltage is more positive than the reversal potential for Na^+ ions, then the arrival at the synapse of an “excitatory” chemical flux that opens the sodium channels will allow an *efflux* of Na^+ ions as the electric field forces sodium ions *outwards*, against their concentration gradient. Thus for this “over-voltage” case, the effect of the EPSP is to *lower* the soma voltage, and the EPSP has become an inhibitory event. This sign reversal of EPSP effect is automatically included in Eq. (1.20) by way of the $(h_e^{\text{rev}} - h_k)$ coefficient that scales the V_{ek} $(k = e, i)$ PSP term. Similarly, if the soma voltage is more negative than the reversal potential for K^+ (or Cl^-) ions (the “under-voltage” case), then the effect of an IPSP becomes excitatory. This sign reversal of EPSP and IPSP events provides a significant physiological constraint on soma voltages, yet apart from the Liley model, seems to have been ignored in all other mean-field models for the cortex.

Three terms contribute on the right of Eq. (1.22): *local* excitatory feedback from within the macrocolumn, *distant* excitatory input from other macrocolumns, and *exogenous* input entering the cortex from the brainstem. Considering the V_{ei} PSP of Eq. (1.22b) for example, the *local* feedback term is $N_{ei}^{\beta}\, \mathcal{S}_e(h_e)$ where N_{ei}^{β} is the estimated average number of $e \longrightarrow i$ connections synapsing on an inhibitory cell, and $\mathcal{S}_e(h_e)$ is the nonlinear sigmoidal function of Eq. (3.6) which maps local soma voltage to locally-generated spike rate. Activity generated by *distant* macrocolumns should be represented by $\phi_{ee}(h_e)$ and $\phi_{ei}(h_e)$, but this nomenclature is abbreviated to $\phi_e(h_e)$ in Eq. (1.22a) and to $\phi_i(h_e)$ in Eq. (1.22b) because long-range couplings from distant inhibitory cortical sources are unlikely (so the forms ϕ_{ie} and ϕ_{ii} never occur in the equations). The $\phi_e(h_e)$ and $\phi_i(h_e)$ cortico-cortical terms are governed by their own second-order differential equation (1.25) listed below. The p_{jk} *exogenous* terms retain a double-subscripting because the Liley model assumes that the input coming up from the brainstem can be of all four types. Typically the four exogenous terms will be set equal to a constant value (see Table 3.1), or will have a small amount of white noise superimposed to provide a weak stochastic driving force.

The time-course for the IPSP at the excitatory and inhibitory populations is given by Eq. (1.23). The form of these equations is identical to that for the EPSP pair, apart from the anticipated absence of cortico-cortical inhibitory-source ϕ-terms.

The IPSP rate-constant is γ_i. In order to model the effect of a GABAergic anaesthetic such as propofol, we will be assuming that the IPSP rate-“constant” (i.e., inverse time-constant) scales inversely with anaesthetic effect, and so replace γ_i in Eq. (1.23) by $\overline{\gamma_i}$ defined as,

$$\gamma_i \longrightarrow \overline{\gamma_i} = \frac{\gamma_i}{\lambda} \tag{1.24}$$

where λ is a dimensionless scale-factor assumed to be proportional to anaesthetic concentration. Thus an increase in λ *reduces* the IPSP rate-constant and *increases* the IPSP duration.

The final pair of equations in the eight-equation Liley set are a form of 1D wave equations for the long-distance macrocolumn contributions to the population EPSP and IPSP events. These equations read:

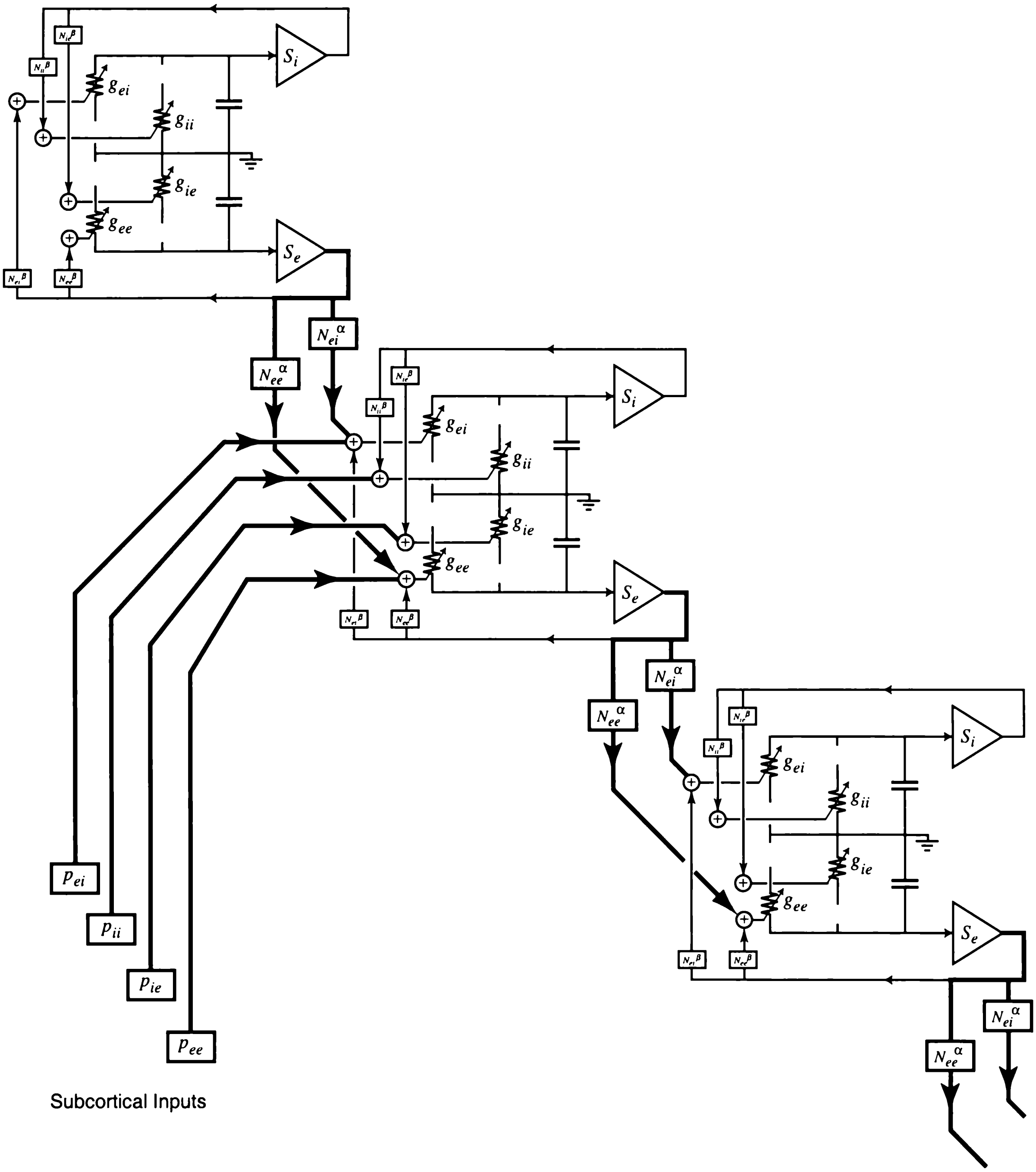

Figure 1.18: Lumped equivalent circuit for the full Liley equations. The cerebral cortex is pictured as a 1D chain of discrete macrocolumns interconnected via their excitatory sigmoid outputs. The Liley model is the continuum limit of this picture, forming a 1D line (or 2D sheet) of macrocolumn "mass." The inter-macrocolumn communication is governed by 1D (or 2D) wave equations to include propagation delay effects. In addition, the entire macrocolumn mass is buffeted by p_{jk} exogenous inputs coming up from excitatory and inhibitory sources in the subcortex. All inputs—local, distant, and external—are combined at the $\oplus$ summing points to determine the g_{jk} synaptic conductances. The resulting synaptic currents are integrated at the soma capacitor to give a soma voltage h_k $(k = e, i)$. To aid clarity, the "batteries" (reversal and resting) have been omitted. The complete schematic would show independent p_{jk} subcortical inputs entering *every* macrocolumn (not just the middle macrocolumn as shown here).

$$\left[\left(\frac{\partial}{\partial t} + \bar{v}\,\Lambda_{ee}\right)^2 - \bar{v}^2 \frac{\partial^2}{\partial x^2}\right] \phi_e(h_e) = \bar{v}\,\Lambda_{ee}\,N_{ee}^{\alpha}\left(\frac{\partial}{\partial t} + \bar{v}\,\Lambda_{ee}\right) \mathcal{S}_e(h_e) \tag{1.25a}$$

$$\left[\left(\frac{\partial}{\partial t} + \bar{v}\,\Lambda_{ei}\right)^2 - \bar{v}^2 \frac{\partial^2}{\partial x^2}\right] \phi_i(h_e) = \bar{v}\,\Lambda_{ei}\,N_{ei}^{\alpha}\left(\frac{\partial}{\partial t} + \bar{v}\,\Lambda_{ei}\right) \mathcal{S}_e(h_e) \tag{1.25b}$$

Here $\bar{v}$ is the mean conduction speed along cortico-cortical fibres; Λ_{ee} and Λ_{ei} are the characteristic inverse-length scales for $e \to e$ and $e \to i$ connections (connectivity is assumed to drop off exponentially with distance); N_{ee}^{α} and N_{ei}^{α} are the estimated total number of $e \to e$ and $e \to i$ connections reaching an excitatory or inhibitory cell via cortico-cortical fibres.

Figure 1.18 completes the circuit diagram of Fig. 1.16 by showing the three classes of input to the macrocolumn conductances—local, long-distance cortical, and subcortical. The macrocolumns are linked to form a continuous 1D line of neural mass; in principle this could be generalized to a 2D mesh to better represent cortical topology.

This thesis will assume that the cortex is spatially uniform, therefore the 1D Laplacian appearing in Eq. (1.25) immediately will be set to zero. I will refer to the resulting spatially-homogeneous set of eight ODEs as the "full Liley equations" since no assumptions have yet been made about separation of PSP and membrane time-scales. A dramatic simplification is achieved if we assume that, compared with the membrane time-constant, the processes associated with the PSP kinetics are very fast, so the PSP inputs to the membrane capacitor can be set equal to their steady-state values. This is done by setting to zero all of the time-derivatives appearing in Eqs (1.22, 1.23, 1.25)—but not Eq. (1.20). The full Liley equations are thereby collapsed to a pair of first-order nonlinear ODEs. These define the "adiabatic equations" that will be the primary focus for the anaesthetics modelling reported here.

1.7.4 A Note on Nomenclature for the PSPs

The four V_{jk} ($j, k \in \{e, i\}$) PSP input terms have the dimensions of voltage. Despite this, in Liley *et al.* (1999) and Liley *et al.* (2002) the authors write the PSP inputs with symbol I_{jk}, giving the unfortunate impression that these are input *currents*. To remain consistent with these source papers (and to avoid possible confusion for the reader attempting to compare the present work with the Liley references) I have (reluctantly) adopted the Liley I_{jk} PSP convention for the remainder of this thesis.[11]

Another point of nomenclature must be flagged. As part of the development to show how the Liley treatment of reversal potentials for the macrocolumn can be viewed as a generalization of the Tuckwell formulation for the subthreshold neuron, I demonstrated that the conductance ratios of Eq. (1.17) become voltage ratios in Eq. (1.20). Thus, for example,

$$\left(h_e^{\text{rev}} - h_i\right)\frac{g_{ei}}{g_i^{\text{rest}}} \longrightarrow \left(h_e^{\text{rev}} - h_i\right)\frac{V_{ei}(h_e)}{\left|h_e^{\text{rev}} - h_i^{\text{rest}}\right|} \tag{1.26}$$

for the $e \to i$ synaptic input term. In the standard Liley nomenclature, the parts on the right involving the reversal potential are combined to define a dimensionless synaptic weighting factor $\psi_{ei}(h_i)$,

---

[11] And may even have referred to these terms as "currents" from time to time—may the author be forgiven!

$$\psi_{ei}(h_i) \equiv \frac{h_e^{\text{rev}} - h_i}{\left|h_e^{\text{rev}} - h_i^{\text{rest}}\right|} \tag{1.27}$$

that multiplies the synaptic input voltage. The right-hand side of Eq. (1.26) then becomes,

$$\left(h_e^{\text{rev}} - h_i\right) \frac{V_{ei}(h_e)}{\left|h_e^{\text{rev}} - h_i^{\text{rest}}\right|} \equiv \psi_{ei}(h_i)\, I_{ei}(h_e) \tag{1.28}$$

where I have applied the $V_{jk} \longrightarrow I_{jk}$ change of symbols.

For convenient reference, here are the eight spatially-homogeneous Liley equations written in "standard" form:

$$\tau_e \frac{dh_e}{dt} = \left(h_e^{\text{rest}} - h_e\right) + \psi_{ee}(h_e)\, I_{ee}(h_e) + \psi_{ie}(h_e)\, I_{ie}(h_i) \tag{1.29a}$$

$$\tau_i \frac{dh_i}{dt} = \left(h_i^{\text{rest}} - h_i\right) + \psi_{ei}(h_i)\, I_{ei}(h_e) + \psi_{ii}(h_i)\, I_{ii}(h_i) \tag{1.29b}$$

$$\left(\frac{d}{dt} + \gamma_e\right)^2 I_{ee}(h_e) = \left[N_{ee}^{\beta}\, \mathcal{S}_e(h_e) + \phi_e(h_e) + p_{ee}\right] G_e \gamma_e e \tag{1.30a}$$

$$\left(\frac{d}{dt} + \gamma_e\right)^2 I_{ei}(h_e) = \left[N_{ei}^{\beta}\, \mathcal{S}_e(h_e) + \phi_i(h_e) + p_{ei}\right] G_e \gamma_e e \tag{1.30b}$$

$$\left(\frac{d}{dt} + \gamma_i\right)^2 I_{ie}(h_i) = \left[N_{ie}^{\beta}\, \mathcal{S}_i(h_i) + p_{ie}\right] G_i \gamma_i e \tag{1.31a}$$

$$\left(\frac{d}{dt} + \gamma_i\right)^2 I_{ii}(h_i) = \left[N_{ii}^{\beta}\, \mathcal{S}_i(h_i) + p_{ii}\right] G_i \gamma_i e \tag{1.31b}$$

$$\left(\frac{d}{dt} + \bar{v}\,\Lambda_{ee}\right)^2 \phi_e(h_e) = \bar{v}\,\Lambda_{ee}\, N_{ee}^{\alpha} \left(\frac{d}{dt} + \bar{v}\,\Lambda_{ee}\right) \mathcal{S}_e(h_e) \tag{1.32a}$$

$$\left(\frac{d}{dt} + \bar{v}\,\Lambda_{ei}\right)^2 \phi_i(h_e) = \bar{v}\,\Lambda_{ei}\, N_{ei}^{\alpha} \left(\frac{d}{dt} + \bar{v}\,\Lambda_{ei}\right) \mathcal{S}_e(h_e)\,. \tag{1.32b}$$

1.8 Alternative Mean-Field Models for Neural Action

I conclude this chapter with a brief survey of other mean-field or "mass action" models for cortical activity.

The first mean-field approach was presented by Beurle (1956). He modelled an exclusively excitatory population of neurons (i.e., no inhibitory neurons included) joined by fibres whose connection densities drop off exponentially with neuron separation. He assumed that a neuron becomes active and fires only when its membrane voltage exceeds a threshold value, and that subsequent to firing, a neuron has a *refractory period* during which it cannot fire again (its threshold potential is dependent on its history: after firing, the threshold is initially very high before decaying to its resting value). Because during the refractory period the neuron is insensitive to further stimulation, the refractory state provides a crude form of control that prevents runaway global firing, but this seems insufficient to provide the level of stability that a real cortex possesses. Griffith (1963) resolved the stability paradox by introducing inhibitory synapses that reduce activity by hyperpolarizing the postsynaptic neuron.

The Wilson and Cowan (1972, 1973) model assumed that synaptic events were much *slower* than the membrane time-constant (i.e., they took the opposite extreme to the "slow-membrane" case we consider here), and their PSPs were effectively rectangular functions differing only in sign for EPSP and IPSP events. Two innovations that have been maintained in later mean-field models include the use of a nonlinear sigmoid function to map from membrane voltage to firing rate, and the notion that inhibition acts purely locally.

Freeman (1975) formalized the concept of cortical "mass action" in terms of an interacting hierarchy of neural sets or aggregates, each set having different interconnection properties. His modelling work included synaptic and dendritic delays, and he noted that the inclusion of delays in feedback loops could lead to oscillatory behaviour in populations of excitatory and inhibitory neurons.

Nunez (1974, 1981) developed an integral wave equation to describe the spatial and temporal variation of cortical voltage generated by neural masses. His model predicted oscillations whose character depended on the relative numbers of excitatory and inhibitory connections between neural aggregates and on the velocity distribution functions for action potential propagation. For certain choices of boundary conditions, standing waves were predicted, and Nunez suggested that these could be the source of cortical rhythms such as alpha (8–14 Hz) seen in the EEG.

Jirsa and Haken (1996, 1997) generalized the work of Wilson and Cowan and of Nunez to derive mean-field equations for the dendritic currents. As with Wilson and Cowan, the Jirsa and Haken EPSC and IPSC functions only differed in sign (and not amplitude or time-course). The activity of the inhibitory population was assumed to be a function of the activity of the excitatory population, rather than being determined by the membrane potential of the inhibitory population itself.

Wright and Liley (1996) used anatomical data to derive expressions for the number of synapses between neurons as a function of neuron type and separation. In their mean-field modelling they used a sigmoid form for the mapping between membrane voltage and spike rate, and approximated the PSPs as triangular functions.

Robinson, Rennie, and Wright (1997) improved on the Wright and Liley model by replacing the triangular PSP with a more physiologically realistic function. They investigated steady-state behaviour, and found that there could be either one or three steady states, and that in the latter case, the middle state was unstable. In their subsequent paper (Robinson, Rennie, Wright, and Bourke, 1998), they classified their steady-state solutions in terms of a ratio ℓ_i/ℓ_e where ℓ_i (ℓ_e) is the nett postsynaptic response per unit synaptic concentration of inhibitory (excitatory) neurotransmitter. They found that the three-state case occurred when $\ell_i/\ell_e \approx 1$, i.e., when the inhibitory and excitatory responses were of similar magnitude. However, if the inhibitory response was strongly dominant over excitatory (or vice versa), the system collapsed to a single steady state. The Robinson ℓ_i "inhibitory response" concept relates directly to the product (IPSP peak) × (IPSP duration) of the present Liley model:

$$\ell_i \sim G_i\,(\overline{\gamma_i})^{-1} \equiv \lambda G_i/\gamma_i \tag{1.33}$$

where, in our case, G_i (IPSP amplitude) and γ_i (IPSP rate-constant) are fixed, but λ varies with anaesthetic concentration. Thus our λ is proportional to the Robinson ℓ_i/ℓ_e ratio: $\lambda \gg 1$ corresponds to extreme inhibition leading to "coma," while at the opposite extreme, $\lambda \ll 1$ corresponds to excessive excitation leading to "seizure."

The work of Liley, Cadusch, and Wright (1999) and of Liley, Cadusch, and Dafilis (2002) extended these earlier theories by improving the treatment of excitatory and inhibitory neurotransmitter kinetics, and by incorporating, apparently for the first time in a mean-field model, the constraints on depolarization and hyperpolarization voltage extremes enforced by cell reversal potentials. It will become apparent later in this thesis that for the purposes of adiabatic (i.e., "slow membrane") modelling of anaesthesia, the inclusion of excitatory and inhibitory ion-reversal potentials is essential.

Chapter 2

Elements of Fourier Transform Theory

In this chapter I present selected elements of Fourier transform theory which are pertinent to the analysis and stochastic simulation of EEG time-series.

2.1 Continuous-Time Representation

EEG signals are *not*, in principle, time-limited. Like the eternal sinewave, they do not have finite energy. This means that we cannot use the "standard" form for the Fourier transform $X(f)$ of a time signal $x(t)$

$$X(f) = \int_{-\infty}^{\infty} x(t)\, e^{-i2\pi ft}\, dt\,. \tag{2.1}$$

More formally, the Fourier transform of an eternal signal does not exist because such a signal violates the *Dirichlet condition*, namely, that the signal be ***absolutely integrable***:

$$\int_{-\infty}^{\infty} |x(t)| < \infty \tag{2.2}$$

i.e., the total area under the "rectified" version of $x(t)$ must be finite. Although the total energy is infinite, the power (energy per unit time) is finite, so we can resolve the non-existence of the Fourier transform by taking a time-limited transform over the time-interval $0 < t < T$. The mod-square of the result, divided by the interval width T, is the power density (power per unit spectral width) for the sample.

Following Gardiner (1985), we define the time-limited transform of $x(t)$ as

$$X(f) = \int_{0}^{T} x(t)\, e^{-i2\pi ft}\, dt \tag{2.3}$$

then compute the *power spectral density* via the limiting process[1]

$$S(f) = \lim_{T\to\infty} \frac{1}{T}\, |X(f)|^2 \tag{2.4}$$

where $-\infty < f < \infty$, and the spectrum is double-sided. If $x(t)$ is measured in volts, then $S(f)$ carries units of volts^2·sec or volts^2/Hz. (We imagine the voltage to have been developed across a 1-Ω resistance, allowing volts^2 to serve as a unit for power.)

---

[1] Not apparent from Eq. (2.4) is the fact that, for a stochastic process, the definition of the power spectral density usually involves an explicit ensemble average. Neglect of some form of averaging leads to spectral estimates that are highly variable, since the distribution of un-averaged normalized spectral estimates for a Gaussian process is chi-squared with two degrees of freedom and hence of equal mean and standard deviation (Kay and Marple, 1981; Newland, 1993). I thank Dr Peter Cadusch, one of the external examiners for this thesis, for bringing this important idea to my attention. The necessity for ensemble averaging is illustrated later in this thesis in Chapter 7 (e.g., see Figs 7.3 and 7.5).

The *Wiener–Khinchin theorem* provides an alternative means for computing the power density spectrum by way of the Fourier transform of the autocorrelation function $G(\tau)$

$$S(f) = \int_{-\infty}^{\infty} G(\tau)\, e^{-i2\pi f\tau}\, d\tau \tag{2.5}$$

where autocorrelation function $G(\tau)$ is given by

$$G(\tau) = \lim_{T\to\infty} \frac{1}{T} \int_0^T x(t+\tau)\, x(t)\, dt\,. \tag{2.6}$$

$G(\tau)$ is defined for all lags $-\infty < \tau < \infty$, and, like the power spectrum, is double-sided and symmetric about the y-axis.

Alternatively, if the spectrum $S(f)$ is known, then its autocorrelation function can be computed from the (inverse) Fourier transform of the spectrum:

$$G(\tau) = \int_{-\infty}^{\infty} S(f)\, e^{+i2\pi f\tau}\, df\,. \tag{2.7}$$

2.1.1 Parseval's Theorem

Parseval's theorem is a statement of energy conservation: The total energy computed in the time domain must be identical to the total energy computed in the frequency domain. In order to apply this theorem to infinite-energy signals such as the EEG, we change the requirement to one of power conservation, i.e., that the *rate* of energy delivery be the same in either domain:

$$\lim_{T\to\infty} \frac{1}{T} \int_0^T |x(t)|^2\, dt = \int_{-\infty}^{\infty} S(f)\, df\,. \tag{2.8}$$

For $x(t)$ in volts, both sides carry units of volt^2 (i.e., power per unit resistance).

2.2 Mapping to Discrete Time

In order to compute the autocorrelation function and spectrum for the EEG signal using a computer, the continuous voltage waveform $x(t)$ detected by scalp electrodes must be converted to a discrete-time representation by sampling $x(t)$ at regular time increments $j\Delta t$. The result is a sequence of voltage samples $\{x_j\}$ which give a discrete approximation to the continuous waveform. A similar discretization of continuous variables must be performed when we wish to numerically simulate the differential equations for the time evolution of the cortical macrocolumn.

2.2.1 Nyquist's Theorem

Although the fidelity of the sample improves as the sampling rate $f_s = 1/\Delta t$ is increased, *Nyquist's theorem* tells us that provided the original waveform contains frequency components no higher than half the sampling rate (i.e., $f_{\text{max}} \leqslant f_s/2$), then the original waveform can be reconstituted without error from the sample. If the Nyquist criterion is violated (i.e., the sampling rate is too low) then the energy present in high-frequency components will "fold" or reflect about the Nyquist point $f_{\text{Ny}} = f_s/2$, producing a spurious boost in the lower-frequency part of the spectrum. These undersampled high-frequency components masquerade as lower-frequency components. Such spectral-aliasing errors are undesirable. To avoid aliasing, it is standard engineering practice to low-pass filter the continuous waveform prior to sampling. For example, the Aspect-1000 EEG monitor,[2] which samples the electrode voltage at $f_s = 256$ samples/s, prefilters the waveforms with a low-pass filter set to 70 Hz, ensuring a good safety margin between the filtered $f_{\max}$ and the Nyquist upper limit of $f_{\mathrm{Ny}} = 128$ Hz.

2.2.2 Discrete Fourier Transform

In order to map the continuous-time results of the previous section to the discrete-time domain, we make the following identifications:

$$\begin{aligned} x(t) &\longrightarrow x(j\Delta t) \equiv x_j && (j \text{ is the time index}) && (2.9a) \\ X(f) &\longrightarrow X(k\Delta f) \equiv X_k && (k \text{ is the frequency index}) && (2.9b) \\ T &= N\Delta t && && (2.9c) \\ \Delta f &= \frac{1}{T} = \frac{1}{N\Delta t}\,. && && (2.9d) \end{aligned}$$

Here, T is the length of the data record which consists of N samples taken at regular time intervals $\Delta t = 1/f_s$. Applying these mappings to the time-limited *continuous* Fourier transform of Eq. (2.3) leads naturally to a definition for the DFT or *discrete Fourier transform* operator:

$$\begin{aligned} X(k\Delta f) &= \sum_{j=0}^{N-1} x_j \exp\left[-i\,2\pi(k\Delta f)(j\Delta t)\right] \Delta t \\ &= \Delta t \sum_{j=0}^{N-1} x_j\, e^{-i2\pi jk/N}, \qquad k = 0, 1, \ldots, N-1 \end{aligned}$$

i.e.,

$$X_k = \Delta t \cdot \mathrm{DFT}\{\mathrm{x}\}_k, \qquad k = 0, 1, \ldots, N-1 \tag{2.10}$$

where $\mathrm{x} = [x_0, x_1, \ldots, x_{N-1}]$ is the vector of N time samples x_j whose discrete Fourier transform is defined by

$$\mathrm{DFT}\{\mathrm{x}\}_k \equiv \sum_{j=0}^{N-1} x_j\, e^{-i2\pi jk/N}\,. \tag{2.11}$$

This is a vector of N discrete-frequency elements that, when scaled by the time-step Δt, give the complex spectral amplitudes X_k. The continuous power spectral density can be *estimated* from these discrete spectral samples by discretizing Eq. (2.4), giving

$$\begin{aligned} S(k\Delta f) &= \frac{1}{N\Delta t}\left|X_k\right|^2 \\ &= \frac{1}{N\Delta t}\left|\Delta t \cdot \mathrm{DFT}\{\mathrm{x}\}_k\right|^2 \\ &= \frac{\Delta t}{N}\left|\mathrm{DFT}\{\mathrm{x}\}_k\right|^2, \qquad k = 0, 1, \ldots, N-1\,. \end{aligned} \tag{2.12}$$

Sometimes it is more convenient to work with rms spectral *amplitude* $\widetilde{X}^{\mathrm{rms}}$ rather than spectral power, and for this purpose we replace Eq. (2.12) by its square root,

---

[2] Aspect Medical Systems, Inc., Natick, MA, USA

$$\widetilde{X}_k^{\mathrm{rms}} \equiv \sqrt{S(k\Delta f)} = \sqrt{\frac{\Delta t}{N}}\left|\mathrm{DFT}\{\mathbf{x}\}_k\right|. \qquad (2.13)$$

As for the continuous case (Eq. 2.4), the units for the discrete spectrum of an EEG signal measured in volts will be V^2/Hz for the power spectral density (and $\mathrm{V}/\sqrt{\mathrm{Hz}}$ and for the rms *amplitude* spectral density). The presence of the Δt multiplier in Eq. (2.12) ensures that the estimate of the energy delivered per second is *independent* of the rate at which the signal is sampled. For example, if we reduce the sampling interval Δt while keeping the number of samples N fixed (i.e., we sample more finely for a smaller length of time, implying a broader, coarser spectrum), then the spectral strengths will be scaled down proportionately in order that the area of the spectral density histogram is conserved.

Window Conditioning

Comparing the continuous Fourier transform of Eq. (2.4) with its N-point Eq. (2.12) discrete approximation, it becomes apparent that the discrete spectrum can only provide an accurate sampling of the continuous spectrum if the time-varying function $x(t)$ is periodic on a time interval T equal to $N\Delta t$, the duration of the recording. In other words, the discrete Fourier transform assumes that the original waveform can be recreated by plotting the N time-samples on a rotating cylinder whose circumference is T seconds.

For most recordings of real world signals, this perfect periodicity ideal is unrealizable. Instead, one would ensure that the total recording time was long enough to provide an adequate frequency resolution $\Delta f = 1/N\Delta t$ in the discrete spectrum. In addition, it important that the end of the record can be "joined" smoothly to the beginning of the record: any step or slope discontinuity at the join will result in high-frequency artifacts in the transform. To minimize such artifacts, it is considered good spectral practice to pre-condition the time-series with a shaping function known as a *window.* A common choice for preconditioning is the Hanning cosine-bell, an N-element vector $\mathbf{W}$ defined by

$$W_j = \frac{1}{2}\left[1 - \cos\left(\frac{2\pi(j+1)}{N+1}\right)\right], \qquad j = 0, 1, \ldots, N-1 \qquad (2.14)$$

and illustrated in Fig. 2.1.

If the time-series has been conditioned with a Hanning or other windowing function, then one should adjust the resulting spectrum to compensate for windowing losses (Krauss *et al.*, 1994). Equations (2.12) and (2.13) for spectral power and amplitude are replaced by their window-compensated counterparts:

$$S(k\Delta f) = \frac{\Delta t}{\|\mathbf{W}\|^2}\left|\mathrm{DFT}\{\mathbf{xW}\}_k\right|^2, \qquad k = 0, 1, \ldots, N-1 \qquad (2.15)$$

and

$$\widetilde{X}_k^{\mathrm{rms}} = \frac{\sqrt{\Delta t}}{\|\mathbf{W}\|}\left|\mathrm{DFT}\{\mathbf{xW}\}_k\right|, \qquad k = 0, 1, \ldots, N-1 \qquad (2.16)$$

where $\mathbf{xW}$ represents the element-by-element product[3] of time-series $\mathbf{x}$ with window $\mathbf{W}$,

---

[3] In MATLAB parlance,

```
xW = x .* W;
```

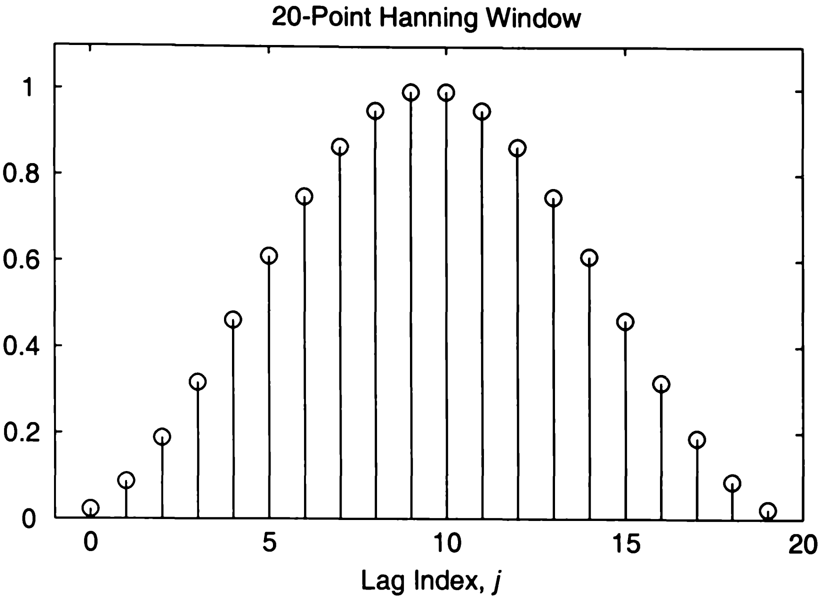

Figure 2.1: The Eq. (2.14) Hanning window function for an $N = 20$-point sample.

$$\mathbf{xW} = [x_0 W_0,\, x_1 W_1,\, \ldots,\, x_{N-1} W_{N-1}] \tag{2.17}$$

and $||\mathbf{W}||$ is the norm or "rms height" of the $\mathbf{W}$ window,

$$||\mathbf{W}|| \equiv \sqrt{\sum_{j=0}^{N-1} W_j^2}\,. \tag{2.18}$$

If the Hanning window is replaced by the identity or "boxcar" window (i.e., a vector of N ones: $\mathbf{W} = [1, 1, \ldots, 1]$), then $||\mathbf{W}||^2 = N$, and equations (2.12, 2.13) are recovered from equations (2.15, 2.16).

2.2.3 Parseval's Theorem for Discrete Time

Applying Parseval's power-conservation theorem to discrete time, the integrals over time and frequency become summations over the discrete time samples $t_j = j\Delta t$ and frequency harmonics $f_k = k\Delta f$. Thus the continuous Eq. (2.8),

$$\lim_{T\to\infty} \frac{1}{T} \int_0^T |x(t)|^2\, dt = \int_{-\infty}^{\infty} S(f)\, df$$

becomes

$$\frac{1}{N\Delta t} \sum_{j=0}^{N-1} |x_j|^2\, \Delta t = \frac{\Delta t}{N} \sum_{k=0}^{N-1} |\mathrm{DFT}\{\mathrm{x}\}_k|^2 \frac{1}{N\Delta t}$$

giving

$$\sum_j |x_j|^2 = \frac{1}{N} \sum_k |\mathrm{DFT}\{\mathrm{x}\}_k|^2\,. \tag{2.19}$$

Therefore, like its continuous counterpart, the discrete Fourier transformation is energy preserving.

2.3 Discrete Approximation for White Noise

In the transformation of a continuous-time stochastic differential equation to a discrete-time numerical simulation, a fundamental question is: What is the correct mapping for the random noise component? The following treatment is an adaptation of the ideas presented by Murthy (1983).

Let $\xi(t)$ be a rapidly fluctuating random function of time, modelled as white noise which has zero mean and is delta-correlated:

$$\langle \xi(t) \rangle = 0, \qquad \langle \xi(t)\, \xi(t') \rangle = \delta(t - t'). \tag{2.20}$$

This second result implies that white noise has the rather pathological feature of infinite variance, so cannot be realized exactly by any real signal. Nevertheless, we wish to simulate the continuous-time $\xi(t)$ with a discrete random sequence $\{\eta_n\}$ of mean zero and variance σ^2:

$$\langle \eta_n \rangle = 0, \qquad \langle \eta_n\, \eta_m \rangle = \sigma^2\, \delta_{n,m} \tag{2.21}$$

where $\delta_{n,m}$ is the unit impulse response. For a time-step Δt sufficiently small,

$$\int_0^T \xi(t)\, dt \simeq \sum_{n=1}^{N} \eta_n\, \Delta t \qquad \text{where} \quad T = N\Delta t \tag{2.22}$$

with both sides going to zero as $T \to \infty$ since both $\xi(t)$ and $\{\eta_n\}$ have zero mean.

For the product $\xi(t)\xi(t')$, the expected value of the integral over all time is

$$\left\langle \lim_{T\to\infty} \int_{-T}^{T} \xi(t)\, \xi(t')\, dt \right\rangle = \int_{-\infty}^{\infty} \langle \xi(t)\, \xi(t') \rangle\, dt = 1 \tag{2.23}$$

which must match the corresponding expectation value for the summation of the discrete products $\{\eta_n \eta_m\}$,

$$\left\langle \lim_{N\to\infty} \sum_{n=1}^{N} \eta_n\, \eta_m\, \Delta t \right\rangle = \lim_{N\to\infty} \sum_{n=1}^{N} \langle \eta_n\, \eta_m \rangle\, \Delta t = \sigma^2\, \Delta t. \tag{2.24}$$

Equating Eqs (2.23) and (2.24), we see that the standard deviation for the discrete sequence must be

$$\sigma = \frac{1}{\sqrt{\Delta t}}. \tag{2.25}$$

For the stochastic simulations presented later in this thesis, we will use MATLAB's **randn** function to generate Gaussian-distributed random numbers $\{\mathcal{R}_n\}$ of zero mean, unit variance:

$$\langle \mathcal{R}_n \rangle = 0, \qquad \langle \mathcal{R}_n\, \mathcal{R}_m \rangle = \delta_{n,m} \tag{2.26}$$

so the **randn**-generated numbers must be multiplied by $1/\sqrt{\Delta t}$ to obtain the correctly scaled $\{\eta_n\}$ stochastic sequence required for numerical simulation:

$$\eta_n = \frac{\mathcal{R}_n}{\sqrt{\Delta t}}. \tag{2.27}$$

This result allows us to specify a mapping from continuous-time white noise $\xi(t)$ to its discrete-time approximation η_n,

$$\xi(t) \longrightarrow \{\eta_n\} = \frac{1}{\sqrt{\Delta t}} \{\mathcal{R}_n\}, \qquad t = n\Delta t. \tag{2.28}$$

We see that in the limit $\Delta t \to 0$, the variance of the $\{\eta_n\}$ tends to infinity, and the discrete sequence better approximates white noise. Thus in any numerical simulation of a white-noise-driven process, use of the Eq. (2.28) mapping should ensure that the stochastic simulation becomes more accurate as the time-step is made smaller.

2.4 Lorentzian Spectrum and Correlation Function

The previous section introduced the notion of *white noise* as a form of extreme fluctuation which is perfectly uncorrelated from one instant to the next. The spectrum for white noise is perfectly flat,

$$S(f) = \text{const.}$$

i.e., the spectrum is a constant function of frequency f. It is named in analogy to white light which has all colours present in equal proportion (at least over the visible portion of the spectrum).

With its properties of infinite variance, infinite power, and infinite bandwidth, white noise cannot exist. Nevertheless, although physically unrealizable, white noise is a useful mathematical idealization for many processes which do occur in nature. A typical model of a spectrum which is nearly flat, and which will turn out to be rather significant for the stochastic modelling of the cortex discussed later in this thesis, is the *Lorentzian spectrum*

$$S(\omega) = \frac{D}{k^2 + \omega^2} \tag{2.29}$$

where $\omega = 2\pi f$ is the angular frequency, D is a diffusion coefficient, and k is a damping constant or decay rate. Example Lorentzian spectra are plotted in Fig. 2.2.

The Lorentzian spectrum is characteristic of diffusion processes such as the irregular fluctuating movements of a pollen grain suspended in water which were first observed by Robert Brown in 1827. The fluctuations arise because the pollen grain is in a state of constant bombardment

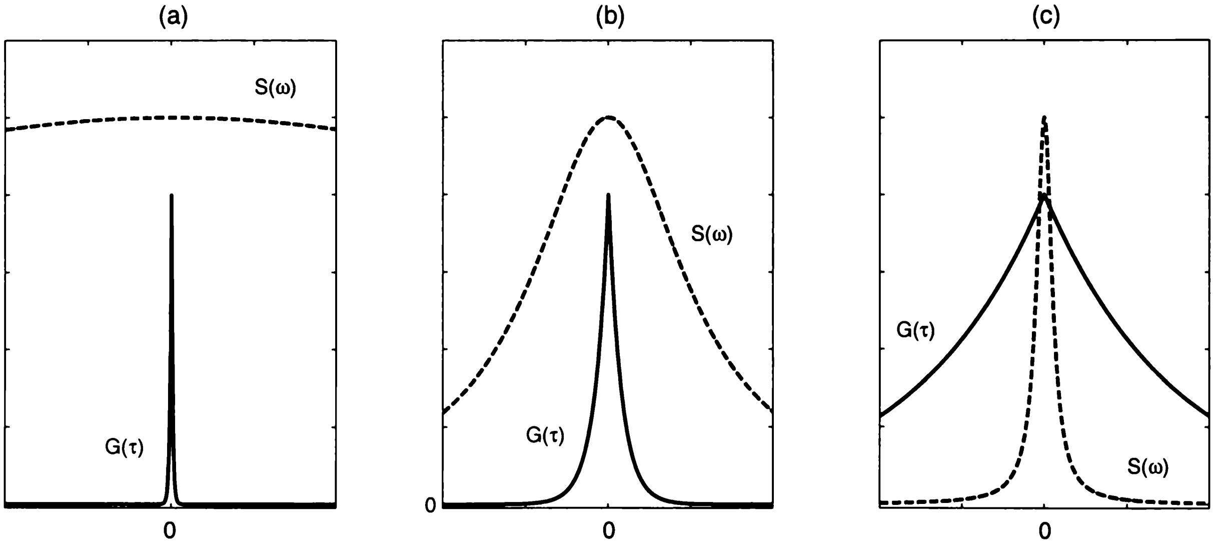

Figure 2.2: Double-sided Lorentzian spectrum $S(\omega)$ and its autocorrelation function $G(\tau)$. (a) A broad spectrum has a narrow correlation function (short correlation time); (b,c) a rapidly decreasing spectrum has an extended correlation time. [Modified from Gardiner (1985, Fig. 1.5)]

from the surrounding water molecules. The motion of the water molecules is so complicated that a deterministic treatment of their effect on the pollen grain is out of the question. Instead, a probabilistic treatment of the exceedingly frequent statistically independent impacts is required (Gardiner, 1985). The term *Brownian motion* is now taken to mean the random motion of any particle in a fluctuating environment.

We can calculate the autocorrelation function for the Brownian-motion spectrum by rewriting the Fourier-transform relation of Eq. (2.7),

$$G(\tau) = \int_{-\infty}^{\infty} S(f)\, e^{i2\pi f\tau}\, df \tag{2.30}$$

as an integration over angular frequency via the change of variable $\omega = 2\pi f$, $d\omega = 2\pi\, df$, giving,

$$G(\tau) = \frac{1}{2\pi}\int_{-\infty}^{\infty} S(\omega)\, e^{i\omega\tau}\, d\omega\,. \tag{2.31}$$

Applying this definition to the Eq. (2.29) Lorentzian spectrum,

$$\begin{aligned}
G(\tau) &= \frac{1}{2\pi}\int_{-\infty}^{\infty} \frac{D}{k^2+\omega^2}\, e^{i\omega\tau}\, d\omega \\
&= \frac{1}{2\pi}\int_{-\infty}^{\infty} \frac{D}{k^2+\omega^2}\cos(\omega\tau)\, d\omega \quad + \quad \frac{i}{2\pi}\int_{-\infty}^{\infty} \frac{D}{k^2+\omega^2}\sin(\omega\tau)\, d\omega \\
&= \frac{1}{\pi}\int_{0}^{\infty} \frac{D}{k^2+\omega^2}\cos(\omega\tau)\, d\omega \quad + \quad 0 \\
&= \frac{D}{2k}\, e^{-k|\tau|} && (2.32) \\
&= \tfrac{1}{2} DT\, e^{-|\tau|/T} \qquad \text{where} \qquad T \equiv 1/k\,. && (2.33)
\end{aligned}$$

On line 2 we have expanded the complex exponential via the Euler identity $\exp(i\theta) = \cos\theta + i\sin\theta$. The first integral on line 2 is an even function of ω, so $\int_{-\infty}^{\infty} \rightarrow 2\int_0^{\infty}$, and the second integral is an odd function of ω, so evaluates to zero. The surviving integral on line 3 is a standard form (Spiegel, 1968, p.96: Eq. 15.40), provided that both k and τ are positive. We take the decay-rate k to be a positive constant, but the lag τ can on take any real value, hence the need for the $|\,|$ operator in the exponent of line 4; this also guarantees that the autocorrelation function will be an even function of τ.

When $\tau = T \equiv 1/k$, the autocorrelation function has decayed to $1/e$ of its zero-lag value. This decay-time is referred to as the *correlation time* T of the fluctuations.

Figure 2.2 illustrates the inverse relationship between spectral width and correlation time. A rapidly-decaying spectrum has a long correlation time (Fig. 2.2c) because most of the spectral energy is concentrated at low frequencies. As the spectrum becomes flatter, the autocorrelation graph decays more rapidly (Fig. 2.2b,a). In the ideal white-noise limit of a perfectly flat spectrum, the autocorrelation function is a delta function at the origin—this is what is meant by the phrase "white noise is delta-correlated."

Chapter 3

Locating the Steady States of the Macrocolumn

3.1 Cortical Equations of Motion

3.1.1 The Liley Equations

Our starting point is Liley's set of eight coupled PDEs (Liley *et al.*, 1999) in which we have assumed complete spatial homogeneity over the region sampled by the EEG electrode. This is a reasonable approximation, given that a scalp electrode has a contact area of approximately 2 cm^2, detecting electrical activity averaged across the underlying 5–10 cm^2 of cerebral cortex. Thus the one-dimensional laplacian $\frac{\partial^2}{\partial x^2}$ (which would have appeared on the LHS of the equation for the long-range potential $\phi(x,t)$, Eq. (3.4) below) is eliminated, and all partial derivatives with time become total derivatives with time. This gives the following set of eight coupled ordinary DEs (the symbols are defined in Table 3.1):

$$\begin{bmatrix} \tau_e & 0 \\ 0 & \tau_i \end{bmatrix} \frac{d}{dt} \begin{bmatrix} h_e \\ h_i \end{bmatrix} = \begin{bmatrix} h_e^{\text{rest}} - h_e \\ h_i^{\text{rest}} - h_i \end{bmatrix} + \begin{bmatrix} \psi_{ee}(h_e)\, I_{ee}(h_e) + \psi_{ie}(h_e)\, I_{ie}(h_i) \\ \psi_{ei}(h_i)\, I_{ei}(h_e) + \psi_{ii}(h_i)\; I_{ii}(h_i) \end{bmatrix}, \tag{3.1}$$

$$\left(\frac{d}{dt} + \gamma_e\right)^2 \begin{bmatrix} I_{ee}(h_e) \\ I_{ei}(h_e) \end{bmatrix} = \left\{ \begin{bmatrix} N_{ee}^{\beta} \\ N_{ei}^{\beta} \end{bmatrix} \mathcal{S}_e(h_e) + \begin{bmatrix} \phi_e(h_e) \\ \phi_i(h_e) \end{bmatrix} + \begin{bmatrix} p_{ee} \\ p_{ei} \end{bmatrix} \right\} G_e \gamma_e e, \tag{3.2}$$

$$\left(\frac{d}{dt} + \gamma_i\right)^2 \begin{bmatrix} I_{ie}(h_i) \\ I_{ii}(h_i) \end{bmatrix} = \left\{ \begin{bmatrix} N_{ie}^{\beta} \\ N_{ii}^{\beta} \end{bmatrix} \mathcal{S}_i(h_i) + \begin{bmatrix} p_{ie} \\ p_{ii} \end{bmatrix} \right\} G_i \gamma_i e, \tag{3.3}$$

$$\begin{bmatrix} \left(\frac{d}{dt} + \bar{v}\Lambda_{ee}\right)^2 \phi_e(h_e) \\ \left(\frac{d}{dt} + \bar{v}\Lambda_{ei}\right)^2 \phi_i(h_e) \end{bmatrix} = \bar{v} \begin{bmatrix} \left(\frac{d}{dt} + \bar{v}\Lambda_{ee}\right) \Lambda_{ee} N_{ee}^{\alpha} \\ \left(\frac{d}{dt} + \bar{v}\Lambda_{ei}\right) \Lambda_{ei} N_{ei}^{\alpha} \end{bmatrix} \mathcal{S}_e(h_e). \tag{3.4}$$

Equation (3.1) gives the time evolution of h_e and h_i, the excitatory and inhibitory soma voltages (also referred to as *membrane potentials*) averaged over the assembly of cooperating neurons. The neural assembly is assumed to be a single resistance-capacitance (RC) compartment or summing point; in effect, we are defining an average neuron for the mass of 10^5 neurons in the macrocolumn.

The first two terms on the right of Eq. (3.1) correspond to an exponential return to a resting voltage $h_{e,i}^{\text{rest}} = -70$ mV. The second pair of terms describe perturbations to the membrane voltage due to synaptic inputs I_{jk} (where $j, k \in \{e, i\}$) to the neural mass. Each of these I_{jk}

Table 3.1: Symbol definitions and model constants for the Liley equations

Symbol	Description	Value	Unit
e, i	(as subscript) excitatory, inhibitory cell populations		
$h_{e,i}$	population mean soma voltage		mV
$\tau_{e,i}$	membrane time constant	0.040, 0.040	s
$h^{\mathrm{rest}}_{e,i}$	cell resting potential	−70, −70	mV
$h^{\mathrm{rev}}_{e,i}$	cell reversal potential (Nernst potential)	45, −90	mV
$I_{ee,ie}$	total $e \longrightarrow e, i \longrightarrow e$ "current" input to excitatory synapses		mV
$I_{ei,ii}$	total $e \longrightarrow i, i \longrightarrow i$ "current" input to inhibitory synapses		mV
ψ_{jk} $(j,k\in\{e,i\})$	weighting factors for the I_{jk} inputs		
$p_{ee,ie}$	exogenous (subcortical) spike input to e population	1100, 1600	s^{-1}
$p_{ei,ii}$	exogenous (subcortical) spike input to i population	1600, 1100	s^{-1}
$\phi_{e,i}$	long-range (cortico-cortical) spike input to e, i populations		s^{-1}
$\Lambda_{ee,ei}$	characteristic cortico-cortical inverse-length scale	0.40, 0.65	$(\mathrm{cm})^{-1}$
EPSP, IPSP	excitatory, inhibitory post-synaptic potential		mV
$\gamma_{e,i}$	neurotransmitter rate constant for EPSP, IPSP	300, 65	s^{-1}
$G_{e,i}$	peak amplitude of EPSP, IPSP	0.18, 0.37	mV
e	(e.g., Eqs (3.2, 3.3)) base of natural logarithms	2.71828...	
$N^{\beta}_{ee,ei}$	total number of local $e \longrightarrow e, e \longrightarrow i$ synaptic connections	3034, 3034	
$N^{\beta}_{ie,ii}$	total number of local $i \longrightarrow e, i \longrightarrow i$ synaptic connections	536, 536	
$N^{\alpha}_{ee,ei}$	total number of synaptic connections from distant e-populations	4000, 2000	
$\bar{v}$	mean axonal conduction speed	700	$\mathrm{cm\,s}^{-1}$
$\mathcal{S}_e(h_e), \mathcal{S}_i(h_i)$	sigmoid function mapping soma voltage to firing rate		s^{-1}
$\mathcal{S}^{\max}_e, \mathcal{S}^{\max}_i$	maximum value for sigmoid function	1000, 1000	s^{-1}
$\theta_{e,i}$	inflexion-point voltage for sigmoid function	−60, −60	mV
$g_{e,i}$	sigmoid slope at inflexion point	0.28, 0.14	$(\mathrm{mV})^{-1}$

inputs is weighted by a dimensionless scale-factor ψ_{jk} whose origin and significance is discussed below.

These equations use a double-indexing scheme to indicate the direction of "flow" or influence. For example, the I_{ie} appearing on the right of Eq. (3.1) is to be read as $I_{i\rightarrow e}$ and can be pictured as the "current" (actually a voltage) which flows *from* the (mass-average) *inhibitory* neuron *to* the (mass-average) *excitatory* neuron. And, ψ_{ie} is the weight factor which modulates this $i \longrightarrow e$ flow.

Examining the equation of motion for h_e (first equation of the (3.1) pair), the resting voltage h^{rest}_e is the asymptote to which h_e will decay in the absence of any inputs. If any perturbing inputs are present (the usual case), then the asymptotic voltage target will be displaced in the positive direction (tending to increase excitability) in the presence of I_{ee} excitatory "self" input, but displaced in the negative direction (tending to decrease excitability) by the I_{ie} input from the inhibitory population. Similarly, in the h_i equation of motion, excitatory input I_{ei} will tend to excite the inhibitory population, and I_{ii} inhibitory self-input will inhibit it.

One of the significant and perhaps surprising features of the model which will become apparent later in this chapter is that although $h^{\mathrm{rest}}_{e,i}$ is the steady-state resting voltage for the *undisturbed* neuron, the presence of excitatory and inhibitory inputs will drive the neuron into one of two distinct states: either a high-firing depolarized state which is more positive than $h^{\mathrm{rest}}_{e,i}$, or a low-firing hyperpolarized state which is more negative that $h^{\mathrm{rest}}_{e,i}$. In short, as soon as the

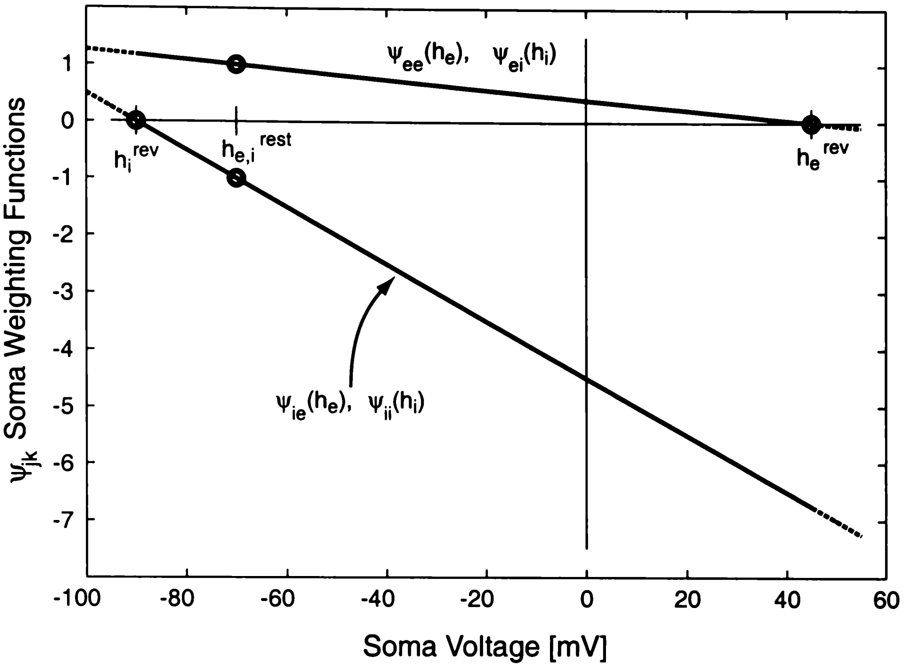

Figure 3.1: Soma-voltage weighting functions. For the normal range of soma voltages $h_i^{\rm rev} < h_{e,i} < h_e^{\rm rev}$, the excitatory weighting functions $\psi_{ee}(h_e), \psi_{ei}(h_i)$ (upper line) are positive, and the inhibitory weighting functions $\psi_{ie}(h_e), \psi_{ii}(h_i)$ (lower line) are negative. If $h_{e,i} > h_e^{\rm rev}$, the upper line goes negative, and all four weights have an inhibitory, hyperpolarizing effect. At the other extreme, for $h_{e,i} < h_i^{\rm rev}$, the lower line goes positive, and all four weights have an excitatory, depolarizing effect.

feedback terms in the model are enabled, the model neuron can no longer come to rest at its $h_{e,i}^{\rm rest} = -70$ mV "resting" voltage.

3.1.2 ψ_{jk} Input Weighting Functions

The four I_{jk} "currents" are always positive. Their excitatory or inhibitory effect is determined by the sign and magnitude of the four ψ_{jk} weighting functions which are defined below and plotted in Fig. 3.1.

$$\psi_{ee}(h_e) = \frac{h_e^{\rm rev} - h_e}{|h_e^{\rm rev} - h_e^{\rm rest}|}, \tag{3.5a}$$

$$\psi_{ei}(h_i) = \frac{h_e^{\rm rev} - h_i}{|h_e^{\rm rev} - h_i^{\rm rest}|}, \tag{3.5b}$$

$$\psi_{ie}(h_e) = \frac{h_i^{\rm rev} - h_e}{|h_i^{\rm rev} - h_e^{\rm rest}|}, \tag{3.5c}$$

$$\psi_{ii}(h_i) = \frac{h_i^{\rm rev} - h_i}{|h_i^{\rm rev} - h_i^{\rm rest}|}. \tag{3.5d}$$

These ψ_{jk} coefficients are the model's representation of two facts: first, that excitation and inhibition are mediated by different ionic species ($h_e^{\rm rev} = +45$ mV $\approx V_{\rm Na}$, the sodium reversal potential; $h_i^{\rm rev} = -90$ mV $\approx V_{\rm K}$, the potassium reversal potential); and second, that the magnitude of the postsynaptic currents depends on the active state of the neuron (Tuckwell, 1988b).

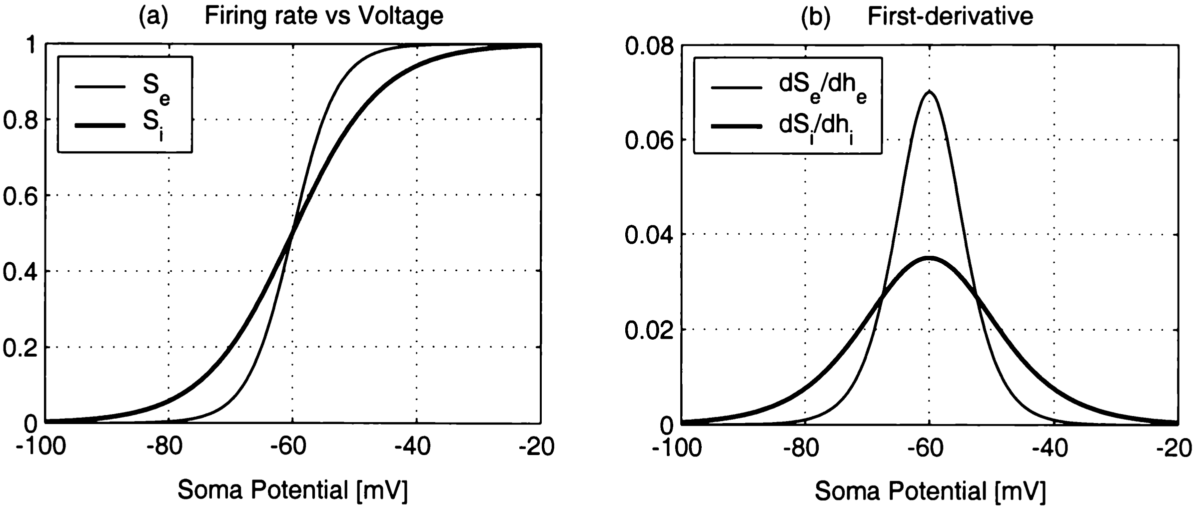

Figure 3.2: Sigmoidal functions relating firing rate to average soma potential. (a) Sigmoid curves: excitatory sigmoid S_e (light curve); inhibitory sigmoid S_i (bold). Both curves have been plotted with a maximum height of unity; in application, the vertical axis will be scaled by $\mathcal{S}_e^{\max}$, $\mathcal{S}_i^{\max}$ repectively. (b) First derivative of sigmoid functions: dS_e/dh_e (light curve); dS_i/dh_i (bold). The points of inflection are set at $\theta_{e,i} = -60$ mV; the mid-point "gains" are $g_{e,i} = 0.28, 0.14\ (\mathrm{mV})^{-1}$ (see Eq. (3.6)).

3.1.3 Sigmoid Transfer Functions

The time evolution of the input terms I_{ee}, I_{ei}, I_{ie}, I_{ii} is governed by Eqs (3.2) and (3.3) which model the variable coupling strength between cells in terms of sigmoid functions $\mathcal{S}_e(h_e)$, $\mathcal{S}_i(h_i)$,

$$\mathcal{S}_e(h_e) = \frac{\mathcal{S}_e^{\max}}{1 + \exp\left[-g_e(h_e - \theta_e)\right]}, \tag{3.6a}$$

$$\mathcal{S}_i(h_i) = \frac{\mathcal{S}_i^{\max}}{1 + \exp\left[-g_i(h_i - \theta_i)\right]}. \tag{3.6b}$$

These are nonlinear S-shaped transfer functions representing the output pulse rate (in pulses per second) of a homogeneous neural mass in response to a mean field of h_e, h_i. $\theta_{e,i}$ and $g_{e,i}$ are constants: $\theta_{e,i}$ is the soma potential at which the function has both maximum gradient and maximum sensitivity to small changes in soma potential; $g_{e,i}$ determines the "gain" at this point of inflexion. See Fig. 3.2 and refer to Table 3.1 for values of the contants. For small values of soma potential, the average firing rate is low; as soma potential increases (becomes less negative), firing rate increases rapidly, eventually levelling off at a maximum value set by the firing rate multiplier $\mathcal{S}_{e,i;\max}$, which in this model is 1000 s^{-1}. At the point of inflexion, the firing rate is half this maximum value. A high firing rate corresponds to a strong interconnectivity between neurons; conversely, a low firing rate corresponds to a weak connectivity. Thus the strength of the interconnection between neurons is determined by the instantaneous value of the mean soma potential.

3.2 Significance of the Steady States

By setting to zero all time derivatives in Eqs (3.1– 3.4), we are able to compute the steady-state values of the soma potentials h_e^0 and h_i^0 as a function of anaesthetic "amount," λ. Contrary to an initial conjecture by an interested party that this zeroing of time-variations would produce a "dead brain," this procedure actually gives us the long-time-limit, equilibrium values for the excitatory and inhibitory soma voltages. In this chapter we will show that for an intermediate range of λ (looking ahead a little, this is region II of Fig. 3.4b), the soma voltages can take on three distinct values, corresponding to three quite different cortical states (two stable, one unstable) which the macrocolumn can switch between. Outside this intermediate range, the soma voltages become single-valued and the range of possible cortical behaviours collapses correspondingly as the brain becomes, in a quantifiable sense, "simpler."

Once these λ-dependent steady states have been located, and their stability status established, we can introduce small-amplitude white-noise perturbations to the sub-cortical inputs in order to generate a fluctuation power spectrum. Of primary interest is how this fluctuation power varies as anaesthetic concentration is increased, and this will be investigated in Chapter 5. The purpose of the remainder of the present chapter is to describe how the steady states are located, then to ponder their physical significance with respect to the state of consciousness of the cortex.

3.3 Stationary Solutions

The soma stationary solutions will be those (h_e, h_i) values which satisfy the eight coupled differential equations (3.1– 3.4) in the long-time limit in which all time variations have vanished. Setting all d/dt terms to zero, we obtain the following set of simplified equations:

$$\begin{aligned} 0 &= h_e^{\text{rest}} - h_e + \psi_{ee}(h_e)\, I_{ee}(h_e) + \psi_{ie}(h_e)\, I_{ie}(h_i), && (3.7a)\\ 0 &= h_i^{\text{rest}} - h_i + \psi_{ei}(h_i)\, I_{ei}(h_e) + \psi_{ii}(h_i)\, I_{ii}(h_i), && (3.7b)\end{aligned}$$

$$\begin{aligned} I_{ee}(h_e) &= \left[N_{ee}^{\beta}\, \mathcal{S}_e(h_e) + \phi_e(h_e) + p_{ee}\right] G_e e/\gamma_e, && (3.8a)\\ I_{ei}(h_e) &= \left[N_{ei}^{\beta}\, \mathcal{S}_e(h_e) + \phi_i(h_e) + p_{ei}\right] G_e e/\gamma_e, && (3.8b)\end{aligned}$$

$$\begin{aligned} I_{ie}(h_i) &= \left[N_{ie}^{\beta}\, \mathcal{S}_i(h_i) + p_{ie}\right] G_i e/\overline{\gamma_i}, && (3.9a)\\ I_{ii}(h_i) &= \left[N_{ii}^{\beta}\, \mathcal{S}_i(h_i) + p_{ii}\right] G_i e/\overline{\gamma_i}, && (3.9b)\end{aligned}$$

$$\begin{aligned} \phi_e(h_e) &= N_{ee}^{\alpha}\, \mathcal{S}_e(h_e), && (3.10a)\\ \phi_i(h_e) &= N_{ei}^{\alpha}\, \mathcal{S}_e(h_e). && (3.10b)\end{aligned}$$

Note that the anaesthetic modulation of the inhibitory neurotransmitter rate constant has now been incorporated in Eqs (3.9a, 3.9b) by replacing γ_i with $\overline{\gamma_i} \equiv \gamma/\lambda$. Thus as anaesthetic effect increases, the $I_{ie}(h_i)$ and $I_{ii}(h_i)$ "currents" generated by the inhibitory neurons will increase linearly with λ.

Observe how in Eq. (3.7a) for h_e, the inhibitory voltage h_i occurs only in the $I_{ie}(h_i)$ current, indirectly as an $\mathcal{S}_i(h_i)$ sigmoid term. So we can obtain an equation giving h_i as a function of h_e in two steps. First, use Eq. (3.9a) to eliminate I_{ie} from Eq. (3.7a), rearranging to make $\mathcal{S}_i(h_i)$ the subject. Effectively this gives an expression for the inhibitory spike rate $\mathcal{S}_i$ as a function of the *excitatory* soma voltage, denoted $\hat{\mathcal{S}}_i(h_e)$. Second, use Eq. (3.6) to invert the inhibitory sigmoid function, thereby extracting the $\hat{h}_i$ which belongs with the given h_e.

Similarly, eliminating I_{ei} from Eq. (3.7b) and solving for $\mathcal{S}_e(h_e)$ will render a parallel equation allowing $\hat{h}_e$ to be retrieved for given h_i. These manipulations result in a pair of coupled nonlinear equations for the equilibrium spike-rates,

$$\hat{\mathcal{S}}_i(h_e) = -\left[\frac{\gamma_i}{G_i e\, \psi_{ie}(h_e)}\left[h_e^{\text{rest}} - h_e + \psi_{ee}(h_e)\, I_{ee}(h_e)\right] + p_{ie}\right] \Big/ N_{ie}^{\beta}, \tag{3.11a}$$

$$\hat{\mathcal{S}}_e(h_i) = -\left[\frac{\gamma_e}{G_e e\, \psi_{ei}(h_i)}\left[h_i^{\text{rest}} - h_i + \psi_{ii}(h_i)\, I_{ii}(h_i)\right] + p_{ei}\right] \Big/ \left(N_{ei}^{\alpha} + N_{ei}^{\beta}\right). \tag{3.11b}$$

Computing the sigmoid-inverses of these spike-rates gives the corresponding membrane voltages,

$$\hat{h}_i(h_e) = \theta_i - \frac{1}{g_i}\ln\left(\mathcal{S}_i^{\max}/\hat{\mathcal{S}}_i(h_e) - 1\right), \tag{3.12a}$$

$$\hat{h}_e(h_i) = \theta_e - \frac{1}{g_e}\ln\left(\mathcal{S}_e^{\max}/\hat{\mathcal{S}}_e(h_i) - 1\right). \tag{3.12b}$$

3.3.1 Root Searching

These equations suggest the following iterative numerical scheme for solving for the (h_e^0, h_i^0) equilibrium soma voltages. Select a first-guess value for a presumed equilibrium value for h_e; call this h_{e_1}. Substitute h_{e_1} into the RHS of Eq. (3.11a) to give a spike rate $\hat{S}_{i_1}$, and, via Eq. (3.12a), the first-guess equilibrium value $\hat{h}_{i_1}$ for the inhibitory population. Now plug $\hat{h}_{i_1}$ into the RHS of Eq.(3.11b) and take its sigmoid-inverse via Eq. (3.12b); call the result h_{e_2}. If h_{e_2} matches the first-guess h_{e_1}, then the coordinate $(h_{e_1}, \hat{h}_{i_1})$ is a soma-voltage equilibrium point on a graph of h_e vs h_i. In the more usual case, h_{e_1} and h_{e_2} will be unequal, but their difference will give an indication of the error in the initial guess.

By keeping track of the sign of the $(h_{e_1} - h_{e_2})$ differences for a range of finely-stepped h_{e_1} initial guesses, we can detect when the h_e^0 root has been bracketted, and then apply a bisection technique, such as MATLAB's `fzero` function, to zero-in on the root to within a specified tolerance. This final stage is referred to as root "polishing."

To illustrate, suppose that h_e achieves equilibrium at $h_e^0 = -71.2377$ mV (this is the middle root of Fig. 3.3a). We can detect the presence of this root by taking a coarse sweep of h_e values from -75.0 to -68.0 mV, in steps of 1.0 mV (more typically, I would use steps 1000 times finer than this to ensure no roots were missed). In the table alongside, the first column is the array of guesses, the second column is the sigmoid-inverse of each guess obtained after traversing the equation sequence (3.11a → 3.12a → 3.11b → 3.12b), and the third column lists the mismatch error between the guess and its sigmoid-inverse. The sign-change in the error indicates that the root must lie somewhere in the interval $-72.0 < h_e^0 < -71.0$ mV: the root has now been bracketted and its precise value will emerge after sufficient polishing.

h_{e_1}	h_{e_2}	$(h_{e_1} - h_{e_2})$
−75.0	−76.5810	+1.5810
−74.0	−75.0226	+1.0226
−73.0	−73.5885	+0.5885
−72.0	−72.2340	+0.2340
−71.0	−70.9318	−0.0682
−70.0	−69.6635	−0.3365
−69.0	−68.4148	−0.5852
−68.0	−67.1732	−0.8268

3.3.2 Roots as Isocline Intersections

Suppose that we use Eq. (3.11a) in isolation to compute a set of $\hat{h}_i$ values which correspond to a given set of (presumed stationary) h_e values, then plot a graph of h_e vs $\hat{h}_i$. Following Wilson and Cowan (1972), we refer to the resulting curve as the $dh_e/dt = 0$ *isocline*. Now perform the corresponding procedure for a set of stationary h_i values applied to Eq. (3.11b) to give a suite of matching $\hat{h}_e$ values, then superimpose this $\hat{h}_e$ vs h_i graph (which defines the $dh_i/dt = 0$ isocline) on the first graph. The intersections of the two isoclines locate those points for which $dh_e/dt = dh_i/dt = 0$, i.e., those points at which h_e and h_i are simultaneously stationary. Thus the isocline intersections define the (h_e^0, h_i^0) equilibrium coordinates. This graphical approach provides a visual confirmation that the iterative scheme described in the previous section has correctly located the stationary points.

Figure 3.3 shows a representative sequence of four isocline graphs illustrating the discovery of multiple roots (first three plots) and a single root (last plot) for anaesthetic effect λ set at

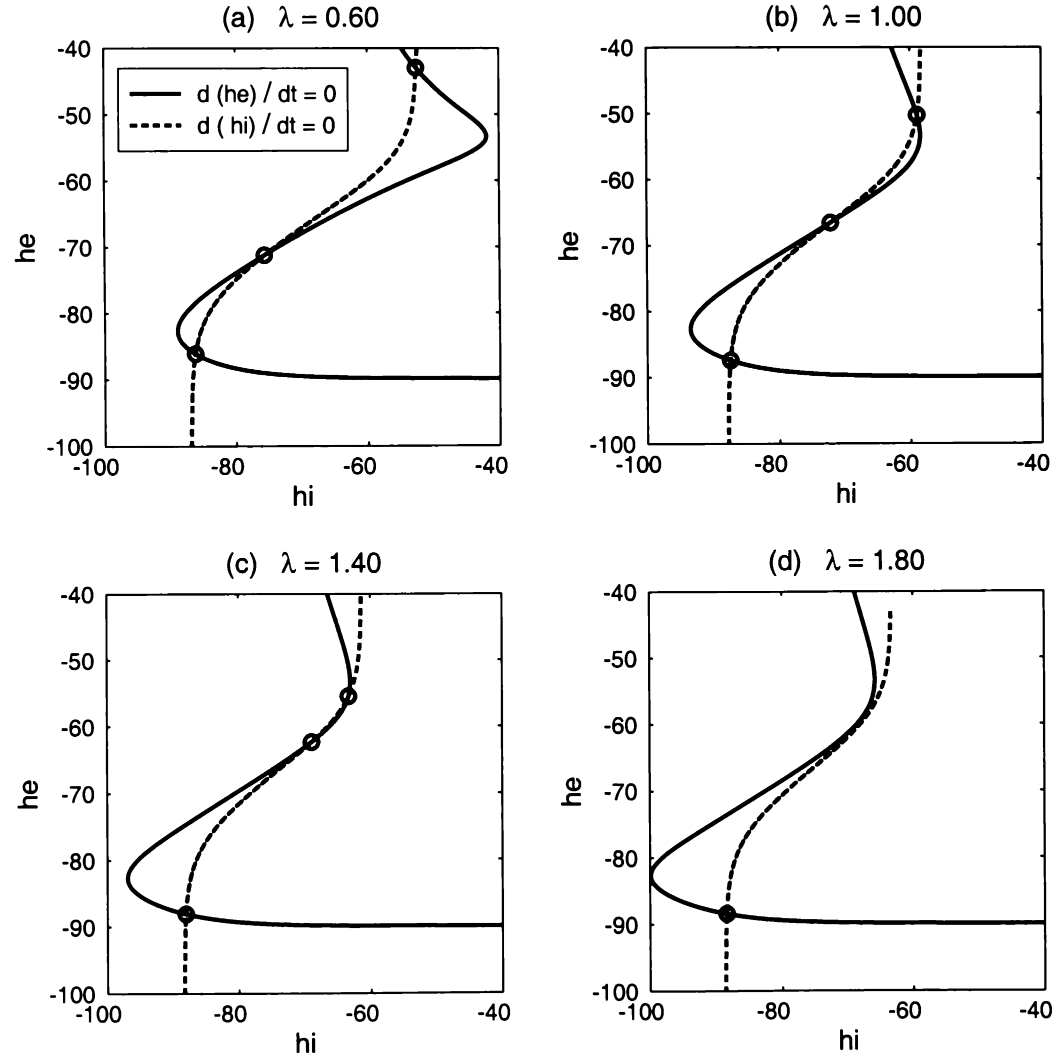

Figure 3.3: Isocline plots for $dh_e/dt = 0$ and $dh_i/dt = 0$. Intersection points locate the equilibrium soma potentials. Multiple intersections (a–c) indicate multiple steady states for a given value of anaesthetic effect. For $\lambda = 1.8$, only one stationary point exists, and this is on the hyperpolarized (low-firing) branch corresponding to comatose-unconsciousness.

0.6, 1.0, 1.4 and 1.8 respectively.

In order to produce a detailed picture showing how the distribution and number of soma-voltage steady states varies with anaesthetic effect, I applied the numerical root-finding procedure of Section 3.3.1 for λ-values ranging from 0 to 1.80 in steps of 0.05, then verified the number and location of the roots on isocline-intersection graphs. This approach worked well for the mid-range $0.30 < \lambda < 1.50$ region where three roots were found, but tended to be rather less successful in the single-root régimes $\lambda \lesssim 0.3$ and $\lambda \gtrsim 1.5$. I will defer until Section 3.3.5 the technical discussion of the strategies I adopted for hunting down these "difficult" roots.

We now examine how the locations and number of the roots change with anaesthetic amount.

3.3.3 Distribution of Roots as a Function of Anaesthetic Effect

Figure 3.4a shows the locus of steady-state excitatory h_e^0 and inhibitory h_i^0 soma voltages as a (multivalued) function of anaesthetic effect λ. The discovered points are marked with circles ($\circ = h_e^0$) and crosses ($\times = h_i^0$), and are joined with a pair of cubic spline curves to aid the eye. A vertical traverse through the locus shows that for the mid-range λ-values, there are three distinct (h_e^0, h_i^0) steady-state pairs. I will show in Section 4 that the steady-state values along the upper and lower branches are *stable* equilibrium points (i.e., can be pictured as a pair of *valleys* on a potential-hill diagram), while the values along the mid-branch are all *unstable* equilibrium points (they define the *crest* of the potential hill which separates the two valleys).

For $\lambda \gtrsim 1.53$, corresponding to strong anaesthetic effect, there is only a single state available, and this is on the bottom branch with the inhibitory and excitatory soma voltages both close to -90 mV: both populations are in their low-firing, *hyperpolarized* state. For $\lambda \lesssim 0.28$, corresponding to strong anti-anaesthetic (i.e., analeptic) effect, again only a single state is available, but this state is on the top branch where, because the soma voltages exceed the sigmoidal inflexion-point voltage $\theta_{e,i} = -60$ mV (see Fig. 3.2), both neuronal populations are firing strongly: this is the *depolarized* state. For $\lambda \to 0$ (i.e., tending to the limit of zero inhibitory effect), both curves converge at the top-left corner to values close to $+45$ mV. At this extremum, both neural populations are firing at their absolute maximum rates.

In Fig. 3.4b, I have traced out the trajectory of steady-state h_e values, and have labelled the three distinct régimes—

Region I ("coma") only the low-firing quiescent state is available to the macrocolumn when λ is large; this is the anaesthetized state

Region II the macrocolumn may be in either of two states: "active" (upper branch) or "quiescent" (lower branch); the macrocolumn may not rest anywhere on the mid-branch since this state is unstable with respect to small perturbations

Region III ("seizure") only the high-firing "active" state is available; for $\lambda \to 0$, firing rate is maximized.

The fact that the locus of steady states is a multiple-valued function of anaesthetic amount is of profound significance. It means that the transition into (and emergence from) unconsciousness *cannot* proceed continuously—there must be a sudden and discontinuous switching of states at a certain critical concentration of anaesthetic. I will discuss these ideas in greater depth in the concluding section of this chapter.

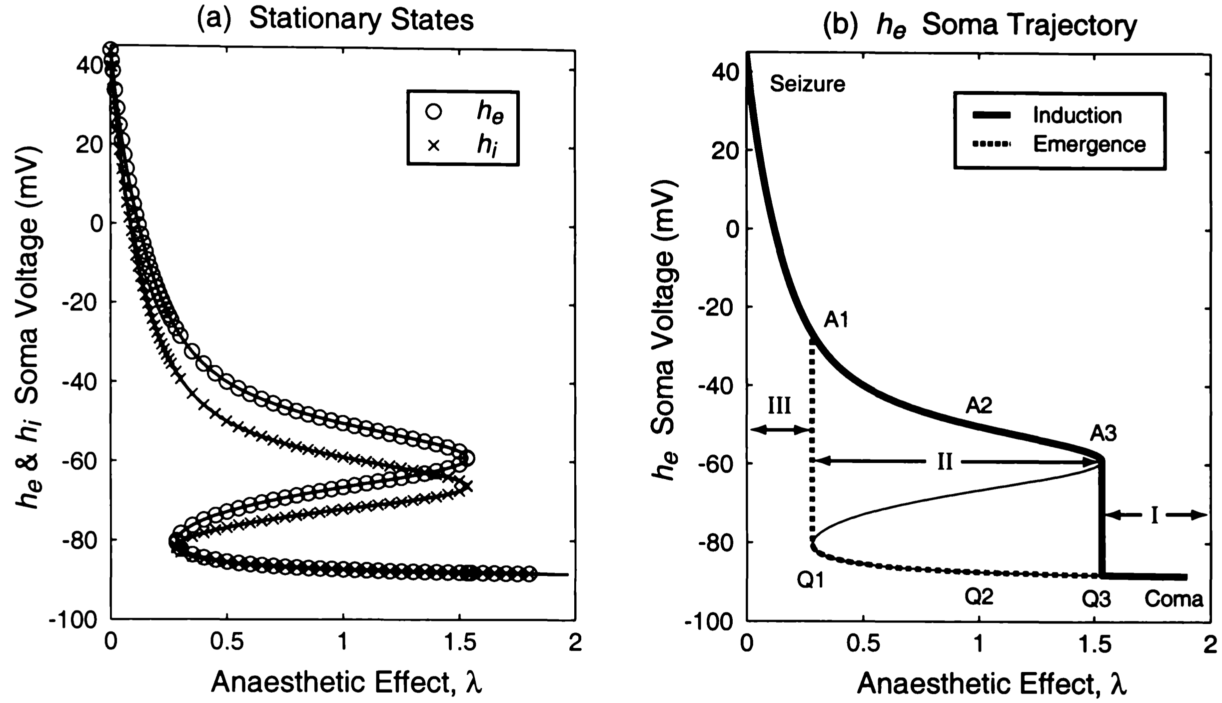

Figure 3.4: (a) Model predictions for the stationary states for h_e (circles) and h_i (crosses) as a function of anaesthetic effect λ. (b) In region II bounded by $A_1A_3Q_3Q_1$, for a given value of λ there are three possible values for h_e, but only two of these are stable: points lying on the upper ("active": A_1A_3) branch, and points on the lower ("quiescent": Q_1Q_3) branch. For $\lambda \gtrsim 1.53$ (region I), h_e becomes single-valued and neural firing is strongly suppressed ("coma"); for $\lambda \lesssim 0.3$ (region III), h_e is again single-valued but now neural firing is maximized ("seizure").

3.3.4 Number of Roots

In the foundation paper of Wilson and Cowan (1972) which describes an abstract model of populations of inhibitory and excitatory neurons containing sigmoid nonlinearities, the authors demonstrated that for sigmoid functions with n inflexion points, there could be up to $2n + 3$ stationary states. The Liley model used in the present work is based on sigmoid functions with a single point of inflexion (see Fig. 3.2a). Applying the Wilson and Cowan result to the Liley model suggests we might expect to find up to *five* stationary states. However, for any given value of λ, I could locate either a single root, or a triple of roots, but never more than three roots.

I attempted a (non-exhaustive) search for the "missing" roots by investigating the effect of systematically altering the values of the model constants listed in Table 3.1, but without success. This finding of (no more than) three roots has been confirmed by other workers: Robinson *et al.* (1998) investigated the nature of the steady-state solutions for a similar sigmoid-coupled model of the cerebral cortex, but, after an extensive parameter-space search, found a maximum of either three steady states or a single steady state. Recent work by Liley *et al.* (2002), working with a model identical to the one used here (lacking only the inclusion of anaesthetic effect), also reported a maximum of three-roots.

3.3.5 The "Pathological" Roots

In Section 3.3.2, I alluded to the fact that for some settings of the λ anaesthetic effect, the (h_e^0, h_i^0) steady states were hard to find. I describe these roots as "pathological"—not because they are ill-behaved, but because they require extra care and numerical effort to locate.

Specifically, for the extreme and diametrically-opposed cases of very large λ (deep coma: macrocolumn is strongly hyperpolarized with very low firing rates) and very small λ (seizure: macrocolumn is strongly depolarized; firing rates are close to maximum), I found that the standard root-search procedures would fail unless the grid spacing of the h_e guesses was made orders of magnitude smaller than a "reasonable" default value of 0.001 mV. The computer resources (memory and machine time) required to locate these extreme roots became a limiting factor, since resource requirements scale directly with the number of points used for the search grid.

Examination of the sigmoid-defining Eqs (3.6) and plots (Fig. 3.2a) provides the first clue as to the source of the problem. The sigmoid graph is approximately linear over its mid-range, but, by design, has a "saturating" characteristic at either end: it tends to zero as $h_{e,i} \to -\infty$, and tends to $\mathcal{S}_{\text{max}}$ as $h_{e,i} \to +\infty$. An essential stage of the root search involves inverting the sigmoid via Eqs (3.12) to find a pair of soma-voltage estimates which bracket the root. If the root is located in one of the saturation zones, the maximum allowable size of the bracketting interval becomes asymmetrically squeezed since there is less and less error "head-room" available: if one of the argument guesses is less than zero (or greater than $\mathcal{S}_{\text{max}}$), its sigmoid-inverse will involve taking the logarithm of a negative number, returning a complex (unphysical) soma-voltage.

Inverse-Sigmoid: Trapping out-of-bound argument

Rather than allowing MATLAB to generate and propagate complex numbers, I detected and marked these unphysical inverse-sigmoid returns as `NaN` (not-a-number), then crafted a customized bisection routine which would iterate Eqs (3.11–3.12) long and hard against the one-sided `NaN` case, endeavouring to convert a trial bracket $[x_1, x_2]$ which returned $[f(x_1), \texttt{NaN}]$ into a real bracket $[x_1, x_3]$ which returned $[f(x_1), f(x_3)]$ such that $f(x_1) \cdot f(x_3) < 0$. This "proper" bracket could then be passed on to MATLAB's `fzero` routine to render a well-polished root.

Asymptotic Limits for $h_{e,i}^0$

Even with these enhancements to locate the roots hiding within the sigmoid saturation zones, it would be reassuring to be able to place upper and lower bounds on the soma-voltage search space. These bounds can be calculated by letting λ take on its two extreme values:

1. For $\lambda \to \infty$ the IPSP becomes infinitely prolonged, and both the inhibitory and excitatory sigmoids are at their zero-firing asymptotic limit at which all neural firing has ceased; this is *deep coma*;
2. For $\lambda \to 0$, the IPSP becomes compressed into a response function of zero width, so there is no inhibitory restraint on the macrocolumn; both inhibitory and excitatory sigmoids are at their $\mathcal{S}_{\text{max}}$ asymptotic limit at which all neurons are firing maximally; this limit corresponds to *epileptic seizure*.

1. Infinite Inhibition: Coma. To obtain the deep-coma limit, set $\mathcal{S}_e(h_e) = \mathcal{S}_i(h_i) = 0$, and allow $\lambda \to \infty$ in Eqs (3.9a,3.9b). This gives

$$I_{ie}(h_i) = \lambda p_{ie} G_i \, e/\gamma_i \tag{3.13a}$$

$$I_{ii}(h_i) = \lambda p_{ii} G_i \, e/\gamma_i \tag{3.13b}$$

so the "currents" from the (subcortical) inhibitory sources will tend to infinity with λ. Meanwhile, zeroing the sigmoids in Eqs (3.8a,3.8b) gives

$$I_{ee}(h_e) = p_{ee} G_e \, e/\gamma_e \tag{3.14a}$$

$$I_{ei}(h_e) = p_{ei} G_e \, e/\gamma_e \tag{3.14b}$$

showing that the currents from excitatory sources will remain finite. Dividing Eq. (3.7a) by I_{ie}, and Eq. (3.7b) by I_{ii}, then allowing $\lambda \to \infty$, collapses these equations to

$$0 = \psi_{ie}(h_e) \equiv \left(h_i^{\text{rev}} - h_e\right) \Big/ \left|h_i^{\text{rev}} - h_e^{\text{rest}}\right| \tag{3.15a}$$

$$0 = \psi_{ii}(h_i) \equiv \left(h_i^{\text{rev}} - h_i\right) \Big/ \left|h_i^{\text{rev}} - h_i^{\text{rest}}\right| \tag{3.15b}$$

from which we conclude that the asymptotic soma voltages for deep-coma must equal the h_i^{rev} reversal potential,

$$h_e^{\text{coma}} = h_i^{\text{coma}} = -90 \text{ mV}. \tag{3.16}$$

2. Zero Inhibition: Seizure. Solving for the zero-inhibition voltages is a little more work. Setting $\lambda \to 0$ causes the inhibitory inputs I_{ie} and I_{ii} to go to zero. In contrast, the excitatory inputs I_{ee} and I_{ei} are maximized because the excitatory sigmoid will be at its saturation maximum $\mathcal{S}_e^{\text{max}}$, thus Eqs (3.8a,3.8b) become

$$I_{ee}(h_e) \to I_{ee}^{\text{seiz}} \equiv \left[(N_{ee}^{\alpha} + N_{ee}^{\beta})\, \mathcal{S}_e^{\text{max}} + p_{ee}\right] G_e e/\gamma_e = 11{,}474 \text{ mV} \tag{3.17a}$$

$$I_{ei}(h_e) \to I_{ei}^{\text{seiz}} \equiv \left[(N_{ei}^{\alpha} + N_{ei}^{\beta})\, \mathcal{S}_e^{\text{max}} + p_{ei}\right] G_e e/\gamma_e = 8{,}213 \text{ mV}. \tag{3.17b}$$

Although cortical $\mathcal{S}_e^{\text{max}}$ and subcortical p_{ee} (p_{ei}) spike inputs are of similar magnitude, the multiplication of $\mathcal{S}_e^{\text{max}}$ by the large number of synaptic connections (see Table 3.1) makes the p_{ee} and p_{ei} subcortical spike inputs completely negligible in this high-firing limit in which the intracortical excitatory inputs dominate. As calculated here, the resulting amplitude of the excitatory seizure amplitudes for I_{ee} and I_{ei} are enormous, generating battery-like voltages(!) which are almost certainly physiologically implausible. Fortunately, the presence of the ψ_{jk} weighting functions in the model provide a voltage-clamp action, ensuring that the actual soma voltages do not "explode" with overexcitation. Substituting these saturation-maxima into Eqs (3.7a,3.7b) then solving for h_e and h_i in turn gives the steady-state soma voltages at the seizure extremum as

$$h_e^{\text{seiz}} = \frac{\left|h_e^{\text{rev}} - h_e^{\text{rest}}\right| h_e^{\text{rest}} + h_e^{\text{rev}} I_{ee}^{\text{seiz}}}{\left|h_e^{\text{rev}} - h_e^{\text{rest}}\right| + I_{ee}^{\text{seiz}}} = +43.9 \text{ mV} \tag{3.18a}$$

$$h_i^{\text{seiz}} = \frac{\left|h_e^{\text{rev}} - h_i^{\text{rest}}\right| h_i^{\text{rest}} + h_e^{\text{rev}} I_{ei}^{\text{seiz}}}{\left|h_e^{\text{rev}} - h_i^{\text{rest}}\right| + I_{ei}^{\text{seiz}}} = +43.4 \text{ mV}. \tag{3.18b}$$

In both cases, the seizure voltages are close to, but a little less than, the $h_e^{\mathrm{rev}} = +45$ mV reversal potential. This state of extreme depolarization appears at the top-left corner of the Fig. 3.4a graph of macrocolumn steady-states.

3.4 Stationary Solutions for the $\psi_{jk} \equiv 1$ System

Although it is standard practice when modelling single neurons to include ionic reversal potentials (e.g., the Hodgkin–Huxley and Tuckwell neurons discussed in Chap. 1), this description of cell behaviour seems to be omitted in the mean-field or neural aggregate theories. Certainly none of the mean-field models surveyed in Sect. 1.8—other than the more recent Liley work (Liley *et al.*, 1999, 2002)—incorporates ion-reversal potentials. This raises the obvious question: If reversal potentials are important for modelling single neurons, why do they become unimportant when modelling populations of neurons? And: Is any "damage" done to model integrity by ignoring reversal potentials?

The Liley model we are using in this thesis *explicitly includes* reversal potentials—these are the ψ weighting functions that scale the synaptic inputs. In order to synthesize a model that *ignores* reversal potentials, we set these weighting functions to plus and minus unity:

$$\psi_{ee}(h_e) = \psi_{ei}(h_i) = +1 \qquad \psi_{ie}(h_e) = \psi_{ii}(h_i) = -1\,. \tag{3.19}$$

Thus the four weighting functions are to become constants, independent of soma voltage. In the work that follows, I investigate the implications of setting the ψ functions to unity.

3.4.1 Pathological Roots Revisited

I now apply the steady-state analysis presented in Section 3.3.5 to the special-case $\psi = \pm 1$ macrocolumn. First, I examine the two extremum cases $\lambda \to \infty$ (coma) and $\lambda \to 0$ (seizure), then I investigate how the distribution of steady states varies with anaesthetic effect.

1. Infinite Inhibition: Coma

Setting $\psi_{ee}(h_e) = \psi_{ei}(h_i) = 1$, and $\psi_{ie}(h_e) = \psi_{ii}(h_i) = -1$ in Eqs (3.7a, 3.7b), then solving for h_e and h_i in the infinite-inhibition, zero-firing limit $S_e(h_e) \to 0$ and $S_i(h_i) \to 0$ gives the following steady-state soma voltages:

$$\begin{aligned} h_e^{\mathrm{coma}} &= h_e^{\mathrm{rest}} + I_{ee} - I_{ie} \\ &= h_e^{\mathrm{rest}} + p_{ee}\, G_e\, e/\gamma_e - \lambda\, p_{ie}\, G_i\, e/\gamma_i \\ &\to -\infty \quad \text{as} \quad \lambda \to \infty \end{aligned} \tag{3.20a}$$

and

$$\begin{aligned} h_i^{\mathrm{coma}} &= h_i^{\mathrm{rest}} + I_{ei} - I_{ii} \\ &= h_i^{\mathrm{rest}} + p_{ei}\, G_e\, e/\gamma_e - \lambda\, p_{ii}\, G_i\, e/\gamma_i \\ &\to -\infty \quad \text{as} \quad \lambda \to \infty \end{aligned} \tag{3.20b}$$

showing that, unlike the standard macrocolumn which enforces an asymptotic lower bound of -90 mV (the h_i reversal potential, h_i^{rev}), the unity-ψ model has steady-state coma voltages which are completely unconstrained, going to minus-infinity with the I_{ie} and I_{ii} inhibitory inputs.

2. Zero Inhibition: Seizure

To obtain the seizure limit, we set $\lambda = 0$, so the inhibitory inputs I_{ie} and I_{ii} must also be zero; and we set the sigmoids at their maximum firing rates, $\mathcal{S}_e(h_e) \rightarrow \mathcal{S}_e^{\max}$ and $\mathcal{S}_i(h_i) \rightarrow \mathcal{S}_i^{\max}$. Then solving Eqs (3.7a, 3.7b) for the soma voltages gives the following seizure extremum values:

$$\begin{aligned} h_e^{\mathrm{seiz}} &= h_e^{\mathrm{rest}} + I_{ee} - I_{ie} \\ &= h_e^{\mathrm{rest}} + \left[(N_{ee}^{\alpha} + N_{ee}^{\beta})\, \mathcal{S}_e^{\max} + p_{ee} \right] G_e e/\gamma_e - 0 \\ &= +11{,}404 \text{ mV} \end{aligned} \tag{3.21a}$$

and

$$\begin{aligned} h_i^{\mathrm{seiz}} &= h_i^{\mathrm{rest}} + I_{ei} - I_{ii} \\ &= h_i^{\mathrm{rest}} + \left[(N_{ei}^{\alpha} + N_{ei}^{\beta})\, \mathcal{S}_e^{\max} + p_{ei} \right] G_e e/\gamma_e - 0 \\ &= +8{,}143 \text{ mV}\,. \end{aligned} \tag{3.21b}$$

Again, in contrast to the standard macrocolumn model which places an upper limit close to $+45$ mV (the h_e reversal potential, h_e^{rev}), the non-inclusion of the ψ weighting functions has cancelled an important moderating influence on the excitatory inputs, resulting in predicted seizure voltages which are completely implausible.

3. Distribution of Steady States

For the unity-ψ macrocolumn, how do the number and location of soma steady-state voltages vary with anaesthetic effect? To answer this question, I applied the same root-searching algorithms described in Sections 3.3.1 and 3.3.5, but found that I needed to vastly extend the λ search domain in order to capture the complete distribution.

The search results are shown in Fig. 3.5, and should be compared with the distribution of steady states for the standard macrocolumn (see Fig. 3.4). The bottom branch no longer tends towards an asymptotic value of $h_i^{\mathrm{rev}} = -90$ mV as λ increases; instead, the bottom branch values decline steeply as λ increases, becoming increasingly more hyperpolarized to a limiting value of about -190 mV. This is a numerical limit arising from the finite precision of the MATLAB calculations (at these very negative soma voltages, the sigmoid function returns an output which is within machine epsilon of zero).[1]

The extended middle branch has positive slope, implying that the macrocolumn becomes *more depolarized* (more excited) as anaesthetic concentration increases. This is a completely unphysical result, so we can expect that, as for the standard macrocolumn, the middle branch will be a locus of *unstable* equilibrium points. A linear stability analysis will confirm this prediction—see Chapter 4.4.

The upper branch is quite truncated, and is only detected for very extreme values of anaesthetic effect. The normal range for anaesthetic-induced increase in the duration of the inhibitory

---

[1] In MATLAB, `eps = 2.22x10`$^{-16}$ is the distance between 1.0 and the next largest floating point number.

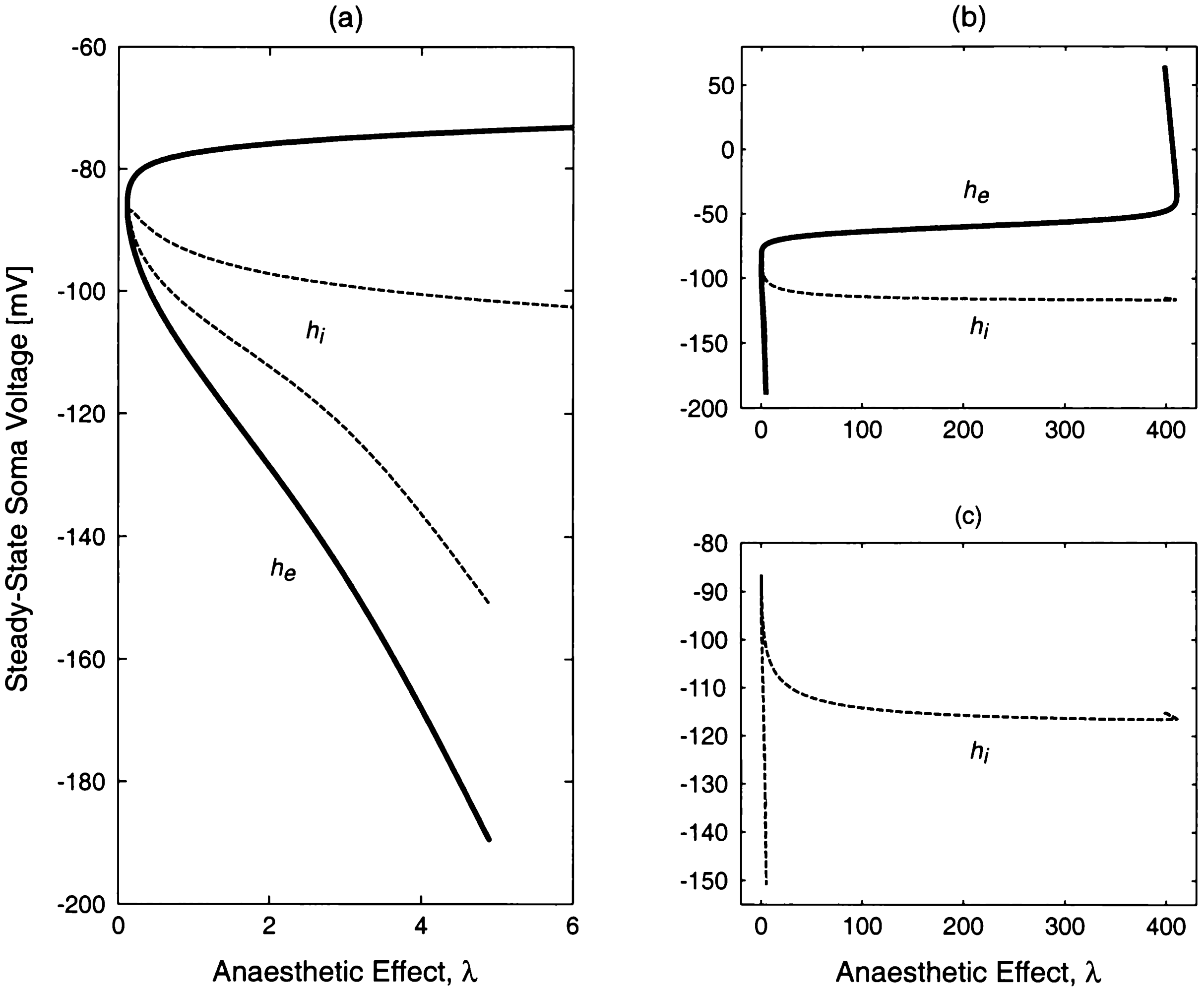

Figure 3.5: Steady-state soma voltages for the unity-ψ macrocolumn. (a) For the range $0 < \lambda < 5$, only two roots for each of h_e and h_i could be found. In principle, the bottom branch is expected to diverge to infinity with λ. (b) To view the complete distribution of roots, the range for anaesthetic effect has to be extended to $0 < \lambda < 420$. Note the eventual appearance of a right-hand knee and top branch for these extreme values of anaesthetic effect. (c) As for (b), but only the h_i roots shown for clarity. The "hook" at the right extreme of h_i matches the knee and upper branch of h_e shown in (b).

post-synaptic potential is of the order of 1.5 to 4 (Gage and Robertson, 1985; Franks and Lieb, 1994; Jones and Harrison, 1993; Antkowiak and Hentschke, 1997). For the standard macrocolumn, the right-hand knee (point A_3 on Fig.3.4) occurs at $\lambda \approx 1.53$; in contrast, for the unity-ψ macrocolumn, it occurs at $\lambda \approx 411$. In principle, when a high-firing, upper-branch (= conscious) macrocolumn is pushed beyond this knee, it must collapse to the low-firing (= unconscious) lower branch, yet, numerically at least, the bottom branch does not exist here!

On the basis of these results, I conclude that, for the purposes of anaesthetic modelling, the unity-ψ macrocolumn is without merit: the algebraic simplifications which result from setting the neurokinetics weighting factors to ±1 come at the cost of a significant loss of physiological fidelity.

3.5 Significance of the Steady States—Revisited

By re-examining the λ-dependent locus of steady-state soma voltages (shown again in Fig. 3.6), we can develop insights into how the cerebral cortex is rendered unconscious with anaesthetic. The significant observations are that the locus of steady states is a multiple-valued function of anaesthetic amount, and that the mid-branch loci are unstable (the stability analysis will be presented in Chapter 4). This means that it is impossible for the macrocolumn to traverse from the upper branch to the lower branch (or the reverse) in a continuous path: there must be discontinuous jump transition between states.

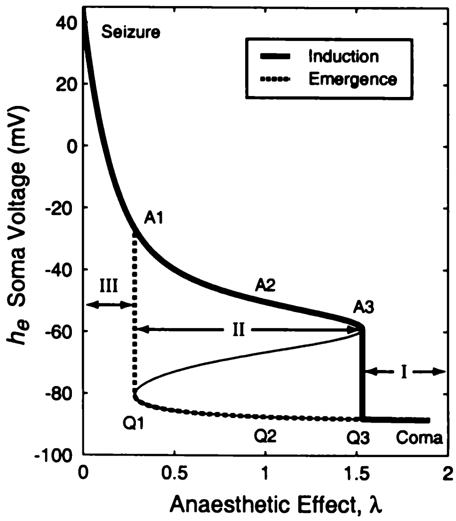

Figure 3.6: Stationary states trajectory for h_e

Suppose the neural assembly is initially at location A_2. As anaesthetic effect λ increases, h_e^0 will slide to the right down the upper branch to A_3, whereupon a sudden jump to Q_3 on the lower branch must occur, since the middle branch is unstable and therefore disallowed. Further increases in λ will then cause h_e^0 to advance along the bottom branch towards the "coma" limit. If instead, the assembly was initially at Q_2 on the lower branch, then increases in λ would lead to a smooth, monotonic decrease in soma voltage towards "coma," with no jump discontinuity.

If the cortex is pictured as a superposition of macrocolumns, some active and some quiescent, then the model predicts that those macrocolumns which are active will undergo a rapid and dramatic active→quiescent change of "phase" at a critical anaesthetic concentration. The signature of this phase change will be a sudden decrease in the soma-average DC voltage as the active neurons become hyperpolarized.

Is this prediction amenable to experimental verification using electrodes affixed to the scalp? Attempting to detect changes in the average DC levels of the cortex via scalp electrodes would seem to be an almost impossibly challenging task. How is one to distinguish the "signal," i.e., the change in cortical polarization, from the "noise"—DC changes arising from gradual changes in the electrode-to-skin impedence, or generated by slow variations in nearby muscle-generated voltages, or generated by slow-wave AC from the cortex itself? Prospecting for the change in the internal DC state via external skin electrodes would seem to be a hopeless proposition.

But, what if the change in the DC polarization state forces a change in the AC characteristics of the scalp-measured EEG signal? It does not seem implausible that the spectral *shape* (i.e., the distribution of spectral energy) of the EEG generated by high-firing active neurons should be distinct from that generated by the much lower-firing quiescent neurons. Even if only a small proportion of macrocolumns are in the activated state, we might expect an anaesthetic-driven downwards transition across the A_3Q_3 gap to produce a measurable change in the EEG signal provided the active macrocolmns are acting synchronously.

In Chapter 5 we drive the model macrocolumn with white noise, and investigate how the resulting fluctuation spectrum varies with anaesthetic effect. We will find that at transition, the theory predicts a dramatic rise in total fluctuation power which is contemporaneous with a pronounced shift—towards lower frequencies—in its spectral distribution. These results are consistent with the fluctuation behaviours observed in the first-order phase transitions of classical thermodynamics. It is very encouraging to be able to report that these qualitative predictions are precisely what is observed in clinical measurements of the EEG patterns for patients undergoing general anaesthesia.

But before examining fluctuation spectra, we need to establish the stability properties of the macrocolumn steady states. This is the business of Chapter 4.

Chapter 4

Stability of the Macrocolumn Stationary States

We wish to establish which of the soma-voltage equilibrium points plotted on Fig. 3.4a are stable with respect to small perturbations, and which points are unstable. If the macrocolumn has settled into a stable configuration, it can be pictured as nestled at the bottom of a potential well where comfortably it can remain in a state of minimum energy. Conversely, an unstable configuration would have the macrocolumn sitting at the crest of a potential hill from which, given the slightest disturbance, it will slide away into a nearby potential valley. Thus the locus of unstable equilibria demarcate the energy barrier which separates the stable equilibrium valleys lying on either side.

Reichl (1980, pp. 683–687) describes a standard technique for determining the stability of a set of coupled first-order ordinary differential equations: one makes a small-perturbation Taylor expansion about the steady state, keeping only the linear terms, then examines the behaviour of the eigenvalues for the linearized system.

In order to apply the Reichl technique to the cortical macrocolumn, we must first rewrite the eight coupled first- and second-order differential equations (DEs) of Eqs (3.1–3.4) as a set of coupled first-order DEs: the four second-order DEs for local "currents" I_{jk} become eight first-order DEs, and the two second-order DEs for long-range spike input $\phi_{e,i}$ from distant excitatory sources are replaced by four first-order DEs. This gives 12 first-order equations for the macrocolumn inputs, plus the two equations for the evolution of the soma voltages, giving a total count of 14 first-order equations. The linear stability analysis would therefore require the calculation of the eigenvalues of a 14×14 system matrix.

However, our primary interest lies with a much simpler version of the Liley equations—the "adiabatic" equations (described below) which recognize that, compared with the h_e and h_i soma voltages, the synaptic inputs evolve on much faster time scales, and can be treated as if they have already achieved steady state. This simplifying assumption collapses the dimensionality of the macrocolumn system from eight independent variables to two, h_e and h_i, and the set of 14 first-order DEs required for the full system is replaced a single pair of DEs giving the time evolution of h_e and h_i. The stability analysis now only requires finding the eigenvalues of a 2×2 system matrix.

4.1 Adiabatic Model of the Macrocolumn

The "adiabatic" approximation[1] is a simplification which arises from a recognition that the input terms (I_{jk}, $\phi_{e,i}$) vary on time scales that are quite distinct from the time scale of the soma voltages h_e and h_i. This becomes apparent when we compare the various relaxation times computed from the numerical values listed in Table 3.1:

$$\begin{aligned}
&\text{relaxation time for } I_{ee}, I_{ei} &&= (\gamma_e)^{-1} \approx 3.3 \text{ ms}\\
&\text{relaxation time for } I_{ie}, I_{ii} &&= (\gamma_i)^{-1} \approx 15.4 \text{ ms}\\
&\text{relaxation time for } \phi_e &&= (\bar{v}\Lambda_{ee})^{-1} \approx 3.6 \text{ ms}\\
&\text{relaxation time for } \phi_i &&= (\bar{v}\Lambda_{ei})^{-1} \approx 2.2 \text{ ms}
\end{aligned}$$

whereas the $\tau_{e,i}$ time-scales for the $h_{e,i}$ soma potentials can be as large as 100 ms (Koch *et al.*, 1996). For our present modelling work we set $\tau_e = \tau_i = 40$ ms, allowing us to make the working assumption that the six neuronal inputs $[I_{ee}, I_{ie}, I_{ei}, I_{ii}, \phi_e, \phi_i]$ equilibrate very much faster than the soma potentials $h_{e,i}$ themselves, so that on $h_{e,i}$ equilibration time-scales, all time-derivatives appearing in the input equations (3.2–3.4) can be set to zero, allowing us to write adiabatically simplified expressions for the six neuronal inputs as functions of h_e and h_i only. This gives the following equations of motion for the adiabatic macrocolumn:

$$\frac{dh_e}{dt} \equiv F_1(h_e, h_i) = \left[h_e^{\text{rest}} - h_e + \psi_{ee}(h_e)\, I_{ee}(h_e) + \psi_{ie}(h_e)\, I_{ie}(h_i)\right] / \tau_e, \tag{4.1a}$$

$$\frac{dh_i}{dt} \equiv F_2(h_e, h_i) = \left[h_i^{\text{rest}} - h_i + \psi_{ei}(h_i)\, I_{ei}(h_e) + \psi_{ii}(h_i)\, I_{ii}(h_i)\right] / \tau_i, \tag{4.1b}$$

$$I_{ee}(h_e) = \left[(N_{ee}^{\alpha} + N_{ee}^{\beta})\, \mathcal{S}_e(h_e) + p_{ee}\right] G_e e/\gamma_e, \tag{4.2a}$$

$$I_{ei}(h_e) = \left[(N_{ei}^{\alpha} + N_{ei}^{\beta})\, \mathcal{S}_e(h_e) + p_{ei}\right] G_e e/\gamma_e, \tag{4.2b}$$

$$I_{ie}(h_i) = \lambda \left[N_{ie}^{\beta}\, \mathcal{S}_i(h_i) + p_{ie}\right] G_i e/\gamma_i, \tag{4.3a}$$

$$I_{ii}(h_i) = \lambda \left[N_{ii}^{\beta}\, \mathcal{S}_i(h_i) + p_{ii}\right] G_i e/\gamma_i. \tag{4.3b}$$

Note that the $\phi_{e,i}$ long-range spike inputs have been folded into the I_{ee} and I_{ei} equations, and that anaesthetic effect λ is shown explicitly in the I_{ie} and I_{ii} equations. The ψ_{jk} weighting functions are repeated here for ease of reference:

$$\begin{aligned}
\psi_{ee}(h_e) &= \frac{h_e^{\text{rev}} - h_e}{|h_e^{\text{rev}} - h_e^{\text{rest}}|}, & \psi_{ei}(h_i) &= \frac{h_e^{\text{rev}} - h_i}{|h_e^{\text{rev}} - h_i^{\text{rest}}|},\\
\psi_{ie}(h_e) &= \frac{h_i^{\text{rev}} - h_e}{|h_i^{\text{rev}} - h_e^{\text{rest}}|}, & \psi_{ii}(h_i) &= \frac{h_i^{\text{rev}} - h_i}{|h_i^{\text{rev}} - h_i^{\text{rest}}|}.
\end{aligned} \tag{4.4}$$

This adiabatic approximation has reduced the dimensionality of the macrocolumn model from the equivalent of 14 first-order differential equations to a single pair of coupled ODEs.

I now present a summary of Reichl's description of linearized stability analysis, paraphrased for application to the two-variable adiabatic macrocolumn equations.

---

[1] The notion of macrocolumn simplification via the adiabatic approach described here was first suggested and developed by M. Steyn-Ross; this philosophy allowed the calculation of the fluctuation spectrum described in our paper Steyn-Ross, Steyn-Ross, Sleigh, and Liley (1999).

4.2 Linear Stability Theory

To establish the stability of the adiabatic model, we assume the macrocolumn has achieved steady state, then allow small perturbations $(\delta h_e, \delta h_i)$ in the excitatory and inhibitory voltages away from their steady-state values (h_e^0, h_i^0):

$$\begin{aligned} \delta h_e(t) &= h_e(t) - h_e^0 & (4.5a) \\ \delta h_i(t) &= h_i(t) - h_i^0 \,. & (4.5b) \end{aligned}$$

If these perturbations tend to decay to zero in time, then the equilibrium is stable with respect to small disturbances; if the perturbations grow, then the equilibrium is unstable. Taking d/dt of Eq. 4.5 gives the time-rate change of the perturbations:

$$\begin{aligned} \frac{d}{dt}(\delta h_e) &= \frac{dh_e}{dt} - 0 = F_1(h_e, h_i) & (4.6a) \\ \frac{d}{dt}(\delta h_i) &= \frac{dh_i}{dt} - 0 = F_2(h_e, h_i) & (4.6b) \end{aligned}$$

in which the F_1 and F_2 rate functions can be expanded as a two-variable Taylor series about steady state

$$\begin{aligned} F_1(h_e, h_i) &= F_1(h_e^0, h_i^0) + \delta h_e \left.\frac{\partial F_1}{\partial h_e}\right|_0 + \delta h_i \left.\frac{\partial F_1}{\partial h_i}\right|_0 + O\left(\delta h_{e,i}^2\right) & (4.7a) \\ F_2(h_e, h_i) &= F_2(h_e^0, h_i^0) + \delta h_e \left.\frac{\partial F_2}{\partial h_e}\right|_0 + \delta h_i \left.\frac{\partial F_2}{\partial h_i}\right|_0 + O\left(\delta h_{e,i}^2\right) \,. & (4.7b) \end{aligned}$$

The zero subscripts indicate that the partial derivatives are to be evaluated at the equilibrium point. For very small values of δh_e, δh_i, (i.e., for solutions very close to equilibrium) we can drop the $O(\delta h_{e,i}^2)$ quadratic correction terms to give the linearized approximation

$$\begin{aligned} F_1(h_e, h_i) &= \delta h_e \left.\frac{\partial F_1}{\partial h_e}\right|_0 + \delta h_i \left.\frac{\partial F_1}{\partial h_i}\right|_0 & (4.8a) \\ F_2(h_e, h_i) &= \delta h_e \left.\frac{\partial F_2}{\partial h_e}\right|_0 + \delta h_i \left.\frac{\partial F_2}{\partial h_i}\right|_0 \,. & (4.8b) \end{aligned}$$

The $F_1(h_e^0, h_i^0)$ and $F_2(h_e^0, h_i^0)$ terms have disappeared since they are identically zero at steady state. Expressing the linear expansion in matrix form (and dropping the $|_0$ "at equilibrium" notation),

$$\begin{bmatrix} \frac{d}{dt}(\delta h_e) \\ \frac{d}{dt}(\delta h_i) \end{bmatrix} = \begin{bmatrix} \frac{\partial F_1}{\partial h_e} & \frac{\partial F_1}{\partial h_i} \\ \frac{\partial F_2}{\partial h_e} & \frac{\partial F_2}{\partial h_i} \end{bmatrix} \begin{bmatrix} \delta h_e \\ \delta h_i \end{bmatrix} \qquad (4.9)$$

or,

$$\frac{d}{dt}\mathbf{h} = \mathbf{J}\,\mathbf{h} \qquad (4.10)$$

where $\mathbf{h} = [\delta h_e \quad \delta h_i]^{\mathrm{T}}$ is the perturbations column vector, and $\mathbf{J}$ is the 2×2 Jacobian matrix of partial derivatives evaluated at equilibrium. Provided $\mathbf{J}$ is non-singular (i.e., $\det \mathbf{J} \neq 0$), then it can be diagonalized (Wiberg, 1971, p.70) by applying a similarity transformation $\mathbf{X}^{-1}\mathbf{J}\mathbf{X}$ where $\mathbf{X}$ is the matrix of the eigenvectors $[\mathbf{x}_1, \mathbf{x}_2]$ of $\mathbf{J}$ corresponding to eigenvalues λ_1, λ_2. The eigenvectors are defined,

$$\mathbf{J}\,\mathbf{x}_1 = \lambda_1 \mathbf{x}_1 \tag{4.11a}$$

$$\mathbf{J}\,\mathbf{x}_2 = \lambda_2 \mathbf{x}_2 \tag{4.11b}$$

so that

$$\mathbf{J}\,\mathbf{X} = \mathbf{X}\,\mathbf{\Lambda} \tag{4.12}$$

where

$$\mathbf{\Lambda} = \begin{bmatrix} \lambda_1 & 0 \\ 0 & \lambda_2 \end{bmatrix} \tag{4.13}$$

is the diagonal matrix of eigenvalues, and

$$\mathbf{X} = \left[\begin{array}{c|c} x_{11} & x_{12} \\ x_{21} & x_{22} \end{array}\right] = [\mathbf{x}_1 \mid \mathbf{x}_2] \tag{4.14}$$

is the partitioned matrix whose columns are the eigenvectors of $\mathbf{J}$. The similarity transformation is equivalent to applying a change of variable

$$\mathbf{h} = \mathbf{X}\,\mathbf{g}, \qquad \text{or} \qquad \mathbf{g} = \mathbf{X}^{-1}\,\mathbf{h}, \tag{4.15}$$

so Eq. (4.10) becomes

$$\frac{d}{dt}(\mathbf{X}\,\mathbf{g}) = \mathbf{J}\,\mathbf{X}\,\mathbf{g} = \mathbf{X}\,\mathbf{\Lambda}\,\mathbf{g} \tag{4.16}$$

where we have made use of the eigenvalue equation (4.12). Left-multiplying both sides by $\mathbf{X}^{-1}$ gives,

$$\frac{d}{dt}\mathbf{g} = \mathbf{X}^{-1}\,\mathbf{X}\,\mathbf{\Lambda}\,\mathbf{g} = \mathbf{\Lambda}\,\mathbf{g} \tag{4.17}$$

or,

$$\begin{bmatrix} \frac{d}{dt}g_1 \\ \frac{d}{dt}g_2 \end{bmatrix} = \begin{bmatrix} \lambda_1 & 0 \\ 0 & \lambda_2 \end{bmatrix} \begin{bmatrix} g_1 \\ g_2 \end{bmatrix}. \tag{4.18}$$

This diagonal system represents a pair of uncoupled differential equations which can be integrated immediately to give the solutions

$$\begin{bmatrix} g_1(t) \\ g_2(t) \end{bmatrix} = \begin{bmatrix} g_1(0)\,e^{\lambda_1 t} \\ g_2(0)\,e^{\lambda_2 t} \end{bmatrix} = \begin{bmatrix} e^{\lambda_1 t} & 0 \\ 0 & e^{\lambda_2 t} \end{bmatrix} \begin{bmatrix} g_1(0) \\ g_2(0) \end{bmatrix} \tag{4.19}$$

Writing $\mathbf{g}(t) = \mathbf{X}^{-1}\mathbf{h}(t)$ and $\mathbf{g}(0) = \mathbf{X}^{-1}\mathbf{h}(0)$, gives

$$\mathbf{X}^{-1} \begin{bmatrix} \delta h_e(t) \\ \delta h_i(t) \end{bmatrix} = \begin{bmatrix} e^{\lambda_1 t} & 0 \\ 0 & e^{\lambda_2 t} \end{bmatrix} \mathbf{X}^{-1} \begin{bmatrix} \delta h_e(0) \\ \delta h_i(0) \end{bmatrix} \tag{4.20}$$

which, after a left-multiplication by $\mathbf{X}$, completes the transformation back to $\mathbf{h}$ for the time-course of the soma fluctuations,

$$\begin{bmatrix} \delta h_e(t) \\ \delta h_i(t) \end{bmatrix} = \mathbf{X} \begin{bmatrix} e^{\lambda_1 t} & 0 \\ 0 & e^{\lambda_2 t} \end{bmatrix} \mathbf{X}^{-1} \begin{bmatrix} \delta h_e(0) \\ \delta h_i(0) \end{bmatrix} . \tag{4.21}$$

Expanding the right-hand side we find

$$\delta h_e(t) = c_1 \, e^{\lambda_1 t} + c_2 \, e^{\lambda_2 t} \tag{4.22a}$$

$$\delta h_i(t) = d_1 \, e^{\lambda_1 t} + d_2 \, e^{\lambda_2 t} \tag{4.22b}$$

where the coefficients c_1, c_2, d_1, d_2 are constants which depend only on the initial perturbations $\delta h_e(0), \delta h_i(0)$ scaled by the x_{jk} elements of the $\mathbf{X}$ eigenvector matrix. Thus the growth behaviour of the perturbations depends entirely on the sign of the real parts of the eigenvalues λ_1, λ_2 of the $\mathbf{J}$ Jacobian matrix (Reichl, 1980):

- If *both* eigenvalues are *real and negative*, then the perturbations will decay exponentially to zero, and the stationary point is *stable*;
- If *either* eigenvalue is *real and positive*, then the perturbations will grow exponentially, and the stationary point is *unstable*;
- If the eigenvalues are complex, i.e., $\lambda_1 = \alpha + i\beta$ and $\lambda_2 = \alpha - i\beta$, then the perturbations will exhibit an oscillatory behaviour whose angular frequency is $\omega = \beta$; these oscillations will decay with time exponentially if $\alpha < 0$ (i.e., stationary state is a *stable* focus), but will grow without limit if $\alpha > 0$ (*unstable* focus).

4.3 Stability Analysis for the Adiabatic Macrocolumn

4.3.1 Adiabatic Equations

In order to establish the stability characteristics along the Fig. 3.4 S-bend of adiabatic steady states, we need to compute the eigenvalues of the Jacobian matrix defined in Eq. (4.9),

$$\mathbf{J} = \begin{bmatrix} \dfrac{\partial F_1}{\partial h_e} & \dfrac{\partial F_1}{\partial h_i} \\[2ex] \dfrac{\partial F_2}{\partial h_e} & \dfrac{\partial F_2}{\partial h_i} \end{bmatrix} . \tag{4.23}$$

From Eqs (4.1–4.3) we compute the matrix elements as:

$$J_{11} \equiv \frac{\partial F_1}{\partial h_e} = \frac{1}{\tau_e} \left[-1 + \frac{\partial \psi_{ee}}{\partial h_e} I_{ee} + \psi_{ee} \frac{\partial I_{ee}}{\partial h_e} + \frac{\partial \psi_{ie}}{\partial h_e} I_{ie} \right] \tag{4.24a}$$

$$J_{12} \equiv \frac{\partial F_1}{\partial h_i} = \frac{1}{\tau_e} \left[\psi_{ie} \frac{\partial I_{ie}}{\partial h_i} \right] \tag{4.24b}$$

$$J_{21} \equiv \frac{\partial F_2}{\partial h_e} = \frac{1}{\tau_i} \left[\psi_{ei} \frac{\partial I_{ei}}{\partial h_i} \right] \tag{4.24c}$$

$$J_{22} \equiv \frac{\partial F_2}{\partial h_i} = \frac{1}{\tau_i} \left[-1 + \frac{\partial \psi_{ei}}{\partial h_i} I_{ei} + \frac{\partial \psi_{ii}}{\partial h_i} I_{ii} + \psi_{ii} \frac{\partial I_{ii}}{\partial h_i} \right] \tag{4.24d}$$

with the four ψ_{jk} weighting-function derivatives given by constants,

$$\frac{\partial\psi_{ee}}{\partial h_e} = \frac{-1}{|h_e^{\mathrm{rev}} - h_e^{\mathrm{rest}}|}, \qquad \frac{\partial\psi_{ei}}{\partial h_i} = \frac{-1}{|h_e^{\mathrm{rev}} - h_i^{\mathrm{rest}}|}, \tag{4.25a}$$

$$\frac{\partial\psi_{ie}}{\partial h_e} = \frac{-1}{|h_i^{\mathrm{rev}} - h_e^{\mathrm{rest}}|}, \qquad \frac{\partial\psi_{ii}}{\partial h_i} = \frac{-1}{|h_i^{\mathrm{rev}} - h_i^{\mathrm{rest}}|}, \tag{4.25b}$$

and the four I_{jk} input-current derivatives given by the expressions,

$$\frac{\partial I_{ee}}{\partial h_e} = (N_{ee}^{\alpha} + N_{ee}^{\beta})\,\frac{G_e e}{\gamma_e}\,\frac{\partial \mathcal{S}_e}{\partial h_e} \tag{4.26a}$$

$$\frac{\partial I_{ei}}{\partial h_e} = (N_{ei}^{\alpha} + N_{ei}^{\beta})\,\frac{G_e e}{\gamma_e}\,\frac{\partial \mathcal{S}_e}{\partial h_e} \tag{4.26b}$$

$$\frac{\partial I_{ie}}{\partial h_i} = \lambda\,\frac{N_{ie}^{\beta} G_i e}{\gamma_i}\,\frac{\partial \mathcal{S}_i}{\partial h_i} \tag{4.26c}$$

$$\frac{\partial I_{ii}}{\partial h_i} = \lambda\,\frac{N_{ii}^{\beta} G_i e}{\gamma_i}\,\frac{\partial \mathcal{S}_i}{\partial h_i}\,. \tag{4.26d}$$

The firing-rate sigmoids $\mathcal{S}_{e,i}$ have derivatives

$$\frac{\partial \mathcal{S}_e}{\partial h_e} = \frac{-g_e\,\mathcal{S}_e^{\max}\exp[-g_e(h_e - \theta_e)]}{\left[1 + \exp[-g_e(h_e - \theta_e)]\right]^2} \tag{4.27a}$$

$$\frac{\partial \mathcal{S}_i}{\partial h_i} = \frac{g_i\,\mathcal{S}_i^{\max}\exp[-g_i(h_i - \theta_i)]}{\left[1 + \exp[-g_i(h_i - \theta_i)]\right]^2}\,. \tag{4.27b}$$

The **J** Jacobian matrix can now be evaluated as a function of GABA anaesthetic effect at arbitrary points along the trajectory of (h_e, h_i) steady states.

4.3.2 Results

Equations (4.24–4.27) were coded into MATLAB and the eigenvalues of the **J** matrix determined using the MATLAB `eig` function. The retrieved eigenvalue pairs are plotted in Fig. 4.1 as a function of λ, the GABA anaesthetic effect.

Only the *dominant* eigenvalue need be inspected in order to determine the stability of a given stationary point. By "dominant" is meant that member of the eigenvalue pair whose signed real part is the larger of the two (i.e., for eigenvalues $(\Lambda_1, \Lambda_2) = (\sigma_1 + i\omega_1, \sigma_2 + i\omega_2)$, Λ_1 is dominant if $\sigma_1 > \sigma_2$). Nevertheless, it is informative to plot the evolution of both eigenvalues as a function of anaesthetic. Figure 4.1b shows the real part of both eigenvalues. When the real-part curves coincide (grey dots), the eigenvalues form complex-conjugate pairs whose imaginary content is displayed in Figure 4.1c. Because all of the complex eigenvalues have large-amplitude *negative* real parts, the oscillatory component will be extremely strongly damped. For example, the complex eigenvalue $-4095.8 + 283.5i$ (which belongs to a point on the upper branch at $\lambda = 1.52$ just prior to the the A_3 turn) suggests an oscillation frequency about steady state of 283.5 rad/s = 45.1 Hz, but the attentuation factor of $e^{-4096} \approx 10^{-1800}$ ensures that this oscillation will never be seen.

The more significant feature Fig. 4.1b is the fact that the dominant eigenvalue crosses zero at the turning points A_3 (induction jump) and Q_1 (emergence return), looping into the positive

(a) Stationary h_e Trajectory

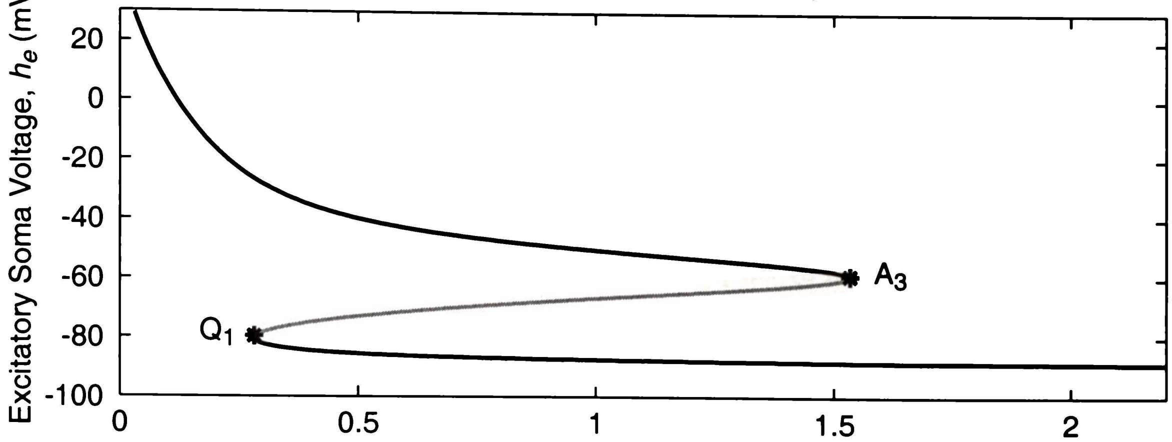

(b) Real [Eig] / 1000

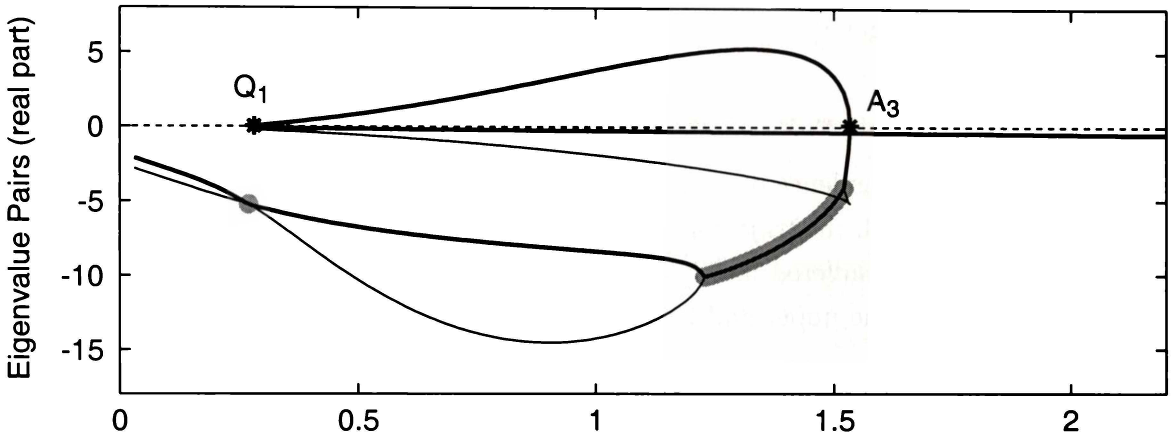

(c) Imag [Eig] / 1000

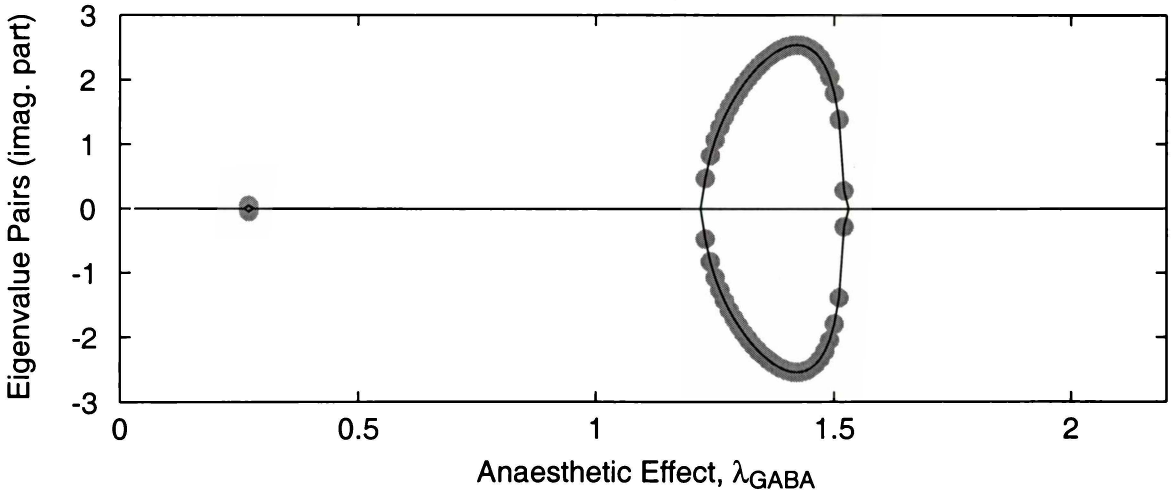

Figure 4.1: Stability chacteristics for the adiabatic macrocolumn. (a) Steady-state trajectory for h_e as a function of λ. The A_3 and Q_1 turning points mark the induction and emergence transition jumps. The unstable midbranch is drawn in grey. (b) Real part of the eigenvalue pairs as a function of λ for small fluctuations away from the steady state trajectory of (a). The dominant eigenvalue trend is drawn bold, the non-dominant eigenvalue is drawn light. The grey dots mark the two regions of complex eigenvalues. For these complex conjugate pairs, the real part is always strongly negative, so there is no possibility of oscillations about steady state. (c) Imaginary part of fluctuation eigenvalues. The grey dots are the sampled points; these have been joined as a guide to the eye.

half-plane, indicating that any small perturbation away from the midbranch stationary states of Fig. 4.1a will grow exponentially. Hence, the *midbranch is unstable.* Conversely, all points along the *upper and lower branches are stable* with respect to small perturbations because, for these regions, the real part of the dominant eigenvalue is always negative.

These stability results confirm the notion that the macrocolumn can persist in one of two stable states: either on the "active" upper branch where firing rates are high, or on the "quiescent" lower branch where firing rates are very subdued. These two stable regions (potential energy valleys) are separated by the potential hill defined by the unstable midbranch which joins the A_3 and Q_1 turning points.

4.4 Stability Analysis for the $\psi \equiv 1$ Macrocolumn

4.4.1 Unity-ψ Equations

In Chapter 3.4 I investigated the consequences of setting the ψ_{jk} neurokinetics coefficients to unity:

$$\psi_{ee} = \psi_{ei} = +1 , \qquad \text{and} \qquad \psi_{ie} = \psi_{ii} = -1 \tag{4.28}$$

thus removing their dependence on soma voltage (see Fig. 3.1). Compared with the standard reverse-S graph of Fig. 3.4, the trajectory of unity-ψ steady states of Fig. 3.5 gives the impression of an S-bend which has suffered multiple traumas: a stretch (by a factor of ~250) along the λ-axis, a truncation of the upper and lower branches, and a rotation about the turning points of these vestigial branches to near vertical. The dominant feature of the graph is the elongated midbranch of positive slope, and the claim was made earlier that because this midbranch has a positive h_e versus λ slope, these midbranch steady states are unphysical. Here I use linear stability analysis to verify the claim: the entire midbranch set of unity-ψ equilibrium states is unstable, and therefore disallowed.

Setting the ψ weights to ±unity simplifies the terms of the **J** Jacobian matrix; thus Eqs (4.24a–4.24d) become:

$$J_{11} \equiv \frac{\partial F_1}{\partial h_e} = \frac{1}{\tau_e}\left[-1 + \frac{\partial \psi_{ee}}{\partial h_e}\right] \tag{4.29a}$$

$$J_{12} \equiv \frac{\partial F_1}{\partial h_i} = \frac{1}{\tau_e}\left[-\frac{\partial I_{ie}}{\partial h_i}\right] \tag{4.29b}$$

$$J_{21} \equiv \frac{\partial F_2}{\partial h_e} = \frac{1}{\tau_i}\left[\frac{\partial I_{ei}}{\partial h_i}\right] \tag{4.29c}$$

$$J_{22} \equiv \frac{\partial F_2}{\partial h_i} = \frac{1}{\tau_i}\left[-1 - \frac{\partial I_{ii}}{\partial h_i}\right] \tag{4.29d}$$

where the form of the four I_{jk} input-current partial derivatives remain unchanged from those listed in Eqs (4.26a–4.26d). The eigenvalues for the revised Jacobian matrix are now presented.

4.4.2 Results

Figure 4.2 illustrates the stability chacteristics for the unity-ψ macrocolumn. The top panel (a) redraws the Fig. 3.5 stretched S-bend of steady-state soma voltages, but now with the midbranch

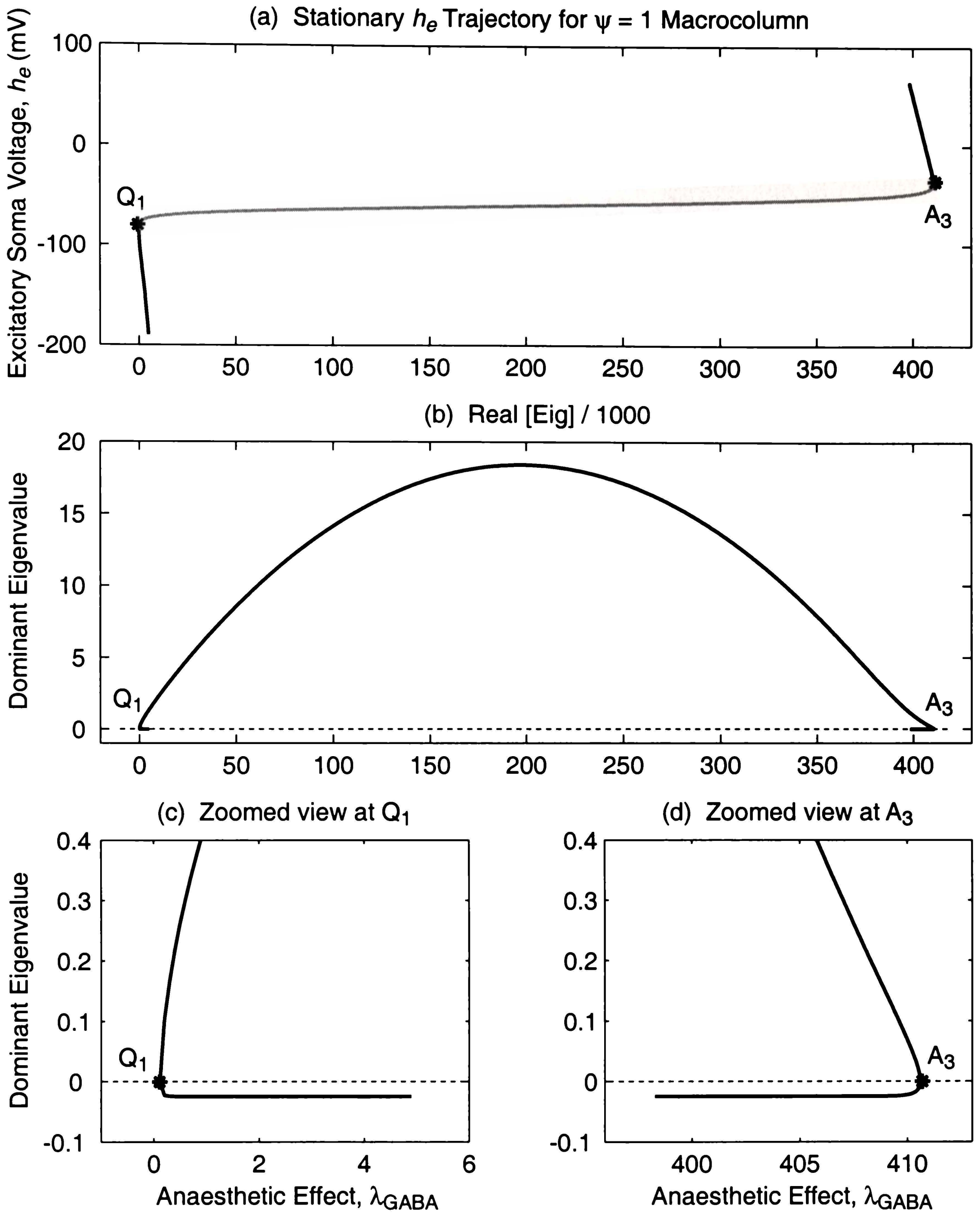

Figure 4.2: Stability chacteristics for the unity-ψ macrocolumn. (a) Steady-state trajectory for h_e as a function of λ. (Refer to Fig. 3.5 for the corresponding h_i trajectory.) The unstable midbranch is drawn in grey. (b) Dominant eigenvalue graph. Only the small hooks below the turning points at the left and right extremes of the graph show a stable (i.e., negative) dominant eigenvalue. (c) and (d) give zoomed-in views in the vicinity of the Q_1 and A_3 turning points respectively.

from turning point Q_1 to turning point A_3 drawn in grey to symbolize its instability. This stability information comes from Figure 4.2b where we see that apart from the easily-overlooked reentrant hook regions at either end, the dominant eigenvalue is almost always positive. Figures 4.2c,d give zoomed in views of the tiny regions of stability: the hyperpolarized bottom branch near Q_1, and the depolarized top branch near A_3.

It is hard to imagine any physiologically plausible significance to these tiny regions of stability which are separated by such a vast distance in λ space. Accordingly, I conclude that the unity-ψ limit for the adiabatic macrocolumn is uninteresting, and no further space will be devoted to its study in this thesis.

Chapter 5

Fluctuation Spectrum for the Macrocolumn

In the first part of this chapter I describe how the Liley equations for the homogeneous macrocolumn are transformed into stochastic differential equations by incorporating a white-noise perturbation about the macrocolumn steady state. The response function, expressed in frequency space, defines a theoretical EEG spectrum. By steadily increasing the λ anaesthetic parameter (i.e., by reducing the inhibitory rate constant $\overline{\gamma_i} = \gamma_i/\lambda$), we are able to investigate how the EEG spectrum is expected to vary during the controlled induction of unconsciousness. Similarly, by reducing λ we can predict the EEG spectral changes expected to occur as a patient emerges from unconsciousness. We will find that the theoretical model makes the following predictions:

1. There will be a strong surge in the EEG fluctuation power as the transition point into unconsciousness is approached;
2. There will be a second, distinct EEG power surge for the emergence phase as the cortex approaches the jump return back to consciousness;
3. These fluctuation maxima will occur at the turning points of the reverse-S equilibrium curve, implying a hysteresis separation of the induction and emergence trajectories: the macrocolumn return to its high-firing state (consciousness) will occur at a *lower* anaesthetic concentration than that required for the initial induction of the low-firing state (unconsciousness);
4. As transition is approached, there will be a change in the distribution of the spectral energy of the fluctuations, with a strong growth in the lower-frequency components occurring at the expense of the higher frequencies;
5. The spectrum for the unconscious cortex will have a pronounced $1/f^2$ characteristic, whereas the spectrum for the conscious cortex will be comparatively flat.

In the final part of this chapter I will compare these model predictions with clinical measurements of the so-called anaesthetic *biphasic effect* performed in The Netherlands by Kuizenga and colleagues in 1998. Kuizenga's work examined the changes in EEG spectral characteristics as a function of anaesthetic blood concentration for the widely-used propofol anaesthetic agent.

Numerical simulation of the model equations will provide a second test of the veracity of the theoretical analysis presented in the present chapter. Description of the simulations will occupy a later chapter of this thesis.

5.1 Stochastic Perturbations to the Adiabatic Steady State

There are two fundamental assumptions in the present work. The first is that the cerebral cortex can be modelled as a (single!) macrocolumn that is never far from one or other of its stable equilibrium[1] states as mapped out in Fig. 3.4. The second assumption is that we may make an adiabatic simplification in which the four I_{jk} input currents to the macrocolumn are taken as being rapidly-varying quantities which have already settled to their final steady-state values. The justification for adiabaticity, in terms of characteristic relaxation times, was given earlier in Chap. 4.1. Adopting Haken's *slaving principle* terminology (Haken, 1978), one would say that the soma voltages are "slow" variables to which the "fast" variables (the input currents) have become *enslaved.*

The resulting adiabatic equations of motion for h_e and h_i, the excitatory and inhibitory voltages, listed in Eq. (4.1), are,

$$\frac{dh_e}{dt} \equiv F_1(h_e, h_i) = \left[h_e^{\text{rest}} - h_e + \psi_{ee}(h_e)\, I_{ee}(h_e) + \psi_{ie}(h_e)\, I_{ie}(h_i)\right] / \tau_e, \tag{5.1a}$$

$$\frac{dh_i}{dt} \equiv F_2(h_e, h_i) = \left[h_i^{\text{rest}} - h_i + \psi_{ei}(h_i)\, I_{ei}(h_e) + \psi_{ii}(h_i)\, I_{ii}(h_i)\right] / \tau_i, \tag{5.1b}$$

where the four I_{jk} input currents are as defined in Eqs (4.2–4.3). By setting the left-hand sides of Eq. (5.1) to zero and solving for (h_e, h_i), we can identify the coordinates of the macrocolumn steady states. This was done in Chap. 3.

We suppose that it is the small fluctuations in h_e about its steady-state value which constitute the source of the scalp-recorded EEG signal, i.e.,

$$\text{EEG}(t) \equiv \delta h_e(t) = h_e(t) - h_e^0 . \tag{5.2}$$

But what causes these δh_e fluctuations? In our model we assume that there is a continuous wash of white-noise variability entering the macrocolumn from the exogenous subcortical connections. Specifically, we say that each of the four p_{jk} subcortical spike rates varies randomly about a predefined mean value $\langle p_{jk} \rangle$. Thus we replace the p_{jk} terms which appeared in the I_{jk} currents of Eqs (4.2–4.3), expressing each as a random variation $(\widetilde{\ldots})$ about its $\langle \ldots \rangle$ mean,

$$p_{ee} \longrightarrow \langle p_{ee} \rangle + \widetilde{p_{ee}}(t) \tag{5.3a}$$

$$p_{ei} \longrightarrow \langle p_{ei} \rangle + \widetilde{p_{ei}}(t) \tag{5.3b}$$

$$p_{ie} \longrightarrow \langle p_{ie} \rangle + \widetilde{p_{ie}}(t) \tag{5.3c}$$

$$p_{ii} \longrightarrow \langle p_{ii} \rangle + \widetilde{p_{ii}}(t) \tag{5.3d}$$

where the $\widetilde{p_{jk}}(t)$ stochastic parts are defined as follows,

$$\widetilde{p_{ee}}(t) = \alpha_{ee} \sqrt{\langle p_{ee} \rangle}\, \xi_1(t) \tag{5.4a}$$

$$\widetilde{p_{ei}}(t) = \alpha_{ei} \sqrt{\langle p_{ei} \rangle}\, \xi_3(t) \tag{5.4b}$$

$$\widetilde{p_{ie}}(t) = \alpha_{ie} \sqrt{\langle p_{ie} \rangle}\, \xi_2(t) \tag{5.4c}$$

$$\widetilde{p_{ii}}(t) = \alpha_{ii} \sqrt{\langle p_{ii} \rangle}\, \xi_4(t) \tag{5.4d}$$

---

[1] Note that although the cortex is a dissipative, energy-consuming system, and therefore, in the strict sense, far from equilibrium, we declare "steady-state" and "equilibrium" to be synonyms here. This invocation of a *local equilibrium* frame of reference is justified in Chap. 6.

The $\xi_n(t)$ are four independent Gaussian-distributed white-noise sources defined to have zero mean,

$$\langle \xi_n(t) \rangle = 0 \tag{5.5a}$$

and delta-function covariances,

$$\langle \xi_m(t)\, \xi_n(t') \rangle = \delta_{mn}\, \delta(t - t'). \tag{5.5b}$$

Given that $\int_{-\infty}^{+\infty} \delta(t)\, dt = 1$, i.e., the total area under the $\delta(t)$ Dirac delta-function is a dimensionless unity, it follows that $\delta(t)$ must carry units of inverse-time, and therefore each $\xi(t)$ noise source has units of $1/\sqrt{\text{time}} = \text{s}^{-1/2}$. (The δ_{mn} Kronecker delta is dimensionless.)

The α_{jk} of Eq. (5.4) are dimensionless scale factors introduced to ensure that the fluctuations always remain very small: if the fluctuations are allowed to become too large, then there exists the possibility that the spike rates could momentarily go negative—this must be disallowed since no physical meaning can be attached to a negative number of spike events per time interval. For our numerical simulations we set all four scale-factors to a common value,

$$\alpha_{jk} = 0.1\,. \tag{5.6}$$

How this value was selected will be discussed in Chap. 7. A correct choice for α becomes rather important when one attempts to use numerical simulations to verify theoretical predictions for the fluctuation spectrum.

It is reasonable to expect that spike rates with a larger mean will have a larger stochastic fluctuation about the mean. However, rather than a direct proportionality[2] of the form $\widetilde{p} \propto \langle p \rangle\, \xi(t)$ (which, because $\xi(t)$ carries units, would be dimensionally improper), we choose the power-law relationship $\widetilde{p} \propto \sqrt{\langle p \rangle}\, \xi(t)$ which retains dimensional integrity for a spike rate:

$$\left[\widetilde{p}\right] = \left[\alpha\sqrt{\langle p \rangle}\, \xi(t)\right] = \left[\alpha\right]\left[\sqrt{\langle p \rangle}\right]\left[\xi(t)\right] = 1 \cdot \text{s}^{-\frac{1}{2}} \cdot \text{s}^{-\frac{1}{2}} = \text{s}^{-1}\,. \tag{5.7}$$

Here, the square brackets [...] are to be thought of as a "dimensions of" operator.

5.2 Stochastic Differential Equations

By incorporating the sub-cortical white-noise sources of Eq. (5.3) into the I_{jk} equations (4.2–4.3), we transform the Eq. (5.1) ordinary differential equations into a pair of coupled stochastic differential equations (SDEs), also known as *Langevin equations*, for the adiabatic macrocolumn.[3] These can be written as the sum of an average or *drift* part, plus a randomly-fluctuating or *diffusive* part:

---

[2] In our original paper (Steyn-Ross *et al.*, 1999), we assumed a direct proportionality between mean and stochastic amplitude: $\widetilde{p} = \langle p \rangle\, \xi(t)$. I subsequently realized that this stochastic mapping was dimensionally inconsistent, and M. Steyn-Ross suggested the careful square-root formulation given above. This revised form was adopted for the Steyn-Ross *et al.* (2001a) and Steyn-Ross *et al.* (2001b) follow-up papers.

[3] This scheme for transforming the Liley cortical equations into a set of stochastic differential equations was developed by M. Steyn-Ross after discussions with D. Liley and J. Sleigh to confirm that its assumptions are physiologically plausible.

$$\frac{d}{dt}\begin{bmatrix} h_e \\ h_i \end{bmatrix} = \underbrace{\begin{bmatrix} F_1(h_e, h_i) \\ F_2(h_e, h_i) \end{bmatrix}}_{\text{drift}} + \underbrace{\begin{bmatrix} \Gamma_e(t) \\ \Gamma_i(t) \end{bmatrix}}_{\text{diffusion}} \tag{5.8}$$

where the F_1 and F_2 drifts define the non-stochastic motion,

$$F_1(h_e, h_i) = \left[h_e^{\text{rest}} - h_e + \psi_{ee}(h_e)\, I_{ee}(h_e) + \psi_{ie}(h_e)\, I_{ie}(h_i)\right] / \tau_e \tag{5.9a}$$

$$F_2(h_e, h_i) = \left[h_i^{\text{rest}} - h_i + \psi_{ei}(h_i)\, I_{ei}(h_e) + \psi_{ii}(h_i)\, I_{ii}(h_i)\right] / \tau_i\,. \tag{5.9b}$$

The I_{jk} currents entering the F_1 and F_2 drifts are as given by Eqs (4.2–4.3), but with the p_{jk} subcortical spike-rate sources replaced by their time-averaged values $\langle p_{jk} \rangle$,

$$I_{ee}(h_e) = \left[(N_{ee}^{\alpha} + N_{ee}^{\beta})\, \mathcal{S}_e(h_e) + \langle p_{ee} \rangle\right] G_e e/\gamma_e \tag{5.10a}$$

$$I_{ei}(h_e) = \left[(N_{ei}^{\alpha} + N_{ei}^{\beta})\, \mathcal{S}_e(h_e) + \langle p_{ei} \rangle\right] G_e e/\gamma_e \tag{5.10b}$$

$$I_{ie}(h_i) = \lambda \left[N_{ie}^{\beta}\, \mathcal{S}_i(h_i) + \langle p_{ie} \rangle\right] G_i e/\gamma_i \tag{5.11a}$$

$$I_{ii}(h_i) = \lambda \left[N_{ii}^{\beta}\, \mathcal{S}_i(h_i) + \langle p_{ii} \rangle\right] G_i e/\gamma_i\,. \tag{5.11b}$$

The $\widetilde{p_{jk}}(t)$ white-noise parts have been factored out to define the $\Gamma_j(t)$ time-dependent diffusion terms,

$$\Gamma_e(t) = b_{ee}\, \xi_1(t) + b_{ie}\, \xi_2(t) \tag{5.12a}$$

$$\Gamma_i(t) = b_{ei}\, \xi_3(t) + b_{ii}\, \xi_4(t) \tag{5.12b}$$

where the b_{jk} coefficients depend on GABA anaesthetic effect λ and (h_e, h_i) soma voltage coordinate,

$$b_{ee} = \psi_{ee}(h_e)\, \alpha_{ee} \sqrt{\langle p_{ee} \rangle}\, G_e e / \gamma_e \tau_e \tag{5.13a}$$

$$b_{ei} = \psi_{ei}(h_i)\, \alpha_{ei} \sqrt{\langle p_{ei} \rangle}\, G_e e / \gamma_e \tau_i \tag{5.13b}$$

$$b_{ie} = \lambda\, \psi_{ie}(h_e)\, \alpha_{ie} \sqrt{\langle p_{ie} \rangle}\, G_i e / \gamma_i \tau_e \tag{5.13c}$$

$$b_{ii} = \lambda\, \psi_{ii}(h_i)\, \alpha_{ii} \sqrt{\langle p_{ii} \rangle}\, G_i e / \gamma_i \tau_i\,. \tag{5.13d}$$

Checking these equations for dimensional consistency, we see that in Eq. (5.13), the $\sqrt{\langle p_{jk} \rangle}\, G_j$ product gives the b_{jk} units of mV/$\sqrt{\text{s}}$ (the G_j is the post-synaptic amplitude in mV—see Table 3.1; the units of the $\gamma_j \tau_k$ product of rate- and time-constants cancel each other; the ψ_{jk} and α_{jk} are dimensionless), so that the Γ diffusion terms of Eq. (5.12) carry units of mV/s, consistent, as they must be, with the units for the F drifts.

5.3 Linearized Langevin Equations

In order to apply the tools of stochastic calculus to the adiabatic macrocolumn, we linearize the stochastic differential equations (5.8) about steady state. Let the macrocolumn lie exactly on an equilibrium point (λ, h_e^0, h_i^0) so that the drift terms are identically zero, i.e.,

$$F_1(h_e, h_i)\big|_0 = F_2(h_e, h_i)\big|_0 = 0\,. \tag{5.14}$$

Now turn on the $\widetilde{p_{jk}}(t)$ subcortical noise sources. This will generate soma voltage perturbations via the $\Gamma_{e,i}(t)$ diffusion terms of Eq. (5.12),

$$\delta h_e(t) = \int \Gamma_e(t)\,dt = h_e(t) - h_e^0 \tag{5.15a}$$

$$\delta h_i(t) = \int \Gamma_i(t)\,dt = h_i(t) - h_i^0\,. \tag{5.15b}$$

From Eq. (5.8), the time-derivative of these perturbations can be written as the sum of drift plus diffusive parts,

$$\frac{d}{dt}(\delta h_e) = \frac{dh_e}{dt} - 0 = F_1(h_e, h_i) + \Gamma_e(t) \tag{5.16a}$$

$$\frac{d}{dt}(\delta h_i) = \frac{dh_i}{dt} - 0 = F_2(h_e, h_i) + \Gamma_i(t)\,. \tag{5.16b}$$

As was done for the linear stability analysis of the adiabatic macrocolumn in Chap. 4.2, we perform a two-variable Taylor expansion of the F_1, F_2 drifts about steady state. To first order in drift (and to zeroth order in diffusion), the linearized Langevin equations read,

$$\begin{bmatrix} \dfrac{d}{dt}(\delta h_e) \\[2ex] \dfrac{d}{dt}(\delta h_i) \end{bmatrix} = \begin{bmatrix} \left.\dfrac{\partial F_1}{\partial h_e}\right|_0 & \left.\dfrac{\partial F_1}{\partial h_i}\right|_0 \\[2ex] \left.\dfrac{\partial F_2}{\partial h_e}\right|_0 & \left.\dfrac{\partial F_2}{\partial h_i}\right|_0 \end{bmatrix} \begin{bmatrix} \delta h_e \\[2ex] \delta h_i \end{bmatrix} + \begin{bmatrix} \Gamma_e(t) \\[2ex] \Gamma_i(t) \end{bmatrix}_{\text{eq.}} \tag{5.17}$$

or,

$$\frac{d}{dt}\,\boldsymbol{\delta}\mathbf{h} = -\mathbf{A}\,\boldsymbol{\delta}\mathbf{h} + \boldsymbol{\Gamma}(t)_{\text{eq.}} \tag{5.18}$$

where $\boldsymbol{\delta}\mathbf{h} = [\delta h_e \quad \delta h_i]^{\mathrm{T}}$ is the perturbations column vector, and $\mathbf{A}$ is the *negative*[4] of the Jacobian matrix of partial derivatives evaluated at equilibrium. Here $\boldsymbol{\Gamma}_{\text{eq.}}$ is the 2×1 diffusion vector also evaluated at equilibrium, so that the b_{jk} diffusion coefficients of Eq. (5.13) become *fluctuation-independent* constants,

$$b_{ee} = \psi_{ee}(h_e^0)\,\alpha_{ee}\sqrt{\langle p_{ee}\rangle}\,G_e e/\gamma_e\tau_e \tag{5.19a}$$

$$b_{ei} = \psi_{ei}(h_i^0)\,\alpha_{ei}\sqrt{\langle p_{ei}\rangle}\,G_e e/\gamma_e\tau_i \tag{5.19b}$$

$$b_{ie} = \lambda\,\psi_{ie}(h_e^0)\,\alpha_{ie}\sqrt{\langle p_{ie}\rangle}\,G_i e/\gamma_i\tau_e \tag{5.19c}$$

$$b_{ii} = \lambda\,\psi_{ii}(h_i^0)\,\alpha_{ii}\sqrt{\langle p_{ii}\rangle}\,G_i e/\gamma_i\tau_i\,. \tag{5.19d}$$

---

[4] The negative sign has been introduced here for consistency with the usual sign convention adopted for the prototypical linear Langevin equation which, in one dimension, reads $dx/dt = -Ax + \Gamma$; for $A > 0$, the system is stable so relaxes to equilibrium.

We emphasize that in this linearization scheme, the diffusion terms are evaluated *exactly* at a given (λ, h_e^0, h_i^0) equilibrium point—by assumption, the four random-noise sources vary only with time, and do not depend on the fluctuations in soma voltage. In other words, although the (λ, h_e^0, h_i^0) steady-state coordinate determines the amplitude of the noise (via the ψ_{jk} functions acting as scale factors), the soma voltage fluctuations themselves (i.e., the EEG signal) have no feedback influence on the diffusion noise which is generating the fluctuations.

5.3.1 Diffusion Matrix

Gardiner (1985, pp. 53 & 96) shows that there is a complete equivalence between an Ito SDE (such as Eq. (5.18)) and a (Fokker–Planck) diffusion process defined by the drift matrix **A** and a diffusion matrix **D** which is calculated from the covariance of the white-noise terms. For the adiabatic macrocolumn, the 2 × 2 diffusion matrix is given by,

$$\mathbf{D}\,\delta(0) = \left\langle \boldsymbol{\Gamma}(t)\,\boldsymbol{\Gamma}(t)^{\mathrm{T}} \right\rangle \tag{5.20a}$$

or, writing out the components in full,

$$\begin{bmatrix} D_{11} & D_{12} \\ D_{21} & D_{22} \end{bmatrix} \delta(0) = \begin{bmatrix} \langle \Gamma_e(t)\,\Gamma_e(t)\rangle & \langle \Gamma_e(t)\,\Gamma_i(t)\rangle \\ \langle \Gamma_i(t)\,\Gamma_e(t)\rangle & \langle \Gamma_i(t)\,\Gamma_i(t)\rangle \end{bmatrix} . \tag{5.20b}$$

Evaluating each element in turn,

$$\begin{aligned} D_{11}\,\delta(0) &= \big\langle \big(b_{ee}\,\xi_1(t) + b_{ie}\,\xi_2(t)\big)\big(b_{ee}\,\xi_1(t) + b_{ie}\,\xi_2(t)\big)\big\rangle \\ &= b_{ee}^2\,\langle \xi_1(t)\,\xi_1(t)\rangle + b_{ie}^2\,\langle \xi_2(t)\,\xi_2(t)\rangle + 2\,b_{ee}b_{ie}\,\langle \xi_1(t)\,\xi_2(t)\rangle \\ &= b_{ee}^2\,\delta(0) + b_{ie}^2\,\delta(0) + 0 \end{aligned} \tag{5.21a}$$

$$\begin{aligned} D_{12}\,\delta(0) &= D_{21}\,\delta(0) \\ &= \big\langle \big(b_{ei}\,\xi_3(t) + b_{ii}\,\xi_4(t)\big)\big(b_{ee}\,\xi_1(t) + b_{ie}\,\xi_2(t)\big)\big\rangle \\ &= b_{ei}b_{ee}\,\langle \xi_3(t)\,\xi_1(t)\rangle + b_{ei}b_{ie}\,\langle \xi_3(t)\,\xi_2(t)\rangle + b_{ii}b_{ee}\,\langle \xi_4(t)\,\xi_1(t)\rangle + b_{ii}b_{ie}\,\langle \xi_4(t)\,\xi_2(t)\rangle \\ &= 0 + 0 + 0 + 0 \end{aligned} \tag{5.21b}$$

$$\begin{aligned} D_{22}\,\delta(0) &= \big\langle \big(b_{ei}\,\xi_3(t) + b_{ii}\,\xi_4(t)\big)\big(b_{ei}\,\xi_3(t) + b_{ii}\,\xi_4(t)\big)\big\rangle \\ &= b_{ei}^2\,\langle \xi_3(t)\,\xi_3(t)\rangle + b_{ii}^2\,\langle \xi_4(t)\,\xi_4(t)\rangle + 2\,b_{ei}b_{ii}\,\langle \xi_3(t)\,\xi_4(t)\rangle \\ &= b_{ei}^2\,\delta(0) + b_{ii}^2\,\delta(0) + 0 \end{aligned} \tag{5.21c}$$

where we have applied the correlation property of Eq. (5.5b) to contract the $\langle \xi_m(t)\,\xi_n(t)\rangle$ white-noise expectations onto delta functions: $\langle \xi(t)\,\xi(t)\rangle = \delta(0)$. Finally, substituting the Eq. (5.19) definitions for the b_{jk} gives the diffusion matrix elements as,

$$D_{11} = \frac{1}{\tau_e^2}\Big\{ \big(\psi_{ee}(h_e^0)\,\alpha_{ee}\,G_e e/\gamma_e\big)^2 \langle p_{ee}\rangle + \lambda^2 \big(\psi_{ie}(h_e^0)\,\alpha_{ie}\,G_i e/\gamma_i\big)^2 \langle p_{ie}\rangle \Big\} \tag{5.22a}$$

$$D_{22} = \frac{1}{\tau_i^2}\Big\{ \big(\psi_{ei}(h_i^0)\,\alpha_{ei}\,G_e e/\gamma_e\big)^2 \langle p_{ei}\rangle + \lambda^2 \big(\psi_{ii}(h_i^0)\,\alpha_{ii}\,G_i e/\gamma_i\big)^2 \langle p_{ii}\rangle \Big\} \tag{5.22b}$$

$$D_{12} = D_{21} = 0\,. \tag{5.22c}$$

Performing a dimensional check on Eq. (5.22) shows that the D_{11} and D_{22} matrix elements carry units of $(\mathrm{mV})^2/\mathrm{s}$, as expected for a voltage diffusion coefficient.

5.3.2 Drift Matrix

The matrix elements of the drift matrix $\mathbf{A}$ follow directly from Eq. (4.24) after replacing $\mathbf{J}$ by $-\mathbf{A}$, giving,

$$A_{11} \equiv -\left.\frac{\partial F_1}{\partial h_e}\right|_0 = -\frac{1}{\tau_e}\left[-1 + \frac{\partial \psi_{ee}}{\partial h_e} I_{ee} + \psi_{ee}\frac{\partial I_{ee}}{\partial h_e} + \frac{\partial \psi_{ie}}{\partial h_e} I_{ie}\right]_{\text{eq.}} \tag{5.23a}$$

$$A_{12} \equiv -\left.\frac{\partial F_1}{\partial h_i}\right|_0 = -\frac{1}{\tau_e}\left[\psi_{ie}\frac{\partial I_{ie}}{\partial h_i}\right]_{\text{eq.}} \tag{5.23b}$$

$$A_{21} \equiv -\left.\frac{\partial F_2}{\partial h_e}\right|_0 = -\frac{1}{\tau_i}\left[\psi_{ei}\frac{\partial I_{ei}}{\partial h_i}\right]_{\text{eq.}} \tag{5.23c}$$

$$A_{22} \equiv -\left.\frac{\partial F_2}{\partial h_i}\right|_0 = -\frac{1}{\tau_i}\left[-1 + \frac{\partial \psi_{ei}}{\partial h_i} I_{ei} + \frac{\partial \psi_{ii}}{\partial h_i} I_{ii} + \psi_{ii}\frac{\partial I_{ii}}{\partial h_i}\right]_{\text{eq.}} \tag{5.23d}$$

where the $\partial I_{jk}/\partial h_j$ partial derivatives of the input currents are given by the Eq. (4.26) expressions,

$$\frac{\partial I_{ee}}{\partial h_e} = \left(N_{ee}^{\alpha} + N_{ee}^{\beta}\right)\frac{G_e e}{\gamma_e}\frac{\partial \mathcal{S}_e}{\partial h_e} \tag{5.24a}$$

$$\frac{\partial I_{ei}}{\partial h_e} = \left(N_{ei}^{\alpha} + N_{ei}^{\beta}\right)\frac{G_e e}{\gamma_e}\frac{\partial \mathcal{S}_e}{\partial h_e} \tag{5.24b}$$

$$\frac{\partial I_{ie}}{\partial h_i} = \lambda\frac{N_{ie}^{\beta} G_i e}{\gamma_i}\frac{\partial \mathcal{S}_i}{\partial h_i} \tag{5.24c}$$

$$\frac{\partial I_{ii}}{\partial h_i} = \lambda\frac{N_{ii}^{\beta} G_i e}{\gamma_i}\frac{\partial \mathcal{S}_i}{\partial h_i}\,. \tag{5.24d}$$

The partial derivatives for the firing-rate sigmoids $\mathcal{S}_{e,i}$ and the ψ_{jk} neurokinetics weighting functions were listed earlier in Eqs (4.27) and (4.25) respectively. It is understood that all soma-voltage-dependent terms in Eqs (5.23–5.24) are to be calculated at a given (λ, h_e^0, h_i^0) equilibrium point.

5.4 Linearized Covariance and Linearized Spectrum

By linearizing about steady-state, we have transformed the stochastic equations of motion for the (h_e, h_i) soma voltages of the adiabatic macrocolumn, as given by Eq. (5.8),

$$\frac{d}{dt}\begin{bmatrix} h_e \\ h_i \end{bmatrix} = \begin{bmatrix} F_1(h_e, h_i) \\ F_2(h_e, h_i) \end{bmatrix} + \begin{bmatrix} \Gamma_e(t) \\ \Gamma_i(t) \end{bmatrix} \tag{5.25}$$

into a pair of linear, constant-matrix equations for $(\delta h_e, \delta h_i)$, the *small fluctuations* about steady-state,

$$\frac{d}{dt}\begin{bmatrix} \delta h_e \\ \delta h_i \end{bmatrix} = -\mathbf{A}\begin{bmatrix} \delta h_e \\ \delta h_i \end{bmatrix} + \sqrt{\mathbf{D}}\begin{bmatrix} \xi_e(t) \\ \xi_i(t) \end{bmatrix} \tag{5.26}$$

where $\mathbf{D}$ is a diagonal matrix, and

$$\sqrt{D_{11}}\,\xi_e(t) \equiv \Gamma_e(t) = b_{ee}\,\xi_1(t) + b_{ie}\,\xi_2(t) \tag{5.27a}$$

$$\sqrt{D_{22}}\,\xi_i(t) \equiv \Gamma_i(t) = b_{ei}\,\xi_3(t) + b_{ii}\,\xi_4(t)\,. \tag{5.27b}$$

This is a two-variable *Ornstein–Uhlenbeck* process[5] whose stationary statistics have been extensively studied and are well documented (e.g., see Gardiner (1985, pp. 109–112)). The statistical descriptors of prime interest for the macrocolumn are the covariance matrix $\boldsymbol{\sigma}$, the time-correlation matrix $\mathbf{G}(\tau)$, and the spectrum matrix $\mathbf{S}(\omega)$.

5.4.1 Covariance Matrix

Following Gardiner (1985, p.111), the stationary *covariance matrix* $\boldsymbol{\sigma}$ (sometimes referred to as the zero-time correlation matrix) for our two-dimensional Ornstein–Uhlenbeck process can be expressed in terms of its drift matrix $\mathbf{A}$ and diffusion matrix $\mathbf{D}$,

$$\boldsymbol{\sigma} = \frac{\mathrm{Det}(\mathbf{A})\,\mathbf{D} + [\mathbf{A} - \mathrm{Tr}(\mathbf{A})\,\mathbf{I}]\,\mathbf{D}\,[\mathbf{A} - \mathrm{Tr}(\mathbf{A})\,\mathbf{I}]^{\mathrm{T}}}{2\,\mathrm{Tr}(\mathbf{A})\,\mathrm{Det}(\mathbf{A})} \tag{5.28a}$$

$$\equiv \begin{bmatrix} \sigma_{11} & \sigma_{12} \\ \sigma_{21} & \sigma_{22} \end{bmatrix} \tag{5.28b}$$

in which $\mathbf{I}$ is the 2×2 identity matrix; Det and Tr are the determinant and trace operators respectively. The individual elements of the covariance matrix are defined,

$$\begin{aligned}\sigma_{11} &\equiv \mathrm{var}\{\delta h_e\} \\ &= \left\langle (\delta h_e - \langle \delta h_e \rangle)^2 \right\rangle = \langle \delta h_e^2 \rangle - \langle \delta h_e \rangle^2 \end{aligned} \tag{5.29a}$$

$$\begin{aligned}\sigma_{22} &\equiv \mathrm{var}\{\delta h_i\} \\ &= \left\langle (\delta h_i - \langle \delta h_i \rangle)^2 \right\rangle = \langle \delta h_i^2 \rangle - \langle \delta h_i \rangle^2 \end{aligned} \tag{5.29b}$$

$$\begin{aligned}\sigma_{12} &\equiv \mathrm{cov}\{\delta h_e, \delta h_i\} \\ &= \left\langle (\delta h_e - \langle \delta h_e \rangle)\,(\delta h_i - \langle \delta h_i \rangle) \right\rangle = \langle \delta h_e\,\delta h_i \rangle - \langle \delta h_e \rangle \langle \delta h_i \rangle \\ &= \sigma_{21}\,. \end{aligned} \tag{5.29c}$$

By writing out Eq. (5.28a) in full, we obtain expressions for the σ_{jk} in terms of the drift and diffusion elements:

$$\sigma_{11} = \frac{\left(A_{11}A_{22} - A_{12}A_{21} + A_{22}^2\right) D_{11} + A_{12}^2\,D_{22}}{2\,(A_{11} + A_{22})\,(A_{11}A_{22} - A_{12}A_{21})} \tag{5.30a}$$

$$\sigma_{22} = \frac{A_{21}^2\,D_{11} + \left(A_{11}^2 + A_{11}A_{22} - A_{12}A_{21}\right) D_{22}}{2\,(A_{11} + A_{22})\,(A_{11}A_{22} - A_{12}A_{21})} \tag{5.30b}$$

$$\sigma_{12} = \sigma_{21} = \frac{-A_{11}A_{12}D_{22} - A_{21}A_{22}D_{11}}{2\,(A_{11} + A_{22})\,(A_{11}A_{22} - A_{12}A_{21})}\,. \tag{5.30c}$$

---

[5] In Chap. 7 we will use the theoretical predictions from a *one-variable* Ornstein–Uhlenbeck process as a simple test-case against which the correctness of our numerical simulation procedures for stochastic differential equations can be checked.

The rms values of the excitatory and inhibitory voltage fluctuations and co-fluctuations about their respective steady-states can be extracted directly from the covariance elements,

$$h_e^{\text{rms}} = \sqrt{\text{var}\{\delta h_e\}} = \sqrt{\sigma_{11}} \tag{5.31a}$$

$$h_i^{\text{rms}} = \sqrt{\text{var}\{\delta h_i\}} = \sqrt{\sigma_{22}} \tag{5.31b}$$

$$h_{ei}^{\text{rms}} = \sqrt{|\text{cov}\{\delta h_e, \delta h_i\}|} = \sqrt{|\sigma_{12}|}\,. \tag{5.31c}$$

From its definition in Eq. (5.29c), one observes that the $\text{cov}\{\delta h_e, \delta h_i\}$ cross-covariance can be negative—this will happen when excitatory and inhibitory fluctuations are anticorrelated, e.g., when a depolarizing (positive-going) fluctuation in h_e leads to a hyperpolarizing (negative-going) fluctuation in h_i, and vice versa. Hence the need for an absolute value in the Eq. (5.31c) definition for h_{ei}^{rms}. However, because it may be useful to distinguish the regions of anticorrelation, I introduce the notion of a "signed rms" value for the square-root of the covariance:

$$h_{ei}^{\pm\text{rms}} = \text{sgn}(\sigma_{12})\sqrt{|\sigma_{12}|} \tag{5.32}$$

where sgn is the signum (sign-of) function. With this definition, $h_{ei}^{\pm\text{rms}}$ will carry the sign of the σ_{12} covariance, thus will be negative when δh_e and δh_i are anticorrelated, and will be positive otherwise.

5.4.2 Time-Correlation Matrix

The autocorrelation function $G(\tau)$ for a time-series $x(t)$ was defined in Eq. (2.6),

$$G(\tau) \equiv \langle x(\tau)\, x(0)\rangle \equiv \lim_{T\to\infty} \frac{1}{T}\int_0^T x(t+\tau)\, x(t)\, dt\,. \tag{5.33}$$

The *autocovariance* of $x(t)$ is defined

$$\text{cov}\{x(\tau),\, x(0)\} \equiv \langle x(\tau)\, x(0)\rangle - \langle x(\tau)\rangle \langle x(0)\rangle\,. \tag{5.34}$$

The autocovariance will be identical to the autocorrelation if the fluctuations $x(t)$ have zero mean. Unless stated otherwise, we will assume that all means have been removed (e.g., the EEG signal, $\delta h_e(t) = h_e(t) - h_e^0$, is the *ac* component of the soma-voltage variation), so that the autocovariance of a time-series $x(t)$ can be taken as its autocorrelation,

$$G(\tau) = \text{cov}\{x(\tau),\, x(0)\}\,. \tag{5.35}$$

For a two-variable system, the autocorrelation function generalizes to a *time-correlation matrix* $\mathbf{G}(\tau)$. Replacing the $x(t)$ above by the soma-voltage fluctuations $\delta h_e(t)$ and $\delta h_i(t)$, their correlation matrix would read,

$$\mathbf{G}(\tau) \equiv \begin{bmatrix} \text{cov}\{\delta h_e(\tau),\, \delta h_e(0)\} & \text{cov}\{\delta h_e(\tau),\, \delta h_i(0)\} \\ \text{cov}\{\delta h_i(\tau),\, \delta h_e(0)\} & \text{cov}\{\delta h_i(\tau),\, \delta h_i(0)\} \end{bmatrix}. \tag{5.36}$$

Gardiner (1985, p. 111) shows that for a two-dimensional Ornstein–Uhlenbeck process, the stationary correlation matrix can be computed directly from the drift matrix $\mathbf{A}$ and covariance matrix $\boldsymbol{\sigma}$:

$$\mathbf{G}(\tau) = \exp\left[-\mathbf{A}\tau\right]\boldsymbol{\sigma}, \qquad \tau > 0 \tag{5.37a}$$

and,

$$= \boldsymbol{\sigma}\exp\left[-\mathbf{A}^{\mathrm{T}}\tau\right], \qquad \tau < 0 \tag{5.37b}$$

with symmetry property (because $\boldsymbol{\sigma} = \boldsymbol{\sigma}^{\mathrm{T}}$),

$$\mathbf{G}(-\tau) = \left[\mathbf{G}(\tau)\right]^{\mathrm{T}}. \tag{5.38}$$

The $\exp\left[-\mathbf{A}\tau\right]$ term denotes a *matrix exponential* (and *not* the exponential of the matrix elements) defined by its Taylor expansion,

$$e^{\mathbf{X}} = \mathbf{I} + \mathbf{X} + \mathbf{X}^2/2 + \mathbf{X}^3/6 + \ldots + \mathbf{X}^k/k! + \ldots \tag{5.39}$$

In the control systems literature, $\exp\left[-\mathbf{A}\tau\right]$ is known as the *transition matrix.* To gain insight into the structure of its elements, we will apply an alternative definition[6] for the matrix exponential expressed in terms of eigenvalues and eigenvectors,

$$e^{\mathbf{X}} = \mathbf{V}\begin{bmatrix} e^{\lambda_1} & 0 \\ 0 & e^{\lambda_2} \end{bmatrix}\mathbf{V}^{-1} \tag{5.40}$$

where $\mathbf{V}$ is the 2×2 matrix of eigenvectors corresponding to the eigenvalues λ_1, λ_2 of the $\mathbf{X}$ matrix. From Wiberg (1971, p. 108), the transition matrix will be

$$e^{-\mathbf{A}\tau} = \mathbf{V}\begin{bmatrix} e^{-\Lambda_1\tau} & 0 \\ 0 & e^{-\Lambda_2\tau} \end{bmatrix}\mathbf{V}^{-1} \tag{5.41}$$

where Λ_1 and Λ_2 are now the $\mathbf{A}$-matrix eigenvalues. The corresponding eigenvector matrix is

$$\mathbf{V} = \begin{bmatrix} v_1 & 1 \\ 1 & v_2 \end{bmatrix} = \begin{bmatrix} \frac{\Lambda_1 - A_{22}}{A_{21}} & 1 \\ 1 & \frac{\Lambda_2 - A_{11}}{A_{12}} \end{bmatrix} \tag{5.42}$$

which follows from the eigenvector definition

$$\mathbf{A}\,\mathbf{V} = \mathbf{V}\,\boldsymbol{\Lambda} = \mathbf{V}\begin{bmatrix} \Lambda_1 & 0 \\ 0 & \Lambda_2 \end{bmatrix}. \tag{5.43}$$

From Eq. (5.37a), the correlation matrix becomes

$$\begin{aligned} \mathbf{G}(\tau) &= e^{-\mathbf{A}\tau}\boldsymbol{\sigma} \\ &= \mathbf{V}\begin{bmatrix} e^{-\Lambda_1\tau} & 0 \\ 0 & e^{-\Lambda_2\tau} \end{bmatrix}\mathbf{V}^{-1}\boldsymbol{\sigma}. \end{aligned} \tag{5.44}$$

Expanding, then selecting the terms for the $G_{11}(\tau)$ element, we obtain the correlation function for the $\delta h_e(t)$ fluctuations as,

$$G_{11}(\tau) = \operatorname{cov}\{\delta h_e(\tau), \delta h_e(0)\} = \alpha_1 e^{-\Lambda_1\tau} + \alpha_2 e^{-\Lambda_2\tau} \tag{5.45}$$

---

[6] This definition appears in the MATLAB help documentation for its `expm` (matrix exponential) function. Also see Wiberg (1971, p. 101, Eq. 5.17).

where

$$\alpha_1 = \frac{\sigma_{11}\, v_1\, v_2 - \sigma_{21}\, v_1}{v_1\, v_2 - 1}\,, \quad \text{and} \quad \alpha_2 = \frac{-\sigma_{11} + \sigma_{21}\, v_1}{v_1\, v_2 - 1}\,. \tag{5.46}$$

Setting $\tau \to 0$ in Eq. (5.45), we see that, as expected, the autocovariance of δh_e collapses to its variance σ_{11},

$$\begin{aligned} G_{11}(0) &= \mathrm{cov}\{\delta h_e(0),\, \delta h_e(0)\} \\ &= \alpha_1 + \alpha_2 \\ &= \sigma_{11} \\ &= \mathrm{var}\{\delta h_e\}\,. \end{aligned} \tag{5.47}$$

It is evident from Eq. (5.45) that the two-time correlation function for δh_e is a linear combination of *two exponential decay processes* whose rate constants are the eigenvalues of the drift matrix. The relative weighting of the exponentials depends on the σ_{11} and σ_{21} entries of the covariance matrix (usefully thought of as the zero-time correlation matrix), and on the v_1 and v_2 eigenvector elements.

Parallel conclusions apply to the correlation functions for the δh_i inhibitory fluctuations and for the $\delta h_{e,i}$ cross-fluctuations.

5.4.3 Generalized Correlation Time

The *correlation time* T was defined in Sect. 2.4 as the time required for the autocorrelation function $G(\tau)$ to decay to $1/e$ of its zero-lag value. This definition assumes the autocorrelation function is a simple, single-exponential decaying function of time of the form,

$$G(\tau) = G(0)\, e^{-k\tau}\,, \qquad \tau \geq 0 \tag{5.48}$$

for which $T = 1/k$. A (semilog) graph of $\ln G(\tau)$ vs τ will give a straight line

$$\ln G(\tau) = \ln G(0) - k\,\tau \tag{5.49}$$

whose slope retrieves k, the inverse of the correlation time.

For our two-dimensional OU (Ornstein–Uhlenbeck) process, the Eq. (5.45) autocorrelation function is the sum of *two* exponential decays, so a simple $1/e$-folding-time (or slope-of-semilog-graph) rule for extracting the correlation time is no longer appropriate.

Gardiner (1985, p. 78) gives a generalized correlation-time definition which can be applied to arbitrary processes,

$$T = \frac{\int_0^\infty \mathrm{cov}\{x(\tau), x(0)\}\, d\tau}{\mathrm{var}\{x\}} \equiv \frac{\int_0^\infty G(\tau)\, d\tau}{G(0)} \tag{5.50}$$

and which certainly works for the single-exponential decay process of Eq. (5.48), retrieving the correlation time

$$T = \frac{\int_0^\infty G(0)\, e^{-k\tau}\, d\tau}{G(0)} = \int_0^\infty e^{-k\tau}\, d\tau = \frac{1}{k}\,, \tag{5.51}$$

as required. Applying Eq. (5.50) to the two-dimensional OU process, we are able to derive two equivalent expressions for the correlation time, the first derivation proceeding via the eigenvector decomposition of Eq. (5.45), and the second proceeding directly from the matrix form of Eq. (5.37a).

Correlation Time: Eigenvector Method

The eigenvector decomposition gave a scalar (sum of exponentials) equation (5.45) for $G_{11}(\tau)$, the δh_e autocorrelation function. Substituting into Eq. (5.50) gives

$$\begin{aligned} T &= \frac{1}{G_{11}(0)} \int_0^\infty G_{11}(\tau)\, d\tau \\ &= \frac{1}{\sigma_{11}} \int_0^\infty \alpha_1\, e^{-\Lambda_1 \tau} + \alpha_2\, e^{-\Lambda_2 \tau}\, d\tau \\ &= \frac{1}{\sigma_{11}} \left(\frac{\alpha_1}{\Lambda_1} + \frac{\alpha_2}{\Lambda_2} \right) \end{aligned} \tag{5.52}$$

where the α_1, α_2 are defined in Eq. (5.46) in terms of the v_1, v_2 eigenvectors, and σ_{11} is the Eq. (5.29a) variance of the δh_e fluctuations.

Correlation Time: Matrix Method

Working directly with the time-correlation matrix $\mathbf{G}(\tau)$ defined in Eq. (5.37a), we can derive an alternative expression for the δh_e correlation time by integrating the matrix exponential,

$$\begin{aligned} \int_0^\infty \mathbf{G}(\tau)\, d\tau &= \int_0^\infty \exp\left[-\mathbf{A}\tau\right] \boldsymbol{\sigma}\, d\tau \\ &= \mathbf{A}^{-1} \boldsymbol{\sigma}\,. \end{aligned} \tag{5.53}$$

Extracting the 1,1 element, and dividing by the δh_e variance σ_{11} gives the alternative expression for the generalized correlation time for the two-dimensional OU process,

$$T = \frac{1}{\sigma_{11}} \left[\mathbf{A}^{-1} \boldsymbol{\sigma}\right]_{11}\,. \tag{5.54}$$

These equivalent forms listed in Eqs (5.52) and (5.54) for correlation time provide a convenient numerical cross-check. This concept of generalized correlation time will be revisited in Chap. 8.

5.4.4 Spectrum Matrix

The power spectral density $S(\omega)$ for a time-series can be calculated from its autocorrelation function via the Wiener–Khinchin theorem of Eq. (2.5),

$$S(\omega) = \frac{1}{2\pi} \int_{-\infty}^{\infty} G(\tau)\, e^{-i\omega\tau}\, d\tau\,. \tag{5.55}$$

Replacing the autocorrelation function $G(\tau)$ in Eq. (5.55) with the correlation matrix $\mathbf{G}(\tau)$ leads to the *spectrum matrix* $\mathbf{S}(\omega)$:

$$\mathbf{S}(\omega) = \frac{1}{2\pi}\int_{-\infty}^{\infty} \mathbf{G}(\tau)\, e^{-i\omega\tau}\, d\tau \tag{5.56a}$$

$$\equiv \begin{bmatrix} S_{11}(\omega) & S_{12}(\omega) \\ S_{21}(\omega) & S_{22}(\omega) \end{bmatrix} \tag{5.56b}$$

For the two-dimensional Ornstein–Uhlenbeck process, Gardiner (1985, p. 111) shows that the stationary spectrum matrix can be expressed in terms of the drift and diffusion matrices,

$$\mathbf{S}(\omega) = \frac{1}{2\pi}\left(\mathbf{A} + i\omega\mathbf{I}\right)^{-1}\mathbf{D}\left(\mathbf{A}^{\mathrm{T}} - i\omega\mathbf{I}\right)^{-1}. \tag{5.57}$$

Expanding Eq. (5.57), we can write explicit expressions for each of the spectral elements:

$$\begin{aligned} S[h_e(\omega)] &= S_{11}(\omega) \\ &= \frac{1}{2\pi}\frac{A_{12}^2 D_{22} + A_{22}^2 D_{11} + D_{11}\omega^2}{\left(A_{11}A_{22} - A_{12}A_{21} - \omega^2\right)^2 + \left(A_{11} + A_{22}\right)^2\omega^2} \end{aligned} \tag{5.58a}$$

$$\begin{aligned} S[h_i(\omega)] &= S_{22}(\omega) \\ &= \frac{1}{2\pi}\frac{A_{11}^2 D_{22} + A_{21}^2 D_{11} + D_{22}\omega^2}{\left(A_{11}A_{22} - A_{12}A_{21} - \omega^2\right)^2 + \left(A_{11} + A_{22}\right)^2\omega^2} \end{aligned} \tag{5.58b}$$

$$\begin{aligned} S[h_{e,i}(\omega)] &= S_{12}(\omega) \\ &= S_{21}^{*}(\omega) \\ &= \frac{1}{2\pi}\frac{-A_{11}A_{12}D_{22} - A_{21}A_{22}D_{11} + i\omega\left(A_{12}D_{22} - A_{21}D_{11}\right)}{\left(A_{11}A_{22} - A_{12}A_{21} - \omega^2\right)^2 + \left(A_{11} + A_{22}\right)^2\omega^2}. \end{aligned} \tag{5.58c}$$

We observe that the excitatory spectrum $S[h_e(\omega)]$ and the inhibitory spectrum $S[h_i(\omega)]$ are both real, even functions of ω, since these are computed from their time-series autocorrelations which have even symmetry about zero lag. In contrast, the $S[h_{e,i}(\omega)]$ cross-spectrum is complex since it comes from a Fourier transformation of the $\langle \delta h_e(\tau), \delta h_i(0)\rangle$ cross-correlation which, in general, will be asymmetric about $\tau = 0$. The two cross-spectra, $S_{12} = S[h_{e,i}(\omega)]$ and $S_{21} = S[h_{i,e}(\omega)]$, are complex conjugates of each other.

The square-roots of the Eq. (5.58) power spectra [units: $(\mathrm{mV})^2/\mathrm{Hz}$] give spectral and co-spectral rms amplitudes [$\mathrm{mV}/\sqrt{\mathrm{Hz}}$] defined as,

$$\tilde{h}_e^{\mathrm{rms}}(\omega) = \sqrt{S_{11}(\omega)} \tag{5.59a}$$

$$\tilde{h}_i^{\mathrm{rms}}(\omega) = \sqrt{S_{22}(\omega)} \tag{5.59b}$$

$$\tilde{h}_{ei}^{\mathrm{rms}}(\omega) = \sqrt{|S_{12}(\omega)|}\,. \tag{5.59c}$$

Because the S_{12} co-spectrum is complex, it is useful to define its phase angle β_{ei},

$$\beta_{ei}(\omega) = \tan^{-1}\left(\frac{\mathrm{Im}[S_{12}(\omega)]}{\mathrm{Re}[S_{12}(\omega)]}\right). \tag{5.60}$$

Before presenting the theoretical variances and spectra, we will examine first the predicted behaviours of the drift and diffusion matrices as a function of GABA anaesthetic effect.

5.5 Drift and Diffusion Response to GABA Anaesthetic

Using Eqs (5.23 and 4.25–4.27), I computed the drift matrix **A** for the range of steady-state versus GABA coordinates illustrated earlier in the reverse-S graph of Fig. 3.4. The results are displayed in Fig. 5.1.

Each curve in Fig. 5.1 exhibits a re-entrant arc joining the A_3 (induction) and Q_1 (emergence) turning points: this arc corresponds to the unstable mid-branch of Fig. 3.4. As expected, the

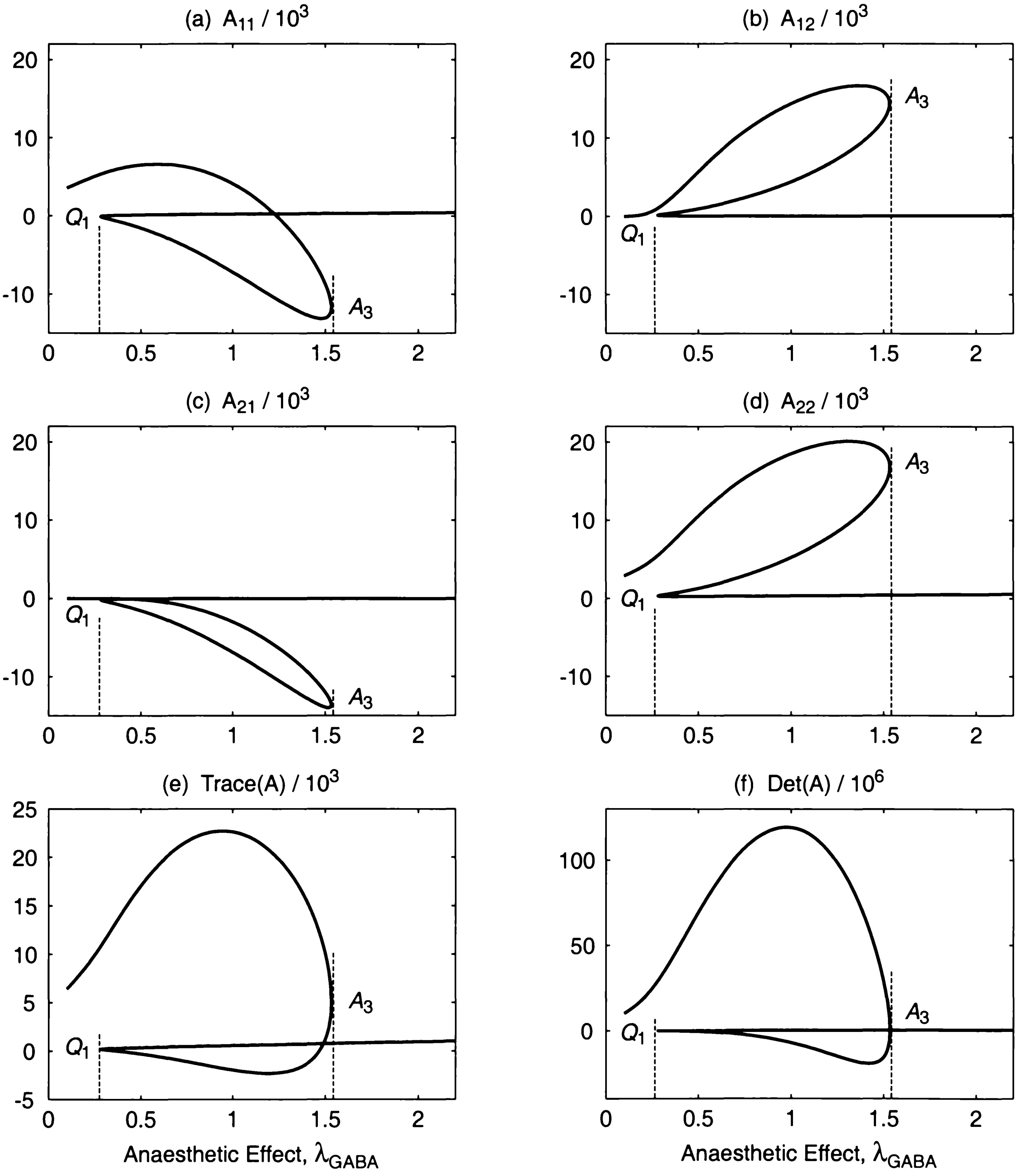

Figure 5.1: Variation of drift matrix **A** with GABA anaesthetic for the adiabatic macrocolumn. The four matrix elements occupy the top four panels: (a) A_{11}; (b) A_{12}; (c) A_{21}; (d) A_{22}. (e) shows the sum of the diagonal elements: $\mathrm{Tr}(\mathbf{A}) = A_{11} + A_{22}$ (equivalent to the sum of eigenvalues), and (f) is the determinant of **A** (product of eigenvalues): $\mathrm{Det}(\mathbf{A}) = A_{11}A_{22} - A_{12}A_{21}$. These graphs belong to the steady-state trajectory of Fig. 3.4. For each curve, the $A_3\,Q_1$ section identifies the unstable branch.

curve in (f) showing Det(**A**) has zeros at its A_3 and Q_1 turning points (the dominant eigenvalue passes through zero at these points—see Fig. 4.1b).

Re-entrant $A_3\,Q_1$ arcs are also evident in Fig. 5.2 which displays the D_{11} and D_{22} elements of the (diagonal) diffusion matrix. These curves, calculated from Eqs (5.22), are always positive, as verified by (c) and (d) showing a zoomed view in the vicinity of the Q_1 cusp.

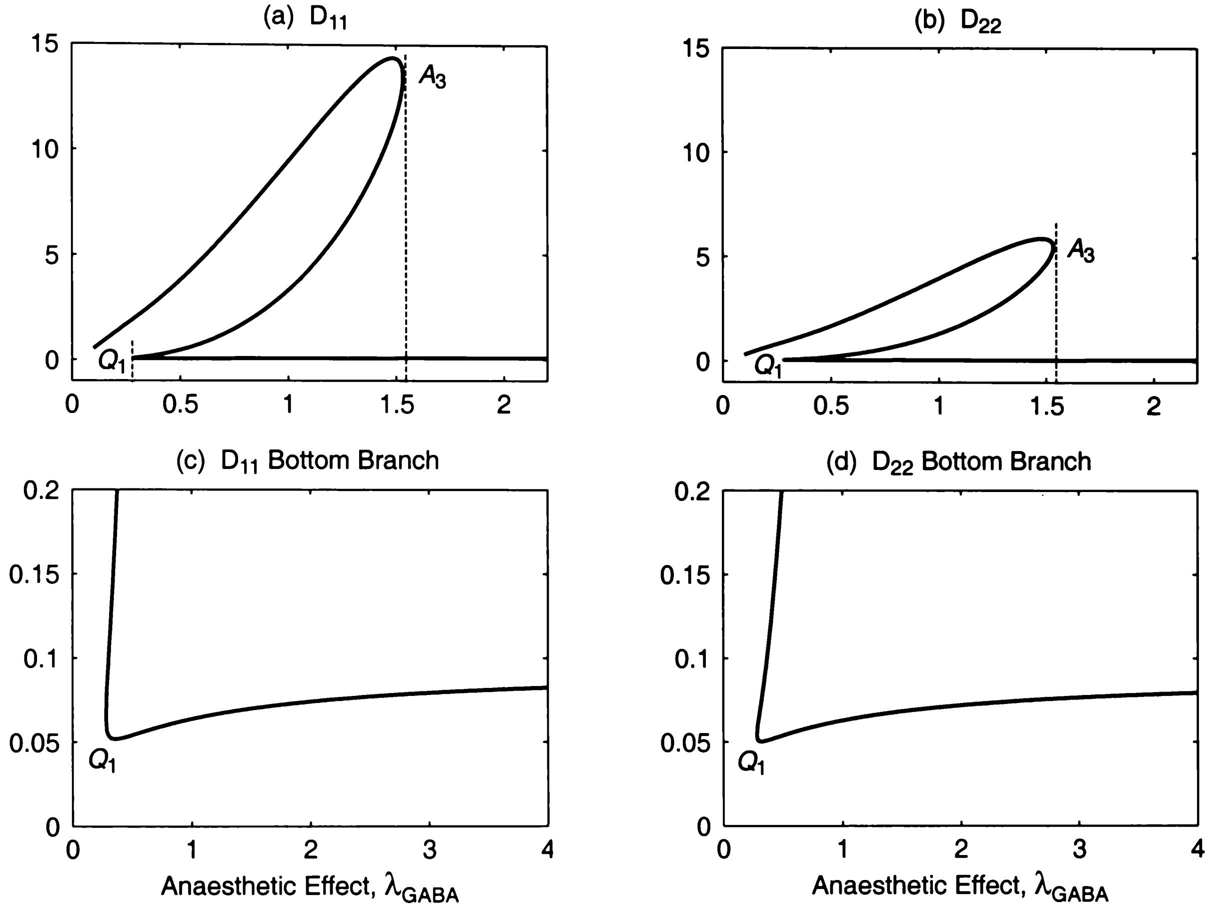

Figure 5.2: Variation of diffusion matrix **D** with GABA anaesthetic. The diffusion matrix elements are shown in the top two panels: (a) D_{11}; (b) D_{22}. Panels (c) and (d) give a close-up view of the Q_1 cusp. Both excitatory and inhibitory diffusion coefficients are always positive, and exhibit a slowly increasing trend with λ on the bottom (hyperpolarized) branch.

5.6 Adiabatic Fluctuations and Spectra

5.6.1 Fluctuation Amplitude vs GABA

Having established the response of the the drift and diffusion matrices to GABA anaesthetic, it is a relatively straightforward matter to compute the covariance matrix σ from Eq. (5.28), and hence determine the macrocolumn predictions for the rms amplitude of the excitatory and inhibitory soma voltage fluctuations about equilibrium. The fluctuation trends are shown in Fig. 5.3.

At first sight, the dramatic surge in fluctuation power as the macrocolumn approaches induction point A_3 on the top ("conscious") branch is astonishing. After all, the prime purpose of general anaesthetic is to dampen down the firing activity of the cerebral cortex to the extent

(a) δh_e rms Fluctuation Amplitude

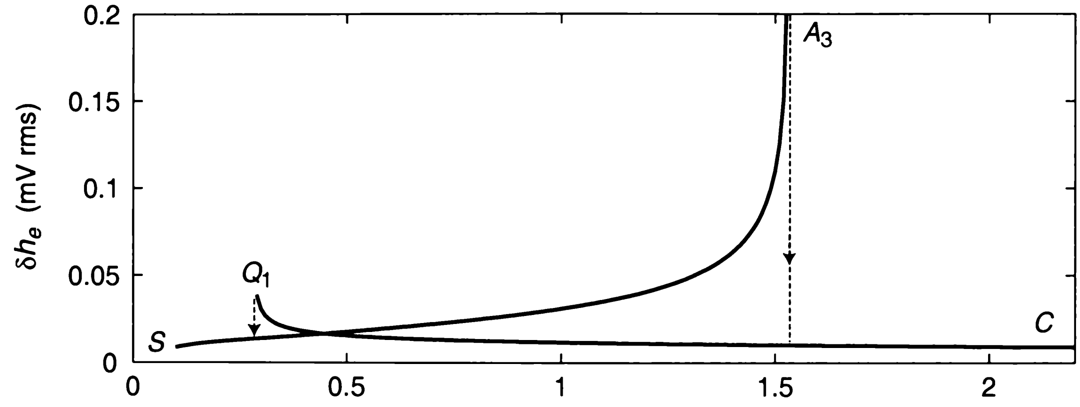

(b) δh_i rms Fluctuation Amplitude

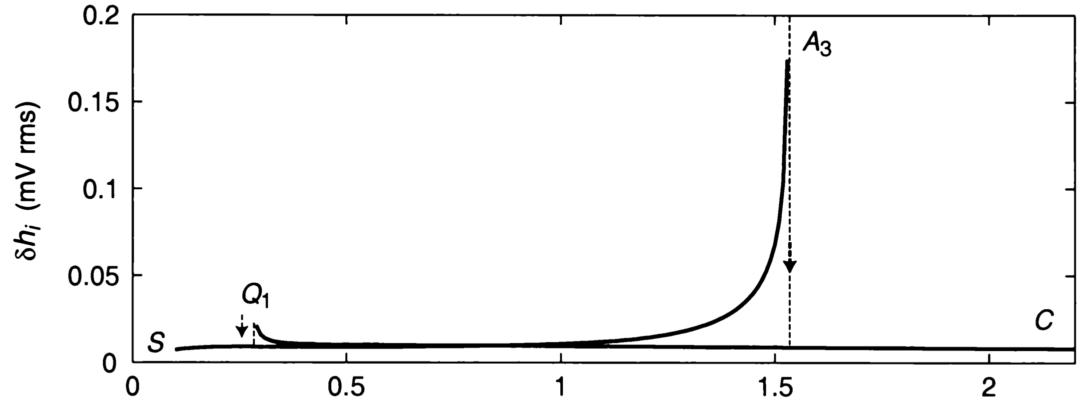

(c) δh_{ei} rms Cross-Fluctuation Amplitude

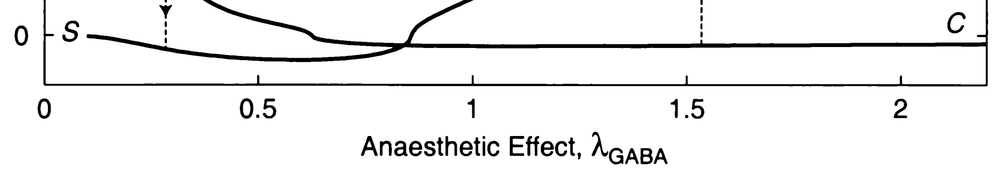

Figure 5.3: Effect of GABA anaesthetic on the fluctuations covariance matrix σ. Plotted here are the standard deviations for the small white-noise-driven fluctuations of soma voltage about equilibrium: (a) excitatory fluctuations, $h_e^{\text{rms}} = \sqrt{\sigma_{11}}$; (b) 0 fluctuations, $h_i^{\text{rms}} = \sqrt{\sigma_{22}}$; and (c) signed excitatory–inhibitory co-fluctuations: $h_{ei}^{\pm\text{rms}} = \text{sgn}(\sigma_{12})\sqrt{|\sigma_{12}|}$. Region SA_3 is the high-firing *active* branch (top-branch of Fig. 3.4); region Q_1C is the low-firing anaesthetized or *quiescent* branch (bottom branch of Fig. 3.4). The unstable A_3Q_1 mid-branch has been suppressed. Note the remarkable surge of fluctuation power on approach to induction (A_3), and again on approach to emergence (Q_1).

that the patient enters the "unconscious" or quiescent state. Yet these graphs show that cortical activity surges to a maximum immediately prior to the induction collapse into quiescence. Moreover, there is a second power surge for the return journey at the Q_1 emergence jump back to consciousness.

The meaning of these power surges becomes clear when we recall that the macrocolumn is exhibiting a pair of hysteretically-separated first-order phase transitions. As Reichl (1980) puts it, the growth in fluctuations as transition is approached is the system's way of readying itself for its impending new state. So we can think of the macrocolumn preparing for an impending step change in its (h_e, h_i) dc voltage by becoming exquisitely sensitive to the incoming white-noise perturbations; although the resulting exaggerated ac excursions are still quite small (~0.2 mVrms) compared with the size of the step change (~30 mV), they enable the macrocolumn to "sample" its dramatically altered potential landscape. (This picture will become clearer in Chap. 6 when we compute the "hills-and-valleys" potential graphs for the macrocolumn.)

We observe from Fig. 5.3b that the inhibitory fluctuations grow in a similar fashion to those of the excitatory population, although with a delayed, then more steeply-rising trend as the A_3 induction point at $\lambda = 1.53$ is approached. Fig. 5.3c is the "signed rms" measure introduced in Eq. (5.32) which is positive when δh_e and δh_i co-vary, and negative when they anti-vary.

5.6.2 Spectral Amplitude vs GABA

Using Eqs (5.58) and (5.59), I calculated the spectral amplitudes for the excitatory and inhibitory fluctuations at three specific point frequencies: 1, 10, and 100 Hz. The results appear in Fig. 5.4.

These single-frequency response pictures are rather similar in character to the total fluctuation graphs of Fig. 5.3: for both sets of graphs there is a strong growth in amplitude as either the A_3 (induction) or the Q_1 (emergence) phase-transition jumps are approached. However, we can now glean some information about the spectral composition of the peaks by comparing the relative amplitudes of the three graphs within a column. While the emergence peak Q_1 contains little high-frequency energy, the induction power surge at A_3 is relatively broad-band, with little attenuation at 100 Hz. This contrast will become more apparent in the following section when we view the complete spectra as three-dimensional "waterfalls."

The co-spectral graphs appear in Fig. 5.5. Because the co-spectrum is complex, the spectral information is split into its amplitude *magnitude* $\widetilde{h}_{ei}^{\mathrm{rms}} = \sqrt{|S_{12}|}$ (left-hand panels) and *spectral phase* $\beta_{ei} = \tan^{-1}[\mathrm{Im}(S_{12})/\mathrm{Re}(S_{12})]$ (right-hand panels).

5.6.3 Spectral Power Waterfalls

In the previous section we evaluated the linearized fluctuation spectrum equations for specified point frequencies. Now we will allow the frequency to vary in fine steps from dc up to a reasonable upper limit to reveal the full *excitatory* spectrum for a given value of anaesthetic effect λ. (For the remainder of this chapter we ignore the inhibitory spectrum and the excitatory–inhibitory cross-spectrum, and focus exclusively on the excitatory spectrum $S_{11}(\omega)$ since it is the δh_e variations which are the putative source of the scalp-measured EEG.)

Using Eq. (5.58a), each value of λ will generate a distinct fluctuation spectrum. If λ is stepped appropriately, the resulting family of spectra can be displayed in a three-dimensional

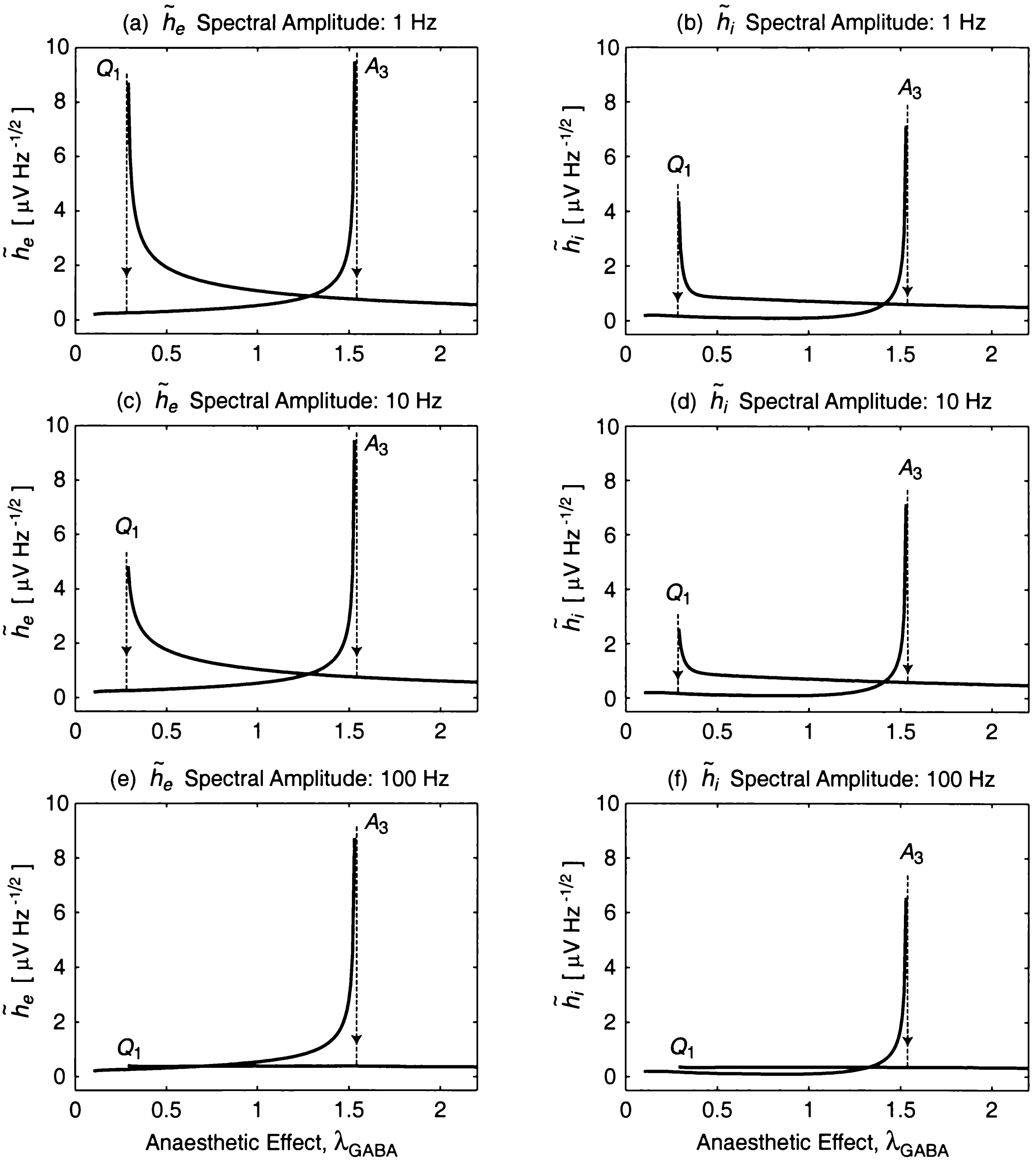

Figure 5.4: Variation of spectral amplitude with GABA anaesthetic at specified point frequencies. Left-hand panels show excitatory spectral amplitude, $\tilde{h}_e^{rms}$; right-hand panels show inhibitory spectral amplitude, $\tilde{h}_i^{rms}$. The point frequencies are (a, b) 1 Hz; (c, d) 10 Hz; (e, f) 100 Hz. Spectral amplitudes carry units of $\mu V/\sqrt{Hz}$.

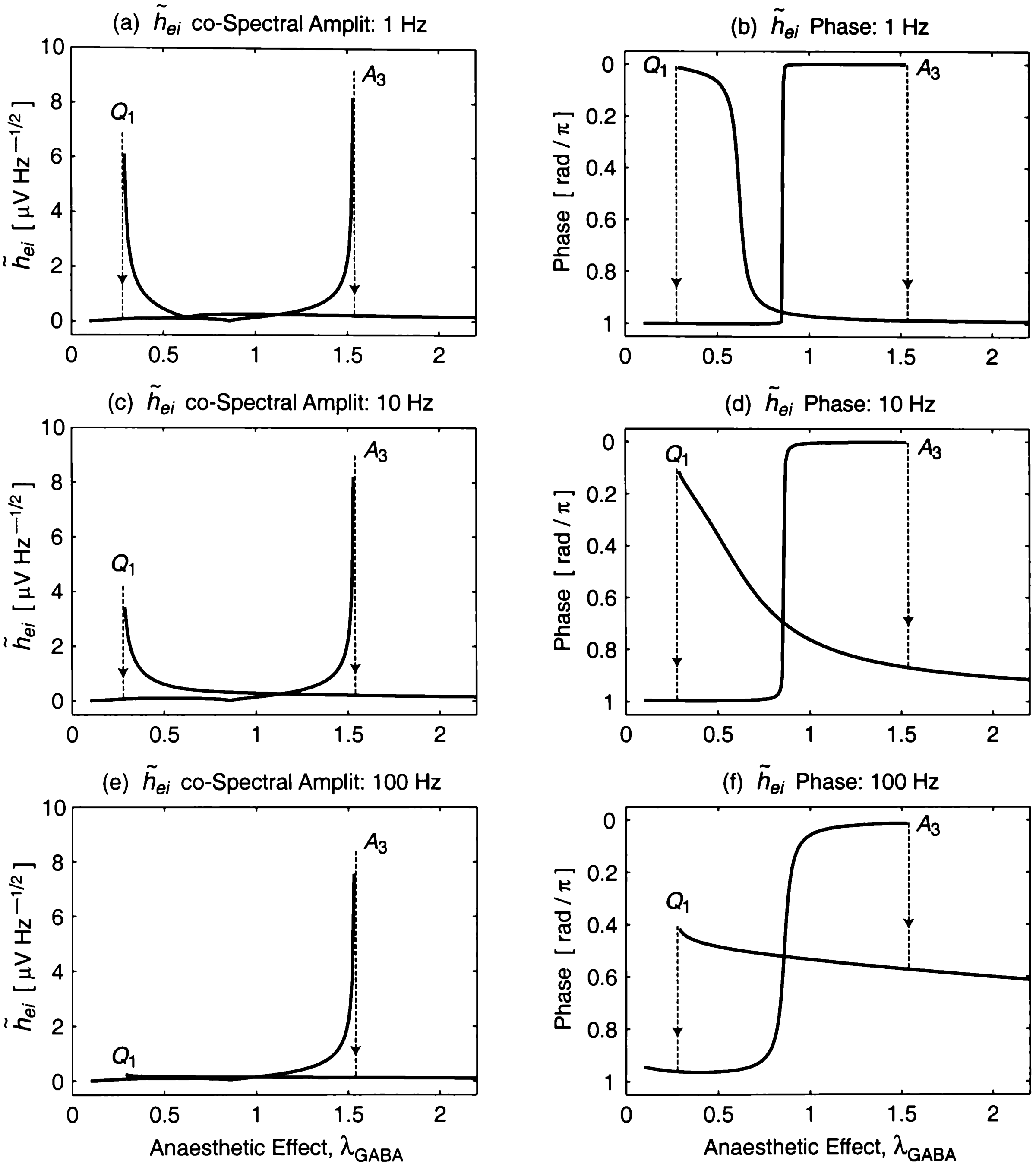

Figure 5.5: Variation of co-spectral amplitude and phase with GABA anaesthetic at specified point frequencies. Left-hand panels show excitatory–inhibitory co-spectral amplitude, $\tilde{h}_{ei}^{\mathrm{rms}}$; right-hand panels show the phase angle β_{ei} for the co-spectrum. The point frequencies are (a, b) 1 Hz; (c, d) 10 Hz; (e, f) 100 Hz. Phase angles are expressed as a fraction of π (i.e., an ordinate of unity corresponds to $\beta = \pi$ rads); the vertical scale for phase angle has been reversed to permit the transition arrows at Q_1 and A_3 to point downwards, consistent with the amplitude graphs.

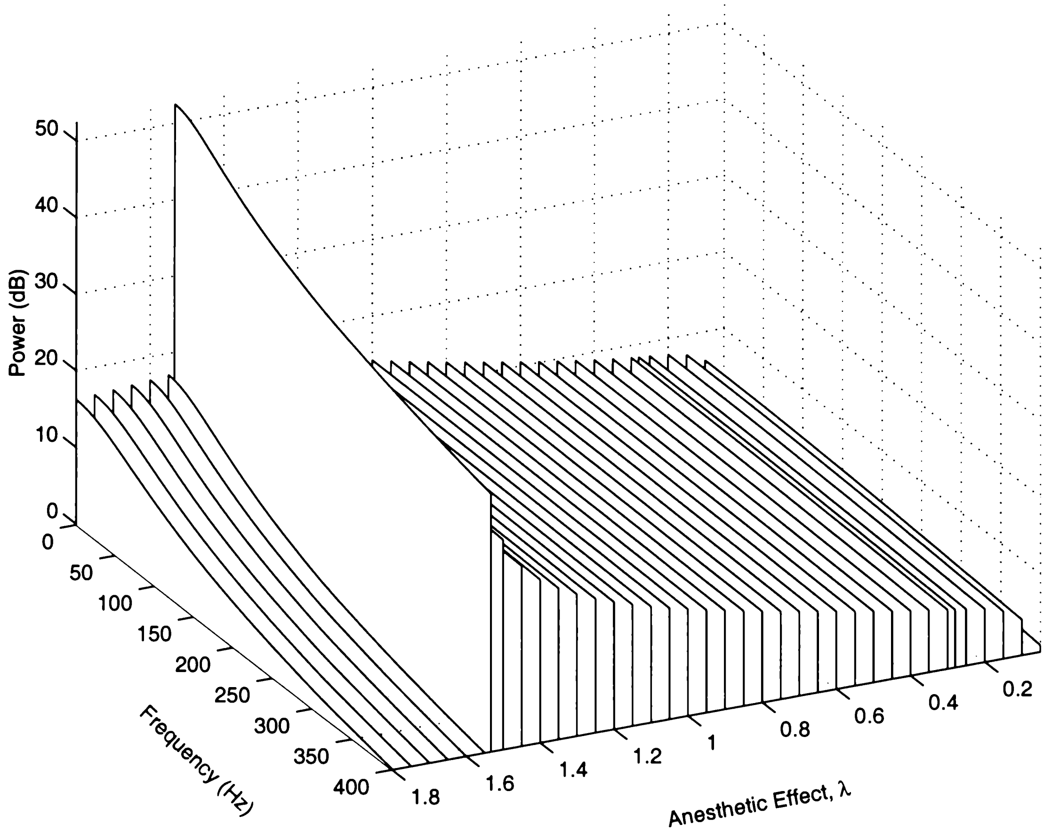

Figure 5.6: Variation of spectral power for anaesthesia-induction path $A_1A_3Q_3C$ of Fig. 3.4. Note the substantial slab of biphasic power at $\lambda = 1.53$ marking the A_3 extremum immediately prior to the $A_3 \rightarrow Q_3$ slump from the active ("conscious") to the quiescent ("unconscious") branch.

"waterfall" presentation showing the "flow" of spectral power (z-axis) versus frequency (y-axis) and versus anaesthetic effect (x-axis).

The 3D waterfall plot for the induction of unconsciousness (path $A_1A_3Q_3C$ in Fig. 3.4) appears in Fig. 5.6. For $\lambda \approx 1$ on the top branch, the spectrum is rather flat over the 0–400-Hz range plotted here. However, the spectral *area* and *shape* change radically on approach to the point of phase change at A_3: the total fluctuation power grows dramatically as the spectrum redistributes energy towards zero frequency, tending to take on the low-frequency character of the post-jump quiescent macrocolumn—albeit at vastly higher power levels (by a factor of ~3000).

The same induction waterfall is pictured in Fig. 5.7(b), but viewed from a different perspective. Figure 5.7(c) and (d) give two views of the $\lambda = 0.28$ *emergence* return to consciousness for the Fig. 3.4 path CQ_1A_1S. The redistribution of fluctuation activity toward zero frequency becomes even more pronounced along the bottom branch as the macrocolumn approaches its Q_1 jump return to the active branch. These characteristic alterations in spectral shape can be quantified using the concept of *spectral entropy*; this notion will be investigated further in Chap. 8.

(a) Induction (view 1) (b) Induction (view 2)

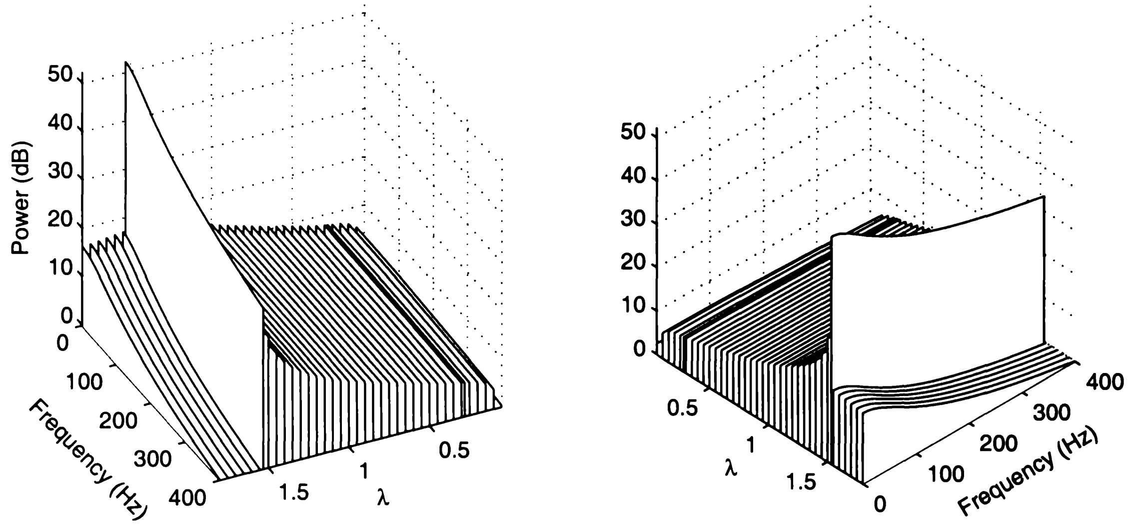

(c) Emergence (view 1) (d) Emergence (view 2)

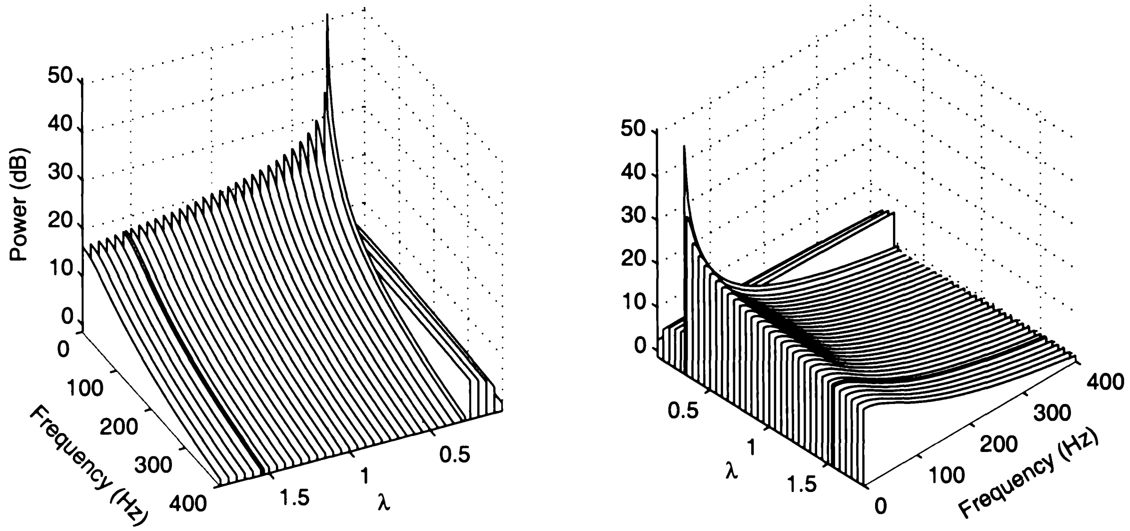

Figure 5.7: Comparative 3D spectral power plots for (a, b) *induction* and (c, d) *emergence*. Two views are shown for each trajectory to allow visual comparison of the relative flatness ("whiteness") of the spectral curves before and after transition. Graph (a) is a repeat of Fig. 5.6. All spectra have maximum power at dc, with the dc-peakiness becoming more pronounced prior to induction at $\lambda = 1.53$ (a, b), and even more pronounced just prior to emergence at $\lambda = 0.28$ (c, d).

5.7 Source and Significance of Fluctuation Surges

5.7.1 Fluctuation Infinities

What is the origin of the Fig. 5.7 surge in fluctuation power as the macrocolumn approaches the A_3 point of induction and the Q_1 point of emergence? The elements of the $\boldsymbol{\sigma}$ covariance matrix were listed in Eq. (5.30). The equation for $\mathrm{var}\{\delta h_e\}$ reads,

$$\mathrm{var}\{\delta h_e\} = \sigma_{11} = \frac{\left(\mathrm{Det}(\mathbf{A}) + A_{22}^2\right) D_{11} + A_{12}^2 D_{22}}{2\,\mathrm{Tr}(\mathbf{A})\,\mathrm{Det}(\mathbf{A})}. \tag{5.61}$$

We will find that the denominator of the right-hand-side expression goes to zero at the turning points of the steady-states trajectory of Fig. 3.4, thus generating a pair of infinities (poles) in the fluctuation variance. To see this, recall from Eq. (5.17) that the drift matrix **A** was defined to be the negative of the Jacobian matrix **J** introduced in Eq. (4.23), thus,

$$\mathrm{Tr}(\mathbf{A}) = A_{11} + A_{22} = -J_{11} - J_{22} = -\mathrm{Tr}(\mathbf{J}) \tag{5.62a}$$

and,

$$\mathrm{Det}(\mathbf{A}) = \mathrm{Det}(-\mathbf{J}) = \begin{vmatrix} -J_{11} & -J_{12} \\ -J_{21} & -J_{22} \end{vmatrix} = \mathrm{Det}(\mathbf{J})\ . \tag{5.62b}$$

Using the matrix property that the *trace* of a matrix equals the *sum* of its eigenvalues, and the *determinant* of a matrix equals the *product* of its eigenvalues,[7] we can write the trace–determinant product in terms of Λ_1 and Λ_2, the eigenvalues of matrix **J**:

$$\mathrm{Tr}(\mathbf{A})\ \mathrm{Det}(\mathbf{A}) = -\mathrm{Tr}(\mathbf{J})\ \mathrm{Det}(\mathbf{J}) = -(\Lambda_1 + \Lambda_2)\cdot(\Lambda_1\,\Lambda_2)\,. \tag{5.63}$$

The Λ_1, Λ_2 eigenvalue pairs for Jacobian matrix **J** were plotted in Fig. 4.1. The A_3 and Q_1 turning points in Fig. 4.1a correspond to the zero-crossing in Fig. 4.1b by the dominant eigenvalue Λ_1; the second eigenvalue Λ_2 is negative. Thus the determinant of the drift matrix is identically zero at the two turning points (t.p.),

$$\lim_{\lambda\to\text{t.p.}} \mathrm{Det}(\mathbf{A}) = \lim_{\lambda\to\text{t.p.}} \mathrm{Det}(\mathbf{J}) = \Lambda_1\,\Lambda_2 = 0\cdot\Lambda_2 = 0 \tag{5.64}$$

and, from Eq. (5.61), the fluctuation variance for δh_e will diverge to positive infinity,

$$\lim_{\lambda\to\text{t.p.}} \sigma_{11} = \frac{A_{22}^2 D_{11} + A_{12}^2 D_{22}}{-2\,(0+\Lambda_2)\,(0\cdot\Lambda_2)} \longrightarrow +\infty\,. \tag{5.65}$$

An identical conclusion applies to the variance for the inhibitory fluctuations, $\mathrm{var}(\delta h_i) = \sigma_{22}$. For the covariance of the cross-fluctuations of Eq. (5.30c),

$$\mathrm{cov}\{\delta h_e, \delta h_i\} = \sigma_{12} = \frac{-A_{11}A_{12}D_{22} - A_{21}A_{22}D_{11}}{2\,\mathrm{Tr}(\mathbf{A})\ \mathrm{Det}(\mathbf{A})} \tag{5.66}$$

it seems, at first sight, that there is a possibility of a divergence to *negative* infinity. Figure 5.2 shows that D_{11} and D_{22}, the diagonal elements of the diffusion matrix, are always positive. From Fig. 5.1 we see that in the vicinity of A_3 the drift-matrix products $A_{11}A_{12}$ and $A_{21}A_{22}$ are negative, so the numerator will be positive, and, because the denominator is also positive, the σ_{12} covariance will behave in fact as indicated in Fig. 5.3c by diverging to *positive* infinity.

---

[7] For a general proof of this property, see Wiberg (1971, p. 88). The demonstration for a 2 × 2 matrix **X** proceeds as follows. Write the characteristic polynomial in eigenvalue-factored form,

$$\mathrm{Det}(\mathbf{X} - \Lambda\mathbf{I}) = (\Lambda - \Lambda_1)(\Lambda - \Lambda_2) = \Lambda^2 - \Lambda\,(\Lambda_1 + \Lambda_2) + \Lambda_1\Lambda_2\,.$$

Now write the polynomial out in full,

$$\begin{aligned} \mathrm{Det}(\mathbf{X} - \Lambda\mathbf{I}) &= \begin{vmatrix} x_{11} - \Lambda & x_{12} \\ x_{21} & x_{22} - \Lambda \end{vmatrix} = (x_{11} - \Lambda)(x_{22} - \Lambda) - x_{12}x_{21} \\ &= \Lambda^2 - \Lambda\,(x_{11} + x_{22}) + x_{11}x_{22} - x_{12}x_{21} \\ &= \Lambda^2 - \Lambda\,\mathrm{Tr}(\mathbf{X}) + \mathrm{Det}(\mathbf{X})\ . \end{aligned}$$

Equating polynomial coefficients between the two expansions gives,

$$\mathrm{Tr}(\mathbf{X}) = \Lambda_1 + \Lambda_2\,, \qquad \text{and} \qquad \mathrm{Det}(\mathbf{X}) = \Lambda_1\Lambda_2\,.$$

5.7.2 Spectral Divergence at Low Frequency

Insight into the spectral character of these infinite fluctuations can be gained by examining the spectrum matrix equations. The excitatory fluctuation spectrum is given by Eq. (5.58a),

$$S_{11}(\omega) = \frac{1}{2\pi}\frac{A_{12}^2 D_{22} + A_{22}^2 D_{11} + D_{11}\omega^2}{[\mathrm{Det}(\mathbf{A}) - \omega^2]^2 + [\mathrm{Tr}(\mathbf{A})]^2\,\omega^2}\,. \tag{5.67}$$

At the phase-change turning points we have $\mathrm{Det}(\mathbf{A}) = 0$ and $\mathrm{Tr}(\mathbf{A}) = -\Lambda_2$ (where Λ_2 is the non-zero eigenvalue of the Jacobian matrix), so the spectrum becomes

$$\lim_{\lambda\to\mathrm{t.p.}} S_{11}(\omega) = \frac{1}{2\pi}\frac{A_{12}^2 D_{22} + A_{22}^2 D_{11} + D_{11}\omega^2}{\omega^4 + \Lambda_2^2\,\omega^2} \tag{5.68}$$

which will be finite everywhere except at zero frequency:

$$\lim_{\omega\to 0}\lim_{\lambda\to\mathrm{t.p.}} S_{11}(\omega) = \frac{1}{2\pi}\frac{A_{12}^2 D_{22} + A_{22}^2 D_{11}}{\Lambda_2^2\,\omega^2} \longrightarrow \infty\,. \tag{5.69}$$

Thus $S_{11}(\omega)$ diverges to infinity as $1/\omega^2$ at the turning points. This means that as the macrocolumn approaches an emergence or induction jump, very low-frequency fluctuations will grow without limit, with the fluctuations becoming infinitely slow at the jump. This is the so-called *critical slowing down* phenomenon which is characteristic of phase transitions. Another way of tracing the progress of a phase change is to measure the lengthening correlation times: the correlation time becomes infinite as the fluctuations slow down to dc. This aspect will be treated in detail in the latter part of Chap. 8.

5.7.3 Lorentzian Limit at High Frequency

It is also of interest to examine the high-frequency spectral limit of Eq. (5.67),

$$\begin{aligned}\lim_{\omega\to\infty} S_{11}(\omega) &= \frac{1}{2\pi}\frac{D_{11}}{\omega^2 - 2\,\mathrm{Det}(\mathbf{A}) + [\mathrm{Tr}(\mathbf{A})]^2}\\ &= \frac{1}{2\pi}\frac{D_{11}}{\omega^2 + k^2}\end{aligned} \tag{5.70}$$

in which

$$k^2 = A_{11}^2 + 2\,A_{12}A_{21} + A_{22}^2\,. \tag{5.71}$$

We recognize the form of Eq. (5.70) as a Lorentzian spectrum (cf Eq. (2.29)) whose −3-dB frequency is k and whose correlation time is $\tau_c = 1/k$. At the phase-change points, Eq. (5.70) simplifies to

$$\lim_{\lambda\to\mathrm{t.p.}}\lim_{\omega\to\infty} S_{11}(\omega) = \frac{1}{2\pi}\frac{D_{11}}{\omega^2 + \Lambda_2^2}\,. \tag{5.72}$$

This means that at a fluctuation pole, the correlation time for the the *high-frequency* components is determined by the value of the non-zero eigenvalue: $\tau_c = |\Lambda_2|^{-1}$.

5.8 Recapitulation: Predictions for Spectral Response

A list of predictions for the anaesthetic-induced alterations in EEG behaviour is given on the opening page of this chapter. To recap, the adiabatic macrocolumn predicts—

- a pronounced growth in fluctuation power as the point of induction into unconsciousness is approached; a second power surge as the moment of return of consciousness is approached (Fig. 5.3); these change-of-phase points will be separated by a hysteresis gap (Fig. 3.4)
- a redistribution of spectral energy towards lower frequencies as transition points are approached (Fig. 5.7)
- a relatively broad spectrum for the top branch; a $1/f^2$ spectrum on the bottom branch (Fig. 5.7 and Eq. (5.69)).

In the next section we present clinical results reported by Kuizenga, Kalkman, and Hennis (1998) that seem to give good support to the first of our model predictions: distinct, hysteretically-separated EEG power surges when the anaesthetized cerebral cortex changes state into unconsciousness and then recovers.

5.9 The Kuizenga Experiment

5.9.1 The Biphasic Response

It is well-known within the anaesthesiology community than many commonly used general-anaesthetic agents exhibit what is referred to as a "biphasic" or activation/depression response: at low (sedative) anaesthetic concentrations there is a significant increase above baseline values in both the total EEG power and in the frequency at which peak power occurs; as concentration is further increased to hypnotic (surgical anaesthesia) levels, the total power and median frequency fall away to levels below baseline. This "biphasic" response has been observed on human volunteers dosed with thiopental (Bührer *et al.*, 1992), and the widely-used propofol (Kuizenga *et al.*, 1998). It has also been measured in rats dosed with thiopental (MacIver *et al.*, 1996; Archer and Roth, 1997). Figure 5.8 shows a typical activation/depression response from one of the patients in the Kuizenga *et al.* (1998) study.

5.9.2 Clinical Details

In their clinical study, Kuizenga *et al.* (1998) examined the biphasic relationship between the concentration of a general anaesthetic agent (propofol) in arterial blood and EEG effects during the transition from the awake state to hypnosis and during subsequent emergence. The subjects were 10 healthy male patients who were scheduled for lower-limb surgery. A scalp electrode pair was placed at the mastoid (bone behind the ear) and the forehead to monitor the differential EEG signal developed across the hemisphere. Each patient received a 10-min infusion of propofol. The EEG was recorded continuously from 5 min before the start of propofol infusion until the patient regained consciousness (approximately 15 min after conclusion of infusion), and thereafter intermittently for 5-min periods, coinciding with blood sampling, until 190 min after start of infusion. Blood samples were drawn from a femoral artery at 2-min intervals during the first 22 min, then at more widely spaced intervals thereafter.

5.9.3 EEG Processing

The EEG signal was processed, over 15-s epochs, into one of six frequency bands (0–5, 6–10, 11-15, 16–20, 21–25, and 26–30 Hz) using "aperiodic analysis." This technique measures the vertical distance between consecutive peaks and valleys in the voltage trace and computes an effective instantaneous frequency from (half the reciprocal of) the time interval for the peak-to-trough excursion. These voltage excursions are then accumulated, unsigned, into one of the six frequency bins to give a total voltage deviation in each frequency band for the 15-s epoch. Dividing each band total by 15 s then gives a measure of the average amplitude "slew-rate," in μV/s, which Kuizenga refers to as "EEG amplitude."

5.9.4 Relationship between Aperiodic and Fourier Analysis

Before we can compare the theoretical spectra against the Kuizenga results, we need to establish the relationship between *Fourier analysis* (which assumes that the EEG fluctuations can be resolved into sinewave vibrations) and *aperiodic analysis.* Paraphrasing Gregory and Pettus (1986), I offer the following brief definition:

> **Aperiodic Analysis:** A method that analyzes the EEG signal in the time-domain by measuring the rate at which the signal slews between consecutive peaks and troughs.

This algorithm, which pre-dates modern *wavelet analysis*, was patented in the 1980s for use in the Neurometrics Lifescan EEG monitor (Diatek Corporation, San Diego, California). It seems that this equipment, and its associated analysis software, is a not uncommon choice at

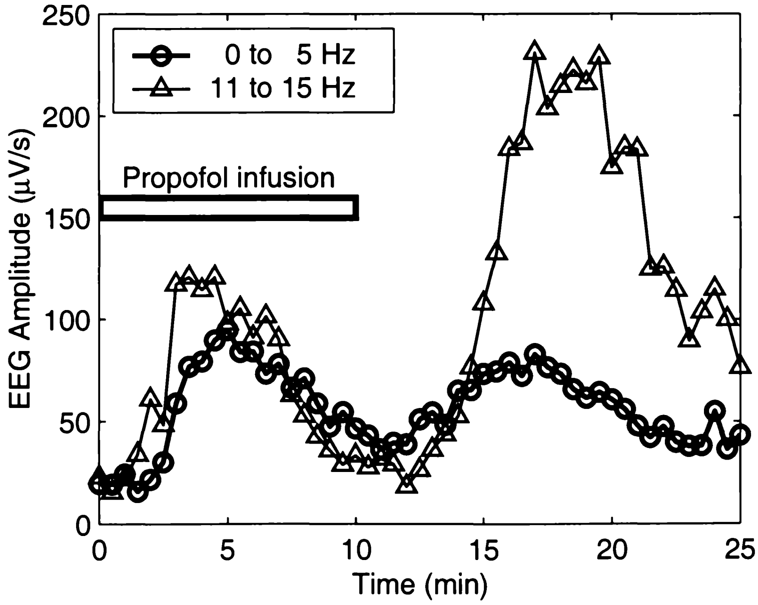

Figure 5.8: Biphasic effect of propofol anaesthetic on 0-5-Hz and 11–15-Hz EEG signal. During the 10 min of propofol infusion, anaesthetic concentration increases steadily. At low concentrations, the EEG signal shows an initial increase in power (activation). EEG power then falls away (inhibition) as concentration is further increased and the patient becomes deeply unconscious. A second EEG activation peak is observed as the anaesthetic concentration declines and the patient begins to emerge from unconsciousness. [Data supplied courtesy of K. Kuizenga, and reported as "Patient 7" in Kuizenga *et al.* (1998).]

anaesthesiology research laboratories around the world. Kuizenga used it to analyze his EEG datasets (Kuizenga *et al.*, 1998, 2001) for propofol anaesthetic, and Bührer found that aperiodic analysis gave a more consistent quantification of the EEG effect of midazolam and thiopental anaesthetics than did the Fourier analysis measures (such as spectral edge and total power) (Bührer *et al.*, 1990, 1992).

To date, no attempt seems to have been made to relate the aperiodic slew-rate measure, measured in μV/s (but misleadingly referred to as "EEG amplitude" (Kuizenga *et al.*, 1998) or "EEG voltage" (Bührer *et al.*, 1990)), to the conventional harmonic measures such as rms voltage obtained by summing Fourier spectral amplitudes across a given frequency range. I will show that for the ideal case of a single-frequency sinewave, the aperiodic analysis gives a result equal to the average absolute slew-rate of the sinewave, and that for more complicated waveforms, the aperiodic analysis is roughly equivalent to a Fourier analysis of the time-derivative of the waveform.

Slew-Rate for a Sinewave

Consider the waveform $y(t) = A\sin(\omega t)$, a pure sinusoid of amplitude A [in, say, μV] and frequency $f = \omega/2\pi$ [Hz] pictured in Fig. 5.9. The aperiodic analysis would detect a peak-to-peak slew of $\Delta y = 2A$ in a half-period $\Delta t = 1/2f = \pi/\omega$, and would accumulate this activity, unsigned, to frequency bin f. The slew-rate contribution from this wave-fragment would be

$$\frac{\Delta y}{\Delta t} = \frac{2A}{\pi/\omega} = \frac{2}{\pi}A\omega \qquad [\text{units: } \mu\text{V/s}]\,. \tag{5.73}$$

Effectively the sinewave has been replaced by a triangular wave formed by drawing a straight line from peak to peak; the calculated slew-rate is the triangle's rate-change of voltage with respect to time.

The actual slew-rate of the sinewave is given by

$$v(t) = \frac{d}{dt}A\sin(\omega t) = A\omega\cos(\omega t) \tag{5.74}$$

which varies over a half-cycle from zero at the sinewave peaks to a maximum of $A\omega$ at the sinewave zero-crossing. The average absolute slew-rate, given by averaging over a (positive-slope) half-period of width $\Delta t = \pi/\omega$, is given by,

$$v_{\text{av}} = \frac{1}{\Delta t}\int_{-\pi/2\omega}^{+\pi/2\omega} v(t)\,dt = \frac{\omega}{\pi}A\sin(\omega t)\Big|_{-\pi/2\omega}^{+\pi/2\omega} = \frac{2}{\pi}A\omega\,, \tag{5.75}$$

exactly matching the value calculated for the equivalent triangular waveform interpolated by aperiodic analysis. Therefore, for a single-frequency sinusoid, the aperiodic analysis is detecting the *average speed* (unsigned) of the simple harmonic vibration.

Slew-Rate for a Mix of Sinewaves

Figure 5.9b illustrates a more realistic signal obtained by summing different-frequency sinewaves. The Gregory and Pettus (1986) algorithm analyzes such a signal on two scales: the "fast-wave" (9–30 Hz) detection looks for *local* excursions between consecutive extrema, while the "slow-wave" (0.5–8.5 Hz) detection requires that the extrema bracket a zero-crossing. These two searches are done in parallel on two differently pre-filtered copies of the signal: for the fast-wave detection, the signal has been low-pass filtered to 30 Hz, and for slow-wave detection, it has been low-pass filtered to 8 Hz. The algorithm will require a specification for the noise threshold (i.e., a minimum voltage excursion considered to be significant), but Gregory and Pettus make no mention of this.

It is clear that the precise output of such a time-domain analysis will be dependent on the implementation details. Nevertheless, it also seems clear that the aperiodic method is performing a kind of "unsigned velocity" analysis of the EEG signal. Ignoring the complications arising from the implied absolute value, I will argue that since derivative in the time-domain corresponds to frequency multiplication in the Fourier domain, a plausible *slew-rate power spectrum* $R(\omega)$ for the macrocolumn can be constructed by scaling the S_{11} excitatory fluctuation spectrum of Eq. (5.58a) by ω^2:

$$R(\omega) = \omega^2 S_{11}(\omega) \tag{5.76}$$

suggesting an rms slewing "velocity" measure v_e^{rms},

$$v_e^{\text{rms}} = \sqrt{\int_{\omega_1}^{\omega_2} \omega^2 S_{11}(\omega)\, d\omega} \tag{5.77}$$

(a) Single Sinewave

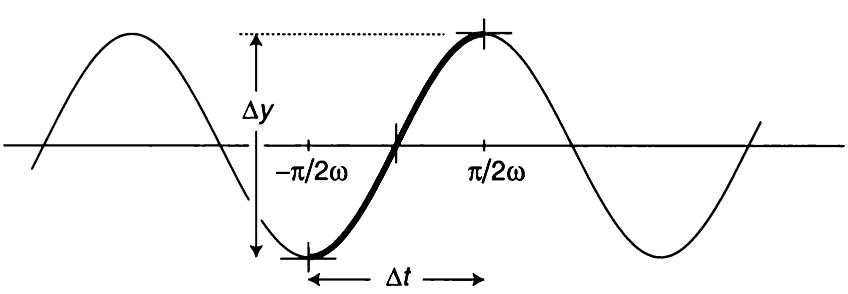

(b) Mix of Sinewaves

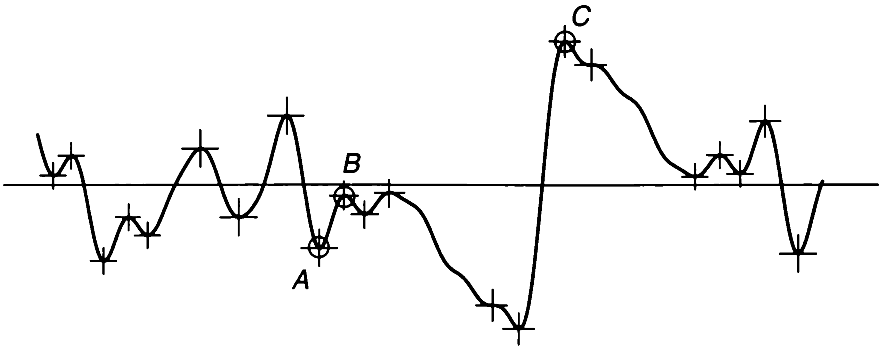

Figure 5.9: Aperiodic analysis is a form of slew-rate estimation for each distinct wave-fragment in a signal. (a) For a single-frequency sinewave $y(t) = A\sin(\omega t)$, the fragment shown in bold slews a vertical distance $\Delta y = 2A$ in a time interval $\Delta t = \pi/\omega$. (b) The aperiodic measure for a more complicated signal will depend on fine details of the algorithm, e.g., number of time-scales over which each fragment is analyzed, noise threshold, amount of pre-filtering. In the Gregory and Pettus (1986) algorithm, AB would be a fast-wave (local) excursion, while AC would be a slow-wave (zero-crossing) excursion.

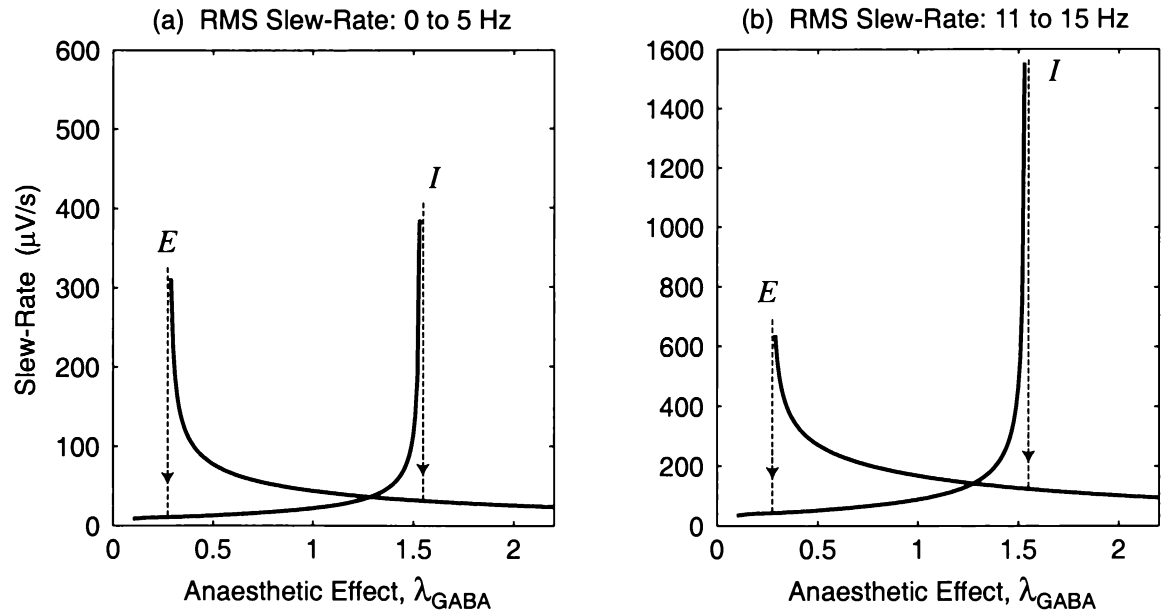

Figure 5.10: Variation of fluctuation slew-rate with GABA anaesthetic. The ordinate is the rms slewing velocity v_e^{rms} predicted by Eq. (5.77) for two frequency bands: (a) 0–5 Hz, and (b) 11–15 Hz. Compare these theoretical curves with Kuizenga's clinical results of Fig. 5.11 obtained via aperiodic analysis of scalp-recorded EEG signals. The peaks are labelled I for induction and E for emergence.

defined so that $(v_e^{\mathrm{rms}})^2$ equals the area under the slew-rate spectrum over the frequency interval $[\omega_1, \omega_2]$.

The macrocolumn predictions for rms slewing velocity for the two frequency bands [0–5 Hz] and [11–15 Hz] are shown in Fig. 5.10. Because of the scaling by ω in the Eq. (5.77) definition, the slew-rate spectrum will have its low-frequency components suppressed, and higher frequency components enhanced. A comparison of the Fig. 5.10 slew-rate activity against the point-frequency amplitudes of Fig. 5.4 bears this out.

5.9.5 Measured EEG Activity vs Anaesthetic Concentration

Figure 5.8 showed the time-course of EEG slew-rate activity for the 0–5 and 11–15-Hz bands for Patient 7 of the Kuizenga *et al.* study, and Fig. 5.11 shows the same information, but now plotted as a function of propofol concentration at the femoral artery. Both bands show a pair of pronounced activation peaks: the first peak occurs during the induction phase as the patient becomes unconscious; the second peak occurs some time later when the concentration is reduced, allowing the patient to emerge from unconsciousness. For the 0–5-Hz band, the induction peak is stronger, while for the 11–15-Hz band the emergence peak is strongly dominant.

Drug–Effect Hysteresis

Comparing the experimental graphs of Fig. 5.11 with the theoretical predictions of Fig. 5.10 shows a very pleasing qualitative agreement in their general shape and character: there are two distinct surges in slew-rate activity, one during induction of anaesthesia and the second during emergence from anaesthesia. These two activity surges are well separated in concentration space: the patient becomes unconscious at a considerably higher propofol (about 2.5×) concentration than that at which she wakes up. The existence of a hysteresis effect (i.e., an emergence

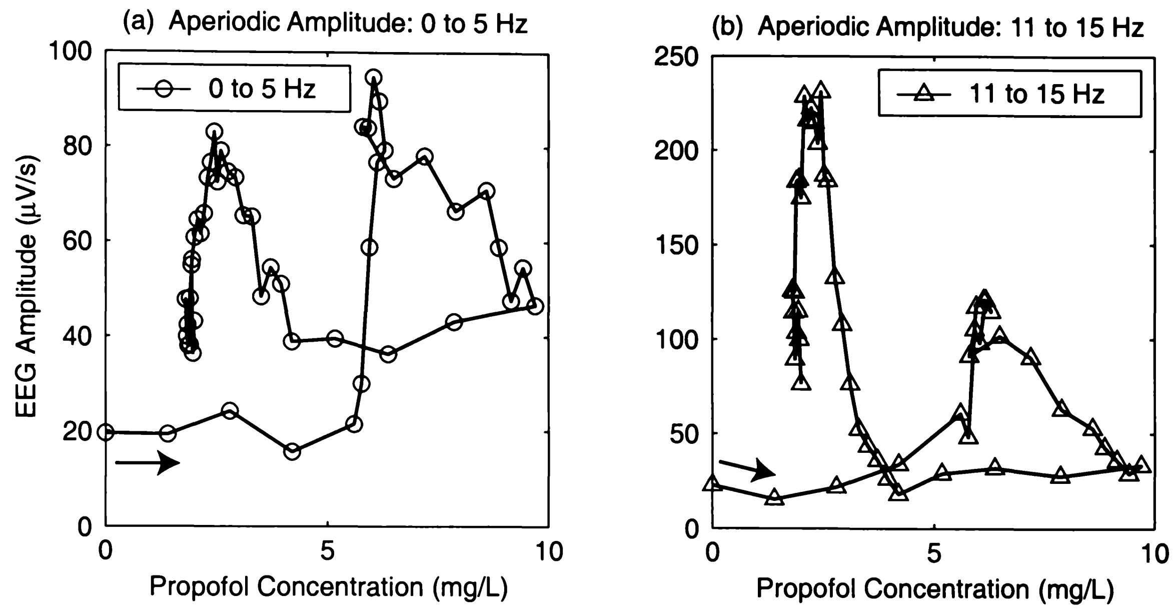

Figure 5.11: EEG "amplitude" (actually *slew-rate*) data from Fig. 5.8 plotted as a function of measured propofol blood concentration. (a) 0–5 Hz; (b) 11–15 Hz. Each trajectory commences at the lower-left corner at zero concentration. For the 0-5-Hz band, the activation peak is stronger during the induction phase (right-hand peak); for the 11–15-Hz band, the activation peak is considerably stronger at emergence (left-hand peak). [Data supplied courtesy of K. Kuizenga, and reported as "Patient 7" in Kuizenga *et al.* (1998).]

trajectory which is distinct from the induction trajectory) is exactly what is expected from the first-order phase-transition model of the macrocolumn.

Some caution is in order. Many anaesthetics researchers would not be convinced that the hysteresis separation is anything other than a *measurement artifact*. In comparing our model with the Kuizenga *et al.* results, we are assuming that our λ-factor (degree of prolongation of the inhibitory time constant) corresponds to propofol concentration at the cortex. However, what was actually measured was the propofol concentration in the femoral artery. The extrapolation from artery concentration to cerebral cortex concentration is a complicated exercise in pharmaco-kinetics modelling (requiring several assumptions about multiple-compartment time-constants) whose intent is to compensate for the fact that the site of anaesthetic action (the cortex) does not coincide with the site of anaesthetic measurement (in this case, the major artery in the thigh). In such modelling it is standard practice to adjust the drug-model parameters until the hysteresis loop closes, so that, in effect, the patient induction and emergence events occur at that *same* extrapolated drug concentration.

However, our phase-transition model asserts that even if the concentration were to be measured at the cortex so that there were no site/effect displacement errors, there should still be a hysteresis effect with emergence occurring at a lower concentration than induction. If our model is correct, then the pharmaco-kineticists are over-compensating when they null the hysteresis loop.

In order to convince the anaesthetics community, one would need an experimental setup that eliminates site/effect timing errors without recourse to a pharmaco-kinetics model. One way of achieving this might be to run a *very slow* induction/emergence experiment in which the anaesthetic concentration is altered so gradually that concentrations at the measurement and effect sites can reasonably be assumed to be identical. Then no pharmaco-kinetics corrections would be required, and the underlying true hysteretic separation between induction and emergence should become apparent.

Biphasic Power

The biphasic power surges predicted in Fig. 5.10 are clearly evident in the clinical record of Fig. 5.11. The theoretical curves suggest that, for the low-frequency band (0–5-Hz), the slew-rate activities at the induction and emergence peaks should be rather similar, while for the high-frequency band (11–15-Hz), the peak at induction should be about four times larger than the emergence peak. The latter prediction is the reverse of what was actually found in Fig. 5.11b.

Another point of distinction concerns the shapes of the curves: the macrocolumn predicts an abrupt collapse into unconsciousness, whereas the clinical records show a gradual "crumbling" of slew-rate activity.

It is likely that these discrepancies arise because the model is predicting the fluctuations in soma voltage for a *single* representative macrocolumn in the cortex, while the EEG measurement is a recording of the superposition of signals from thousands of macrocolumns in the vicinity of the scalp electrodes, after attenuation and filtering by the intervening cerebro-spinal fluid, skull and skin. The fact that the activation peaks can be detected at all suggests that, near the critical points, a significant fraction of the macrocolumns must be behaving coherently.

Chapter 6

Thermodynamics Analogy for the Conscious-to-Unconscious Transition

A common characteristic of thermodynamic phase transitions is the observation of divergences in one or more parameters. The fact that EEG power appears to diverge at a critical point during induction motivates the present chapter's attempt to understand the nature of this transition from a statistical mechanics perspective. The approach will be to assert a formal correspondence between the cortical system (the adiabatic macrocolumn) and a classical system which can be described using the language and ideas of equilibrium thermodynamics. These ideas were first presented in our Steyn-Ross *et al.* (2001a) paper. M. Steyn-Ross provided the theoretical backbone, J. Sleigh located the clinical evidence in support, and I performed all numerical calculations.

First we discuss what is meant by "equilibrium" for the (dissipative) cortical system. From the Langevin equations for the adiabatic macrocolumn we derive a Fokker–Planck equation for the time evolution of the probability density function (PDF) for the h_e and h_i soma voltages. The uncoupled stationary PDFs for h_e and h_i are generated by treating the stationary state diagram of Fig. 3.4 as an effective equation of state which allows h_i to be expressed as a variable offset from h_e: $h_i = h_e - \Delta$. From the stationary PDFs we can extract *potential functions* $U_{e,i}$, so-called because when plotted as a function h_e, we see a hills-and-valleys picture whose maxima and minima locate the unstable and stable equilibrium points. These potential function diagrams evolve with anaesthetic in such a way that the zero-gradient points always coincide with the coordinates defined by the Fig. 3.4 graph of stationary points.

To continue the analogy, we need to choose a quantity for the cortex which *behaves like* the physical temperature of a classical thermodynamic phase transition. For guidance, we examine how the predominant intracellular ion processes in the anaesthetic-damped cortex might be viewed from a canonical ensemble perspective, then discuss the ferroelectric phase transition as an example of a true thermodynamic phase transition which has stronger similarities to the cortical transition than do some of the more familiar phase changes (e.g., liquid → solid, para- → ferromagnetic). These considerations lead us to argue that anaesthetic effect *behaves like an inverse temperature*, but to avoid confusion with physical temperature we christen this temperature-like entity *excitability*, symbol Θ, and claim that excitability and anaesthetic effect must be, in some functional form, oppositely proportional: $\Theta \sim \lambda^{-1}$.

Having identified a temperature analogue, we can map from potential function U to effective Helmholtz free energy V, and from there to cortical entropy and cortical "heat capacity." But then we need to pause to ask, "Do these theoretical cortical constructs have any physical reality?" While it is not obvious how one might test the model predictions for cortical entropy, there does appear to be clinical evidence for a "latent heat" effect in the research reported by Stullken and colleagues (Stullken Jr. *et al.*, 1977). Their investigation looked at the change in metabolic energy requirements of the cortex as anaesthetic concentration is slowly increased. Rather than a gradual decline in energy consumption, Stullken *et al.* found an abrupt decrease which coincided with changes in the character of the EEG waveform.

6.1 What is "Equilibrium" in an Open Dissipative System?

We need to elucidate what we mean by applying the words "thermodynamics" and "equilibrium" to the phase transition of a complex biological system such as the cerebral cortex. First, we are *not* implying that the phase transition is in any way caused by changes in the thermometer-measured physical temperature of the cortex. Rather, we are asserting that the anaesthetic acts in a temperature-like manner to drive the cortex through its "anaestheto-dynamc" phase transition into unconsciousness, and that once a suitable anaesthetic-effect/analogous-temperature mapping has been established, we are free to use generalized thermodynamics concepts to describe the change.

Second, the equilibrium assumption is fundamental to our model: At all times the cortex never deviates far from the anaesthetic-determined equilibrium points defined by the inverse-S curve of steady-states shown in Fig. 3.4. The assumption that the cortex can be regarded as being in an equilibrium state requires justification—after all, the conventional picture of the cortex would say that it is an open, dissipative biological system which is *far from equilibrium* because its steady-state behaviour is maintained by a continuous flux of chemical energy associated with nutrients and oxygen required for metabolic functioning. We argue that our equilibrium treatment can be justified on the basis of (1) localization, and (2) scale.

1. Local equilibrium: Glansdorff and Prigogine (1974) explain how it is possible to ascribe a state of *local equilibrium* to a small mass element (in our case, the macrocolumn) which is part of a larger system (i.e., the cerbral cortex) which, as a whole, is out of equilibrium. This can be done if the local state (i.e., the soma voltage) is completely described by an equation of state which is independent of the gradients (e.g., of chemical energy). In our case, the equation of state is represented by Fig. 3.4: the anaesthetic-determined trajectory of soma-voltage steady states.

This adoption of local equilibrium is analogous to a technique used in engineering mechanics whereby an accelerated body is treated as if it were in static equilibrium by mapping to an accelerated frame of reference in which the body is *locally* at rest. One incorporates into the equations of motion the inertial forces which arise from the fact that the measurements are now being performed in the accelerated frame [see, e.g., Tipler (1990, p. 121); Kleppner and Kolenkow (1978, p. 346); Steyn-Ross and Ivey (1992)].[1] For the cortex, the "inertial" forces would be the

---

[1] The *principle of equivalence* asserts that the laws of physics in a uniformly accelerated system are identical to those in an inertial system provided that one introduces a fictitious force to act on each particle, $\mathbf{F}_{\text{fict}} = -m\mathbf{a}$. An acceleration $\mathbf{a}$ produces an effect which locally is indistinguishable from a gravitational field $\mathbf{g} = -\mathbf{a}$; this equivalence underlies Einstein's general theory of relativity.

generalized forces responsible for the flow of energy and matter driving the intracellular processes which maintain the biological state of the cortex.

2. **Scale:** Glansdorff and Prigogine emphasize that

> "...the local equilibrium assumption implies that dissipative processes are sufficiently dominant to exclude large deviations from statistical equilibrium...There must be sufficient dissipative 'collisions' to compensate for the effect of imposed gradients."

For the cortex, we picture these dissipative processes as the myriad openings and closings of the millions of ion channels which service an individual neuron. These collisions occur on timescales several orders of magnitude faster than timescales of our "mesoscale" soma-voltage model, so the requirement for plentiful collisions is well satisfied. Further, because we are modelling at the meso scale of the neural assembly, and not at the microscopic scale of the molecular and ionic channel processes, it is not unreasonable to replace the fine details of biological maintenance with steady-state parameters in the model (e.g., the ψ_{jk} weighting functions represent the time-averaged neurokinetics), then to treat the steady state as if it were a true equilibrium.

6.2 Langevin Equations in the Adiabatic Limit

In Chap. 4.1 we inspected the various time-scales for the $h_{e,i}$ soma voltages and the four I_{jk} input currents, and showed that it was reasonable to assume that the input currents would equilibrate much faster than the soma voltages. This justified the so-called "adiabatic" simplification in which we eliminated the time-variation of the currents (i.e., we set to zero all d/dt terms appearing in Eqs (3.2–3.4)), giving the reduced set of adiabatic differential equations listed as Eqs (4.1–4.3). These were transformed in Chap. 5.1 into a pair of stochastic differential equations by incorporating into each of the I_{jk} input currents a white-noise term originating from the subcortex via fluctuations about a mean value in its p_{jk} spike rate. The resulting stochastic equations are,

$$\frac{d}{dt}\begin{bmatrix} h_e \\ h_i \end{bmatrix} = \begin{bmatrix} F_1(h_e,h_i) \\ F_2(h_e,h_i) \end{bmatrix} + \begin{bmatrix} \Gamma_e(h_e,t) \\ \Gamma_i(h_i,t) \end{bmatrix}, \tag{6.1}$$

where the drift terms are

$$\begin{aligned} F_1(h_e,h_i) &= \Big\{ \left(h_e^{\text{rest}} - h_e\right) + \psi_{ee}(h_e)\left[\left(N_{ee}^{\alpha} + N_{ee}^{\beta}\right) S_e(h_e) + \langle p_{ee}\rangle\right] G_e e/\gamma_e \\ &\quad + \lambda\, \psi_{ie}(h_e)\left[N_{ie}^{\beta} S_i(h_i) + \langle p_{ie}\rangle\right] G_i e/\gamma_i \Big\} / \tau_e\,, \end{aligned} \tag{6.2a}$$

$$\begin{aligned} F_2(h_e,h_i) &= \Big\{ \left(h_i^{\text{rest}} - h_i\right) + \psi_{ei}(h_i)\left[\left(N_{ei}^{\alpha} + N_{ei}^{\beta}\right) S_e(h_e) + \langle p_{ei}\rangle\right] G_e e/\gamma_e \\ &\quad + \lambda\, \psi_{ii}(h_i)\left[N_{ii}^{\beta} S_i(h_i) + \langle p_{ii}\rangle\right] G_i e/\gamma_i \Big\} / \tau_i\,, \end{aligned} \tag{6.2b}$$

and the corresponding diffusion terms are

$$\begin{aligned} \Gamma_e(h_e,t) &= \Big\{ \psi_{ee}(h_e)\, \alpha_{ee} \sqrt{\langle p_{ee}\rangle}\, \xi_1(t)\, G_e e/\gamma_e \\ &\quad + \lambda\, \psi_{ie}(h_e)\, \alpha_{ie} \sqrt{\langle p_{ie}\rangle}\, \xi_2(t)\, G_i e/\gamma_i \Big\} / \tau_e\,, \end{aligned} \tag{6.3a}$$

$$\begin{aligned}\Gamma_i(h_i,t) &= \Big\{\psi_{ei}(h_i)\,\alpha_{ei}\sqrt{\langle p_{ei}\rangle}\,\xi_3(t)\,G_e e/\gamma_e \\ &\quad + \lambda\,\psi_{ii}(h_i)\,\alpha_{ii}\sqrt{\langle p_{ii}\rangle}\,\xi_4(t)\,G_i e/\gamma_i\Big\}/\tau_i\,. \qquad (6.3\text{b})\end{aligned}$$

Whereas in Chap. 5 we linearized these coupled equations about steady state in order to compute the fluctuation spectrum for h_e, here we will use the h_e-vs-λ and h_i-vs-λ steady-state curves to extract the highly nonlinear and λ-dependent steady-state voltage *difference* $(h_e^0 - h_i^0)$. Knowing the voltage offset then allows us to decouple the Langevin equations, and hence obtain a pair of uncoupled Fokker–Planck equations for the soma voltage probability distribution functions.

6.3 Fokker–Planck Equation for the Macrocolumn

In order to explore the statistical mechanics nature of the anaestheto-dynamic phase transition, we need to derive probability distribution functions P_e and P_i for the excitatory and inhibitory neuron populations of the macrocolumn. We generate an expression for the time-evolution of the joint probability distribution $P(h_e, h_i)$ by writing down the Fokker–Planck equation[2] equivalent to the coupled Langevin equations of the preceding section, giving,

$$\begin{aligned}\frac{\partial P(h_e,h_i,t)}{\partial t} &= -\frac{\partial}{\partial h_e}\left[F_1(h_e,h_i)\,P(h_e,h_i,t)\right] - \frac{\partial}{\partial h_i}\left[F_2(h_e,h_i)\,P(h_e,h_i,t)\right] \\ &\quad + \frac{1}{2}\frac{\partial^2}{\partial h_e^2}\left[D_{11}(h_e)\,P(h_e,h_i,t)\right] + \frac{1}{2}\frac{\partial^2}{\partial h_i^2}\left[D_{22}(h_i)\,P(h_e,h_i,t)\right]\,. \qquad (6.4)\end{aligned}$$

The D_{11} and D_{22} are the diffusion terms defined by the delta-correlation requirement of Eq. (5.20),

$$\langle\Gamma_e(t)\,\Gamma_e(t')\rangle = D_{11}\,\delta(t-t') \qquad (6.5\text{a})$$

$$\langle\Gamma_i(t)\,\Gamma_i(t')\rangle = D_{22}\,\delta(t-t') \qquad (6.5\text{b})$$

so that

$$D_{11}(h_e) = \frac{1}{\tau_e^2}\Big\{\big(\psi_{ee}(h_e)\,\alpha_{ee}\,G_e e/\gamma_e\big)^2\langle p_{ee}\rangle + \lambda^2\big(\psi_{ie}(h_e)\,\alpha_{ie}\,G_i e/\gamma_i\big)^2\langle p_{ie}\rangle\Big\} \qquad (6.6\text{a})$$

$$D_{22}(h_i) = \frac{1}{\tau_i^2}\Big\{\big(\psi_{ei}(h_i)\,\alpha_{ei}\,G_e e/\gamma_e\big)^2\langle p_{ei}\rangle + \lambda^2\big(\psi_{ii}(h_i)\,\alpha_{ii}\,G_i e/\gamma_i\big)^2\langle p_{ii}\rangle\Big\}\,. \qquad (6.6\text{b})$$

---

[2] Gardiner (1985, p. 119) gives the general Fokker–Planck equation as

$$\frac{\partial p(\mathbf{z},t)}{\partial t} = -\sum_j \frac{\partial}{\partial z_j}A_j(\mathbf{z},t)\,p(\mathbf{z},t) + \frac{1}{2}\sum_{j,k}\frac{\partial^2}{\partial_j\partial_k}B_{jk}(\mathbf{z},t)\,p(\mathbf{z},t)$$

which can be rewritten in terms of the gradient of the *probability currents* J_j

$$\frac{\partial p(\mathbf{z},t)}{\partial t} = -\sum_j \frac{\partial}{\partial z_j}J_j(\mathbf{z},t)$$

where the J_j are defined

$$J_j(\mathbf{z},t) = A_j(\mathbf{z},t)\,p(\mathbf{z},t) - \frac{1}{2}\sum_k \frac{\partial}{\partial_k}B_{jk}(\mathbf{z},t)\,p(\mathbf{z},t)\,.$$

In order to compute equilibrium parameters, such as entropy, using a statistical mechanics framework, we require the *stationary* distribution function $\overline{P}(h_e, h_i)$. This is found by setting $\partial P/\partial t = 0$ in Eq. (6.4), then solving for $\overline{P}$, subject to appropriate boundary conditions.

6.3.1 Boundary Conditions

To solve the Fokker–Planck equation (6.4) we need to impose boundary conditions at the ends of the interval over which the soma voltages are constrained. Soma voltage cannot go more positive than $h_e^{\text{rev}} = +45$ mV (sodium reversal potential), and cannot go more negative than $h_i^{\text{rev}} = -90$ mV (potassium reversal potential).[3] Thus the excitatory and inhibitory voltages are constrained by,

$$h_i^{\text{rev}} < h_{e,i} < h_e^{\text{rev}} \tag{6.7a}$$

i.e.,

$$-90 \text{ mV} < h_{e,i} < +45 \text{ mV} \tag{6.7b}$$

and soma voltages outside these bounds cannot occur in the model. These hard limits constitute what Gardiner (1985, p. 121) describes as a "reflecting barrier": there is no net flow of probability across the boundary, so the probability "particles" must be reflected there.

Because the drifts (Eq. (6.2)) and diffusions (Eq. (6.3)) are time-independent, the macrocolumn is a homogeneous system whose steady-state probability currents must settle down to zero (Gardiner, 1985, pp. 124, 146), so the task of solving the second-order Fokker–Planck equation (6.4) at steady state is replaced by the task of solving a pair of coupled first-order DEs obtained by setting the excitatory and inhibitory probability currents to zero. If the system has sufficient symmetry such that it satisfies the *potential conditions* (defined below), then the DEs can be solved to yield a joint potential-energy function $V(h_e, h_i)$. We will find that the macrocolumn does *not* satisfy the potential conditions, and this will motivate an alternative approach to deriving separated potential energy functions $V(h_e)$ and $V(h_i)$ by uncoupling the h_e and h_i Langevin equations and their associated Fokker–Planck probability currents.

6.3.2 Potential Conditions

The probability currents (see footnote on p. 98) for the excitatory and inhibitory neural populations of the macrocolumn are given by,

$$J_e = F_1(h_e, h_i)\, P(h_e, h_i, t) - \frac{1}{2}\frac{\partial}{\partial h_e}\left[D_{11}\, P(h_e, h_i, t)\right] - \frac{1}{2}\frac{\partial}{\partial h_i}\left[D_{12}\, P(h_e, h_i, t)\right] \tag{6.8a}$$

$$J_i = F_2(h_e, h_i)\, P(h_e, h_i, t) - \frac{1}{2}\frac{\partial}{\partial h_e}\left[D_{21}\, P(h_e, h_i, t)\right] - \frac{1}{2}\frac{\partial}{\partial h_i}\left[D_{22}\, P(h_e, h_i, t)\right] \tag{6.8b}$$

where the D_{12} and D_{21} off-diagonal elements of the diffusion matrix are actually zero. For steady state, we set the probability currents to zero and replace $P(h_e, h_i, t)$ by its time-independent steady value $\overline{P}(h_e, h_i)$. Expanding the derivatives in Eq. (6.8) and rearranging, we have

---

[3] Refer to earlier discussion in Chap. 3.3.5 on the seizure ($\lambda_{\text{GABA}} \to 0$) and coma ($\lambda_{\text{GABA}} \to \infty$) asymptotic limits for soma voltage.

$$\begin{aligned}\frac{1}{\overline{P}(h_e,h_i)}\frac{\partial}{\partial h_e}\left[\overline{P}(h_e,h_i)\right] &= \frac{1}{D_{11}}\left[2F_1(h_e,h_i)-\frac{\partial D_{11}}{\partial h_e}\right]\\ &\equiv Z_1(h_e,h_i)\end{aligned} \tag{6.9a}$$

$$\begin{aligned}\frac{1}{\overline{P}(h_e,h_i)}\frac{\partial}{\partial h_i}\left[\overline{P}(h_e,h_i)\right] &= \frac{1}{D_{22}}\left[2F_2(h_e,h_i)-\frac{\partial D_{22}}{\partial h_i}\right]\\ &\equiv Z_2(h_e,h_i)\,.\end{aligned} \tag{6.9b}$$

The left-hand sides can be written as gradients

$$\frac{\partial}{\partial h_e}\left[\log_e \overline{P}(h_e,h_i)\right] = Z_1(h_e,h_i) \tag{6.10a}$$

$$\frac{\partial}{\partial h_i}\left[\log_e \overline{P}(h_e,h_i)\right] = Z_2(h_e,h_i)\,. \tag{6.10b}$$

Equations (6.10) can be solved analytically if the $Z_{1,2}$ are also gradients. A necessary and sufficient condition for this is that the curl should vanish (Gardiner, 1985, p. 147):

$$\frac{\partial Z_1}{\partial h_i} = \frac{\partial Z_2}{\partial h_e} \tag{6.11}$$

in which case the steady-state probability $\overline{P}$ is obtained by solving the line integral

$$\overline{P}(h_e,h_i) \overset{?}{=} \exp\left[\int^{h_e,h_i} Z_1\,dh_e' + Z_2\,dh_i'\right]\,. \tag{6.12}$$

The question-sign above the equality in Eq. (6.12) emphasizes that the equation is true only if the so-called *potential conditions* of Eq. (6.11) hold.

We will find that the potential conditions do *not* hold for the macrocolumn model. Inspecting Eq. (6.6), we see that the D_{11} diffusion term is a linear function of h_e only (via the ψ_{ee} and ψ_{ie} weighting functions), and similarly D_{22} is a linear function of h_i only, so the diffusion terms (and their derivatives) make zero contribution to the curl. But the $F_{1,2}$ drift terms make asymmetric contributions: evaluating the cross-derivatives of the $Z_{1,2}$ in Eq. (6.9) for the drifts defined in Eq. (6.2), we obtain,

$$\begin{aligned}\frac{\partial Z_1}{\partial h_i} &= \frac{2}{D_{11}}\frac{\partial F_1}{\partial h_i}\\ &= \frac{2\,\lambda\psi_{ie}N_{ie}^{\beta}G_i e}{D_{11}\gamma_i\tau_e}\,\frac{\partial \mathcal{S}_i}{\partial h_i}\end{aligned} \tag{6.13a}$$

and

$$\begin{aligned}\frac{\partial Z_2}{\partial h_e} &= \frac{2}{D_{22}}\frac{\partial F_2}{\partial h_e}\\ &= \frac{2\,(N_{ei}^{\alpha}+N_{ei}^{\beta})\psi_{ei}G_e e}{D_{22}\gamma_e\tau_i}\,\frac{\partial \mathcal{S}_e}{\partial h_e}\,.\end{aligned} \tag{6.13b}$$

It is clear that Eqs (6.13a) and (6.13b) cannot be equal: the first depends on anaesthetic effect λ and on the slope of the inhibitory firing-rate sigmoid $\partial\mathcal{S}_i/\partial h_i$, while the second is independent of anaesthetic and proportional to the slope of the excitatory sigmoid $\partial\mathcal{S}_e/\partial h_e$.

6.4 Decoupling the Langevin Equations

We have just observed that the two-variable adiabatic macrocolumn system does not satisfy the potential conditions of Eq. (6.11), so an analytic expression for the steady-state probability distribution $\overline{P}(h_e, h_i)$ is unavailable to us.

However, an approximate solution for $\overline{P}$ is achievable if we use the equilibrium values of Fig. 3.4 to decouple the Langevin equations Eq. (6.1) into two independent equations, one for h_e alone and a second for h_i alone. From the separated Langevin pair will follow a pair of now independent Fokker–Planck equations whose respective long-time solutions will give us the desired $\overline{P}(h_e)$ and $\overline{P}(h_i)$ stationary probability distribution functions. First, though, we must explain precisely how the decoupling is to be done, then check the quality of the decoupling by asking the question: Have the essential features of the anaestheto-dynamic phase transition been preserved in the transformation to a single-variable system?

Inspection of Fig. 3.4 shows that the λ-dependence of h_e and h_i is rather similar: the curves are almost coincident on the bottom branch, become distinct on the middle and upper branches, then converge again as they approach the top-left seizure corner. So it seems not unreasonable to express the locus of equilibrium values of h_i as an h_e-dependent offset from the matching locus of equilibrium values of h_e:

$$h_i^0 = h_e^0 - \Delta(h_e) \tag{6.14}$$

where the offset term $\Delta(h_e)$, obtained numerically from the Fig. 3.4 stationary curves, is shown in Fig. 6.1 plotted as a function of h_e and of λ. We will assume that the $\Delta(h_e)$ offset formula, which is exact for the locus of equilibrium points, can also be applied to points nearby which are *very close to equilibrium*, so generalize Eq. (6.14) to read

$$h_i = h_e - \Delta(h_e)\,. \tag{6.15}$$

This generalization is equivalent to making a Taylor expansion about equilibrium and requiring that the first-order term in the expansion, the gradient $(\partial\Delta/\partial h_e)\big|_0$, be small.

Examining Fig. 6.2c, we see that the absolute value of the offset slope is generally less than ~0.2, except along the unstable branch A_3Q_1 (which is of little interest since the macrocolumn can never remain here) and in the vicinity of the jump points A_3 and Q_1; and also approaching seizure point S where the slope has magnitude ~0.35. For these regions, Eq. (6.15) will not be very accurate, but this is of little consequence for the stationary potential and probability distribution function curves that are to be derived shortly, since it the locations of the distribution maxima and minima which are of prime interest, and for these points, Eq. (6.15) is exact. (The inaccuracies in the distribution curves will manifest as shape errors *between* the distribution extrema, and might compromise calculations for first-passage times, but this is not the focus of our present work.)

Applying the offset relationship decouples the original Langevin equations (6.1) into two independent, stochastic equations of motion, one for h_e, and one for h_i,

$$\frac{dh_e}{dt} = \widetilde{F_1}(h_e) + \Gamma_e(t) \tag{6.16a}$$

$$\frac{dh_i}{dt} = \widetilde{F_2}(h_i) + \Gamma_i(t) \tag{6.16b}$$

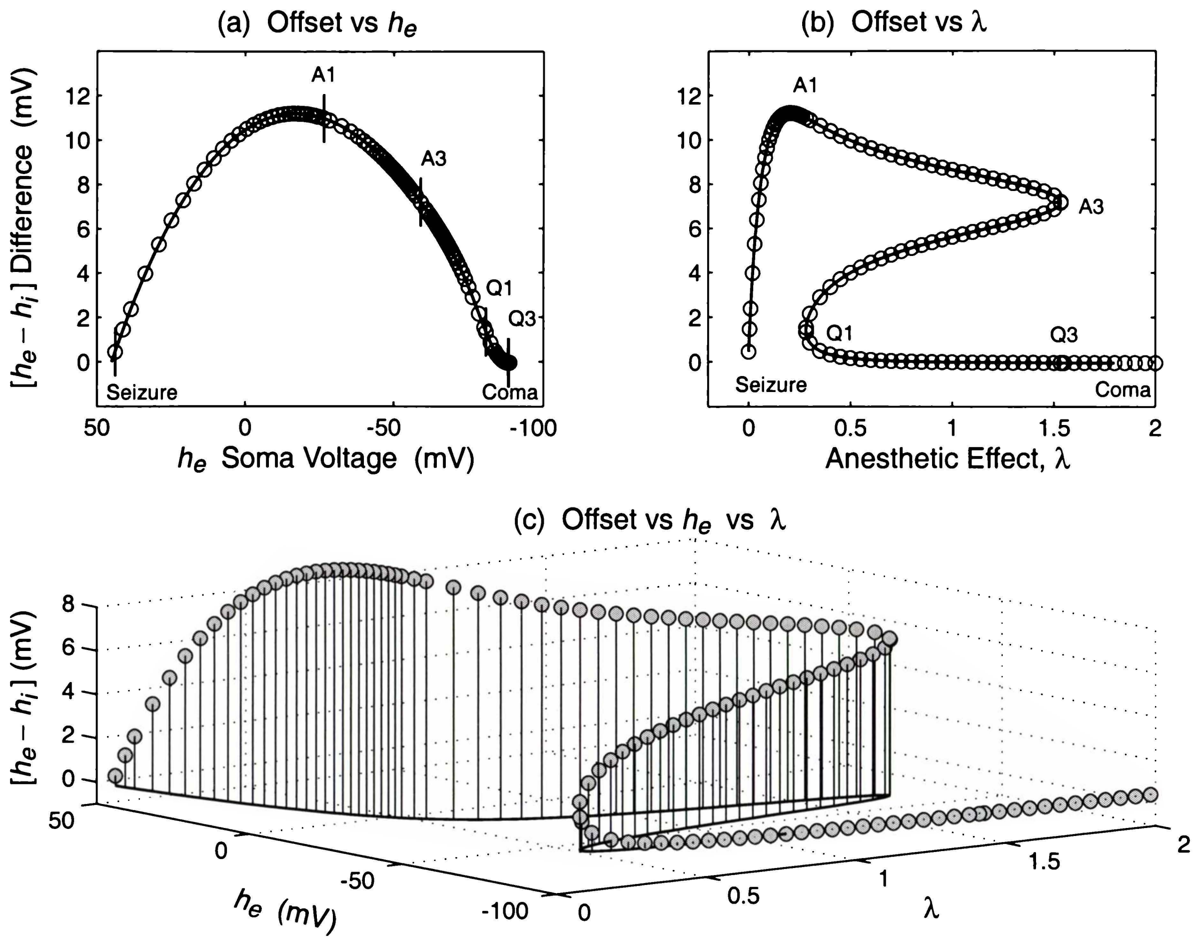

Figure 6.1: Offset between excitatory and inhibitory soma voltages for the steady-state trajectory of Fig. 3.4. The offset, defined $\Delta(h_e) = h_e^0 - h_i^0$, tends to zero at the seizure and coma extremes. See also Fig. 6.2.

where the overtilde variables are defined

$$\widetilde{F_1}(h_e) \equiv F_1(h_e, h_e - \Delta) \qquad (6.17a)$$

$$\widetilde{F_2}(h_i) \equiv F_2(h_i + \Delta, h_i)\,. \qquad (6.17b)$$

6.5 Behaviour of the Uncoupled Pseudocolumns

A truly fundamental feature of the cortical macrocolumn is the strong feedforward and feedback interconnectedness of the excitatory and inhibitory neural populations. Yet we seem to have boldly severed these connections by invoking internal knowledge of the soma voltage offsets which pertain at equilibrium. Effectively, the offset ruse has allowed us to engineer a pair of new, and *apparently independent* excitatory and inhibitory systems that I shall refer to as *pseudocolumns* to distinguish them from the fully-coupled macrocolumn. It is our hope that the essential physics arising from the excitatory–inhibitory coupling has not been lost from the pseudocolumns, but is now encapsulated within the offset itself. The first test will be to examine the stability characteristics of the excitatory and inhibitory pseudocolumns defined by Eq. (6.16).

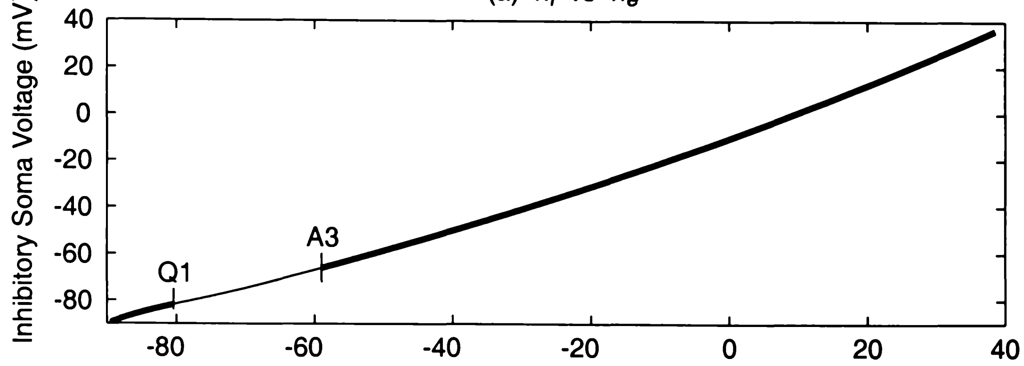

(a) h_i vs h_e

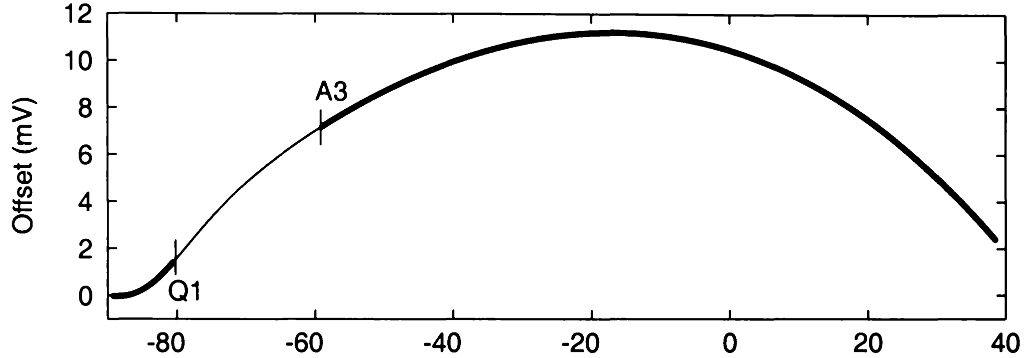

(b) $(h_e - h_i)$ Offset vs h_e

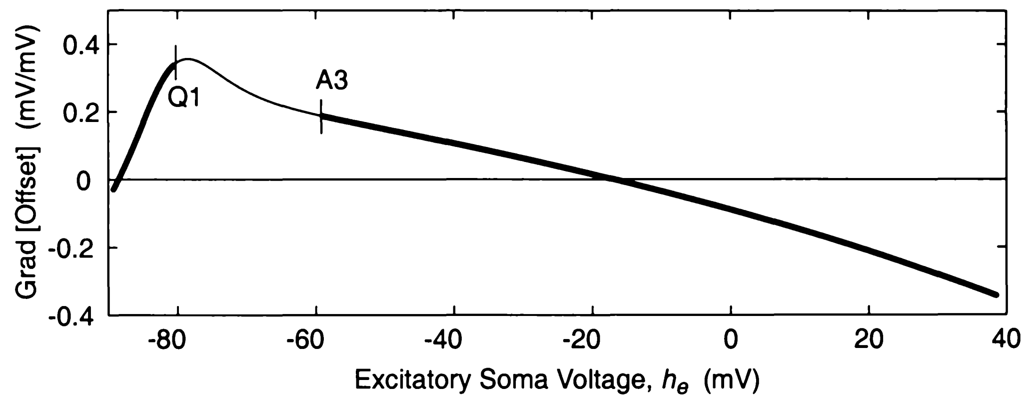

(c) Gradient of $(h_e - h_i)$ Offset

Figure 6.2: Relationship between stationary h_e and h_i expressed as (a) actual values; (b) an offset $\Delta = (h_e - h_i)$; and (c) the gradient of the offset, $d\Delta/dh_e$. Panel (b) shows the same information as Fig. 6.1a, but with data-point markers removed and replaced with a spline fit for clarity, and with horizontal axis restored to conventional presentation (i.e., increasing to the right). Unstable A_3Q_1 branch is drawn with a thin pen.

6.5.1 Pseudocolumn Rate Equations

The pseudocolumn rate equations are generated by replacing h_i by $(h_e - \Delta)$ in Eq. (4.1a), and h_e by $(h_i + \Delta)$ in Eq. (4.1b),

$$\widetilde{F_1}(h_e) = \left[h_e^{\text{rest}} - h_e + \psi_{ee}(h_e)\, I_{ee}(h_e) + \psi_{ie}(h_e)\, I_{ie}(h_e - \Delta)\right] / \tau_e \tag{6.18a}$$

$$\widetilde{F_2}(h_i) = \left[h_i^{\text{rest}} - h_i + \psi_{ei}(h_i)\, I_{ei}(h_i + \Delta) + \psi_{ii}(h_i)\, I_{ii}(h_i)\right] / \tau_i\,. \tag{6.18b}$$

Following the linear stability analysis of Chap. 4.2, we assess the sensitivity of the pseudocolumn to soma voltage perturbation by examining the drift gradients $d\widetilde{F_1}/dh_e$ and $d\widetilde{F_2}/dh_i$,

$$\frac{d\widetilde{F_1}}{dh_e} = \frac{1}{\tau_e}\left[-1 + \frac{d\psi_{ee}}{dh_e}I_{ee} + \psi_{ee}\frac{dI_{ee}}{dh_e} + \frac{d\psi_{ie}}{dh_e}I_{ie} + \psi_{ie}\frac{dI_{ie}(h_e - \Delta)}{dh_e}\right] \tag{6.19a}$$

$$\frac{d\widetilde{F_2}}{dh_i} = \frac{1}{\tau_i}\left[-1 + \frac{d\psi_{ei}}{dh_i}I_{ei} + \psi_{ei}\frac{dI_{ei}(h_i + \Delta)}{dh_i} + \frac{d\psi_{ii}}{dh_i}I_{ii} + \psi_{ii}\frac{dI_{ii}}{dh_i}\right]. \tag{6.19b}$$

The coupling-term derivatives appearing in these two equations can be rewritten

$$\frac{dI_{ie}(h_e - \Delta)}{dh_e} = \frac{d}{dh_e}I_{ie}(h_i) = \frac{dI_{ie}}{dh_i}\frac{dh_i}{dh_e} = \frac{dI_{ie}}{dh_i}\left(1 - \frac{d\Delta}{dh_e}\right) \tag{6.20a}$$

$$\frac{dI_{ei}(h_i + \Delta)}{dh_i} = \frac{d}{dh_i}I_{ei}(h_e) = \frac{dI_{ei}}{dh_e}\frac{dh_e}{dh_i} = \frac{dI_{ei}}{dh_e}\left(1 + \frac{d\Delta}{dh_i}\right). \tag{6.20b}$$

The right-hand sides of Eq. (6.19) can now be re-expressed as paired combinations of the elements of the **J** Jacobian matrix for the fully-coupled system presented in Eq. (4.24):

$$\frac{d\widetilde{F_1}}{dh_e} = J_{11} + \left(1 - \frac{d\Delta}{dh_e}\right)J_{12} \equiv K_1 \tag{6.21a}$$

$$\frac{d\widetilde{F_2}}{dh_i} = \left(1 + \frac{d\Delta}{dh_i}\right)J_{21} + J_{22} \equiv K_2. \tag{6.21b}$$

I will now demonstrate that it is the sign of K_1 and K_2 which determines pseudocolumn stability.

6.5.2 Stability

Let the pseudocolumn pair suffer small independent perturbations δh_e, δh_i away from the equilibrium soma voltages h_e^0, h_i^0:

$$\delta h_e(t) = h_e(t) - h_e^0 \tag{6.22a}$$

$$\delta h_i(t) = h_i(t) - h_i^0. \tag{6.22b}$$

The time rate-of-change of these perturbations determines the stability of the stationary state:

$$\frac{d}{dt}(\delta h_e) = \frac{dh_e}{dt} - 0 = \widetilde{F_1} \approx \widetilde{F_1}\Big|_0 + \delta h_e\frac{d\widetilde{F_1}}{dh_e}\bigg|_0 \tag{6.23a}$$

$$\frac{d}{dt}(\delta h_i) = \frac{dh_i}{dt} - 0 = \widetilde{F_2} \approx \widetilde{F_2}\Big|_0 + \delta h_i\frac{d\widetilde{F_2}}{dh_i}\bigg|_0 \tag{6.23b}$$

where we have neglected quadratic and higher-order terms in the Taylor expansion about steady state. By the definition of steady state, $\widetilde{F_1}\big|_0 = \widetilde{F_2}\big|_0 = 0$, and from Eq. (6.21), $(d\widetilde{F_1}/dh_e)\big|_0 = K_1$ and $(d\widetilde{F_2}/dh_i)\big|_0 = K_2$, so Eq. (6.23) leads to a pair of fractional-change equations for the perturbations,

$$\frac{d}{dt}(\delta h_e) = K_1\,\delta h_e \tag{6.24a}$$

$$\frac{d}{dt}(\delta h_i) = K_2\,\delta h_e \tag{6.24b}$$

leading to exponential growth or decay depending on the sign of the K coefficients:

$$\delta h_e(t) = \delta h_e(0)\, e^{K_1 t} \tag{6.25a}$$

$$\delta h_i(t) = \delta h_i(0)\, e^{K_2 t}\,. \tag{6.25b}$$

These perturbations will decay with time if both K_1 and K_2 coefficients are negative. Thus, the condition for the stability of a given equilibrium state of the uncoupled excitatory (or inhibitory) pseudocolumn is simply,

$$K_1 < 0, \qquad K_2 < 0. \tag{6.26}$$

Figure 6.3(a) plots the variation of the K_1 (as defined by Eq. (6.21a)) and K_2 (from Eq. (6.21b)) pseudocolumn rate constants for the trajectory of soma voltage steady states mapped out earlier in Fig. 3.4. The overall shape for the rate-constants graph (a) is very similar to that shown in Fig. 6.3(b) for the dominant and non-dominant eigenvalue pair of the two-variable coupled macrocolumn system of Eq. (4.1). In particular, the zero-crossings of $K_{1,2}$ at A_3 (induction) and Q_1 (emergence) exactly match those of the dominant eigenvalue plotted in (b). Therefore, for both coupled macrcocolumn and uncoupled pseudocolumn systems, the A_3Q_1 mid-branch of stationary states is unstable.

Since $K_{1,2}$ goes to zero at the A_3 and Q_1 turning points, it follows that the amplitude of the stochastic fluctuations about equilibrium will grow without limit as the pseudocolumn

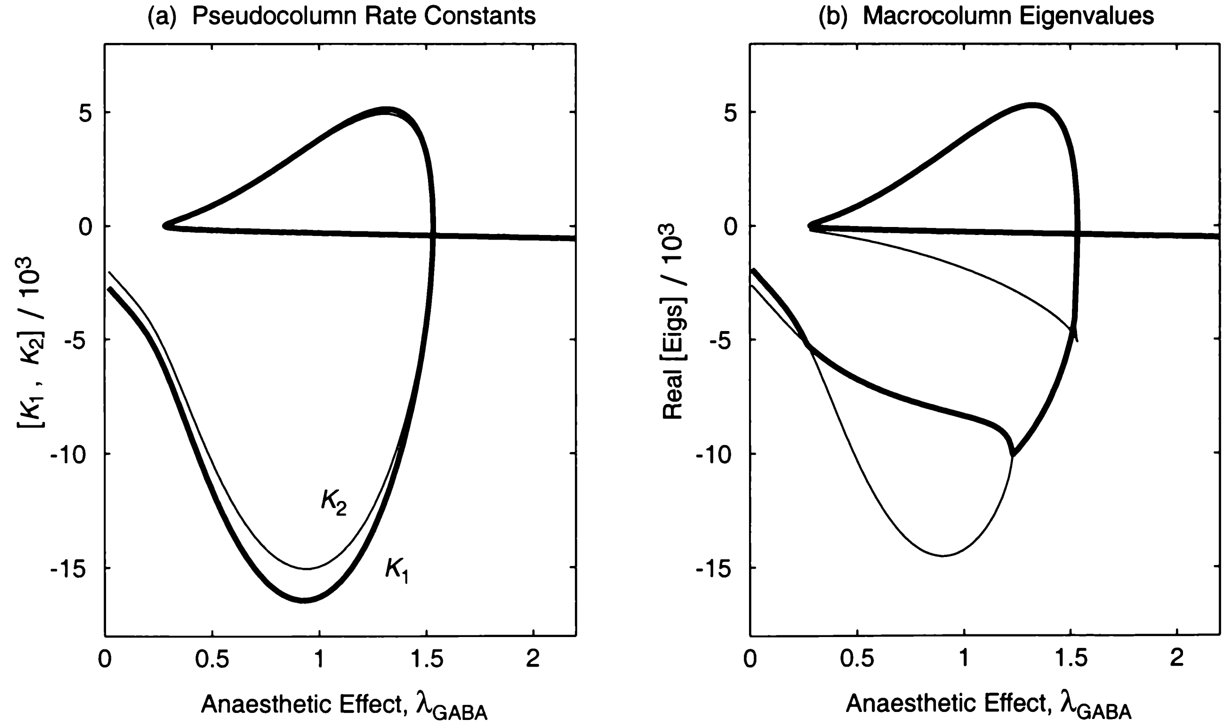

Figure 6.3: Stability comparision between the decoupled pseudocolumn model (left) and the standard adiabatic macrocolumn (right). (a) Variation with anaesthetic effect of pseudocolumn rate constants K_1 (excitatory: bold line) and K_2 (inhibitory: thin line). For comparison, (b) shows the real part of the dominant (bold line) and non-dominant (thin line) eigenvalues for standard macrocolumn. (Panel (b) is a copy of Fig. 4.1(b) with the imaginary part suppressed).

approaches the turning point; this will be demonstrated in the following section. Thus the first-order phase-transition behaviours of the macrocolumn have been preserved in the transformation to (apparently) independent pseudocolumns.

6.5.3 Ornstein–Uhlenbeck Equations for the Pseudocolumn

By applying the offset relationship of Eq. (6.15), we have uncoupled the drift terms[4] of the Langevin equations of Eqs (5.8, 6.1)

$$\frac{d}{dt}\begin{bmatrix} h_e \\ h_i \end{bmatrix} = \begin{bmatrix} F_1(h_e, h_i) \\ F_2(h_e, h_i) \end{bmatrix} + \begin{bmatrix} \Gamma_e(h_e, t) \\ \Gamma_i(h_i, t) \end{bmatrix}, \tag{6.27}$$

to give the independent Langevin pair of Eq. (6.16)

$$\frac{dh_e}{dt} = \widetilde{F_1}(h_e) + \Gamma_e(h_e, t) \tag{6.28a}$$

$$\frac{dh_i}{dt} = \widetilde{F_2}(h_i) + \Gamma_i(h_i, t)\,. \tag{6.28b}$$

We are interested in the magnitude and spectral character of the random voltage fluctuations about pseudocolumn steady state, so, as was done in Sect. 5.3, we linearize about steady state while retaining the diffusion terms. Thus Eqs (6.28) become (cf. Eq. (5.17))

$$\frac{d}{dt}(\delta h_e) = \left.\frac{d\widetilde{F_1}}{dh_e}\right|_0 \delta h_e + \left.\Gamma_e(h_e, t)\right|_0 \tag{6.29a}$$

$$\frac{d}{dt}(\delta h_i) = \left.\frac{d\widetilde{F_2}}{dh_i}\right|_0 \delta h_i + \left.\Gamma_i(h_i, t)\right|_0 \tag{6.29b}$$

which we can rewrite as a pair of independent Ornstein–Uhlenbeck equations (cf. Eq. (5.26) and Gardiner (1985, p. 106))

$$\frac{d}{dt}(\delta h_e) = -A_1\,\delta h_e + \sqrt{D_{11}}\,\xi_e(t) \tag{6.30a}$$

$$\frac{d}{dt}(\delta h_i) = -A_2\,\delta h_i + \sqrt{D_{22}}\,\xi_i(t) \tag{6.30b}$$

where the D_{jj} were given in Eq. (6.6), and the $\xi_{e,i}$ noises were defined in Eq. (5.27). The $A_{1,2}$ drift factors are the negative of the rate coefficients evaluated at equilibrium:

$$A_1 \equiv -K_1 = -\left.\frac{d\widetilde{F_1})}{dh_e}\right|_0 \tag{6.31a}$$

$$A_2 \equiv -K_2 = -\left.\frac{d\widetilde{F_2})}{dh_i}\right|_0 . \tag{6.31b}$$

Following Gardiner (1985, pp. 106–107), we can write down expressions for steady-state variance, time-correlation, and spectrum for the uncoupled pseudocolumn fluctuations, and these can be compared with the coupled macrocolumn results of Sect. 5.4.

---

[4] Unlike the $F_{1,2}$ drifts, the diffusion terms (see Eqs (5.22, 6.6)) have been uncoupled from the outset; i.e., $D_{11} = D_{11}(h_e)$, $D_{22} = D_{22}(h_i)$.

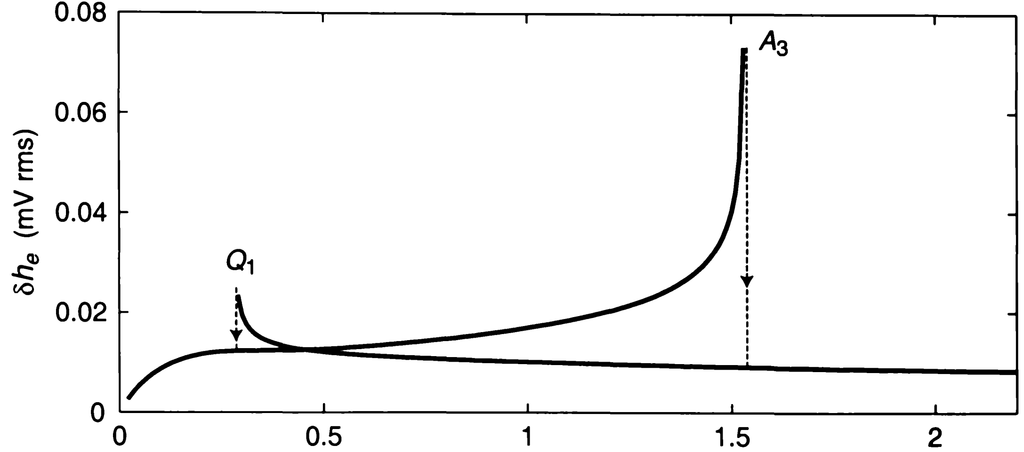

(a) Pseudocolumn δh_e Fluctuation Amplitude

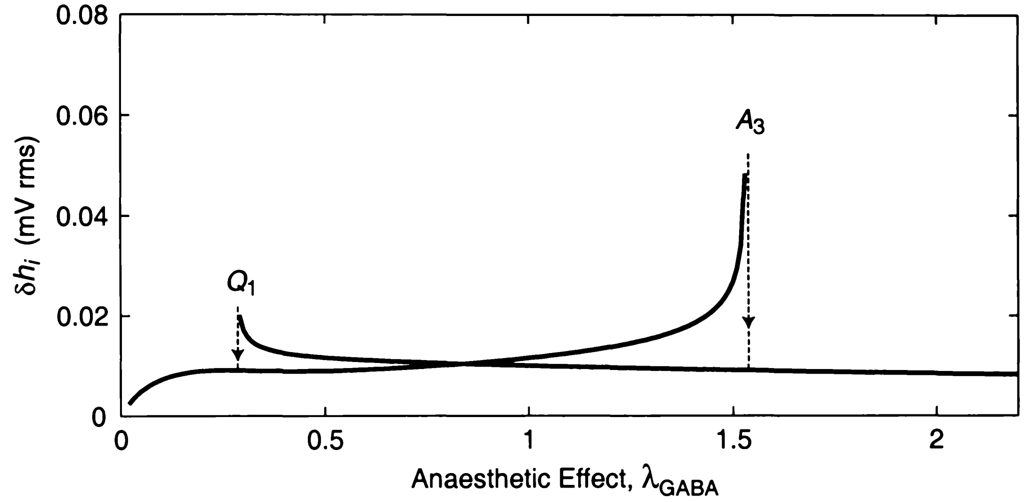

(b) δh_i Fluctuation Amplitude

Figure 6.4: Fluctuation amplitude for the pseudocolumn model. (a) $\delta h_e^{\mathrm{rms}}$ versus λ; (b) $\delta h_i^{\mathrm{rms}}$ versus λ. Comparing these graphs with those in Fig. 5.3 shows that the pseudocolumn fluctuations are about one-third as large as those for the macrocolumn on approach to induction at A_3, and have an overall shape which is rather similar to the $\delta h_{ei}^{\mathrm{rms}}$ cross-fluctuations of Fig. 5.3(c).

Variance of the Fluctuations

The fluctuation variance for the excitatory and inhibitory pseudocolumns at steady state is,

$$\mathrm{var}(\delta h_e) = \frac{D_{11}}{2A_1} \tag{6.32a}$$

$$\mathrm{var}(\delta h_i) = \frac{D_{22}}{2A_2}. \tag{6.32b}$$

Contrast these single-dimensional results with the macrocolumn covariance matrix listed in Eq. (5.28). Fluctuation amplitude will grow without limit as $A_{1,2} \to 0$ on approach to the turning points; this is shown in Fig. 6.4.

Time-Correlation for Fluctuations

The stationary autocorrelation functions for the pseudocolumns are given by,

$$\langle \delta h_e(\tau), \delta h_e(0) \rangle = \frac{D_{11}}{2A_1} \exp\left[-A_1 \tau\right] \tag{6.33a}$$

$$\langle \delta h_i(\tau), \delta h_i(0) \rangle = \frac{D_{22}}{2A_2} \exp\left[-A_2 \tau\right] . \tag{6.33b}$$

Here the correlations decay with a single time-constant, whereas the macrocolumn autocorrelation functions are the sum of two exponential decays (see Eq. (5.45)).

Fluctuations Spectrum

The steady-state fluctuation spectrum for the pseudocolumn will have a pure Lorentzian profile (see Eq. (2.29)),

$$S_1(\omega) = \frac{1}{2\pi} \frac{D_{11}}{A_1^2 + \omega^2} \tag{6.34a}$$

$$S_2(\omega) = \frac{1}{2\pi} \frac{D_{22}}{A_2^2 + \omega^2} . \tag{6.34b}$$

These spectra will develop a $1/\omega^2$ power-law characteristic as the pseudocolumn approaches its induction or emergence turning points with $A_{1,2} \to 0$. Thus the growth in fluctuation power will be entirely at the low-frequency end of the spectrum, with the dc spectral component diverging to infinity at the point of phase-change.

These investigations of the single-dimensional pseudocolumn model demonstrate that, despite the decoupling simplification, the significant features of macrocolumn behaviour (regions of stability, divergent fluctuations, growth of low-frequency power) have been preserved. This gives us some confidence that the work which follows, applying a thermodynamics analogy to the pseudocolumn, has relevance also to the two-variable macrocolumn.

6.6 Steady-State Probability Distribution for the Pseudocolumn

This decoupling of the Langevin equations, as discussed in the preceding section, leads to two *independent* Fokker–Planck equations which are expected to be valid for points close to equilibrium:

$$\frac{\partial \widetilde{P_e}(h_e,t)}{\partial t} = -\frac{\partial}{\partial h_e}\left[\widetilde{F_1}(h_e)\,\widetilde{P_e}(h_e,t)\right] + \frac{1}{2}\frac{\partial^2}{\partial h_e^2}\left[D_{11}(h_e)\,\widetilde{P_e}(h_e,t)\right] \tag{6.35a}$$

$$\frac{\partial \widetilde{P_i}(h_i,t)}{\partial t} = -\frac{\partial}{\partial h_i}\left[\widetilde{F_2}(h_i)\,\widetilde{P_i}(h_i,t)\right] + \frac{1}{2}\frac{\partial^2}{\partial h_i^2}\left[D_{22}(h_i)\,\widetilde{P_i}(h_i,t)\right] . \tag{6.35b}$$

The corresponding probability currents $\widetilde{J}_e$ and $\widetilde{J}_i$ (see Eq. (6.8)) also become uncoupled:

$$\widetilde{J}_e(h_e) = \widetilde{F_1}(h_e)\,\widetilde{P_e}(h_e,t) - \frac{1}{2}\frac{\partial}{\partial h_e}\left[D_{11}(h_e)\,\widetilde{P_e}(h_e,t)\right] \tag{6.36a}$$

$$\widetilde{J}_i(h_i) = \widetilde{F_2}(h_i)\,\widetilde{P_i}(h_i,t) - \frac{1}{2}\frac{\partial}{\partial h_i}\left[D_{22}(h_i)\,\widetilde{P_i}(h_i,t)\right] . \tag{6.36b}$$

These currents go to zero in the steady state. Setting $\widetilde{J}_e = \widetilde{J}_i = 0$ in Eq. (6.36), and replacing the time-varying probabilities $\widetilde{P_e}(h_i,t)$, $\widetilde{P_i}(h_i,t)$ with their steady values $\overline{P}_e(h_e)$, $\overline{P}_i(h_i)$, gives

$$2\widetilde{F_1}(h_e)\overline{P}_e(h_e) = \overline{P}_e(h_e)\frac{d}{dh_e}\Big[D_{11}(h_e)\Big] + D_{11}(h_e)\frac{d}{dh_e}\Big[\overline{P}_e(h_e)\Big] \qquad (6.37a)$$

$$2\widetilde{F_2}(h_i)\overline{P}_i(h_i) = \overline{P}_i(h_i)\frac{d}{dh_i}\Big[D_{22}(h_i)\Big] + D_{22}(h_i)\frac{d}{dh_i}\Big[\overline{P}_i(h_i)\Big]. \qquad (6.37b)$$

Rearranging for $\overline{P}_e$, $\overline{P}_i$ we have,

$$\frac{d\overline{P}_e(h_e)}{\overline{P}_e(h_e)} = \frac{1}{D_{11}(h_e)}\left[2\widetilde{F_1}(h_e) - \frac{d}{dh_e}\left[D_{11}(h_e)\right]\right] dh_e \qquad (6.38a)$$

$$\frac{d\overline{P}_i(h_i)}{\overline{P}_i(h_i)} = \frac{1}{D_{22}(h_i)}\left[2\widetilde{F_2}(h_i) - \frac{d}{dh_i}\left[D_{22}(h_i)\right]\right] dh_i \qquad (6.38b)$$

which integrates to

$$\log_e\left[\frac{\overline{P}_e(h_e)}{\overline{P}_e(-90)}\right] = \int_{-90}^{h_e}\frac{2\widetilde{F_1}(h_e')}{D_{11}(h_e')}\,dh_e' - \log_e\left[\frac{D_{11}(h_e)}{D_{11}(-90)}\right] \qquad (6.39a)$$

$$\log_e\left[\frac{\overline{P}_i(h_i)}{\overline{P}_i(-90)}\right] = \int_{-90}^{h_i}\frac{2\widetilde{F_2}(h_i')}{D_{22}(h_i')}\,dh_i' - \log_e\left[\frac{D_{22}(h_i)}{D_{22}(-90)}\right] \qquad (6.39b)$$

where the lower bound for both integrations has been set to −90 mV (potassium reversal potential), and the upper bound will be +45 mV (sodium reversal potential). Solving Eq. (6.39) for $\overline{P}_e$, $\overline{P}_i$ gives

$$\begin{aligned}\overline{P}_e(h_e) &= \mathcal{N}_1\exp\left[\int_{-90}^{h_e}\frac{2\widetilde{F_1}(h_e')}{D_{11}(h_e')}\,dh_e' - \log_e\left[D_{11}(h_e)\right]\right]\\ &\equiv \mathcal{N}_1\exp\left[-U_e(h_e)\right] \end{aligned}\qquad (6.40a)$$

$$\begin{aligned}\overline{P}_i(h_i) &= \mathcal{N}_2\exp\left[\int_{-90}^{h_i}\frac{2\widetilde{F_2}(h_i')}{D_{22}(h_i')}\,dh_i' - \log_e\left[D_{22}(h_i)\right]\right]\\ &\equiv \mathcal{N}_2\exp\left[-U_i(h_i)\right] \end{aligned}\qquad (6.40b)$$

where the $\mathcal{N}_1$ and $\mathcal{N}_2$ are constants which normalize their respective probability distributions to unit area:

$$\int_{-90}^{+45}\overline{P}_e(h_e)\,dh_e = \int_{-90}^{+45}\overline{P}_i(h_i)\,dh_i = 1. \qquad (6.41)$$

Equations (6.40) constitute the steady-state probability distributions for the decoupled macrocolumn which shortly we will evaluate numerically. First, though, we wish to focus on the argument of the exponential terms which define the excitatory and inhibitory *potential functions* U_e and U_i:

$$U_e(h_e) = \log_e\left[D_{11}(h_e)\right] - \int_{-90}^{h_e}\frac{2\widetilde{F_1}(h_e')}{D_{11}(h_e')}\,dh_e' \qquad (6.42a)$$

$$U_i(h_i) = \log_e\left[D_{22}(h_i)\right] - \int_{-90}^{h_i}\frac{2\widetilde{F_2}(h_i')}{D_{22}(h_i')}\,dh_i'. \qquad (6.42b)$$

The potential functions serve as statistical mechanics building blocks from which expressions for macrocolumn free energy, entropy, and "heat capacity" can be derived.

6.6.1 The U Potential Functions

Equations (6.42) define the pseudocolumn potential functions U_e and U_i, so named because their negative gradient can be pictured as a generalized force. Thus we interpret $-dU_e/dh_e$ as a force that drives the excitatory neuron voltage, and similarly $-dU_i/dh_i$ as a force driving the inhibitory voltage. This abstract notion becomes more concrete when we evaluate Eq. (6.42) numerically[5] for several representative values of λ, the GABA anaesthetic parameter, then examine the resulting hills-and-valleys graphs displayed in Fig. 6.5.

Figure 6.5 which shows how the $U_{e,i}$ potential functions vary with soma voltage $h_{e,i}$. The points on these curves at which the gradient is zero are the "zero-force" or equilibrium coordinates. The stability or otherwise of a given equilibrium point is determined by the sign of the curvature in the region immediately bracketing the point. Thus if the equilibrium point lies at the bottom of a potential valley (positive curvature), any small deviations away from the local minimum will be opposed by a force acting to restore the equilibrium, making it stable. The converse is true for the equilibrium point at the top of a potential hill (region of negative curvature): a small perturbation away from the peak will produce a force tending to enhance the perturbation, so the equilibrium there will be unstable.

Figures 6.5(a–g) show graphs of $U_{e,i}$ as a function of $h_{e,i}$ for the seven representative values of λ shown in (h), the last panel of the figure. These seven slices provide a coarse sweep through regions III (seizure), region II (upper branch), and into region I (coma) of Fig. 3.4.

We observe that the extrema of the $U_{e,i}$ potential functions coincide with the equilibrium soma voltages highlighted by the vertical lines marked on Fig. 6.5(h).[6] For example, in Fig. 6.5(a), U_e exhibits a single valley minimum whose (λ, h_e) coordinate belongs to the upper-left "seizure" corner of the equilibrium soma trajectory in (h). This is consistent with the vertical slice through this coordinate (labelled "a" in Fig. 6.5(h)) cutting the h_e trajectory once only, implying that for $\lambda = 0.25$ only a single equilibrium state is possible. The potential function is a minimum here, so this state is stable.

In Fig. 6.5(b) for $\lambda = 0.50$, three well-defined extrema have developed (two unequal valleys separated by small hill), corresponding to three distinct steady-state solutions and therefore three intersections on the (b)-slice of Fig. 6.5(h). Only the two valley-point equilibria (upper branch at $h_e = -40$ mV, and lower branch at $h_e = -85$ mV) are stable, while the mid-branch equilibrium point defined by the potential-function peak (at $h_e = -73$ mV) which separates the two valleys is unstable. In principle, the macrocolumn could sit delicately balanced at the top of this hill, but given the slightest nudge, would "slide" off the hill to nestle into one of the adjacent valleys.

The relative depth of the two valleys changes as λ varies, indicating that the probability of occupation also changes with λ. For $\lambda < 1$, the upper (high-firing) branch is more likely;

---

[5] The fast quadrature algorithm I developed to evaluate the F/D integral is described in Appendix B. As it turns out, there is an equivalent algorithm, **trapz**, built into MATLAB, but I only became aware of its existence much later.

[6] Actually, this is not quite true. The extrema of the potential functions can only coincide with the equilibrium soma voltages in the particular case that the D diffusion terms are *constant functions* that are independent of the noise. However, if the diffusion functions are small compared to the F drift functions, as is the case here, then this shift in the stable states will be small. I am grateful to external examiner Dr Daniel Gillespie for pointing out this "slight swindle" in my analysis. [The noise dependence of the locations for the steady states of a univariate Markov process is discussed in Gillespie (1992, Secs. 3.5–3.9).]

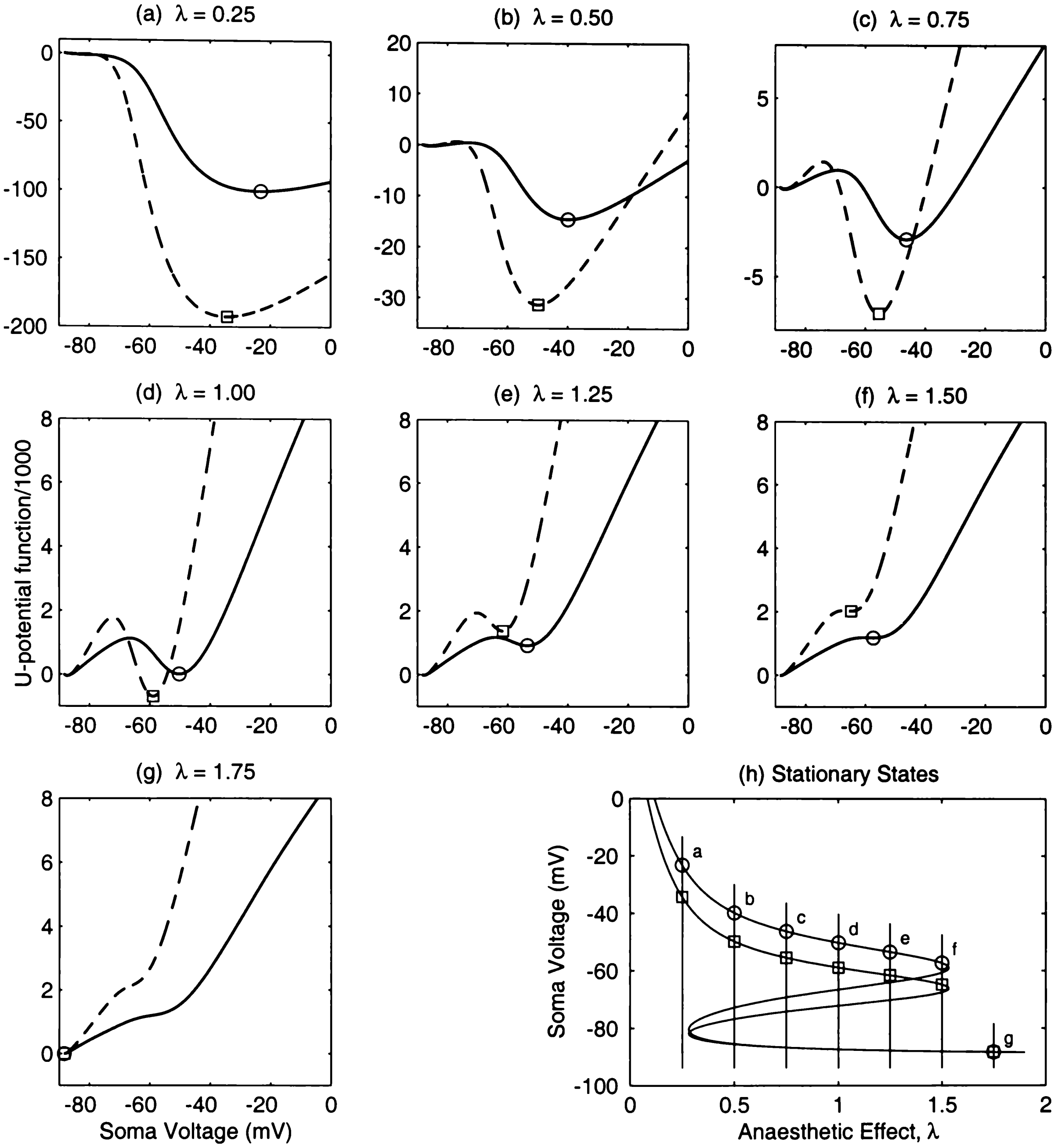

Figure 6.5: Hills-and-valleys potential function diagrams for the decoupled macrocolumn. (a)–(g) $U_{e,i}$ potential functions for seven representative values of λ. Solid curve: U_e; dashed curve: U_i. (h) Copy of Fig. 3.4 showing the seven vertical slices through the stationary-state trajectory which were used to evaluate the displayed U-functions. Circles: h_e; squares: h_i. (b)–(f) show two valleys separated by a hill; the valleys belong to the stable upper (high-firing) and lower (low-firing) branches of the trajectory curve, while the hill belongs to the unstable mid-branch. Each of the labelled points in (h) maps to a valley point (local minimum) in the correspondingly labelled figure. Note that for $\lambda = 1$, the two valleys are approximately symmetric. The cortical state "rides" the upper-branch valley as the U-curve is distorted by the anaesthetic, until the cortical state is "tipped out" into unconsciousness in (g).

while for $\lambda > 1$ the lower (low-firing) branch is favoured. For $\lambda \approx 1$, both stable-branch values for h_e are equally likely; and if there are perturbations of sufficient magnitude to overcome the potential hill, then there is the possibility that the macrocolumn could repeatedly switch between the upper- and lower-branch stable states.

In statistical thermodynamics, it is the Helmholtz free energy V which is minimized when the system is in equilibrium. The fact that our $U_{e,i}$ potential functions have minima which correctly locate the stable equilibria leads us to suggest that these potential functions behave like Helmholtz free energy functions for the macrocolumn. We expand on this idea later in this chapter. Before doing so, we will examine the Eq. (6.40) stationary probability distributions obtained from the negative exponential of the $U_{e,i}$ potential functions.

6.6.2 The $\overline{P}$ Stationary PDFs

From Eq. (6.40) I calculated $\overline{P}_e$ and $\overline{P}_i$, the stationary probability distributions for the decoupled excitatory and inhibitory macrocolumn populations. The results appear in Fig. 6.6.

In the hills-and-valleys potential graphs of Fig. 6.5 we could picture the macrocolumn as a "particle" that would slide to the bottom of valley to minimize its potential energy. The PDF diagrams flip this orographic notion on its head: now it is the *probability peaks* that show where, in soma voltage space, the macrocolumn particle is most likely to be found, with each probability peak in Fig. 6.6 mapping precisely to a potential trough in Fig. 6.5.

For $\lambda = 0.25$, the depolarized upper branch at $h_e \approx -22$ mV is strongly favoured; this is point (a) on Fig. 6.6(h). As λ increases, this peak migrates to the left and lowers in height as a new probability peak close to -90 mV on the lower branch begins to emerge, with the depolarized (upper branch) and hyperpolarized (lower branch) peaks being of approximately equal height at $\lambda = 1.0$ (point (c)). By $\lambda = 1.5$ (f) the hyperpolarized peak is stronger, and by $\lambda = 1.75$ (g) the depolarized option has disappeared altogether.

Although the soma voltage bounds for Eq. (6.41) were set by Eq. (6.7) at

$$-90 \text{ mV} < h_{e,i} < +45 \text{ mV}, \tag{6.43}$$

I chose to truncate the PDF graphs in Fig. 6.6 to an upper bound of $h_{e,i} = +20$ mV for display purposes since no interesting probability "events" were apparent in the fully-depolarized $\lambda \rightarrow 0$ regime (i.e., top-left corner of Fig. 3.4). The PDF graphs are normalized to unity on the interval $[-90, +45]$ mV, and are abruptly zero outside this interval.

6.6.3 The V Free-Energy Functions

We wish to construct a statistical mechanics description of the anaesthetic-induced cortical phase transition. We proceed by deriving a (phenomenological) *free energy* function V. The "free energy" concept is very useful in statistical mechanics as its negative rate-change with temperature, at constant internal energy E, gives entropy:

$$S = -\partial V / \partial T\big|_E \,. \tag{6.44}$$

But this step will require us to identify carefully exactly what is meant by the "temperature" of the cerebral macrocolumn; by macrocolumn "temperature" we do *not* mean the physical temperature measured with a thermometer. In the next section we present a line of argument, based on the idea of a canonical ensemble, to enable identification of a plausible cortical temperature analogue.

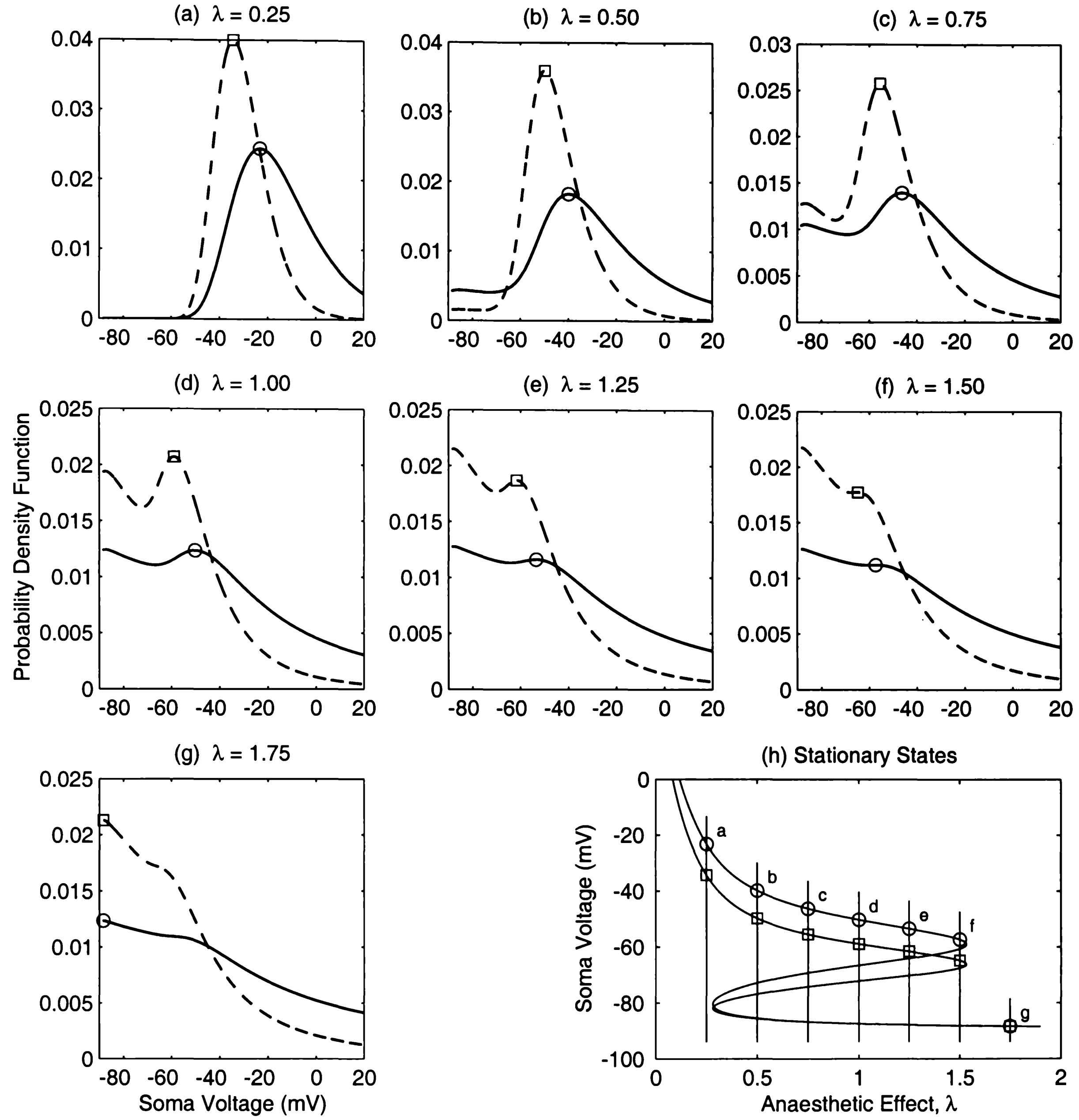

Figure 6.6: (a)–(g) Stationary probability distributions $\overline{P}_{e,i}$ for the decoupled macrocolumn at the seven representative values of λ shown in (h). Solid curve: $\overline{P}_e$; dashed curve: $\overline{P}_i$. These probability pictures correspond to the potential functions of Fig. 6.5: the highest probability peaks here map to the deepest (most stable) potential wells. The evolution of twin probability peaks as λ increases corresponds to the appearance of double potential wells, indicating that the macrocolumn can exist in either of two stable states. The boundaries at -90 mV (left edge) and at $+45$ mV (not shown) are reflecting, so the PDFs are zero beyond these bounds.

The construction of our statistical mechanics theory is motivated by the obvious similarities between the form of the $U_{e,i}$ potential functions of Fig. 6.5 and the potential-well description of phase transitions common in quantum optics (Gibbs, 1985). For a quantum optics system described in terms of a parameter x, Lugiato and Bonifacio (1978) write the stationary probability distribution $\overline{P}(x)$ in the form,

$$\overline{P}_{\mathrm{LB}}(x) = \mathcal{N} \exp\left[-V(x)/k_0\right] \qquad \text{(Lugiato \& Bonifacio)} \qquad (6.45)$$

Table 6.1: A mapping between thermodynamics theory and the macrocolumn model of the cortex.

Thermodynamic Space		Cortical Space	
Temperature	T	Excitability	Θ
Internal energy	E	Internal energy of macrocolumn	$E_{e,i}$
Helmholtz free energy	$V = E - TS$	Cortical free energy	$V_{e,i} = E_{e,i} - \Theta\, S_{e,i}$
Entropy	$S = -(\partial V/\partial T)\vert_E$	Cortical entropy	$S_{e,i} = -(\partial V_{e,i}/\partial \Theta)\vert_E$
Heat capacity	$C = T\,(\partial S/\partial T)\vert_E$	Cortical "heat" capacity	$C_{e,i} = \Theta\,(\partial S_{e,i}/\partial \Theta)\vert_E$
Latent heat	$T\,\Delta S$	Cortical latent "heat"	$\Theta\,\Delta S_{e,i}$

where $\mathcal{N}$ is a normalization constant, and k is a constant introduced to ensure dimensional consistency. The quantity $V(x)$ plays the role of a "generalized free energy" (Lugiato and Bonifacio, 1978; Graham, 1973). Haken (1978) follows a similar approach in his Fokker–Planck treatment of an analogous phase transition, but in his exponential term the denominator is the product of Boltzmann's constant k_B and a parameter he identifies as an equivalent temperature T,

$$\overline{P}_{\rm H}(x) = \mathcal{N} \exp\left[-V(x)/k_B T\right] \qquad \text{(Haken)} \qquad (6.46)$$

which is very suggestive of the Boltzmann distribution. The assertion in Eqs (6.45, 6.46) that $V(x)$ is a free energy is justified phenomenologically on the grounds that the extrema of V locate the equilibrium states.

We postulate that there exists a formal equivalence between (one or other of) the probability distribution functions of Eqs (6.45) or (6.46) and the cortical PDFs of Eq. (6.40), and assume that the cortical phase transition can be described in a space which is dual to that of statistical thermodynamics. The proposed dual-space mapping is set out in Table 6.1;[7] the various elements of this table will be discussed at relevant points later in this chapter.

Equating the cortical potential function U from Eq. (6.40) first with the exponential argument of Eq. (6.46) (Haken form), then with the exponential argument of Eq. (6.45) (Lugiato and Bonifacio form), we obtain two alternative thermodynamic ↔ cortical mappings for the free energy of the cortex:

$$U(x) \equiv V(x)/k_B T \implies V_{\rm H}(h_{e,i}) = k_B\, \Theta\, U(h_{e,i}) \qquad \text{(Haken)} \qquad (6.47a)$$

$$U(x) \equiv V(x)/k \implies V_{\rm LB}(h_{e,i}) = k_0\, U(h_{e,i}) \qquad \text{(Lugiato \& Bonifacio)} \qquad (6.47b)$$

From Table 6.1 and Eqs (6.47, it will be apparent that for the cortical system we have introduced the symbol Θ, which we define to be *cortical excitability*, and which, as we show using plausibility arguments developed later in the chapter, plays a role in the cortex analogous to that of temperature T in thermodynamic systems. We will show that excitability Θ is inversely related to anaesthetic effect λ. This (λ, Θ) mapping provides the crucial link between the cortical general-anaesthetic phase transition and the world of thermodynamic phase transitions, and allows us to apply the language and concepts of thermodynamics (e.g., entropy, heat capacity) to the cortical transition.

---

[7] These correspondences were crafted by M. Steyn-Ross, and first appeared in Steyn-Ross *et al.* (2001a). I selected the name "excitability" to convey the notion of an inverse-anaesthetic effect on the cortex, with symbol Θ after the nomenclature used in meteorology for the potential temperature of a parcel of air.

6.6.4 Relating Anaesthetic Effect to Cortical Excitability

In our model, for $\lambda \gtrsim 1.53$ the macrocolumn must reside on the low-firing quiescent branch. As anaesthetic concentration is increased, the duration of the inhibitory post-synaptic potential (IPSP) is prolonged, producing greater inhibition and reduced neuronal firing. Increased anaesthetic depth λ corresponds to reduced cortical excitability Θ, so λ and Θ are inversely related. In the $\lambda \to \infty$ limiting case of extreme anaesthesia, there can be no activity in the presence of an infinitely-prolonged IPSP, so $\Theta = 0$ in this extreme frozen limit. This point is our absolute zero "temperature" at which all neurons are fully hyperpolarized.

For the emergence trajectory, Θ will increase as the hyperpolarization ordering diminishes with reductions in λ, and more neurons become depolarized (able to fire). With sufficient reduction in λ, the macrocolumn will eventually reach the seizure extremum (top-left corner of Fig. 3.4) at which point all neurons are fully depolarized and firing maximally, since $\lambda = 0$ means that the IPSP has zero duration so there is no inhibitory restraint on macrocolumn firing activity. At this seizure extremum, cortical excitability will have its maximum value Θ_{max}.

From a biological energy resources perspective, it is reasonable to argue that Θ_{max} will have a large but finite value, while from a mathematical modelling perspective one might argue that $\Theta_{\text{max}} \to \infty$ as $\lambda \to 0$ and then avoid the finite resources problem by asserting that $\lambda = 0$ is a model abstraction which will never occur in practice. In either case, we seek a mapping whose model predictions for entropy change are not unduly sensitive to the finiteness or otherwise of Θ_{max}.

The mathematical equation relating Θ to λ is unknown, but based on the foregoing discussion a plausible mapping would have all of the following properties:

(i) $\Theta \to 0$ as $\lambda \to \infty$ (deep coma);
(ii) Θ is a monotonic decreasing function of λ;
(iii) $\Theta \to \Theta_{\text{max}}$ as $\lambda \to 0$ (extreme seizure), where Θ_{max} may be finite or infinite.

Two of the simplest inverse relationships which satisfy these criteria are

$$\Theta_{\text{I}} = c_0/\lambda^{c_1}, \quad \text{and} \tag{6.48a}$$

$$\Theta_{\text{II}} = \Theta_{\text{max}} \exp(-c_0\,\lambda^{c_1}) \tag{6.48b}$$

where c_0 and c_1 are positive constants. Both functions decay smoothly to zero as $\lambda \to \infty$; for the $\lambda \to 0$ seizure extreme, $\Theta_{\text{I}} \to \infty$ while $\Theta_{\text{II}} \to \Theta_{\text{max}}$, a finite maximum value. For definiteness and simplicity, we will set $c_0 = 1$, $\Theta_{\text{max}} = 1$, and only the c_1 exponent will be altered. Fig. 6.7 shows sample Θ-vs-λ mappings for $c_1 = 0.2$ (curves 1 and 3), $c_1 = 3$ (curve 2), and $c_1 = 1.0$ (curve 4). Curves 1 and 2 correspond to infinite activity at $\lambda = 0$ (i.e., Θ_{I}-mapping), while curves 3 and 4 have finite activity $\Theta = \Theta_{\text{max}}$ at $\lambda = 0$ (i.e., Θ_{II}-mapping).

6.6.5 Cortical Entropy

The entropy definition of Eq. (6.6.3) is now rewritten as the cortical excitability gradient of the free energy,

$$S = -\partial V/\partial \Theta\,. \tag{6.49}$$

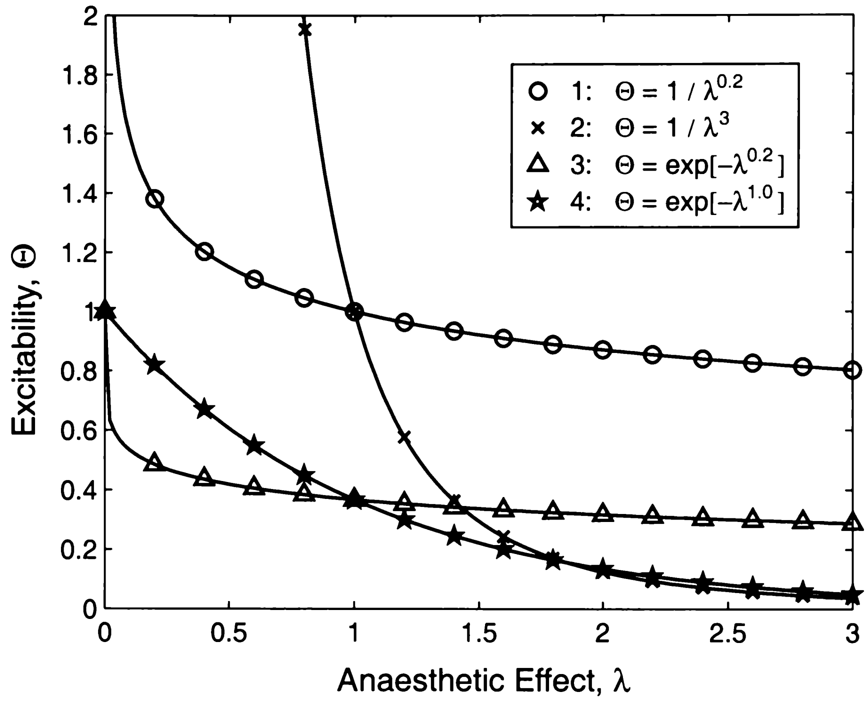

Figure 6.7: Plausible excitability Θ versus anaesthetic effect λ mappings. Curves 1 and 2 have unbounded excitability ("temperature") as $\lambda \rightarrow 0$; curves 3 and 4 have finite excitability at $\lambda = 0$.

We have two candidate free energy formulations (Haken: Eq. (6.47a), and Lugiato and Bonifacio: Eq. (6.47b)), and two excitability–effect mappings (Eqs (6.48a, 6.48b)), giving a total of four possible entropy expressions,

$$S_{\text{I, Haken}} = k_B \left(\frac{\lambda}{c_1} \frac{\partial U}{\partial \lambda} - U \right) \tag{6.50a}$$

$$S_{\text{II, Haken}} = k_B \left(\frac{\lambda^{1-c_1}}{c_0 c_1} \frac{\partial U}{\partial \lambda} - U \right) \tag{6.50b}$$

$$S_{\text{I, L\&B}} = k_0 \frac{\lambda^{1+c_1}}{c_0 c_1} \frac{\partial U}{\partial \lambda} \tag{6.50c}$$

$$S_{\text{II, L\&B}} = k_0 \frac{\lambda^{1-c_1}}{c_0 c_1 \Theta_{\max}} \exp\left[c_0 \lambda^{c_1}\right] \frac{\partial U}{\partial \lambda} \tag{6.50d}$$

where, for example, Eq. (6.50c) was derived by applying the Maxwell relation $S = -\partial V / \partial \Theta$ to the Lugiato and Bonifacio potential form $V = kU$ and using the chain rule:

$$S_{\text{I, L\&B}} = -\frac{\partial V}{\partial \Theta_{\text{I}}} = -k \frac{\partial U}{\partial \Theta_{\text{I}}} = -k \frac{\partial U}{\partial \lambda} \frac{\partial \lambda}{\partial \Theta_{\text{I}}} = -k \frac{\partial U}{\partial \lambda} \bigg/ \frac{\partial \Theta_{\text{I}}}{\partial \lambda} \tag{6.51}$$

with the Θ_{I}-mapping giving the partial-derivative result

$$\frac{\partial \Theta_{\text{I}}}{\partial \lambda} = -c_0 c_1 / \lambda^{1+c_1} . \tag{6.52}$$

Graphs showing the λ-dependence of the Haken and LB entropies appear in Fig. 6.8. All three graphs assume the type-I "temperature" mapping $\Theta = 1/\lambda^{c_1}$ (the type-II mappings give qualitatively similar results, so are not shown here), with $c_1 = 0.2$ for graphs (a) and (b), and

$c_1 = 3$ for graph (c). Note that for the smaller value of c_1, the Haken and LB entropy graphs are very similar, showing a maximum entropy in the top-left corner (seizure), and minimum entropy in the bottom-right corner (coma). The upper (active) and lower (quiescent) branches are separated by step discontinuities at A_3 (induction point), and at Q_1 (emergence point).

Inspection of Eqs (6.50a–6.50c) shows that the Haken and LB forms will give entropy curves which become more alike for small c_1. This is because the potential gradient $\partial U/\partial\lambda$, which is scaled by $1/c_1$, will tend to dominate the U-potential term. For large c_1, the entropy curves become dissimilar. However, the presence of the subtractive U term in the Haken form places an upper bound on the maximum permissible value for c_1: we found that for $c_1 \gtrsim 0.4$ the Haken entropy becomes negative on the upper branch when $\lambda \gtrsim 1.4$. Since we require entropy to be always positive (reaching zero only in the limit of perfect order), then the range of permissible power-law exponents for the Θ-vs-λ mapping is limited to $0 < c_1 \lesssim 0.4$ for Haken entropy.

The absence of the U subtraction in the LB form means that in principle there is no upper bound for the c_1 exponent in the LB entropy expression. We have selected $c_1 = 3$ as a representative "large" exponent value since this produces an LB entropy curve (Fig. 6.8(c)) which has strong qualitative similarity to the theoretical *spectral* entropy curves presented later in Chapter 8.

Compared with the small-c_1 entropy graphs of Figs 6.8(a) and (b), the large-c_1 graph (c) shows a significantly different profile: the position of maximum entropy has shifted from the top-left seizure corner to a position on the upper branch in the vicinity of $\lambda = 1$. This feature suggests that the normal conscious state is associated with maximum entropy, and that both the coma and seizure extremes have reduced entropy (increased order).

While this is an intuitively attractive result, the supporting evidence is sparse at present. The work of Viertiö-Oja and colleagues Viertiö-Oja *et al.* (2000) shows that EEG *spectral* entropy diminishes during anaesthetic induction (discussed later in Chapter 8). Spectral entropy also appears to diminish for the cortical transition into epileptic seizure (Quiroga *et al.*, 2000, Figs 2, 3). These early findings indicate that the large-c_1 LB entropy graph of Fig. 6.8(c) is at least plausible, assuming that there exists a direct relationship between thermodynamic entropy (availability of cortical microstates) and spectral entropy (availability of electrical vibration modes).

We note that for both Haken and LB forms there is an abrupt and discontinuous negative change in the macrocolumn entropy at the A_3 point of induction. A step change in entropy, ΔS, is characteristic of a first-order thermodynamic phase transition, and implies the existence of an analogous "latent heat," $\Theta\Delta S$, for the cortex. The detection of this latent effect should provide a direct clinical means by which we can determine the amount of energy which must be removed from each macrocolumn in order to transform the cortex from a depolarized, disordered, conscious state to a hyperpolarized, ordered, hypnotic state.

6.6.6 Cortical "Heat Capacity" and "Latent Heat"

For a thermodynamic system consisting of a sample and its environment, the *heat capacity* of the sample is the energy required to raise the temperature of the sample by one kelvin. This is a "heating" experiment in which energy flows inwards, from the environment to the sample.

(a) Haken Entropy for $\Theta = 1/\lambda^{0.2}$

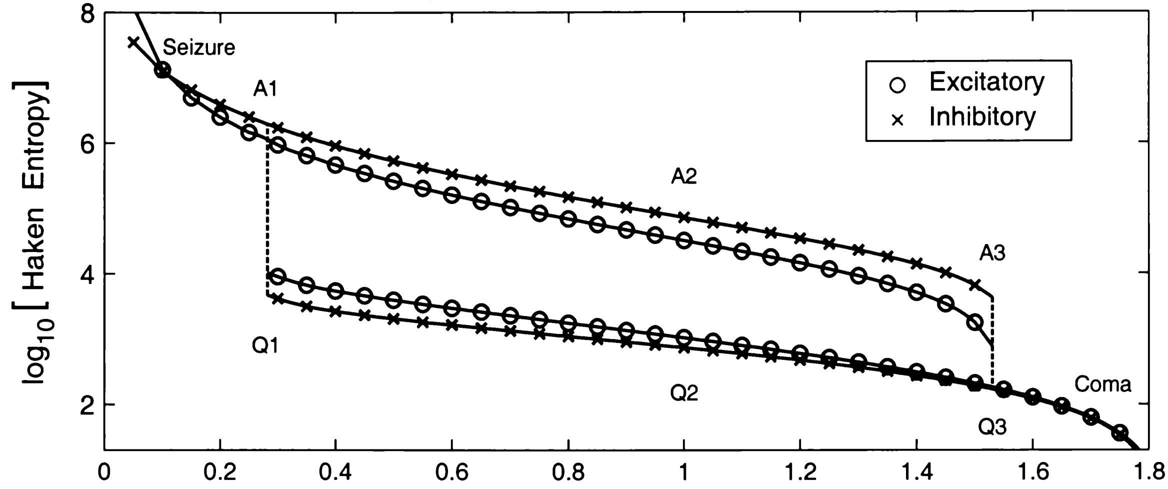

(b) L&B Entropy for $\Theta = 1/\lambda^{0.2}$

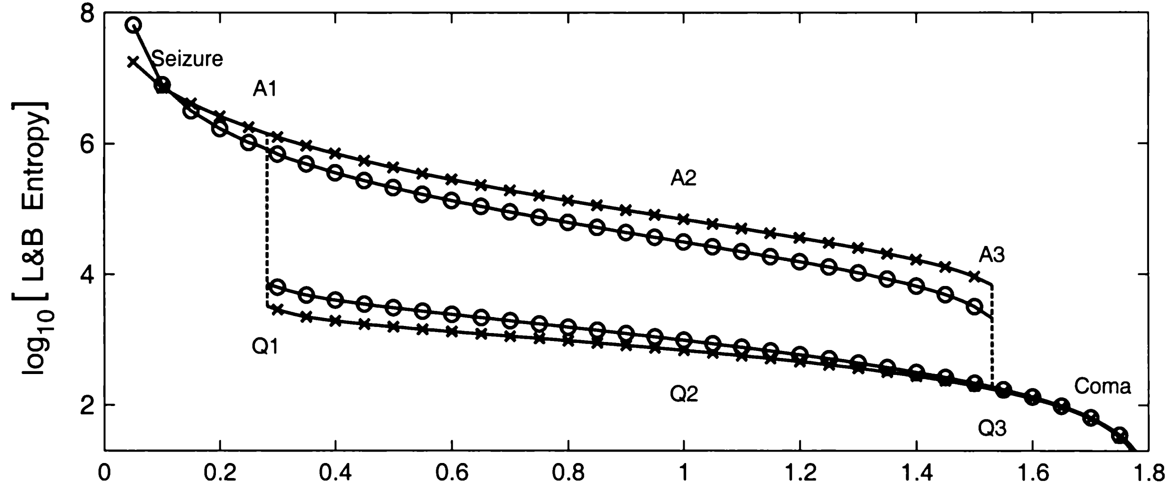

(c) L&B Entropy for $\Theta = 1/\lambda^{3}$

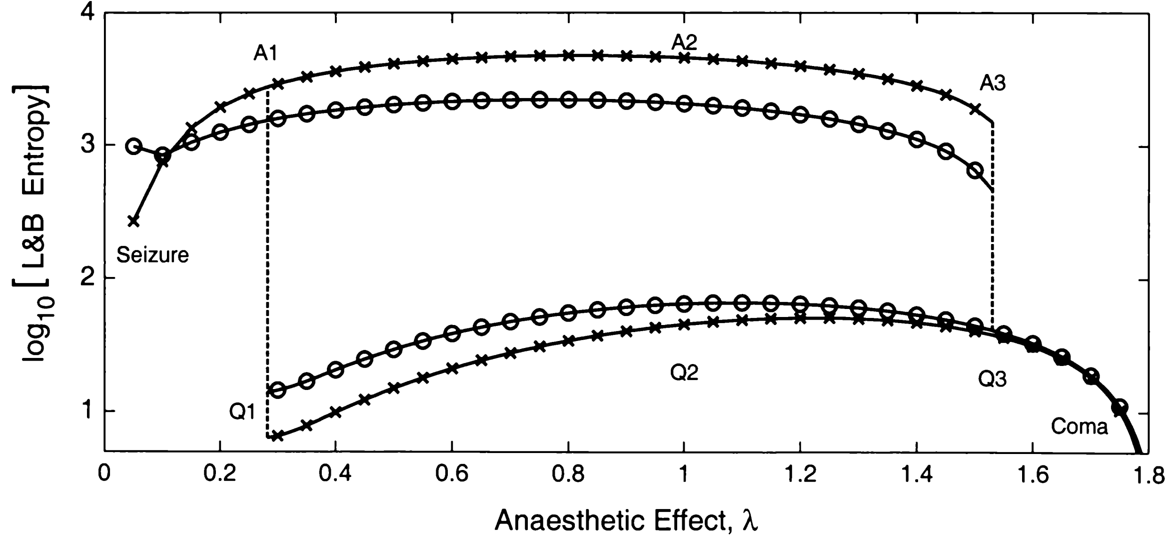

Figure 6.8: Theoretical cortical entropy curves for the excitatory and inhibitory neural populations of the macrocolumn as a function of anaesthetic effect. Assumed excitability ("temperature") mapping is $\Theta = 1/\lambda^{c_1}$. (a) Haken form, $c_1 = 0.2$. (b) Lugiato and Bonifacio form, $c_1 = 0.2$. (c) Lugiato and Bonifacio form, $c_1 = 3$.

Equivalently, heat capacity can be determined in a "cooling" experiment which measures the energy required to lower the temperature of the sample by 1 K; in this case the energy flow is outwards, from the sample to its environment. For the cortex, we seek to design an experiment which measures the outflow of energy from the cortex as it is "cooled" (its excitability reduced) under the influence of a general anaesthetic.

The heat capacity depends on the *phase* or bonding structure of the sample. If the sample changes phase during the cooling experiment, then we should expect the change of phase to show up as an anomalous peak in the heat capacity. For a ferromagnetic substance cooled through its Curie temperature, the transition from the disordered, non-magnetic state to the ordered, magnetically-aligned state is smooth and continuous, and the transition is classified as second-order. In contrast, the freezing of water and the cooling of a ferroelectric material through its Curie point are classified as first-order transitions, since both exhibit an abrupt and discontinuous change in order, quantifiable as a negative step change ΔS in entropy as the sample transforms from its liquid water (c.f. non-polarized ferroelectric) disordered state to its crystalline (c.f. polarized ferroelectric) ordered state. This discontinuous change in entropy is detectable as a sudden release of latent energy equal to $|T_c \Delta S|$, where T_c is the temperature at transition.

Our model of the cortex predicts that as anaesthetic effect is increased, the soma voltage h_e and associated free energy V will change abruptly at a critical value for anaesthetic effect λ. If the unconscious state is the more ordered, then the entropy change for the transition from the disordered, conscious state to the well-ordered, unconscious state will be negative, and latent energy should be *released* at the instant of transition. However, because of the uncertainty introduced by the presence of subcortical noise, we would not expect all 10^5 macrocolumns of the cortex to jump simultaneously (the larger the noise input into a given macrocolumn, the larger the probability that it will jump "early"). Instead, the downward jumps into unconsciousness will occur over the noise-broadened range $\lambda_1 < \lambda_{\text{jump}} < \lambda_{A_3}$, where $\lambda_1 > 1.0$ and $\lambda_{A_3} = 1.53$ (see Fig. 3.4). For small subcortical noise, $\lambda_1 \to 1.53$ and the transition range will be quite narrow; for large subcortical noise, the transition range will be comparatively broad.

What are the requirements for the definitive thermodynamics experiment applied to the anaesthetic-damped cortex? Essentially we need to know how the energy uptake of the cortex varies as a function of anaesthetic concentration. Ideally there would be simultaneous recordings of the EEG waveforms in order to correlate cortical electrical activity with cortical energy consumption as the brain moves into comatose unconsciousness.

Recently J. Sleigh located an historical paper by Stullken Jr. *et al.* (1977) that investigated the changes in cerebral metabolic rate induced by general anaesthetic agents. In the next section we examine the Stullken paper and compare its clinical findings against our macrocolumn model predictions.

6.7 The Stullken Experiment

The "cortical cooling" experiment we seek was performed over 20 years ago by Stullken Jr., Milde, Michenfelder, and Tinker (1977), albeit for purposes quite different from ours. Stullken and colleagues were investigating the response in dogs of the cerebral metabolic rate for oxygen

($\mathrm{CMR}_{\mathrm{O}_2}$) to increasing concentrations of four different anaesthetic agents: halothane, enflurane, isoflurane, and thiopental.

Cerebral oxygen consumption was determined by measuring the change in blood oxygen concentration for blood entering and leaving the cerebral hemispheres, then multiplying this difference by the cerebral blood flow rate. The shapes of the anaesthetic dose–response curves for $\mathrm{CMR}_{\mathrm{O}_2}$ were examined by multiple measurements made at small, progressive concentration increments. For example, the six dogs in the halothane group received increasing concentrations of halothane such that the measured end-tidal (end-of-breath) concentration increased at a rate of 0.05 per cent (of atmospheric pressure) every five minutes to 1.1 per cent, and thereafter, at increments of 0.10 per cent every five minutes. The EEG was continuously recorded and changes in EEG patterns from "awake" to "anaesthetic" were correlated with changes in anaesthetic concentration and $\mathrm{CMR}_{\mathrm{O}_2}$. The points of EEG change for "awake" to transitional "shifting" patterns, and from "shifting" to "anaesthetic" patterns were determined by inspection of rhythm, amplitude, and frequency. High-frequency, low-amplitude activity (15 ± 5 Hz, 50 ± 40 μV) was classified as an "awake" pattern, while onset of persistent lower-frequency and higher-amplitude activity (10 ± 8 Hz, 300 ± 150 μV) was classified as an "anaesthetic" pattern. "Shifting" patterns showed alternation between "awake" and "anaesthetic" characteristics.

Prior to the Stullken *et al.* experiment, it had been assumed that there was a *linear* negative-slope relationship between cerebral oxygen consumption ($\mathrm{CMR}_{\mathrm{O}_2}$) and anaesthetic concentration, but these earlier inferences of linear dose–response had been based on a small number of isolated measurements. In contrast, Stullken's careful and detailed study revealed that $\mathrm{CMR}_{\mathrm{O}_2}$ dose–response curves are nonlinear at anaesthetic concentrations less than 1 MAC (minimum anaesthetic concentration at which half the subjects are unresponsive to surgical incision; the MAC is a standard measure of anaesthetic potency). For all four anaesthetic agents studied (three inhalational, one intravenous), Stullken found that $\mathrm{CMR}_{\mathrm{O}_2}$ decreased precipitously until a stable "anaesthetic" EEG pattern was observed; thereafter $\mathrm{CMR}_{\mathrm{O}_2}$ decreased only slowly. These results demonstrate that the change in EEG pattern from "awake" to "anaesthetic" is accompanied by an abrupt metabolic depression, and the researchers speculated that these events coincide with the onset of functional depression (loss of conscious awareness). The Stullken graph for the variation of metabolic rate with halothane concentration is shown in Fig. 6.9a.

It is pertinent to emphasize an important distinction between a "standard" thermodynamics cooling experiment designed to determine the heat capacity of a closed, thermally-insulated physical sample, and the biological experiment performed by Stullken and coworkers. In the latter case, the "sample" is the living and metabolizing cerebral cortex of a dog which is necessarily an energy-dissipative, open system. In order to maintain an equilibrium state of the cortex, there must be a continuous flux of energy (oxygen plus nutrients) from the arterial blood to the cortex, and then from the cortex to the venous blood (metabolic waste products). As discussed earlier in Section 6.1, this molecular metabolic activity is occurring at spatial and temporal scales several orders of magnitude below that of our model, and serve to maintain the macrocolumn in its (local) equilibrium state. We picture the biological system as analogous to a non-ideal "lossy" physical system.

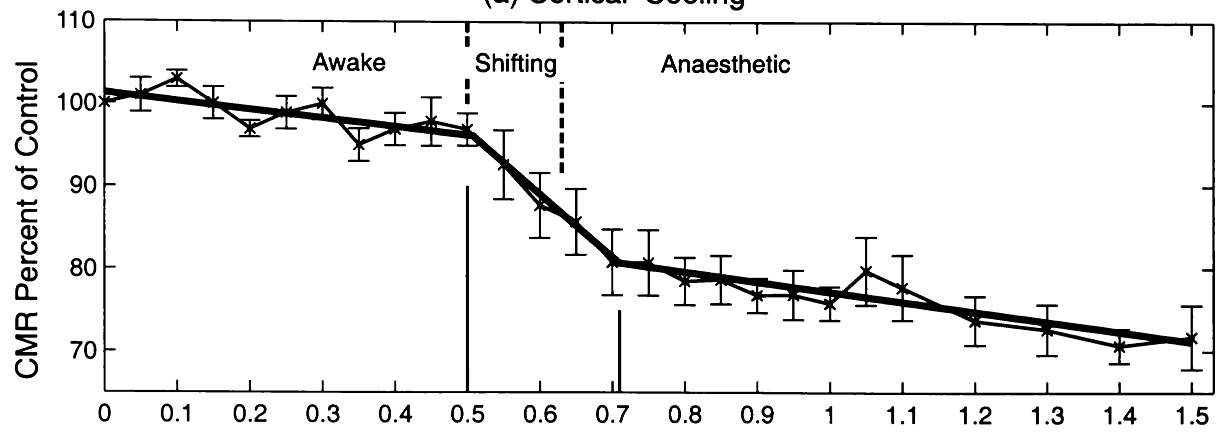

(a) Cortical Cooling

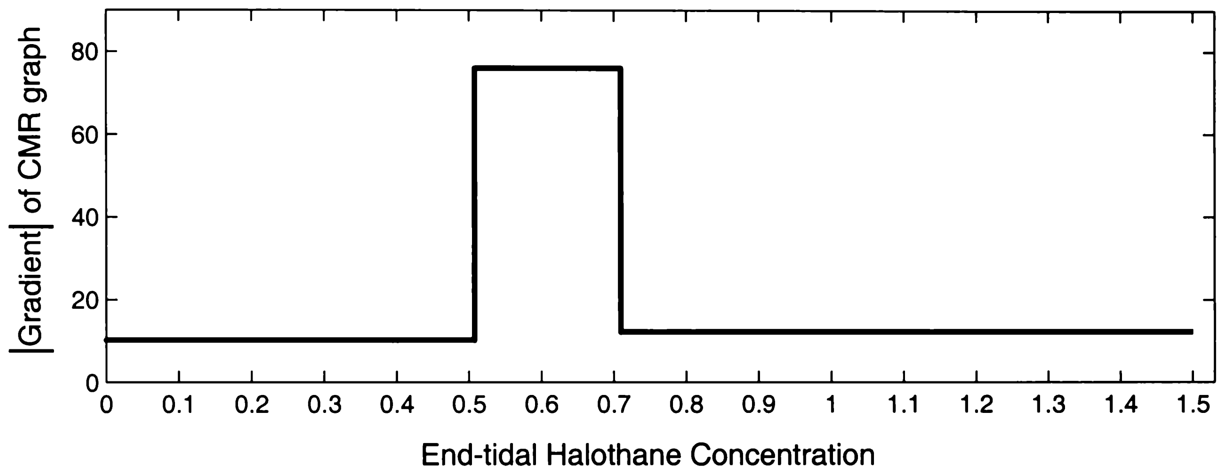

(b) Latent Heat Release

Figure 6.9: Effect of general anaesthetic (halothane) on the cerebral metabolic rate (CMR via oxygen consumption) for dog, as reported by Stullken Jr. *et al.* (1977, Fig. 3) (a) CMR (as per cent of control) is plotted versus end-of-exhalation halothane concentration (as per cent of atmospheric pressure). Regression lines for changes in metabolic rate are drawn for each EEG-determined region. (b) Here I have computed the negative slope of the regression lines of (a) to give the rate of decrease of metabolic rate with increasing anaesthetic. The abrupt change in metabolic sensitivity to anaesthetic during the transition stage is very suggestive of a "latent heat" effect signaling a change of phase to the more ordered state.

6.7.1 Biological "Heat Capacity"

A reasonable working definition for "heat capacity" of a dissipative biological system such as the cortex might be

> "the amount by which the metabolic rate must change in order to change, by one unit, the state of excitability of the cortex,"

where "excitability" is an inverse measure of anaesthetic effect (see Section 6.6.4). This definition implies that it is the rate of energy delivery which determines the state of the neuron, whereas in fact the causality is the other way around: it is the state of the cell, as set by the anaesthetic concentration, which determines the metabolic requirement and hence the bloodflow. With this caveat in mind, we will apply this working definition to the Stullken experiment.

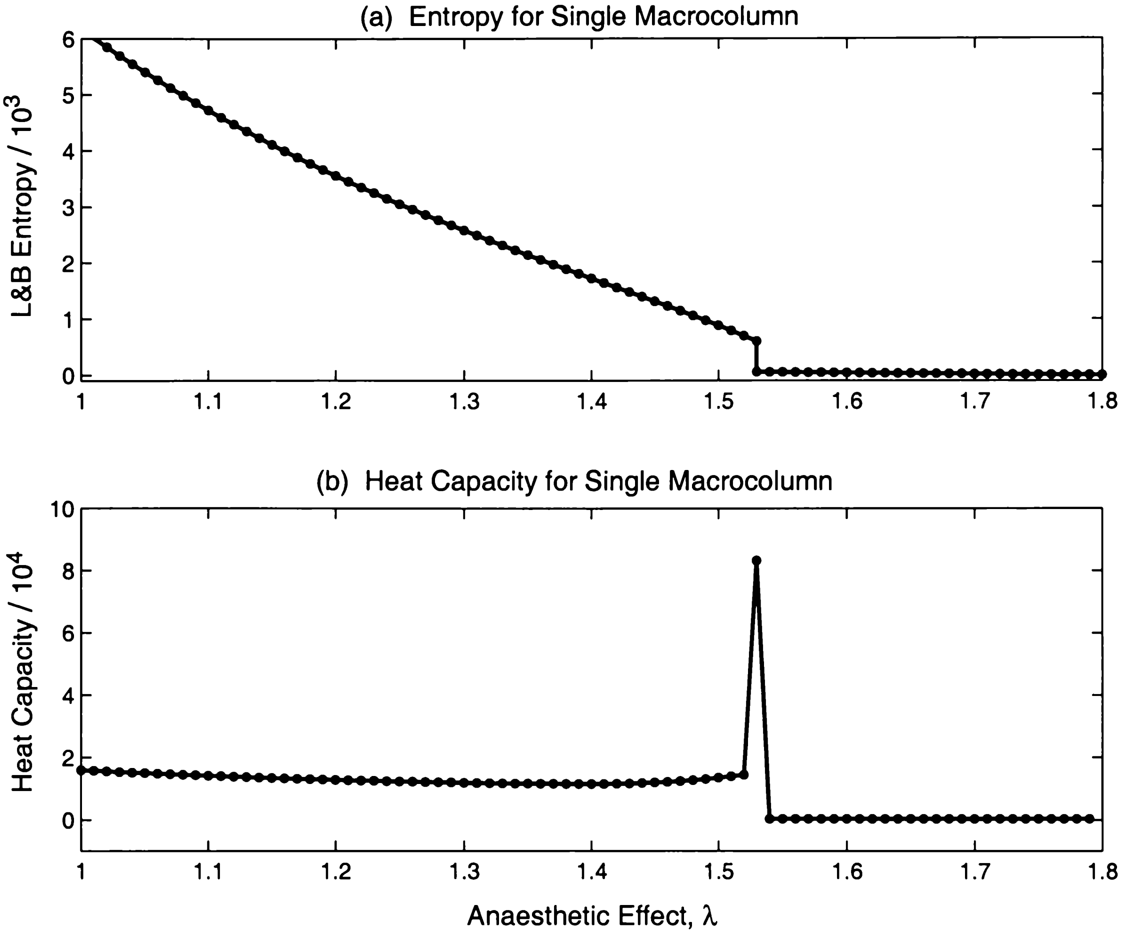

Figure 6.10: Predicted variation in (a) entropy and (b) heat capacity for the excitatory neurons of a single macrocolumn during induction of anaesthesia. The entropy curve assumes a simple inverse mapping between excitability ("temperature") and anaesthetic effect: $\Theta = 1/\lambda$, and follows the Lugiato and Bonifacio scheme for free energy (see Eqs 6.45, 6.50c). The heat capacity is computed from the derivative of the entropy curve, $C = -\lambda(\partial S/\partial\lambda)$. The negative step-discontinuity in entropy at $\lambda = 1.53$ produces a positive delta-function in the heat capacity which we approximate as a triangular spike of area $1.53|\Delta S|$ and half-width equal to the sampling resolution of λ.

The halothane results of the Fig. 6.9a graph show that the overall trend is for metabolic rate to diminish as anaesthetic depth increases. The gradient of this graph is negative, and its magnitude gives the percentage reduction in metabolic rate per unit increase in halothane concentration, or equivalently, per unit *decrease* in excitability (assuming an inverse relationship between halothane concentration and cortical excitability). Thus the slope magnitude can be interpreted as a cortical heat capacity; see Fig. 6.9b.

Unlike the "awake" and "anaesthetic" regions which have similar (gentle) slopes and therefore similar heat capacities, the intermediate "shifting" region has dramatically steeper slope. This is the heat capacity anomaly which signals the thermodynamic phase change from the high-firing, high-metabolic-rate upper branch to the low-firing, low-metabolic-rate quiescent branch. The area of the anomaly gives the average decrease in the rate of energy consumption ($\approx$14%) during transition. We may also interpret this area as a measure of the rate of latent energy release from the cortex arising from the loss of entropy (gain in order) as the cortex transits to its unconscious state. Thus, during transition, the metabolic requirements of the cortex are offset by the latent energy which becomes available to the cortex as it "crystallizes" into hyperpolarized order.

In order to compare the Stullken experimental results with the model predictions for a single macrocolumn, we will focus on the excitatory neuron population (inhibitory results are very similar), assuming the Lugiato and Bonifacio form for free energy, and taking a "temperature" mapping $\Theta = c_0/\lambda^{c_1}$, with $c_0 = c_1 = 1.0$. This gives the LB entropy trajectory for induction shown in Fig. 6.10a which lies between those shown in Fig. 6.8b ($c = 0.2$) and Fig. 6.8c ($c = 3$).

Applying the assumed temperature mapping to the definition for cortical "heat capacity" listed in Table 6.1, we obtain

$$C = \Theta \frac{\partial S}{\partial \Theta} = -\lambda \frac{\partial S}{\partial \lambda}. \tag{6.53}$$

The resulting single-macrocolumn heat capacity is shown in Fig. 6.10b. As expected, the step decrease in entropy produces a heat capacity anomaly corresponding the release of latent "heat" as the model "freezes" into its hyperpolarized state. Only a single latent-heat spike is shown. This narrow peak would be expected to broaden if the contributions of all 10^5 macrocolumns participating in the $\mathrm{CMR}_{\mathrm{O}_2}$ bloodflow experiment could be summed, taking into account the expected variability for the various biological parameters (threshold voltage, input spike rates, noise amplitudes, etc). This qualitative agreement between our preliminary theory and clinical experiment is very encouraging.

6.8 Chapter Summary

The cerebral cortex is an open, dissipative, biological system whose far-from-equilibrium steady state is maintained by a continuous flux of energy. However, because for the two-variable adiabatic macrocolumn we have an effective equation of state (Fig. 3.4) linking the population-average excitatory and inhibitory soma voltages, it is possible to treat each (λ, h_e^0, h_i^0) steady state as if it were a *local* equilibrium. This effective equation of state, as re-plotted in Figs 6.1 and 6.2, allowed us to decouple the Langevin and Fokker–Planck equations, and to derive hills-and-valleys potential functions U (Fig. 6.5) and their corresponding stationary PDFs (Fig. 6.6).

In order to derive thermodynamics-like equilibrium statistics such as entropy and heat capacity, we needed to identify an *analogous temperature* and also a free-energy function V. We argued that the analogous temperature, named *excitability*, Θ, should scale inversely with anaesthetic effect λ, and posited two simple functional forms for $\Theta = \Theta(\lambda)$ (Eq. (6.48)).

Previous work by Lugiato and Bonifacio (1978) and Haken (1978) suggested that the V free-energy function could be obtained from the potential function U either directly (LB form: Eq. (6.47b)), or after scaling by temperature (Haken form: Eq. (6.47a)). Applying the Maxwell relation $S = -\partial V/\partial\Theta$ gave us four possible entropy expressions (Eq. (6.50)). By allowing anaesthetic effect to vary along the induction and emergence steady-state trajectories, we obtained graphs of entropy as a function of anaesthetic effect (Fig. 6.8). These graphs showed a discontinuous step reduction in entropy at induction, and a step increase at emergence. A discontinuous change in thermodynamic entropy implies that there will be a "latent heat" anomaly at phase change: if the quiescent state is the more ordered, then energy will be *released* from the macrocolumn at induction.

This suggestion of latent energy release was able to be tested in a qualitative way by examining the experiment of Stullken Jr. *et al.* (1977). The fact that the experiment showed a sudden reduction in metabolic energy requirement as the EEG waveforms were shifting from their "awake" to their "anaesthetic" characteristic pattern provides support for the prediction of a first-order change of phase to a more ordered state.

The Kuizenga experiment of Chapter 5 provided the first test of the adiabatic macrocolumn predictions, and the presently-described Stullken dog experiments constitute the second. The third clinical test will use spectral entropy to compare the spectral flatness of the theoretical fluctuation spectrum against that measured from EEG records for patients undergoing general anaesthesia. However, before discussing spectral entropy in Chap. 8, in Chap. 7 we will examine the results of stochastic simulations of the Langevin equations to verify numerically the correctness of the Chap. 5 predictions for fluctuation growth and spectral change as anaesthetic is varied.

Chapter 7

Numerical Simulations and Verification of Adiabatic Predictions

Thus far we have described two clinical experiments that provide *qualitative* confirmation of the major predictions of the adiabatic macrocolumn model: the Kuizenga experiment (Sect. 5.9) showing biphasic fluctuation power growth at induction and at emergence; and the Stullken dog experiment (Sect. 6.7) illustrating a "heat capacity" anomaly at the conscious-to-unconscious change of phase. Before proceeding further, it would be prudent to seek *quantitative* verification of the adiabatic theory. This is the motivatation for the present chapter's focus on numerical simulation of the macrocolumn stochastic differential equations.

As a careful and conservative first step towards numerical validations, I chose to simulate a simple but non-trivial Langevin equation whose stationary properties are well documented: the Ornstein–Uhlenbeck process. I refer to this preliminary investigation as a "calibration" experiment since its intention is to provide guidance as to appropriate choices for important numerical details, such as: quadrature time-increment, random-number scaling, windowing functions for the time-series, Fourier transform scale factors for spectral amplitude normalization.

The Ornstein–Uhlenbeck equation is an appropriate choice as a calibration test case since the *linearized* macrocolumn of Sect. 5.4 constitutes a two-dimensional Ornstein–Uhlenbeck system which decouples into a pair of one-dimensional Ornstein–Uhlenbeck processes in the pseudocolumn treatment of Sect. 6.5.3.

This conservative approach of running an initial calibration experiment seems not unwise given some salutory messages in the literature. Gardiner (1985) states that "differential equations which include white noise as a driving term have to be handled with great care." Craig and McNeil (1989) show that when simulating a quantum optical system using complex noise, unexpected "spiking" behaviours can occur which are *not* numerical artifacts (e.g., poor time resolution giving degraded stochastic accuracy), but actually are caused by the stochastic phase fluctuations pushing the sytem into deterministically unstable trajectories.[1] In his recent text, Gardiner (Gardiner and Zoller, 2000, pp. 209–210) describes some of the characteristics exhibited by quantum stochastic simulations which have gone bad.

In constrast to the Craig and Gardiner experiences, we do not anticipate pathological behaviours in our macrocolumn simulations. We do not have stochastic phase terms, so our simulations are modelling what is essentially a classical diffusion problem, and this is expected

---

[1] Spiking misbehaviours in quantum stochastic simulations had been observed a decade earlier by M. Steyn-Ross (1979) in her MSc thesis investigations of molecular vibrational modes.

to be quite well-behaved—provided that care is taken to ensure that the noise perturbations remain small. This aspect will be discussed later in Sect. 7.2.1.

7.1 The Ornstein-Uhlenbeck Calibration Experiment

7.1.1 Historical Context

The Ornstein–Uhlenbeck (OU) process is the oldest example of a stochastic differential equation (Arnold, 1974, p. 134):

$$\frac{dv(t)}{dt} = -A\,v(t) + \sqrt{D}\,\xi(t)\,. \tag{7.1}$$

This is the Langevin equation describing the velocity v of a Brownian particle, such as a pollen grain suspended in water. The positive constant A is a damping or fluid friction coefficient, $\xi(t)$ is random forcing function, and D is a diffusion coefficient. The particle is buffeted by $\sim 10^{21}$ collisions per second from all sides. Each collision causes a sudden and random velocity change, but any imposed velocity tends to be damped out by subsequent collisions. Thus the molecules of the suspension liquid induce two counteracting effects: the myriad random kicks from $\xi(t)$ make v spread out over an ever broadening range of values, while the frictional damping $-Av$ tries to bring v back to zero (van Kampen, 1981, p. 238).

For a spherical particle of mass m, radius a suspended in a fluid of viscosity η [units: $\mathrm{kg\,m^{-1}\,s^{-1}}$] and temperature T, the damping and diffusion constants are given by [Arnold (1974, p. xii); Schuss (1980, p. 91)],

$$A = \frac{6\pi a\eta}{m} \qquad [\text{units: s}^{-1}] \tag{7.2}$$

$$D = \frac{2k_BTA}{m} \qquad [\text{units: (m/s)}^2\,\text{s}^{-1}] \tag{7.3}$$

where k_B is Boltzmann's constant. These latter two equations show that there is a monotonic relation between the fluctuation coefficient $\sqrt{D}$ and the dissipative drag coefficient A. This is an expression of the *fluctuation–dissipation* theorem (Gillespie, 1993).

The damping constant A, carrying units of frequency, is a parameter that describes the frequency of collisions. Between collisions the constant straight-line motion of the particle is perfectly correlated. Therefore A is an inverse measure of the correlation between velocities of a Brownian particle at various times (Schuss, 1980, p. 92).

The random fluctuation $\xi(t)$ [units: $\mathrm{s}^{-1/2}$] is a Gaussian-distributed white noise of zero mean,

$$\langle \xi(t) \rangle = 0 \tag{7.4}$$

and zero autocorrelation everywhere except at lag $\tau = 0$,

$$\langle \xi(\tau)\,\xi(0) \rangle = \delta(\tau)\,. \tag{7.5}$$

Gillespie (1996a) defines the white noise $\xi(t)$ as the $dt \to 0$ limit of a temporally uncorrelated normal random variable with mean zero and variance $1/dt$.

Equation (7.1) is often written in terms of differentials (Gardiner, 1985, p. 106),

$$\begin{aligned} dv(t) &= -A\,v(t)\,dt + \sqrt{D}\,\xi(t)\,dt && (7.6a) \\ &= -A\,v(t)\,dt + \sqrt{D}\,dW(t) && (7.6b) \end{aligned}$$

where

$$dW(t) \equiv \xi(t)\,dt \tag{7.7}$$

is a temporally uncorrelated normal random variable with mean 0 and variance *dt*. The increment $dW(t)$ is the differential of a random process $W(t)$ given by

$$W(t) = \int_0^t \xi(t')\,dt'\,. \tag{7.8}$$

If the observations of the Brownian particle are at time intervals much larger than the characteristic settling time $1/A$, then $W(t)$ gives a measure of the temporally coarse-grained *position* of the particle. Gillespie (1996a; 1996b) refers to $W(t)$ as the *driftless Wiener process.*

Because of the presence of white noise, the Langevin equation 7.1 is, strictly speaking, mathematically improper (Gillespie, 1996b). To give the equation meaning, we take the *dv* infinitesimal to have an Ito forward-difference interpretation of "pointing towards the future"

$$dv(t) = v(t+dt) - v(t) \tag{7.9}$$

so that the differential form of Eq. (7.6a) can now be interpreted as an updating formula for v:

$$v(t+dt) = v(t) - A\,v(t)\,dt + \sqrt{D}\,\xi(t)\,dt\,. \tag{7.10}$$

Equation (7.10) is the form we will use for the numerical simulations of the Ornstein–Uhlenbeck process.

7.1.2 Solutions of the Ornstein-Uhlenbeck Process

In the limit of zero diffusion ($D = 0$), Eq. (7.1) predicts that any initial velocity $v(t = 0)$ will decay exponentially to rest with characteristic time-constant $1/A$,

$$v(t) = v(0)\,e^{-At} \qquad (t \geq 0)\,. \tag{7.11}$$

In the presence of diffusion, it is the *time-averaged* velocity that follows an exponential decay trajectory to zero (Gardiner, 1985, p. 106),

$$\langle v(t) \rangle = v(0)\,e^{-At} \tag{7.12a}$$

with variance

$$\operatorname{var}\{v(t)\} = \frac{D}{2A}\left[1 - e^{-2At}\right]. \tag{7.12b}$$

Of primary interest are the $t \longrightarrow \infty$ steady-state (ss) characteristics,

$$\langle v(t)\rangle\big|_{\mathrm{ss}} = 0 \qquad \text{(mean)} \tag{7.13a}$$

$$\operatorname{var}\{v(t)\}\big|_{\mathrm{ss}} = \frac{D}{2A} \qquad \text{(variance)} \tag{7.13b}$$

$$G(\tau) = \operatorname{cov}\{v(\tau), v(0)\}\big|_{\mathrm{ss}} = \frac{D}{2A}e^{-A|\tau|} \qquad \text{(autocorrelation)} \tag{7.13c}$$

$$S(\omega)\big|_{\mathrm{ss}} = \frac{D}{A^2+\omega^2} \qquad \text{(intensity spectrum)}\,. \tag{7.13d}$$

7.1.3 Quadrature

Following the Murthy (1983) scheme of Sect. 2.3, we approximate the infinite-variance white noise $\xi(t)$ with a sequence of (dimensionless) Gaussian-distributed random numbers $\{\mathcal{R}_n\}$ scaled by $1/\sqrt{\Delta t}$,

$$\xi(t) \longrightarrow \frac{1}{\sqrt{\Delta t}}\{\mathcal{R}_n\}\,, \qquad t = n\Delta t \tag{7.14}$$

where $\mathcal{R}_n$ is explicitly defined to be the normal random variable with mean 0 and variance 1, and Δt is an appropriately chosen time-step. Replacing the infinitesimal dt in Eq. (7.10) with finite time-step Δt, and substituting $\mathcal{R}_n/\sqrt{\Delta t}$ for $\xi(t)$ gives an approximate finite-difference updating rule for v_n,

$$\begin{aligned} v_{n+1} &= v_n - A\,v_n\,\Delta t + \sqrt{D}\,\xi(t)\,\Delta t \\ &= v_n(1 - A\,\Delta t) + \mathcal{R}_n\sqrt{D\Delta t}\,. \end{aligned} \tag{7.15}$$

This Euler one-step quadrature should give accurate results provided the time-step Δt is much smaller[2] than the $1/A$ relaxation time, i.e., provided $|A\Delta t| \ll 1$.

7.1.4 Simulation Results for an OU Process

In order to verify the OU updating formula of Eq. (7.15) against the theoretical predictions of Sect. 7.1.2, I fixed the diffusion constant at $D = 1$ m^2/s^3, and set the drift constant A at one of three values: [1, 10, 100] s^{-1}, corresponding to relaxation times of [1, 0.1, 0.01] s respectively. The time-step was set at $\Delta t = 10^{-3}$ s, sufficiently fine to give good temporal resolution for the most rapidly evolving case ($A = 100$ s^{-1}). A vector of 6000 unit-normal random numbers were generated (via MATLAB's **randn** function) and stored; this stored sequence was re-used for each run in order to highlight the effect of variations in the A rate constant.

The results are illustrated in Fig. 7.1. For the three panels on the left (a, c, e), the initial condition was set at $v_0 = 1$ m/s, allowing us to view the relaxation to steady-state $\langle v(\infty)\rangle = 0$. As expected, the relaxation becomes increasingly rapid as the A rate constant is increased, with the fluctuations following the Eq. (7.12a) prediction for average velocity.

---

[2] Because the OU process is analytically solvable, it is possible to derive an updating formula which is *exact* for *any* positive value of Δt (Gillespie, 1996a):

$$v_{n+1} = v_n e^{-A\Delta t} + \mathcal{R}_n\sqrt{\frac{D}{2A}\left(1 - e^{-2A\Delta t}\right)}\,.$$

which reduces to Eq. (7.15) when $|A\Delta t| \ll 1$. Thus Eq. (7.15) is a first-order approximation to Gillespie's exact updating formula.

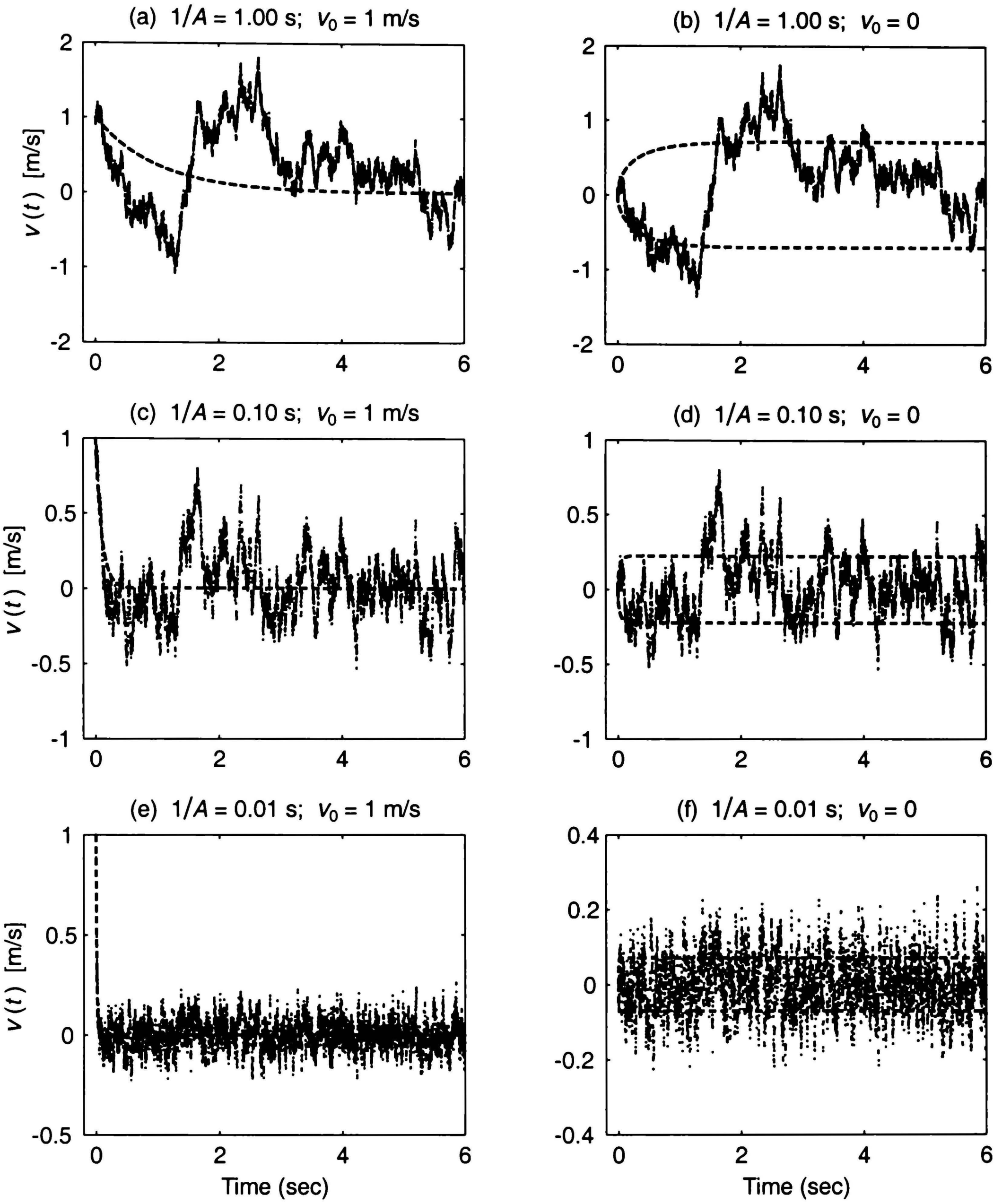

Figure 7.1: Six simulations for the velocity of an OU process computed from the Eq. (7.15) updating rule. Each run used the identical set of 6000 unit-normal random numbers. The timestep was $\Delta t = 10^{-3}$ s, and the diffusion constant D was set at unity. The drift constant A was varied over three orders of magnitude (from top to bottom). The initial velocity was set at 1 m/s for the left-hand panels (a, c, e), and at 0 for the right-hand panels (b, d, f). For the left panels, the dashed curve shows the Eq. (7.12a) prediction for average velocity. For the right panels, the dashed curves show the ± 1 standard deviation envelope calculated from the Eq. (7.12b) variance. [After Gillespie (1996a, Figs 3–5)]

For the three right-hand panels (b, d, f) of Fig. 7.1, the system was started with initial condition $v_0 = 0$, allowing us to view the fluctuations about steady state. The pair of dashed curves give the ± 1 standard-deviation envelope predicted by Eq. (7.12b): the velocity values are expected to lie inside this envelope approximately two-thirds of the time.

The correlations for the steady-state fluctuations were calculated using the discrete autocorrelation formula of Eq. (7.17), and plotted in Fig. 7.2; the corresponding Eq. (7.13c) autocorrelation predictions are drawn with a dashed line.

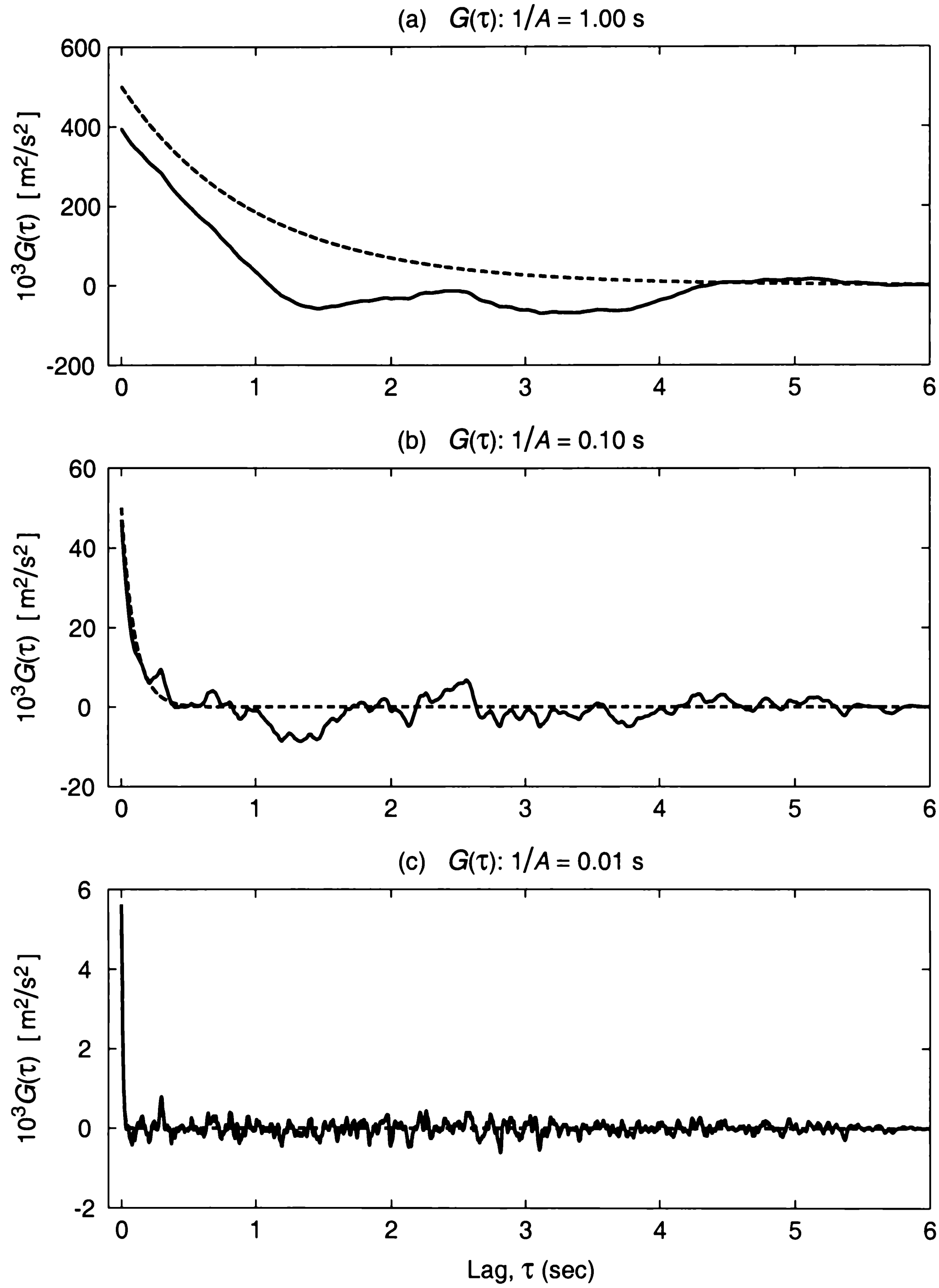

Figure 7.2: Autocorrelation functions for the time-series pictured in Fig. 7.1(b, d, f). The dashed trends are the theoretical predictions from Eq. (7.13c); the joined lines are calculated from the simulation time-series using Eq. (7.17).

These simulation runs[3] confirm that $1/A$ determines not only the correlation time for fluctuations about steady state (Fig. 7.2 and Eq. (7.13c)), but also sets the relaxation time for a perturbed OU process to recover its steady state (left panels of Fig. 7.1 and Eq. (7.12a)).

---

[3] For completeness, I compared the present results against those obtained using the Gillespie (1996a) exact updating formula listed in the footnote on p. 128. At the scale of the graphs plotted in Fig. 7.1, the Gillespie results are indistinguishable from mine. However, this situation changes dramatically if the timestep Δt is made *larger* than the relaxation time $1/A$: the Eq. (7.15) first-order Euler approximation becomes numerically unstable, while the Gillespie exact algorithm remains reliable and accurate.

The agreement between experiment and theory for these simulation test runs has so far been entirely satisfactory. All that remains is to verify the steady-state *spectrum* prediction of Eq. (7.13d).

7.1.5 OU Simulation Spectrum

The steady-state spectral *amplitudes* $\widetilde{V}_k^{\mathrm{rms}}$ [units: (m/s) Hz$^{-1/2}$] for the OU velocity simulation can be estimated either *directly* from the discrete Fourier transform of the time-series, or *indirectly* via a discretized version of the Wiener–Khinchin theorem of Eq. (2.5). The direct method substitutes the time-series vector $\mathbf{v}$ into the Eq. (2.13) discrete spectral amplitude expression to give,

$$\widetilde{V}_k^{\mathrm{rms}} = \sqrt{\frac{\Delta t}{N}}\left|\mathrm{DFT}\{\mathbf{v}\}_k\right| \qquad k = 0, 1, \ldots, N-1 \tag{7.16}$$

where $\mathbf{v} = [v_0, v_1, \ldots, v_{N-1}]$ is the N-element vector of random velocity samples generated via Eq. (7.15), k is the frequency index, and DFT denotes the discrete Fourier transform operator.

The indirect method first computes $\mathbf{G}$, the autocorrelation vector estimate[4] of $2N-1$ lagged products formed from the time-series via

$$G_j = \frac{1}{N}\sum_{i=-N+1}^{N-1} v_{i+j}\, v_i\,, \qquad j = -(N-1), \ldots, N-1\,. \tag{7.17}$$

The Fourier transform of $\mathbf{G}$ gives the spectral power, and the square root of the spectral power yields the rms spectral amplitude estimate,

$$\widetilde{V}_k^{\mathrm{rms}} = \sqrt{\Delta t \cdot \left|\mathrm{DFT}\{\mathbf{G}\}_k\right|}\,, \qquad k = 0, 1, \ldots, N-1\,. \tag{7.18}$$

In the event that the $\mathbf{v}$ time-series vector has been pre-conditioned by a Hanning (or other) shaping window $\mathbf{W}$, the N appearing in the denominator of Eqs (7.16) and (7.17) should be replaced by $||\mathbf{W}||^2$, the square of the window-norm (see Eq. (2.18)).

Results

Fig. 7.3 illustrates log-log and semilog graphs for the spectral amplitudes $\widetilde{V}_k^{\mathrm{rms}}$ of time-series corresponding to the steady-state ($v_0 = 0$) fluctuations plotted in the right-hand panels of Fig. 7.1. The drift coefficient A was set at 1 s^{-1} (top pair), 10 s^{-1} (middle pair), or 100 s^{-1} (bottom pair); the diffusion constant was left fixed at $D = 1$ m^2/s^3 throughout. For each setting of the drift coefficient, 10 Ornstein–Uhlenbeck velocity simulations were run using the Eq. (7.15) first-order updating rule with a time-step $\Delta t = 10^{-3}$ s. The amplitude spectrum for each 6000-point simulation run was computed via Eq. (7.16). I compared these results with those obtained using the autocorrelation method of Eq. (7.18), but observed no significant difference in the spectral amplitude estimates. For both methods, the spectra were quite noisy, so the 10 successive spectral runs were averaged to provide some smoothing.

---

[4] In MATLAB, Eq. (7.17) is evaluated via the code

```
G = xcorr(v, 'biased');
```

returning a *biased* estimate of the autocorrelation since no correction is made for the the fact that there are fewer lagged-product contributions at the wings of the correlation function. The *unbiased* version scales the raw autocorrelation by $1/(N - |j|)$, but this correction typically results in very noisy wings.

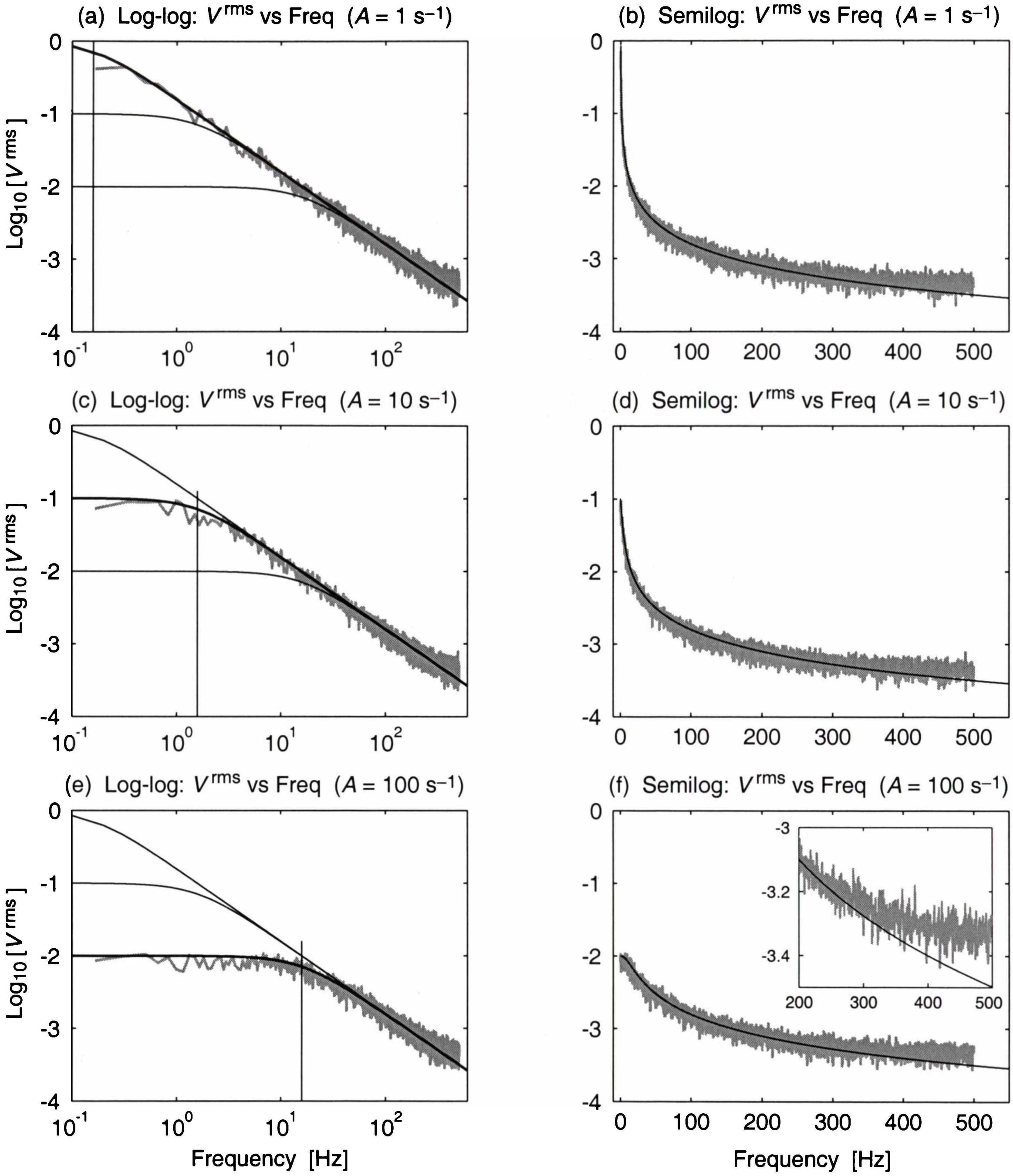
(a) Log-log: V^{rms} vs Freq ($A = 1$ s^{-1})

(b) Semilog: V^{rms} vs Freq ($A = 1$ s^{-1})

(c) Log-log: V^{rms} vs Freq ($A = 10$ s^{-1})

(d) Semilog: V^{rms} vs Freq ($A = 10$ s^{-1})

(e) Log-log: V^{rms} vs Freq ($A = 100$ s^{-1})

(f) Semilog: V^{rms} vs Freq ($A = 100$ s^{-1})

Figure 7.3: Amplitude spectra for the OU steady-state ($v_0 = 0$) stochastic time-series illustrated in Fig. 7.1(b, d, f): $D = 1$ m^2/s^3, $\Delta t = 10^{-3}$, $A \in \{1, 10, 100\}$ s^{-1} as indicated. The spectra are presented here both as log-log plots (left-hand panels) and as semilog plots (right-hand panels). The smooth curves are the OU theoretical prediction given by the square-root of Eq. (7.13d); the grey background traces are the average of 10 experimental spectra computed by applying Eq. (7.16) to the simulation time-series. The vertical markers in (a, c, e) indicate the frequency $f = A/2\pi$ at which the spectral amplitude has decayed to $1/\sqrt{2}$ of its dc value (i.e., the half-power frequency). The smoothed inset in (f) highlights the aliasing error evident on approach to the 500-Hz Nyquist frequency limit.

Minor Spectral Errors: High-frequency aliasing

As can be seen from Fig. 7.3, the agreement between theoretical prediction (the square-root of the Lorenztian spectrum of Eq. (7.13d)) and experiment is very good, except perhaps for a small imperfection at the high-frequency end where the experimental values somewhat overestimate

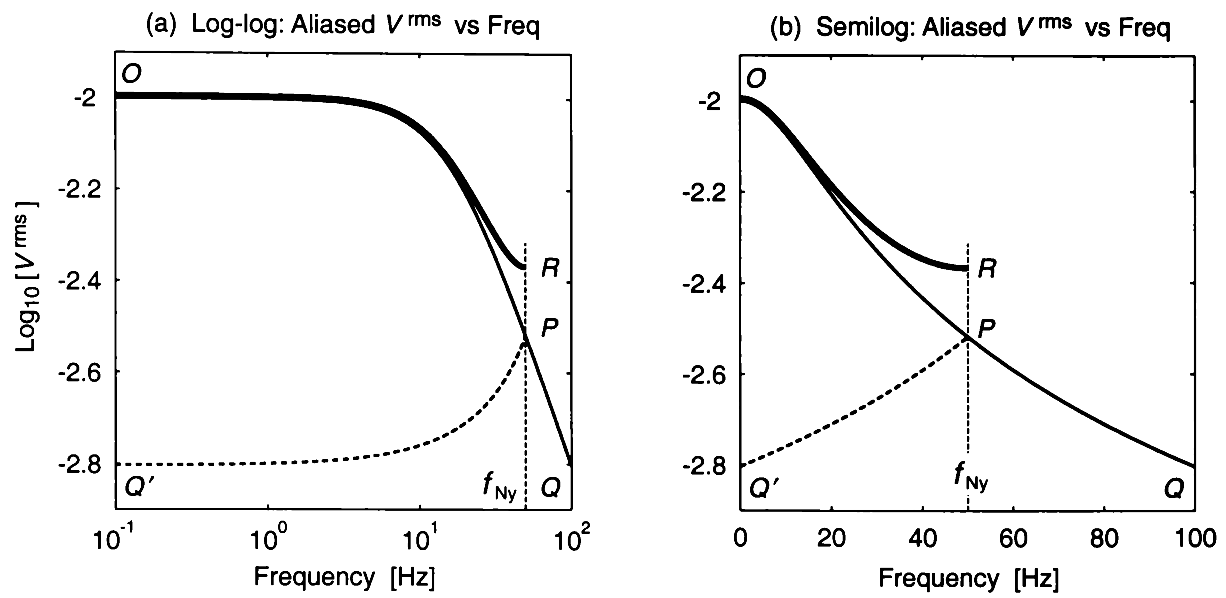

Figure 7.4: Aliased amplitude spectrum generated by taking the discrete Fourier transform of a non-bandlimited Lorentzian process; plotted (a) on a logarithmic frequency axis, and (b) on a linear frequency axis. The full curve OPQ is the theoretical Lorentzian amplitude $\tilde{V}^{\rm rms}(f) = [D/(A^2 + (2\pi f)^2)]^{1/2}$ with $D = 1$ m^2/s^3, $A = 100$ s^{-1}. The dashed segment PQ' is the reflection of segment PQ in the Nyquist mirror, here set at $f_{\rm Ny} = 50$ Hz (corresponding to a sampling interval of $\Delta t = 10^{-2}$ s). The bold curve OR is the sum of the true spectrum OP plus the $Q'P$ reflection ("alias") of QP. The discrepency RP is $\frac{1}{2}\log_{10} 2 = 0.15$.

the expected spectral trend. This is highlighted in the inset graph of Fig. 7.3(f) which has been additionally smoothed by applying a 5-point moving average filter.[5]

This small but systematic high-frequency error is *not* eliminated by applying a Hanning pre-conditioning window. (In fact, I found that provided the time-series was started at steady-state (i.e., $v_0 = 0$), the all-ones ("boxcar") and Hanning windows produced spectra which were virtually indistinguishable).

All of the Fig. 7.3 graphs show the same high-frequency blemish, irrespective of the setting for the Ornstein–Uhlenbeck decay rate A. Close inspection of the high-frequency tail at the $f_{\rm Ny} = 500$ Hz Nyquist frequency shows that in all cases, the time-series amplitude spectrum overestimates the theoretical OU prediction by ~0.15 on the base-10 logarithm scale,

$$\log_{10}\left[\tilde{V}^{\rm rms}_{\rm expt}(f_{\rm Ny})\right] - \log_{10}\left[\tilde{V}^{\rm rms}_{\rm theory}(f_{\rm Ny})\right] = 0.15 \tag{7.19}$$

giving,

$$\frac{\tilde{V}^{\rm rms}_{\rm expt}(f_{\rm Ny})}{\tilde{V}^{\rm rms}_{\rm theory}(f_{\rm Ny})} = 10^{0.15} \approx \sqrt{2}. \tag{7.20}$$

Squaring this amplitude ratio, we see that the spectral *intensity* is too high by a factor of 2. This is precisely the error magnitude expected at the Nyquist point for a (moderately) aliased power spectrum—assuming that only first-order aliasing (i.e., a single fold about the Nyquist frequency) need be considered. This is elucidated in Fig. 7.4.

---

[5] A moving-average filter is equivalent to a convolution with a vector of ones. Thus a 5-point smoother for a vector `X` can be implemented in MATLAB as,

```
X = conv(X, [1 1 1 1 1]/5);
```

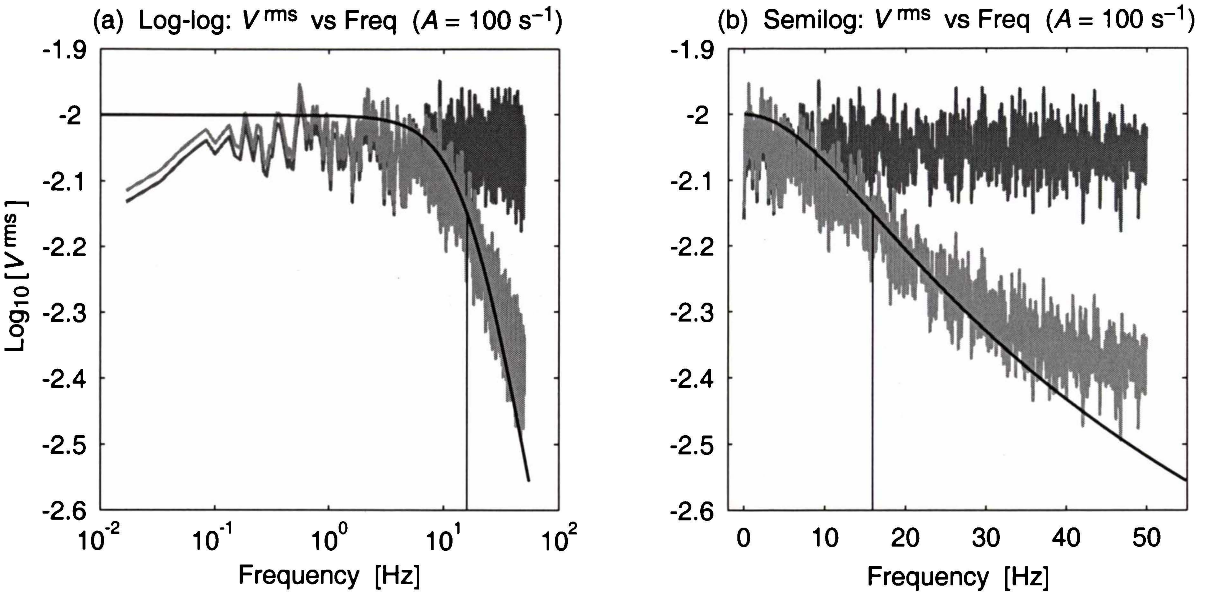

Figure 7.5: Spectral damage caused by inadequate temporal resolution in the stochastic simulation; plotted (a) on a logarithmic frequency axis, and (b) on a linear frequency axis. The dark-grey background trace shows the amplitude spectrum obtained from the DFT of a time-series generated using the Eq. (7.15) updating rule with $D = 1$ m^2/s^3, $A = 100$ s^{-1}, and $\Delta t = 10^{-2}$ s. Although the dark-grey high-frequency spectrum is grossly incorrect, there is reasonable agreement with theory (black curve) at low frequencies. The light-grey foreground trace is the spectrum calculated for the Gillespie-generated time-series. Apart from the not unexpected aliasing effect (giving the spurious $\sqrt{2}$ amplitude boost at the 50-Hz Nyquist frequency), the Gillespie time-series gives a reliable spectrum. The vertical lines mark the $A/2\pi = 15.9$ Hz half-power frequency.

It seems that such spectral aliasing is an unavoidable consequence of the stochastic simulation itself. With a time-step of $\Delta t = 10^{-3}$ s, the discrete Fourier transform has a Nyquist upper-frequency limit of $f_{\mathrm{Ny}} = 1/2\Delta t = 500$ Hz. Any activity in the time-series which has frequency components higher than this 500-Hz limit will be undersampled: activity at frequency $f_{\mathrm{Ny}} + \varepsilon$ will appear in the DFT spectrum at its mirror frequency $f_{\mathrm{Ny}} - \varepsilon$. And yet, by design, the simulation experiences a random kick $\mathcal{R}_n$ at *every* step, so is being driven at *twice* the Nyquist frequency. Despite this, the resulting spectral discrepency is surprisingly small, with the distortion being confined to the high-frequency tail. This is presumably because the high-frequency random kicks tend to be damped out by the viscous drag term, acting rather like an integrating capacitor in an *RC* low-pass filter circuit.

Gross Spectral Errors: Temporal undersampling

It was pointed out earlier in Sect. 7.1.3 that the Euler one-step quadrature of Eq. (7.15) can only be expected to give accurate results provided $\Delta t \ll 1/A$. Here I demonstrate the spectral consequences of violating this "small time-step" condition by deliberately setting the time-step equal to the decay-time, $\Delta t = 1/A = 0.01$ s. As is obvious in Fig. 7.5, the resulting DFT spectrum (dark-grey background trace) is ruined.

This ruination occurs because the fidelity of the simulation itself has been compromised: the large time-step prevents the time-series from adequately sampling the velocity relaxation which follows each stochastic kick.

However, because an *exact* updating formula for the OU process exists (Gillespie (1996a); and see footnote on p. 128 of this thesis), it is in fact possible to run a "low temporal fidelity" simulation and still recover the correct spectrum. That this is so is demonstrated in the light-grey foreground spectrum in Fig. 7.5. This Gillespie result is instructive, but is really a rather special case. For most SDEs, the exact solution is unknown, and therefore a "suitably small" value for Δt is mandatory in any SDE simulation which adopts an Euler-type quadrature scheme.

This completes the Ornstein–Uhlenbeck calibration experiments. We are now ready to simulate the stochastic differential equations that define the white-noise-driven macrocolumn model for the cerebral cortex. The primary purpose of these macrocolumn simulations is to give quantitative verification of the various theoretical predictions made in earlier chapters. In particular, we will find that these simulation experiments—

- Confirm the predicted number, character, and location of the macrocolumn steady states as a function of anaesthetic effect;
- Establish the range over which the adiabatic and full equations give similar results, and identify the point at which their behaviours are expected to diverge;
- Give numerical demonstration of the growth in fluctuation power (the "biphasic effect") as the conscious→unconscious transition point is approached.

7.2 Mapping the Macrocolumn SDEs to Difference Equations

7.2.1 Adiabatic Difference Equations

The *adiabatic* macrocolumn stochastic equations of motion (Langevin equations) were listed earlier as Eqs (6.1–6.3). Recasting the Eq. (6.1) pair of first-order differential equations as a pair of *difference* equations in h_e and h_i, we obtain,

$$h_e^{n+1} = h_e^n + F_1^n\,\Delta t + \Gamma_e^n\,\Delta t \tag{7.21a}$$

$$h_i^{n+1} = h_i^n + F_2^n\,\Delta t + \Gamma_i^n\,\Delta t \tag{7.21b}$$

where the superscript n means "value at time-step n," and Δt is the time increment. Thus the h_e and h_i soma voltages evolve in response to two counteracting influences: a diffusive term $\Gamma\Delta t$ (proportional to $\sqrt{\Delta t}$; see below) that randomly perturbs the voltage away from steady state, and a drift term $F\Delta t$ that causes these voltage perturbations to die away, allowing the macrocolumn to return to its equilibrium state. The $F_{1,2}^n$ drift coefficients are straightforward discretizations of Eqs (6.2):

$$\begin{aligned} F_1^n = \Big\{ & \left(h_e^{\text{rest}} - h_e^n\right) \\ & + \psi_{ee}(h_e^n)\left[\left(N_{ee}^\alpha + N_{ee}^\beta\right)\mathcal{S}_e(h_e^n) + \langle p_{ee}\rangle\right] G_e e/\gamma_e \\ & + \lambda\,\psi_{ie}(h_e^n)\left[N_{ie}^\beta\,\mathcal{S}_i(h_i^n) + \langle p_{ie}\rangle\right] G_i e/\gamma_i \Big\} \Big/ \tau_e\,, \end{aligned} \tag{7.22a}$$

$$\begin{aligned} F_2^n = {} & \Big\{ \left(h_i^{\text{rest}} - h_i^n\right) \\ & + \psi_{ei}(h_i^n) \left[\left(N_{ei}^{\alpha} + N_{ei}^{\beta}\right) \mathcal{S}_e(h_e^n) + \langle p_{ei} \rangle \right] G_e e / \gamma_e \\ & + \lambda\, \psi_{ii}(h_i^n) \left[N_{ii}^{\beta}\, \mathcal{S}_i(h_i^n) + \langle p_{ii} \rangle \right] G_i e / \gamma_i \Big\} \Big/ \tau_i \,. \end{aligned} \tag{7.22b}$$

The discretization of the diffusion equations (6.3) requires some care; the resulting equations read,

$$\begin{aligned} \Gamma_e^n = {} & \Big\{ \psi_{ee}(h_e^n)\, \alpha_{ee} \sqrt{\langle p_{ee} \rangle}\, \frac{\mathcal{R}_1^n}{\sqrt{\Delta t}}\, G_e e / \gamma_e \\ & + \lambda\, \psi_{ie}(h_e^n)\, \alpha_{ie} \sqrt{\langle p_{ie} \rangle}\, \frac{\mathcal{R}_2^n}{\sqrt{\Delta t}}\, G_i e / \gamma_i \Big\} \Big/ \tau_e \,, \end{aligned} \tag{7.23a}$$

$$\begin{aligned} \Gamma_i^n = {} & \Big\{ \psi_{ei}(h_i^n)\, \alpha_{ei} \sqrt{\langle p_{ei} \rangle}\, \frac{\mathcal{R}_3^n}{\sqrt{\Delta t}}\, G_e e / \gamma_e \\ & + \lambda\, \psi_{ii}(h_i^n)\, \alpha_{ii} \sqrt{\langle p_{ii} \rangle}\, \frac{\mathcal{R}_4^n}{\sqrt{\Delta t}}\, G_i e / \gamma_i \Big\} \Big/ \tau_i \,. \end{aligned} \tag{7.23b}$$

The $\psi_{jk}(h_k)$ $(j, k \in \{e, i\})$ are the voltage-dependent psi-weighting functions of Eq. (3.5),

$$\psi_{ee}(h_e^n) = \left(h_e^{\text{rev}} - h_e^n\right) \Big/ \left|h_e^{\text{rev}} - h_e^{\text{rest}}\right| \tag{7.24a}$$

$$\psi_{ie}(h_e^n) = \left(h_i^{\text{rev}} - h_e^n\right) \Big/ \left|h_i^{\text{rev}} - h_e^{\text{rest}}\right| \tag{7.24b}$$

$$\psi_{ei}(h_i^n) = \left(h_e^{\text{rev}} - h_i^n\right) \Big/ \left|h_e^{\text{rev}} - h_i^{\text{rest}}\right| \tag{7.24c}$$

$$\psi_{ii}(h_i^n) = \left(h_i^{\text{rev}} - h_i^n\right) \Big/ \left|h_i^{\text{rev}} - h_i^{\text{rest}}\right| \tag{7.24d}$$

and the $\mathcal{S}_{e,i}$ are the Eq. (3.6) sigmoidal coupling strengths (voltage-to-firing-rate transfer functions), which are also soma-voltage dependent,

$$\mathcal{S}_e(h_e^n) = \mathcal{S}_e^{\max} \Big/ \left[1 + \exp\left(-g_e(h_e^n - \theta_e)\right)\right] \tag{7.25a}$$

$$\mathcal{S}_i(h_i^n) = \mathcal{S}_i^{\max} \Big/ \left[1 + \exp\left(-g_i(h_i^n - \theta_i)\right)\right] \,. \tag{7.25b}$$

Other symbols are as defined in Table 3.1.

Simulation of White-Noise Sources

There are two points to note regarding the discretized diffusion equations (7.23). First, each of the four independent white-noise sources $\xi_k, (k \in \{1, \ldots, 4\})$ appearing in Eq. (6.3) has been replaced in the simulation equations by its discrete approximation $\mathcal{R}_k/\sqrt{\Delta t}$ where the $\mathcal{R}_k$ are Gaussian-distributed zero-mean unit-variance random numbers. (This is the Murthy scheme discussed earlier in Sect. 7.1.3.) The division by $\sqrt{\Delta t}$ ensures that the diffusion increment $\Gamma \Delta t$ scales as the *square root* of the time increment as required for a Wiener process.

Second, as stated in Sect. 5.1, the four stochastic terms are scaled by dimensionless "safety factors" α_{jk} to ensure that the random fluctuations in the p_{jk} subcortical inputs always remain small. How these safety factors are determined will now be discussed.

For definiteness, consider p_{ie}, the i–e spike-rate for events originating from subcortical sources giving inhibitory modulation of the excitatory neuronal population of the macrocolumn. In Sect. 5.1 we transformed p_{ie} from a *sure* number ($p_{ie} = 1600\ \mathrm{s}^{-1}$—see Table 3.1) into a Gaussian-distributed *random* number

$$p_{ie}(t) \;=\; \langle p_{ie}\rangle + \alpha_{ie}\sqrt{\langle p_{ie}\rangle}\,\xi(t) \tag{7.26}$$

which we now wish to simulate by mapping the $\xi(t)$ white-noise source to its $\mathfrak{R}/\sqrt{\Delta t}$ discrete approximation. The continuous-time $p_{ie}(t)$ of Eq. (7.26) is then replaced by the discrete random sequence $\{p_{ie}\}$,

$$p_{ie}(t) \;\longrightarrow\; p_{ie}^{n} \;=\; \langle p_{ie}\rangle + \alpha_{ie}\sqrt{\langle p_{ie}\rangle}\,\frac{\mathfrak{R}^n}{\sqrt{\Delta t}}\,, \qquad t \;=\; n\Delta t \tag{7.27}$$

which is Gaussian-distributed with mean $\langle p_{ie}\rangle = 1600\ \mathrm{s}^{-1}$ and standard deviation

$$\mathrm{sdev}\{p_{ie}\} \;=\; \alpha_{ie}\sqrt{\langle p_{ie}\rangle/\Delta t}\,. \tag{7.28}$$

For a time-step of $\Delta t = 10^{-4}$ s, the ±3 standard-deviation bounds on p_{ie} are

$$\langle p_{ie}\rangle \;\pm\; 3\,\mathrm{sdev}\{p_{ie}\} \;=\; 1600 \;\pm\; 12\,000\,\alpha_{ie} \qquad [\text{units: s}^{-1}]. \tag{7.29}$$

Eq. (7.29) indicates that the spike-rate can go negative. This is unphysical, since our model assumes that the noise enters the macrocolumn *from* the subcortex, and can never reverse direction to "flow" back to the subcortex from the macrocolumn; therefore we require that the probability of generating a negative spike-rate be made vanishingly small. Accordingly, we will work at the −3-standard-deviation limit in Eq. (7.29), and require that

$$1600 \;-\; 12\,000\,\alpha_{ie} \;>\; 0 \tag{7.30a}$$

giving an upper bound for the α_{ie} scale-factor

$$\alpha_{ie} \;<\; 0.133\,. \tag{7.30b}$$

For a Gaussian distribution, the probability of an excursion which is more than 3 standard deviations *below* the mean is 0.0013. So by setting the scale-factor at $\alpha_{ie} = 0.133$, we are tolerating the fact that about once every one-thousand calls to the random-number generator we will obtain a (slightly) negative, and therefore (slightly) unphysical, subcortical spike-rate.

Applying the same 3-standard-deviation criterion to each of the other three α_{jk}, we derive safety scale-factors

$$\alpha_{ie,ei} < 0.133 \quad \text{for } p_{ie},\, p_{ei}\,, \qquad \text{and} \qquad \alpha_{ee,ii} < 0.111 \quad \text{for } p_{ee},\, p_{ii}\,. \tag{7.31}$$

For simplicity, we set $\alpha = 0.1$ as a conservative safety scale-factor which applies to *all four* subcortical noise inputs.

Quadrature Initialization

To start the integration, the initial values for soma voltages h_e and h_i typically would be set equal to their zero-noise equilibrium values, derived from Fig. 3.4, appropriate to the given value of anesthetic effect λ:

$$h_e^0 = h_e^{\text{eq.}}(\lambda)\,, \qquad h_i^0 = h_i^{\text{eq.}}(\lambda)\,. \tag{7.32}$$

For λ in the range $0.28 < \lambda < 1.53$, the equilibrium curve has a multi-valued ordinate, so we would select either the top-, middle-, or bottom-branch $(h_e^{\text{eq.}}, h_i^{\text{eq.}})$ equilibrium values, depending on the particular numerical experiment we wished to run.

7.2.2 Full, Non-Adiabatic Difference Equations

Simulating the full *non-adiabatic* DEs requires rather more effort. If we do not wish to impose the simplifying adiabatic assumption of slow soma voltages, fast input currents, then we must work with the full set of *eight* coupled partial-differential equations for the spatially homogeneous macrocolumn listed in Eqs (3.1–3.4). This equation set consists of a pair of first-order DEs for the h_e and h_i soma voltages; these are coupled to four second-order DEs, one for each of the four input currents I_{ee}, I_{ei}, I_{ie}, I_{ii}; plus a pair of second-order DEs for the long-range spike inputs ϕ_e, ϕ_i from distant macrocolumns.

For simulation purposes, the two first-order DEs for h_e and h_i are replaced by first-order difference equations, and each of the six second-order DEs are recast as a pair of first-order difference equations; this gives a total of 14 coupled first-order difference equations which can be integrated using a simple Euler one-step quadrature scheme.

The conversion to *stochastic* difference equations proceeds exactly as for the adiabatic case described in Sect. 5.1: each of the four p_{jk} subcortical spike-rates entering the I_{jk} currents is converted from a sure value to a Gaussian-distributed random value defined by

$$p_{jk} \longrightarrow \langle p_{jk}\rangle + \widetilde{p_{jk}}(t) \tag{7.33}$$

where the randomly fluctuating part

$$\widetilde{p_{jk}}(t) = \alpha_{jk}\sqrt{\langle p_{jk}\rangle}\,\xi_{jk}(t) \tag{7.34}$$

will be approximated in simulation as

$$\widetilde{p_{jk}}^{\,n} = \alpha_{jk}\sqrt{\langle p_{jk}\rangle}\,\frac{\mathcal{R}_{jk}^n}{\sqrt{\Delta t}}\,, \tag{7.35}$$

and $\alpha_{jk} = 0.1$ is the "small fluctuations" safety factor.

Appendix A lists the 14 discretized equations and explains how the quadrature is initialized.

7.3 Verification of Macrocolumn Steady States

The theoretical distribution of macrocolumn steady states illustrated in Fig. 3.4 were verified numerically by running simulations of both the full equations (see Appendix A) and of the

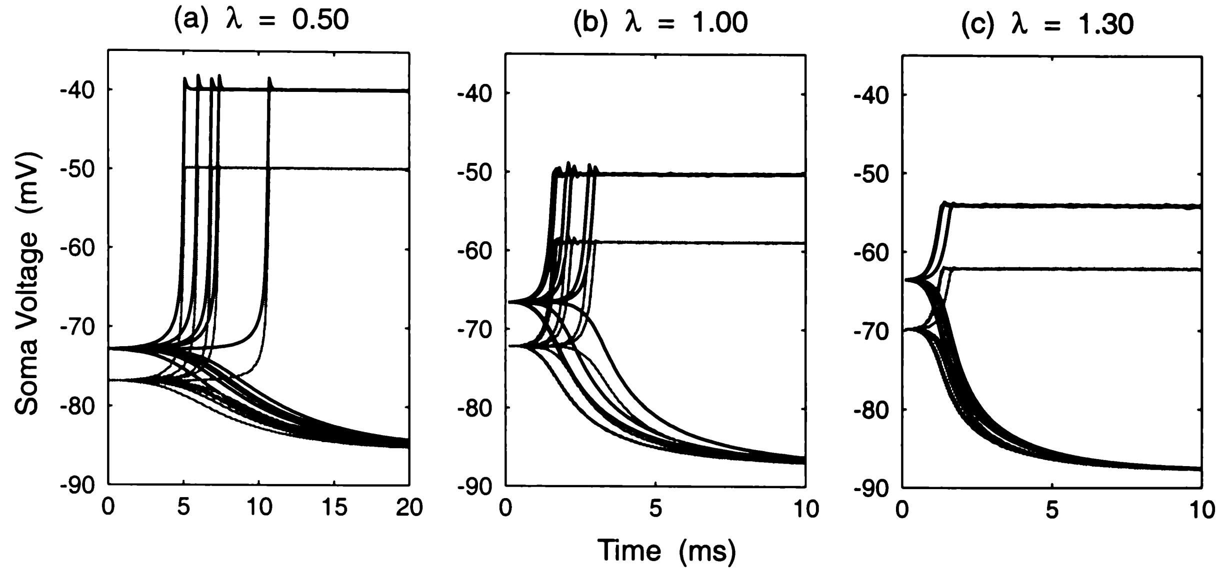

Figure 7.6: Relaxation to stable equilibrium for stochastic simulations of the *adiabatic* equations (see Eqs (6.1–6.3, (7.21–7.23)) for three values of anaesthetic effect lying within region II of the S-bend (see Fig. 3.4 on p. 47): (a) $\lambda = 0.5$; (b) $\lambda = 1.0$; (c) $\lambda = 1.3$. The four random noise sources for the p_{jk} subcortical spike inputs each have scale-factor $\alpha = 0.1$. Time-step is $\Delta t = 10^{-4}$ s. Dark (light) curves show time evolution for h_e (h_i). For each λ-value, 10 independent runs are shown. Each run is started on the unstable (h_e^0, h_i^0) equilibrium point at the crest of the potential hill separating the two valleys (see Fig. 6.5, p. 111), but cannot remain there. Random fluctuations cause the soma voltages to roll off the hill into either valley with equal probability. The upper stable equilibrium is the high-firing, active state; the lower stable equilibrium is the hyperpolarized, quiescent state. [Source: Adiabatic simulation dataset from Wilcocks (2001)]

adiabatically-simplified equations (Sect. 7.2.1). The integration scheme was an Euler one-step, with a time-step of $\Delta t = 10^{-4}$ s. A small time-step is necessary because the equations are strongly nonlinear, and the Euler method fails dramatically (becomes unstable) for large time-steps. We established that 10^{-4} s was a safe value by confirming that the deterministic behaviour of the simulations was unchanged if re-run using smaller time-step values. The noise consisted of four independent Wiener-process inputs as described earlier.

These simulation runs showed that the steady-state values calculated in Sect. 3.3.3 are correct, that the upper and lower branches are stable (with the exception of the high-λ top branch for the full equations; this is discussed below), and that the middle branch is unstable. We demonstrated this by starting the system on the middle (unstable) equilibrium point. The macrocolumn would never sit there, but would "fall" off the potential hill, settling into either the upper-branch (high-firing) equilibrium valley, or the lower-branch (low-firing) equilibrium valley. The "splitting probability" (i.e., the probability of falling into a given valley) was found to be ~50%. See Figs 7.6 and 7.7.

Figure 7.6 shows that the adiabatic runs settle to one of the stable states within about 200 samples (20 ms). It appears that the time required to settle decreases with increasing λ.

Figure 7.7 illustrates the much slower evolution of the full equations, typically taking an order of magnitude longer (2000 samples, 200 ms) than the adiabatic equations to settle to one of the stable steady-states. We also see that for $\lambda = 1.3$ (Fig. 7.7c), the upper branch is unstable: all runs which go to the upper branch develop an exponentially-growing oscillation about that branch before collapsing to the bottom branch.

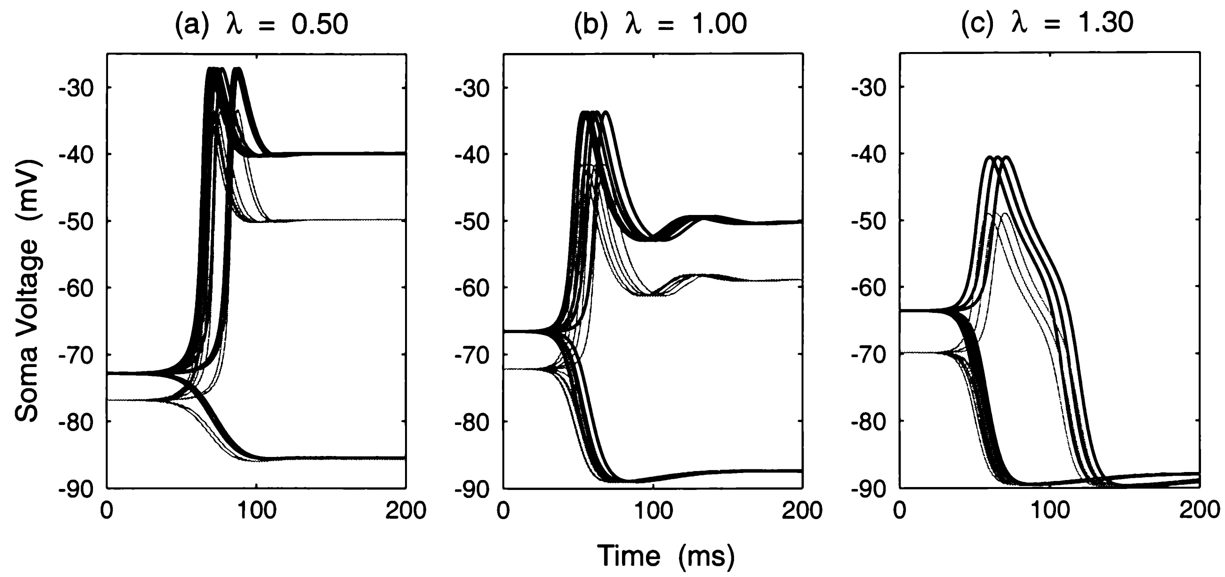

Figure 7.7: Relaxation to stable equilibrium for the stochastic simulations of the *full, non-adiabatic* equations (see Eqs (3.1–3.4), and Appendix A) for (a) $\lambda = 0.5$; (b) $\lambda = 1.0$; (c) $\lambda = 1.3$. Initial settings, noise scale-factor, and time-step as in Fig. 7.6. Full-equation runs generally demonstrate the same steady-state asymptotes as the adiabatic runs, but note that settling times are an order of magnitude longer here, and the upper branch is now characterized by an oscillatory dynamic, of frequency ~10 Hz, which is strongly damped for small λ, but becomes much less damped as λ is increased. For $\lambda \gtrsim 1.3$, the oscillation about the upper branch becomes so strong that the upper equilibrium becomes dynamically unstable, causing trajectories originally headed towards the high-firing branch to deviate and collapse into the hyperpolarized quiescent branch. [Source: Full, non-adiabatic simulation dataset from Wilcocks (2001)]

This oscillation has a frequency of ~10 Hz, lying within the so-called EEG *alpha-band* (8–14 Hz). These time-series results indicate that, along the top branch of steady states, the *full* equations can be characterized as having the impulse response of a damped, single-frequency (~10 Hz) sinewave, whose damping diminishes (i.e., whose resonance spectrum becomes narrower and stronger) as the macrocolumn approaches the top-branch A_3 induction point.

However, time-frequency analysis of clinically-measured EEG waveforms (e.g., the Kuizenga results presented in Figs 5.8 and 5.11) do *not* show a preferential growth of alpha-band power during anaesthetic induction. Instead, the clinical traces show a broad transfer of power from higher to lower frequencies as the induction point is approached, just as predicted by the simpler, adiabatic theory (e.g., see waterfall spectra in Fig 5.7, slew-rate spectra of Fig. 5.10; also Fig. 7.9 discussed later in the present chapter).

For the purposes of modelling anaesthetic induction, the simpler, adiabatic theory seems to provide a better match with clinical measurement than does the full, non-adiabatic theory. For this reason, this thesis focuses on the adiabatic predictions.

7.4 Verification of Fluctuation Divergence at Induction

Figure 5.3 (p. 80) illustrated the (linearized) adiabatic-theory prediction of a dramatic increase in rms amplitude for the fluctuations in soma voltage as the conscious → unconscious transition is approached. This prediction compares nicely with the actual results for a (nonlinear) adiabatic simulation run presented in Fig. 7.8. We see that the simulation produces an h_e time-series

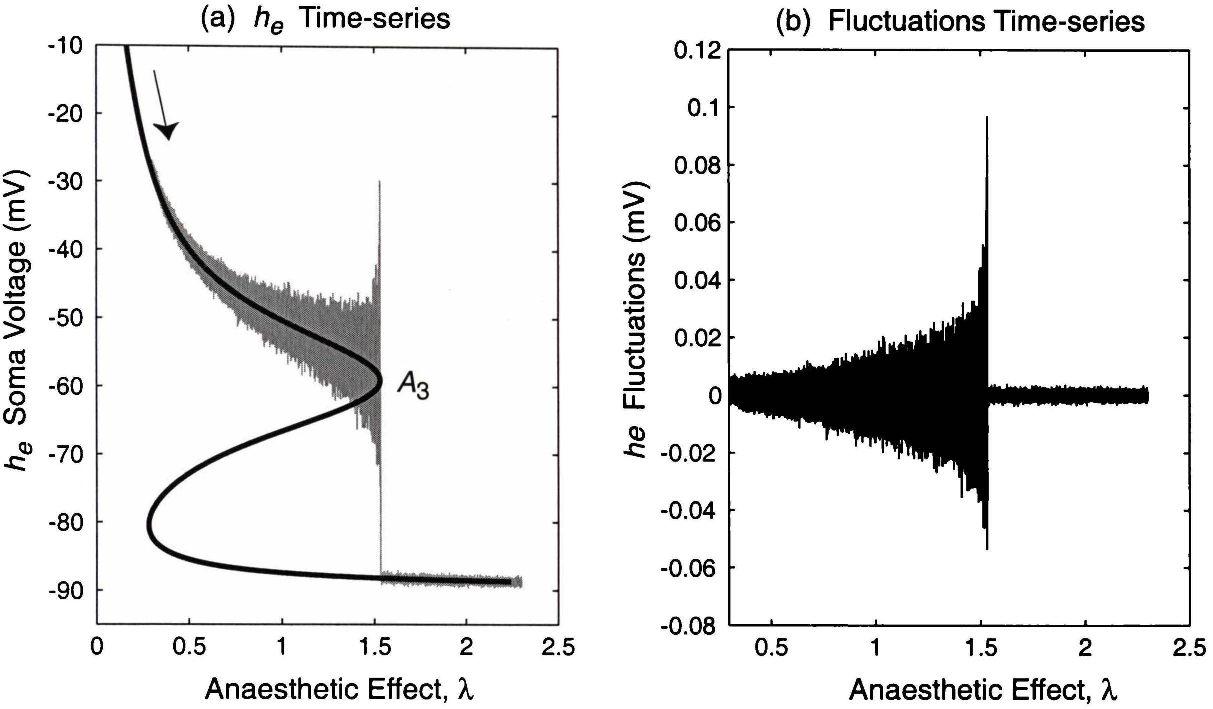

Figure 7.8: Time-series of excitatory soma voltage h_e for induction into unconsciousness: fluctuation amplitude grows strongly as the induction point A_3 is approached. (a) Time development (in grey) along the equilibrium curve (black); (b) fluctuations as the ac residual after subtraction of the dc equilibrium component. The h_e time-series was generated by a 30-s *adiabatic* simulation run in which λ was steadily increased from 0.3 to 2.3 during the course of the run. Time-step: $\Delta t = 10^{-4}$ s for 300,000 samples; noise scale-factor $\alpha = 0.1$. In (a), the fluctuations are displayed at 300× actual size in order to make them visible on the equilibrium voltage scale. Their true scale is shown in (b). [Adiabatic induction time-series in (a) abstracted from Wilcocks (2001)]

whose fluctuations about steady state grow markedly as the macrocolumn nears the A_3 critical point.

The adiabatic macrocolumn is started at $\lambda = 0.3$ on the upper-branch of the Fig. 3.4 S-curve trajectory of steady states. During a 30-s simulation run, anaesthetic effect is slowly and steadily increased to reach a final value of $\lambda = 2.3$ after 300,000 iterations with a time-step $\Delta t = 10^{-4}$ s. The simulation results in Fig. 7.8 show a flaring cornucopia of soma-voltage fluctuations which reach their maximal extent at the moment of transition, then abruptly collapse immediately after the jump to the much lower values characteristic of a low-firing, hyperpolarized macrocolumn.

As discussed earlier in Chap. 5.9.1, such a power surge in the EEG signal would be described by the anaesthesiology community as the "biphasic" or activation–depression response to general anaesthetic. This growth in fluctuation power is reminiscent of the divergent behaviour observed in many physical phase transitions, supporting the notion that the conscious $\leftrightarrow$ unconscious transition is analogous to a physical change of state.

7.5 Verification of EEG Spectral Changes

7.5.1 Spectrum for Adiabatic Simulations

The theoretical fluctuation spectrum for the (linearized) Langevin equations describing the adiabatic macrocolumn was stated in Eq. (5.58a) (p. 77) and plotted as a set of waterfall graphs in Fig. 5.7 (p. 85). These provide the spectral reference against which the simulation results are tested.

The simulation spectra were computed by Fourier transforming the pseudo-EEG waveforms generated by iterating the coupled, nonlinear adiabatic equations of motion listed in Eqs (7.21–7.23). We started the macrocolumn at the upper- or lower-branch stable equilibrium point corresponding to a given value of λ, then induced fluctuations about steady state by driving the four subcortical inputs $(p_{ee}, p_{ie}, p_{ei}, p_{ii})$ with four independent white-noise sources $(\xi_1, \xi_2, \xi_3, \xi_4)$. The simulated EEG waveform $h(t)$ is extracted from the resulting time-series as the *deviation* of the $h_e(t)$ excitatory voltage from its known steady-state value h_e^0:

$$\mathrm{EEG}(t) \equiv h(t) = h_e(t) - h_e^0 . \tag{7.36}$$

A simulation run consisted of 100,000 iterations with a time-step $\Delta t = 10^{-4}$ s, giving a 10-s pseudo-EEG record. Simulation runs were recorded for λ values ranging from 0.3 to 1.8 in steps of 0.1.

Each 10-s record was split into 10 non-overlapping 1-s sections, tapered with a 10,000-point Hanning window W (defined in Eq. (2.14)) to reduce spectral leakage, then fast Fourier transformed, giving an $N = 10,000$-point intensity spectrum $S(k\Delta f)$ [units: $(\mathrm{mV})^2/\mathrm{Hz}$] with a resolution of $\Delta f = 1/N\Delta t = 1$ Hz from 0 to 5000 Hz (the Nyquist frequency),

$$S(k\Delta f) = \frac{\Delta t}{\|\mathbf{W}\|^2} \left|\mathrm{DFT}\{\mathbf{hW}\}_k\right|^2 , \qquad k = 0, 1, \ldots, N/2 \tag{7.37}$$

where $\mathbf{hW}$ is the element-by-element product of the pseudo-EEG time-series vector $\mathbf{h}$ with Hanning windowing vector $\mathbf{W}$,

$$\mathbf{hW} = [h_0 W_0,\ h_1 W_1,\ \ldots,\ h_{N-1} W_{N-1}] . \tag{7.38}$$

(Because the spectrum is symmetric about dc, we can ignore negative frequencies, i.e., index values $N/2 < k < N$ in Eq. (7.37).) The scaling by time-step in Eq. (7.37) ensures that the rate of energy delivery (area under the power spectral density curve) is independent of sample rate. As was discussed in Sect. 2.2.2, the division by the squared norm of the Hanning window (i.e., the sum of the squares of the window function) is required to compensate for the loss of power due to the tapering; for a rectangular ("boxcar") window, the squared norm evaluates to N, and for the Hanning window $\| \|^2 \approx N/2.7$.

Each run produced 10 power spectral density estimates which were averaged, then smoothed with a 5-point moving average filter. See Fig. 7.9.

For frequencies below 400 Hz, we see excellent agreement between the theoretical Ornstein–Uhlenbeck spectrum of Eq. (5.58a) and the Eq. (7.37) experimental spectrum calculated from the Fourier transform of the numerical simulation. However, at higher frequencies, the simulation spectra overestimate the theoretical result, particularly when the macrocolumn is predicted to have a relatively flat spectral response (e.g., $\lambda = 0.3$ and $\lambda = 1.0$ on the top branch: see Figs 7.9(a),(b)). Agreement at high frequencies is more convincing in those cases for which the macrocolumn is predicted to have a strongly low-pass filtering characteristic (Figs 7.9(c)–(f)).

When we first reported these results [see Fig. 5 of Steyn-Ross *et al.* (2001b)], we asserted that these high-frequency spectral discrepancies between theory and experiment are an inevitable

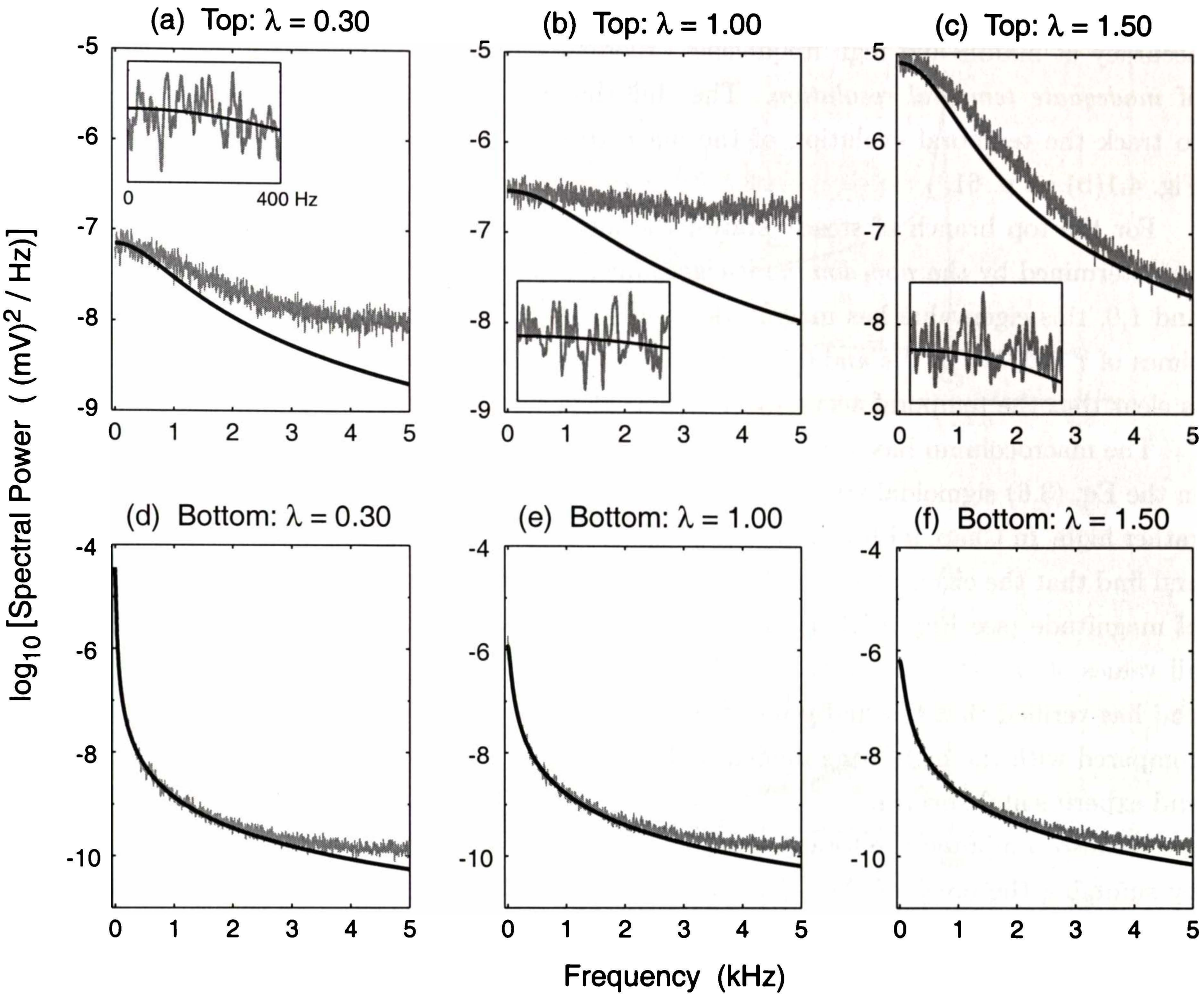

Figure 7.9: Comparison of theoretical fluctuation spectra (black curves) with stochastic simulation spectra (gray curves) for the adiabatic equations. (Time-step and noise scale-factor as for Fig. 7.6.) Simulation graphs were computed as the averaged spectra for 10 1-s time-series segments (10,000 samples per segment) which were then smoothed with a 5-point moving-average filter. Plots (a)–(c) are fluctuation spectra for three representative anaesthetic values on the top (high-firing) branch; plots (d)–(f) are the corresponding spectra for the bottom (low-firing, quiescent) branch. At low frequencies, agreement between theory and simulation is excellent (see inset graphs for 0–400-Hz detail in (a)–(c)). At higher frequencies, simulation spectra become inaccurate. Spectral accuracy improves when the macrocolumn has a strong low-pass filtering characteristic (e.g., bottom branch: (d)–(f), and top branch near transition: (c)), but degrades when the macrocolumn frequency response is relatively flat. [Adiabatic time-series abstracted from Wilcocks (2001)]

aliasing artifact arising from the fact that the macrocolumn is being driven by unfiltered white noise, so the only "antialiasing protection" in the sampled pseudo-EEG time-series is that provided by the low-pass filtering characteristic of the macrocolumn itself. Indeed, the discrepancy of 0.3 (on the base-10 logarithmic power scale) that we see in Figs 7.9(d)–(f) at the $f_{\mathrm{Ny}} = 5000$-Hz Nyquist frequency limit corresponds to the anticipated *spurious power-doubling* arising from a first-order "folding" of the spectrum about the Nyquist limit. This effect was illustrated (as an rms *amplitude* error of $\times\sqrt{2}$) in Fig. 7.4 (p. 133).

But the spectral errors apparent in Figs 7.9(a),(b) are far too severe to be explained away as aliasing artifact. A plausible explanation suggests itself when we observe how similar are the patterns of spectral ruination evident both here in Figs 7.9(a),(b) and seen previously in

Fig. 7.5: fair agreement with theory at low frequencies, but flattened spectrum with degraded accuracy at middle and high frequencies. Evidently these ruinations are one of the signatures of *inadequate temporal resolution.* The clue that our quadrature time-stepping is too coarse to track the temporal evolution of the macrocolumn is provided by the eigenvalues graph of Fig. 4.1(b) on p. 61.

For the top branch of steady states, the high-frequency response of the macrocolumn will be determined by the *non-dominant* eigenvalue,[6] since it has the larger magnitude. At $\lambda = 0.3$ and 1.0, this eigenvalue has magnitude 5836 s^{-1} and 14,240 s^{-1} respectively, giving $1/e$ decay times of $\tau = 1.7 \times 10^{-4}$ s and 0.7×10^{-4} s. With our time-step setting of $\Delta t = 1.0 \times 10^{-4}$ s, it is clear that the temporal accuracy criterion $\Delta t \ll \tau$ has been violated.

The macrocolumn has a maximum neuronal firing rate, set by the S_e^{max} and S_i^{max} constants in the Eq. (3.6) sigmoidal transfer functions, of 1000 s^{-1} (see Table 3.1). This is physiologically rather high. In Chap. 9 I investigate the impact of lowering this saturation firing rate to 100 s^{-1}, and find that the eigenvalues for the low-firing-rate macrocolumn are lowered by about an order of magnitude (see Fig. 9.7(b)), indicating that a time-step of $\Delta t = 10^{-4}$ s should be safe for all values of anaesthetic effect. L. Wilcocks (2001) has run numerical simulations for this case, and has verified that the half-power frequency is also reduced by about an order of magnitude compared with the high-firing model, with consequent improved agreement between theoretical and experimental spectra.

We also computed the total fluctuation power in the range dc to 5000 Hz and dc to 400 Hz by summing the areas of the 1-Hz histogram bins. The comparisons between simulation and prediction are shown in Fig. 7.10. The biphasic power peaks demarcating the induction and emergence transition points are of similar magnitude for both frequency bands, indicating that most of the fluctuation power near transition resides in the lower frequencies. We observe that the agreement between simulation and theory is excellent for the 0–400 Hz band (Fig. 7.10b), but degraded for 0–5000 Hz band (Fig. 7.10(a)) for the upper branch where temporal undersampling errors are likely to be most apparent.

The band-limited total-power curves of Fig. 7.10(a) can be cross-checked against the predicted $\delta h_e(t)$ rms fluctuation amplitudes of Fig. 5.3(a) on p. 80. Both graphs show an intersection between the induction (top-branch) and emergence (bottom-branch) traces (implying equal fluctuation activity in the active and quiescent states) at $\lambda \approx 0.5$. For the top branch at $\lambda = 1$, Fig. 5.3(a) predicts an rms amplitude of $\delta h_e \approx 0.032$ mV, implying a fluctuation power level [in $(\text{mV})^2$] of $\log_{10}(0.032^2) = -3.0$. As expected, this is larger than, but not too dissimilar from, the area under the $\lambda = 1$ band-limited (0–5000-Hz) waterfall slice.

7.5.2 Spectrum for Non-Adiabatic Simulations

As mentioned earlier, numerical simulations of the full 14-equation model (Eqs A.2–A.14) showed that the non-adiabatic macrocolumn becomes unstable along the upper branch for $\lambda > 1.3$. Unlike the adiabatic case, small soma-voltage fluctuations about the upper-branch steady state would evolve into a ~10-Hz oscillation whose amplitude would grow inexorably until the macrocolumn collapsed "early" to the low-firing-rate lower branch, whereupon the oscillations would

---

[6] The *dominant* eigenvalue determines the stability of a given equilibrium point. See p. 60 for a definition.

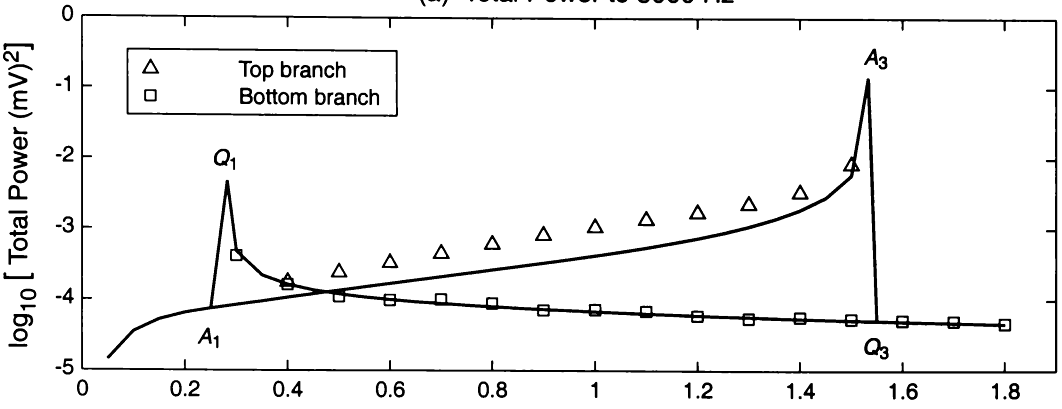

(a) Total Power to 5000 Hz

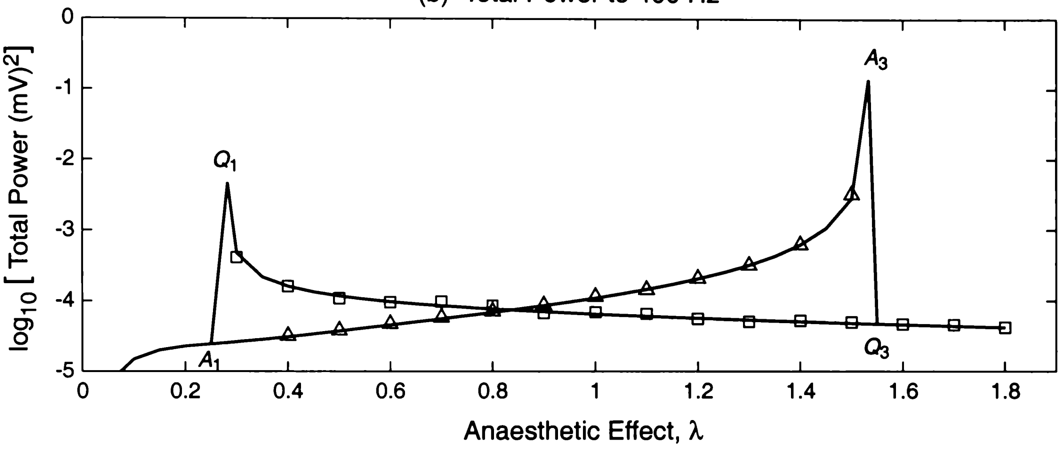

(b) Total Power to 400 Hz

Figure 7.10: Total fluctuation power (a) to 5000 Hz, (b) to 400 Hz for the macrocolumn as a function of anaesthetic effect; solid lines: theoretical prediction; points: simulation results. Curves show the predicted trends in fluctuation power computed from the area under the theoretical spectral density curves of Fig. 5.7. Points are obtained from the power spectra of the pseudo-EEG $h(t)$ time-series generated by numerical simulation of the adiabatic equations (timestep $\Delta t = 10^{-4}$ s; noise scale-factor $\alpha = 0.1$). Total power was estimated by summing into 1-Hz bins the area under the power spectral density curves from 0–5000 Hz (a) and 0–400 Hz (b). [Simulation data points from Wilcocks (2001)]

vanish. It is therefore not possible to define a steady-state fluctuation spectrum for the $\lambda > 1.3$ regime using the full equations, since the deterministic growth completely swamps the stochastic behaviour.

7.6 Chapter Summary

The Ornstein–Uhlenbeck (OU) velocity process for a Brownian particle provided a calibration test-bed for proving the quadrature techniques to be applied to the stochastic equations of motion for the macrocolumn. These preliminary calibration experiments provided the following guidance:

- the time-step Δt should be small compared with the relaxation time of the drift; if the time-step is not small, then the Euler update rule will give inaccurate time-series and ruined spectral estimates;

- a white-noise infinite-variance Wiener process can be simulated accurately using appropriately scaled Gaussian-distributed unit-variance random numbers (this is the Murthy (1983) scheme of Eq. (7.14));
- application of a Hanning window to a stochastic time-series improves the accuracy of its spectrum *if* the process is still evolving towards steady state; once the process has settled, the window has negligible effect on the spectrum, but its continued use is probably good signal-processing practice;
- to obtain the correct magnitude and dimension for spectral intensity, the mod-square of an N-point DFT of a time-series should be scaled by $\Delta t/N$ (see Eq. (2.12)), or by $\Delta t/||\mathbf{W}||^2$ if a window function W has been applied (Eq. (2.15));
- the DFT spectrum will exhibit a spurious power doubling, relative to theoretical OU prediction, at the Nyquist frequency—this is a predictable (see Fig. 7.4) and (apparently) unavoidable aliasing artifact in any unfiltered white-noise-driven numerical simulation.

Applying these lessons to the macrocolumn model of the cerebral cortex, we were able to demonstrate numerically that—

- the mid-branch set of steady states for the *adiabatic* macrocolumn is unstable, and the upper and lower branches are stable (Fig. 7.6);
- the full *non-adiabatic* macrocolumn has similar stability characteristics, except that the upper branch becomes dynamically unstable for $\lambda \gtrsim 1.3$, causing the macrocolumn to collapse to quiescence "early" (Fig. 7.7);
- the adiabatic macrocolumn exhibits a dramatic increase in fluctuation power on approach to the A_3 critical point on the upper branch (Fig. 7.8);
- after allowance has been made for aliasing and temporal undersampling errors, the simulation-derived fluctuation spectra show the expected and pronounced redistribution of spectral energy towards zero-frequency as the A_3 (induction: Fig. 7.9(c)) and Q_1 (emergence: Fig. 7.9(d)) change-of-phase points are approached.

We now turn our attention to the time-correlation properties of the fluctuations about macrocolumn steady state. We seek to examine and quantify the inverse relationship between correlation time and frequency distribution.

Chapter 8

Spectral Entropy and Correlation Time

The state of disorder of a system is naturally expressed in terms of its *entropy* which gives a measure of the *availability* of accessible states. For the cerebral cortex there are many candidate entropies which could be used. The three entropies I choose to discuss here are thermodynamic, statistical, and spectral. In the section which follows I will present a brief overview of these three entropies in order to establish the relative utility of each measure. This will be followed by a more detailed discussion of the properties of spectral entropy, both for discrete and continuous functions of frequency. I will demonstrate that the standard sampled-frequency definition for spectral entropy does *not* pass over to the expected continuous-frequency result in the limit of an infinitesimal frequency step, i.e., in the limit $\Delta\omega \to d\omega$. However, the continuous-domain result *can* be recovered provided an appropriate correction to the discrete-frequency formula is made. This finding is significant because it permits one to make meaningful intercomparisons of spectral entropy measurements for clinical EEG reported by different research groups.

I will then investigate the application of spectral entropy to the adiabatic macrocolumn model, and examine how the model predictions compare against clinical results for patient EEG reported by colleagues in Finland. The chapter concludes by establishing a quantitative inverse link between spectral entropy, a relatively modern concept, and correlation time, a fundamental concept used to quantify temporal order in fluctuating systems.

8.1 Entropies for the Macrocolumn

8.1.1 Excitability Entropy

An implicit assumption in the present work is that the model behaviour of a single macrocolumn of $\sim 10^5$ cooperating neurons can serve as a proxy for the bulk behaviour of the $\sim 10^6$ macrocolumns comprising the $\sim 10^{11}$ neuron population of the cortex. This "one speaks for all" macrocolumn picture is probably not too unreasonable when applied to the task of characterizing the gross changes which occur when there is a massive switchover in cortical function from active-consciousness to comatose-unconsciousness. After all, these gross changes can be, and routinely are, detected using a single EEG electrode which is only sampling $\sim 1\%$ of the total macrocolumn population. In Ch. 6 I described how, once a feasible mapping between anaesthetic effect and "temperature" has been established, it is possible to use the language and concepts of thermodynamics to quantify this gross change in state in terms of a "cortical entropy" defined as the negative rate of change of macrocolumn free energy with respect to its excitability,

$$H_\Theta = -\frac{dV}{d\Theta} \qquad \text{(cortical excitability entropy).} \qquad (8.1)$$

8.1.2 Microstate Entropy

Another means for quantifying the state of orderliness of the cortex would be to use statistical mechanics to define an entropy H_Ω in terms of Ω, the statistical weight of the macrostate (i.e., the number of *micro*states equivalent to the given macrostate),

$$H_\Omega = k_B \log_e \Omega\,, \qquad \text{(microstate entropy)} \qquad (8.2)$$

where k_B is Boltzmann's constant. H_Ω is a measure of the availability or spread of the microstates, indicating their degree of randomness or disorder. For the macrocolumn picture, a microstate is one particular depolarized/hyperpolarized electrical configuration of the 10^5 neurons within the macrocolumn. The weight for this microstate would be the number of distinct voltage configurations of the 10^5 excitatory and inhibitory neurons, whose net effect, when summed over the whole macrocolumn, is to produce a given excitatory and inhibitory (λ, h_e, h_i) voltage "coordinate." The equilibrium state for a given value of GABA anaesthetic effect λ would then be that state which maximizes the number of available microstates.

Our model has no detailed knowledge of the state of its constituent neurons, so cannot be used to count microstates (except perhaps for the fully-hyperpolarized state of extreme coma: in this case all neurons are assumed to be in the same zero-firing state at -90 mV, giving a microstate count of unity). Clinical measurements of scalp-detected EEG are also unable to reveal microscopic details of the individual neuron states. This is because the recordings are the summation of the electrical activity of the several hundred macrocolumns in the vicinity of the electrode: all internal microstate structure has been irretrievably blurred out by the spatial and temporal averaging.

8.1.3 Internal Physics from External Measures?

Despite the fact that knowledge of the internal microstate structure is unavailable to us, our simple macrocolumn model has demonstrated considerable utility with respect to the anaesthetic transition: it predicts the "biphasic" power peak and the sudden loss of higher frequency components in the EEG spectrum, and predicts a "latent heat" effect in which cortical energy requirements will be dramatically lowered during transition. This predictive utility suggests that the model equations provide a not unreasonable coarse-grained picture of the bulk behaviour of the anaestheto-dynamic phase transition.

This leads us to ask: Can the model be used to infer some of the internal physics of the brain from the external EEG signal? Specifically, can we uncover and quantify the link between the externally-measurable EEG *spectral* entropy (defined below) and the internal state of disorder of the cerebral cortex during the transition into unconsciousness?

That there is a link between EEG and brain-state is well established. For example, Steriade *et al.* (1993) observe:

> "The rapid patterns characteristic of the aroused state are replaced by low-frequency, synchronized rhythms of neuronal activity when the brain falls asleep"

so the unconscious brain has a relatively simple EEG spectrum, whereas the spectrum for the conscious brain is noisier and more complex.

8.1.4 Shannon Information and Spectral Entropy

Following recent work by Rezek and Roberts (1998) and Quiroga *et al.* (2000), EEG complexity can be quantified by applying to the computed EEG frequency spectrum the Shannon (Shannon and Weaver, 1949)[1] definition for discrete *information entropy* H_I

$$H_\text{I} = -\sum_{i=1}^{N} p_i \ln p_i \qquad \text{(Shannon information entropy).} \qquad (8.3)$$

In the Shannon formula, p_i is the probability that a communication channel is in cell i of its phase space, and H_I is the entropy of its set of probabilities $p_1, p_2, \ldots, p_N$. H_I is maximized when every cell is equally likely with $p_1 = p_2 = \ldots = \frac{1}{N}$. (The leading minus sign ensures that the entropy is always positive: each of the $\ln p_i$ terms is negative.)

In a similar vein, given a set of *spectral* probabilities (derived from a histogrammed power spectrum), one can compute an entropy for the distribution of spectral power. If over the range of sampled frequencies the spectrum is "flat" with all frequency bins equally populated, then the spectral entropy will be maximized. Conversely, if the spectrum is "rough" (e.g., has resonance peaks, or follows a power-law decay $\sim 1/f^n$), then the spectral entropy will be diminished.

Our phase-transition model for the cortex suggests that cortical entropy H_Θ will be smaller in the hyperpolarized (unconscious) state. Since the cortex will have fewer microstates available to it in this well-ordered state, its firing behaviour and resulting EEG spectrum should be relatively simple, so it is reasonable to expect that spectral entropy should also be smaller in the unconscious state. In the more complex, relatively disordered, active state, both kinds of entropy should be larger. So changes in the measured spectral entropy should track changes in the internal thermodynamic entropy, thereby providing an external measure of the internal state of the cortex.

We now examine how the Shannon information entropy is generalized to define an entropy for spectral power, and in the process uncover an important, and apparently overlooked, subtlety in the application of the discrete Shannon formula to the continuous-frequency case of EEG signals.

8.2 Properties of Spectral Entropy

8.2.1 Shannon Form of Spectral Entropy

In order to use the Shannon definition of Eq. (8.3) to calculate the entropy of a continuous power spectrum $S(\omega)$, the continuous-frequency distribution must be approximated by a histogram obtained by sampling $S(\omega)$ at N discrete frequencies $\omega_i = i\Delta\omega$, $i = 1, 2, \ldots, N$. Figure 8.1

---

[1] Shannon's classic 1949 paper "A mathematical theory of communication" is conveniently accessed in a recently published volume of his collected papers edited by Sloane and Wyner (1993).

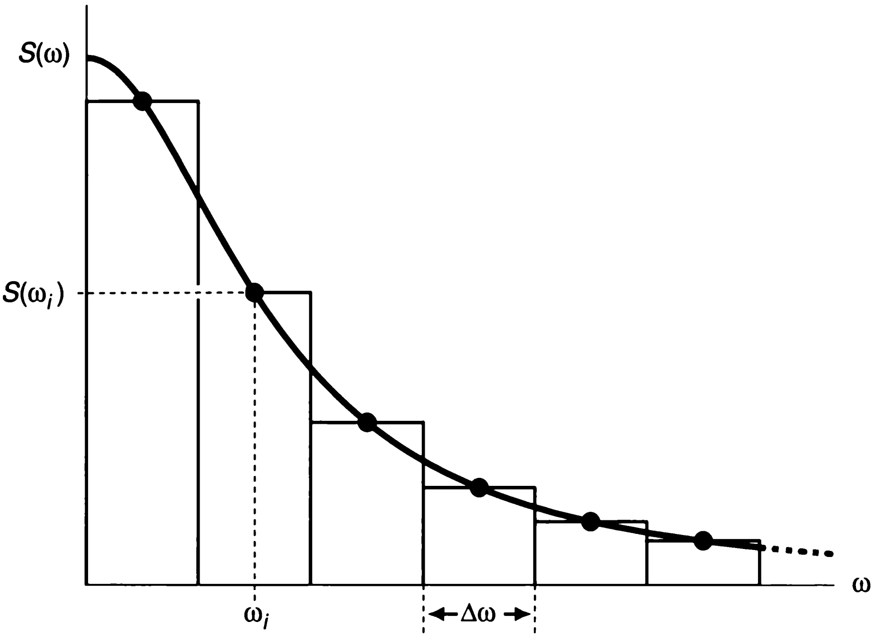

Figure 8.1: Histogram approximation to a continuous-frequency spectrum. The spectrum $S(\omega)$ is sampled at discrete frequencies ω_i with a sampling resolution (histogram binwidth) of $\Delta\omega$.

illustrates the procedure. We assume that the frequency resolution $\Delta\omega$ is fine enough to give reasonable fidelity. The relative height of each histogram bin provides the distribution of discrete spectral probabilities p_i,

$$p_i = \frac{S(\omega_i)}{\sum_{j=1}^{N} S(\omega_j)} \qquad \text{where} \qquad \sum_{i=1}^{N} p_i = 1\,. \tag{8.4}$$

Unfortunately we discover that the naive replacement of a continuous frequency function $S(\omega)$ by its histogram samples $S(\omega_i)$ produces *incorrect* entropy results. This is because a $\Delta\omega \to 0$ limiting value for information entropy *does not exist*: taking ever finer frequency samples improves the spectral resolution but gives a spectral entropy which grows monotonically with the number of samples, so does not converge. For example, consider an N-sample spectrum that is perfectly flat over the region of interest, and that therefore has maximal entropy. For such a band-limited white spectrum, the N bin-probabilities are equal,

$$p_i = \frac{1}{N}, \qquad i = 1, 2, \ldots, N \tag{8.5}$$

giving a discrete spectral entropy of

$$\begin{aligned} H_1 &= -\left(p_1 \ln p_1 + p_2 \ln p_2 + \ldots + p_N \ln p_N\right) \\ &= -\left(\tfrac{1}{N} \ln \tfrac{1}{N} + \tfrac{1}{N} \ln \tfrac{1}{N} + \ldots + \tfrac{1}{N} \ln \tfrac{1}{N}\right) \\ &= -\ln \tfrac{1}{N} \\ &= \ln N \end{aligned} \tag{8.6}$$

which increases without limit as $N \to \infty$. This result suggests the replacement of Eq. (8.3) with a normalized form,

$$H_1^{\mathrm{norm}} = -\frac{1}{\ln N}\sum_{i=1}^{N} p_i \ln p_i \qquad \text{(normalized discrete entropy)} \tag{8.7}$$

that is guaranteed to have a value in the range $[0, 1]$. However, this revised definition is also unsatisfactory, since *any* reasonable spectrum, no matter how non-uniform, will, in the $N \to \infty$ limit, tend to an entropy value of unity. I will demonstrate this later for the case of a band-limited Lorentzian spectrum.

8.2.2 Histogram Spectral Entropy

While Eqs (8.3) and (8.7) are correct representations for the entropy of a distribution which is truly discrete, what we require is a form which retrieves an accurate estimate of the entropy of the *underlying continuous spectrum* from which the discrete spectral samples were drawn.

We assume that the underlying spectrum $S(\omega)$ is upper-band limited to some maximum frequency $\omega_{\lim}$, i.e., $S(\omega) = 0$ for $\omega > \omega_{\lim}$. Let $s(\omega)$ be the PDF (probability density function) of $S(\omega)$, where $0 \leq \omega \leq \omega_{\lim}$, then

$$\int_0^{\omega_{\lim}} s(\omega)\, d\omega = 1\,. \tag{8.8}$$

The spectral entropy for the continuous $S(\omega)$ will be given by the integral

$$H_\omega = -\int_0^{\omega_{\lim}} s(\omega) \ln s(\omega)\, d\omega \qquad \text{(continuous spectral entropy).} \tag{8.9}$$

From the $s(\omega)$ density function we construct a histogram of binwidth $\Delta\omega$ using the set of PDF spectral samples s_i. We require the histogram to have unit area, so

$$\sum_{i=1}^{N} s_i\, \Delta\omega = 1 \tag{8.10}$$

and the entropy for the area-normalized histogram will be

$$H_2 = -\Delta\omega \sum_{i=1}^{N} s_i \ln s_i \qquad \text{(histogram spectral entropy)} \tag{8.11}$$

where $N\Delta\omega = \omega_{\lim}$. Unlike the H_1 discrete entropy of Eq. (8.3), the histogram entropy H_2 has the desired property of converging to the "true" H value in the limit as $N \to \infty$ and $\Delta\omega \to 0$. Thus H_2 is an *unbiased estimator* for H_ω. This assertion will be demonstrated in Sect. 8.4.

8.2.3 Linking Histogram Entropy to Shannon Information

What is the link between histogram entropy H_2 and information entropy H_1? Comparing the unit-summation equations (8.4) and (8.10) gives

$$1 = \sum_{i=1}^{N} p_i = \sum_{i=1}^{N} s_i\, \Delta\omega \tag{8.12}$$

so

$$s_i = \frac{p_i}{\Delta\omega}\,. \tag{8.13}$$

Substituting this result in Eq. (8.11) provides the linking relationship,

$$\begin{aligned} H_2 &= -\sum_{i=1}^{N} \frac{p_i}{\Delta\omega} \ln\left(\frac{p_i}{\Delta\omega}\right) \Delta\omega \\ &= -\sum p_i \ln p_i + \sum p_i \ln \Delta\omega \\ &= H_1 + \ln \Delta\omega\,. \end{aligned} \tag{8.14}$$

Thus H_1 and H_2 are identical only in the special case $\Delta\omega = 1$. Rearranging,

$$H_1 = H_2 - \ln \Delta\omega \tag{8.15}$$

so as $\Delta\omega \to 0$, H_1 will overestimate H_2, with the discrepency growing to infinity as $\ln\left(\frac{1}{\Delta\omega}\right)$. In view of this inherent $\Delta\omega$-dependent bias, the discrete information entropy H_1 is *not* a useful measure of the spectral flatness of continuous-frequency signals such as EEG. Instead, the histogram entropy H_2 should be used since it provides an unbiased estimate of the underlying continuous spectral entropy H_ω.

8.2.4 Normalizations for Spectral Entropy

It is convenient to normalize H_ω and H_2 so that they return maximum values of unity for an ideal band-limited flat spectrum. From Eq. (8.8), such a spectrum has the rectangular PDF

$$\begin{aligned} s(\omega) &= \frac{1}{\omega_{\text{lim}}}\,, && 0 \le \omega \le \omega_{\text{lim}} \\ &= 0\,, && \text{otherwise} \end{aligned} \tag{8.16}$$

giving a two-level block histogram

$$\begin{aligned} s_i &= \frac{1}{N\Delta\omega}\,, && 1 \le i \le N \\ &= 0\,, && i > N\,. \end{aligned} \tag{8.17}$$

Substitututing these probability distributions into Eqs (8.9) and (8.11), we obtain expressions for the spectral entropy upper bounds,

$$H_\omega^{\max} = -\int_0^{\omega_{\text{lim}}} \frac{1}{\omega_{\text{lim}}} \ln\left[\frac{1}{\omega_{\text{lim}}}\right] d\omega = \ln \omega_{\text{lim}} \tag{8.18}$$

and

$$H_2^{\max} = -\sum_{i=1}^{N} \frac{1}{N\Delta\omega} \ln\left[\frac{1}{N\Delta\omega}\right] \Delta\omega = \ln\left[N\Delta\omega\right] \tag{8.19}$$

and hence the final equations for spectral entropy, normalized with respect to an upperband-limited flat spectrum, are

$$H_\omega^{\text{norm}} = \frac{H_\omega}{H_\omega^{\max}} = -\frac{1}{\ln \omega_{\text{lim}}} \int_0^{\omega_{\text{lim}}} s(\omega)\ \ln\ s(\omega)\, d\omega \tag{8.20a}$$

(normalized continuous entropy)

where

$$s(\omega) = \frac{S(\omega)}{\int_0^{\omega_{\text{lim}}} S(\omega)\, d\omega} \tag{8.20b}$$

and

$$H_2^{\text{norm}} = \frac{H_2}{H_2^{\max}} = -\frac{\Delta\omega}{\ln\,[N\Delta\omega]} \sum_{i=1}^{N} s_i \ln s_i \tag{8.21a}$$

(normalized histogram entropy)

where

$$s_i = \frac{S_i}{\Delta\omega \sum S_i}\,. \tag{8.21b}$$

It is interesting to recognize that for any sufficiently jagged spectrum, both histogrammed and continuous entropies can return *negative* results, unlike the discrete entropy H_1 which can never be smaller than zero. Since $H_2 = H_1 + \ln \Delta\omega$ (Eq. 8.14), a negative H_2 entropy will occur whenever the spectral resolution $\Delta\omega$ is sufficiently fine that its logarithm "swamps" the positive H_1 information entropy, i.e.,

$$\Delta\omega < \exp(-H_1) \quad \Longrightarrow \quad H_2 < 0\,. \tag{8.22}$$

Table 8.1 summarizes the three kinds of spectral entropy discussed in this chapter.

8.3 Spectral Entropy for Lorentzian and Gaussian Distributions

8.3.1 Lorentzian Distribution

I will now derive the entropy of a Lorentzian spectral distribution. The continuous-frequency Lorentzian is of particular relevance to any white-noise-driven system—such as our adiabatic macrocolumn—which can be modelled as a Brownian or diffusive process. As well as being of theoretical interest, this continuous-frequency result provides an ideal test-bed against which

Table 8.1: Summary of discrete and continuous spectral entropies. All summations assume N samples indexed from 1 (i.e., $\sum_{i=1}^{N}$) at frequency spacing $\Delta\omega$ up to maximum frequency $\omega_{\text{lim}} = N\Delta\omega$. The continuous entropy is defined over the band-limited frequency domain $0 \le \omega \le \omega_{\text{lim}}$ via integrals of the form $\int_0^{\omega_{\text{lim}}} \ldots d\omega$.

Name	Definition	PDF	Normalized Entropy
Shannon information	$H_1 = -\sum p_i \ln p_i$	$p_i = \frac{S(\omega_i)}{\sum S(\omega_i)}$	$H_1^{\text{norm}} = \frac{H_1}{\ln N}$
Histogram entropy	$H_2 = -\Delta\omega \sum s_i \ln s_i$	$s_i = \frac{S_i}{\Delta\omega \sum S_i}$	$H_2^{\text{norm}} = \frac{H_2}{\ln[N\Delta\omega]}$
Continuous-frequency entropy	$H_\omega = -\int s(\omega) \ln s(\omega)\, d\omega$	$s(\omega) = \frac{S(\omega)}{\int S(\omega)\, d\omega}$	$H_\omega^{\text{norm}} = \frac{H_\omega}{\ln \omega_{\text{lim}}}$

the predicted properties of the discrete H_1 and H_2 spectral entropy estimators can verified. For example, using this theoretical result we will be able to demonstrate that the H_2 discrete entropy provides an unbiased estimate of H_ω continous entropy.

Consider the prototypical single-sided Lorentzian spectrum

$$\begin{aligned} S(\omega) &= \frac{1}{k^2+\omega^2}, \qquad 0 \le \omega < \infty \\ &= 0, \qquad \text{otherwise} \end{aligned} \tag{8.23}$$

whose decay-rate k sets the half-power or -3-dB frequency. Following Eq. (8.20b) with $\omega_{\lim} \to \infty$, we convert the spectrum to a probability density function (PDF) by normalizing with respect to total spectral area

$$s(\omega) = \frac{S(\omega)}{\int_0^\infty S(\omega)\,d\omega}. \tag{8.24}$$

The area for the Lorentzian distribution is

$$\int_0^\infty S(\omega)\,d\omega = \int_0^\infty \frac{d\omega}{k^2+\omega^2} = \frac{1}{k}\tan^{-1}\left(\frac{\omega}{k}\right)\Big|_0^\infty = \frac{\pi}{2k} \tag{8.25}$$

giving the Lorentzian PDF

$$s(\omega) = \frac{2k}{\pi}\frac{1}{k^2+\omega^2}. \tag{8.26}$$

The continuous spectral entropy H_ω is obtained by evaluating the negative of the expectation value of $\ln s(\omega)$:

$$\begin{aligned} H_\omega &= -\int_0^\infty s(\omega)\,\ln s(\omega)\,d\omega \\ &= -\int_0^\infty \frac{2k}{\pi}\frac{1}{k^2+\omega^2}\ln\left[\frac{2k}{\pi}\frac{1}{k^2+\omega^2}\right]d\omega \\ &= -\frac{2k}{\pi}\left\{\ln\left[\frac{2k}{\pi}\right]\int_0^\infty \frac{d\omega}{k^2+\omega^2} - \int_0^\infty \frac{\ln\left[k^2+\omega^2\right]}{k^2+\omega^2}\,d\omega\right\} \\ &= -\frac{2k}{\pi}\left\{\frac{\pi}{2k}\ln\left[\frac{2k}{\pi}\right] - I_1\right\}. \end{aligned} \tag{8.27}$$

The value of the definite integral I_1 is tabulated [see formula 4.295.7 on p.560 of Gradshteyn and Ryzhik (1965)[2]]:

$$I_1 = \frac{\pi}{k}\ln 2k, \tag{8.28}$$

thus enabling us to write the spectral entropy H_ω for the continuous Lorentzian spectrum in a simple and elegant closed form which depends only on k, the Lorentzian decay-rate:

---

[2] The tabulated integral reads:

$$\int_0^\infty \ln\left(a^2+b^2x^2\right)\cdot\frac{1}{c^2+g^2x^2}\,dx = \frac{\pi}{cg}\ln\left[\frac{ag+bc}{g}\right], \qquad a,b,c,g>0$$

which solves our integral when $b=g=1$ and $a=c=k$.

$$H_\omega = \ln(2\pi k) \qquad \text{(Lorentzian spectral entropy).} \tag{8.29}$$

Examining this result, we see that the Lorentzian spectral entropy H_ω exhibits the following limiting and scaling behaviours:

1. $H_\omega \to +\infty$ as $k \to \infty$. As decay-rate k increases, we approach the white-noise flat-spectrum limit in which energy is uniformly distributed over all frequencies, giving extreme maximum spectral entropy.
2. $H_\omega = 0$ when $k = 1/2\pi$. If the spectrum is sufficiently jagged, its entropy can be zero, and a more jagged spectrum will have a negative entropy. This possibility of a negative continuous entropy is quite unlike the behaviour of the discrete Shannon entropy of Eq. (8.3) which can never go negative.
3. $H_\omega \to -\infty$ as $k \to 0$. In this limit the Lorentzian distribution tends to the infinitely-peaked delta-function $\delta(\omega)$ which is zero everywhere except at zero frequency. For this delta-spike spectrum, spectral entropy reaches its extreme negative value.
4. The numerical value for spectral entropy is *frequency-scale dependent.* Consider the transformation of the prototypical Lorentzian of Eq. (8.23) from angular frequency ω [rad/s] to linear frequency f [Hz] via the change of variable $\omega = 2\pi f$. Then Eq. (8.23) is rewritten

$$\begin{aligned} S(f) &= \frac{1}{k^2 + (2\pi f)^2} \\ &= \frac{\frac{1}{4\pi^2}}{K^2 + f^2} \end{aligned} \tag{8.30}$$

where $K = k/2\pi$, leading to a revised spectral entropy H_f

$$H_f = \ln(2\pi K) = \ln k\,. \tag{8.31}$$

Comparing Eqs (8.29) and (8.31), we see that H_f is *smaller* than H_ω:

$$\begin{aligned} H_f &= \ln k \\ &= \ln(2\pi k) - \ln(2\pi) \\ &= H_\omega - \ln(2\pi)\,, \end{aligned} \tag{8.32}$$

a rather surprising result. It seems that the numerical value for spectral entropy depends on the choice of spectral unit [rad/s or Hz]. On reflection, this can be understood in terms of the relative size of the two units. The hertz is the larger unit, so when a given Lorentzian spectrum is graphed against a horizontal frequency scale expressed in Hz, the spectrum will decay more rapidly with respect to the numerical values on that scale, consequently the spectrum will be "less flat," giving a smaller entropy result. Still, this scale-dependence of the continuous spectral entropy is a little disconcerting.

Normalization for Lorentzian Spectral Entropy

Any real experiment involving a Lorentzian process will necessarily be band-limited to some upper limit frequency ω_{lim}. In principle we could determine the spectral entropy of a band-limited

Lorentzian by replacing ∞ by ω_{lim} in the integrals of Eqs (8.24) and (8.27), but unfortunately the resulting expression for H cannot be integrated analytically and must be computed numerically.

An alternative approach to band-limiting is to reference the entropy of the unlimited Lorentzian against the maximum entropy achievable on the band-limited domain $0 \leq \omega \leq \omega_{\text{lim}}$ as illustrated in Fig. 8.2. The reference is then the rectangular spectrum of Eq. (8.16) which is flat up to ω_{lim}, and zero beyond:

$$\begin{aligned} s^{\text{rect}} &= \frac{1}{\omega_{\text{lim}}}, \qquad 0 \leq \omega \leq \omega_{\text{lim}} \\ &= 0, \qquad \text{otherwise} \end{aligned} \tag{8.33}$$

and whose spectral entropy (from Eq. 8.18) H_ω^{rect} is,

$$H_\omega^{\text{rect}} = \ln \omega_{\text{lim}} . \tag{8.34}$$

Thus we may define a Lorentzian spectral entropy H_ω^{norm} which has been normalized with respect to a band-limited rectangular reference,

$$H_\omega^{\text{norm}} = \frac{H_\omega}{H_\omega^{\text{rect}}} = \frac{\ln(2\pi k)}{\ln \omega_{\text{lim}}} \qquad \text{(normalized Lorentzian entropy).} \tag{8.35}$$

With this normalization, $H_\omega^{\text{norm}} = 1$ when $k = \omega_{\text{lim}}/2\pi$, meaning that for this value of decay-rate k, the entropy of the open-ended Lorentzian matches that of a rectangular reference spectrum which is upper-band limited to ω_{lim}.

8.3.2 Gaussian Distribution

Is the simple Eq. (8.29) $H_\omega \propto \ln k$ relationship between spectral entropy and decay rate k unique to the Lorentzian distribution? It seems that the answer is *no*, since the Gaussian distribution also shares this property. Consider the single-sided Gaussian spectral distribution,

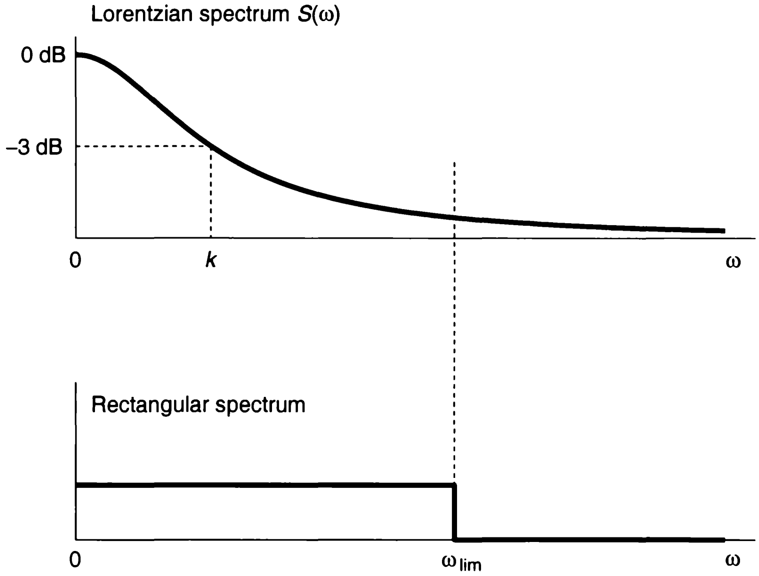

Figure 8.2: Establishing a rectangular reference for an open-ended Lorentzian spectrum $S(\omega) = 1/(k^2 + \omega^2)$; decay-rate constant k sets the half-power point. The entropy of a band-limited rectanglular spectrum can be used to normalize the entropy of the open-ended Lorentzian.

$$
\begin{aligned}
S(\omega) &= \exp\left[-\omega^2/2k^2\right], && 0 < \omega < \infty \\
&= 0, && \text{otherwise.}
\end{aligned}
\tag{8.36}
$$

The PDF for the one-sided Gaussian is

$$s(\omega) = \frac{e^{-\omega^2/2k^2}}{\mathcal{N}} \tag{8.37}$$

where the area normalization $\mathcal{N}$ is

$$\mathcal{N} = \int_0^\infty e^{-\omega^2/2k^2}\, d\omega = \tfrac{1}{2}\sqrt{2\pi}\, k\,. \tag{8.38}$$

which was obtained via an integral identity.[3] The spectral entropy for the half-Gaussian is then

$$
\begin{aligned}
H_\omega &= -\int_0^\infty s(\omega)\, \ln s(\omega)\, d\omega \\
&= -\int_0^\infty \frac{S(\omega)}{\mathcal{N}} \ln\left[\frac{S(\omega)}{\mathcal{N}}\right] d\omega \\
&= -\frac{1}{\mathcal{N}}\left\{\int_0^\infty S(\omega)\, \ln S(\omega)\, d\omega \;-\; \ln\mathcal{N}\int_0^\infty S(\omega)\, d\omega\right\} \\
&= -\frac{1}{\mathcal{N}}\left\{I_1 \;-\; \mathcal{N}\ln\mathcal{N}\right\}
\end{aligned}
\tag{8.39}
$$

where the integral I_1 is

$$I_1 = \int_0^\infty e^{-\omega^2/2k^2}\left(\frac{-\omega^2}{2k^2}\right) d\omega = -\frac{1}{2k^2}\int_0^\infty \omega^2\, e^{-\omega^2/2k^2}\, d\omega = -\frac{k}{4}\sqrt{2\pi} \tag{8.40}$$

and we have made use of a second exponential identity.[4] Substituting I_1 in Eq. (8.39) gives the result we seek,

$$
\begin{aligned}
H_\omega &= -\frac{I_1}{\mathcal{N}} + \ln\mathcal{N} \\
&= \tfrac{1}{2} + \ln\left[\tfrac{1}{2}\sqrt{2\pi}\, k\right] \\
&= \ln e^{1/2} + \ln\left[\tfrac{1}{2}\sqrt{2\pi}\, k\right] \\
&= \ln\left[\tfrac{1}{2}\sqrt{2\pi e}\, k\right] \qquad \text{(half-Gaussian spectral entropy).}
\end{aligned}
\tag{8.41}
$$

For completeness, I have also calculated the entropies for the *full* (i.e., double-sided) Gaussian and Lorentzian distributions; the results are summarized in Table 8.2. Because the double-sided distributions have even symmetry about zero frequency, there is a factor of two difference between the single- and double-sided area normalizations, and this comes through as a factor of two difference in the logarithm arguments for entropy (refer to last column of Table 8.2).

---

[3] Spiegel (1968), p.98, integral 15.72:

$$\int_0^\infty e^{-ax^2}\, dx = \frac{1}{2}\sqrt{\frac{\pi}{a}}$$

[4] Spiegel (1968), p.98, integral 15.77:

$$\int_0^\infty x^2\, e^{-ax^2}\, dx = \frac{\Gamma(\frac{3}{2})}{2a^{3/2}} = \frac{1}{4}\sqrt{\frac{\pi}{a^3}}$$

Table 8.2: Spectral entropy values for Lorentzian and Gaussian spectra. Here $\mathcal{N}$ is the area normalization, $\mathcal{N} = \int S(\omega)\, d\omega$, from which the spectral PDF is constructed: $s(\omega) = S(\omega)/\mathcal{N}$.

Spectral Shape	Domain	$\mathcal{N}$	Spectral Entropy
Half-Lorentzian	$[0, \infty)$	$\pi/2k$	$\ln(2\pi k)$
Lorentzian	$(-\infty, \infty)$	π/k	$\ln(4\pi k)$
Half-Gaussian	$[0, \infty)$	$\frac{1}{2}\sqrt{2\pi}\, k$	$\ln\left(\frac{1}{2}\sqrt{2\pi e}\, k\right)$
Gaussian	$(-\infty, \infty)$	$\sqrt{2\pi}\, k$	$\ln\left(\sqrt{2\pi e}\, k\right)$

It is instructive to compare the form of the PDF for the double-sided Gaussian spectrum drawn from Table 8.2

$$s(\omega) = \frac{1}{k\sqrt{2\pi}}\, e^{-\omega^2/2k^2} \tag{8.42}$$

with that of a standard Gaussian PDF $p(x)$ whose mean is zero and whose standard deviation is σ,

$$p(x) = \frac{1}{\sigma\sqrt{2\pi}}\, e^{-x^2/2\sigma^2}\,. \tag{8.43}$$

It becomes immediately clear that for the special case of the double-sided Gaussian spectrum, the decay-rate parameter k is identical to the standard deviation σ. So our $H_\omega \propto \ln k$ result permits the intuitively pleasing conclusion that the spectral entropy of a Gaussian spectrum is directly proportional to the logarithm of the standard deviation of the distribution. In fact, the Gaussian distribution is a significant limiting case since, of all possible PDFs, it is the one which, for a given standard deviation, has maximum entropy. This was proved by Shannon using the calculus of variations (Shannon and Weaver, 1949).

Figure 8.3 compares the Lorentzian and Gaussian double-sided spectral profiles. Relative to the Gaussian, the Lorentzian is peakier, yet decays to zero much more slowly—so has "heavier tails."

8.4 Numerical Verification of Spectral Entropy Properties

In this section I will verify numerically the claims made earlier regarding the theoretical properties of the three forms of spectral entropy: Shannon information, histogram entropy, and continuous-frequency entropy. In particular, I will demonstrate that histogram entropy H_2 provides an unbiased estimator for continuous-frequency entropy H_ω.

From the previous work we know that the spectral entropy of a Lorentzian spectrum is directly proportional to the logarithm of the decay constant k. Provided the spectrum is sampled sufficiently finely, i.e., provided $\Delta\omega$ is sufficiently small, we would expect that an unbiased discrete entropy measure should recover this underlying logarithmic relationship.

For the numerical experiments I chose a frequency range $0 \leq \omega \leq 1000$ rad/s, and computed the discrete entropies for a comprehensive set of Lorentzian spectra whose decay rates varied

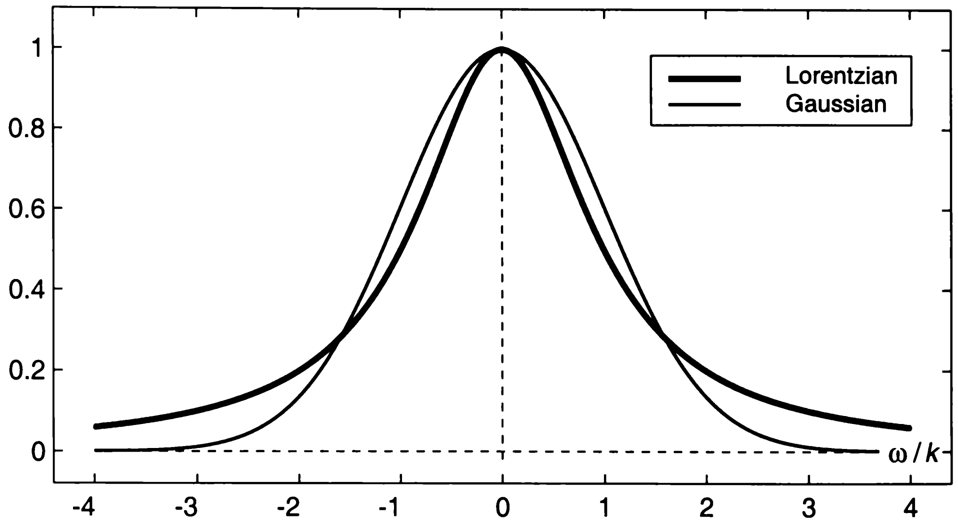

Figure 8.3: Comparison of Lorentzian and Gaussian spectral profiles. The Lorentzian profile is $S^{\mathrm{Lor}}(\omega) = k^2/(k^2+\omega^2)$, and the Gaussian is $S^{\mathrm{Gau}}(\omega) = \exp(-\omega^2/2k^2)$. For both distributions, the spectral entropy is logarithmically proportional to the decay constant: $H_\omega \propto \ln k$.

over $5\frac{1}{2}$ decades, from $k = 0.01$ rad/s, an extremely dc-peaked spectrum, to $k = 2560$ rad/s, a relatively flat spectrum. The effect of k variation is illustrated in Figure 8.4 where we see three sample spectra with successive k-values spaced at geometric intervals of ×16 (i.e., $k \in \{k_0, 16k_0, 16^2k_0\}$ with $k_0 = 5\ \mathrm{s}^{-1}$), covering a range in k of $\sim 2\frac{1}{2}$ decades.

For each single-sided, continuous Lorentzian curve, I sampled the spectrum at three different frequency resolutions, $\Delta\omega \in \{0.1, 1, 10\}$ rad/s, over the frequency range $0 \le \omega \le 1000$ rad/s,

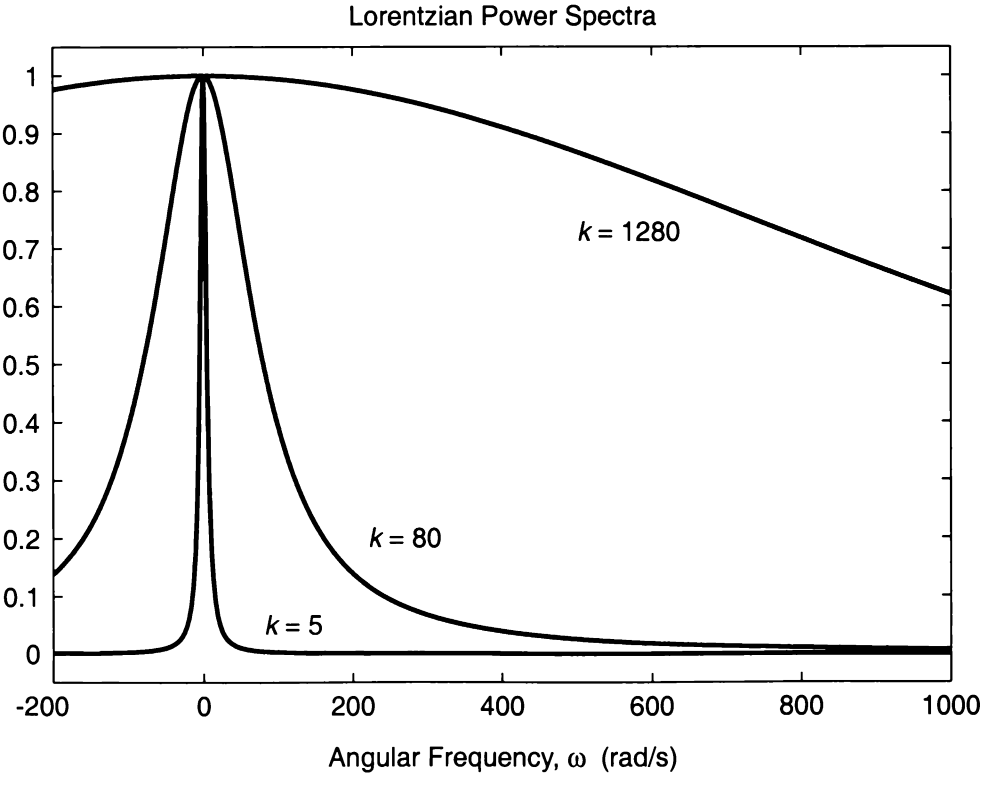

Figure 8.4: Three double-sided Lorentzian power spectra illustrating the influence of the k decay-rate constant.

and, for each resolution, computed the corresponding Shannon (H_1) and histogram (H_2) discrete entropies. These discrete values could then be compared with the continous entropy prediction $H_\omega = \ln(2\pi k)$. In all, a total of 19 spectra were assessed. The 19 k-values were chosen to be at octave intervals [$k/k_0 \in \{2^{-9}, 2^{-8}, 2^{-7}, \ldots, 2^{9}\}$ with $k_0 = 5\ \mathrm{s}^{-1}$] in order to give uniformly-spaced points when plotted on a logarithmic axis.

Figure 8.5(a) demonstrates that the magnitude of the H_1 Shannon entropy depends on the frequency resolution $\Delta\omega$. Only when $\Delta\omega = 1$ rad/s ($\triangle$ points) do the H_1 measurements line up with the H_ω prediction for continuous open-ended Lorentzian spectra (bold linear trend). For the coarser sampling of $\Delta\omega = 10$ rad/s ($\times$ points), the number of sample points per spectrum is reduced by a factor of 10, and the Shannon entropy reduces by $\ln 10 = 2.3026\ldots$, resulting in a downwards offset of these points relative to the $\Delta\omega = 1$ trend. If the sampling density is *increased* to $\Delta\omega = 0.1$ rad/s ($\circ$ points), the H_1 values *rise* by $\ln 10$. Thus it becomes apparent that Shannon information will grow without limit as the frequency resolution is made ever finer.

At the high-k end of the range, the discrete entropy curves of Fig. 8.5(a) deviate away from the expected $\ln(2\pi k)$ trend towards individual saturation plateaus. This is an unavoidable consequence of the fact that all sampled spectra are necessarily band-limited, in this case to an upper-frequency limit of $\omega_{\mathrm{lim}} = 1000$ rad/s (as plotted in Fig. 8.4). The bold line of constant slope is the (unachievable) theoretical ideal for an *open-ended* Lorentzian which goes on to infinite frequency, hence its $H_\omega(\infty)$ label. The curved trend-line labelled $H_\omega(\mathrm{lim})$ is the numerically-computed entropy graph for Lorentzian spectra which are abruptly truncated at (i.e., assumed to be zero beyond) the limiting frequency $\omega_{\mathrm{lim}} = 1000$ rad/s. It is reassuring to note that the $\Delta\omega = 1$ measurements ($\triangle$ points) accurately follow this curved trend-line.

At the low-k end of Fig. 8.5(a), the discrete entropy measurements "bottom-out" to a limiting value of zero, deviating away from the $H_\omega(\infty)$ line which inexorably approaches negative infinity as k goes to zero. This mismatch can be regarded as a sampling-fidelity error: the low-k spectra are so strongly dc-peaked that they become like $\delta(\omega)$ functions, and therefore can only be adequately represented if they are sampled very finely indeed. Note that of the three sampling intervals tested, the curve which exhibits the least low-k "distortion" is that which has the best sampling resolution ($\circ$ points: $\Delta\omega = 0.1$ rad/s).

Figure 8.5(b) demonstrates the effect of dividing the Shannon entropy measurements by a normalization factor $\ln N$, where $N = 1 + \omega_{\mathrm{lim}}/\Delta\omega$ is the number of spectral samples drawn from each spectrum. For the continuous entropy, the normalization is $\ln \omega_{\mathrm{lim}}$, so that $H_\omega^{\mathrm{norm}}(\infty) = 1$ when $\ln(2\pi k) = \ln \omega_{\mathrm{lim}}$, giving $k = 1000/2\pi$ and $\log_{10} k = 2.2018$ (see vertical dashed line drawn to the x-axis). Although the three sets of Shannon measurements are now constrained to lie in the interval $[0, 1]$, they no longer share the same mid-range gradient: in fact, the gradient *increases* with the number of sample points, and, in the limit $\Delta\omega \to 0$, the normalized Shannon entropy will converge unhelpfully to unity.

Figures 8.5(c) and (d) are the corresponding set of graphs for the H_2 histogrammed entropy. The vertical offsets apparent in Fig. 8.5(a) have disappeared in Fig. 8.5(c), and there is now excellent agreement between the discrete H_2 and continuous $H_\omega(\mathrm{lim})$ curves for the mid- and high-k range of spectra. The distortion arising from undersampling at the low-k extreme is still present, of course, but it is clear that the distortion is reduced as the sampling fidelity is improved. It is also apparent that the histogrammed entropy has the correct limiting behaviour: in the limit $\Delta\omega \to 0$, the underlying continuous entropy curve is recovered, demonstrating graphically that H_2 is an unbiased estimator for the (band-limited) H_ω.

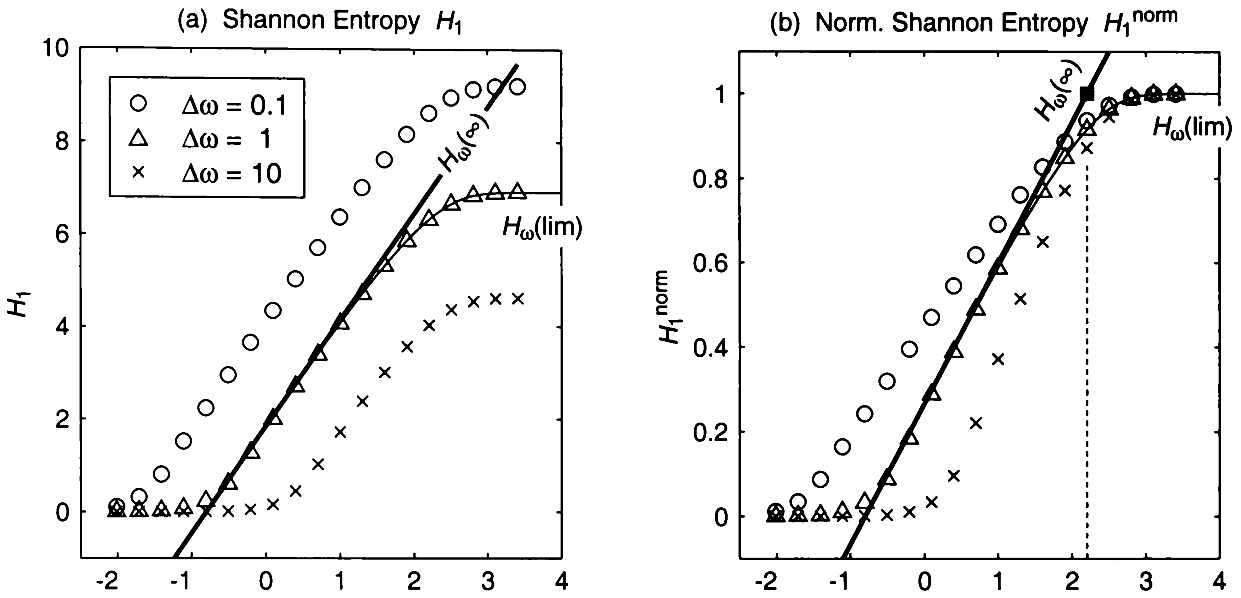
(a) Shannon Entropy H_1

(b) Norm. Shannon Entropy H_1^{norm}

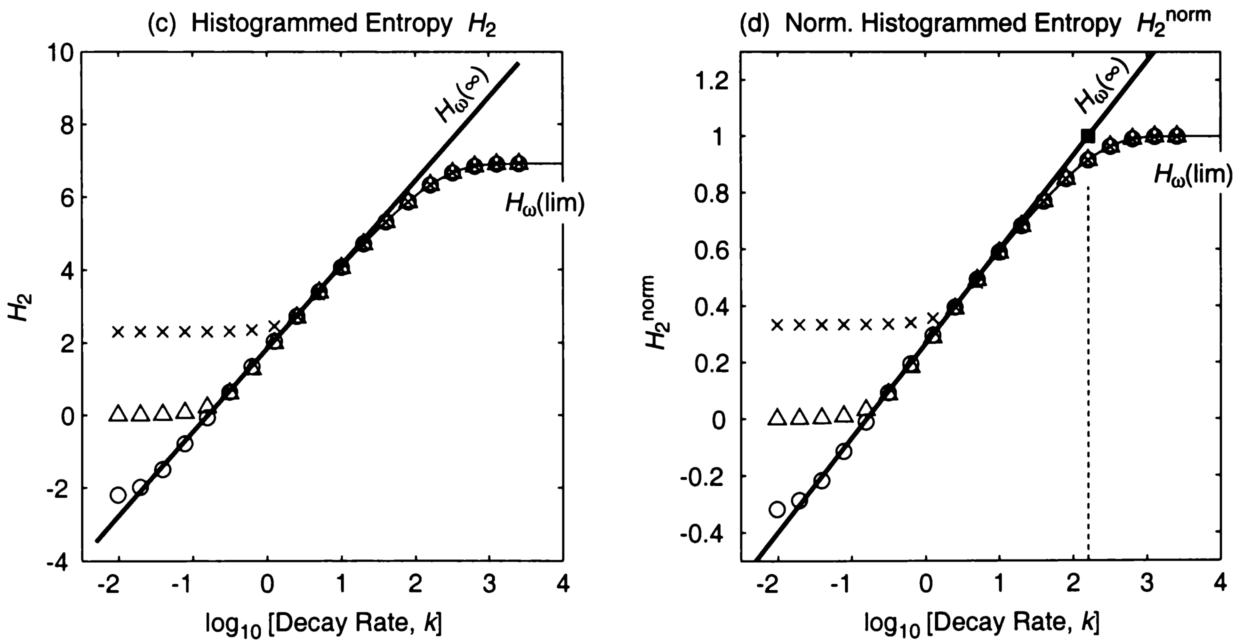
(c) Histogrammed Entropy H_2

(d) Norm. Histogrammed Entropy H_2^{norm}

Figure 8.5: Comparison of Shannon and histogrammed entropies for 19 Lorentzian spectra. The band-limited spectra, defined over the frequency range $0 \leq \omega \leq 1000$ rad/s, were sampled with three different frequency resolutions: $\Delta\omega = 10$ (×), 1 (△), and 0.1 rad/s (○). The bold straight line labelled $H_\omega(\infty)$ gives the theoretical open-ended continuous-frequency entropy $H_\omega = \ln 2\pi k$, and the non-bold curve labelled $H_\omega(\text{lim})$ gives the entropy for a Lorentzian which is truncated abruptly at frequency $\omega_{\text{lim}} = 1000$ rad/s. (a) Shannon entropy H_1 increases in absolute value as frequency resolution is made smaller, and does not recover the underlying continuous entropy except for the special case $\Delta\omega = 1$ rad/s. (b) Normalized Shannon entropy exhibits an increase in *gradient* as $\Delta\omega$ is made smaller. (c) Histogrammed entropy H_2 recovers the underlying H_ω entropy with improving fidelity as $\Delta\omega$ is made smaller. (d) The normalized histogram entropy H_2^{norm} is a well-behaved estimator of H_ω^{norm}. The point marked with a filled square (■) in (b) and (d) highlights the value of decay constant k at which the open-ended spectral entropy reaches a normalized value of unity.

This excellent limiting behaviour of the H_2 measure is in no way spoiled when we normalize it via a division by $\ln[N\Delta\omega]$ (Fig. 8.5(d)). The $H_2^{\rm norm}$ values are thereby constrained to a maximum positive value of unity. If $\Delta\omega$ is made sufficiently small, and the spectrum is strongly dc-peaked (i.e., has a very small k-value), then $H_2^{\rm norm}$ can go negative as it tracks the theoretical $\ln(2\pi k)$ trend. This is quite unlike Shannon information whose minimum value is zero.

8.5 Applications of Spectral Entropy

8.5.1 Spectral Entropy for the Adiabatic Macrocolumn

Having completed this rather detailed investigation of the general properties of spectral entropy and its estimation via discrete measures, we finally are ready to apply this statistic to the steady-state fluctuation spectra generated by the adiabatic macrocolumn. We are particularly interested in tracking the changes in spectral entropy as the macrocolumn changes state under the influence of a GABA anaesthetic agent; both induction and emergence transitions will be examined.

The theoretical form of the linearized fluctuation spectrum for the adiabatic macrocolumn was presented earlier as Eq. (5.58a),

$$S[h_e(\omega)] = \frac{1}{2\pi}\,\frac{A_{12}^2 D_{22} + A_{22}^2 D_{11} + D_{11}\omega^2}{\left(A_{11}A_{22} - A_{12}A_{21} - \omega^2\right)^2 + \left(A_{11} + A_{22}\right)^2 \omega^2} \tag{8.44}$$

where the elements of the drift matrix $\mathbf{A}$ and diffusion matrix $\mathbf{D}$ were listed in Eqs (5.23) and (5.22) respectively. Three-dimensional waterfall graphs of the adiabatic spectral variation with GABA anaesthetic effect λ appeared in Fig. 5.7 (p. 85).

Using the fluctuation spectra calculated from Eq. (8.44), I computed the normalized histogram entropy $H_2^{\rm norm}$ (Eq. 8.21) with 1-Hz histogram bins for frequency ranges 0–5000 Hz and 0–400 Hz. See Fig. 8.6. Superimposed on these graphs are the point data measurements extracted from adiabatic simulation runs performed by L. Wilcocks (2001), and described in Sect. 7.5.1.

For both frequency bands, the spectral entropy is higher on the high-firing upper branch, and lower on the bottom branch. This is consistent with the notion that spectral entropy will be large when the spectrum is relatively flat or "white" (all frequency bins equally populated), and small for a peaked spectrum (low-frequency bins more favoured than high-frequency bins). As the 3D plots in Fig. 5.7 show, for small values of λ the shape of the adiabatic power spectra for the top branch is considerably flatter than for the bottom branch. As $\lambda \to 1.53$ along the top branch, the total fluctuation power rises to a peak, but its spectral distribution becomes increasingly concentrated towards lower frequencies, so the spectral entropy decreases to a local minimum at the A_3 critical point immediately prior to the $A_3 \to Q_3$ induction jump.

For the $Q_3 \to Q_1$ emergence trajectory along the bottom branch, the fluctuation spectra become even more dc-peaked, hence the steep decline in spectral entropy in anticipation of the $Q_1 \to A_1$ jump return to the upper branch.

8.5.2 Spectral Entropy for the Anaesthetized Patient

We have recently become aware of clinical research by Viertiö-Oja and colleagues (Viertiö-Oja *et al.*, 2000) investigating the feasibility of using spectral entropy of patient EEG as a robust measure of depth of anaesthesia. 105 patients undergoing routine general anaesthesia were monitored using 12-lead EEG. The state of consciousness was manually scored by an expert observer using the 6-level OAAS scale (observer's assessment of alertness and sedation: 5 = fully awake; 0 = deep anaesthesia). Loss of consciousness is defined as the transition from OAAS 3 to OAAS 2. After the transition, the patient no longer responds to spoken commands and the eyelid reflex is lost.

The OAAS scores were compared with the EEG spectral entropy values, and it was found that the entropy tracked the anaesthesiologist's rating, with loss of consciousness occurring at a universal critical value of entropy ($H_1^{\text{norm}} = 0.73$) which was found to be patient independent. Figure 8.7 illustrates the strong correlation between the EEG measure and the observer

(a) Spectral Entropy to 5000 Hz

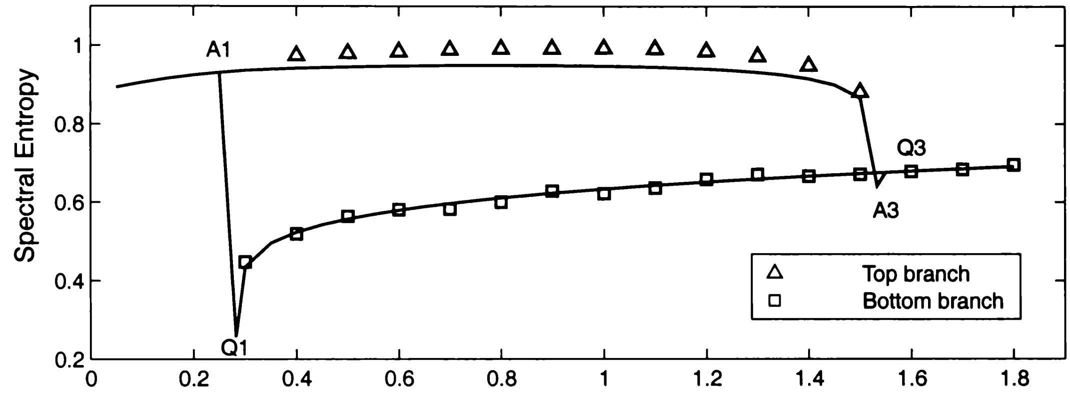

(b) Spectral Entropy to 400 Hz

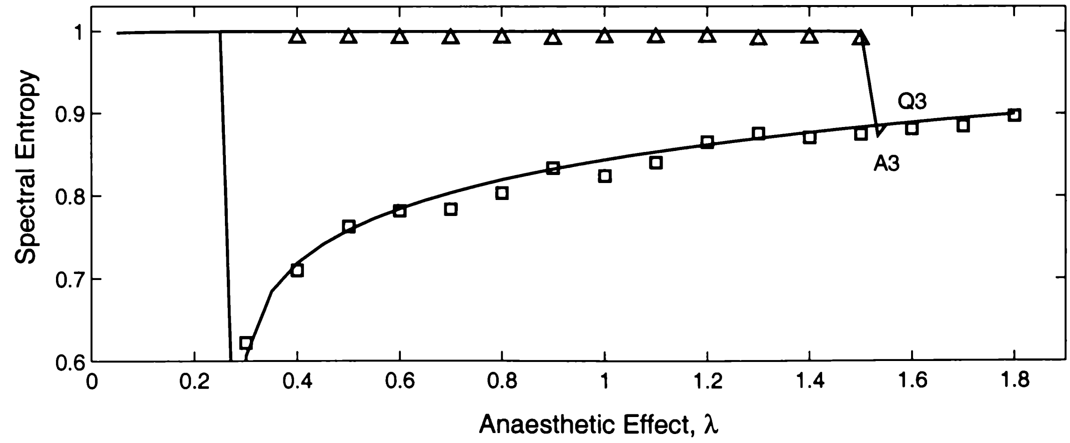

Figure 8.6: Theoretical prediction and simulation results for spectral entropy H_2^{norm} for (a) 0–5000 Hz, (b) 0–400 Hz; solid lines: prediction; discrete points: simulation results. Spectral entropy is typically high on the upper (active) branch, and low on the quiescent branch. For induction into unconsciousness, spectral entropy declines steeply but continuously. In contrast, during emergence into consciousness the spectral entropy makes a discontinuous upwards jump at transition. The points labeled A_3 and Q_1 mark the cusps in fluctuation power which occur at the instant preceding induction into unconsciousness, and preceding emergence from unconsciousness, respectively. [Source: Discrete points furnished by L.Wilcocks (2001)]

(a) Spectral Entropy

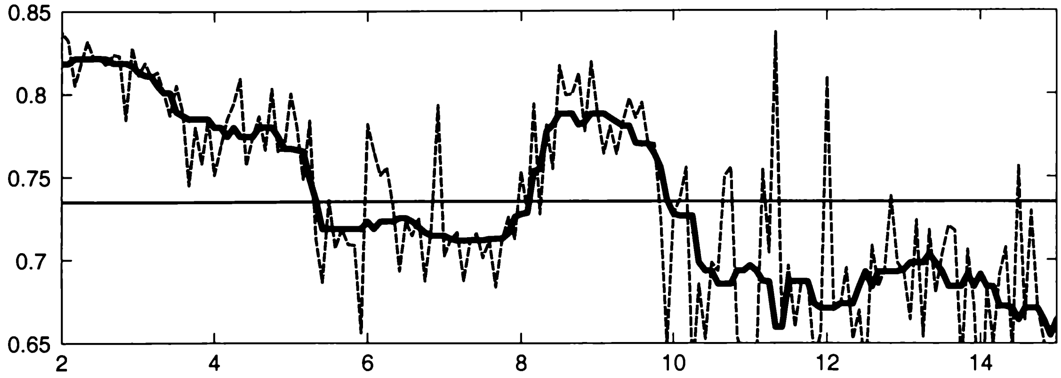

(b) OAAS Level

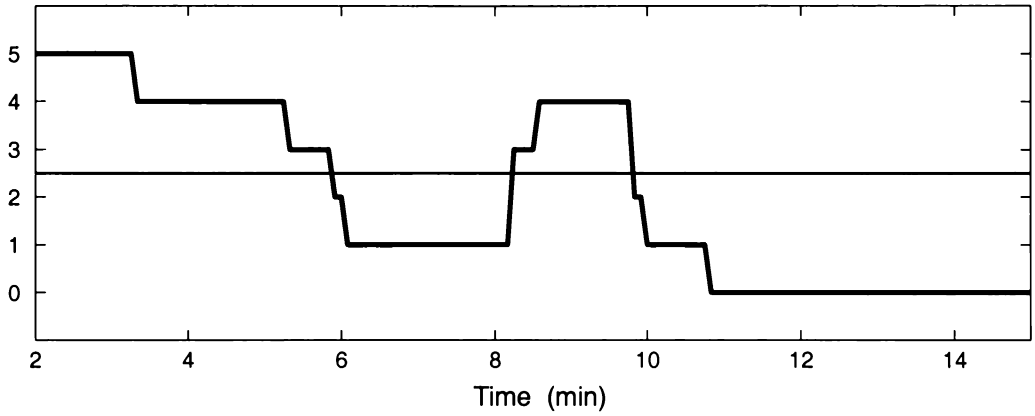

Figure 8.7: (a) Spectral entropy derived from patient scalp EEG during induction of anaesthesia. Dashed curve shows 5-s averages; heavy curve shows one-minute median-filtered averages. The EEG was sampled at 10,000 s^{-1}, decimated to 500 s^{-1}, and processed in 5-s segments. For each segment, spectral entropy was calculated using a frequency-histogram binwidth of 0.2 Hz. (b) OAAS (observer's assessment of alertness and sedation) level as assessed by an anaesthesiologist. Level-5 is fully awake; level-0 is a deep hypnotic state in which the patient shows no response to tetanic stimulation of the ulnar nerve (50 mA, 5 s). In both figures, the horizontal line shows the level at which transition from consciousness to unconsciousness occurs (OAAS 3 $\rightarrow$ 2). [Data supplied courtesy H. Viertiö-Oja, and reported as patient 75 in *Anesthesiology News*, vol. 26, no. 4, 2000.]

assessment of consciousness.

Comparing the clinical results of Fig. 8.7 against the adiabatic prediction of Fig. 8.6, there is good qualitative agreement for the induction trajectory: adiabatic spectral entropy declines as the macrocolumn transits from the high-firing upper branch to the low-firing quiescent branch; this parallels the decline in clinical spectral entropy as the patient becomes anaesthetized. In both cases, the rate of decline is steepest at transition.

However, theory and experiment diverge for the emergence trajectory. The adiabatic theory predicts that once the macrocolumn has reached the low-firing branch, reducing the anaesthetic concentration should lead to ever-diminishing spectral entropy as the macrocolumn approaches the Q_1 critical point from the right, yet the clinical measurements seem to bottom-out at a minimum value of $\sim$0.66.

A possible explanation for this discrepancy might be that the stochastic fluctuations for the bottom-branch macrocolumn are expected to be very much smaller than for the top-branch (compare the "before" and "after" fluctuation amplitudes of Fig. 7.8), consequently the stochastic component of the unconscious cortex could easily be swamped by any broad-band cortical resonances generated by the relatively ordered macrocolumns of the hyperpolarized cortex.

It is interesting to observe that the critical spectral entropy value of 0.73 (horizontal line drawn in Fig. 8.7(a)), identified by Viertiö-Oja as separating the conscious and unconscious states, would serve equally well to demarcate the active and quiescent branches of the adiabatic macrocolumn of Fig. 8.6(a).

Unfortunately I suspect that this apparent congruence may be somewhat fortuitous, for two reasons. First, the adiabatic model predicts the raw, unfiltered soma voltage fluctuations for a single macrocolumn, whereas any real EEG measurement will be the spatial sum of the voltages generated by the thousands of macrocolumns sampled by the scalp electrode, and which have been low-pass filtered by the intervening cerebro-spinal fluid, skull, and skin. Our modelling ignores filtering and spatial averaging effects. In addition, as remarked earlier in Sect. 7.5.1, our saturation firing rates of $\mathcal{S}_e^{\max} = \mathcal{S}_i^{\max} = 1000\ \mathrm{s}^{-1}$ are probably too high by an order of magnitude, leading to a theoretical fluctuation spectrum which is over-broad.

Second, in her calculations for spectral entropy, Viertiö-Oja applied the Shannon information formula[5] $H_1^{\mathrm{norm}} = -\sum p \ln p / \ln N$ (see Table 8.1 on p. 153), rather than the H_2^{norm} histogram form which would have compensated for the non-unity ($\Delta f = 0.2$ Hz) frequency interval. Based on the numerical experiments summarized earlier in Fig. 8.5(b) on p. 161, since $\Delta f < 1$, the critical Shannon value of 0.73 is likely to be an *overestimate* of the underlying continuous-entropy value at induction. We can generate a corrected value for the critical entropy if we know the number of frequency bins used in the analysis. Let us suppose, for definiteness, that the EEG frequency analysis extended to 47 Hz (this allows a 3-Hz safety margin in order to stay clear of any 50-Hz mains-induced electrical artifacts). Then, for $\Delta f = 0.2$ Hz, we have

$$N\Delta f = 47\ \mathrm{Hz} \qquad \Longrightarrow \qquad N = 235\ \mathrm{bins}.$$

From Eq. (8.14), writing Δf for the frequency interval,

$$H_2 = H_1 + \ln \Delta f\,. \tag{8.45}$$

Dividing through by $\ln[N\Delta f]$ gives the normalized histogram entropy,

$$\begin{aligned}\frac{H_2}{\ln[N\Delta f]} &\equiv H_2^{\mathrm{norm}} \\ &= \frac{H_1}{\ln[N\Delta f]} + \frac{\ln \Delta f}{\ln[N\Delta f]} \\ &= \frac{\ln N}{\ln[N\Delta f]} H_1^{\mathrm{norm}} + \frac{\ln \Delta f}{\ln[N\Delta f]} \end{aligned} \tag{8.46}$$

which, after substituting the assumed value for N, and the known values for H_1^{norm} and Δf, gives the revised (and lowered) value for critical entropy:

$$H_2^{\mathrm{norm}} = 0.62 \tag{8.47}$$

---

[5] Personal communication, H. Viertiö-Oja (2000)

Even after histogram correction for a non-unity frequency interval, it is clear that the signature value for spectral entropy (i.e., the critical entropy level which separates the conscious and unconscious states) will depend on the bandwidth used in the spectral analysis.

8.6 Correlation Time and its Relationship to Spectral Entropy

For the single-sided Lorentzian fluctuation spectrum whose half-power frequency is k [rad/s]

$$\begin{aligned} S(\omega) &= \frac{D}{k^2+\omega^2}, \qquad 0 \le \omega < \infty \\ &= 0, \qquad\qquad \text{otherwise} \end{aligned} \tag{8.48}$$

we have demonstrated (see Table 8.2) that the spectral entropy is

$$H_\omega = \ln(2\pi k). \tag{8.49}$$

By applying the Wiener–Khinchin theorem (see Sect. 2.4) to Eq. (8.48), we obtain the autocorrelation function,

$$\begin{aligned} G(\tau) &= \frac{D}{4k} e^{-k|\tau|} \\ &= \frac{DT}{4} e^{-|\tau|/T} \end{aligned} \tag{8.50}$$

where we define $T \equiv 1/k$ as the *correlation time* of the fluctuations. (T is sometimes referred to as the *decorrelation* time since for lags $\tau > T$ the fluctuations are effectively uncorrelated.) Substituting T in Eq. (8.49) gives the inverse relationship between correlation time and spectral entropy,

$$H_\omega = -\ln(2\pi T) \tag{8.51}$$

or, if the spectrum is written as a function of linear frequency f, from Eq. (8.31) we get

$$H_f = -\ln T. \tag{8.52}$$

Thus a short correlation time is associated with an extended k half-power frequency (i.e., a "flat" spectrum), and a large spectral entropy. Conversely, a long correlation time is associated with a small k value giving a strongly dc-peaked spectrum and a small spectral entropy.

8.6.1 Correlation Function for the Adiabatic Macrocolumn

To what extent can these ideas linking correlation time with spectral shape be extended to the two-dimensional Ornstein–Uhlenbeck macrocolumn model? We know from Eq. (5.45) that the correlation function for δh_e, the excitatory fluctuations of the macrocolumn, is the sum of *two* exponential decay processes whose decay rates are the eigenvalues $\Lambda_{1,2}$ of the 2×2 **A** drift matrix:

$$G_{11}(\tau) = \alpha_1 e^{-\Lambda_1 \tau} + \alpha_2 e^{-\Lambda_2 \tau} \tag{8.53}$$

where the α_1, α_2 scale factors were defined in Eq. (5.46) in terms of the eigenvectors and covariance matrix entries.

In Fig. 8.8 I have plotted $G_{11}(\tau)$, and its two exponential-decay components, for six different locations on the Fig. 3.4 trajectory of steady states. The top three panels (a)–(c) belong to the top branch, and show the evolution of $G_{11}(\tau)$ as GABA anaesthetic effect is increased towards the point of induction at A_3. In the waterfall graph of Fig. 5.6 (p. 84) we saw a prediction for a surge in spectral power and a narrowing of the spectrum at the A_3 critical point. The power surge appears in Fig. 8.8(c) as a pronounced increase in autocorrelation height at zero lag, and the spectral narrowing is evidenced as a broadening of the correlation function. The value for (generalized) correlation time T printed in each panel was calculated from the Eq. (5.52) definition,

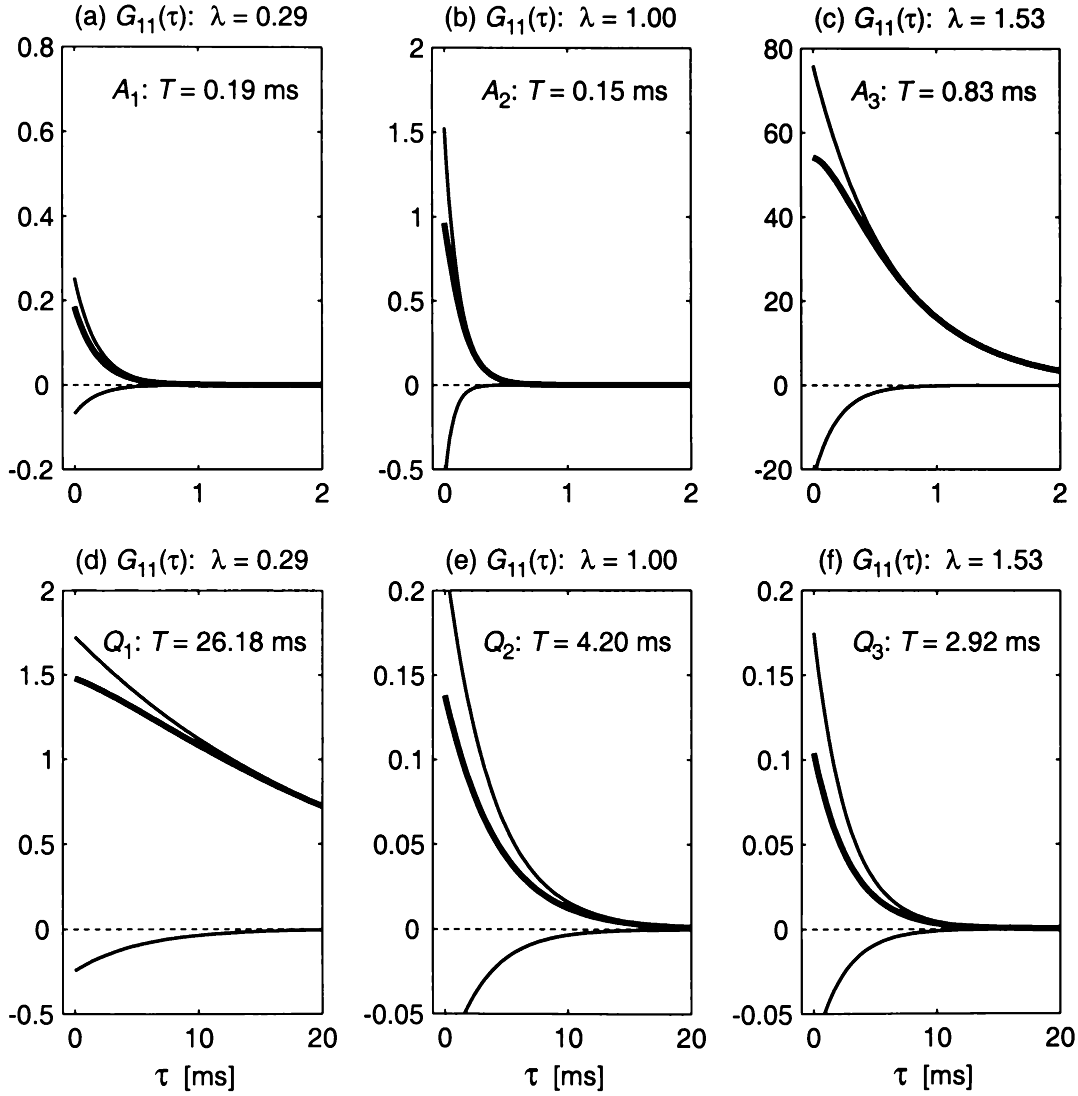

Figure 8.8: Macrocolumn autocorrelation functions for three values of anaesthetic effect on the top (active) branch (a–c), and for the same three anaesthetic values on the bottom (quiescent) branch (d–f). The generalized correlation time T, calculated from Eq. (5.52), increases for the induction trajectory ($A_1 \rightarrow A_3 \rightarrow Q_3$), and increases further for return journey along the bottom branch ($Q_3 \rightarrow Q_1$), before collapsing abruptly at emergence ($Q_1 \rightarrow A_1$). Note the ×10 change in scale for the lag axis for the bottom-branch graphs (d–f). The bold curve shows the $G_{11}(\tau)$ autocorrelation function of Eq. (8.53); its two exponential-decay components, $\alpha_1 e^{-\Lambda_1 \tau}$ and $\alpha_2 e^{-\Lambda_2 \tau}$, are drawn with a thin pen.

$$\begin{aligned} T &= \frac{1}{G_{11}(0)} \int_0^\infty G_{11}(\tau)\, d\tau \\ &= \frac{1}{\sigma_{11}} \left(\frac{\alpha_1}{\Lambda_1} + \frac{\alpha_2}{\Lambda_2} \right) \end{aligned} \tag{8.54}$$

and cross-checked against the Eq. (5.54) formula

$$T = \frac{1}{\sigma_{11}} \left[\mathbf{A}^{-1} \boldsymbol{\sigma} \right]_{11} , \tag{8.55}$$

the two methods returning values for T that, to within expected precision (i.e., to within a small multiple of machine epsilon), were identical.

Correlation time increases by a factor of ~4 for the $A_1 \rightarrow A_3$ approach to induction (panels (a)→(c) of Fig. 8.8), increases by a similar amount across the $A_3 \rightarrow Q_3$ phase jump (panels (c)→(f); note the decade change in scale between top and bottom panels), compounding further by almost an order of magnitude along the $Q_3 \rightarrow Q_1$ emergence trajectory (panels (f)→(d)). The emphatically extended correlation time in panel (d) corresponds to the exceedingly dc-peaked waterfall slice of Fig. 5.7(d) (p. 85) at $\lambda = 0.29$. At this point, the macrocolumn is about to make its jump return from the quiescent bottom branch to the active top-branch. These pictures provide an excellent illustration of the critical slowing down and divergent growth of fluctuations in the vicinity of a first-order phase transition.

8.6.2 Correlation Time and Anaesthetic Effect

By repeating the Eq. (8.54) generalized correlation-time determinations for finely-stepped increments in GABA anaesthetic effect ($\Delta\lambda_{\text{GABA}} = 0.01$), a detailed picture showing the T-vs-λ_{GABA} dependence emerges—see Fig. 8.9.

The graph shows that correlation time is longer on the low-firing Q_1–Q_3 quiescent branch, and shorter (i.e., fluctuations are less correlated) on the A_1–A_3 active branch where, because the average firing rate is higher, the intensity spectrum is broader. On both branches, correlation time rises to a local maximum value (on the top branch at the A_3 induction; on the bottom branch at the Q_1 emergence) in the immediate vicinity of the change of state, although for the active branch, the peak at A_3 only becomes readily discernible in Fig. 8.9(b) where correlation time is plotted on a logarithmic scale.

8.6.3 Correlation Time and Spectral Entropy

The second panel of Fig. 8.9 bears a remarkable mirror symmetry with the band-limited spectral entropy H_2^{norm} plotted earlier in Fig. 8.6(a). To explore this apparent symmetry, I have replotted the spectral entropy and correlation-time graphs in a pair of opposing panels in Fig. 8.10. Now the x-axis reflection symmetry becomes obvious: it seems that for the two-dimensional adiabatic macrocolumn, the spectral entropy of the excitatory fluctuations is, to fair approximation, proportional to the negative of the logarithm of the generalized correlation time of those fluctuations.

(a) Correlation Time vs Anaesthetic Effect

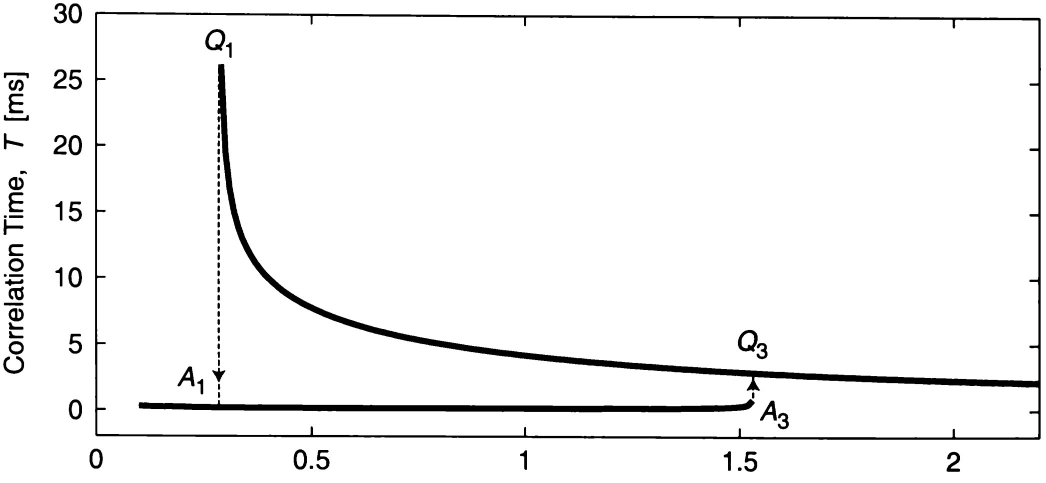

(b) Log Correlation Time vs Anaesthetic Effect

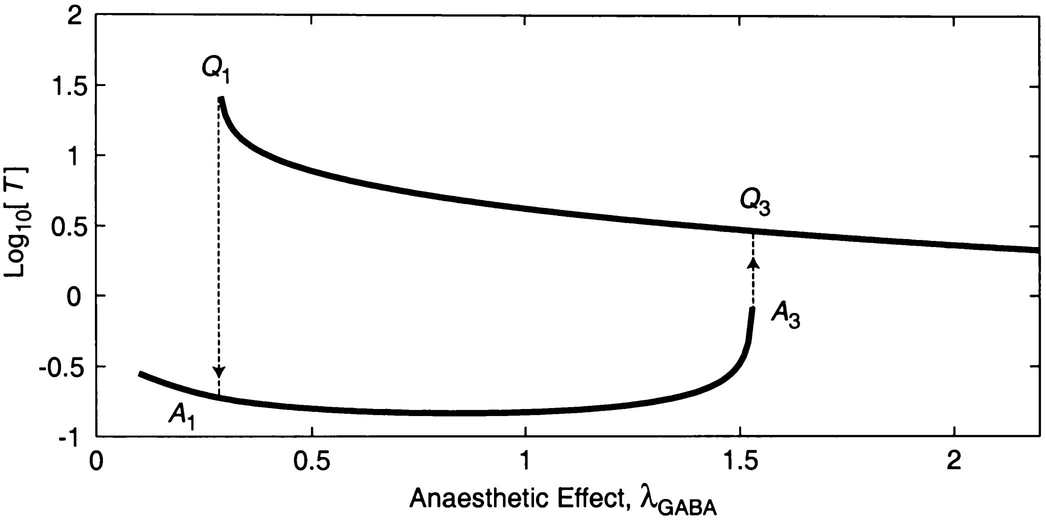

Figure 8.9: Generalized correlation time T as a function of anaesthetic effect for the adiabatic macrocolumn plotted (a) with linear axes, and (b) with a logarithmic y-axis. Correlation time is small on the conscious (active) branch A_1A_3, and large on the unconscious (quiescent) branch Q_3Q_1. For both branches, maximum correlation time occurs at the A_3 (induction) or Q_1 (emergence) phase transition point.

To test this assertion, Fig. 8.11 plots spectral entropy versus generalized correlation time, first with (a) linear axes, giving a close-to-exponential decay curve; and second, with a (b) logarithmic correlation-time axis, giving an almost-linear trend line of negative slope. (The gap in the thick-pen lines corresponds to the set of inaccessible (T, H_2^{norm}) coordinates belonging to the unstable equilibrium points on the A_3Q_1 midbranch of Fig. 3.4.)

Superimposed with a thin pen on Fig. 8.11 is the normalized entropy prediction which would apply if the autocorrelation function could be represented as a *single* exponential decay curve whose time constant is given by T, the generalized correlation time of Eq. (8.54). The thin-pen prediction is

$$H_f^{\text{norm}} = -\frac{\ln T}{\log 5000} \tag{8.56}$$

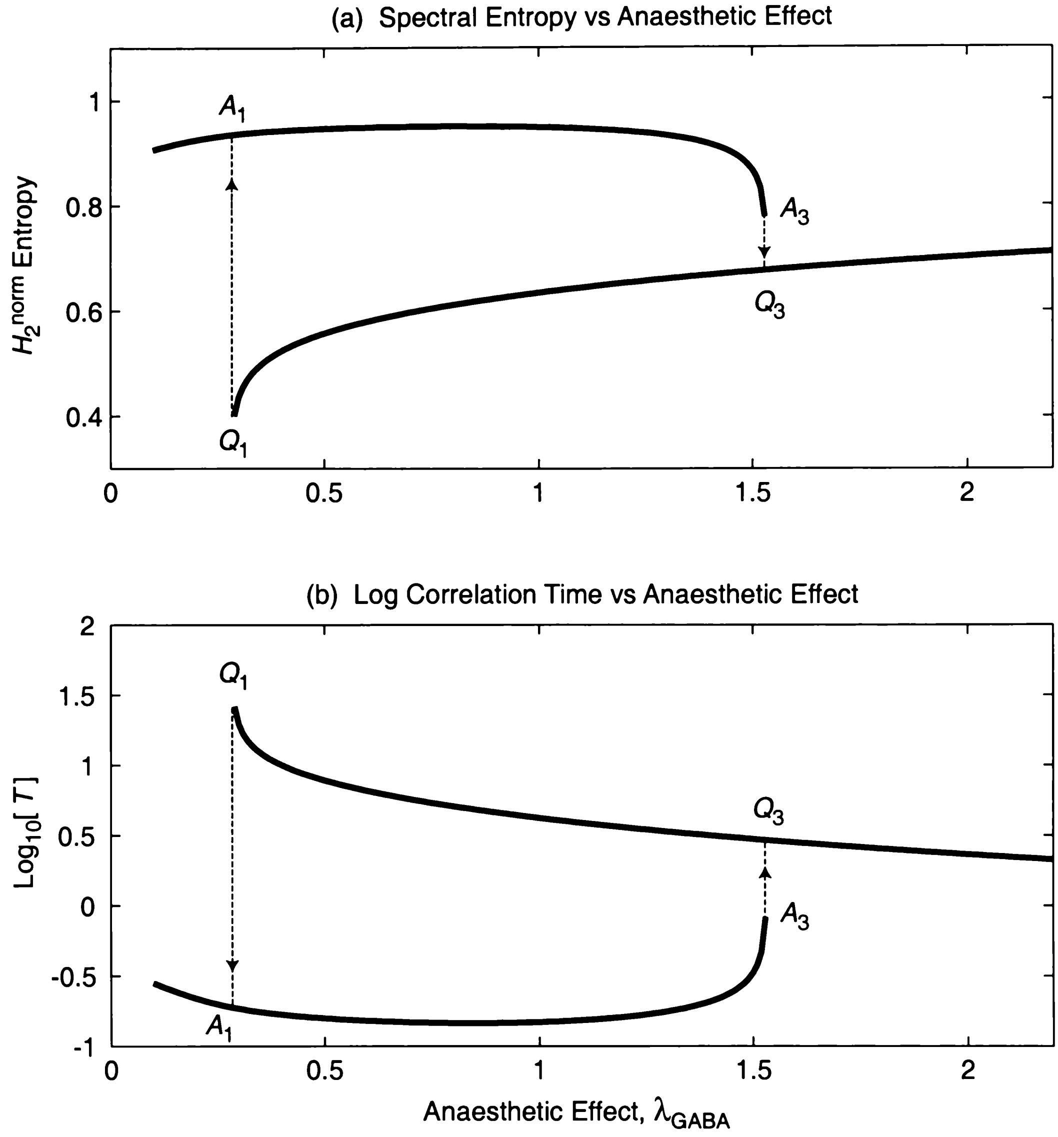

Figure 8.10: Comparision of the anaesthetic dependence of (a) spectral entropy and (b) generalized correlation time. (a) Spectral entropy H_2^{norm} calculated by applying Eq. (8.21a) to the δh_e fluctuation spectrum of Eq. (8.44), and normalized to a frequency upper limit of 5000 Hz. [This graph is the same as Fig. 8.6(a), but plotted to a finer resolution (0.01 steps in λ_{GABA}), with steady-state coordinates located with a different root finder (presented later in Sect. 9.2).] Note the close mirror symmetry between the spectral entropy graph of (a) and the correlation-time graph of Fig. 8.9(b), duplicated here for ease of comparison.

where the log 5000 denominator provides the normalization to Eq. (8.52) by referencing to a rectangular spectrum which is flat on the frequency interval $0 \leq f \leq 5000$ Hz (see Fig. 8.2)—this matches the frequency range used to calculate the normalized histogram entropy H_2^{norm}.

Because the autocorrelation function for a two-dimensional Ornstein-Uhlenbeck process is the sum of two exponential decays, it is not surprising that the attempt at a single time-constant fit in Fig. 8.11(b) is not particularly accurate. Nevertheless, the general conclusion that: *for OU processes, spectral entropy and correlation time are inversely related* provides a fair rule-of-thumb for two-dimensional processes, and becomes an exact statement for the special case of a one-dimensional system.

(a) Spectral Entropy vs Correlation Time

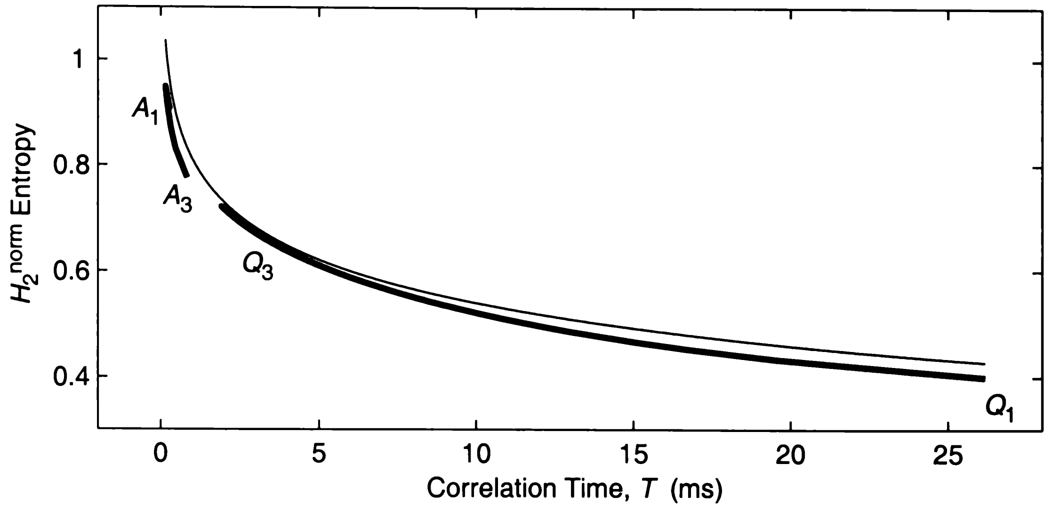

(b) Spectral Entropy vs Log [Correlation Time]

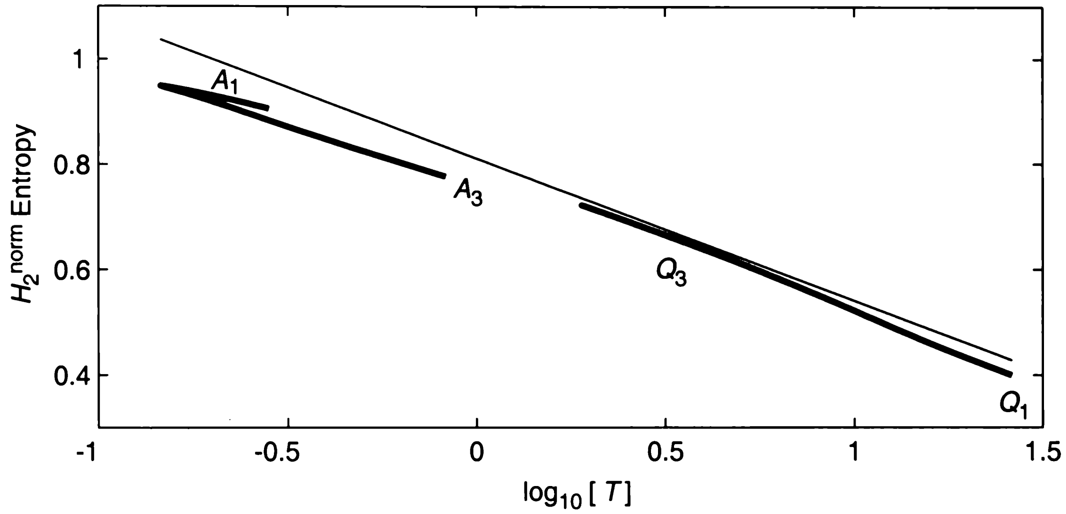

Figure 8.11: Spectral entropy versus generalized correlation time plotted with (a) linear axes, and (b) a logarithmic x-axis. The bold curves are the data extracted from Fig. 8.10; the gap corresponds to the region of correlation-time–entropy space belonging to the unstable midbranch, therefore inaccessible to the macrocolumn. The continuous thin line is the entropy prediction $H_f^{\text{norm}} = -\ln T/\ln 5000$ given by assuming that the autocorrelation function can be approximated by a *single* exponential decay whose decay constant is given by T, the generalized correlation time.

This conclusion suggests that instead of tracking cortical state in the frequency domain by way of changes in spectral entropy, one could examine the time-domain properties of the EEG signal, looking for increases in correlation time as an indicator of an imminent change of phase. This should be a particularly sensitive detector for the *return* of conscious awareness, since it is for this transition that the growth and subsequent collapse of correlation time is most dramatic. How robust this measure would be with respect to contamination from non-stochastic variations (e.g., alpha rhythms, mains electrical interference) and other artifacts (e.g., muscle-generated voltages) would be a matter requiring further investigation.

8.7 Context of Present Chapter and Paper 2

Some of the work in the present chapter has been reported in paper 2 (Steyn-Ross *et al.*, 2001b), but the reader will find that the state of knowledge reported in this thesis has advanced somewhat. I wish to establish the context of the present chapter with respect to paper 2, both for the record, and also because it nicely demonstrates the role of serendipity and surprise in the uncovering of new knowledge.

It was recognized in paper 2 that at the high-frequency limit, the steady-state fluctuation spectrum of Eq. (8.44) is Lorentzian. (This was discussed earlier in Sect. 5.7.3; note that Eq. (5.70) corrects an error in Eq. (3.3) in paper 2.) Because the decay rate of the Lorentzian profile can be interpreted as the inverse of a correlation time for the fluctuations, I was interested in learning how the correlation time varied with anaesthetic effect.

To extract the correlation times, I computed the autocorrelation functions of the theoretical adiabatic spectra shown in Fig. 5.7. This was done numerically[6] by converting each single-sided spectrum to a dc-centred, double-sided spectrum, applying a Hanning window, then taking the absolute value of its discrete inverse-Fourier transform. The autocorrelation graphs showed an approximately exponential decay from a peak at zero lag. The decay time T was determined as the negative of the inverse-slope for a straight-line best-fit to each of the semilog plots of autocorrelation versus lag-time (see Eq. (5.49)). When I compared the resulting T-vs-λ graph (Fig. 9 of paper 2) with the spectral entropy-versus-λ graph (Fig. 7(a) of paper 2), I was struck by their almost perfect mirror symmetry, convincing me that there must exist a direct and simple relationship between spectral entropy and correlation time. This motivated the spectral entropy investigation reported in Sect. 8.3.1, revealing the direct logarithmic proportionality $H_\omega = \ln(2\pi k) = \ln(2\pi/T)$ for an ideal Lorentzian spectrum. Then followed the attempt to estimate the (continuous) H_ω entropy from the (discrete) Shannon information H_1, and the discovery that a histogram correction was required if the frequency resolution for the sampled spectrum was other than unity.

Finally came the realization that the Gardiner (1985, p. 111) expression for the 2×2 time-correlation matrix for a two-dimensional Ornstein-Uhlenbeck process involved a matrix exponential that could be expressed in terms of drift-matrix eigenvalues and eigenvectors, and this lead naturally to the Eq. (5.45) sum-of-exponentials formula for the autocorrelation function, and to the notion of a generalized correlation time given by Eq. (5.52). Thus the correlation time for the macrocolumn can now be calculated directly from the eigenvalues, giving Fig. 8.10(b) as the accurate and informed replacement for Fig. 9 of paper 2.

---

[6] At that time I was unaware that this information could be extracted from the time-correlation matrix; the exposition in Sect. 5.4.2 and the development of the notion of a generalized correlation time came much later.

Chapter 9

Modelling NMDA Effects in the Adiabatic Macrocolumn

9.1 Adiabatic Equations for NMDA Anaesthetic

9.1.1 Modelling the NMDA Effect

The cerebral cortex can be made less active via anaesthetic agent in either of two complementary ways. Either: The overall level of inhibition can be increased by *lengthening* the duration of the *inhibitory* post-synptic potential (PSP)—this is the mode of action of the GABA-enhancing class of general anaesthetics (such as propofol). Or: The overall level of excitation can be decreased by *shortening* the duration of the *excitatory* PSP—this is thought to be the mode of action of the NMDA-suppression class of anaesthetics (e.g., xenon, nitrous oxide). The earlier work presented in this thesis assumes a GABA-enhancing pro-inhibitory action which acts by reducing the γ_i inhibitory rate-constant; the present chapter investigates the NMDA-suppressing anti-excitatory action which increases the γ_e rate-constant (i.e., reduces the γ_e^{-1} time-constant).

The GABA-enhancement adiabatic equations were presented as Eqs (4.1a–4.3b). In order to adapt these to incorporate NMDA effects, I will replace the excitatory rate-constant γ_e appearing in Eqs (4.2a, 4.2b) with an expression dependent on a dimensionless parameter labelled λ_{NMDA} which is presumed to increase monotonically with concentration of anti-NMDA anaesthetic agent:

$$\gamma_e^{-1} \longrightarrow \gamma_e^{-1} + \frac{\mathcal{S}_{\text{NMDA}}(h_e)}{\lambda_{\text{NMDA}}} \equiv \tau_E(h_e, \lambda_{\text{NMDA}}), \tag{9.1}$$

where $\mathcal{S}_{\text{NMDA}}(h_e)$ is a sigmoid function of the excitatory soma voltage,

$$\mathcal{S}_{\text{NMDA}}(h_e) = \frac{\mathcal{S}_{\text{NMDA}}^{\max}}{1 + \exp[-g_{\text{NMDA}}(h_e - \theta_{\text{NMDA}})]}. \tag{9.2}$$

The experimental basis for the sigmoid form will be given in the following section. Note that the NMDA-dependent time-"constant" τ_E defined in Eq. (9.1) depends on both the anti-NMDA anaesthetic concentration parameter λ_{NMDA} and on the average membrane voltage h_e of the excitatory neurons in the macrocolumn.

A graph for τ_E for variable λ_{NMDA} appears in Fig. 9.1. Note that in the limit of $\lambda_{\text{NMDA}} \to \infty$, $\tau_E \to \gamma_e^{-1}$, all NMDA effect has been suppressed, and the original pure-GABA model with $\gamma_e^{-1} = 3.3$ ms is recovered. The curve shown for $\lambda_{\text{NMDA}} = 1$ is my (deliberately approximate)

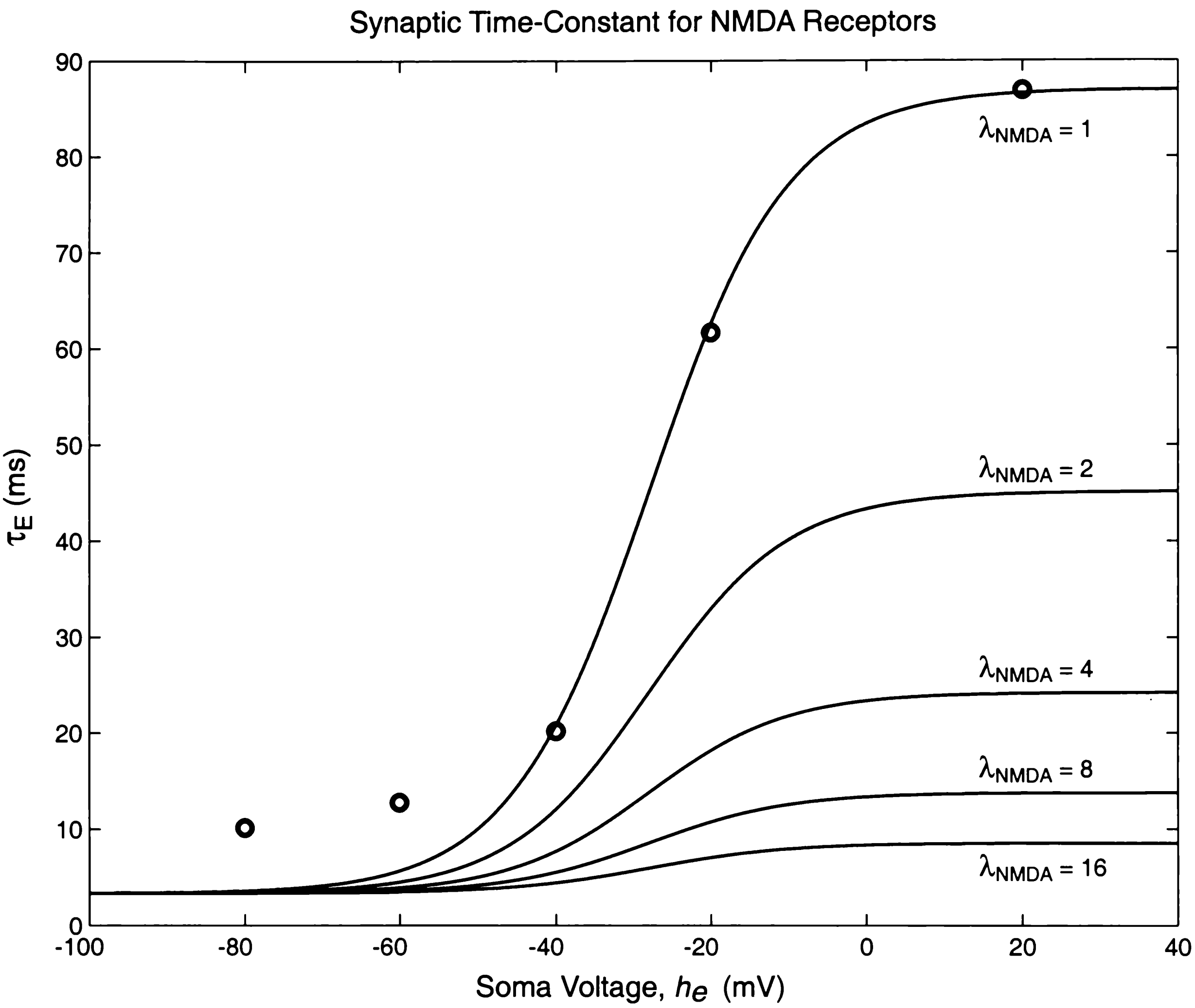

Figure 9.1: Dependence of NMDA-mediated time-constant τ_E on soma voltage. Unlike GABA-enhancing anaesthetics whose IPSP time-decay-constant depends only on anaesthetic concentration, NMDA-suppressing anaesthetics have an EPSP duration which depends on *both* concentration *and* membrane voltage. Maximum time-constant occurs for a fully-depolarized neuron (top-right of graph); minimum time-constant for a hyperpolarized neuron (lower-left). Circles are time-constants extracted from work reported by Hestrin *et al.* (1990); the $\lambda_{\text{NMDA}} = 1$ curve is our approximate fit to these data via Eqs (9.1) and (9.2): $S_{\text{NMDA}}^{\text{max}} = 83.7$ ms, $g_{\text{NMDA}} = 0.11$ (mV)$^{-1}$, $\theta_{\text{NMDA}} = -28$ mV (see Section 9.1.2 for details). Anaesthetic effect deepens as λ_{NMDA} increases.

sigmoid fit[1] to data extracted from NMDA-effect measurements first reported by Hestrin, Nicoll, Perkel, and Sah (1990), and subsequently included in one of the standard neuroscience textbooks (Kandel and Schwartz, 1991, p. 159). The data of Hestrin *et al.* are plotted in Fig. 9.1 as bold circles. My treatment of their measurements will now be described.

9.1.2 Measurements of Hestrin, Nicoll, Perkel, and Sah

Figure 9.2 shows the results reported by Hestrin *et al.* (1990) indicating the presence of two distinct components in the excitatory post-synaptic current for a hippocampus neuron: an "early" rapidly-decaying current pulse due to AMPA receptors, on which is superimposed a "late" slowly-decaying trend due to NMDA receptors. By applying APV, an NMDA-blocking

---

[1] It was the suggestion of M. Steyn-Ross (personal communication) to try fitting a sigmoid function to the NMDA current-decay data of Hestrin *et al.* (1990).

agent, this late-phase current is suppressed, revealing the underlying early-phase current. The significant observation from these Hestrin graphs is the fact that the decay-rate for the NMDA component depends on the membrane potential h_e: the more depolarized the membrane, the greater the NMDA current and the slower its rate of decay. Note that these experiments are an instantiation of the *extreme adiabatic* assumption (i.e., h_e varies on extremely slow time-scales) since the membrane voltage is held constant at preset levels by a voltage clamp.

Estimating τ_{early}

The decay-constant τ_{early} for the fast AMPA process can be estimated by comparing the excitatory current at $t = 25$ ms with the peak excitatory current at $t = 0$. Let α be the slope of the fitted line for peak current $I(0)$ versus h_e (▲ symbols in Fig. 9.2), and β the slope of the NMDA-suppressed trend line (o symbols); then

$$I^{\text{early}}(0) = \alpha\, h_e \tag{9.3}$$

and

$$I^{\text{early}}(t) = I^{\text{early}}(0)\, e^{-t/\tau_{\text{early}}} = \beta\, h_e \tag{9.4}$$

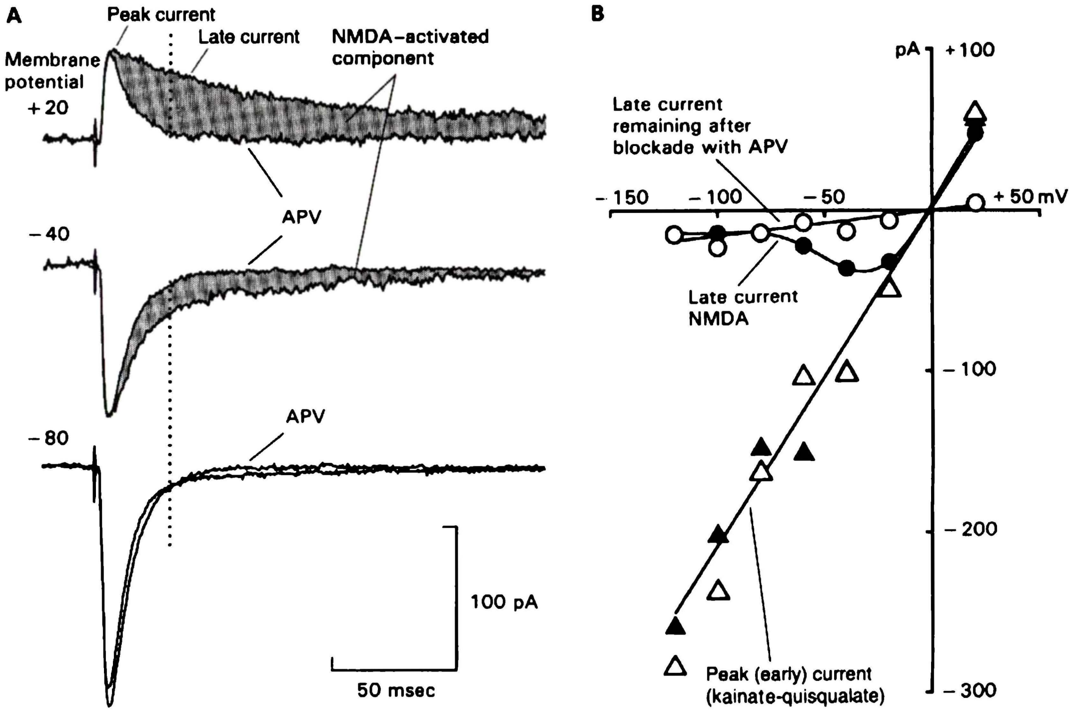

Figure 9.2: Early and late components of the excitatory post-synaptic current. NMDA receptors are responsible for a "late," slowly-decaying component of the current which can be suppressed with application of APV, an NMDA-blocking agent. The underlying "early," rapidy-decaying component remains. (A) Synaptic current shown for three different membrane potentials before and during application of APV. The shaded areas indicate the size of the NMDA (APV-sensitive) component. The vertical dotted line indicates 25 ms after the $I(t = 0)$ current peak. (B) At each of seven membrane voltages, the peak synaptic current $I(t = 0)$ was recorded for no exposure to APV (▲), and with exposure to APV (△). The circles show the synaptic current at 25 ms for no APV exposure (•), and with APV exposure (o). Note that the decay-rate of the APV-sensitive component (•) is dependent on membrane voltage. [Source: (Kandel and Schwartz, 1991, Fig.11-6, p.159), after Hestrin *et al.* (1990)]

where $t = 25$ ms and, measuring from Fig. 9.2B, the slope-ratio is $\alpha/\beta = 12.57$. Solving Eqs (9.3) and (9.4) for τ_{early} gives

$$e^{-t/\tau_{\text{early}}} = \frac{\beta}{\alpha} \quad \Rightarrow \quad \tau_{\text{early}} = \frac{25 \text{ ms}}{\ln(\alpha/\beta)} = 9.88 \text{ ms}. \tag{9.5}$$

Encouragingly, this result is of the same order-of-magnitude as the inverse of the excitatory rate-constant assumed in the Liley model: $\gamma_e^{-1} = 3.3$ ms.

Estimating τ_{late}

A similar procedure estimates the slow-process decay "constant" (not really a constant because of its h_e dependence). We write the decay equation for the total current as $I(t)$,

$$I(t) = I(0)\, e^{-t/\tau_E} \tag{9.6}$$

where the composite time-constant τ_E is defined as the sum

$$\begin{aligned} \tau_E \quad &\equiv \quad \tau_{\text{early}} \quad + \quad \tau_{\text{late}}(h_e)\,. \\ &\quad\ \text{(constant)} \quad \text{(voltage-gated)} \end{aligned} \tag{9.7}$$

Solving Eq. (9.6) for τ_{late} gives

$$\tau_{\text{late}} = \frac{t}{\ln\,[I(0)/I(t)]} - \tau_{\text{early}} \tag{9.8}$$

with the ratio in the denominator measured directly from the ($\blacktriangle = I(0)$) and ($\bullet = I(t)$) points on Fig. 9.2B at time $t = 25$ ms. The calculated values for τ_E which appear in Table 9.1 are plotted as circles in Fig. 9.1. We choose to fit a sigmoid which passes through the underlined (h_e, τ_E) table entries for the depolarized regime, but allow the sigmoid to deviate from the tabulated results in the hyperpolarized limit in order to match the $\gamma_e^{-1} = 3.3$ ms Liley value. This permits a smooth modelling transition from the pure-GABA results of the previous chapters (which ignore all slow-NMDA effects) to the NMDA-inclusive work of this chapter.

Table 9.1: Variation of excitatory post-synaptic time-"constant" τ_E with excitatory membrane voltage h_e calculated from Eq. (9.8) for the Hestrin *et al.* (1990) measurements. We modify the Liley model by curve-fitting to the three most depolarized entries (shown underlined). See Fig. 9.1.

h_e (mV)	τ_E (ms)	τ_{early} (ms)	τ_{late} (ms)
+20	$\underline{86.9}$	9.9	77.0
−20	$\underline{61.7}$	9.9	51.8
−40	$\underline{20.2}$	9.9	10.3
−60	12.8	9.9	2.9
−80	10.2	9.9	0.25
−100	9.9	9.9	0

9.1.3 Justification for the Extreme Adiabatic Assumption

We wish to incorporate slow-NMDA effects into the macrocolumn model by assuming that on the time-scale of the excitatory events arriving at the post-synapse of the excitatory mean-field neuron, the membrane voltage h_e of that neuron is effectively constant. While this condition is precisely true of the Hestrin measurements reported in Section 9.1.2 (since the cell voltage was held fixed for each recording via voltage-clamping circuitry), at first glance it does not seem to be a valid assumption for the Liley model. Up until this point, we have taken the membrane time-constants to be $\tau_e = \tau_i = 40$ ms, which is comfortably larger than the default synaptic time-constants $\gamma_e^{-1} = 3.3$ ms, $\gamma_i^{-1} = 15.4$ ms. But when we wish to include the slow-NMDA effects, it is clear from Fig. 9.1 that in order to use Eq. (9.1) to replace γ_e^{-1} with $\tau_E(h_e)$ in Eqs (4.2a, 4.2b) for the I_{ej}, we are requiring that variations in h_e be on time-scales slower than $\tau_E^{\max} = 87$ ms. We describe this requirement for slow h_e variations as the *extreme adiabatic assumption* (since it is a more severe requirement than that needed for the earlier GABA-anaesthetic modelling).

There do not appear to exist any compelling *a priori* justifications for extreme adiabaticity. But we will find that if we allow h_e to be "as slow as necessary," then the theory predicts that instead of three soma-voltage steady-states (two of them stable), there can be up to *five* steady-states with *three* of these being stable to small perturbations. The discovery of this extra state, lying between full consciousness and coma, helps explain why the anti-NMDA anaesthetics do not, when used alone, induce fully-developed unconsciousness. Instead, they seem to induce a "disconnected" or "dream-like" state in which the EEG patterns are almost indistinguishable from normal wakefulness.

There is another *a posteriori* justification for extreme adiabaticity. We will show that the model predicts that as the NMDA-anaesthetic concentration is increased, there will be a first-order (discontinuous) transition from the upper to the intermediate stable-state at a critical value of concentration. This state-transition will be heralded by fluctuations of growing amplitude and slowing frequency, i.e., there will be a "critical slowing down" during which the spectrum of the h_e fluctuations will develop a strong peak at zero-frequency. Thus the assumption of slow-h_e becomes precisely true at the point of transition, and, in a sense, the assumption has become self-fulfilling since it allows for state transitions which generate the critical slowness.

The correctness of the adiabaticity assumption can be tested by comparing the model predictions for spectral and temporal changes at NMDA transition against clinical EEG measurements of patients treated with anti-NMDA anaesthetic agents.

9.1.4 Incorporating τ_E into the Macrocolumn Model

As discussed in the previous section, we will assume that h_e varies rather slowly (i.e., the membrane voltage equilibrates on a much longer time-scale than its synaptic stimulation) so that we are justified in replacing γ_e^{-1} in Eqs (4.2a, 4.2b) with $\tau_E(h_e)$ defined in Eq. (9.1). The revised adiabatic equations for the macrocolumn are now as follows:

$$\frac{dh_e}{dt} \equiv F_1(h_e, h_i) = \left[h_e^{\text{rest}} - h_e + \psi_{ee}(h_e)\, I_{ee}(h_e) + \psi_{ie}(h_e)\, I_{ie}(h_i)\right] / \tau_e, \tag{9.9a}$$

$$\frac{dh_i}{dt} \equiv F_2(h_e, h_i) = \left[h_i^{\text{rest}} - h_i + \psi_{ei}(h_i)\, I_{ei}(h_e) + \psi_{ii}(h_i)\, I_{ii}(h_i)\right] / \tau_i, \tag{9.9b}$$

$$\begin{aligned} I_{ee}(h_e) &= \left[(N_{ee}^{\alpha} + N_{ee}^{\beta})\,\mathcal{S}_e(h_e) + p_{ee}\right] G_e e\,\tau_E(h_e, \lambda_{\text{NMDA}}), && \text{(9.10a)} \\ I_{ei}(h_e) &= \left[(N_{ei}^{\alpha} + N_{ei}^{\beta})\,\mathcal{S}_e(h_e) + p_{ei}\right] G_e e\,\tau_E(h_e, \lambda_{\text{NMDA}}), && \text{(9.10b)} \end{aligned}$$

$$\begin{aligned} I_{ie}(h_i) &= \lambda_{\text{GABA}} \left[N_{ie}^{\beta}\,\mathcal{S}_i(h_i) + p_{ie}\right] G_i e/\gamma_i, && \text{(9.11a)} \\ I_{ii}(h_i) &= \lambda_{\text{GABA}} \left[N_{ii}^{\beta}\,\mathcal{S}_i(h_i) + p_{ii}\right] G_i e/\gamma_i. && \text{(9.11b)} \end{aligned}$$

For convenient reference, we repeat the definition for the synaptic-current time-"constant" τ_E,

$$\tau_E(h_e, \lambda_{\text{NMDA}}) = \gamma_e^{-1} + \frac{\mathcal{S}_{\text{NMDA}}(h_e)}{\lambda_{\text{NMDA}}} \tag{9.12}$$

with its sigmoid function of membrane voltage,

$$\mathcal{S}_{\text{NMDA}}(h_e) = \frac{\mathcal{S}_{\text{NMDA}}^{\max}}{1 + \exp[-g_{\text{NMDA}}(h_e - \theta_{\text{NMDA}})]}\,. \tag{9.13}$$

It is clear from these equations that we now have the scope to vary either the inhibition-enhancement parameter λ_{GABA} (simulating a pro-GABA anaesthetic such as propofol), or the excitation-suppression parameter λ_{NMDA} (simulating an anti-NMDA anaesthetic, e.g., APV, nitrous oxide, xenon), or to vary both simultaneously (simulating a dual-effect anaesthetic cocktail; some anaesthetic agents are thought to behave in this manner).

In the next section we will determine the new steady-states, and trace their evolution as a function of anaesthetic effect. We will establish the stability of these states, then compute the theoretical spectra for white-noise-driven fluctuations about the stable steady-states.

9.2 Steady States for the NMDA-Sensitive Macrocolumn

9.2.1 Root Searching

Finding the steady-states for the NMDA-sensitive macrocolumn requires a somewhat different iterative scheme from that used in section 3.3.1 for the original GABA-only macrocolumn. This is because the I_{ej} current equations now contain two distinct sigmoidal functions of h_e (the firing-rate sigmoid $\mathcal{S}_e(h_e)$ and the synaptic time-constant sigmoid $\mathcal{S}_{\text{NMDA}}(h_e)$), so it is no longer possible to "invert the excitatory sigmoid" to extract iterated $\hat{h}_e$ trial-root values.

The revised root-extraction scheme proceeds as follows:

1. Set $dh_e/dt = 0$ in Eq. (9.9a). Observe that while h_e appears multiple times in this equation, h_i occurs only in the $I_{ie}(h_i)$ current. Rearrange Eq. (9.9a) to make I_{ie} the subject,

$$\hat{I}_{ie} = -\left[h_e^{\text{rest}} - \hat{h}_e + \psi_{ee}(\hat{h}_e)\,I_{ee}(\hat{h}_e)\right] \Big/ \psi_{ie}(\hat{h}_e) \tag{9.14}$$

where $\hat{I}_{ie}$ is the i–e current computed from the first-guess $\hat{h}_e$ stationary voltage, and $I_{ee}(\hat{h}_e)$ is the corresponding e–e current computed from Eq. (9.10a):

$$I_{ee}(\hat{h}_e) = \left[(N_{ei}^{\alpha} + N_{ei}^{\beta})\,\mathcal{S}(\hat{h}_e) + p_{ei}\right] G_e e\,\tau_E(\hat{h}_e, \lambda_{\text{NMDA}})\,. \tag{9.15}$$

2. Rearrange Eq. (9.11a) to make $\mathcal{S}_i$ the subject, and replace its $I_{ie}(h_i)$ term by the $\hat{I}_{ie}$ values from Eq. (9.14):

$$\hat{\mathcal{S}}_i = \left[\frac{\hat{I}_{ie}}{\lambda_{\text{GABA}} G_i e/\gamma_i} - p_{ie}\right] \Big/ N^\beta_{ie} \tag{9.16}$$

The inhibitory sigmoid-inverse of $\hat{\mathcal{S}}_i$ yields the first-guess $\hat{h}_i$ stationary values:

$$\hat{h}_i = \mathcal{S}_i^{-1}\left(\hat{\mathcal{S}}_i\right) \tag{9.17}$$

where the inhibitory sigmoid function is defined in Eq. (3.6b).

3. Set $dh_i/dt = 0$ in Eq. (9.9b), and rearrange to make I_{ei} the subject (I_{ei} is the only term dependent on h_e). Call this $I^0_{ei}(\hat{h}_i)$ since this provides an estimate for the I_{ei} steady-state based on the $\hat{h}_i$ values from Eq. (9.17),

$$I^0_{ei}(\hat{h}_i) = -\left[h_i^{\text{rest}} - \hat{h}_i + \psi_{ii}(\hat{h}_i)\, I_{ii}(\hat{h}_i)\right] \Big/ \psi_{ei}(\hat{h}_i)\,. \tag{9.18}$$

4. Unlike the pure-GABA case discussed in Chapter 3, it is no longer possible to retrieve $\hat{h}_e$ by computing the excitatory sigmoid-inverse of $I^0_{ei}(\hat{h}_i)$; this is because there are now *two* independent sigmoidal functions of h_e in Eq. (9.10b). Instead, we allow Eq. (9.10b) to provide a second estimate, $I^0_{ei}(\hat{h}_e)$, this new estimate based on the initial $\hat{h}_e$ values entered in Eq. (9.14),

$$I^0_{ei}(\hat{h}_e) = -\left[(N^\alpha_{ei} + N^\beta_{ei})\,\mathcal{S}(\hat{h}_e) + p_{ei}\right] G_e e\, \tau_E(\hat{h}_e, \lambda_{\text{NMDA}})\,. \tag{9.19}$$

5. The difference between the Eqs (9.18) and (9.19) estimates for I^0_{ei} provides an error function ΔI_{ei},

$$\Delta I_{ei}(\hat{h}_e, \hat{h}_i) = I^0_{ei}(\hat{h}_e) - I^0_{ei}(\hat{h}_i) \tag{9.20}$$

which will be zero when $(\hat{h}_e, \hat{h}_i)$ is a stationary soma-voltage coordinate, and which will exhibit a sign-change as the soma voltages traverse a stationary point. By locating the sign-changes in ΔI_{ei}, we are able to bracket the stationary-state roots, then iterate to convergence using the MATLAB `fzero()` bisection routine.

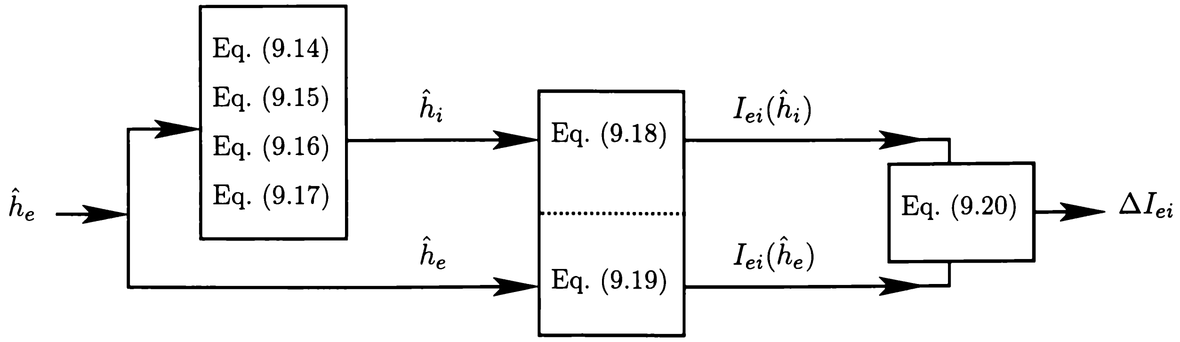

Figure 9.3: Calculation of the $\Delta I_{ei}(\hat{h}_e, \hat{h}_i)$ error function for the NMDA-sensitive macrocolumn. $\hat{h}_e$ is a first-guess for the excitatory steady-state voltage; $\hat{h}_i$ is the corresponding first-guess for the inhibitory steady-state. $\Delta I_{ei} = 0$ at an actual (h^0_e, h^0_i) steady-state coordinate.

The calculation sequence required to compute the ΔI_{ei} error function is summarized in Fig. 9.3.

As was the case for the pure-GABA macrocolumn, I found that unless the mesh of $\hat{h}_e$ trial values was made extremely fine, it was often the case that roots in the firing-rate sigmoid tails would be missed. To avoid the need for a dense (and computationally expensive) search grid, I adopted the same NaN boundary-pushing scheme described in Section 3.3.5.

Unfortunately, and apparently because of the presence of the third sigmoid function (the NMDA term of Eq. (9.13)), these boundary-point explorations now unearthed several additional "roots" which were clearly spurious since, although the retrieved h_e^0 values seemed plausible, the retrieved h_i^0 values were invariably "stuck" at +45 mV, and the F_2 rate equation (9.9b) for dh_i/dt was far from zero. In order to detect and reject these spurious roots, I added a final check for stationarity: a putative root must satisfy $dh_e/dt = 0$ and $dh_i/dt = 0$ within tolerance. While this test should have been completely unnecessary (since the numerical algorithm was derived on the *assumption* of stationarity in the first place), the need for it seems to arise from the numerical stresses occurring at the NaN/real-number boundary.

9.2.2 Distribution of Steady States

1. Reduction to Pure-GABA Case: Infinite NMDA suppression

In the limit of complete NMDA suppression (i.e., $\lambda_{\text{NMDA}} \to \infty$), the behaviour of the NMDA-enabled macrocolumn should collapse to that of the pure-GABA macrocolumn previously analyzed in Chapter 3. I used this idea to check the correctness of the steady-state roots retrieved via the I_{ei} algorithm of Eqs (9.14–9.20), in the infinite anti-NMDA limit, against those retrieved via the dual sigmoid-inverse method of Chapter 3. The graphs of Fig. 9.4 show the comparison. It is clear from Fig. 9.4a that the two algorithms retrieve $(\lambda_{\text{GABA}}, h_e^0)$ steady-state coordinates which, to printing resolution, *appear* identical: the dots (I_{ei} retrievals for h_e^0) are co-centred with the circles (inverse-sigmoid retrievals for h_e^0); similarly, the crosses (I_{ei} retrievals for h_i^0) are co-centred with the boxes (inverse-sigmoid retrievals for h_i^0). That the two methods are distinct and do *not* return identical results can be established by differencing one from the other to compute the *mismatch residues* for h_e and h_i:

$$\Delta h_e = h_e^{[I_{ei}]} - h_e^{[\text{inv.sig.}]}, \tag{9.21a}$$

$$\Delta h_i = h_i^{[I_{ei}]} - h_i^{[\text{inv.sig.}]}. \tag{9.21b}$$

To quantify the numerical agreement achieved by the two algorithms, Fig. 9.4b presents a 3-D plot showing the mismatch residues for Δh_e and Δh_i, plotted on the z-axis, versus soma voltage and λ_{GABA}. As might be anticipated, the largest residue excursions occur along the bottom (hyperpolarized) branch where the firing-rate sigmoids are close to zero and root-retrievals are consequently difficult. (The opposite extreme of saturated firing in the top-left corner also presents numerical difficulties: large residues become evident for $\lambda_{\text{GABA}} < 0.15$, but are not shown here.) Nevertheless, for the 99 coordinates of Fig. 9.4b, the mismatch statistics (mean ±

(a) Comparison of Inv.Sig. and I_{ei} Root-Retrieval Methods

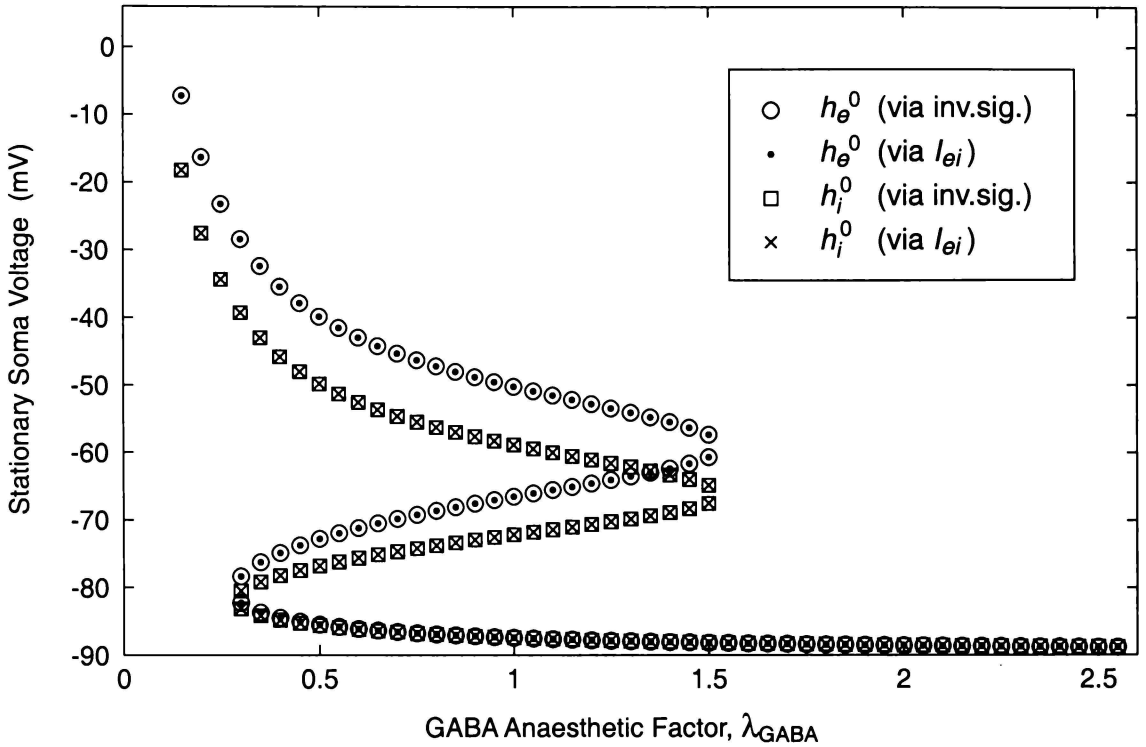

(b) Error Residues from Root Determinations

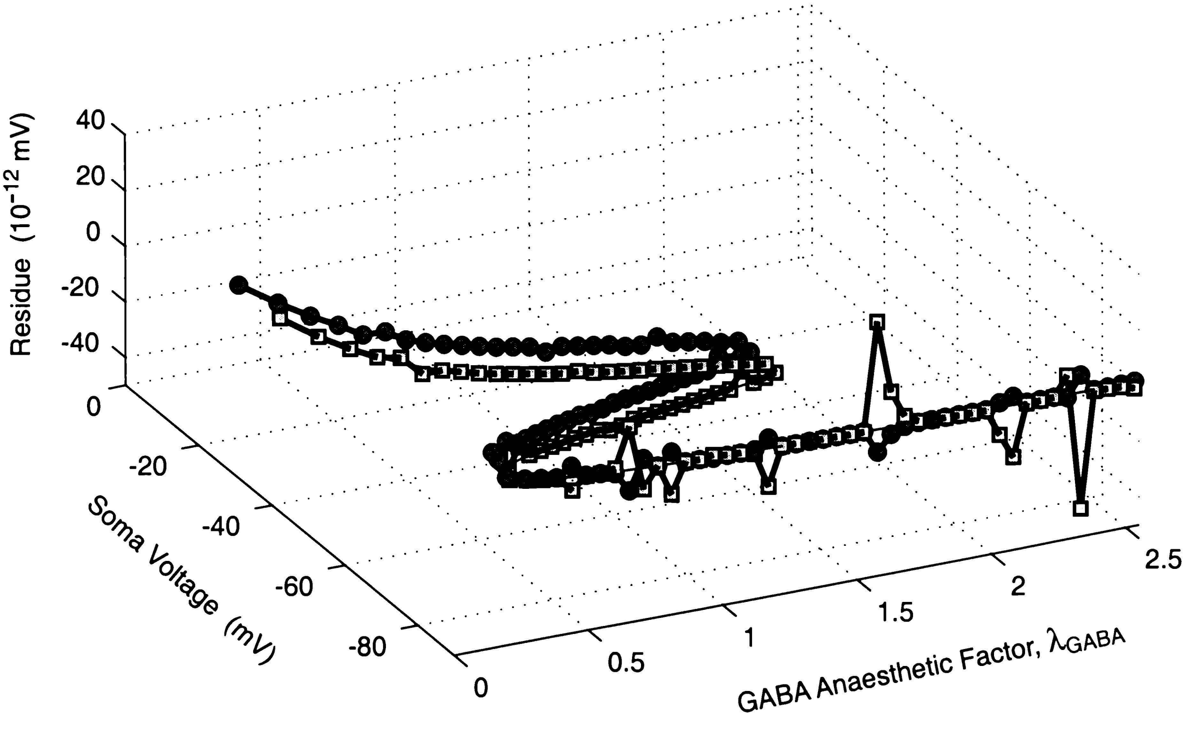

Figure 9.4: Comparison of inverse-sigmoid and I_{ei}-based root retrieval results. (a) Upper curve shows inverse-sigmoid retrievals for h_e^0 as open-circle (o), and I_{ei} retrievals for h_e^0 as bold-dot (·) within the circle. Second curve shows inverse-sigmoid retrievals for h_i^0 as square (□), and I_{ei} retrievals for h_i^0 as a cross (×) within the square. (b) Error residuals Δh_e and Δh_i versus soma voltage vs λ_{GABA}. Circles show Δh_e^0; squares show Δh_i^0.

standard deviation) are quite satisfactory:

$$\begin{aligned}\overline{\Delta h_e} &= (0.14 \pm 1.74) \times 10^{-12}\ \text{mV}\\ \overline{\Delta h_i} &= (-0.26 \pm 6.85) \times 10^{-12}\ \text{mV}.\end{aligned}$$

This excellent agreement between the two algorithms gives me confidence that the I_{ei}-based root-retrieval code is working properly.

2. Variable NMDA Suppression

We have now verified that in the $\lambda_{\text{NMDA}} \to \infty$ limit, the NMDA-sensitive macrocolumn can exist in either one or three λ_{GABA}-determined steady states, and that the distribution of these steady states is identical to that obtained for the original GABA-only adiabatic model of Chapter 3. Here, we will allow λ_{NMDA} to be relaxed from this infinitely-suppressed limit in order to investigate the effect of including the slow-acting NMDA neurophysiology into the model. We will find that the presence of the slow NMDA τ_E term in Eqs (9.10a–9.10b) permits new macrocolumn steady-states to come into existence.

Figure 9.5 shows the results of a search for soma-voltage steady states for the NMDA-enabled macrocolumn for a range of λ_{NMDA} NMDA-suppression factors. The $\lambda_{\text{NMDA}} = 1$ curves in Fig. 9.5 corresponds to incorporation of a fully-extended excitatory response, giving an EPSP decay time (see Eqs (9.1, 9.2) and Fig. 9.1), for a maximally depolarized macrocolumn, of

$$\tau_E^{\max} = \gamma_e^{-1} + \frac{S_{\text{NMDA}}^{\max}}{\lambda_{\text{NMDA}}} = 3.3 + \frac{83.7}{1} = 87.0\ \text{ms}.$$

The five other curves, corresponding to $\lambda_{\text{NMDA}} = 2, 3, \ldots, \infty$, demonstrate the effect of incremental increases in NMDA suppression. As expected, for $\lambda_{\text{NMDA}} = \infty$ the pure-GABA curve of Fig. 9.4a is recovered.

The significant feature of Fig. 9.5 is the appearance of a new turning point in the vicinity of the $\theta_{\text{NMDA}} = -28$ mV threshold voltage. The magnitude and curvature of this NMDA feature scales inversely with λ_{NMDA}. The discovery of an additional turning point means that there can now be up to *five* stationary solutions for a given λ_{GABA} value. For example, consider the $\lambda_{\text{NMDA}} = 3$ curve: there are five $(\lambda_{\text{GABA}}, h_{e,i}^0)$ intersections with vertical lines drawn through $\lambda_{\text{GABA}} = 1.5$ in Figs 9.5a,b. I will demonstrate shortly that for the 5-root NMDA macrocolumn, three states are stable. This has important implications for predicted neural behaviour.

For the pure-GABA macrocolumn with two stable states, only a single downward transition is possible: from the depolarized upper branch to the hyperpolarized lower branch. With the incorporation of NMDA effect into the macrocolumn, there is now the possibility of a new family of first-order phase transitions: an initial jump from the strongly depolarized upper branch to the intermediate branch at a critical value of GABA concentration, and then as λ_{GABA} increases further, a second downward transition from the intermediate to the hyperpolarized branch. The presence of the intermediate branch also permits interesting hysteresis behaviours with implications for the modelling of memory and learning.

3. Effect of Firing-Rate on NMDA Steady States

Note that the inclusion of an NMDA term in the model means that, because the excitatory post-synaptic potentials now have extended duration, for a given value of λ_{GABA}, the macrocolumn

(a) h_e^0 (high-firing case)

(b) h_i^0 (high-firing case)

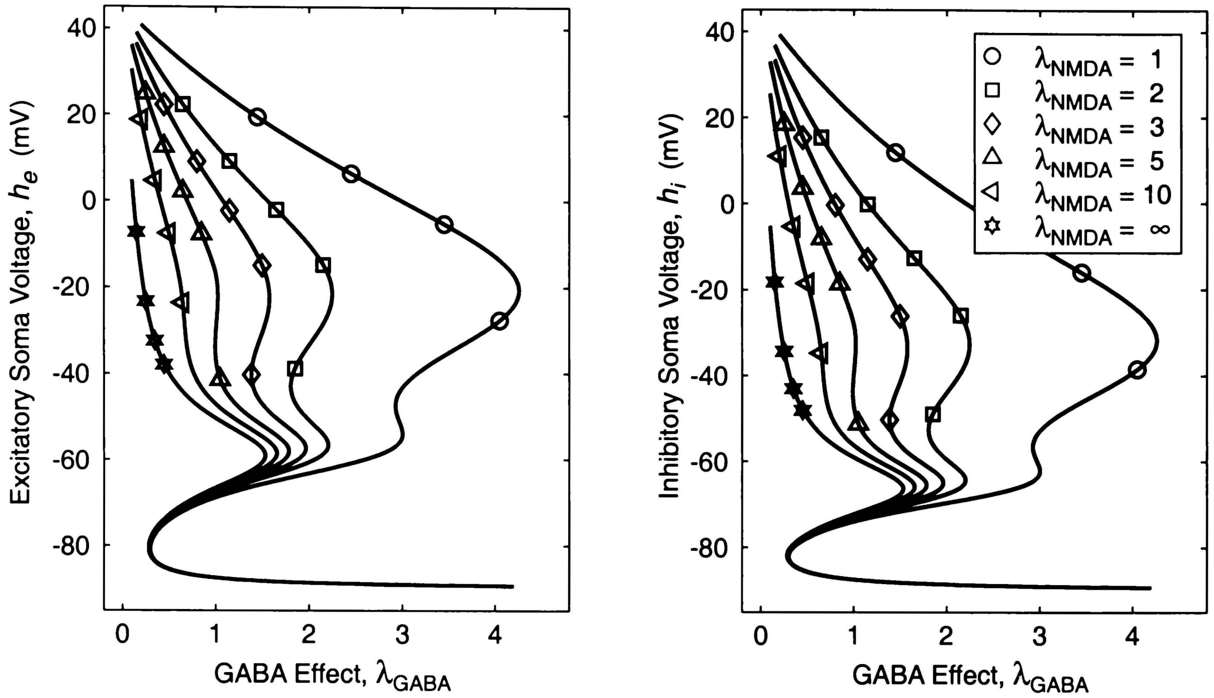

(c) h_e^0 (low- vs high-firing)

(d) h_i^0 (low- vs high-firing)

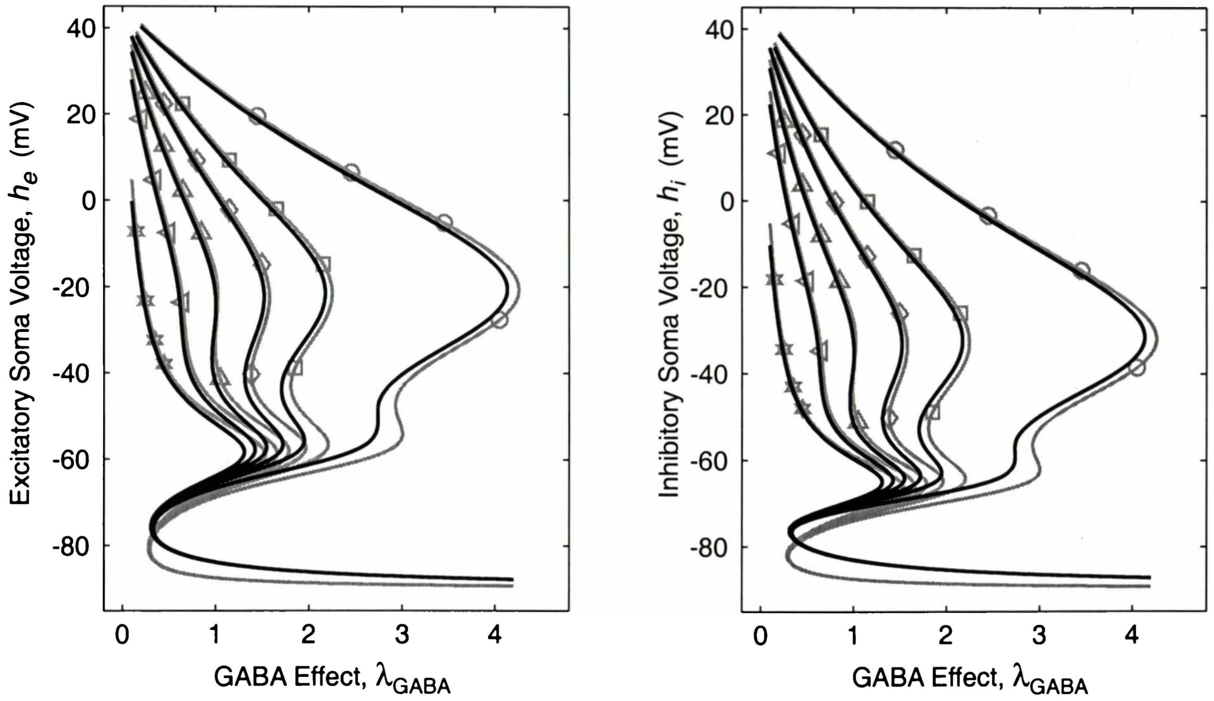

Figure 9.5: Distribution of soma-voltage steady states as a function of λ_{GABA} for the NMDA-enabled macrocolumn. Roots were recovered at 0.05 steps in λ_{GABA}, with additional searching undertaken to accurately locate each turning point. Roots were sorted by soma potential, then spline-fitted to give the continuous curves shown here. Top two panels show (a) excitatory (h_e^0) and (b) inhibitory (h_i^0) steady states for the default high-firing case ($\mathcal{S}_e^{\max} = \mathcal{S}_i^{\max} = 1000\,\text{s}^{-1}$). Bottom two panels (c, d) show alteration in distribution of steady states when the maximum firing rate is lowered to $\mathcal{S}_e^{\max} = \mathcal{S}_i^{\max} = 100\,\text{s}^{-1}$ (black curves). For ease of comparison, the high-firing curves of (a, b) are replicated in grey.

will tend to be *more* excited (i.e., more neurons firing) than previously. So if $\lambda_{\text{GABA}} = 1$ in the previous pure-GABA model represented some sort of "normal" range of excitation, then enabling the NMDA terms will tend to give a relatively "over-excited" macrocolumn. This NMDA boost in excitation can be seen clearly in the upper-branch regions of Fig. 9.5a,b by comparing the pure-GABA ($\lambda_{\text{NMDA}} = \infty$) curve with, say, the $\lambda_{\text{NMDA}} = 10$ curve: for a given value of λ_{GABA}, we see that the upper-branch steady-state values for h_e^0 and h_i^0 have been raised (made more depolarized). Equivalently, for a given soma voltage, a larger GABA concentration is required in order to reach the turning point at which the transition to the hyperpolarized bottom branch can occur.

In short, the amount of inhibition required to anaesthetize the macrocolumn has to be increased in order to compensate for the excitatory boost generated by the NMDA effect.

We can partly compensate for this (presumed) over-excitation by adjusting the saturation setting of the $\mathcal{S}_e(h_e)$ and $\mathcal{S}_i(h_i)$ firing-rate sigmoid functions downwards from their 1000 s^{-1} default value: a maximum setting of 100 s^{-1} is perhaps more physiologically plausible. The result of such adjustment is shown in Fig. 9.5c,d. By comparing the low-firing curves (in black) with the high-firing curves (in grey), we see that the upper-branch turning points have been shifted to the *left* by the reduction in firing rate (a smaller GABA concentration is required to achieve anaesthesia). However, for the hyperpolarized branch, the lower-left turning point has been *raised* and shifted to the *right*, indicating that in this régime the low-firing macrocolumn has actually become *more* rather than less excited. This occurs because although the inhibitory neurons dominate here, their average firing rate has been lowered, so there is less inhibition.

4. Standard λ_{NMDA} Settings for Low-Firing-Rate Macrocolumn

In view of the fact that the pure-GABA model seems to have predictive veracity (it successfully predicts the power surge, the frequency shift, and spectral entropy changes observed in clinical settings), it seems wise to retain the pure-GABA model as a baseline against which the behaviour of the NMDA-enabled macrocolumn can be compared. I will assume that the inclusion of NMDA effects is in the nature of a perturbative correction to the GABA model, rather than a dramatic replacement for what has gone before. Thus, rather than taking the "strong" $\lambda_{\text{NMDA}} = 1$ curves of Fig. 9.5 as being typical, I will opt for the "moderately weak" NMDA effect given by setting the NMDA-suppression at $\lambda_{\text{NMDA}} = 4$, and setting the maximum firing rates at $\mathcal{S}_e^{\max} = \mathcal{S}_i^{\max} = 100\ \text{s}^{-1}$. This prototypical NMDA curve, which has a maximum of five steady states, is plotted in Fig. 9.6. Also shown is the weaker $\lambda_{\text{NMDA}} = 8$ trajectory which is sufficiently NMDA-suppressed that the pair of (local) maximum and minimum λ_{GABA} turning points which would have appeared at about -20 and -30 mV respectively have flattened out, being replaced by a point of inflection at $\sim\!-30$ mV. Like the pure-GABA ($\lambda_{\text{NMDA}} = \infty$) case, this weaker pro-NMDA setting permits a maximum of only three steady states.

Listed in Table 9.2 are the four "standard" pro-NMDA settings which will be used for comparison purposes when examining stability and spectral predictions for the NMDA-enabled adiabatic macrocolumn.

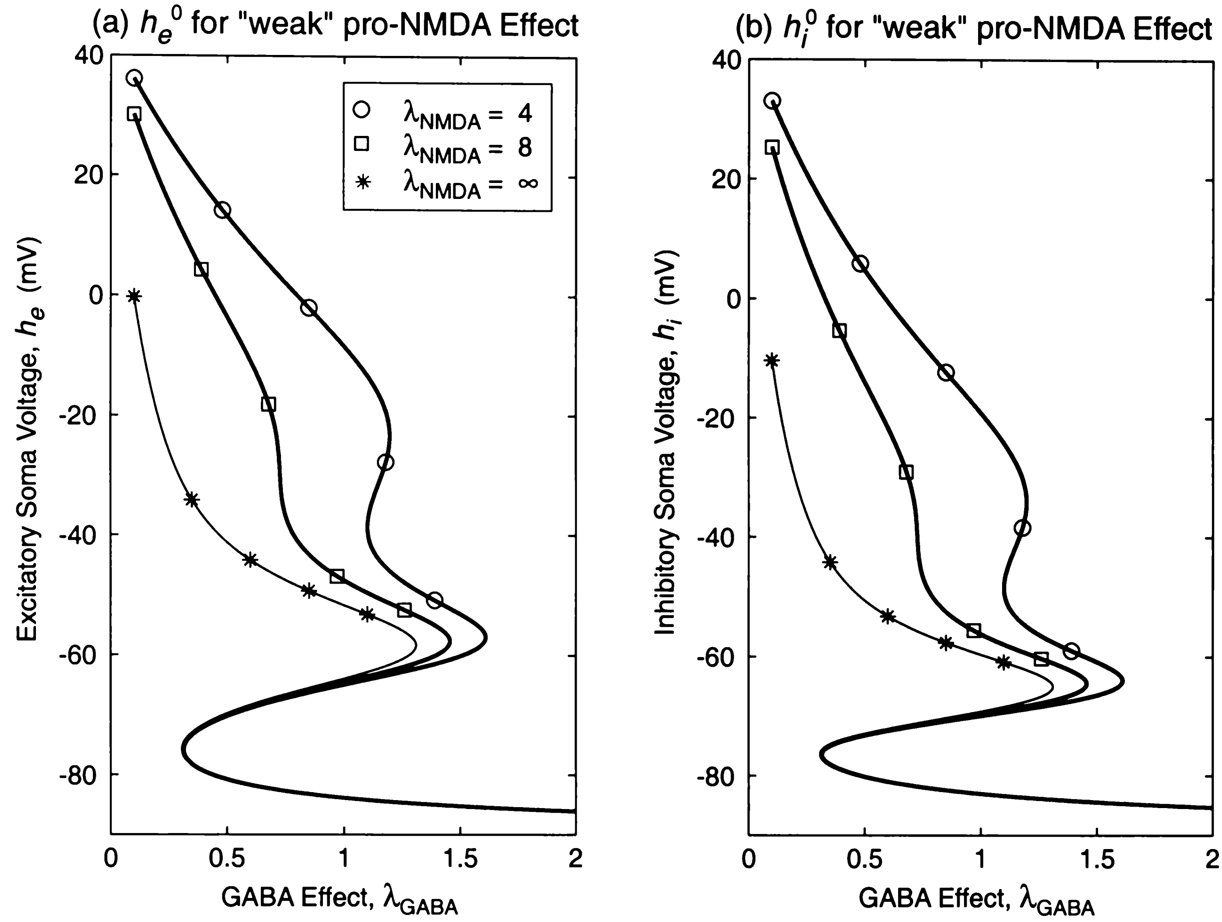

Figure 9.6: Excitatory (left) and inhibitory (right) soma-voltage steady states as a function of λ_{GABA} for the "moderately" ($\lambda_{\text{NMDA}} = 4$) and "weakly" ($\lambda_{\text{NMDA}} = 8$) NMDA-enabled macrocolumn. Maximum firing rates are $S_e^{\max} = S_i^{\max} = 100\ \text{s}^{-1}$. Roots were recovered at 0.01 steps in λ_{GABA}, with additional searching undertaken to accurately locate each turning point. Roots were sorted by soma potential, then spline-fitted to give the continuous curves shown here. (a) h_e^0 vs λ_{GABA}; (b) h_i^0 vs λ_{GABA}. For reference, the distribution of steady states for the pure-GABA ($\lambda_{\text{NMDA}} = \infty$) low-firing model is drawn with a thin pen.

9.3 Stability of the NMDA-Enabled Macrocolumn

We have established that the inclusion of NMDA neurotransmitter in the cortical model (via extension of the time-course of the excitatory post-synaptic potential) alters both the *distribution*

Table 9.2: Reference settings for NMDA-enabled macrocolumn. Five-root (four turning-point) behaviour is observed only for "moderate" pro-NMDA settings. If the pro-NMDA setting is too strong (e.g., $\lambda_{\text{NMDA}} \leqslant 1$: unsuppressed NMDA excitation), or too weak (e.g., $\lambda_{\text{NMDA}} \geqslant 8$: NMDA excitation strongly suppressed), then no more than three steady states are available.

λ_{NMDA}	$\tau_E^{\max}$ (ms)	max. number of steady states	pro-NMDA Effect
1	87.0	3	"strong" (i.e., no NMDA suppression)
4	**24.2**	**5**	**"moderate"**
8	13.8	3	"weak"
∞	3.3	3	"zero" (i.e., complete NMDA suppression)

and *number* of soma-voltage steady states. For a moderate NMDA-suppression factor of $\lambda_{\text{NMDA}} = 4$, the number of possible steady states increases to five, two more than for the pure-GABA model. By performing a linear stability analysis, I will demonstrate that two of these five states are unstable, leading to the interesting possibility that the NMDA-sensitive macrocolumn can exist on one of three stable branches—active, intermediate, and quiescent—with first-order jump transitions being required to move between branches.

9.3.1 Stability Analysis: Equations

To establish the stability characteristics of the steady states for the NMDA-sensitive macrocolumn, I will follow the small-fluctuations stability analysis technique described in Chaper 4. This involves examination of the eigenvalues for the 2×2 Jacobian matrix

$$\mathbf{J} = \begin{bmatrix} \dfrac{\partial F_1}{\partial h_e} & \dfrac{\partial F_1}{\partial h_i} \\[2ex] \dfrac{\partial F_2}{\partial h_e} & \dfrac{\partial F_2}{\partial h_i} \end{bmatrix} \tag{9.22}$$

evaluated at the (h_e^0, h_i^0) points resulting from the stationarity requirement $F_1 \equiv dh_e/dt = 0$ and $F_2 \equiv dh_i/dt = 0$. The adiabatic equations for the NMDA-sensitive macrocolumn were listed as Eqs(9.9a–9.13). Using these, the four elements of the $\mathbf{J}$ matrix are evaluated as follows:

$$J_{11} \equiv \frac{\partial F_1}{\partial h_e} = \frac{1}{\tau_e}\left[-1 + \frac{\partial \psi_{ee}}{\partial h_e} I_{ee} + \psi_{ee}\frac{\partial I_{ee}}{\partial h_e} + \frac{\partial \psi_{ie}}{\partial h_e} I_{ie}\right] \tag{9.23a}$$

$$J_{12} \equiv \frac{\partial F_1}{\partial h_i} = \frac{1}{\tau_e}\left[\psi_{ie}\frac{\partial I_{ie}}{\partial h_i}\right] \tag{9.23b}$$

$$J_{21} \equiv \frac{\partial F_2}{\partial h_e} = \frac{1}{\tau_i}\left[\psi_{ei}\frac{\partial I_{ei}}{\partial h_i}\right] \tag{9.23c}$$

$$J_{22} \equiv \frac{\partial F_2}{\partial h_i} = \frac{1}{\tau_i}\left[-1 + \frac{\partial \psi_{ei}}{\partial h_i} I_{ei} + \frac{\partial \psi_{ii}}{\partial h_i} I_{ii} + \psi_{ii}\frac{\partial I_{ii}}{\partial h_i}\right]. \tag{9.23d}$$

The four partial derivatives of the ψ_{jk} weighting-functions were listed earlier in Eq. (4.25). The derivatives of the NMDA-enhanced I_{ee} and I_{ei} input currents defined by Eq. (9.10) are altered by the presence of the voltage-gated τ_E time-factor, and now read,

$$\frac{\partial I_{ee}}{\partial h_e} = G_e e\,(N_{ee}^{\alpha} + N_{ee}^{\beta})\,\frac{\partial S_e}{\partial h_e}\,\tau_E + G_e e\left[(N_{ee}^{\alpha} + N_{ee}^{\beta})\,S_e + p_{ee}\right]\frac{\partial \tau_E}{\partial h_e} \tag{9.24a}$$

$$\frac{\partial I_{ei}}{\partial h_e} = G_e e\,(N_{ei}^{\alpha} + N_{ei}^{\beta})\,\frac{\partial S_e}{\partial h_e}\,\tau_E + G_e e\left[(N_{ei}^{\alpha} + N_{ei}^{\beta})\,S_e + p_{ei}\right]\frac{\partial \tau_E}{\partial h_e} \tag{9.24b}$$

$$\frac{\partial I_{ie}}{\partial h_i} = \lambda_{\text{GABA}} \cdot \frac{G_i e\, N_{ie}^{\beta}}{\gamma_i}\,\frac{\partial S_i}{\partial h_i} \tag{9.24c}$$

$$\frac{\partial I_{ii}}{\partial h_i} = \lambda_{\text{GABA}} \cdot \frac{G_i e\, N_{ii}^{\beta}}{\gamma_i}\,\frac{\partial S_i}{\partial h_i} \tag{9.24d}$$

where the derivative of the NMDA time-"constant" is

$$\frac{\partial \tau_E}{\partial h_e} = \frac{1}{\lambda_{\text{NMDA}}} \cdot \frac{g_{\text{NMDA}}\, S_{\text{NMDA}}^{\max}\, \exp[-g_{\text{NMDA}}(h_e - \theta_{\text{NMDA}})]}{\left[1 + \exp[-g_{\text{NMDA}}(h_e - \theta_{\text{NMDA}})]\right]^2}. \tag{9.25}$$

Note that there is no NMDA effect in the I_{ie} and I_{ii} currents originating from the inhibitory neurons, so Eqs (9.24c,d) are unchanged from the pure-GABA case. The derivatives for the firing-rate sigmoids $\mathcal{S}_{e,i}$ were listed earlier in Eq. (4.27).

Each (h_e^0, h_i^0) coordinate on the S-bend graph of stationary states will return a pair of eigenvalues. The stability of the stationary state is determined by the larger (i.e., least negative) of the eigenvalue pair: if the real part of the dominant eigenvalue is negative, the state is stable with respect to small perturbations; if the real part is positive, perturbations will grow, so the point is unstable; and if the eigenvalue is zero, the point has neutral stability, indicative of a turning point in the S-graph. If the eigenvalues are complex, then there is the possibility of oscillations, but these will be rapidly damped out if the real part of the eigenvalue is negative.

Equations (9.23–9.25) were coded into MATLAB and applied to each of the standard λ_{NMDA} settings listed in Table 9.2 for a finely-stepped range of λ_{GABA} values. The results of these computations now follow.

9.3.2 Results

The top row of trajectories of Fig. 9.7 plot the soma voltage steady states as a function of λ_{GABA} for four representative values of NMDA suppression: $\lambda_{\text{NMDA}} = \infty, 8, 4, 1$. Below each steady-state trajectory is a pair of graphs showing the distribution of the real (second row) and imaginary (third row) parts of the eigenvalues. Only the dominant eigenvalues are plotted, since these determine system stability.

The left-hand column of three panels of Fig. 9.7(a–c) give the results for a low-firing ($\mathcal{S}_{e,i}^{\max} = 100\ \text{s}^{-1}$) macrocolumn in which all NMDA activity has been suppressed ($\lambda_{\text{NMDA}} = \infty$). The results in (a)–(c) are similar to those presented in Chap. 3 for the high-firing ($\mathcal{S}_{e,i}^{\max} = 1000\ \text{s}^{-1}$) GABA-only macrocolumn, except that the induction transition point now occurs earlier at $\lambda_{\text{GABA}} \approx 1.3$. The pair of S-bend turning points labelled "3" and "4" in (a) correspond to the pair of zero-valued eigenroots in (b). Between these two zero crossings, the intermediate eigenvalues loop up into the positive half-plane, indicating that, as expected, the S-bend region of positive slope in (a) is unstable. In contrast, regions above "3" (depolarized), or below "4" (hyperpolarized), are always stable.

There are three regions (indicated with grey shading in (b) and (c)) which return complex eigenvalues, but these cannot support oscillations because in all cases the real part of the eigenvalue is very strongly negative.

Panels (d) and (g) of Fig. 9.7 show the respective effects of weak ($\lambda_{\text{NMDA}} = 8$) and moderate ($\lambda_{\text{NMDA}} = 4$) enabling of NMDA prolongation of the EPSPs. The steepening negative gradient at $h_e \approx -30$ mV in (d) becomes, in (g), a fully developed positive-gradient region, bracketted by a new pair of steady-state turning points labelled "1" and "2." Inspection of the eigenvalues trajectory of (h) shows that the dominant eigenvalue now loops twice into the positive half-plane, with each of the four zero-crossings in (h) coinciding with one of the four numbered turning points of (g). Thus there are now *three* stable steady-state branches for the $\lambda_{\text{NMDA}} = 4$ macrocolumn:

- $h_e > h_{e,1}$ strongly depolarized *upper* branch;
- $h_{e,2} < h_e < h_{e,3}$ moderately depolarized *middle* branch;

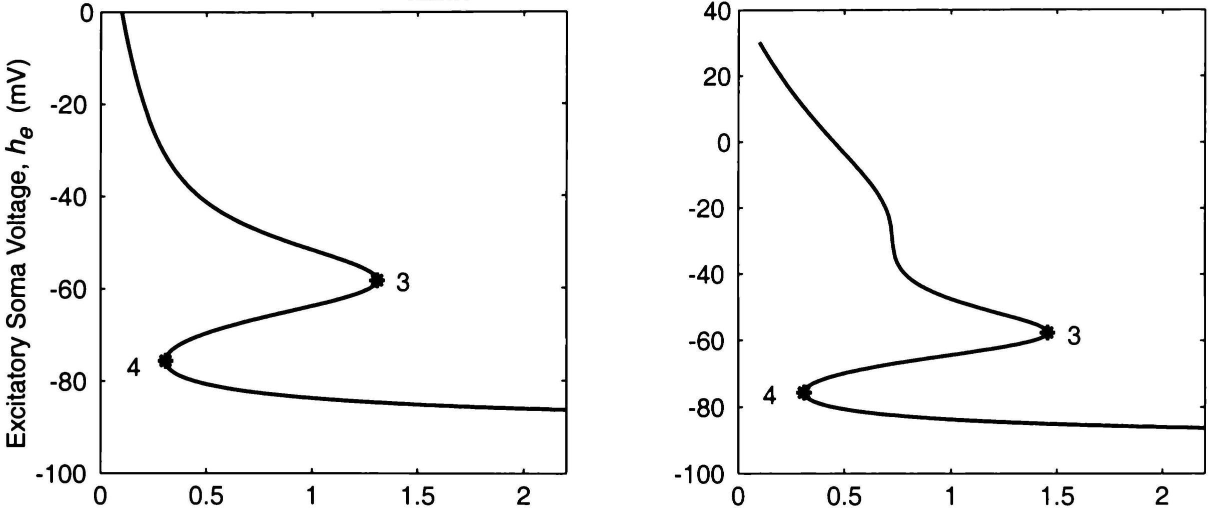
(a) Stationary h_e for $\lambda_{NMDA} = \infty$

(d) Stationary h_e for $\lambda_{NMDA} = 8$

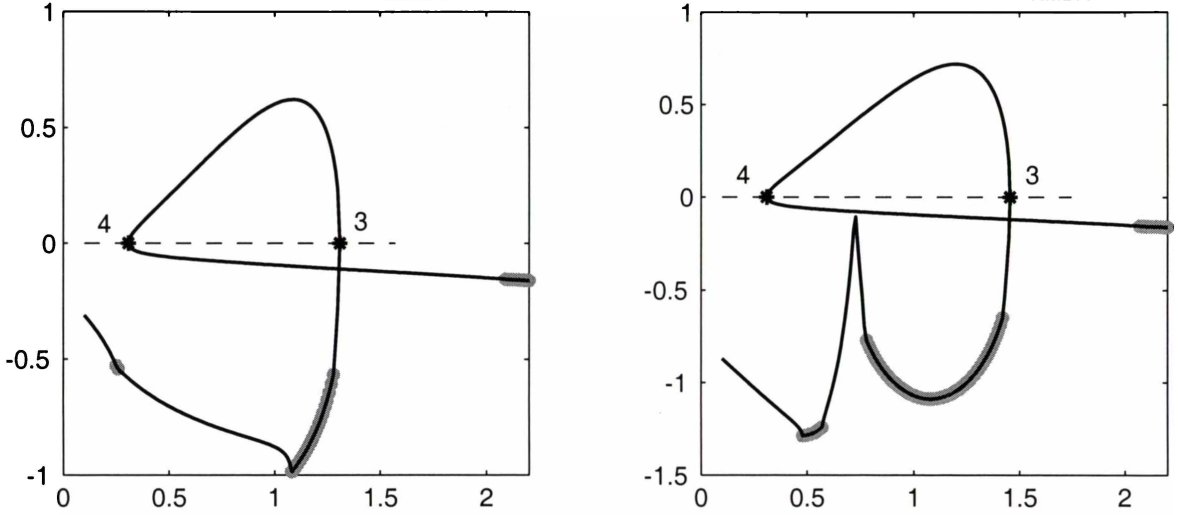
(b) Real [Eig] / 1000 for $\lambda_{NMDA} = \infty$

(e) Real [Eig] / 1000 for $\lambda_{NMDA} = 8$

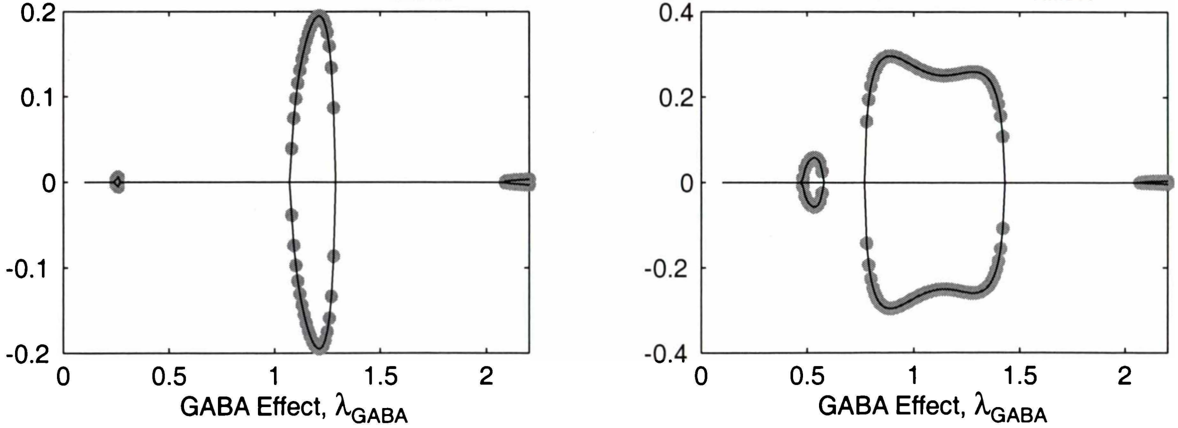
(c) Imag [Eig] / 1000 for $\lambda_{NMDA} = \infty$

(f) Imag [Eig] / 1000 for $\lambda_{NMDA} = 8$

Figure 9.7: Distribution of steady states and their eigenvalues for four representative values of NMDA suppression: $\lambda_{\text{NMDA}} = \infty$ (panels a–c), $\lambda_{\text{NMDA}} = 8$ (d–f), $\lambda_{\text{NMDA}} = 4$ (g–i: next page), $\lambda_{\text{NMDA}} = 1$ (j–l: next page). *Top panels* (a, d on this page; g, j on next page): S-bend and double-S-bend equilibrium soma voltages as a function of pro-GABA anaesthetic effect; numbered asterisks ($*$) mark the S-bend turning points. *Middle panels:* Real part of dominant (i.e., least negative) eigenvalue; eigenvalue becomes complex at positions marked with filled-grey circles. *Bottom panels:* Imaginary parts of eigenvalues.

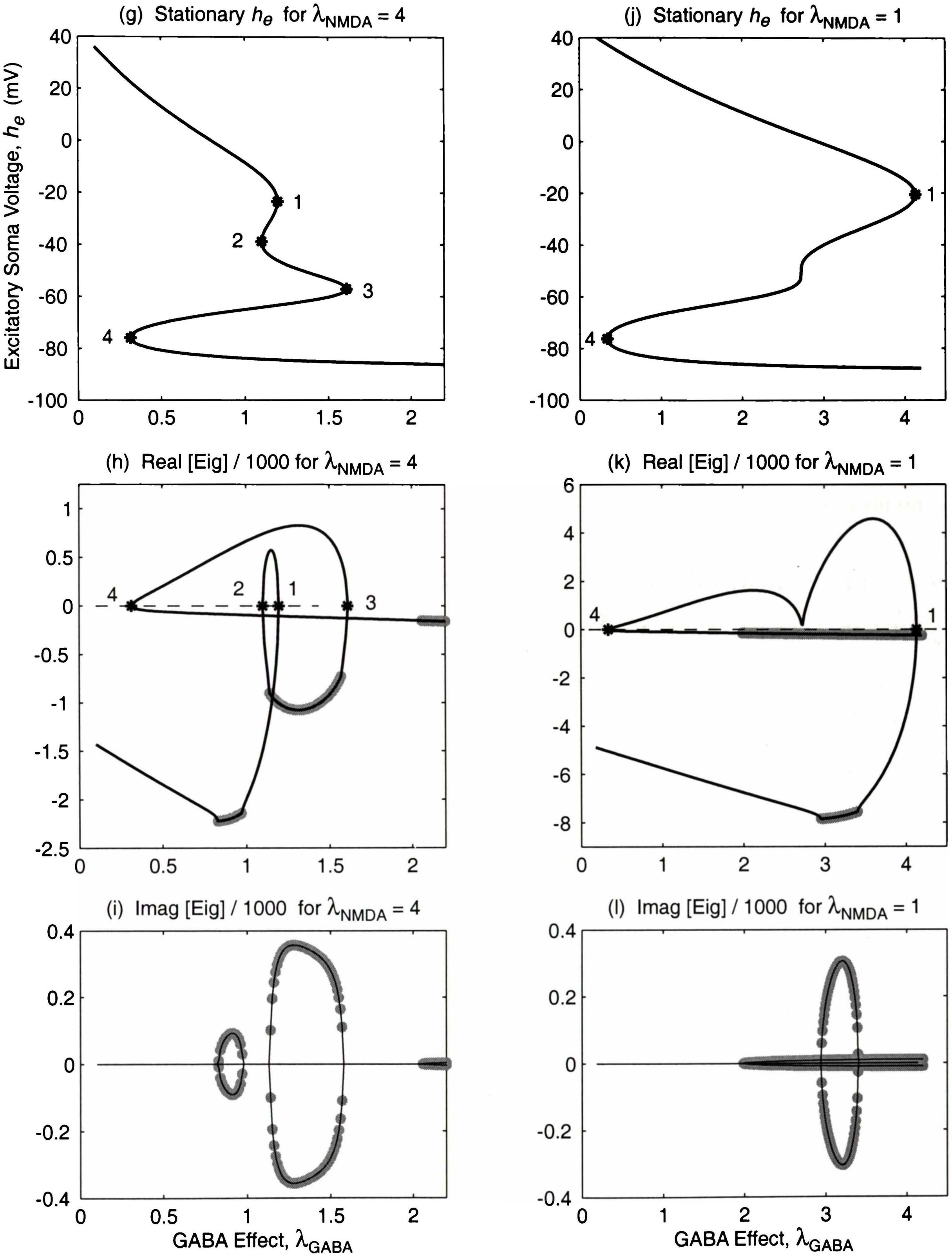

Figure 9.7 **(*cont.*):** Distribution of steady states and eigenvalues for weak ($\lambda_{\text{NMDA}} = 4$: left panels) and zero ($\lambda_{\text{NMDA}} = 1$: right panels) NMDA suppression. (g) Only the $\lambda_{\text{NMDA}} = 4$ setting exhibits the full complement of four turning points; for higher (j) and lower (a, d on previous page) λ_{NMDA} settings, two of the turning points have disappeared. S-bend regions of positive slope (e.g., regions 1–2 and 3–4 of panel g) are associated with a positive eigenvalue, and are therefore unstable.

- $h_e < h_{e,3}$ hyperpolarized *bottom* branch.

The emergence of an isolated and stable mid-branch is the significant NMDA contribution to model behaviour, since it now permits the macrocolumn to exist in a "half-way" polarization state lying between the extremes of hyperpolarized quiescence and strongly depolarized activity. This leads to the interesting possibility of first-order jump transitions to and from this intermediate state, and to the prediction of *two* biphasic power surges as the GABA anaesthetic damps the conscious brain from normal activity into unconsciousness—this idea will be discussed in the next section.

Figure 9.7(j) shows the result of allowing the full extent of EPSP prolongation ($\lambda_{\text{NMDA}} = 1$, $\tau_E \to 84$ ms for the completely depolarized macrocolumn; see Fig. 9.1) permitted by the model. Access to the 2–3 intermediate zone has been lost because the entire 1–4 region is now unstable, so once again the macrocolumn has only two stable branches available to it. The induction transition which would have occurred at the $h_e \approx -60$ mV turning point labelled "3" in (a), (d), or (g) now occurs at turning point "1" ($h_e \approx -20$ mV), and requires a much larger GABA concentration to compensate for the enhanced EPSP duration.

9.4 Fluctuation Analysis for NMDA Model

9.4.1 Fluctuation Analysis: Equations

As was the case for the pure-GABA adiabatic macrocolumn examined earlier, the NMDA-enabled macrocolumn is a two-dimensional Ornstein–Uhlenbeck process whose covariance matrix $\boldsymbol{\sigma}$ and spectrum matrix $\mathbf{S}(\omega)$ can be expressed in terms of its drift matrix $\mathbf{A}$ and its diffusion matrix $\mathbf{D}$. The 2×2 drift matrix $\mathbf{A}$ is the negative of the Jacobian matrix,

$$\mathbf{A} = -\begin{bmatrix} \dfrac{\partial F_1}{\partial h_e} & \dfrac{\partial F_1}{\partial h_i} \\[2ex] \dfrac{\partial F_2}{\partial h_e} & \dfrac{\partial F_2}{\partial h_i} \end{bmatrix} \tag{9.26}$$

thus the elements of $\mathbf{A}$ are the negative of the right-hand sides of Eq. (9.23).

The NMDA-enabled diffusion matrix is obtained by editing the pure-GABA diffusion matrix of Chap. 5: each occurrence of the excitatory inverse-rate constant γ_e^{-1} is replaced by the NMDA-dependent time-"constant" τ_E as highlighted with double underlines as below,

$$\begin{aligned} D_{11} &= \frac{1}{\tau_e^2}\Big\{(\psi_{ee}\,\alpha_{ee}\,G_e e/\underline{\underline{\gamma_e}})^2\langle p_{ee}\rangle + \lambda_{\text{GABA}}^2\cdot(\psi_{ie}\,\alpha_{ie}\,G_i e/\gamma_i)^2\langle p_{ie}\rangle\Big\}_{\text{eq.}} \\ &\longrightarrow \frac{1}{\tau_e^2}\Big\{(\psi_{ee}\,\alpha_{ee}\,G_e e\,\underline{\underline{\tau_E}})^2\langle p_{ee}\rangle + \lambda_{\text{GABA}}^2\cdot(\psi_{ie}\,\alpha_{ie}\,G_i e/\gamma_i)^2\langle p_{ie}\rangle\Big\}_{\text{eq.}}, \end{aligned} \tag{9.27a}$$

and

$$\begin{aligned} D_{22} &= \frac{1}{\tau_i^2}\Big\{(\psi_{ei}\,\alpha_{ei}\,G_e e/\underline{\underline{\gamma_e}})^2\langle p_{ei}\rangle + \lambda_{\text{GABA}}^2\cdot(\psi_{ii}\,\alpha_{ii}\,G_i e/\gamma_i)^2\langle p_{ii}\rangle\Big\}_{\text{eq.}} \\ &\longrightarrow \frac{1}{\tau_i^2}\Big\{(\psi_{ei}\,\alpha_{ei}\,G_e e\,\underline{\underline{\tau_E}})^2\langle p_{ei}\rangle + \lambda_{\text{GABA}}^2\cdot(\psi_{ii}\,\alpha_{ii}\,G_i e/\gamma_i)^2\langle p_{ii}\rangle\Big\}_{\text{eq.}}, \end{aligned} \tag{9.27b}$$

where the definition for τ_E, the voltage-gated NMDA duration, was listed earlier in Eqs (9.1–9.2):

$$\tau_E(h_e, \lambda_{\text{NMDA}}) = \gamma_e^{-1} + \frac{1}{\lambda_{\text{NMDA}}} \cdot \frac{\mathcal{S}_{\text{NMDA}}^{\max}}{1 + \exp[-g_{\text{NMDA}}(h_e - \theta_{\text{NMDA}})]} . \tag{9.28}$$

The two-variable Ornstein–Uhlenbeck theory presented in Sect. 5.4 gave Eq. (5.30a) for the variance of the excitatory fluctuations,

$$\begin{aligned} \text{var}(h_e) &= \sigma_{11} \\ &= \frac{(A_{11}A_{22} - A_{12}A_{21} + A_{22}^2)\, D_{11} \;+\; A_{12}^2\, D_{22}}{2\,(A_{11} + A_{22})\,(A_{11}A_{22} - A_{12}A_{21})} \end{aligned} \tag{9.29}$$

and Eq. (5.58a) for their spectral intensity,

$$\begin{aligned} S[h_e(\omega)] &= S_{11}(\omega) \\ &= \frac{1}{2\pi}\, \frac{A_{12}^2 D_{22} \;+\; A_{22}^2 D_{11} \;+\; D_{11}\omega^2}{(A_{11}A_{22} - A_{12}A_{21} - \omega^2)^2 + (A_{11} + A_{22})^2\, \omega^2} . \end{aligned} \tag{9.30}$$

We can now examine how the character of these fluctuations is altered by the inclusion of NMDA sensitivity.

9.4.2 Results

Figure 9.8 shows the Eq. (9.29) predictions for $h_e^{\text{rms}} = \sqrt{\sigma_{11}}$, the rms value of the h_e voltage fluctuations, as a function of GABA effect (which sets the inhibitory post-synaptic duration) for four representative values of λ_{NMDA}. The maximum firing rate was set at $\mathcal{S}_{e,i}^{\max} = 100\ \text{s}^{-1}$. In Fig. 9.8(a), setting $\lambda_{\text{NMDA}} = \infty$ has suppressed all NMDA excitatory effect, giving the expected pure-GABA response which exhibits biphasic fluctuation surges at both induction and at emergence. The induction surge occurs for a macrocolumn moving to the right with increasing λ_{GABA} along the top-branch locus of steady states shown previously in Fig.9.7(a): the approach towards the turning-point labelled "3" there corresponds to the climb towards the peak labelled I (induction) here which precedes the sudden downward jump into unconscious quiescence. The emergence power surge occurs for the return path when the macrocolumn is moving to the left with decreasing λ_{GABA} along the bottom-branch of Fig.9.7(a) towards turning-point "4"—this heralds the point of re-emergence E to conscious activity in Fig. 9.8(a).

In Fig. 9.8(b), we see the dramatic effect of allowing even a modest amount of NMDA activity: $\lambda_{\text{NMDA}} = 8$.[2] In addition to the expected surge of fluctuation power as $\lambda_{\text{GABA}} \to 1.4$ (the point of induction), there is now a new peak, labelled D, which develops in the vicinity of $\lambda_{\text{GABA}} = 0.7$ and which is associated with the NMDA-induced point of inflexion, apparent at $h_e \approx -30$ mV in Fig. 9.7(d), and highlighted by a pronounced spike-like eigenvalue excursion towards the positive half-plane in Fig. 9.7(e).

If we take $\lambda_{\text{GABA}} = 1$ (on the upper branch of Fig. 9.7(d)) as the normal macrocolumn "operating point" for consciousness, then the D power surge of Fig. 9.8(b) will only be encountered if the macrocolumn is moved along the top branch to the *left* towards smaller λ_{GABA} values by,

---

[2] Setting $\lambda_{\text{NMDA}} = 8$ allows the duration of the excitatory post-synaptic potential to take values which range from its default minimum of $\gamma_e^{-1} = 3.3$ ms (fully hyperpolarized quiescent macrocolumn) out to a maximum of $\tau_E = 3.3 + \mathcal{S}_{\text{NMDA}}^{\max}/8 = 13.8$ ms (fully-depolarized, maximally active macrocolumn); see Fig. 9.1.

for example, administering an *anti*-GABA (i.e., an analeptic) anaesthetic agent to the patient. In the more usual case, the macrocolumn will start from $\lambda_{\rm GABA} = 1$ and will be moved to the *right* via pro-GABA drugs: for this Fig. 9.8(b) case of weakly-enabled NMDA effect, the model predicts that only a single surge in fluctuation power will be detected, and this peak will occur at the moment of collapse to the bottom branch.

The situation changes if we allow a stronger pro-NMDA effect. For the $\lambda_{\rm NMDA} = 4$ graph of Fig. 9.8(c), we see that not only does the D peak occur to the *right* of $\lambda_{\rm GABA} = 1$ (so *will* be encountered during a GABA-propelled traversal into unconsciousness), but also that the peak has changed character by evolving into a pair of discontinuous jump transitions at $\lambda_{\rm GABA} \approx 1.2$ (for motion along the top branch of Fig. 9.7(g) towards turning-point "1"), and at $\lambda_{\rm GABA} \approx 1.1$ (reversed motion along the mid-branch of Fig. 9.7(g) towards turning-point "2").

These jump discontinuities arise because the eigenvalue-spike excursion visible in Fig. 9.7(e) for $\lambda_{\rm NMDA} = 8$ has evolved for $\lambda_{\rm NMDA} = 4$ into a fully-fledged loop into the positive half-plane in Fig. 9.7(h), and all steady states of Fig. 9.7(g) between turning points "1" and "2" are unstable.

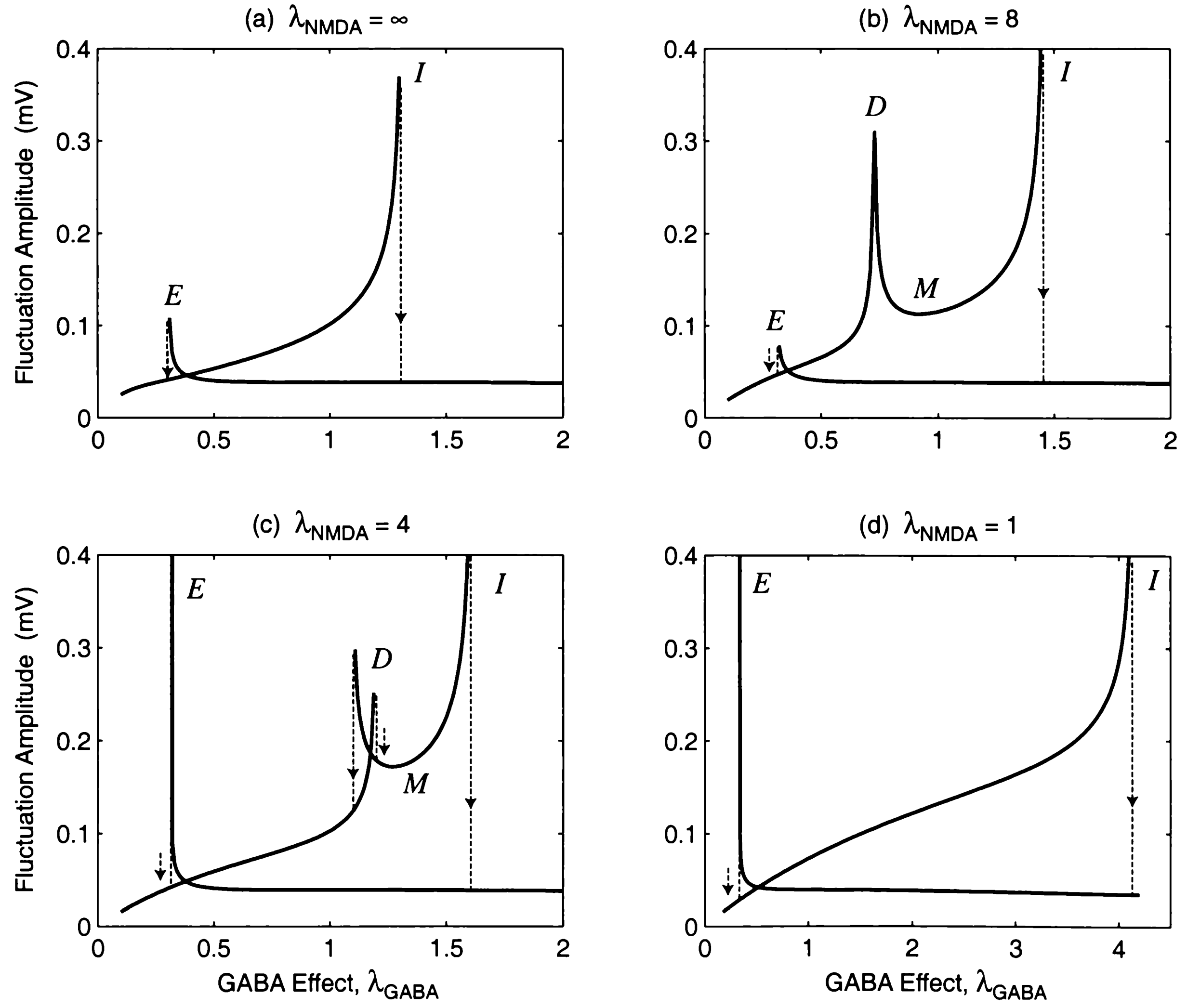

Figure 9.8: Fluctuation amplitude of h_e soma voltage as a function of GABA effect for the NMDA-enabled macrocolumn. These are rms values calculated from the leading element of the σ covariance matrix: $h_e^{\rm rms} = \sqrt{\sigma_{11}}$. Fluctuations grow strongly at onset of induction (labelled I), at the point of emergence from unconsciousness E, and at D, marking the approach to (or emergence from) the NMDA-generated midbranch M. (Only the stable-branch trajectories are shown.)

Thus the NMDA effect has allowed a new stable branch, suspended between turning points "2" and "3," to come into existence. Because the NMDA-enabled transitions at turning points "1" and "2" are discontinuous (as are the pre-existing GABA-dependent transitions at "3" and "4"), these new turning points define a new pair of first-order phase transitions which, at their critical points, exhibit the expected singularity in fluctuation power. There should also be a pronounced redistribution of spectral power towards low frequencies at these points ("critical slowing down"). These critical-point changes in spectral characteristics will be examined later in this chapter.

The situation changes again if we allow yet more NMDA effect—see Fig. 9.8(d) showing the $\lambda_{\text{NMDA}} = 1$ graph for a fully-prolonged EPSP duration. The NMDA effect is now so pronounced that the turning point "1" in Fig. 9.7(j) has been pushed out to $\lambda_{\text{GABA}} \approx 4.1$, well beyond the previous $\lambda_{\text{GABA}} \approx 1.6$ induction turning point "3" of Fig. 9.7(g), and the "2"–"3" NMDA-enabled mid-branch has been completely lost. As a result, the Fig. 9.8(d) fluctuations graph has considerably simplified, having much in common with the pure-GABA graph of Fig. 9.8(a): a single pair of induction and emergence fluctuation peaks, albethey much more widely separated in the $\lambda_{\text{NMDA}} = 1$ case—a much greater concentration of GABA agent is required to overcome the enhanced excitation arising from the fully-prolonged EPSPs.

In summary, the adiabatic model predicts that the inclusion of NMDA effects can lead to the generation of a *second biphasic power surge* as the macrocolumn moves into unconsciousness via GABA anaesthetic agent. This prediction can be tested against clinical measurements by looking for the occurrence of a double-peak in the EEG power recorded for a patient undergoing general anaesthesia.

Fluctuation Spectra for NMDA Macrocolumn

We now examine how the inclusion of NMDA sensitivity alters the spectral character of the macrocolumn voltage fluctuations.

Figure 9.9 presents a set of 3D "waterfall" views of the spectral amplitude (in units of $\text{mV}/\sqrt{\text{Hz}}$) as a function of frequency and GABA effect. These waterfall slices were calculated by fixing λ_{NMDA} at one of the four standard values (∞, 8, 4, or 1), then evaluating Eq. (9.30) to give the spectral power $\mathcal{S}[h_e(\omega)]$ (in units of mV^2/Hz) over the frequency range $0 \leq f \leq 100$ Hz for finely-stepped increments in λ_{GABA}. The displayed spectral amplitudes $h_e(\omega)$ are the square-root of the Eq. (9.30) spectral power,

$$h_e(\omega) = \sqrt{\mathcal{S}[h_e(\omega)]}\,. \tag{9.31}$$

The Fig. 9.9 waterfall graphs verify the rms fluctuation trends shown earlier in Fig. 9.8: there is a surge in fluctuation activity on approach to an S-bend turning point associated with induction (I), emergence (E), or NMDA mid-branch (M). In all cases the spectral curves become more steeply dc-peaked prior to transition, and this dc-peakiness is particularly evident at emergence. This is consistent with the notion of a *critical slowing down* prior to a jump transition—the macrocolumn readies itself for the imminent large change in dc operating point by a pronounced redistribution, towards the dc end of the spectrum, of the white-noise driving energy entering the macrocolumn from the sub-cortex.

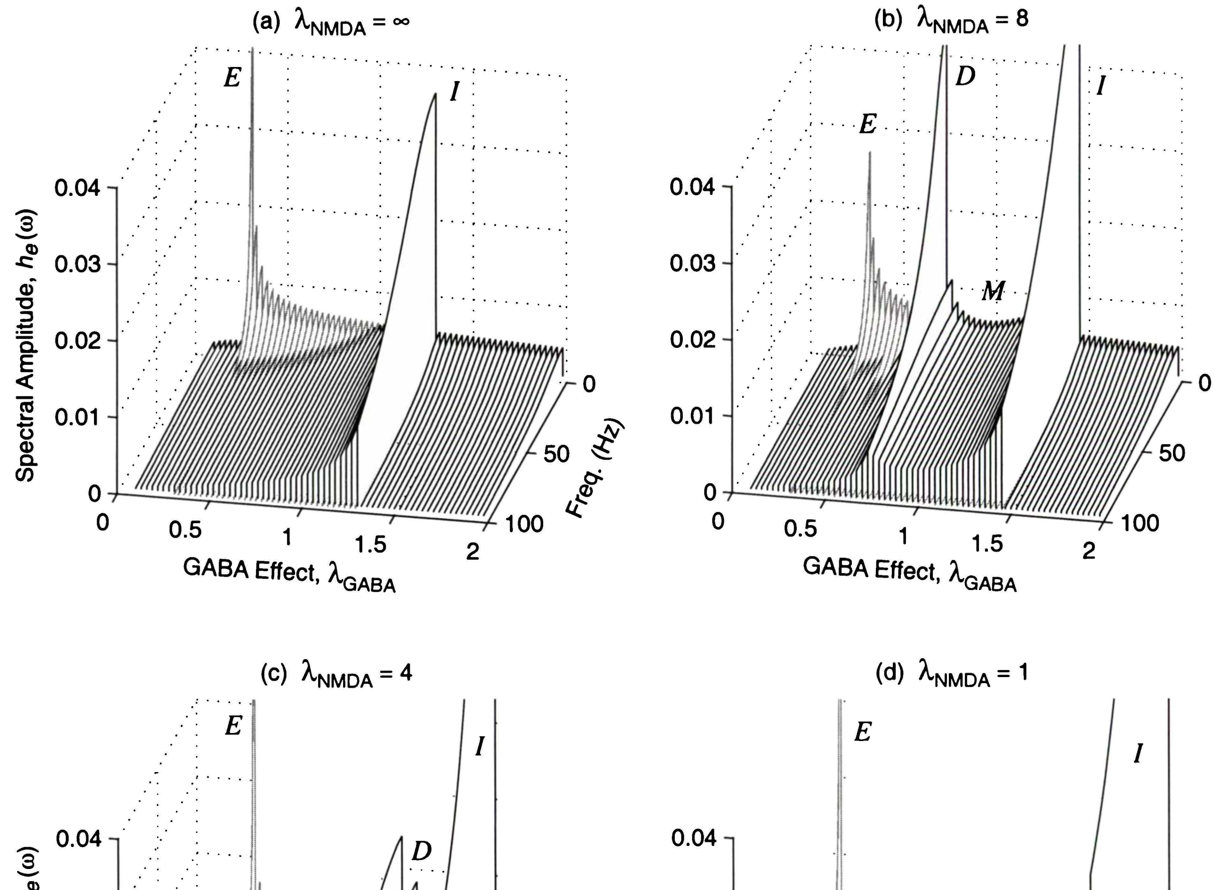

Figure 9.9: Spectral amplitude waterfalls for $h_e(\omega)$ (units: mV/$\sqrt{\text{Hz}}$) as a function of GABA effect for the NMDA-enabled macrocolumn. The black curves correspond to *increasing* GABA effect as the macrocolumn traverses from the active (conscious) branch to the lower quiescent (unconscious) branch; the gray curves are for *decreasing* GABA effect as the macrocolumn is revived from its comatose state. The fluctuation surges at induction (I), emergence (E), and on approach to the NMDA-generated midbranch (M) are accompanied by a pronounced redistribution of spectral power towards zero frequency.

9.5 Clinical Evidence for Biphasic Peak-Splitting

If NMDA effects are included in the macrocolumn model, then the adiabatic theory predicts that, depending on the background level of NMDA-determined excitation, there can be either one *or two* distinct EEG power surges for a GABA-anaesthetic journey into unconsciousness.

For example, suppose the macrocolumn operates at a "weak" pro-NMDA level (i.e., $\lambda_{\text{NMDA}} = 8$; see Table 9.2), and suppose that it begins its GABA journey at $\lambda_{\text{GABA}} = 1$ on the top branch of Fig. 9.8(b). Then only the single fluctuation surge at I will be encountered as the macrocolumn transits to its quiescent state. In contrast, for a "moderate" pro-NMDA level (i.e., $\lambda_{\text{NMDA}} = 4$), a GABA traverse in Fig. 9.8(c) from $\lambda_{\text{GABA}} = 1$ (top branch) to $\lambda_{\text{GABA}} = 2$ (quiescent branch) will generate the additional power surge at D as the macrocolumn negotiates the transition to the intermediate mid-branch region (2–3 of Fig. 9.7(g)).

Thus the prediction is that for "moderate" levels of NMDA neurotransmitter, there should be two distinct peaks in EEG activity in the GABA-anaesthetic traversal between conscious and unconscious states. I will refer to the occurrence of a double-peak as "biphasic peak-splitting."

A recent paper by Kuizenga, Wierda, and Kalkman (2001) reports biphasic EEG changes during induction of general anaesthesia for five different anaesthetic agents. This new study is similar to that described in Sect. 5.9 (Kuizenga *et al.*, 1998), except that this time the focus was on establishing whether or not there existed a consistent relationship between the time of loss-of-consciousness (LOC) and the time of peak biphasic activity in the EEG slewrate. Although their findings were negative (i.e., it appears that there is no consistent timing relationship between LOC and biphasic peak), the EEG activity graphs for some of their propofol patients (Fig. 2 of Kuizenga *et al.* (2001)) seemed to show *double* peaks, so we requested access to these datasets.

Figure 9.10 shows their aperiodic analysis results for the 11–15 Hz band for the five propofol patients. Two graphs are shown for each patient: the left panel analyzes the EEG activity for a pair of scalp electrodes connected between top-of-head (Cz) and centre-forehead (Fpz); the right panel corresponds to EEG activity for a second pair of electrodes connected between right-hand mastoid (M_2: bone behind the ear) and right forehead (Fpz_2). Following a 3-min recording of EEG to establish baseline activity, patients were infused with propofol.[3] Loss of consciousness occurred about 2–3 min after commencement of drug infusion.

As expected from our first-order phase transition model, all five patients show a surge in cortical activity in the vicinity of loss of consciousness. For three patients (2, 4, 5), we observe two distinct peaks: the first peak close to the time of LOC, and the second about 3 min later. I have labelled these peaks as a and b, and our theory would suggest that peak-a is associated with the NMDA-enabled mid-branch transition D, and peak-b is associated with the I transition to quiescence.

Two patients do not show peak-splitting in EEG activity: patient-3 is lacking the first peak, and patient-1 is lacking the second.

---

[3] The drug was infused at a constant rate of 0.5 mg per "kg" per min, where the "kg" pseudo-unit represents the effective dose body weight (DBW) given by subtracting 100 from the patient's *height* H in cm:

$$\text{DBW (in "kg")} = H \text{ (in cm)} - 100$$

This is a way of estimating *lean* body mass; actual body mass is less useful for dose calculations because of the lower blood flow to fat. Presumably this rule of thumb is only applied to adult patients of normal stature...

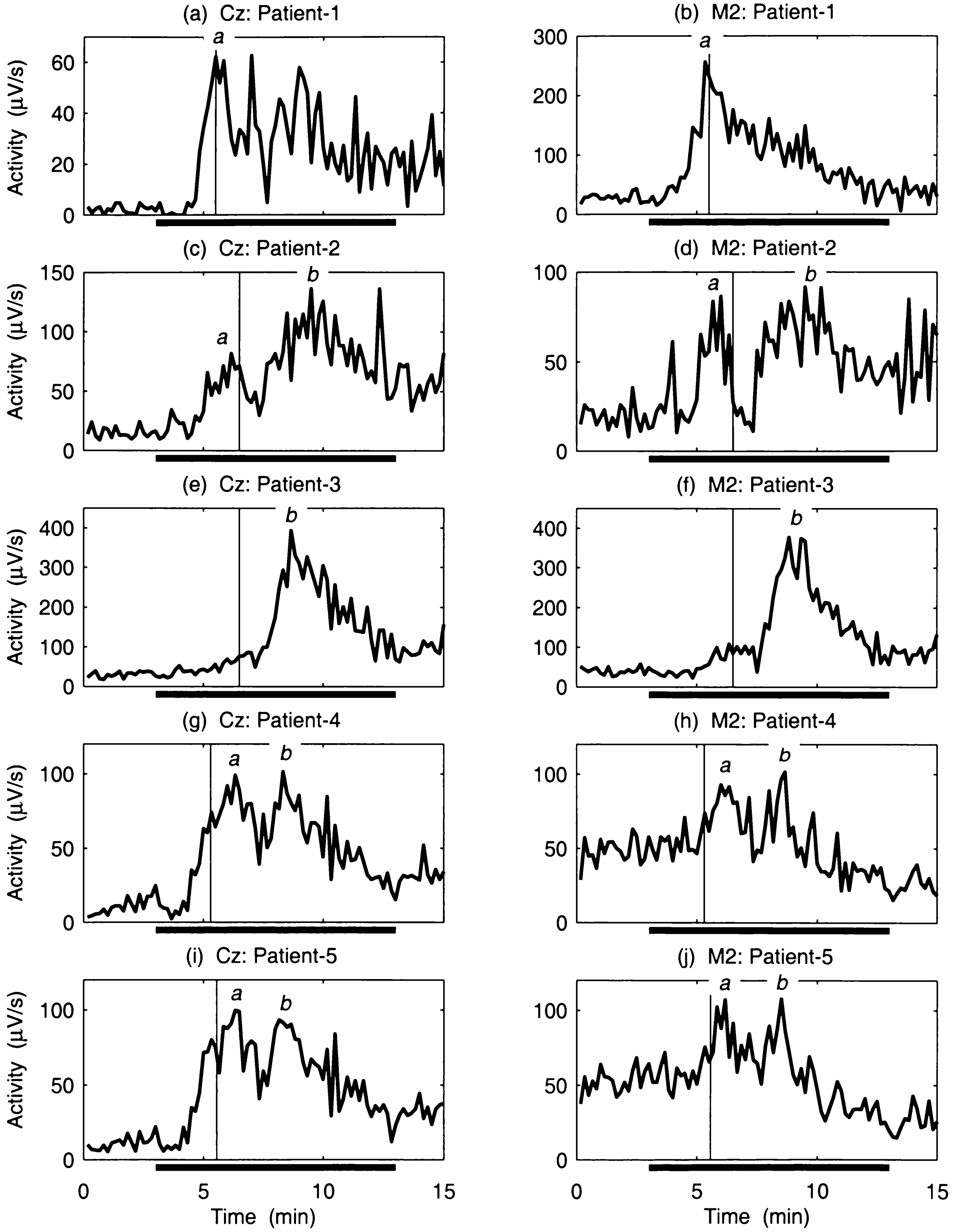

Figure 9.10: Aperiodic analysis of the 11–15-Hz EEG slew-rate activity for five patients undergoing propofol-induced anaesthesia. Left column is for the Cz–Fpz electrode pair; right column is for the M_2–Fpz_2 electrode pair. Vertical lines mark the time of loss of responsiveness (patient stops responding to verbal command). For each patient, the 10-min propofol infusion began 3 min into the recording (infusion duration indicated with a horizontal bar under the time axis). Patients 2, 4, and 5 show *two* EEG activity peaks labelled *a* and *b*; patients 1 and 3 appear to have a single activity peak. [Graphs plotted from data supplied courtesy of K. Kuizenga (personal communication, 2001)]

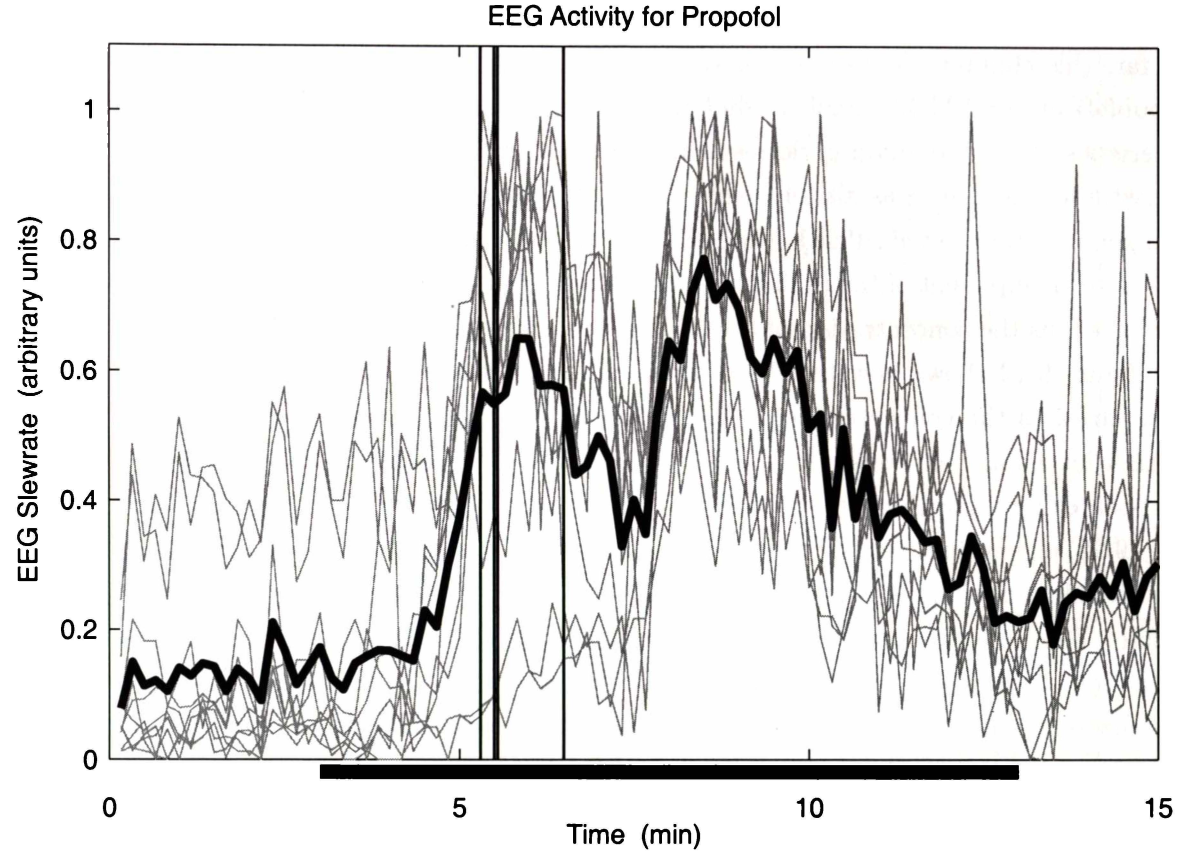

Figure 9.11: Average time-course for 11–15-Hz EEG slewrate activity for propofol induction. Bold curve is the average obtained from the 10 plots (5 patients; 2 traces per patient) shown in Fig. 9.10. Each slewrate curve was prescaled to give a vertical range of [0, 1] prior to averaging; the scaled curves appear as grey background traces. The horizontal bar gives the duration of propofol infusion; the vertical lines mark the time of loss of responsiveness for each patient.

The individual traces of Fig. 9.10 are quite noisy. Since each patient is exposed to a nominally identical time-course of drug concentration (a 10-min exposure commencing at the third minute, and a dose-rate adjusted for body size), it seems not unreasonable to average the time course of EEG activity across all five patients in an attempt to extract a smoothed "average patient" response. The averaged propofol-response curve is presented in Fig. 9.11.

Figure 9.11 is quite unambiguous: the averaged induction curve for propofol exhibits a double biphasic peak. As far as I am aware, the observation of a peak splitting for induction has not previously been reported. Had the infusion been performed at "normal" clinical rates (typically the bolus of propofol would be administered over a period of, say, 20 s rather than over the extended duration of 10 min used in the Kuizenga experiment), the valley separating the peaks would almost certainly *not* have been resolvable in the more rapidly evolving EEG time-series.

The observation of peak splitting is a very encouraging endorsement of our adiabatic macrocolumn theory. It suggests that the patient response to propofol GABA anaesthetic can be modelled as a moderately-NMDA-enabled (i.e., $\lambda_{\mathrm{NMDA}} = 4$) macrocolumn whose inhibitory PSP duration is set by the concentration of the anaesthetic (i.e., by the value of λ_{GABA}).

9.6 Steady States for an NMDA Anaesthetic

So far, this chapter has focused on the effect of a standard GABA-type anaesthetic (such as propofol) on an NMDA-enabled adiabatic macrocolumn. Now I wish to investigate the characteristics of the induction cycle resulting from the application of a purely NMDA-suppressing anaesthetic agent such as nitrous oxide (N_2O: "laughing gas" (Jevtovic-Todorovic *et al.*, 1998)) and xenon (Franks *et al.*, 1998). Both of these gases are thought to act in a similar way to APV: the "late" component of the excitatory post-synaptic current is suppressed, and then completely abolished, as the concentration of the NMDA-blocking agent is increased; see Fig. 9.2 on p. 175.

Figure 9.12 shows how the distribution of steady states for the excitatory neural population varies as the concentration of NMDA-antagonist agent is increased. For each curve, the GABA level was held constant at the labelled value. The steady states were located using the root-searching algorithm described in Sect. 9.2. A small-perturbations stability analysis of the Eq. (9.22) eigenvalues verified that, as was the case for the stepped NMDA curves of Fig. 9.7, the positive-slope regions (i.e., sections in which the curve becomes re-entrant) of Fig. 9.12 are unstable. Thus a first-order transition to quiescent state Q *is* achievable for an NMDA-antagonist induction, but *only* if the GABA level is held rather high (i.e., $\lambda_{\text{GABA}} \gtrsim 1.5$). However, once the macrocolumn has reached quiescence, it cannot recover to its active high-firing state via reduction of anti-NMDA agent alone—the GABA level must also be reduced to achieve recovery (this observation becomes clearer after examining the 3D manifold of steady states of Fig. 9.14).

The most interesting observation from Fig. 9.12 is that for low or moderate values of GABA (i.e., $\lambda_{\text{GABA}} < 1.0$), infusion of an NMDA-antagonist anaesthetic moves the macracolumn smoothly to a "mid-state" M that lies *between* normal activity A and quiescent inactivity Q. It seems plausible that this state of intermediate activity corresponds to the "dissociated" state in which the patient has become disconnected from her surroundings and unaware of painful stimuli—the patient is *neither* fully conscious *nor* fully unconscious. Nitrous oxide and xenon are both classified as *dissociative* anaesthetics.[4]

Figure 9.13 places the (a) stepped-NMDA and (b) stepped-GABA steady-state graphs alongside each other. We observe that while the range of GABA responsiveness of the macrocolumn is sensibly explored using a linear scale for λ_{GABA}, exploration of NMDA response requires a logarithmic scale. This is because the two effects enter the adiabatic model in mathematically distinct ways. GABA-effect enters as a direct *linear* scaling by λ_{GABA} of the I_{ie} and I_{ii} inhibitory currents (see Eq. (9.11)); in contrast, NMDA effect is represented as an (almost) *inverse* scaling by λ_{NMDA} of the I_{ee} and I_{ei} excitatory currents (see Eqs (9.12) and (9.10)), with complete NMDA suppression requiring $\lambda_{\text{NMDA}} \to \infty$.

By comparing the two graphs of Fig. 9.13, and by examining their co-presentation on orthogonal axes of the 3D manifold of Fig. 9.14, it is clear that, by appropriate manipulations of NMDA and GABA levels, the "half-way" or dissociated M-state can be reached via a multitude of different paths. For example, one could fix the level of NMDA suppression at $\lambda_{\text{NMDA}} = 4$ in Fig. 9.13(a), then steadily increase the GABA prolongation of the IPSP from $\lambda_{\text{GABA}} = 1$ to $\lambda_{\text{GABA}} \approx 1.4$. Or, considering an orthogonal trajectory, one could fix $\lambda_{\text{GABA}} = 1$ in Fig. 9.13(b), then steadily increase the level of NMDA suppression to $\lambda_{\text{NMDA}} = 10$ (i.e., $\log_{10} \lambda_{\text{NMDA}} = 1$).

---

[4] In contrast, propofol belongs to the class of *induction* anaesthetics.

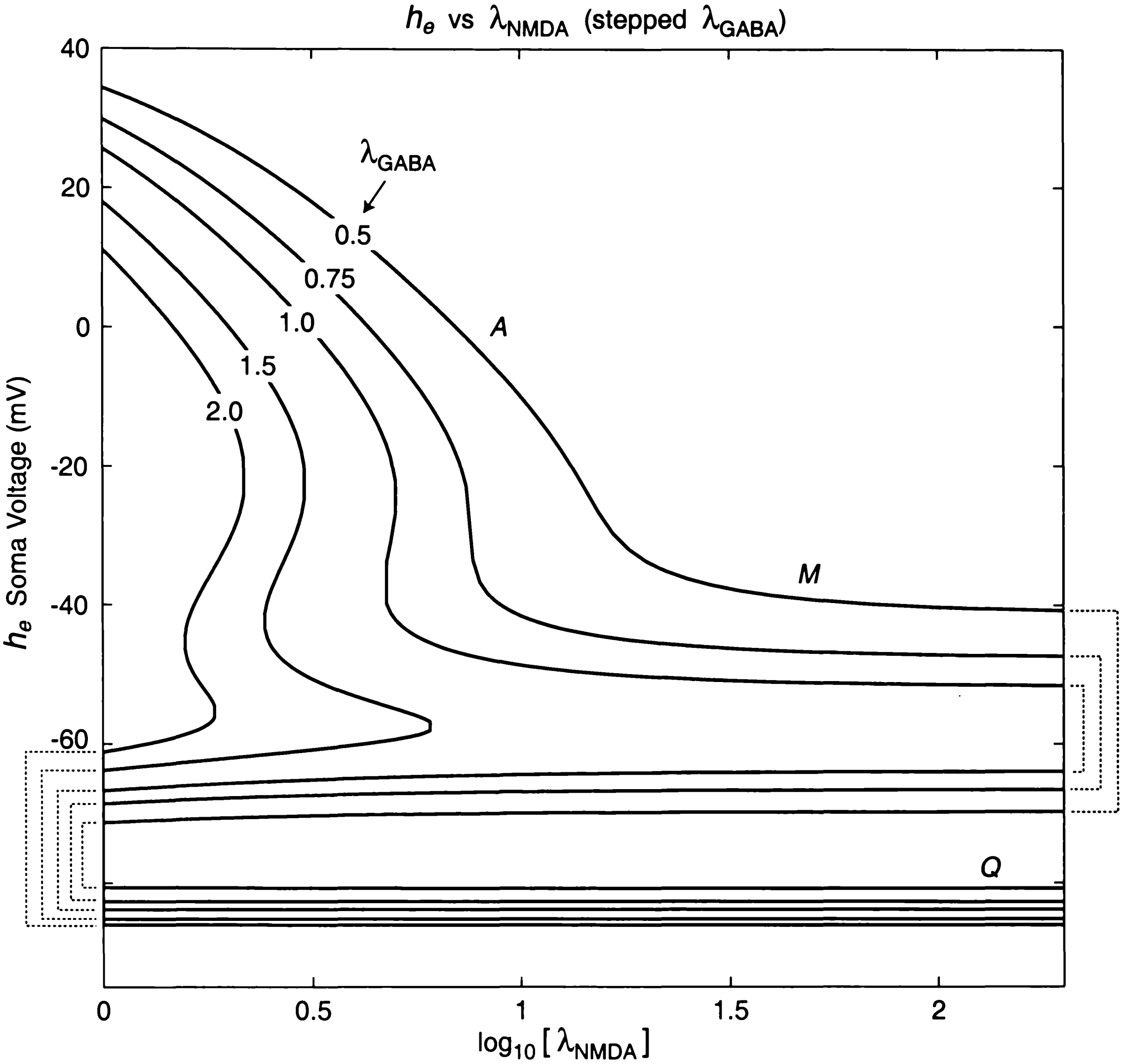

Figure 9.12: Distribution of excitatory steady states as a function of λ_{NMDA}, the NMDA suppression factor. For each curve, the level of GABA effect was fixed at the value indicated by the label. Note that in the absence of GABA enhancement (i.e., $\lambda_{\text{GABA}} \leq 1$), the low-firing quiescent state Q is *inaccessible* from the high-firing active state A; instead, only the medium-firing intermediate state M can be reached. The dashed end-caps identify which segments belong to a given λ_{GABA} trajectory.

9.7 Fluctuation Amplitude and Spectrum for an NMDA Anaesthetic

Figure 9.15 shows the predicted amplitude and spectral composition for the steady-state fluctuations in excitatory soma voltage for an adiabatic macrocolumn infused with a steadily increasing concentration of NMDA-antagonist agent. Each pair of graphs corresponds to a constant-GABA slice through the Fig. 9.14 manifold of steady states. In all cases there is a surge in low-frequency activity as the turning point (point of inflexion) between the active (A) and mid-branch (M) steady states is traversed. As GABA effect is increased, the slope of the manifold along the NMDA direction steepens, and the fluctuation surge becomes more pronounced.

Figures 9.15(a)–(d) suggest another clinical test for the model. For moderate (i.e., $\lambda_{\text{GABA}} \lesssim 1.0$), fixed GABA levels, the induction of the mid-state M via NMDA anaesthetic is predicted to be smooth, continuous, and exactly reversible. This means that the return path $A \leftarrow M$ should

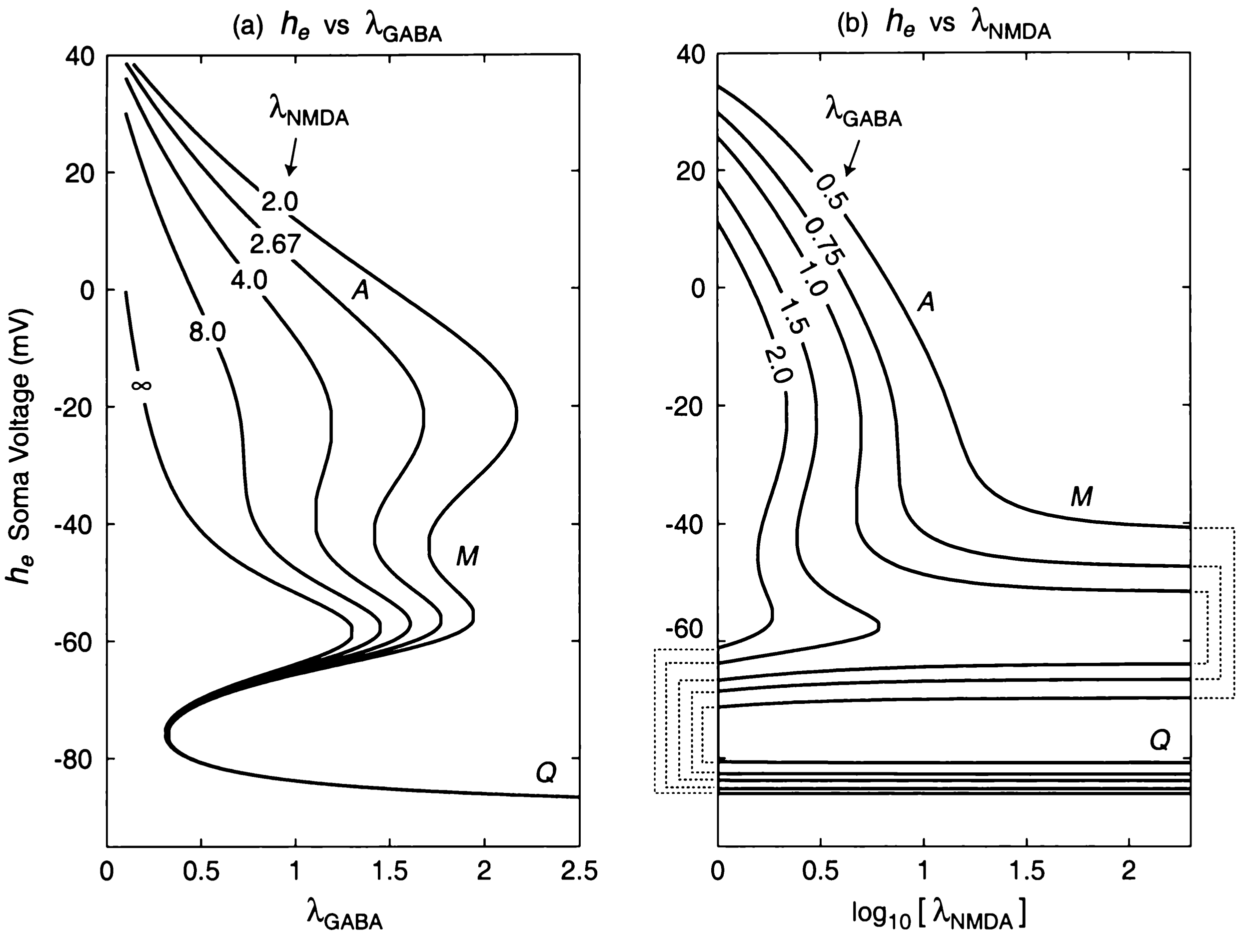

Figure 9.13: Distribution of excitatory steady states as (a) a continuous function of λ_{GABA} for stepped values of λ_{NMDA}, and as (b) a continous function of λ_{NMDA} for stepped values of λ_{GABA}. In (a), the NMDA suppression factor λ_{NMDA} was set at each of the 5 labelled values in turn (these curves belong to the same family shown in Fig. 9.5(c) and Fig. 9.6(a)). (b) is copy of Fig. 9.12, repeated here to allow easy comparison between GABA and NMDA effect.

be an exact retracing of the induction path $A \rightarrow M$, so there should be *no hysteresis* between EEG effect and drug concentration: the patient should awaken at the same drug concentration as that at which she went to sleep. This is quite unlike the prediction for an $A \rightarrow Q$ induction of quiescence via GABA infusion—the active and quiescent states are separated by a jump discontinuity, so the drug concentration at the point of induction is expected to be much greater than at the point of emergence.

9.8 Adiabatic States for a Slow Propofol Infusion

This chapter has demonstrated that, by incorporating a voltage-gated τ_E term representing the NMDA contribution to the excitatory post-synaptic potential, it becomes possible for the adiabatic macrocolumn to reside in a new stable state M lying somewhere between normal activity A and anaesthetic quiescence Q. It is well established in the anaesthesiology community that infusion with a dissociative anaesthetic such as xenon, ketamine, or N_2O (i.e., increasing levels of NMDA suppression with GABA levels remaining fixed) induces a dreamy, disconnected

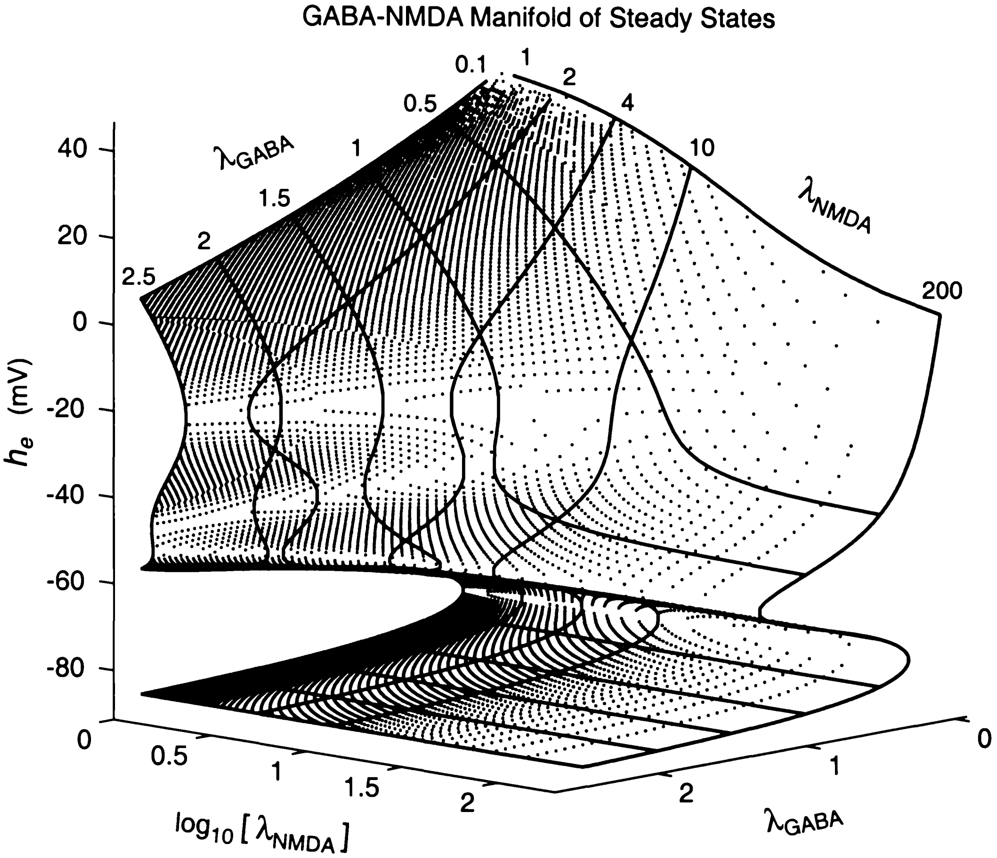

Figure 9.14: Three-dimensional view of the GABA-NMDA manifold of excitatory steady states. The dots form a point cloud of steady states; the superimposed curves are parallel and orthogonal "slices" though the manifold giving trajectories for constant NMDA effect (cf Fig. 9.13(a)), and for constant GABA effect (cf Fig. 9.13(b)).

state.[5] Thus it seems that there exists a direct mapping between the stable steady states of the adiabatic macrocolumn and the major states of human consciousness (at least as viewed from the specific and narrow perspective of a clinical anaesthetist). Table 9.3 summarizes our putative state mapping.

This mapping is consistent with the Kuizenga *et al.* (2001) aperiodic analysis of the slow propofol-induction experiment presented earlier in Fig. 9.11. If the adiababic model is correct, then we can identify the valley separating the pair of slew-rate peaks as the marker for the dissociated M-state. Figure 9.16 is a copy of Figure 9.11, but with the individual patient traces removed and with the state labellings of Table 9.3 superimposed. I have christened the first

---

[5] J. Sleigh, personal communication

Table 9.3: Proposed mapping between stationary states of the macrocolumn and the anaesthetic states of consciousness

Macrocolumn Steady State		State of Consciousness
A: Active firing	$\Longleftrightarrow$	Conscious awareness
M: Mid-level	$\Longleftrightarrow$	Dreamy dissociation
Q: Quiescent, low-firing	$\Longleftrightarrow$	Unresponsive unconsciousness

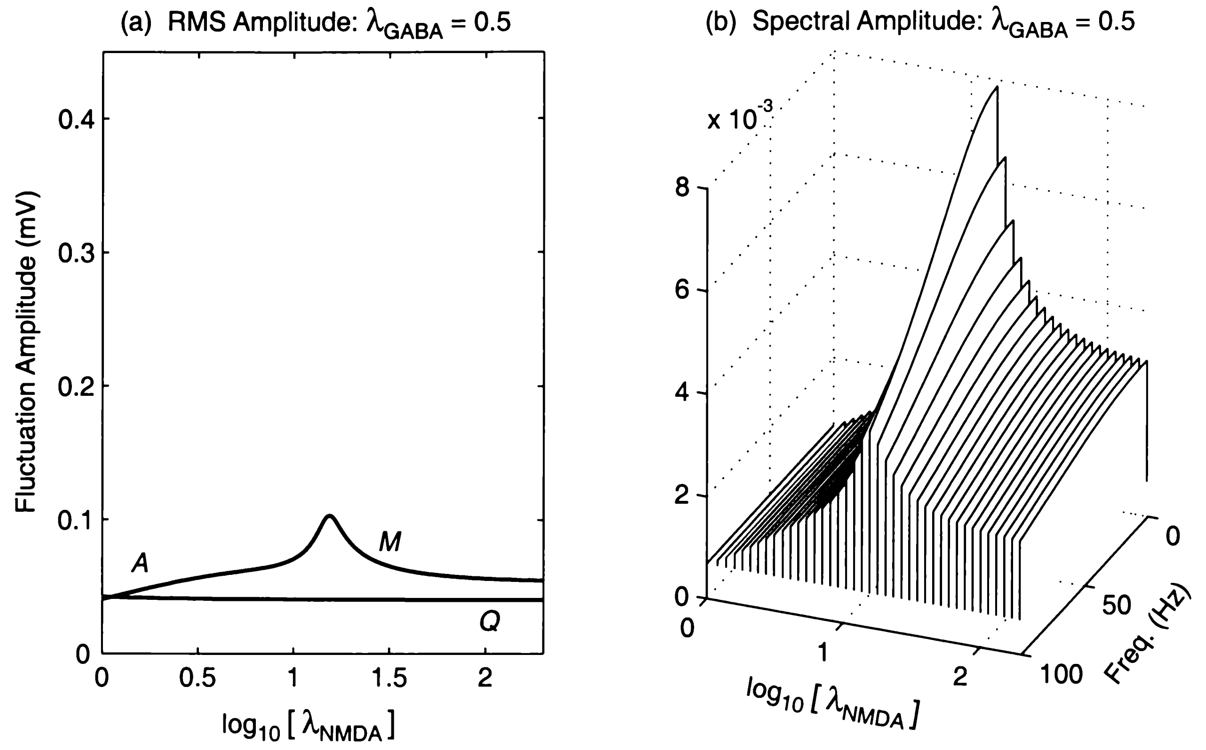

(a) RMS Amplitude: $\lambda_{\text{GABA}} = 0.5$

(b) Spectral Amplitude: $\lambda_{\text{GABA}} = 0.5$

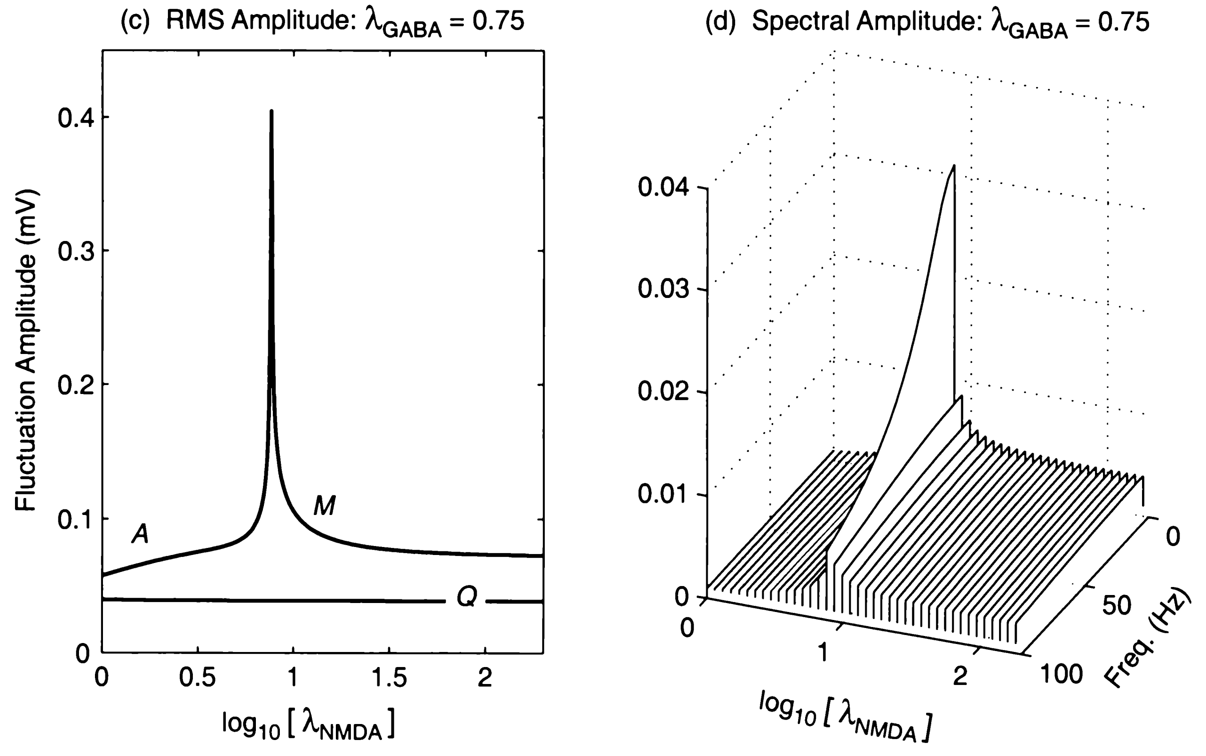

(c) RMS Amplitude: $\lambda_{\text{GABA}} = 0.75$

(d) Spectral Amplitude: $\lambda_{\text{GABA}} = 0.75$

Figure 9.15: Fluctuation amplitude h_e^{rms} (left) and its spectral structure $h_e(\omega)$ [mV/$\sqrt{\text{Hz}}$] (right) for an induction using an NMDA-antagonist anaesthetic agent. Each left–right pair of graphs corresponds to a distinct constant-λ_{GABA} slice through the Fig. 9.14 manifold of steady states. The waterfalls on the right are for a traversal along the upper branch of Fig. 9.13(b) from A (active) to M (mid-state); for these selected GABA values [(a), (b): $\lambda_{\text{GABA}} = 0.5$; (c), (d): $\lambda_{\text{GABA}} = 0.75$], the Q quiescent state cannot be reached by application of a purely anti-NMDA anaesthetic.

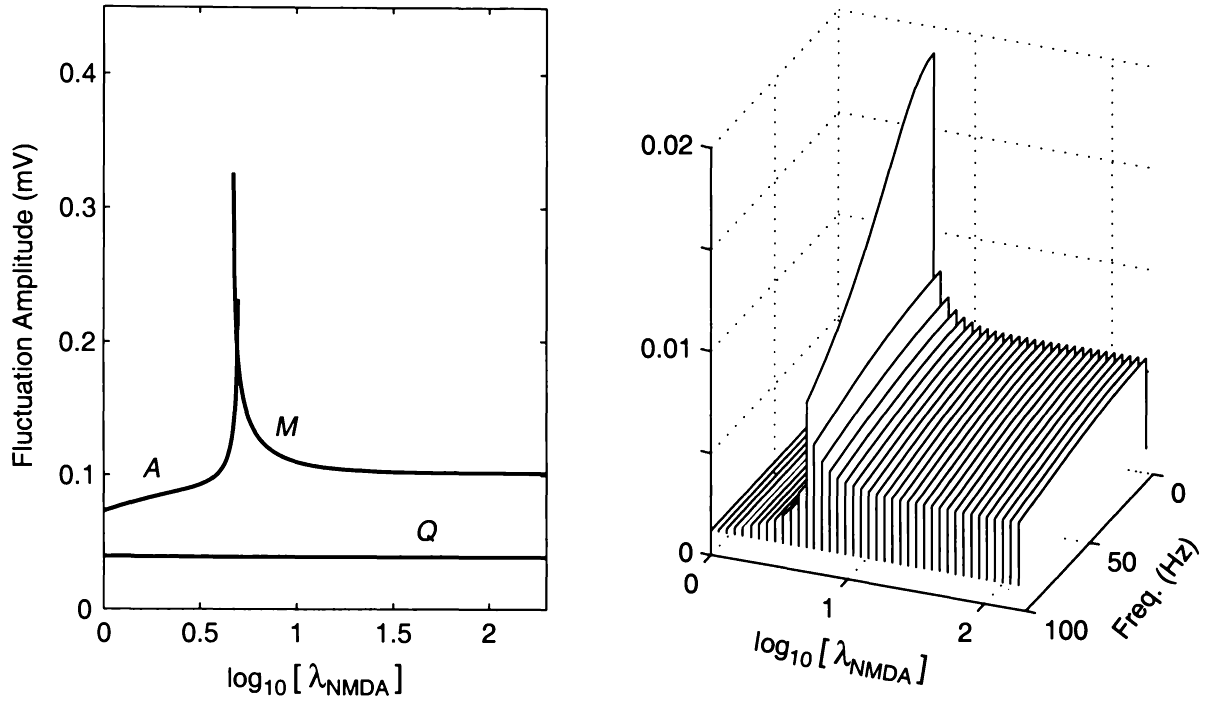
(e) RMS Amplitude: $\lambda_{GABA} = 1.0$

(f) Spectral Amplitude: $\lambda_{GABA} = 1.0$

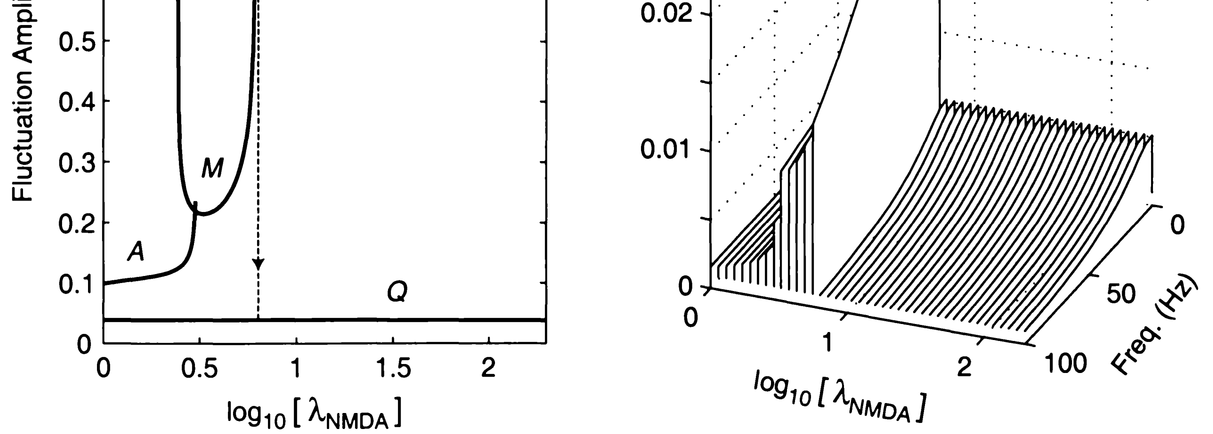
(g) RMS Amplitude: $\lambda_{GABA} = 1.5$

(h) Spectral Amplitude: $\lambda_{GABA} = 1.5$

Figure 9.15 (*cont.*): Fluctuation amplitude and spectrum for an NMDA-antagonist induction with GABA levels fixed at (e), (f) $\lambda_{\text{GABA}} = 1.0$, and at (g), (h) $\lambda_{\text{GABA}} = 1.5$. Only at the higher level of GABA effect is a full induction to the low-firing quiescent state Q achievable, but the macrocolumn cannot then exit from this quiescent state via reduction of NMDA-antagonist effect: emergence would require a simultaneous reduction in GABA effect.

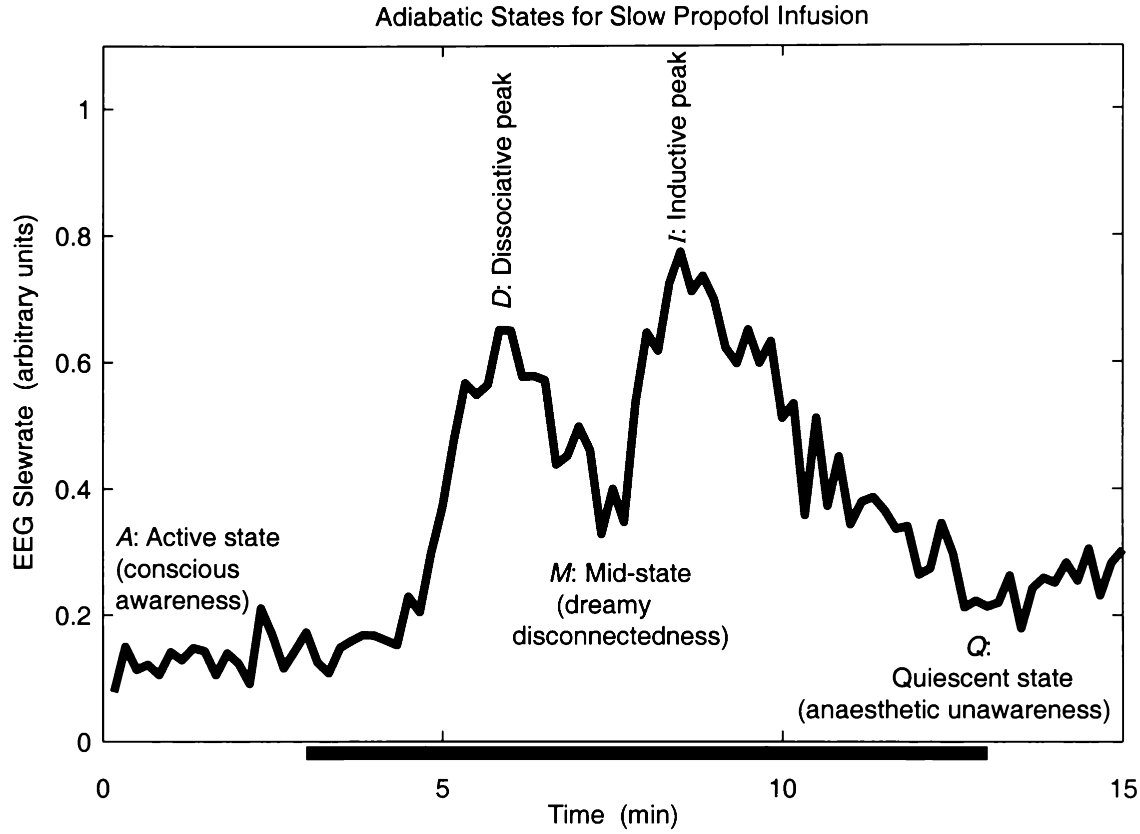

Figure 9.16: Adiabatic state labellings for a slow propofol infusion. The macrocolumn model leads us to believe that the distinct EEG activity peaks mark the passage to distinct states of consciousness.

of the slew-rate maxima the *dissociative peak*, since this fluctuation surge signals the passage to the dissociated state, and the second maximum as the *inductive* peak since it presages the induction of full, non-responsive anaesthesia.

9.9 Slow-Infusion Tests of the Adiabatic Theory

Figures 9.15 and 9.16 suggest several slow anaesthetic-infusion experiments that could be run to test the various predictions of the adiabatic theory.

$A \rightleftharpoons M$ dissociative round trip via NMDA-antagonist The dissociative EEG activity peak should occur at the *same* drug concentration on emergence as it did on entry (e.g., see Fig. 9.15(c)). This absence of drug–effect hysteresis—after proper compensation for timing offsets arising from displacement between measurement site (e.g., femoral artery) and effect site (i.e., cerebral cortex)—is expected when the A active state and the M dissociated state both lie on the same locus of stable equilibria. This is the case, for example, for the $\lambda_{\text{GABA}} = 0.75$ curve of Fig. 9.13(b).

$A \rightleftharpoons M$ dissociative round trip via GABA In this case, the presence or absence of drug-effect hysteresis will depend on the background level of NMDA. Figure 9.13(a) predicts a small hysteresis for $\lambda_{\text{NMDA}} = 4$, but none for $\lambda_{\text{NMDA}} = 8$.

$A \rightleftharpoons Q$ inductive round trip via GABA Here, the prediction of pronounced hysteresis is quite unambiguous. The inductive peak I will occur at a much greater drug concentration than the emergence peak E. This was demonstrated in Figures 9.9 and 9.8.

$A \nrightarrow Q$ via NMDA-antagonist For an anti-NMDA anaesthetic acting alone, it should be virtually impossible to progress beyond the dissociative state to achieve the fully unresponsive unconscious state Q. Figure 9.12 shows that the M half-conscious state lies on a saturation plateau which is close to horizontal.

Chapter 10

Summary and Future Work

10.1 Summary

This thesis has investigated the construction and performance of an electrical model for the effects of a general anaesthetic agent on EEG. The model incorporates the ion-channel theory of Franks and Lieb which asserts that anaesthetic agents act on specific synaptic receptors to control the flow of ions through the lipid membrane of the nerve cells in the cerebral cortex, thereby altering the transmembrane voltage of the nerve cell. GABAergic anaesthetics tend to inhibit brain action by increasing the duration of each inhibitory PSP (postsynaptic potential), holding the $\mathrm{GABA_A}$ chloride channels open longer, thereby allowing an increased number of $\mathrm{Cl^-}$ ions to diffuse down their concentration gradient into the cell. As a result, the cortical neurons become hyperpolarized (more negative) and therefore less likely to fire. Thus a GABAergic anaesthetic agent *increases* the effectiveness of each *inhhibitory* postsynaptic event. The dissociative class of anaesthetics has a quite different mode of action. These anaesthetics are thought to reduce the duration of the *excitatory* postsynaptic potentials mediated by the slow-acting NMDA receptor, thereby limiting the influx of sodium ions and consequently lowering the overall level of excitability of the postsynaptic cell. Thus dissociative anaesthetics *reduce* the effectiveness of each *excitatory* postsynptic event.

Liley Mean-Field Equations

The Liley equations adopted here describe the spatially-averaged or mean-field behaviour of strongly interacting populations of excitatory and inhibitory neurons residing within a small volume of cerebral cortex. These interacting populations define a "macrocolumn." A one- or two-dimensional assembly of such macrocolumns, driven by subcortical inputs and interacting via long-range excitatory connections, might define a plausible spatial model for the cerebral cortex. However, for these investigations I chose to explore the behaviour of a spatially homogeneous cortex in which all macrocolumns are identical.

In order to apply this spatially homogeneous picture to the problem of modelling anaesthetic action, the Liley model was modified to incorporate drug-mediated changes in the postsynaptic response functions, and then collapsed to an "adiabatic" subset that replaces the detailed time evolution of the postsynaptic potentials by their steady-state values.

Modelling Anaesthetic Action

The drug-mediated changes were modelled as alterations to either the IPSP time-constant (γ_i^{-1} is *increased* for GABAergic induction anaesthetics), or to the EPSP time-constant (voltage-gated $\tau_E = \gamma_e^{-1} + \frac{S_{\text{NMDA}}(h_e)}{\lambda_{\text{NMDA}}}$ is *reduced* for NMDA-antagonist dissociative anaesthetics). The adiabatic simplification is based on the notion that, compared to the time-constant of the average nerve cell ($\tau_e, \tau_i \approx 40$ ms), the neurotransmitter-induced synaptic inputs have *fast* kinetics which rapidly settle to steady-state. This permitted setting dI_{jk}/dt to zero in each of the equations of motion for the four I_{jk} synaptic inputs, and the adiabatic macrocolumn could then be described using a pair of first-order nonlinear differential equations in the $h_{e,i}$ soma voltage (in contrast, the full Liley set consists of eight DEs).

Stability Analysis

A linear stability analysis of the adiabatic equations showed that, depending on the level of anaesthetic, there could be either one or three steady states, and that in the latter case, the middle state is unstable to small perturbations. This implies the possibility of sudden state switching at particular (critical) levels of anaesthetic effect.

Fluctuation Variance and Spectrum

Incorporating white-noise perturbations into the p_{jk} subcortical inputs transformed the adiabatic equations into 2D Langevin equations for which theoretical predictions for fluctuation variance and spectral distribution could be made. The significant findings were:

- the intensity of the random fluctuations about steady state will grow strongly as the state-change jump points are approached;
- the spectral distribution of the fluctuations will shift towards low frequencies on approach to state-change;
- the cortical state will depend on both the level of anaesthetic and on the previous history of cortical states—in other words, the cortical model exhibits hysteresis.

Thermodynamic Analogy

The excitatory and inhibitory populations can be uncoupled by applying the trajectory of steady states as an "equation of state." Then, after proposing possible mappings between analogous temperature ("excitability," Θ) and anaesthetic effect, we were able to extract analogous entropy and "heat" capacity for the excitatory population of the macrocolumn. The prediction of a discontinuity in biological "heat" capacity seems to receive support in the Stullken (1977) dog experiments.

Simulations, Spectral Entropy, and Correlation Time

Simulations of the *adiabatic* equations were in qualitative and quantitative agreement with theoretical predictions. Simulations of the *full* Liley equations demonstrated an unexpected narrow resonance on the top branch of steady states at moderate ($\lambda_{\text{GABA}} \approx 1.2$) levels of anaesthetic effect; at higher values of anaesthetic, the resonance developed into a dynamic instability that caused premature collapse to the bottom branch. I suspect, but have not yet confirmed, that this failure of the *full* equations occurs because the prolonged IPSP now has a duration which is similar to the membrane time-constant. This means that the IPSP conductance is no longer neglibible, so the effective membrane time-"constants" τ_e and τ_i can no longer be taken as a fixed, pre-determined number. I discussed this possibility in Sect. 1.7.1 (p. 21).

Investigations of the theoretical properties of fluctuation spectral entropy showed that, for the special case of a Lorentzian spectrum, there is a direct and simple relationship between spectral entropy and correlation time. The investigations also indicated that considerable care is required when attempting to use a discrete sample to estimate the entropy of a continuous function. In particular, the discrete formula for spectral entropy as given in several recent EEG papers will only render correct results when the spectral interval is unity. For non-unity spectral steps, a histogram form for spectral entropy should be used.

Reversal Potentials

One of the distinguishing characteristics of the Liley equations, compared with other mean-field cortical models, is the inclusion of reversal potentials as ψ_{jk} weighting factors. For example, synaptic input I_{ei} (that is, excitatory input to the inhibitory population) is scaled by a factor proportional to $(h_e^{\mathrm{rev}} - h_i)$. This factor will be positive (therefore depolarizing) in the usual case of $h_i < h_e^{\mathrm{rev}}$, but will become negative (a hyperpolarizing effect) in the unusual over-depolarized case of $h_i > h_e^{\mathrm{rev}}$. If $h_i = h_e^{\mathrm{rev}}$, the I_{ei} input is neutral and has no effect on the nerve cell.

How significant are reversal potentials for cortical modelling? To answer this question, I varied the λ_{GABA} anaesthetic effect and compared the distribution of steady states both with (i.e., using standard ψ weights) and without (i.e., unity-ψ case: $\psi_{ek} = +1$, $\psi_{ik} = -1$, where $k = e, i$) the reversal-potential scale-factors. For the standard ψ-enabled case, the $h_{e,i}$ steady-state voltages mapped out a reverse-S trajectory whose $\lambda_{\mathrm{GABA}} \to 0$ depolarized extreme ("seizure") was close to the sodium reversal potential of +45 mV, and whose $\lambda_{\mathrm{GABA}} \to \infty$ hyperpolarized extreme ("coma") matched the potassium (or chloride) reversal potential of −90 mV. In contrast, the unity-ψ case was wildly under-constrained, giving a depolarized limiting soma voltage of several thousand millivolts, and a hyperpolarized voltage asymptote of $-\infty$(!) I conclude that inclusion of the reversal potentials is crucial for a physiologically plausible mathematical model of nerve cell response to a GABAergic anaesthetic agent.

Modelling NMDA-antagonist Action: Extreme Adiabatic Limit

While the adiabatic assumption is reasonable for the PSP effects of GABAergic anaesthetics (since they act on the relatively fast-responding GABA$_\mathrm{A}$ receptor), it seems distinctly dubious for slow NMDA effects lasting, say, ~100 ms or more. In order to make progress on a model for NMDA receptor disruption by dissociative anaesthetics, I made the working hypothesis that the membrane time-constant could be made "as long as necessary." The validity of this working hypothesis can be assessed by testing clinically the predictions of the adiabatic NMDA-enabled macrocolumn. If the modelling assumptions are correct, then the following behaviours should be observed in the clinical EEG records:

- a slow GABAergic induction should show *two* EEG activity peaks: the first signalling the transition to the "dissociated" unconscious state; the second, at a higher anaesthetic concentration, marking the discontinuous transition to the hyperpolarized, unresponsive state of unconsciousness required for safe surgery;
- there should be *little or no hysteresis* for a slow GABAergic return journey to and from the *dissociated state* (i.e., dissociation and emergence should occur at the *same* level of anaesthetic).

10.2 Future Work

Spatial Variability

An obvious and deliberate limitation of the present study is the neglect of spatial variability among populations of connected macrocolumns. The possibility of such variablity is built into the Liley model equations for ϕ_e and ϕ_i, the excitatory and inhibitory inputs from distant excitatory cortical sources. The simplest spatial case would consider a one-dimensional "line" of continuous macrocolumn "mass." There are three possibilities for boundary conditions: (i) periodic (the "line" is deformed into a "circle"); (ii) zero-flux (no excitation enters at either end); or (iii) an infinite line of macrocolumn mass (in which case there are no boundaries). If a macrocolumn contains 10^4 to 10^5 neurons, then the $\sim 10^{11}$ neurons of the cerebral cortex will be distributed across 10^6 to 10^7 macrocolumns, so, on the scale of a single macrocolumn, the picture of the cortex as of an infinite 1D line of macrocolumn mass is not too unreasonable.

The adiabatic philosophy identified h_e as the "slow" state variable of interest. Relative to its time-scale, the input PSPs relax rapidly to their final states, so their time evolution can be ignored—this was the "temporally adiabatic" treatment (of the I_{jk} synaptic inputs) used in this thesis. As a first step towards solving for spatial variations, we can apply a "spatially adiabatic" treatment to the 1D $\phi_e(h_e)$ and $\phi_i(h_e)$ wave equations. Assume that ϕ_e and ϕ_i are both slowly varying functions of space, and that h_e is never far from its spatially homogeneous steady-state value. Then, by applying a Born-like approximation for small perturbations in ϕ_e about its spatially uniform state, we can derive a first-order solution for the steady-state spatial distribution for h_e.

Very recently, M. Steyn-Ross (personal communication) has derived an analytic result for the spatial covariance of h_e fluctuations in this spatially adiabatic limit for the infinite 1D case, and I have evaluated the correlation lengths as a function of GABAergic effect. Our preliminary results suggest that the covariance can either decay exponentially with space, or can be periodic in space. This latter finding is most intriguing, for it suggests that *non-adjacent regions* of the cortex can have *correlated* activity, and that these "islands of cooperation" will be separated by intervening cortical space that exhibts no correlation. The critical parameter which determines the type of spatial behaviour is $R = \Lambda_{ee}/\Lambda_{ei}$, the ratio of connectivity decay rates for the cortico-cortical $e \longrightarrow e$ and $e \longrightarrow i$ couplings. This work is continuing, and will be written up for publication shortly.

Drug–Effect Hysteresis

It is now well established in the anaesthetics community that there is a strong surge in EEG activity (the so-called "biphasic peak") at the point of induction of anaesthetic unconsciousness, followed by a distinct second surge that occurs later as the anaesthetic dissipates and the patient emerges from unconsciousness. The Kuizenga results of Fig. 5.11 (p. 93) show that the measured propofol concentration in the blood is significantly larger at induction than at emergence. The fact that the induction and emergence EEG-activity peaks are not coincident (i.e., do not occur at the same anaesthetic concentration) indicates an apparent history dependence or *hysteresis* between drug effect and drug concentration. This observation of a hysteresis effect is entirely consistent with our anaestheto-dynamic phase transition theory, but this phase transition idea is too new to have achieved any currency among anaesthetics modellers.

The traditional explanation for drug–effect hysteresis is that the measurement site (e.g., femoral artery in the thigh) is displaced from the effect site (the cerebral cortex), and that it takes some time (1–2 min) for the drug to diffuse across the blood–brain barrier. It has therefore been the goal of pharmacokinetics modellers to tune their model parameters (specifically the time-constants of the multiple "compartments") in such a way that the history dependence is eliminated, thereby "closing" the hysteresis loop. The implicit assumption of such modelling is that the hysteresis is due *entirely* to measurement-displacement error.

However, if we accept the anaestheto-dynamic model prediction of a first-order phase transition, then a true hysteresis effect is expected, and therefore a pharmacokinetics-based nulling of the hysteresis loop is in fact an over-compensation. To establish the reality of hysteresis, we need an induction–recovery cycle which is so slow and gradual that the drug concentrations in blood and brain are close to steady state and the measurement-displacement errors become negligible. I have begun analyzing some very recent (2001) Kuizenga recordings for three consecutive propofol induction–emergence cycles: the first two cycles each had propofol-infusion periods of 10 min, and the third cycle had a 20-min infusion. My preliminary analysis indicates that the blood concentration at induction is $\sim 4\times$ the concentration of emergence, and that this ratio is independent of the rate of infusion. This research is continuing, and when complete should be written up for one of the anaesthesiology journals.

Sleep

There are EEG-pattern similarities between anaesthetic unconsciousness and natural sleep. However, modelling sleep processes is a vastly more difficult problem than modelling anaesthesia. For anaesthetic "sleep," the externally-administered drug provides the quantifiable forcing function that determines (albeit in a highly nonlinear way) the cortical response. In contrast, the cycling between consciousness and normal sleep, and the subcycling between REM (rapid eye-movement) sleep and nonREM sleep, are all under the control of locally-generated hormones and neurotransmitters—there is no easily identified "forcing function" driving the sleep cycles. If there are phase transitions in natural sleep, then we might expect to find biphasic surges in EEG activity as the brain switches state. Thus a preliminary investigation might look for such activity surges, seeking to correlate these with traditional measures for sleep staging. Perhaps a phase-transition theory of sleep might allow us to begin to begin to understand the underlying mechanisms and functions of sleep.

Appendix A

Difference Equations for the Full, Non-Adiabatic Macrocolumn

This appendix shows how the eight first- and second-order stochastic DEs (Eqs 3.1–3.4) for the non-adiabatic cortical macrocolumn can be solved numerically by iterating 14 first-order difference equations.

The Euler one-step method is a simple iteration scheme which predicts the value of the soma voltage $h_{e,i}$ at timestep $n+1$ (i.e., at time $t = (n+1)\Delta t$) via linear extrapolation from the previous timestep n:

$$h_{e,i}^{n+1} = h_{e,i}^{n} + \left[\frac{dh_{e,i}}{dt}\right]^n \Delta t\,. \tag{A.1}$$

The implicit assumption is that the iteration will give an accurate estimate for $h_{e,i}^{n+1}$ provided the timestep Δt is sufficiently small. The rates of change of the soma voltages at timestep n, $(dh_{e,i}/dt)^n$, are given by recasting the first pair of Liley differential equations (3.1) as difference equations:

$$\left[\frac{dh_e}{dt}\right]^n = \frac{1}{\tau_e}\left[h_e^{\text{rest}} - h_e^n + \psi_{ee}^n\, I_{ee}^n + \psi_{ie}^n\, I_{ie}^n\right] \tag{A.2a}$$

$$\left[\frac{dh_i}{dt}\right]^n = \frac{1}{\tau_i}\left[h_i^{\text{rest}} - h_i^n + \psi_{ei}^n\, I_{ei}^n + \psi_{ii}^n\, I_{ii}^n\right]. \tag{A.2b}$$

The equations for the four I_{jk} "currents" $(I_{ee}, I_{ei}, I_{ie}, I_{ii})$ are second-order DEs. Equation (3.2) for I_{ee}, for example, reads,

$$\frac{d^2 I_{ee}}{dt^2} + 2\gamma_e \frac{dI_{ee}}{dt} + \gamma_e^2 I_{ee} = \left[N_{ee}^{\beta}\mathcal{S}_e(h_e) + \phi_e + \langle p_{ee}\rangle\right] G_e \gamma_e e + \Gamma_1 \tag{A.3}$$

so we define an ancillary variable $J_{ee} = dI_{ee}/dt$, then recast the DE as the pair of difference equations for $(dI_{ee}/dt)^n$ and $(dJ_{ee}/dt)^n$,

$$\left[\frac{dI_{ee}}{dt}\right]^n = J_{ee}^n \tag{A.4a}$$

$$\left[\frac{dJ_{ee}}{dt}\right]^n = \left[N_{ee}^{\beta}\mathcal{S}_e(h_e^n) + \phi_e^n + \langle p_{ee}\rangle\right] G_e \gamma_e e + \Gamma_1^n - 2\gamma_e J_{ee}^n - \gamma_e^2 I_{ee}^n \tag{A.4b}$$

which, on application of an Euler one-step, give the updating equations for I_{ee} and J_{ee},

$$I_{ee}^{n+1} = I_{ee}^{n} + \left[\frac{dI_{ee}}{dt}\right]^{n} \Delta t \tag{A.5a}$$

$$J_{ee}^{n+1} = J_{ee}^{n} + \left[\frac{dJ_{ee}}{dt}\right]^{n} \Delta t\,. \tag{A.5b}$$

A similar recasting gives the difference equations for the I_{ei} input term,

$$\left[\frac{dI_{ei}}{dt}\right]^{n} = J_{ei}^{n} \tag{A.6a}$$

$$\left[\frac{dJ_{ei}}{dt}\right]^{n} = \left[N_{ei}^{\beta}\mathcal{S}_e(h_e^n) + \phi_i^n + \langle p_{ei}\rangle\right] G_e\gamma_e e + \Gamma_3^n - 2\gamma_e J_{ei}^n - \gamma_e^2 I_{ei}^n\,. \tag{A.6b}$$

For the I_{ie} and I_{ii} equations (3.3), we incorporate the effect of anesthetic by replacing the inhibitory rate constant γ_i by γ_i/λ, where λ is the IPSP prolongation factor dependent on anesthetic concentration. The difference equations for I_{ie} and I_{ii} are then given by

$$\left[\frac{dI_{ie}}{dt}\right]^{n} = J_{ie}^{n} \tag{A.7a}$$

$$\left[\frac{dJ_{ie}}{dt}\right]^{n} = \left[N_{ie}^{\beta}\mathcal{S}_i(h_i^n) + \langle p_{ie}\rangle\right] G_i\frac{\gamma_i}{\lambda}e + \Gamma_2^n - 2\frac{\gamma_i}{\lambda}J_{ie}^n - \left[\frac{\gamma_i}{\lambda}\right]^2 I_{ie}^n \tag{A.7b}$$

$$\left[\frac{dI_{ii}}{dt}\right]^{n} = J_{ii}^{n} \tag{A.8a}$$

$$\left[\frac{dJ_{ii}}{dt}\right]^{n} = \left[N_{ii}^{\beta}\mathcal{S}_i(h_i^n) + \langle p_{ii}\rangle\right] G_i\frac{\gamma_i}{\lambda}e + \Gamma_4^n - 2\frac{\gamma_i}{\lambda}J_{ii}^n - \left[\frac{\gamma_i}{\lambda}\right]^2 I_{ii}^n\,. \tag{A.8b}$$

The long-range spike-input equations are also second-order. For example, equation (3.4) for ϕ_e reads

$$\frac{d^2\phi_e}{dt^2} + 2\bar{v}\Lambda_{ee}\frac{d\phi_e}{dt} + \bar{v}^2\Lambda_{ee}^2\phi_e = \bar{v}\Lambda_{ee}N_{ee}^{\alpha}\frac{d\mathcal{S}_e}{dt} + \bar{v}^2\Lambda_{ee}^2 N_{ee}^{\alpha}\mathcal{S}_e \tag{A.9}$$

so we define ancillary variable $\Phi_e = d\phi_e/dt$, giving

$$\frac{d\Phi_e}{dt} = \bar{v}\Lambda_{ee}\left[N_{ee}^{\alpha}\frac{d\mathcal{S}_e}{dt} + \bar{v}\Lambda_{ee}N_{ee}^{\alpha}\mathcal{S}_e - 2\Phi_e - \bar{v}\Lambda_{ee}\phi_e\right]\,. \tag{A.10}$$

Applying the chain rule to the time-derivative of the sigmoid function,

$$\frac{d\mathcal{S}_e}{dt} = \frac{\partial\mathcal{S}_e}{\partial h_e}\frac{dh_e}{dt} = Q_e\frac{dh_e}{dt} \tag{A.11}$$

where

$$Q_e = \frac{g_e\,\mathcal{S}_e^{\max}\exp\left(-g_e(h_e-\theta_e)\right)}{\left[1+\exp\left(-g_e(h_e-\theta_e)\right)\right]^2}\,, \tag{A.12}$$

leads to the following difference equations for ϕ_e,

$$\left[\frac{d\phi_e}{dt}\right]^{n} = \Phi_e^{n} \tag{A.13a}$$

$$\left[\frac{d\Phi_e}{dt}\right]^{n} = \bar{v}\Lambda_{ee}\left[N_{ee}^{\alpha}\,Q_e^n\left(\frac{dh_e}{dt}\right)^{n} + \bar{v}\Lambda_{ee}N_{ee}^{\alpha}\mathcal{S}_e(h_e^n) - 2\Phi_e^n - \bar{v}\Lambda_{ee}\phi_e^n\right]\,. \tag{A.13b}$$

Finally, for ϕ_i we have

$$\left[\frac{d\phi_i}{dt}\right]^n = \Phi^n_i \tag{A.14a}$$

$$\left[\frac{d\Phi_i}{dt}\right]^n = \bar{v}\Lambda_{ei}\left[N^\alpha_{ei}\, Q^n_e \left(\frac{dh_e}{dt}\right)^n + \bar{v}\Lambda_{ei}N^\alpha_{ei}\mathcal{S}_e(h^n_e) - 2\Phi^n_i - \bar{v}\Lambda_{ei}\phi^n_i\right] . \tag{A.14b}$$

The $\Gamma_{1 \ldots 4}$ stochastic terms in Eqs (A.4–A.8) are given by

$$\Gamma^n_1 = \alpha_{ee}\sqrt{\langle p_{ee}\rangle}\, G_e \gamma_e e \frac{\mathfrak{R}^n_1}{\sqrt{\Delta t}} \tag{A.15a}$$

$$\Gamma^n_2 = \alpha_{ie}\sqrt{\langle p_{ie}\rangle}\, G_i \gamma_i e \frac{\mathfrak{R}^n_2}{\sqrt{\Delta t}} \tag{A.15b}$$

$$\Gamma^n_3 = \alpha_{ei}\sqrt{\langle p_{ei}\rangle}\, G_e \gamma_e e \frac{\mathfrak{R}^n_3}{\sqrt{\Delta t}} \tag{A.15c}$$

$$\Gamma^n_4 = \alpha_{ii}\sqrt{\langle p_{ii}\rangle}\, G_i \gamma_i e \frac{\mathfrak{R}^n_4}{\sqrt{\Delta t}} \tag{A.15d}$$

where the $\mathfrak{R}_{1 \ldots 4}$ are independent Gaussian-distributed random numbers with mean zero, variance unity. As was the case for the adiabatic simulations, the noise-amplitude scale-factor α_{jk} is set to 0.1 in all four stochastic terms.

To start the integration, we fix λ, then read off the appropriate $(h^0_e(\lambda), h^0_i(\lambda))$ coordinate from the soma voltage steady-states curve (Fig. 3.4) The matching steady-state values for I_{ee}, I_{ei}, I_{ie}, I_{ii}, ϕ_e, ϕ_i are determined by solving Eqs (3.2–3.4) in the limit of zero noise and zero time-derivatives, giving:

$$I^0_{ee} = \left[N^\beta_{ee}\mathcal{S}_e(h^0_e) + \phi^0_e + \langle p_{ee}\rangle\right] G_e e/\gamma_e \tag{A.16a}$$

$$I^0_{ei} = \left[N^\beta_{ei}\mathcal{S}_e(h^0_e) + \phi^0_i + \langle p_{ei}\rangle\right] G_e e/\gamma_e \tag{A.16b}$$

$$I^0_{ie} = \left[N^\beta_{ie}\mathcal{S}_i(h^0_i) + \langle p_{ie}\rangle\right] G_i e\lambda/\gamma_i \tag{A.16c}$$

$$I^0_{ii} = \left[N^\beta_{ii}\mathcal{S}_i(h^0_i) + \langle p_{ii}\rangle\right] G_i e\lambda/\gamma_i \tag{A.16d}$$

where the ϕ^0_e and ϕ^0_i are

$$\phi^0_e = N^\alpha_{ee}\mathcal{S}_e(h^0_e) \tag{A.16e}$$

$$\phi^0_i = N^\alpha_{ei}\mathcal{S}_e(h^0_e) \tag{A.16f}$$

and the six ancillary variables have initial value zero:

$$J^0_{ee} = J^0_{ei} = J^0_{ie} = J^0_{ii} = \Phi^0_e = \Phi^0_i = 0 . \tag{A.16g}$$

The numerical simulation proceeds by iterating up from this initial state with a time-step of $\Delta t = 10^{-4}$ s.

Appendix B

Approximate Quadrature via Cumulative Sum

In Chapter 6.6 we compute the negative of the area under the "driving-force" versus soma voltage curves to obtain the U_e and U_i potential curves, e.g.,

$$U_e(h_e) = \log_e [D_{11}(h_e)] - \int_{-90}^{h_e} \frac{2\widetilde{F}_1(h'_e)}{D_{11}(h'_e)}\, dh'_e \tag{B.1}$$

where the $\widetilde{F}/D$ drift-on-diffusion integrand is evaluated numerically for finely stepped increments in h_e. Let $\mathbf{f} = [f_1, f_2, \ldots, f_N]$ be the N-element vector of $\widetilde{F}/D$ values sampled at uniformly-spaced soma voltages $[h_1, h_2, \ldots, h_N]$ with sample spacing Δh. $\widetilde{F}/D$ is a smoothly-varying function of h_e, so provided the voltage step Δh is sufficiently small, the area can be well approximated by summing the areas of the individual trapeziums defined by the f_j sample points illustrated in Fig. B.1.

The trapezium area can be evaluated directly from the cumulative sum of the elements of $\mathbf{f}$ (in MATLAB: `cumsum(f)`) after making appropriate end-value corrections as described below. But why bother with a trapezium estimate of the area when very accurate quadrature functions (quad and quad8) are available in MATLAB? The primary reason is speed: quad is a recursive function which would need to be called once for every one of the ~2500 sampled points along the soma-voltage axis, thus the area calculation cannot be vectorized. In contrast, `cumsum` is a very fast built-in vector operation which allows all of the cumulative areas to be computed in a

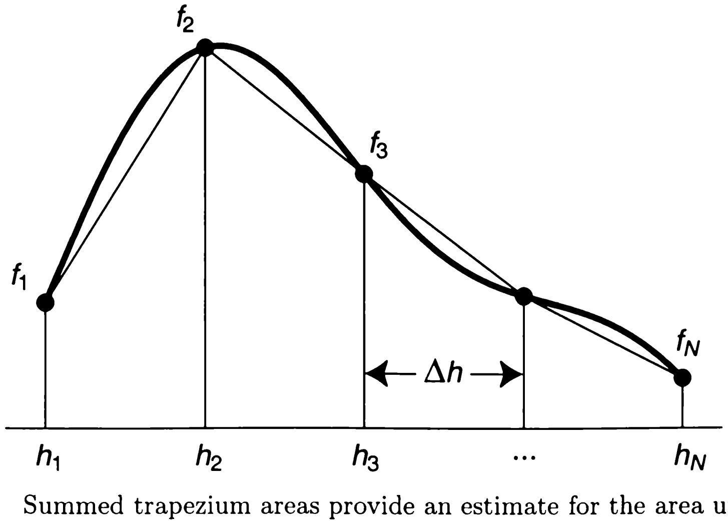

Figure B.1: Summed trapezium areas provide an estimate for the area under a curve.

single call. Provided Δh is sufficiently small (e.g., ~0.05 mV), the accuracy of the cumulative sum method can be made quite acceptable.

The method proceeds as follows. Let `Trap` be the MATLAB vector of cumulative trapezium areas to be defined as

$$\mathrm{Trap}(1) = 0 \tag{B.2a}$$

$$\mathrm{Trap}(2) = \tfrac{1}{2}(f_1 + f_2)\,\Delta h \tag{B.2b}$$

$$\mathrm{Trap}(3) = \tfrac{1}{2}(f_1 + f_2)\,\Delta h + \tfrac{1}{2}(f_2 + f_3)\,\Delta h = \tfrac{1}{2}(f_1 + 2f_2 + f_3)\,\Delta h \tag{B.2c}$$

$$\mathrm{Trap}(N) = \tfrac{1}{2}(f_1 + 2f_2 + 2f_3 + 2f_4 + \cdots + 2f_{N-1} + f_N)\,\Delta h \tag{B.2d}$$

which exhibits the $1, 2, 2, \ldots, 2, 1$ coefficient pattern characteristic of the trapezium-quadrature rule. Compare `Trap` with the vector `CS` of *cumulative sums* which would be returned by the MATLAB call: `CS = cumsum(f)`,

$$\mathrm{CS}(1) = f_1 \tag{B.3a}$$

$$\mathrm{CS}(2) = f_1 + f_2 \tag{B.3b}$$

$$\mathrm{CS}(3) = f_1 + f_2 + f_3 \tag{B.3c}$$

$$\mathrm{CS}(N) = f_1 + f_2 + f_3 + f_4 + \cdots + f_N. \tag{B.3d}$$

By comparing corresponding elements in the `Trap` and `CS` vectors we see that the cumulative trapezium areas may be recovered from the cumulative sums after appropriate adjustment to the end-point contributions to each sum,

$$\mathrm{Trap}(1) = \tfrac{1}{2}\,[2\,\mathrm{CS}(1) - (f_1 + f_1)]\,\Delta h \tag{B.4a}$$

$$\mathrm{Trap}(2) = \tfrac{1}{2}\,[2\,\mathrm{CS}(2) - (f_1 + f_2)]\,\Delta h \tag{B.4b}$$

$$\mathrm{Trap}(3) = \tfrac{1}{2}\,[2\,\mathrm{CS}(3) - (f_1 + f_3)]\,\Delta h \tag{B.4c}$$

$$\vdots$$

$$\mathrm{Trap}(N) = \tfrac{1}{2}\,[2\,\mathrm{CS}(N) - (f_1 + f_N)]\,\Delta h. \tag{B.4d}$$

Writing this in vectorized notation,

$$\mathrm{Trap}(1:N) = \tfrac{1}{2}\big[2\,\mathrm{CS}(1:N) - \big(f_1 + \mathbf{f}(1:N)\big)\big]\Delta h \tag{B.5}$$

where the idiom $f_1 + \mathbf{f}(1:N)$ indicates that the f_1 scalar (first element of vector $\mathbf{f}$) is to be added to all N elements of $\mathbf{f}$. This vectorized form translates directly into a single line of MATLAB code as,

```
trapsum = del_h/2*(2*cumsum(f) - (f(1) + f))          (B.6)
```

where `del_h` is the soma voltage sampling interval Δh, and `trapsum` is the returned N-element vector containing the N cumulative trapezium areas for the $\widetilde{F}/D$ sample vector $\mathbf{f}$.

References

Antkowiak, B. and H. Hentschke. Cellular mechanisms of gamma rhythms in rat neocortical brain slices probed by the volatile anaesthetic isoflurane. *Neuroscience Letters*, **231**, pp. 87–90 (1997).

Archer, D. P. and S. H. Roth. Pharmacodynamics of thiopentone: Nocifensive reflex threshold changes correlate with hippocampal electroencephalography. *British Journal of Anaesthesia*, **79**, pp. 744–749 (1997).

Arnold, L. *Stochastic Differential Equations: Theory and Applications.* John Wiley & Sons, New York (1974).

Beurle, R. L. Properties of a mass of cells capable of regenerating pulses. *Transactions of the Royal Society (London)*, **240**, pp. 55–94 (1956).

Braitenberg, V. and A. Schüz. *Anatomy of a Cortex: Statistics and Geometry.* Springer-Verlag, Berlin (1991).

Bührer, M., P. O. Maitre, O. R. Hung, W. F. Ebling, S. L. Shafer, and D. R. Stanski. Thiopental pharmacodynamics: I. Defining the pseudo-steady-state serum concentration–EEG effect relationship. *Anesthesiology*, **77**, pp. 226–236 (1992).

Bührer, M., P. O. Maitre, O. R. Hung, and D. R. Stanski. Electroencephalographic effects of benzodiazepines: Choosing an electroencephalographic parameter to measure the effect of midazolam on the central nervous system. *Clinical Pharmacology and Therapeutics*, **48**, pp. 544–554 (1990).

Craig, I. J. D. and K. J. McNeil. Quantum simulations of nonlinear optical damping: An exact solution for the stochastic differential equations and an interpretation of "spiking". *Physical Review A*, **39**, pp. 6267–6270 (1989).

Flohr, H., U. Glade, and D. Motzko. The neural correlate of consciousness and the mechanisms of general anaesthesia. In: *Molecular Pharmacology of Anaesthesia*, edited by J. Schultz am Esch, J. Scholz, and P. H. Tonner, pp. 12–24. Pabst Science Publishers, Lengerich (2000).

Franks, N. P., R. Dickenson, S. L. M. de Sousa, A. C. Hall, and W. R. Lieb. How does xenon produce anaesthesia? *Nature*, **396**, p. 324 (1998).

Franks, N. P. and W. R. Lieb. Molecular and cellular mechanisms of general anaesthesia. *Nature*, **367**, pp. 607–613 (1994).

Franks, N. P. and W. R. Lieb. Anaesthetics set their sites on ion channels. *Nature*, **389**, pp. 334–335 (1997).

Freeman, W. J. *Mass Action in the Nervous System.* Academic Press, New York (1975).

Gage, P. W. and B. Robertson. Prolongation of inhibitory postsynaptic currents by pentobarbitone, halothane and ketamine in CA1 pyramidal cels in rat hippocampus. *British Journal of Pharmacology*, **85**, pp. 645–681 (1985).

Gardiner, C. W. *Handbook of Stochastic Methods for Physics, Chemistry, and the Natural Sciences*, volume 13 of *Springer Series in Synergetics.* Springer-Verlag, Berlin (1985).

Gardiner, C. W. and P. Zoller. *Quantum Noise: A Handbook of Markovian and non-Markovian Quantum Stochastic Methods with Applications to Quantum Optics.* Springer Series in Synergetics. Springer-Verlag, Berlin (2000).

Gibbs, H. M. *Optical Bistability: Controlling Light with Light.* Academic Press, Orlando (1985).

Gillespie, D. T. *Markov Processes: An Introduction for Physical Scientists.* Academic, San Diego (1992).

Gillespie, D. T. Fluctuation and dissipation in Brownian motion. *American Journal of Physics*, **61**, pp. 1077–1083 (1993).

Gillespie, D. T. Exact numerical simulation of the Ornstein–Uhlenbeck process and its integral. *Physical Review E*, **54**, pp. 2084–2091 (1996a).

Gillespie, D. T. The mathematics of Brownian motion and Johnson noise. *American Journal of Physics*, **64**, pp. 225–240 (1996b).

Glansdorff, P. and I. Prigogine. *Thermodynamic Theory of Structure, Stability, and Fluctuations.* Wiley–Interscience, John Wiley & Sons Ltd, New York (1974).

Gradshteyn, I. S. and I. M. Ryzhik. *Table of Integrals, Series, and Products.* Academic Press, New York (1965).

Graham, R. *Quantum Statistics in Optics and Solid-State Physics*, volume 66 of *Springer Tracts in Modern Physics.* Springer-Verlag, New York (1973).

Gregory, T. K. and D. C. Pettus. An electroencephalographic processing algorithm specifically intended for analysis of cerebral electrical activity. *Journal of Clinical Monitoring*, **2**, pp. 190–197 (1986).

Griffith, J. S. On the stability of brain-like structures. *Biophysical Journal*, **3**, pp. 299–308 (1963).

Guedel, A. E. *Inhalational Anesthesia: A Fundamental Guide.* Macmillan, New York (1937).

Haken, H. *Synergetics: An Introduction: Nonequilibrium Phase Transitions and Self-organization in Physics.* Springer-Verlag, Berlin (1978).

Halsey, M. J. and E. B. Smith. Effects of anaesthetics on luminous bacteria. *Nature*, **227**, pp. 1363–1365 (1970).

Hammond, C. *Cellular and Molecular Neurobiology.* Academic Press, Orlando, Florida (2001).

Hestrin, S., R. A. Nicoll, D. J. Perkel, and P. Sah. Analysis of excitatory synaptic action in pyramidal cells using whole-cell recording from rat hippocampal slices. *Journal of Physiology*, **422**, pp. 203–225 (1990).

Hodgkin, A. L. and A. F. Huxley. A quantitative description of membrane current and its application to conduction and excitation in nerve. *Journal of Physiology*, **117**, pp. 500–544 (1952).

Jevtovic-Todorovic, V., S. M. Todorovic, S. Menneric, S. Powell, K. Dikranian, N. Benshoff, C. F. Zorumski, and J. W. Olny. Nitrous oxide (laughing gas) is an NMDA antagonist, neuroprotectant and neurotoxin. *Nature Medicine*, **4**, pp. 460–464 (1998).

Jirsa, V. K. and H. Haken. A field theory of electromagnetic brain activity. *Physical Review Letters*, **77**, pp. 960-963 (1996).

Jirsa, V. K. and H. Haken. A derivation of a macroscopic field theory of the brain from the quasi-microscopic neural dynamics. *Physica D*, **99**, pp. 503–526 (1997).

Johnson, F. H. and E. A. Flagler. Activity of narcotised amphibia larvae under hydrostatic pressure. *Journal of Cellular and Comparative Physiology*, **37**, p. 15 (1951).

Johnson, F. H. and K. W. Miller. Antagonism of pressure and anaesthesia. *Nature*, **228**, p. 75 (1970).

Jones, M. V. and N. L. Harrison. Effects of volatile anesthetics on the kinetics of inhibitory postsynaptic currents in cultured rat hippocampal neurons. *Journal of Neurophysiology*, **70**, pp. 1339–1349 (1993).

Kandel, E. R. and J. H. Schwartz. Directly gated transmission at central synapses. In: *Principles of Neural Science*, edited by E. R. Kandel, J. H. Schwartz, and T. M. Jessell, chapter 11, pp. 153–172. Prentice-Hall International, London (1991).

Kay, S. M. and S. L. Marple. Spectrum analysis: A modern perspective. *Proceedings of the IEEE*, **69(11)**, pp. 1380–1419 (1981).

Kleppner, D. and R. Kolenkow. *An Introduction to Mechanics.* International Student Edition. McGraw-Hill, Singapore (1978).

Koch, C., M. Rapp, and I. Segev. A brief history of time (constants). *Cerebral Cortex*, **6**, pp. 93–101 (1996).

Koester, J. Membrane potential. In: *Principles of Neural Science*, edited by E. R. Kandel, J. H. Schwartz, and T. M. Jessell, chapter 6, pp. 81–94. Prentice-Hall International, London (1991).

Krauss, T. P., L. Shure, and J. N. Little. *Matlab Signal Processing Toolbox User's Guide.* The Mathworks, Inc, Natick, Mass (1994).

Kuizenga, K. *Pharmacokinetic pharmacodynamic modelling of EEG effects in hypnotic drugs used in anaesthesia.* Ph.D. thesis, Groningen University Hospital, Groningen, The Netherlands (2001).

Kuizenga, K., C. J. Kalkman, and P. J. Hennis. Quantitative electroencephalographic analysis of the biphasic concentration–effect relationship of propofol in surgical patients during extradural analgesia. *British Journal of Anaesthesia*, **80**, pp. 725–732 (1998).

Kuizenga, K., J. M. K. H. Wierda, and C. J. Kalkman. Biphasic EEG changes in relation to loss of consciousness during induction with thiopental, propofol, etomidate, midazolam or sevoflurane. *British Journal of Anaesthesia*, **86**, pp. 354-360 (2001).

Liley, D. T. J. A continuum model of the mammalian alpha rhythm. In: *Spatiotemporal Models in Biological Artificial Systems*, edited by F. L. Silva, pp. 89–96. IOS Press, Amsterdam (1997).

Liley, D. T. J., P. J. Cadusch, and M. P. Dafilis. A spatially continuous mean field theory of electro-cortical activity. *Network: Computation in Neural Systems* (2002). In press.

Liley, D. T. J., P. J. Cadusch, and J. J. Wright. A continuum theory of electro-cortical activity. *Neurocomputing*, **26–27**, pp. 795–800 (1999).

Lugiato, L. A. and R. Bonifacio. Mean field theory of optical bistability and resonance fluorescence. In: *Coherence in Spectroscopy and Modern Physics*, edited by F. T. Arecchi, R. Bonifacio, and M. O. Scully, volume 37 of *NATO Advanced Study Institute, series B*, pp. 85–109. Plenum Press, New York (1978).

MacIver, M. B., J. W. Mandema, D. R. Stanski, and B. H. Bland. Thiopental uncouples hippocampal and cortical synchronized electroencephalographic activity. *Anesthesiology*, **84**, pp. 1411–1424 (1996).

Murthy, K. P. N. Monte Carlo methods: An introduction. In: *Stochastic Processes Formalism and Applications*, edited by G. S. Agarwal and S. Dattagupta, Lecture Notes in Physics, no. 184, pp. 116–121. Springer–Verlag, Berlin (1983).

Newland, D. E. *Random Vibrations, Spectral and Wavelet Analysis.* Addison Wesley Longman, New York, third edition (1993).

Nunez, P. L. The brain wave function: A model for the EEG. *Mathematical Biosciences*, **21**, pp. 279–297 (1974).

Nunez, P. L. *Electric Fields of the Brain: The Neurophysics of EEG.* Oxford University Press, New York (1981).

Quiroga, R. Q., J. Arnhold, K. Lehnertz, and P. Grassberger. Kulback–Leibler and renormalized entropies: Applications to electroencephalograms of epilepsy patients. *Physical Review E*, **62**, pp. 8380–8386 (2000).

Reichl, L. E. *A Modern Course in Statistical Physics.* University of Texas Press, Austin (1980).

Rezek, I. A. and S. J. Roberts. Stochastic complexity measures for physiological signal analysis. *IEEE Transactions on Biomedical Engineering*, **45**, pp. 1186–1191 (1998).

Robinson, P. A., C. J. Rennie, and J. J. Wright. Propagation and stability of waves of electrical activity in the cerebral cortex. *Physical Review E*, **56**, pp. 826–840 (1997).

Robinson, P. A., C. J. Rennie, J. J. Wright, and P. D. Bourke. Steady states and global dynamics of electrical activity in the cerebral cortex. *Physical Review E*, **58**, pp. 3557–3571 (1998).

Schuss, Z. *Theory and Applications of Stochastic Differential Equations.* John Wiley & Sons, New York (1980).

Shannon, C. E. and W. Weaver. *The Mathematical Theory of Information.* University of Illinois Press, Urbana, Illinois (1949).

Silbernagl, S. and A. Despopoulos. *Sesam Atlas van de Fysiologie.* Bosch & Keuning, Baarn, Germany (1996).

Sloane, N. J. A. and A. D. Wyner, editors. *Claude Elwood Shannon: Collected papers.* IEEE Press, New York (1993).

Spiegel, M. R. *Mathematical Handbook of Formulas and Tables.* Schaum's Outline Series. McGraw-Hill, New York (1968).

Steriade, M., D. A. McCormick, and T. J. Sejnowski. Thalamocortical oscillations in the sleeping and aroused brain. *Science*, **262**, pp. 679–685 (1993).

Steyn-Ross, M. L. *Laser excitation of vibrational modes of molecules.* Master's thesis, University of Waikato, Hamilton, New Zealand (1979).

Steyn-Ross, D. A. and D. G. Ivey. Frames of reference revisited. *American Journal of Physics*, **60(12)**, pp. 1069–1085 (1992).

Steyn-Ross, M. L., D. A. Steyn-Ross, J. W. Sleigh, and D. T. J. Liley. Theoretical electroencephalogram stationary spectrum for a white-noise-driven cortex: Evidence for a general anesthetic-induced phase transition. *Physical Review E*, **60**, pp. 7299–7311 (1999).

Steyn-Ross, M. L., D. A. Steyn-Ross, J. W. Sleigh, and L. C. Wilcocks. Toward a theory of the general anesthetic-induced phase transition of the cerebral cortex: I. A statistical mechanics analogy. *Physical Review E*, **64**, p. 011917 (2001a).

Steyn-Ross, D. A., M. L. Steyn-Ross, L. C. Wilcocks, and J. W. Sleigh. Toward a theory of the general anesthetic-induced phase transition of the cerebral cortex: II. Stochastic numerical simulations, spectral entropy, and correlations. *Physical Review E*, **64**, p. 011918 (2001b).

Stullken Jr., E. H., J. H. Milde, J. D. Michenfelder, and J. H. Tinker. The nonlinear responses of cerebral metabolism to low concentrations of halothane, enflurane, isofluorine, and thiopental. *Anesthesiology*, **46**, pp. 28–34 (1977).

Thomas, J. D. and E. P. Riley. Fetal alcohol syndrome: Does alcohol withdrawal play a role? *Alcohol Health and Research World*, **22**, pp. 47–53 (1998).

Tipler, P. A. *Physics for Scientists and Engineers*, volume 1. Worth, New York, third edition (1990).

Tuckwell, H. C. *Introduction to Theoretical Neurobiology: Linear Cable Theory and Dendritic Structure*, volume 1. Cambridge University Press, Cambridge (1988a).

Tuckwell, H. C. *Introduction to Theoretical Neurobiology: Nonlinear and Stochastic Theories*, volume 2. Cambridge University Press, Cambridge (1988b).

Ueda, I. Effects of diethyl ether and halothane on firefly luciferin bioluminescence. *Anesthesiology*, **26**, pp. 603–606 (1965).

Ueda, I. Molecular mechanisms of anesthesia. *Keio Journal of Medicine*, **50**, pp. 20–25 (2001).

van Kampen, N. G. *Stochastic Processes in Physics and Chemistry.* North-Holland, Amsterdam (1981).

Viertiö-Oja, H. E., R. Drachman-Mertsalmi, V. Jäntti, P. Meriläinen, R. Remes, A. Seljänperä, M. Särkelä, P. Talja, H. Tolvanen-Laakso, J. Tuukkanen, and A. Yli-Hankala. New method to determine depth of anesthesia from EEG measurements. *Journal of Clinical Monitoring and Computing*, **16**, p. 60 (2000).

White, D. C. and C. R. Dundas. The effect of anaesthetics on emission of light by luminous bacteria. *Nature*, **226**, pp. 456–458 (1970).

Wiberg, D. M. *State Space and Linear Systems.* Schaum's Outline Series. McGraw-Hill, New York (1971).

Wilcocks, L. C. *Investigation of a stochastic model of the electrical behaviour of the cerebral cortex.* Master's thesis, University of Waikato, Hamilton, New Zealand (2001).

Wilson, H. R. and J. D. Cowan. Excitatory and inhibitory interactions in localized populations of model neurons. *Biophysical Journal*, **12**, pp. 1–24 (1972).

Wilson, H. R. and J. D. Cowan. A mathematical theory of the functional dynamics of cortical and thalamic nervous tissue. *Kybernetik*, **13**, pp. 55–80 (1973).

Wright, J. J. and D. T. J. Liley. Dynamics of the brain at global and microscopic scales: Neural networks and the EEG. *Behavioral and Brain Science*, **19**, pp. 285–316 (1996).